



HAL
open science

Experimental study and modelling of high temperature creep flow and damage behaviour of 9Cr1Mo-NbV

Vincent Gaffard

► **To cite this version:**

Vincent Gaffard. Experimental study and modelling of high temperature creep flow and damage behaviour of 9Cr1Mo-NbV. Mechanics [physics.med-ph]. École Nationale Supérieure des Mines de Paris, 2004. English. NNT : 2004ENMP1269 . tel-00162118

HAL Id: tel-00162118

<https://pastel.hal.science/tel-00162118>

Submitted on 16 Jul 2007

HAL is a multi-disciplinary open access archive for the deposit and dissemination of scientific research documents, whether they are published or not. The documents may come from teaching and research institutions in France or abroad, or from public or private research centers.

L'archive ouverte pluridisciplinaire **HAL**, est destinée au dépôt et à la diffusion de documents scientifiques de niveau recherche, publiés ou non, émanant des établissements d'enseignement et de recherche français ou étrangers, des laboratoires publics ou privés.



Collège doctoral

THESE

Pour obtenir le grade de
Docteur de l'Ecole Nationale Supérieure des Mines de Paris
Spécialité : Sciences et Génie des Matériaux

Présentée et soutenue publiquement par

Vincent Gaffard

Ingénieur de l'Institut National Polytechnique de Grenoble (ENSEEG)

Le 13 décembre 2004

Experimental study and modelling of high temperature creep flow and
damage behaviour of 9Cr1Mo-NbV steel weldments
(Etude expérimentale et modélisation, du comportement, de l'endommagement et de la
rupture en fluage à haute température de joint soudés en acier 9Cr1Mo-NbV)

**Directeur et directrice de thèse: M. Jacques Besson
& Mme Anne-Françoise Gourgues-Lorenzon**

Jury

M. Gunther Eggeler	Ruhr-Universität Bochum	Rapporteur
M. Helmut Klöcker	ENSMSE	Rapporteur
M. Claude Prioul	ECP	Examineur
M. Jacques Besson	ENSMP	Examineur
Mme Anne-Françoise Gourgues-Lorenzon	ENSMP	Examinatrice
M. Roland Piques	ENSMP	Membre invité
Mme Marie-Thérèse Cabrillat	CEA Cadarache	Membre invité
M. Sylvain Leclercq	EdF	Membre invité
M. Jean-Marc Cloué	Framatome	Membre invité
M. Jean-Christophe Brachet	CEA Saclay	Membre invité

Centre des Matériaux P.M. Fourt de l'Ecole Nationale Supérieure des Mines de Paris
BP87 91003 Evry Cedex France

« Comme un iceberg se renverse, la mathématique, globalement a viré, en début de ce siècle, au formalisme. Elle a délaissé l'intuition. Elle a oublié l'intuition. Elle a même, parfois, condamné l'intuition... La ruée logique, axiomatique, formelle, ne fut pas seulement propre aux mathématiques... Le tsunami a touché tous les rivages de la mer Encyclopédie. Physiciens ou philosophes, sociologues ou biologistes, nous étions tous des formalistes. Jusqu'à la rigueur, certes, et puis, jusqu'à l'excès. Quand je voulais connaître une bête, je lisais un livre sur cette bête, où jamais je ne voyais la bête, jamais. Nous sommes fatigués de ne plus rien voir. Je veux voir enfin derrière ces grimoires, et brûler ces écrans de mots et de signes. Voici. L'intuition revient. »

M. Serres *Le Passage du Nord-Ouest*, Les Editions de Minuit (1980)

Introduction

Context: New materials for future power stations

The efficiency of all type of power plant depends on the heat transfers between the vessel and the boiler. Therefore increasing service pressure and temperature should ensure better efficiency. Pressure of 240 bar and temperature of 550°C are currently the maximum service conditions encountered in the classical fossil fuel power plants. The great challenge for the new supercritical and ultra supercritical power plants is to match service values pressure larger than 300 bar and temperature larger than 650°C. Indeed, it will lead to a better efficiency of the production of electricity with two consequences :

1. Lower production costs.
2. A positive impact on environment as CO₂ emissions would be reduced by 2% if efficiency is 1% better (Note that the electrical power generation is responsible for over 20% of the worldwide emissions of CO₂).

To reach this goal, it is necessary to develop new high temperature resistant materials to replace 316 and 304 austenitic stainless steels that are the most commonly used materials for reactor vessel, primary and secondary loops in power plants. Among all materials, chromium martensitic stainless steels have been largely studied during the last three decades. Research programs have been simultaneously conducted in the United States (EPRI), Japan (EFDC) and Europe (COST 501 and 522). The objective of COST 501 and 522 (see Staubli et al 2001)) programs are service conditions of 280 bar / 600-650°C. The next European program THERMIE which has started in 1998 has the objective to reach 375 bar / 700-720°C in 2013: it essentially concerns Ni-base alloys. The objectives in terms of in-service conditions of the new generation of power plants are given in **figure In.1** and as underlined by Vandstone (1998), the typical basis of the power plant design is to reach in service durations of 100,000 hours. It is admitted that the life assessment generally requires long term tests at high temperature for at least one percent of the service life (i.e. 1,000 hours for a lifetime of 100,000 hours) to ensure the extrapolation accuracy.

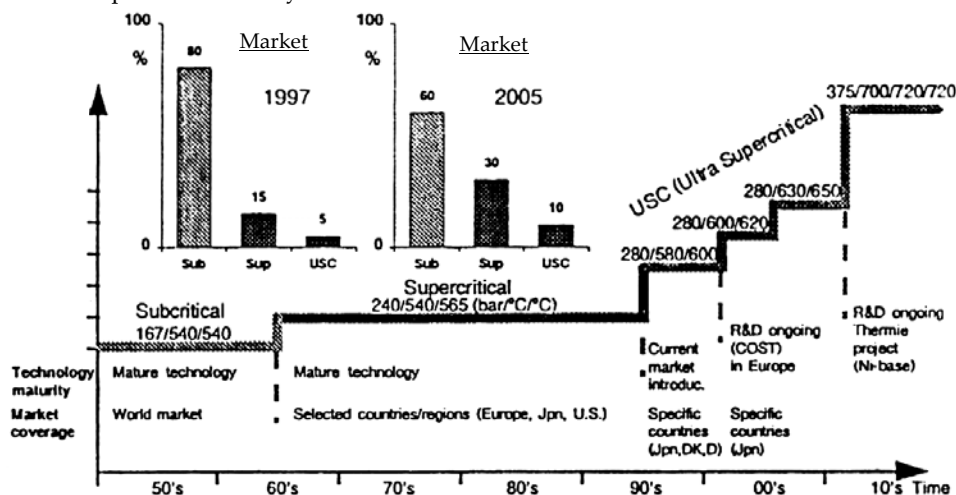


Figure In.1. In service conditions in classical and future power plants (extracted from Metcalfe and Scarlin (1998))

The main advantages of the chromium ferritic and martensitic stainless steels are:

1. Good corrosion resistance.
2. Interesting mechanical properties up to 600°C thanks to the addition of several strengthening alloy elements like V, Nb or Mo.
3. Good thermal conductivity and low thermal expansion coefficient ensure good weldability of the steel.
4. A low nuclear activation energy provided Mo, Ni, Nb and V contents are limited.
5. A lower material cost than austenitic stainless steels mainly as chromium is cheaper than nickel.

2.25Cr-1Mo stainless steels were the first generation of chromium steels that have been integrated in power plants, for example as tubing material in the evaporator of Phenix. Then, many efforts have been made these 20 last years to develop new alloys starting from the first 9Cr1Mo steel (already used in petrochemical applications since the 1950's) which exhibited limited weldability, forgeability and fracture toughness. The initial composition of the steel has then been modified in the United States with the addition of niobium and vanadium (P91/T91 steels) whereas it was chosen to increase the chromium content and to add tungsten in Japan leading to the P92/P122/E911 series. The evolution of the alloy composition as well as the corresponding predicted long term creep properties are reported in **figure In.2** (see also Von Hagen and Bendick (2001), Klueh and Harries (2001), Fujita (2001) and Von Hagen and Scarlin (1998)).

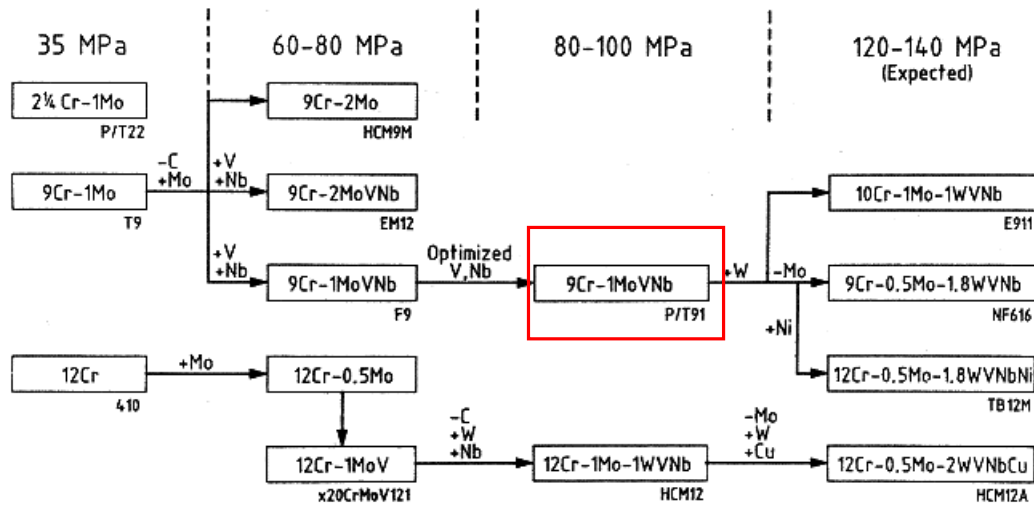


Figure In.2. Progress in chromium stainless steel designs (Hald (1996))

The present study is concerned with 9Cr1Mo-NbV steels which are not the last generation of chromium steels. They are already used in power plants for boiler and steam line (see Blum and Hald (1998)) like in Lippendorf (267 bar, 550-580°C), Boxberg (267 bar, 555-578°C) and Nordjylland (290 bar – 580°C) plants. They are also candidates for structural materials for the Fast Breeder Reactor in India and for the DEMO fusion reactor that would follow the ITER reactor. Therefore, there is a strong need to predict the evolution of their metallurgical and mechanical properties for long term service exposures.

Aim of the present study

The present study has benefited from a strong financial support from Electricité de France (EdF), le Commissariat à l’Energie Atomique (CEA) and Framatome and is a part of a large research program (see Cabrillat et al (2004)). It deals with studying **creep flow and damage behaviour of 9Cr1Mo-NbV base metal and weldments in the temperature range from 450°C to 650°C**. Indeed, the use of 9Cr1Mo-NbV steels as structural materials in industrial facilities implies to join large components as can be shown in **figure In.3**. The most common joining method is welding. This operation leads to several changes in the mechanical properties of the resulting structure that may have dramatic influences on the creep strength.



Figure In.3. Example of the welding operation on a pipe (source www.altavista.com)

More generally, several problems can be related to the welding operation:

1. The solidification of the weld metal may lead to the formation of cracks especially for very thick components.
2. The solidification is accompanied by a metal contraction leading to stress concentrations that may be significant. As a consequence a post weld heat treatment (PWHT) is performed to relax residual stresses.

3. Local heating of the base metal induces phase transformations and several microstructural and mechanical properties changes in the so called heat affected zone whose thickness is not much larger than 5 mm.

One critical point in the design of 9Cr1Mo-NbV weldments is their very high sensitivity to type IV cracking (i.e. rupture in the HAZ parallel to the fusion line) in high temperature creep conditions. Six incidents of cracking and failure have yet been reported especially in the West Burton power plant in the United Kingdom after only 20,000 hours at 565°C i.e. largely under the maximum design temperature of 600°C. These incidents are reported in Shibli (2002), Brett et al (2001), Brett et al (1999), Allen et al (1999) and Middleton et al (1990). Even if Brett et al (1999) and Allen et al (1999) concluded that these incidents were probably due to incorrect heat treatment during manufacturing, they evidenced a great need to finely investigate the effects of welding on the microstructural and mechanical properties of 9Cr1Mo-NbV steel welded components. This need to predict the risk of type IV failure in 9Cr1Mo-NbV weldments is of particular importance as the steel is actually used at its maximum design temperature (i.e. 600°C) in Japan. Note also that in the synthesis of Parrot and Shibli (2004), the failure of a secondary superheater tube operating at 540°C and under an internal pressure of 8.2 MPa is reported after 63,000 hours of service.

The present study was performed in the framework of the local approach to fracture whose guideline principles are to “combine a detailed experimental analysis of the considered materials and of their specific damage mechanisms, a realistic modelling of these mechanisms and the implementation of these models into a numerical simulation of the response of the structural components under investigation” (A. Zaoui in Berdin et al (2004)).

The first part of this work (**Part A**) is dedicated to the description of material microstructures and general mechanical properties as they strongly determine the material creep strength. The effects of thermal ageing are especially studied as the microstructural stability is a key point in the material ability to retain its creep strength after long term exposure.

Then, creep flow and damage behaviour of the base metal is analysed (**Part B**). Numbers of experiments, mainly creep tests, were performed at 625°C to investigate damage mechanisms and their relationships with mechanical fields. To predict creep time to failure up to 100,000 hours, a new creep model integrating coupled influences of creep flow and damage behaviour was designed. The accuracy of the extrapolation of creep results from about 1,000 hours to 100,000 hours is especially questioned. From literature data and experimental results, the model was extended to the temperature range from 550°C to 650°C. It is shown in the present manuscript that extrapolations above or below this domain may be extremely hazardous.

Special attention was then focused on determining the creep properties of the weldments (**Part C**). The reduction in the creep lifetime is due to the lower creep strength of part of the heat affected zone. To identify the intrinsic creep flow and damage behaviour of the weakest part of the heat affected zone, a Gleeble 1500 thermal mechanical simulator was used to obtain bulk specimens having the same metallurgical properties as this zone but on a larger volume. The new creep model used for the base metal was also used to fit on the creep response of this simulated microstructure.

Moreover, creep flow properties of the weld metal were also studied. Consequently, one model, with three different sets of parameters, i.e. for the base metal, for the weld metal and for the heat affected zone, integrating coupled influence of creep flow and damage mechanisms, were determined. Using this three-material representation, simulation of the creep response of weldments was possible (**Part D**). Structural effects due to mismatch in material creep properties could thus be evaluated. Finite element (FE) calculations were performed to investigate the effects of geometrical parameters (weld angle, relative proportion of each material, specimen diameter ...) on the weldment creep response. The ability to use the model for design purposes was finally investigated.

*For the sake of clarity, the synthesis of experimental results and descriptions of experimental techniques are given in **appendices A and B**. All the micrographs presented in this study were taken using the two scanning electron microscopes (the LEO 1450VP and the Field Emission Gun 200 DSM 982 Gemini) of the Centre des Matériaux of the Ecole Nationale Supérieure des Mines de Paris. Transmission micrographs were taken both at the CEA Saclay and the CEA Grenoble. All mechanical tests were carried out at the Centre des Matériaux of the Ecole Nationale Supérieure des Mines de Paris and at the Centre de recherches des Renardières of EdF. The author wishes associate to the experimental results of the present study: M. Rousselot (ENSMP), F. Grillon (ENSMP), J. Valy (ENSMP), A. Naslot (ENSMP), D. Pachoutinsky (ENSMP), Y. Rousseleau (EdF), G. Lindet (EdF), B. Brugier (Framatome), Dr. L. Guetaz (CEA), Dr. Y. Decarlan (CEA), C. Meurin (ENSMP), J. Gibier (ENSMP), G. Cassas (ENSMP), J.L. Ajzenberg (ENSMP), J. Labrousse (ENSMP) and A. Laurent (ENSMP). Dr. Roland Piques who largely contributed to the birth of this research project is also strongly acknowledged and associated to the present study. Many thanks are due to Marie-Thérèse Cabrillat and Bruno MICHEL (CEA Cadarache), Sylvain Leclercq (EdF) and Jean-Marc Cloué (Framatome).*

I'm very grateful to my supervisors : Anne Françoise Gourgues-Lorenzon and Jacques Besson for fruitful discussions and their strong support in experimental and theoretical developments of the present work.

This PhD thesis is dedicated to my parents.

References

- Allen D.J., Brett S.J. (1999). Premature failure of a P91 header encap weld: minimising the risks of additional failures. *Proceedings of the conference on case histories in failure investigation – Milan*. 133-143.
- Berdin C., Besson J., Bugat S., Desmorat R., Feyel F., Forest S., Lorentz E., Maire E., Pardoën T., Pineau A., Tanguy B. (2004). Local approach to fracture. *Edited by J. Besson in les presses de l'école des mines de Paris*. Préface. 9-10.
- Blum R., Hald J. (1998). Benefit of advanced steam power plants. *Materials for advanced power engineering - 6th Liege Conference*. 1009-1016.
- Brett S.J., Allen D.J., Pacey J. (1999). Failure of a modified 9Cr header endplate. *Proceedings of the conference on case histories in failure investigation – Milan*. 873-884.
- Brett S.J. (2001). Identification of weak thick section modified 9Cr forgings in service. *Proceedings of the Swansea creep conference*. CDRom.
- Cabrillat M.T., Reytier M., Sauzay M., Mottot M., Gaffard V., Seran J.L., Billot P., Riou B. (2004). Studies on mechanical behavior of mod. 9Cr-1Mo steel - CEA R&D program. *HTR 2004 conference - Beijing China*.
- Fujita T. (2001). Advances in 9-12%Cr heat resistant steels for power plants. *Advances in materials technology for fossil power plants – Edited by Viswanathan R*. 33-65.
- Hald J. (1996). Metallurgy and creep properties of new 9-12%Cr steels. *Steel research*. **67(9)**. 369-374.
- Clueh R.L. and Harries D.R. (2001). High chromium ferritic and martensitic steels for nuclear applications. *American Society for Testing Materials*
- Metcalfe E., Scarlin B. (1998). Advanced high efficiency power plant. *Materials for advanced power engineering - 6th Liege Conference*. 33-51.
- Middleton C., Metcalfe E. (1990). A review of laboratory type IV cracking data in high chromium ferritic steels. *Paper C386/027 published in ImechE proceedings – London*.
- Parrot A., Shibli A. (2004). Performance du P91 et des autres aciers martensitiques à 9%Cr : Expérience industrielle et en laboratoire. *EdF report n°HT-26/02/006/A. In French (Private communication)*.
- Shibli I.A. (2001). Overview of the HIDA project. *International journal of pressure vessels and piping*. **78**. 729-735.
- Staubli M., Mayer K.H., Kern T.U., Vandstone R.W., Hanus R., Stief J., Schonfeld K.H. (2001). Cost 522 – Power generation into the 21st century; advanced steam power plant. *Advances in materials technology for fossil power plants – Edited by Viswanathan R*. 15-32.
- Tavassoli A.A.F (1998). Materials design data for fusions reactors. *Journal of nuclear materials*. **258-263**. 85-96.
- Vandstone R.W. (1998). Alloy design and microstructural control for improved 9-12%Cr power plants steels. *Materials for advanced power engineering - 6th Liege Conference*. 1035-1047.
- Von Hagen I., Bendick W. (2001). Creep resistant ferritic steels for power plants. *Niobium science and technology – proceedings of the international symposium Niobium 2001*. 753-776.
- Von Hagen I., Scarlin B. (1998). Advanced high efficiency power plant. *Materials for advanced power engineering - 6th Liege Conference*. 33-51.
- Viswanathan R., Bakker W.T. (2000). Materials for boilers in ultra supercritical power plants. *Proceedings of the International joint power generation conference*. 1-22.

Contexte : de nouveaux matériaux pour les futures unités de production d'électricité

L'efficacité des unités de production électrique dépend intimement des pertes énergétiques lors des différents transferts de chaleur. C'est pourquoi, une augmentation des pressions et températures admissibles en service devraient assurer une amélioration non négligeable du rendement des unités de production électrique. Une pression de 240 bars et une température de 550°C sont actuellement les conditions de service dans les centrales thermiques classiques. Le développement de nouvelles unités de production dites supercritiques et ultra-supercritiques dont la pression et la température en service visées sont respectivement de 300 bar et 650°C est un objectif ambitieux. De telles unités présenteraient cependant des rendements bien meilleurs avec pour conséquence :

3. Une diminution des coûts de production.
4. Un impact positif sur l'environnement avec une réduction de 2% des émissions de CO₂ pour une augmentation de 1% du rendement.

Pour atteindre un tel objectif, il est apparu nécessaire de développer de nouveaux matériaux résistants aux sollicitations haute température pour remplacer les aciers inoxydables austénitiques type 304 et 316 et les aciers ferritiques type 1Cr-Mo ou 2.25Cr-Mo qui sont actuellement des matériaux couramment utilisés. Parmi les matériaux pressentis, les aciers martensitiques à 9-12% de chrome sont les plus largement étudiés depuis les trente dernières années. De nombreux programmes de recherches ont été entrepris aux Etats Unis (EPRI), au Japon (EFDC) et en Europe (COST 501 et 522). L'objectif des programmes COST 501 et 522 (cf. Staubli et al 2001)) était d'identifier les matériaux susceptibles de résister aux sollicitations de fatigue et fluage pour des conditions de service de 280 bar / 600-650°C. Le projet européen suivant : THERMIE qui a débuté en 1998 est encore plus ambitieux puisque les conditions de service visées sont de 375 bar / 700-720°C à l'horizon 2013.

Les objectifs des différents programmes de recherche en termes de conditions de service sont résumés **figure In.1**. Comme l'indique Vandstone (1998), le critère de résistance en fluage retenu est la contrainte maximale admissible permettant d'atteindre une durée de vie de 100000 heures en fluage. La pratique courante est de réaliser des essais en laboratoire avec des temps d'essais beaucoup plus courts à partir desquels les prédictions de durée de vie à 100000 heures sont établies (i.e. 1000 heures d'essais en laboratoire pour prédire la durée de vie à 100000 heures).

Les avantages des aciers martensitiques inoxydables au chrome sont nombreux :

6. Une bonne résistance à la corrosion.
7. De très bonnes propriétés mécaniques jusqu'à 600°C grâce à une optimisation de la composition en V, Nb ou Mo.
8. Une bonne conductivité thermique et un faible coefficient d'expansion thermique (Bonne soudabilité).
9. Une faible sensibilité à l'irradiation si les teneurs en Mo, Ni, Nb et V sont limitées.
10. Un coût très inférieur à celui des aciers austénitiques (Prix du chrome inférieur celui du nickel).

Les aciers inoxydables 1Cr-Mo et 2.25Cr-1Mo constituent les deux premières générations d'aciers inoxydables au chrome qui sont déjà utilisés comme matériaux de structure dans les centrales thermiques du parc EDF. Ces trente dernières années, de nombreux efforts ont été consacrés à l'optimisation de la composition des aciers 9Cr1Mo afin d'améliorer leur résistance mécanique mais aussi leur soudabilité. La composition initiale du matériau a ainsi été modifiée aux Etats-Unis avec l'optimisation de la teneur en niobium et vanadium (aciers P91/T91) tandis qu'il a été choisi au Japon d'augmenter la teneur en chrome et d'ajouter du tungstène (aciers P92/P122/E911). Les évolutions de la composition chimique de l'acier et la tenue en fluage des nuances ainsi obtenues sont répertoriées **figure In.2** (voir aussi Von Hagen et Bendick (2001), Klueh et Harries (2001), Fujita (2001) et Von Hagen et Scarlin (1998)).

Notre étude concerne les aciers 9Cr1Mo-NbV qui ne sont pas la dernière génération des aciers au chrome. Ils sont notamment déjà largement utilisés dans les circuits vapeurs (cf. Blum and Hald (1998)) d'unités de production comme à Lippendorf (267 bar, 550-580°C), Boxberg (267 bar, 555-578°C) et Nordjylland (290 bar – 580°C). Par conséquent, il est important d'être capable de prédire l'évolution des propriétés mécaniques et métallurgiques de ces alliages pour des sollicitations de fluage longue durée.

Objectif de l'étude

Ce travail de thèse a été financé par Electricité de France (EdF), le Commissariat à l'Energie Atomique (CEA) et Framatome. Il s'inscrit dans un vaste programme de recherche (cf. Cabrillat et al (2004)). **Il s'intéresse au comportement, à l'endommagement et à la rupture en fluage de l'acier 9Cr1Mo-NbV et de ces produits soudés dérivés dans la gamme de température 450 - 650°C.** En effet, l'utilisation des aciers 9Cr1Mo-NbV comme matériaux de structure sur les

installations industrielles requiert l'assemblage de composants de grande taille comme le montre la **figure In.3**. La méthode d'assemblage la plus couramment utilisée est le soudage. Cette opération conduit à des modifications microstructurales qui peuvent avoir une influence très importante sur les propriétés mécaniques et plus particulièrement la tenue en fluage.

D'une manière générale, l'opération de soudage peut induire plusieurs types de problèmes:

4. la solidification du métal d'apport peut conduire à la formation de criques notamment pour les produits épais.
5. Le retrait consécutif à la solidification du métal déposé engendre des contraintes résiduelles importantes. Un traitement de détensionnement post-soudage est ainsi quasi-systématiquement réalisé.
6. L'échauffement local du métal de base dans la Zone dite Affectée Thermiquement (ZAT) induit des transformations de phases qui s'accompagnent de modifications plus ou moins importantes de la microstructure et des propriétés mécaniques.

Le point le plus critique des assemblages soudés en acier 9Cr1Mo-NbV est leur très grande sensibilité à la rupture de type IV (i.e. rupture dans la ZAT parallèlement à la ligne de fusion) dans les conditions de fluage à haute température.

Six incidents majeurs ont déjà été reportés comme dans l'unité de production électrique de West Burton en Angleterre où la rupture d'un assemblage soudé a été constatée après 20000 heures de fonctionnement à 565°C c'est à dire pour une température très inférieure à 600°C qui était la température d'utilisation maximale conseillée. Ces incidents sont décrits dans Shibli (2002), Brett et al (2001), Brett et al (1999), Allen et al (1999) et Middleton et al (1990). Même si Brett et al (1999) et Allen et al (1999) ont conclu que ces incidents étaient probablement dus à un mauvais traitement thermique lors de la fabrication des composants, ils ont mis en évidence la nécessité de comprendre plus finement les effets du soudage sur la tenue en fluage des aciers 9Cr1Mo-NbV.

Notre étude a été réalisée dans le cadre de l'approche locale de la rupture qui combine une analyse expérimentale détaillée des matériaux considérés, de leurs propres mécanismes d'endommagement, une modélisation représentative de ces mécanismes et l'implémentation de ces modèles pour la simulation numérique de structures réelles.

La première partie de ce travail (**Partie A**) est dédiée à la description des microstructures des matériaux et de leurs propriétés mécaniques car elles influencent fortement la tenue en fluage. Les effets de vieillissements thermiques statiques sont également étudiés car la stabilité microstructurale est représentative de la capacité du matériau à conserver sa résistance mécanique en fluage pour des temps d'exposition longs à haute température.

Ensuite, le comportement et l'endommagement de fluage du métal de base sont étudiés (**Partie B**). De nombreux essais mécaniques (principalement de fluage) ont été réalisés à 625°C pour identifier les mécanismes d'endommagement. Pour prédire la durée de vie en fluage à 100000 heures, un nouveau modèle de fluage intégrant plusieurs mécanismes de déformation et d'endommagement a été formulé. La validité de l'utilisation de résultats d'essais de laboratoire n'excédant pas 1000 heures voir 10000 heures pour prédire des durées de vie à 100000 heures est en particulier remise en cause. A partir de données de la littérature et de résultats expérimentaux, le modèle a pu être utilisé dans la gamme de température 550 - 650°C. Il est montré dans ce manuscrit que des extrapolations en dehors de ce domaine de température peuvent être dangereuses (Modification des mécanismes physiques de déformation et d'endommagement).

Une attention toute particulière a été apportée à la détermination de la résistance en fluage des joints soudés (**Partie C**). Il est notamment mis en évidence une réduction significative de la résistance en fluage qui est attribuée à la mauvaise tenue de la ZAT intercritique en fluage. Pour déterminer les propriétés de fluage intrinsèques de cette ZAT faible, un simulateur thermo-mécanique Gleeble 1500 a été utilisé pour simuler sur de larges volumes la microstructure de cette ZAT faible. Le nouveau modèle de fluage identifié pour le métal de base a aussi été utilisé pour représenter la réponse en fluage de la microstructure simulée.

Les propriétés intrinsèques du métal d'apport ont également été déterminées. Ainsi à partir d'un seul modèle intégrant plusieurs mécanismes de déformation et d'endommagement, trois jeux de paramètres différents i.e. pour le métal de base, pour le métal d'apport et la zone affectée thermiquement ont été identifiés. A partir d'une représentation à trois matériaux, la simulation de la réponse des assemblages soudés à la sollicitation de fluage a ainsi été possible (**Partie D**). Nous avons notamment pu, à partir de ces simulations, évaluer les effets de structure induits par les hétérogénéités de comportement et de résistance au fluage. Les calculs éléments finis ont également permis d'étudier l'effet de différents paramètres géométriques (angle de la soudure, taille des éprouvettes testées, largeur de ZAT ...). L'aptitude du modèle à prédire la durée de vie en fluage de composants industriels a également été démontrée.

Table of contents
(*Table des matières*)

<u>Part A. Materials</u>	17
Chapter A.I. Base metals	21
Chapter A.II. Weldments	49
<u>Part B. Creep flow and damage mechanisms of 9Cr1Mo-NbV steels at high temperature: Experiments and Modelling</u>	67
Chapter B.I. State of the art.	71
Chapter B.II. Experimental investigations of creep mechanisms and cavitation processes in P91 steel at 625°C (smooth round specimens).	103
Chapter B.III. Modelling creep mechanical and damage behaviour of the P91 steel at 625°C: “Creep failure model of a tempered martensitic stainless steel integrating multiple deformation and damage mechanisms”. V. Gaffard, J. Besson, A.F. Gourgues-Lorenzon. <i>Submitted to international journal of fracture.</i>	117
Chapter B.IV. Validation of the model: Ability of the model to represent creep tests on CT and plate notched specimens.	145
Chapter B.V. Formulation and use of a locally coupled version of the model.	155
Chapter B.VI. Creep flow and damage behaviour of the T91 steel at 450°C and 550°C.	161
<u>Part C. Creep flow and damage mechanisms of 9Cr1Mo-NbV weldments at high temperature. Experimental evaluation and modelling of creep flow and damage behaviour of the weakest area of weldments</u>	175
Chapter C.I. State of the art	179
Chapter C.II. Comparison between creep flow and damage behaviour of the P91 base metal and the WJP91 weldment at 625°C: “High temperature creep flow and damage properties of 9Cr1Mo-NbV steels: base metal and weldment” V. Gaffard, A.F. Gourgues-Lorenzon and J. Besson. <i>Intended to be submitted to Nuclear engineering and design.</i>	188
Chapter C.III. Creep flow and damage properties of the weakest area of the WJP91 weldment at 625°C: “High temperature creep flow and damage properties of the weakest area of 9Cr1Mo-NbV steel weldments”, V. Gaffard, A.F. Gourgues-Lorenzon and J. Besson. <i>Intended to be submitted to ISIJ international.</i>	205
Chapter C.IV. Modelling creep flow and damage behaviour of the weakest area of the WJP91 weldment: “Modelling high temperature creep flow and damage properties of the weakest area of 9Cr1Mo-NbV steel weldments”, V. Gaffard, J. Besson. and A.F. Gourgues-Lorenzon. <i>Intended to be submitted to engineering fracture mechanics.</i>	227
<u>Part D. Modelling creep flow and damage behaviour of weldments</u>	249
Chapter D.I. State of the art.	253
Chapter D.II. Modelling coupled creep flow and damage behaviour of weldments: “Modelling high temperature creep flow and damage behaviour of 9Cr1MoNbV steel weldments”. <i>Intended to be submitted to european journal of mechanics.</i>	269
Chapter D.III. Predictions of creep lifetime of cross-weld specimens by means of elasto-viscoplastic calculations and the use of a rupture criterion in post-calculation.	289
Chapter D.IV. Modelling creep flow and damage behaviour of the WJT91 weldment at 450°C and 550°C.	297
Chapter D.V. Use of the model to predict creep lifetime of welded components for industrial applications.	307
<u>Conclusions and further works</u>	321

Part A

Materials
(Matériaux)

Introduction

This first part is dedicated to the description of the materials of the study which consist in two base metals of type 9Cr1Mo-NbV steels and two weldments that are studied in terms of metallurgical and general mechanical properties. Effects of ageing are also explored.

In the following:

1. P91 and T91 will refer to base metals.
2. WJP91 and WJT91 will refer to weldments respectively corresponding to the P91 and the T91 base metal.
3. WMP91 and WMT91 will refer to weld metals respectively used for the WJP91 and the WJT91 weldments.

Attention is first focused on base metals (**chapter A.I**) which are tempered chromium martensitic stainless steels. Alloy composition and thermal treatment characteristics are described. The presentation of the resulting microstructure is made throughout optical, scanning electron microscope (SEM) and transmission electron microscope (TEM) observations. A description of inclusions and of the precipitation behaviour is also included.

Then, evaluation of general mechanical properties throughout tensile tests at high temperature is presented. Strain rate effects on tensile response are in particular explored. The last part about base metals is dedicated to the study of thermal ageing. T91 and P91 steels were respectively submitted to 450°C, 550°C and 550°C, 625°C thermal ageings for 1,000 hours, 5,000 hours and 10,000 hours. Identification of second phase particles and measurements of the evolution of the average particle size, using carbon extraction replicas, were done. TEM and electron backscattered diffraction (EBSD) investigations were also performed to explore the microstructural changes during thermal ageing.

Attention is then focused on welded components (**chapter A.II**). The welding procedures, the composition and the properties of the weld metals are described. Some recommendations to ensure the integrity of the weldments are also given. The main point that is explored is the modification of metallurgical and mechanical properties in the so called heat affected zone of weldments. This heat affected zone is classically divided into three main parts related to local phase transformations. Hardness measurements, SEM and TEM investigations are performed to characterise the resulting microstructures.

Contents

Chapter A.I. Base metal

Chapter A.II. Weldments

Chapter A.I. Base Metal

1. Alloy composition and general feature of the microstructure

The P91 steel was supplied by Mannesmann and Vallourec as a seamless pipe of 295 mm in outer diameter and 55 mm in thickness. The T91 steel was supplied by Creusot Loire as a plate of 150 mm in thickness. The chemical composition of the steels of this study is shown in **table A.I.1**.

	C	Si	Mn	P	S	Al	Cr	Ni	Mo	V	Nb	N
P91	0.09	<i>0.31</i>	0.41	<i>0.014</i>	<i>0.005</i>	0.016	8.56	0.26	0.92	0.21	0.065	0.042
T91	0.105	<i>0.240</i>	0.44	<i>0.008</i>	<i>0.00016</i>	0.013	8.41	0.08	0.95	0.25	0.08	0.033

Table A.I.1. Chemical composition of the steels examined in the present study (wt %)

One should notice several differences between P91 and T91 alloys composition as nuclear specifications require a strict control of segregating elements like P, S or Si. Some comments can be done about roles of elements:

1. Cr is added to ensure a good resistance to corrosion and good mechanical properties.
2. Nb, V restrict the austenite grain growth during austenitization and have a strengthening effect by precipitation of MX particles during tempering.
3. Mo is added for solid solution strengthening.
4. P and S contents are strictly controlled as they are potentially segregating elements at grain boundaries.
5. Ni is detrimental by forming a brittle Fe rich phase but also considerably lowers the A_{c1} temperature so that its addition must be strictly controlled.

For the sake of completeness, the synthesis of Maruyama et al (2001) about the role of elements is given in **figure A.I.1**, where the role of the newly used alloy elements as W or Re, are also reported (Note that "D" designates the austenite grain size in **figure A.I.1**).

Element	Merit	Demerit
B	Improve creep strength and quench hardenability. Stabilize $M_{23}C_6$ particles and delay their coarsening.	Reduce impact toughness.
C	Necessary to make $M_{23}C_6$ and NbC.	
Co	Suppress δ -ferrite. Decrease D .	
Cr	Improve oxidation resistance. Lower M_s . Raise A_1 . Main element of $M_{23}C_6$.	Increase D .
Cu	Suppress δ -ferrite.	Promote precipitation of Fe_2M .
Mn		Increase D and reduce creep strength. Lower A_1 . Promote M_6C precipitation.
Mo	Lower M_s . Raise A_1 . Solid solution hardening.	Accelerate growth of $M_{23}C_6$.
N	Necessary to make VN.	
Nb	Form MX and contribute to strengthening.	Promote precipitation of Z phase.
Ni		Increase D and reduce creep strength. Lower A_1 .
Re	Prevent the loss of creep rupture strength. Lower M_s .	Lower A_1 .
Si	Improve oxidation resistance.	Increase D and reduce creep strength.
V	Form MX and contribute to strengthening.	
W	Lower M_s . Raise A_1 . Delay coarsening of $M_{23}C_6$ particles. Solid solution hardening.	

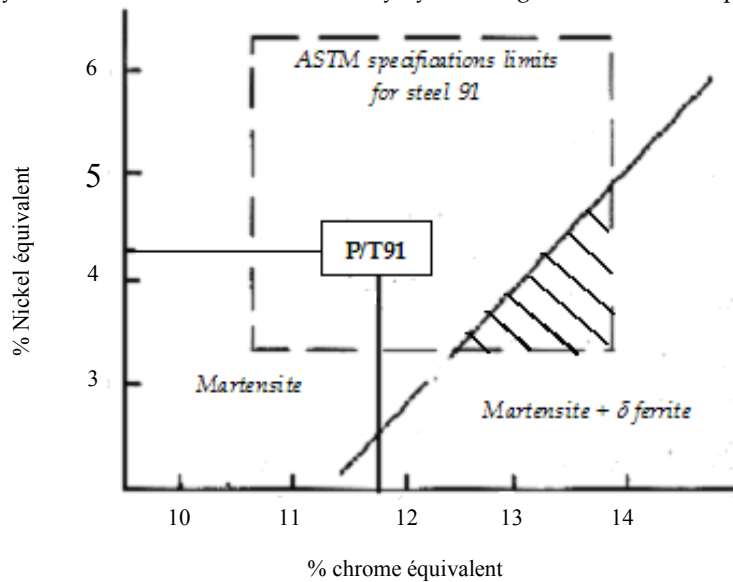
Figure A.I.1. Role of elements (Extracted from Maruyama et al (2001))

Moreover, the balance between all elements must be controlled to avoid δ ferrite formation. Schneider's sketch and equivalent Ni and Cr percentages formulae are often used to predict possible presence of δ ferrite. For chromium steels, equivalent Ni and Cr percentages are given by:

$$\%_{\text{eq}} \text{Ni} = \% \text{Ni} + \% \text{Co} + 0.5\% \text{Mn} + 0.3\% \text{Cu} + 25\% \text{N} + 30\% \text{C} \quad (\text{in wt } \%) \quad (\text{eq. A.I.1})$$

$$\%_{\text{eq}} \text{Cr} = \% \text{Cr} + 2\% \text{Si} + 1.5\% \text{Mo} + 5.5\% \text{Al} + 5\% \text{V} + 1.75\% \text{Nb} + 1.5\% \text{Ti} + 0.75\% \text{W} \quad (\text{in wt } \%) \quad (\text{eq. A.I.2})$$

where the compositions are in wt%. The calculated values of $\%_{\text{eq}} \text{Ni}$ and $\%_{\text{eq}} \text{Cr}$ are reported in the Schneider (1960) diagram of **figure A.I.2** established by Orr and DiFrancesco (1993) from a study on 9Cr1Mo-NbV steels. It shows that no δ ferrite should appear during P91 and T91 steels elaboration. This prediction was experimentally confirmed as no δ ferrite was detected in any of the two base metals of this study by scanning electron microscopy (SEM) investigations.



*Figure A.I.2. Schneider diagram established by Orr and DiFrancesco for 12CrMoV type steels
Evaluation of P91 and T91 $\%_{\text{Ni}^{\text{eq}}}$ and $\%_{\text{Cr}^{\text{eq}}}$*

Note also in **figure A.I.2** that the steels of the study are within the specifications limits of the ASTM with $\%_{\text{Cr}^{\text{eq}}} \approx 11.8\%$ and $\%_{\text{Ni}^{\text{eq}}} = 4.2\%$, and also that it exists chemical compositions of steel 91, set within the ASTM ranges, that could result in a material containing up to 10% of δ ferrite for $\%_{\text{eq}} \text{Cr}^{\text{eq}} > 12.5\%$.

The two steels are martensitic chromium stainless steels obtained after normalising at high temperature and rapid quench followed by a tempering treatment. The resulting microstructure is a lath martensite arranged in packets in prior austenite grain boundary (**figure A.I.3**). Microstructure of the steel is also characterised by a high dislocation density and the precipitation of numbers of carbides of mainly M_{23}C_6 type at grains boundaries (preferentially at lath interfaces and dislocations: see Jones et al (1991)) but also precipitates of type MX which are both located at prior austenite grain boundary and along dislocations in the matrix of martensite lath (see Kaneko et al (2004) and Taneike et al (2004)). Although primary carbides, contain a balance of Nb and V, it was shown by Suzuki et al (2003) that a two phase separation of primary MX into V rich and Nb rich precipitates occurs during tempering. This point is also confirmed by the present study. Taneike et al (2004) have also shown that MX precipitates along grain boundaries contain more vanadium and less niobium than these found within lath martensite. Note finally that in the steels of the present study, no M_2X precipitates were detected.

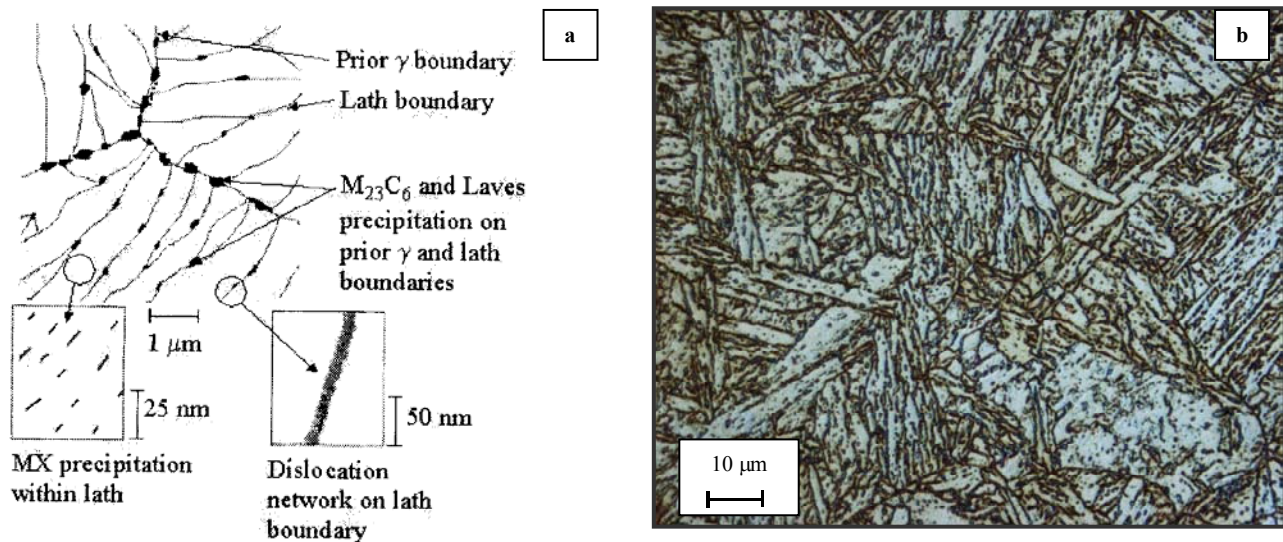


Figure A.I.3. (a) Sketch of P91 steel microstructure extracted from Masuyama (2001) (b) Optical micrograph after villeda etching

Inclusion characterisation:

The volume fraction of inclusions is said to be very low in 9Cr1Mo-NbV steels and Zhang et al (2000) have reported that it does not exceed $5 \cdot 10^{-4}$. In the present study, no measurement of the volume fraction of inclusions was carried out but X-ray dispersive wavelength spectroscopy analysis, using a Castaing electron microprobe, was performed. Results of the study are reported in **table A.I.2** (Note that only qualitative results are given as the small size of the inclusion did not allow to determine the exact chemical compositions of inclusions).

Material	Inclusion type	Size	Reference
P91	Al, Mn, O	2 μm – 3 μm	Soussan (2000)
T91	Al, Cu, Mn, O / SiO ₂	1 μm – 2 μm	This study

Table A.I.2. Inclusions in base metal

Formation of these inclusions is mainly due to the elaboration process. Indeed, desoxidation is necessary as oxygen that is trapped during the solidification step may lead to the formation of a high number of cavities. Therefore, elements like Si, Al or Mn which have a strong affinity for oxygen are added. As it has already been underlined by Bush (2001) this step is critical because these elements, especially Al, have also a great affinity for nitrogen and may avoid carbonitrides of type MX or M₂X precipitation during tempering. Note also that SiO₂ and Mn₂O₃ inclusions can come from the refractory materials which are in contact with the steel in the liquid state. No MnS particles were detected which is a good point as they would lower the impact toughness but it also shows that the sulphur probably segregates at grain boundaries. As optical and SEM observations confirm a very low inclusion content, no quantification of the area fraction of inclusion was performed. It will also be shown later on, that inclusions play a negligible role in the high temperature creep cavitation process for the steel of the study.

2. Heat treatments and resulting properties

The determination of the prior austenite grain size is quite difficult. Several techniques are proposed especially by Brachet (1991) who proposed both a technique based on a two step cooling (a dwell near 600°C is especially performed) which promotes the formation of pro-eutectoid ferrite at austenite grain boundaries and a use of a special etching reagent (Béchet-Beaujard = saturated aqueous picric acid and 1% of surfactant sodium tridecylbenzene sulfonate). A technique of thermal etching is also proposed by Garcia de Andres et al (2001). It consists in heating a polished sample to the austenitization temperature under vacuum. It follows that grooves form at austenite grain boundaries due to surface tension effects.

In the present study an etching reagent (100 ml of water solution saturated in picric acid + 10 ml of Xylen + 5 ml of Photoflo produced by Kodak®), already successfully used by Schacht and Richter (1998) for a 2^{1/4}Cr steel, was used. The size of the martensitic packet was determined after Villeda etching of the material microstructure. The determination of the average austenite grain and packet sizes were done from the image analysis of optical micrographs using a public domain analysis software Scion® (see **appendix B.H** for a finer description of the technique). In both cases, the average

grain size was determined from the analysis of more than four hundred grains. The size of the lath martensite i.e. their thickness was determined from transmission electron microscopy (TEM) investigations.

To study the precipitation state, second phase particles were extracted on carbon replicas. The procedure described in the following is largely used in the present study:

1. Mechanical grinding and then polishing with diamond paste up to 1 μm .
2. Villela etching: 100 ml methanol, 5 ml hydrochloric acid and 1g picric acid (For information, note that another etching reagent is proposed by Grobner and Hagel (1980) and Vitek et al (1983) who recommended the use of a 10 ml HCl, 1 ml tartaric acid and 100 ml methanol for extraction).
3. Carbon deposition under vacuum (The carbon layer deposited on the specimen surface is of few hundreds nanometers in thickness).
4. Extraction in Villela and cleaning in methanol before deposition on 3 mm diameter copper grids.

In a second step, the same carbon extraction replicas were observed with the field emission gun scanning electron microscope (FEG-SEM) of type Gemini DSM 982. The X-ray dispersive energy spectroscopy (EDS) facility was used to identify the chemical composition of the second phase particles. Moreover image analysis could be performed on SEM micrographs and then, using the Scion® public domain image analysis software the average particles sizes were determined from the analysis of more than four hundred particles. Finally, hardness measurements were done as a first characterisation of the steel mechanical properties. The corresponding characteristics of P91 and T91 microstructures are given in **table A.I.3**.

Material	Normalising	Quenching	Tempering	Grain sizes (Optical and TEM observations)	Vickers hardness HV 0.5	Precipitates (Carbon extraction replica)
P91	1065°C (1h00)	Air	765°C (2 h)	PAG = 90 – 100 μm Packet = 30 – 40 μm Lath = 0.4 – 1.0 μm	230	M ₂₃ C ₆ (90 - 100 nm) MX (10 - 20 nm)
T91	1070°C (4h30)	Water	765°C (6h45) + 750°C (15h18)	PAG = 100 – 120 μm Packet = 50 – 60 μm Lath = 1.0 – 2.0 μm	215	M ₂₃ C ₆ (130 - 140 nm) MX (10 - 20 nm)

Table A.I.3. Characteristics of the steels examined in the present study

The evolution of the austenitic grain size dependence on normalising temperature and time has been described by Barcelo and Brachet (1994). They found that the mean diameter of the austenite grain followed:

$$D_{\text{moy}} = Kt^n \text{ where } K = K_0 \exp\left(-\frac{E_a}{RT}\right) \quad (\text{eq. A.I.3})$$

with the activation energy $E_a = 113 \pm 12 \text{ kJmol}^{-1}$, $K_0 = 1 \text{ ms}^{-0.13}$ and $n = 0.13$. This formula was used to compare calculated and experimentally measured austenite grain sizes. Good agreement was found between measured and calculated values. The model gives: $D_{\text{moy, calc}} = 110 \mu\text{m}$ for 1h at 1065°C and for 4h30 at 1070°C: $D_{\text{moy, calc}} = 140 \mu\text{m}$, which corresponds to values of grain size slightly higher than those experimentally measured.

One should notice that the T91 steel was subjected to two tempering treatments. The second one is currently performed on welded components. A double tempering treatment was also carried out on several P91 base metal specimens (765°C 2h + 760°C 2h). It could then be ensured that, despite a decrease in measured hardness at room temperature, the steel exhibits similar creep properties after one or two tempering treatments.

It is also very interesting to determine the phase transformation points and their relative position in comparison with temperatures of thermal treatments. To do so, dilatometric tests were performed on small cylindrical specimens (10 mm in length and 3.0 mm in diameter) at low heating rates respectively 1.0 °C s⁻¹ and 0.5 °C s⁻¹. They consisted in a heating at a constant rate up to 1000°C immediately followed by a rapid helium cooling in order to induce the martensitic transformation (The maximum temperature of 1000°C was chosen imposed by the specifications of the furnace used for these experiments). The results are given in **table A.I.4**.

Material	Rates	Transformations	Start	End
P91 steel	1.0 °C s ⁻¹ *	Austenitic	A _{c1} = 852 °C	A _{c3} = 888 °C
		Martensitic	M _s = 395°C	M _f = 287 °C
T91 steel	60 °C s ⁻¹ **	Austenitic	A _{c1} = 840 °C	A _{c3} = 890 °C
		Martensitic	M _s = 402 °C	M _f = 306 °C
P91 steel	0.5 °C s ⁻¹ *	Austenitic	A _{c1} = 849 °C	A _{c3} = 890 °C
		Martensitic	M _s = 383°C	M _f = 295 °C
T91 steel	60 °C s ⁻¹ **	Austenitic	A _{c1} = 854 °C	A _{c3} = 901 °C
		Martensitic	M _s = 404 °C	M _f = 308 °C

Table A.I.4. Phase Transformation points for the base metals (* = heating, ** = cooling)

The positions of A_{c1} and A_{c3} temperatures are quite similar for the two steels. A_{c1} is also 100°C higher than the tempering temperature which should ensure no significant formation of austenite during tempering. The measured values of M_s can be compared with the results given by the formula proposed by Beres et al (2001) from a study on 350 types of martensitic stainless steels:

$$M_s = 454 - 210C + \frac{4.2}{C} - 27Ni - 7.8 Mn - 9.5 (Cr + Mo + V + W + 1.5Si) - 21Cu \quad (\text{in wt\%}) \quad (\text{eq. A.I.4})$$

The calculated value of M_s (≈ 375°C) is lower than the measured ones. This difference can be explained by the non dissolution of existing precipitates which leads to lower carbon and chromium contents in the solid solution both because no dwell at the austenitising temperature was done and because the normalising temperature was maybe too low especially to dissolve all MX precipitates. Moreover, M_s is higher in T91 than in P91 steel, probably because carbides are larger in size in the T91 steel and are consequently more difficult to dissolve.

An experiment of differential scanning calorimetry was also carried out to determine the temperature of M₂₃C₆ carbides dissolution. The event was unfortunately not observed but the Curie temperature could be determined as T_{Curie} = 760°C.

Attention was then focused on heat treatments as materials properties strongly depend on them. Normalising temperature must not be too high for two reasons:

1. To avoid precipitation of δ ferrite that is very harmful for creep strength .
2. To avoid growth and coarsening of the austenite grain. Note that Orr et al (1993) experimentally evidenced that the coarsening of austenite grain starts at 1125°C. They also showed that for normalising at 1050°C or 1100°C and up to 24 hours, the austenite grain only slightly coarsen and confirms by TEM investigations that part of Nb(C,N) and VN carbides remains undissolved at 1050°C - 1100°C.

However, a normalising temperature as high as possible is necessary to dissolve main parts of primary carbonitrides. As a matter of fact normalising conditions must be carefully chosen. To obtain martensitic structure during quench, cooling rates must be up to 20°C per hours (Klueh and Harries (2001)). The martensite transformation is not diffusive as it occurs by shear of prior austenite. In its pioneering work, Kelly (1965) has distinguished two shear systems:

System I: (110)_A [1-11]_A ⇔ (112)_M [11-1]_M

System II: (111)_A [1-21]_A ⇔ (101)_M [10-1]_M

(A = Austenite, M = Martensite)

However both theory and observations have largely evolved. The habit plane of the lath martensite is not well determined: (557)_γ or (223)_γ according to Sandwick and Wayman (1983). Laths organisation also depends on carbon weight percentage which was studied by Maki et al (1980). For wt %C < 0.2 (i.e. for P91 and T91 steels), laths of same orientations are gathered in packets. It is obviously confirmed by microstructural observations of the steels of the present study (see **figure A.I.2**). The resulting microstructure has, in fact, a very complex crystallography. Morito et al (2003) have carefully described the lath morphology and crystallography. The orientation relationships between lath martensite and austenite nearly matched one of the 24 Kurdjumov and Sachs (1930) orientation relationships. The 24 K.S. variants can be divided into fourth categories of 6 variants depending on the four main planes orientation between austenite and martensite:

1. (111)_γ // (011)_{α'}
2. (1-11)_γ // (011)_{α'}
3. (-111)_γ // (011)_{α'}
4. (11-1)_γ // (011)_{α'}

Packets are characterised by lath that have the same plane parallel relationship (i.e. one of the fourth previous). Blocks which corresponds to laths of single variants are sometimes distinguished and Morito et al (2003) deduced from TEM and EBSD investigations that the 6 blocks of all variants are randomly distributed in packets.

The particularity of the quench martensite is to be very hard (HV 0.5 up to 400) but with a low ductility level and a low impact toughness (see Materkowski and Krauss (1979)). Consequently, performing a tempering treatment which softens martensite but increases mechanical strength is necessary. The tetragonality of the martensite crystal structure is given by:

$$\frac{c}{a} = 1.000 + 0.045[C]_{ss} \quad (\text{eq. A.I.5})$$

(see also **figure A.I.4**) therefore, when all the carbon is in the solid solution, the tetragonality of the crystal structure, $c/a = 1.004$ for the P91 steel and $c/a = 1.0047$ for the T91 steel. The ratio c/a is nearly equal to 1.0 which means that the martensite crystal structure of the studied steels is nearly body-centred-cubic like ferrite. This crystallography particularly increases the sensitivity of the microstructure to softening mechanisms such as recovery or recrystallisation.

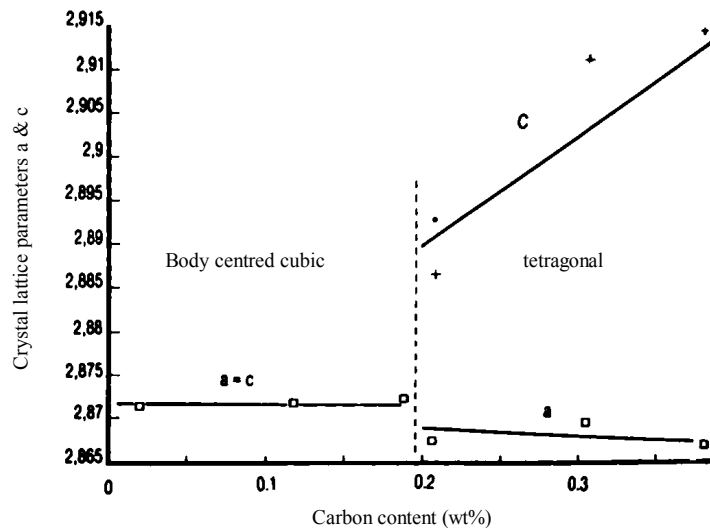


Figure A.I.4. Effect of carbon content on the structure of the martensite

The evolution of the microstructure from the quench state (i.e. high dislocation density martensite over-saturated in carbon and no precipitates) strongly depends on the temperature of the tempering heat treatment (see Shantsky et al (2000)):

1. In the temperature range between 450°C and 500°C, penny shaped M_2X particles precipitates.
2. In the temperature range between 500°C and 550°C, the precipitation of carbides of type M_7C_3 occurs and coarsening of M_2X is reported.
3. For temperatures higher than 550°C: M_7C_3 carbides and M_2X precipitates are replaced by MX precipitates and $M_{23}C_6$ carbides. Moreover low angle boundary configurations start to form (i.e. recovery proceeds).
4. For temperatures higher than 650°C, carbide coarsening starts and is accompanied by the formation of subgrains.
5. For temperatures higher than 750°C, the recovery of the lath martensite into equiaxed subgrains but also carbide coarsening largely occur. It is reported that for tempering times larger than one hour, all the carbon initially in solid solution is precipitated into $M_{23}C_6$ carbides.

As can be shown in **table A.I.3**, 9Cr1Mo-NbV steels are mainly submitted to high temperature tempering (> 750°C) on which attention will be focused in the following. During the high temperature tempering treatment (>750°C), the precipitation of carbides occurs following the sequence described by Laha et al (2000) and Vitek and Klueh (1983). Their precipitation is said to be un coherent or semi coherent with the matrix (Cadek et al (1997)):



This sequence is confirmed by Bjarbo and Hattestrand (2001) who performed thermodynamical calculations to follow nucleation and growth of $M_{23}C_6$ and M_7C_3 particles. Their calculations show that the dissolution of M_7C_3 occurs after 400s at 750°C. Sometimes, the precipitation of M_6C , M_7C and M_3C carbides is reported but Andrews (1972) have concluded that for 9Cr1Mo steels only $M_{23}C_6$ precipitation occurs. Note also that Jones et al (1991) indicated the formation of a Cr_2C phase preceding that of $M_{23}C_6$ carbide. Another precipitation sequence is reported by Robson and Bhadhesia (1997a and 1997b) for tempering up to 600°C:



From experimental results, one should assume that the sequence reported by Robson and Bhadhesia (1997a and 1997b) does not well describe the precipitation in P91 and T91 steels during tempering $> 750^\circ\text{C}$ as rather MX than M_2X particles were experimentally detected in the tempering state (see also Okamura et al (1996)). The proposed precipitation sequence for tempering at temperatures larger than 750°C is as follows:



Note also that as shown by Shantsky and Inden (1997) the presence of molybdenum was evidenced in $M_{23}C_6$ carbides. Moreover, the MX precipitates, which are generally of type Nb(C,N) or V(C,N), are very stable. They only dissolve at very high temperature (larger than 1100°C) as shown in **figure A.I.5a and A.I.5b**.

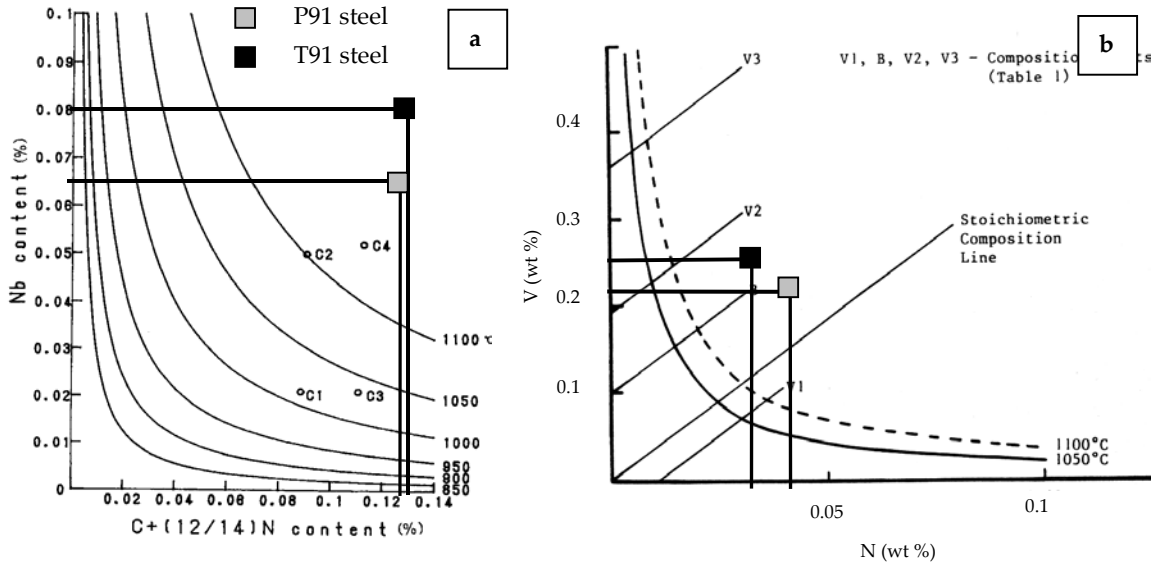


Figure A.I.5. Solubility of Nb(C,N) and VN in 9Cr1Mo-NbV steels from Ootoguro et al (2000) and Orr and Di Francesco (1993) (The solubility limit in the P91 and the T91 steel are also reported)

The solubility curves given in **figure A.I.5** have been determined by Ootoguro et al (2000) and Orr and Di Francesco (1993). Dutta and Palmiere (1998) gave the following expression for Nb(C,N) solubility in wt%:

$$\log[\text{Nb}] \left[\text{C} + \frac{12}{14} \text{N} \right] = 2.06 - \frac{6700}{T} \quad (\text{eq. A.I.9})$$

The **equation A.I.9** was modified by Klueh and Harries (2001) to take into account interactions between carbon, nitrogen and chromium:

$$\log[\text{Nb}] \left[\text{C} + \frac{12}{14} \text{N} \right] = 2.06 - \frac{6700}{T} - \frac{1}{2} e_C^{\text{Cr}} + e_N^{\text{Cr}} [\text{Cr}] \quad (\text{eq. A.I.10})$$

$$\log[\text{V}][\text{N}] = 5.2 - 10500/T - e_N^{\text{Cr}} [\text{Cr}] \quad (\text{eq. A.I.11})$$

$$\text{with: } e_C^{\text{Cr}} = 0.09 - \frac{180}{T} \quad \text{and} \quad e_N^{\text{Cr}} = -0.056 - \frac{145.8}{T} + 0.017 \log(T)$$

Other parameters than the tempering temperature strongly influence the evolution of the microstructure. Parameswaran et al (1996) studied both the effect of the cooling rate and the effect of the tempering time on carbide precipitation for a 9Cr1Mo-NbV steel after a normalising treatment at 1050°C . They have plotted in the same representation (**figure A.I.6a**) the corresponding TRC and TTT diagrams.

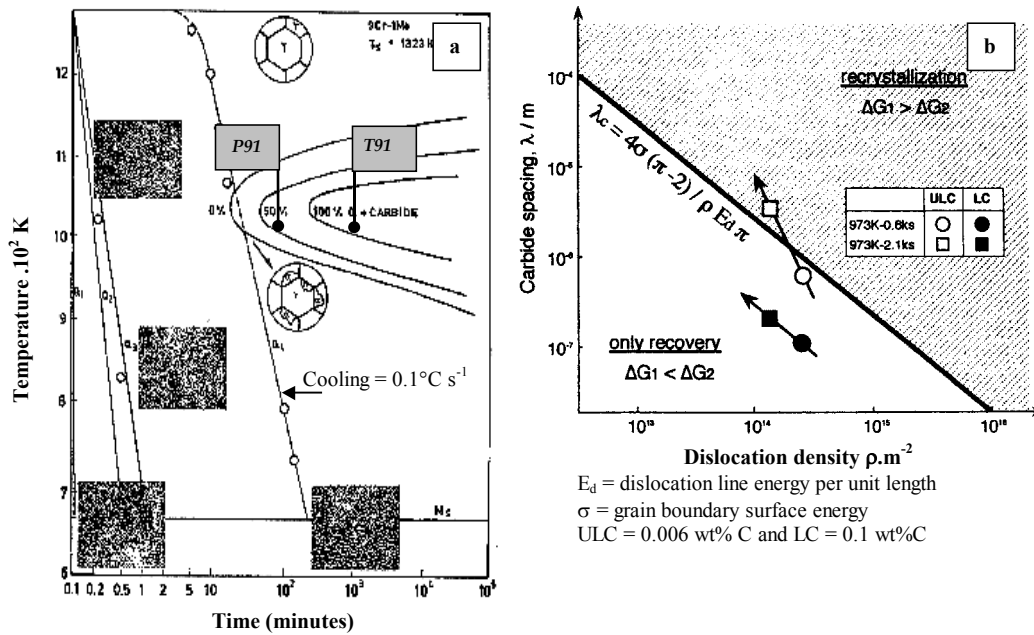


Figure A.I.6. Evolution of the 9Cr1Mo-NbV steel microstructure during tempering (a) evolution of the precipitation state from Parameswaran et al (1996) and (b) softening mechanisms from Tsuchiyama et al (2001)

From the results of Parameswaran et al (1996), it can be first concluded that no ferrite should appear during quench as it would require cooling rates lower than $0.1 \text{ } ^\circ\text{C s}^{-1}$, then, more than 50% of carbides have precipitated after 2 hours at 765°C for the P91 steel and as a double tempering treatment of more than seventeenth hours on the whole is performed, Parameswaran et al (1996) predict that nearly 100% of carbides have precipitated for the T91 steel.

The sensitivity of low carbon steels, like the chromium steels, to recovery during tempering is reported by Klueh and Harries (2001) for tempering larger than 1 hour at 750°C . The steps of the recovery are described as follow:

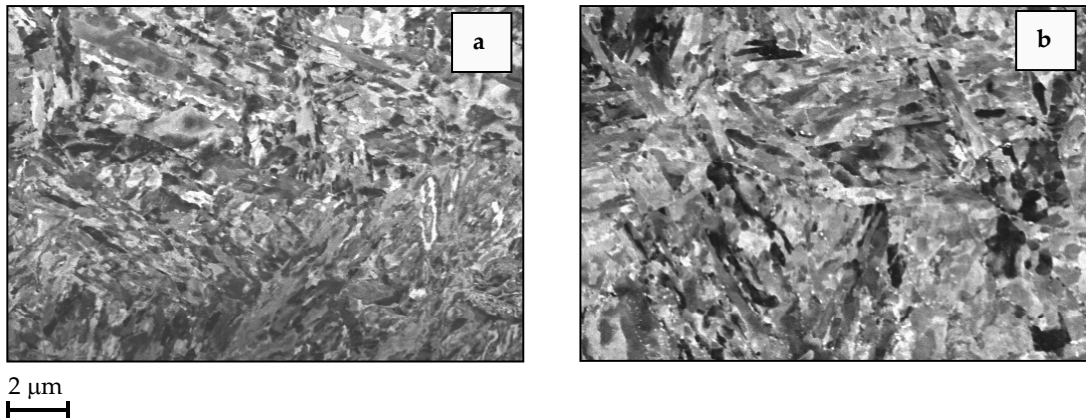
1. Growth and coarsening of the new carbides of type M_{23}C_6 .
2. Decrease in dislocation density. The evolution of dislocation density during tempering has already been measured by Pesicka et al (2003). It drops from $4.2 \cdot 10^{14} \text{ m}^{-2}$ for the as quenched microstructure to $0.79 \cdot 10^{14} \text{ m}^{-2}$ after 0.25 hours of tempering at 750°C and $0.06 \cdot 10^{14} \text{ m}^{-2}$ after 100 hours. They also evidenced that the dislocation density is very heterogeneous as some subgrains exhibited a very low and other a very high dislocation density.
3. Polygonisation of the dislocation substructure leading to formation and growth of subgrains within laths (Also observed by Fougères (1975) and Carron and Krauss (1972)). This sensitivity of low carbon steel to recovery processes is obviously due to the growth and coarsening of the precipitates which induces the ability for dislocations to move more freely.

Lath recovery during tempering was recently investigated by Sawada et al (2003) who performed TEM in situ observations during a temper of 4 hours at 730°C . They observed a change in lath morphology from an elongated shape to an equiaxed one. The lath boundary moves by repeated migration of local parts. Sawada et al (2003) consider that the driving force for lath recovery is the strain accumulated during martensitic transformation as recovery is not homogeneous and proceeds only in the high thickness area of the foil. The recovery process observed by Sawada et al (2003) is in quite good agreement with the Li's mechanism as already proposed by Guttman D. (1974) for a microalloyed martensitic steel. Tsuchiyama et al (2001) studied the effect of a 700°C tempering and showed that the evolution of the microstructure both depends on the dislocation density and the carbide spacing. Thus, in the case of a low carbon content (LC \Leftrightarrow 0.1 wt% C), they evidenced that recovery of the lath martensite occurs and that for a ultra low carbon content (ULC \Leftrightarrow 0.006 wt% C) recrystallisation of the microstructure may occur (see figure A.I.6b).

In the present study, TEM and SEM investigations were carried out to determine the characteristics of the tempered microstructures. On the TEM micrograph (see figure A.II.9a in the following), one can see lath martensite with M_{23}C_6 carbides at boundaries and formation of polygon dislocations substructures of only few microns in size within lath martensite.

It was evidenced in the present study that light optical observations after etching do not allow to evidence the recovery of the lath martensite microstructure as carbides remain aligned following the initial lath boundary. To do so, it is necessary to perform SEM investigations with the backscattered (BSE) channelling contrast after colloidal silica polishing

of the specimens. In this case, image contrasts corresponds to changes in crystallographic orientations. SEM-BSE micrographs are shown in **figures A.I.7a** and **A.I.7b**. Both the two micrographs evidence breaks in the laths and the beginning of their decomposition into fine equiaxed grains. The comparison between the P91 and the T91 steel also evidences a higher lath thickness in the T91 steel which can be related to the longer tempering time.



*Figure A.I.7. Microstructures (a). Tempered P91 steel (SEM observation after colloidal silica polishing)
(b). Tempered T91 steel (SEM observation after colloidal silica polishing)*

3. Mechanical properties

3.1. Manufacturing reports

For the P91 steel, no information about mechanical properties of the steel was given. However, Prunier et al (1998) have reported a 0.2 proof stress of 325 MPa and 538 MPa respectively at 625°C and 22°C, and tensile strengths of 338 MPa and 688 MPa respectively at 625°C and 22°C. Unfortunately, Prunier et al (1998) did not give the testing conditions, especially the strain rate that is a very important factor as it will be shown later. For the T91 steel, both Charpy impact tests at – 20°C, 0°C and + 20°C and tensile tests at 20°C and 550°C were carried out. Tensile properties of the T91 steel are reported in **table A.I.5**. No differences in tensile properties in the rolling and transverse directions were evidenced at 20°C and 550°C.

Direction	Test temperature	0.2 % proof stress	Tensile strength	Final elongation	Reduction of area
Rolling direction	20°C	466 MPa	639 MPa	25.0 %	74.2 %
Rolling direction	550°C	323 MPa	378 MPa	21.0 %	84.8 %
Transverse direction	20°C	458 MPa	634 MPa	27.0 %	75.1 %
Transverse direction	550°C	331 MPa	374 MPa	21.0 %	84.8 %

Table A.I.5. Tensile properties of the T91 steel reported in the fabrication report (Welding Framatome (2003))

The values of KCV at 20°C ranged from 25.8 to 27.8 daJcm⁻² whereas the specification for acceptance is 9.0 daJcm⁻² (minimum accepted value).

3.2. Tensile strength and 0.2% proof stress calculations

In Bestwick and Escaravage (1998), equations of evolution of the 0.2% proof stress, $R_p^{0.2}$ in the following, and the tensile strength, R_m in the following, with respect to the temperature have been determined for 9Cr1Mo-NbV steels as:

$$R_p^{0.2} = 494.636 - 0.45486T + 1.3264 \cdot 10^{-3} T^2 - 1.9024 \cdot 10^{-6} T^3 \quad (T \text{ en } ^\circ\text{C}) \quad (\text{eq. A.I.12})$$

$$R_m = 677.95 - 1.4279T + 6.6248 \cdot 10^{-3} T^2 - 13.187 \cdot 10^{-6} T^3 + 7.4131 \cdot 10^{-9} T^4 \quad (T \text{ en } ^\circ\text{C}) \quad (\text{eq. A.I.13})$$

($R_p^{0.2} = 260$ MPa at 625°C, 326 MPa at 550°C and 383 MPa at 450°C and $R_m = 285$ MPa at 625°C, 381 MPa at 550°C and 479 MPa at 450°C). Note that **equations A.I.12** and **A.I.13** were established from results of tensile tests probably carried out at a strain rate of 10⁻⁵ s⁻¹ and at two temperatures: the room temperature i.e. 20°C and 550°C so that their validity is questionable.

Warreing (1994) has established the following formulas for the Young's modulus:

$$E(T) = 207300 - 64.58.T(20^\circ\text{C} < T < 500^\circ\text{C}) \text{ and } E(T) = 295000 - 240.T(500^\circ\text{C} < T < 650^\circ\text{C}) \quad (\text{eq. A.I.14})$$

($E = 150,000 \text{ MPa}$ at 625°C , $163,000 \text{ MPa}$ at 550°C and $178,000 \text{ MPa}$ at 450°C).

Some authors like Pickering (1997), have suggested that the 0.2% proof stress can be described by an Hall-Petch type relationship with adding the strengthening contribution of carbides precipitates:

$$\sigma_{0.2} = A + Bd^{-1/2} + \sigma_p \quad (\text{eq. A.I.15})$$

$$\sigma_p = \frac{C}{\lambda} \ln \frac{D}{2b} \quad (\text{eq. A.I.16})$$

where λ = interparticle spacing, D = particle diameter and b = burgers vector of slip dislocations and C is a constant .

3.3. Experiments and results

The experimental facility used to carry out the tensile tests of the present study is described in **appendix B.D**. Tensile tests were performed on smooth cylindrical bars having a maximum gauge length of 19 mm and a gauge diameter of 3 mm (see **figure A.I.8**) at 450 and 550°C on the T91 steel and 625°C on the P91 steel in the strain rate domain from 10^{-5} to 10^{-2} s^{-1} . The elongation of the specimen was determined, using a linear variable transducer with a sensitivity of 1 μm , as:

$$\varepsilon = \frac{\Delta L_g}{L_{g0}} \quad (\text{eq. A.I.17})$$

where ΔL_g is the elongation of the gauge length and L_{g0} is the initial gauge length equal to 10 mm.

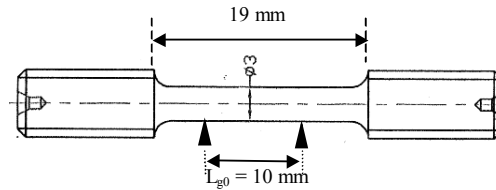


Figure A.I.8. Geometry of the smooth round tensile specimens

Tensile tests were both carried out using specimens manufacturing in the transverse (T) and longitudinal (L) directions of the pipe for the P91 steel and the sheet for the T91 steel. Results show no difference between both loading direction so that the two materials exhibit isotropy in mechanical properties. A similar study was carried out by Sasaki et al (1991) on a pipe of the same origin than the P91 steel with the conclusion that the tensile properties were very similar along L and T directions.

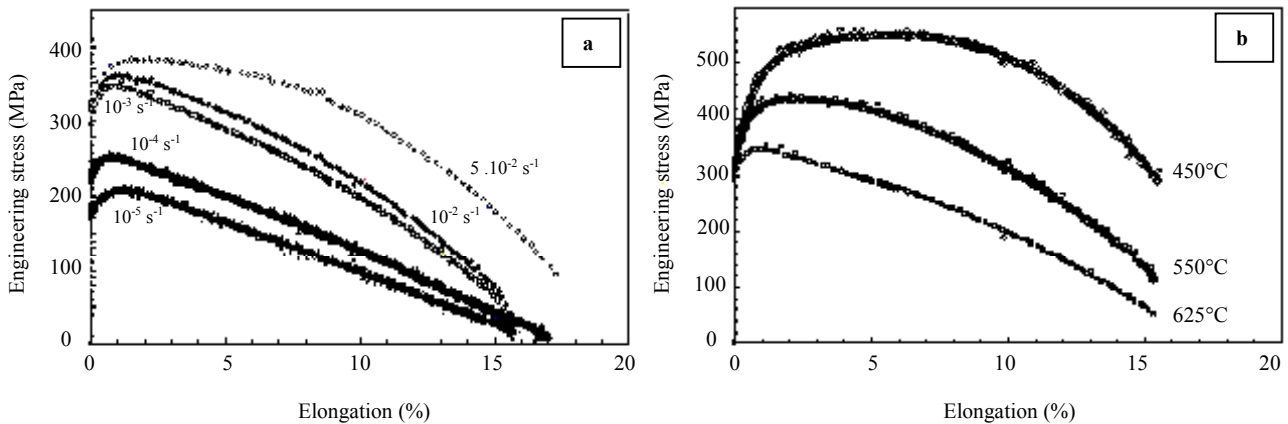


Figure A.I.9. Tensile tests on P91 steel - (a) at 625°C and strain rates of 5.10^{-2} , 10^{-2} , 10^{-3} , 10^{-4} and 10^{-5} s^{-1} (b) at 1.10^{-3} s^{-1} and temperatures of 450°C, 550°C and 625°C

Young's modulus were found to be in accordance with those given by **equation A.I.14**. 0.2% proof stress, tensile strength, uniform elongation and reduction of area are given in **table A.I.6** where the uniform elongation is the value of elongation when the value of the tensile strength, R_m , is reached. More experimental results are given in **appendix A table A.A.1**. The results are also in agreement with these of Sasaki et al (1991). It can be noticed in **table A.I.6** that the material ductility, represented by the reduction of the specimen area, does not depend on the tensile strain rate at 625°C.

Temperature	Initial strain rate	$R_p^{0.2}$	Uniform elongation	R_m	Final Elongation	Reduction of area
625°C	$5.10^{-2} s^{-1}$	360 MPa	2.5 %	380 MPa	17.3 %	78.9 %
625°C	$10^{-2} s^{-1}$	345 MPa	0.9 %	360 MPa	15.4 %	79.6 %
625°C	$10^{-3} s^{-1}$	335 MPa	0.8 %	350 MPa	15.3 %	79.1 %
625°C	$10^{-4} s^{-1}$	235 MPa	0.7 %	250 MPa	16.8 %	79.8 %
625°C	$10^{-5} s^{-1}$	190 MPa	1.1 %	210 MPa	15.8 %	78.7 %

Table A.I.6. Main results of tensile tests at 625°C – Effect of the strain rate (P91 steel)

Complementary tests were carried out at 450°C and 550°C with strain rate of $10^{-3} s^{-1}$ to evaluate the effects of the temperature on general mechanical properties (see **table A.I.7**).

Temperature	Initial strain rate	$R_p^{0.2}$	Uniform elongation	R_m	Final elongation	Reduction of area
625°C	$10^{-3} s^{-1}$	330 MPa	0.8 %	350 MPa	15.7 %	79.1 %
550°C	$10^{-3} s^{-1}$	360 MPa	2.6 %	435 MPa	15.8 %	69.3 %
450°C	$10^{-3} s^{-1}$	390 MPa	4.9 %	550 MPa	15.6 %	54.2 %

Table A.I.7. Tensile properties of P91 steel at 450, 550 and 625°C with the same strain rate $10^{-3} s^{-1}$ – Effect of temperature

Very low uniform elongations ($\approx 1.0\%$ at 625°C and $\approx 3.0 - 4.0\%$ at 450°C and 550°C) before material softening were found. This point has been investigated by Guetaz et al (2003) in the case of a 9Cr1W-V steel who performed TEM investigations and also TEM in-situ tensile tests at both 20°C and 550°C.

The main conclusions of the study of Guetaz et al (2003) that can explained the role of the temperature on tensile properties are as follow:

1. The Burgers vector of the mobile dislocations is $\frac{1}{2} \langle 111 \rangle$. The dislocation core is laid out in the three {110} planes containing the Burgers vector $\frac{1}{2} \langle 111 \rangle$.
2. When increasing temperature higher than 200°C, the Peierls stress is very low (< 10 MPa in α iron see Jaoul (1965)). Note however, that this transition temperature is probably higher as chromium strongly modify the dislocation core and increases the Peierls stress.
3. The material exhibits initially a very high dislocation density which increases rapidly within the lath martensite.
4. Both dislocation cross-slip and climb are facilitated due to thermal agitation so that the dislocation recovery occurs all the more quickly than the temperature is high.

It can also be noticed in **table A.I.7** that the material ductility, represented by the reduction of the specimen area, decreases with the tests temperature.

Tensile tests were carried out in the same strain rate range for the T91 steel at 450°C and 550°C. The measured tensile properties are listed in **table A.I.8**. More experimental results are given in **appendix A table A.B.1** and **table A.B.2**. It can be especially noticed that the tensile strain rate has a negative effect on the material ductility, represented by the reduction of the specimen area, at both 450°C and 550°C whereas this effect did not exist at 625°C.

Temperature	Initial strain rate	$R_p^{0.2}$	Uniform elongation	R_m	Final elongation	Reduction of area
450°C	$10^{-2} s^{-1}$	415 MPa	5.4 %	470 MPa	15.4 %	50.0 %
450°C	$10^{-3} s^{-1}$	410 MPa	3.7 %	460 MPa	13.6 %	53.5 %
450°C	$10^{-4} s^{-1}$	390 MPa	3.7 %	460 MPa	13.2 %	57.9 %
450°C	$10^{-5} s^{-1}$	385 MPa	3.2 %	455 MPa	11.6 %	63.6 %
550°C	$10^{-2} s^{-1}$	350 MPa	3.7 %	400 MPa	17.2 %	61.0 %
550°C	$10^{-3} s^{-1}$	340 MPa	2.4 %	380 MPa	17.5 %	66.0 %
550°C	$10^{-4} s^{-1}$	330 MPa	1.2 %	345 MPa	15.5 %	71.0 %
550°C	$10^{-5} s^{-1}$	300 MPa	1.1 %	320 MPa	15.5 %	72.7 %

Table A.I.8. Tensile properties of T91 steel at 450 and 550°C for strain rate of 10^{-2} , 10^{-3} , 10^{-4} and $10^{-5} s^{-1}$

The corresponding experimental curves are plotted in **figure A.I.10**. The strain rate sensitivity of the tensile response is clearly evidenced at 550°C (see **figure A.I.10b**) whereas a very limited, but still positive, strain rate sensitivity is observed at 450°C (see **figure A.I.10a**). This point will be explored in the next section.

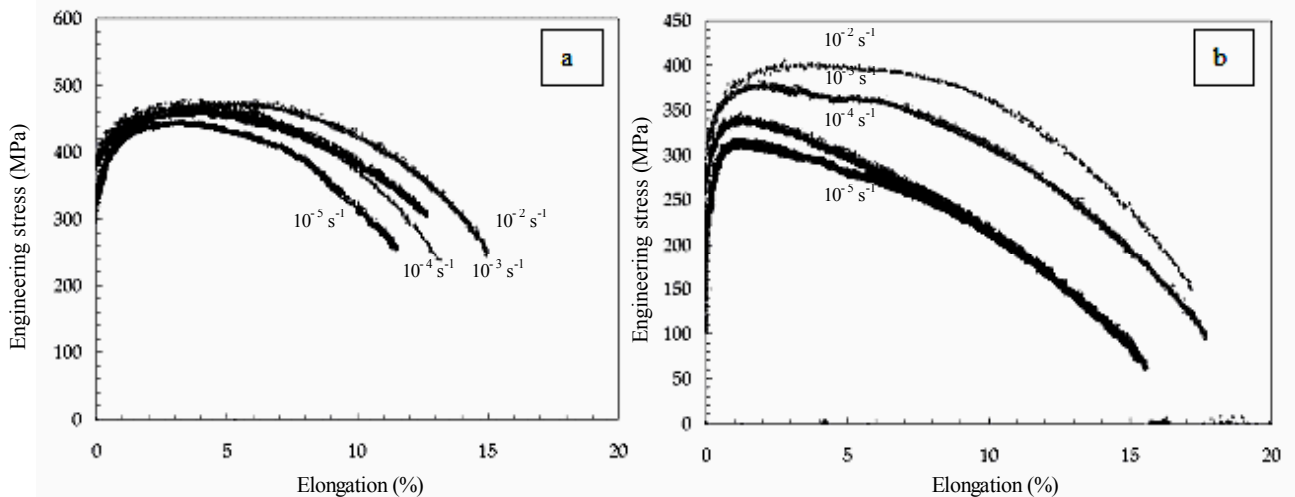
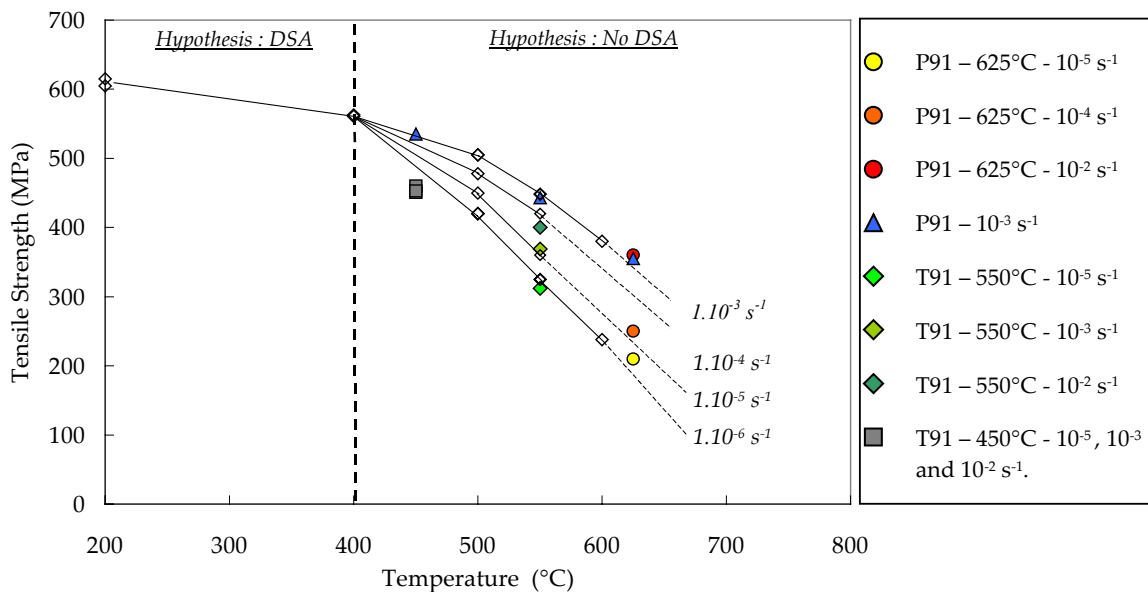


Figure A.I.10. Tensile tests on the T91 steel - (a) at 450°C - (b) at 550°C for strain rates of 10^{-2} , 10^{-3} , 10^{-4} and 10^{-5} s^{-1}

In addition, a comparison of tensile properties at 450°C and 550°C between the P91 and the T91 steels could be made. It showed that the 0.2% proof stress and the tensile strength are considerably lower in the T91 steel. It can be explained by the difference in the tempering heat treatments. Metallurgical changes due to the double tempering treatment for T91 steel led to a more recovered martensitic microstructure with a lower initial dislocation and a lower number of M_{23}C_6 carbides per unit volume. These metallurgical differences are obviously responsible for the lower tensile strength of the T91 steel at 450°C and 550°C.

3.4. Strain rate sensitivity

Tensile tests in the temperature range between 450°C and 625°C showed that the strain rate sensitivity change with the test temperature. A synthesis of strain rate effects on tensile strength for different temperatures is plotted in **figure A.I.11** where experimental results of the present study were added to these of Yaguchi and Takahashi (1999) established for a 9Cr1Mo-NbV steel normalised for 1.5 hour at 1060°C and twice tempered first at 760°C for 1 hour and second at 740°C for 5 hours. A quite good agreement is evidenced with the experimental results of the present study.



** Black lines and open symbols are data from Yaguchi and Takahashi (1999) at 1.10^{-3} , 1.10^{-4} , 1.10^{-5} and 1.10^{-6} s^{-1} .

Figure A.I.11. Effect of temperature and strain rate on tensile strength of P/T 91 steels

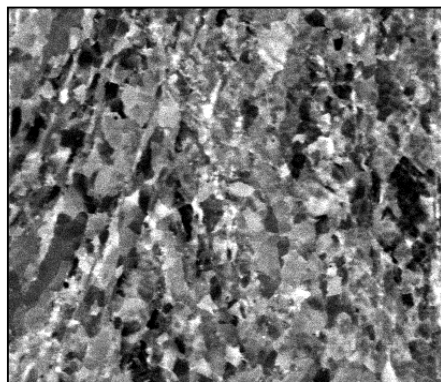
The plots in **figure A.I.11** show that the influence of the strain rate on the tensile response experimentally evidenced is also confirmed by Yaguchi and Takahashi (1999a and 1999b). This influence strongly depends on the testing

temperature. For temperatures larger than 400°C for both the P91 steel and the T91 steel, tensile properties are known to increase with the strain rate. Brinkman et al (1993) confirmed this increase of both the 0.2 % proof stress and the tensile strength with the strain rate. For temperatures below 400°C for the P91 steel and the T91 steel, the strain rate has no more effect which can be related to the dynamic strain ageing (DSA). The DSA phenomenon has already been outlined by Massol and Leclercq (2003), Nagesha et al (2002), Armas et al (1998) and Van der Schaege et al (1992) in low cycle fatigue conditions. In the temperature range between 27°C and 450°C, it was observed that the peak tensile stress of the hysteresis loops increased when lowering the strain rate. Yaguchi, Takahashi (1999a) and Choudhary et al (1999a) have observed the DSA during tensile deformation below 450°C. Choudhary et al (1999b) performed calculations of the activation energy for solute migration leading to the value of 83 kJmol⁻¹ (This result is valid between 27 and 400°C) which is consistent with the diffusion of interstitial solutes like C in bcc metals.

The DSA is due to the interaction of solute atoms (essentially C and N) with dislocations during plastic deformation (see Krauss (1999)). The dislocations which are saturated with carbon or nitrogen atoms are unable to cross-slip and generate new dislocations necessary to maintain plastic deformation and a serrated yielding is reached. Choudhary et al (1999b) showed that prior thermal ageing reduces DSA effects, with respect to the tempered state, as C and N concentrations in solid solution are lowered. However, Mohan and Marschall (1998) remind that the amount of dissolved nitrogen or carbon necessary to cause DSA is extremely low: 0.0004 – 0.002 wt%. Position of the DSA domain are difficult to define for the P91 and the T91 steels as tensile tests at 400°C would have give more arguments to state about this point. However, as the strain rate is still positive but very limited at 450°C, DSA related metallurgical evolutions probably starts to proceed at this temperature.

3.5. Metallurgical changes during tensile deformation

Very few cavities are observed in cross-sections of tensile tested specimens for both the P91 and the T91 steel in the temperature range from 450°C to 625°C. Moreover, these cavities are only located in highly deformed area (i.e. in the necking area with a reduction of area larger than 60%). Final reduction of area of specimens is larger than 75% at 625°C (consistent with Brinkman et al (1993)) and from SEM investigations (see **figure A.I.12**), one can see that either recovery or recrystallisation of the material occurs as the initial lath martensite microstructure has disappeared. The micrograph of **figure A.I.12** shows a microstructure of equiaxed grains which are not elongated despite the high strain level reached in the necking area.



20 μm


Figure A.I.12. Evidences of the modification of the initial lath microstructure during tensile deformation (MEB observation after colloidal silica polishing)

An additional study using the electron backscattered diffraction (EBSD) facility was performed to investigate the changes in lath morphology. The EBSD map in **figure A.I.13** confirms that the lath morphology has totally disappeared with a final microstructure composed of small equiaxed grains (Note that the EBSD map was performed along the loading direction).

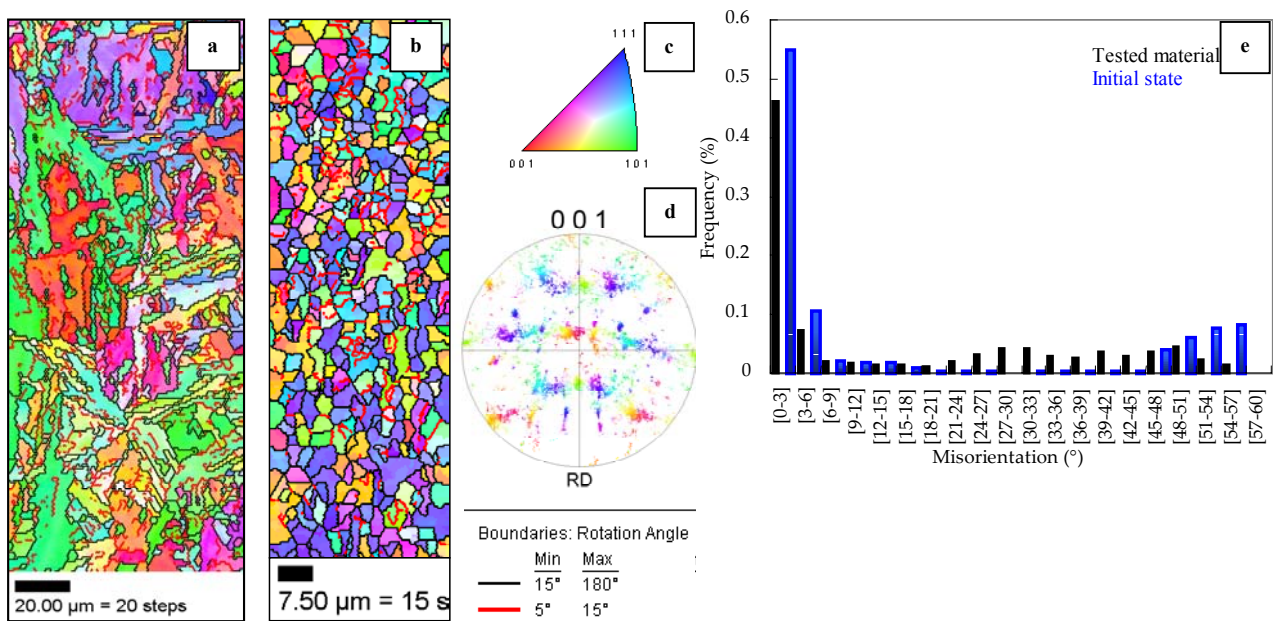


Figure A.I.13. EBSD maps (a) initial state, (b) in the necking area after tensile test at 625°C (10^{-3} s^{-1}), (c) colour key, (d) {001} pole figure and (e) Misorientation angle histogram (between neighbouring grains)

Angles misorientation distributions can be compared with the same plot for the initial state. One can show that angles misorientation are higher than in the initial state even if the fraction of low angle boundaries is still very high. Moreover, it is shown in **figure A.I.13b** that the grain boundaries of the small equiaxed grains are high angle boundaries ($> 15^\circ$) and the pole figure indicates that the material is textured, which confirms that the recrystallisation of the initial microstructure has probably proceeded. The material softening during tensile deformation is not reported in the literature. However, many authors like Armas et al (2002) and Nagesha et al (2002) have already evidenced such microstructural changes in cyclic loading conditions.

3.6. Conclusions

The main results of tensile tests experiments are:

1. For $T > 450^\circ\text{C}$, the sensitivity of the tensile strength to the strain rate is positive.
2. For $T < 450^\circ\text{C}$, dynamic strain ageing probably occurs. Solute atmospheres formed around dislocations and the strain rate sensitivity is inverted.
3. For the three temperatures experimentally explored, a quite low deformation level before the onset of material softening is evidenced particularly at 625°C. This observation let foresee a rapid recovery of the material microstructure during creep at high temperature.

4. Effects of thermal ageing

4.1. Background

The long-time creep strength of the material is strongly related to its microstructural stability. Therefore, many studies have addressed the evaluation of the effects of thermal ageing in terms of both:

1. Metallurgical changes (Evolution of the precipitation state and of the lath martensite microstructure: recovery or recrystallisation).
2. Evolution of mechanical properties (tensile properties or tenacity).

Many studies were concerned with evaluating the effect of ageing on 9Cr and 12Cr steels: Hofer et al (2000), Lundin et al (2000), Schaffernack et al (2000), Hofer et al (1999), Okamura et al (1999), Alamo et al (1996), Brinkman et al (1993), Saroja et al (1993), Brachet (1991), Zhang et al (1991), Sasaki et al (1991) and Schinkel et al (1984). These works were concerned with ageing in the temperature range between 400°C to 650°C with ageing durations up to 75,000 hours. The effects of ageing were evaluated from TEM observations, analysis of carbon extraction replicas, hardness measurements and mechanical tests of mainly impact toughness and tensile types. The main conclusions which can be given are:

1. Hardness measurements evidence a slight softening with ageing duration (typically 20 HV after 5,000 hours) and tensile tests revealed a decrease in the 0.2% proof stress and the tensile strength after ageing at temperatures higher than 500°C.
2. Laves phase (Fe₂Mo or (Fe,Cr)₂Mo) precipitation occurs after 1,000 hours for ageing at temperatures higher than 600°C. The Laves phase precipitation is promoted for high Si contents (> 0.3 wt%). It is also outlined that Laves phase precipitate near M₂₃C₆ carbides and that their coarsening rate is between 2 and 4 times lower than that of the M₂₃C₆ carbides.
3. Carbides coarsening occurs for ageing at temperatures larger than 500°C and can be well represented by the Lifshitz-Slyosov-Wagner equation (Lifshitz and Slyosov (1961), Wagner (1961)).
4. The precipitation of a complex carbo-nitride, the modified Z-phase, is reported for long term ageing (after more than 30,000 hours at 600°C). The properties of this phase are unfortunately poorly characterised yet.
5. A decrease in the impact properties is observed. Alamo et al (1996) considered that it is due to Laves phase precipitation under the form of brittle thin films on boundaries. Sasaki et al (2000) have also attributed the decrease of the Charpy energy, after ageing at 600-650°C, to the Laves phase precipitation.

Many experimental studies were concerned with evaluating the evolution of the Laves phase precipitation during thermal ageing. Korkacova et al (2001) and then Dimmler et al (2004) introduced a technique based on the use of the SEM with backscattered electron channelling contrast. Indeed, the backscattered signal can be related to the atomic number of atoms by: $\eta = -0.0254 + 0.016Z - 0.000186Z^2 - 0.0000083Z^7$ where Z is the atomic number (Note that it was shown, according to Monte Carlo simulations, that the backscatter coefficient η does not depend on the acceleration voltage in the range 3kV - 30kV). They used the higher backscattered signal of Laves phase to identify them among the other particles.

Stocker et al (2002) and Dimmler et al (2004) used their observations to quantitatively determine the evolution of Laves phase surface fraction using a classical Johnson-Mehl-Avrami representation:

$$f_{Lp} = f_{max} \left[1 - \exp \left(- \left(\frac{t}{t_0} \right)^n \right) \right] \quad (\text{eq. A.I.18})$$

Their results are given in **figure A.I.14** in terms of f_{Lp}/f_{max} for thermal ageing at 650°C and 600°C. It shows that Laves phase precipitation is nearly complete after 30,000 hours at 600°C for 9Cr1Mo-NbV steels. The predicted Laves phase precipitation diagram are quite different from one author to another as Laves phase precipitation behaviour obviously strongly depend on both thermal treatments and the chemical composition of the steel.

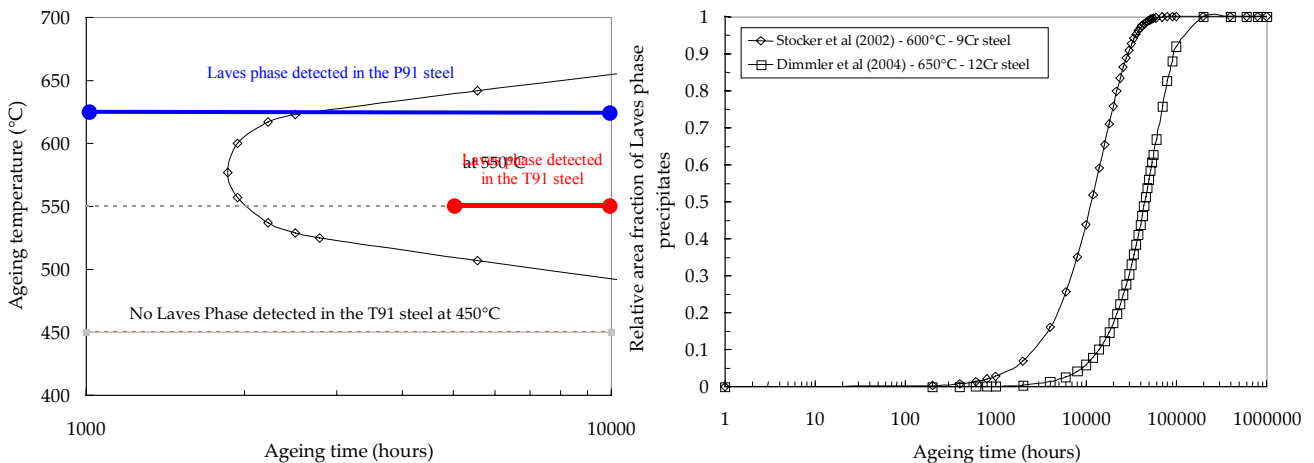


Figure A.I.14. Laves phase precipitation diagram from Klueh and Harries (2001),Stoker et al (2002) and Dimmler et al (2004)

The following step (i.e. for $f_{Lp} = f_{max}$) corresponds to the Laves phase particles coarsening that can be well represented by the Lifshitz-Slyosov-Wagner equation (Lifshitz and Slyosov (1961), Wagner (1961)). Laves phase solubility is also simply described by Senior (1989) as:

$$\ln([Si]^{0.7} [Mo]^{0.8}) = 3.47 - \frac{33.572}{T} \quad (\text{eq. A.I.18})$$

The evolution of the total weight of carbides during ageing were measured by numbers of authors. The experimental procedure consists in selective dissolution of carbides in electrolyte. Mujahid et al (1999) proposed a 10% solution of HCl in methanol for matrix dissolution and a 10g solution of oxalic acid in water to dissolve carbides. Solignac (1994) indicated a current of extraction of 0.1 Acm². Following this technique, an attempt was made to measure the evolution of weight fractions of precipitate during ageing. It was not possible to process the results because the residues resulting

from the extraction where not only composed of extracted precipitates. However, some results found in literature are given in **figure A.I.15**. Slight variations in total weight of precipitates are recorded for ageing up to 80,000 hours between 480°C and 650°C. The tendencies are quite different from one author to another which shows that the experimental measurement of the total weight of carbides is a quite difficult work.

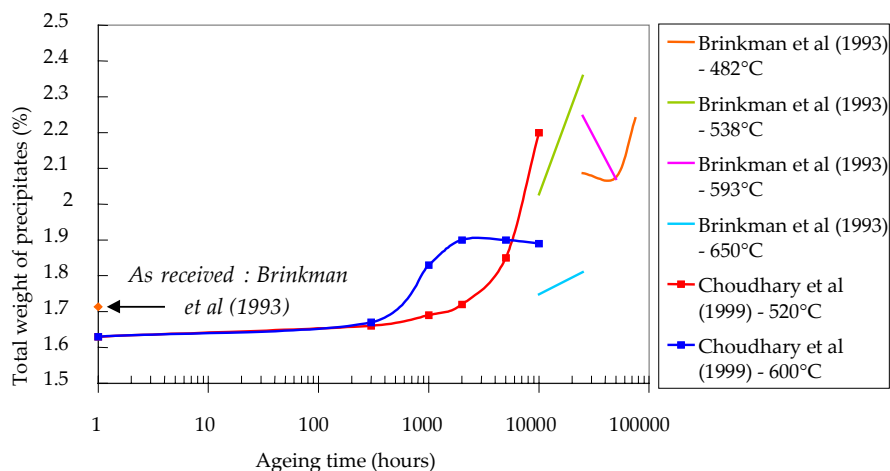


Figure A.I.15. Evolution of total weight fraction of carbides during thermal ageing (Synthesis)

As phosphorous and sulphur both enter in the chemical composition of the alloys, one should be interested in evaluating their ability to segregate at grain boundaries. Phosphorous segregation in 9Cr1Mo-NbV steels during thermal ageing is reported by Perhacova et al (2001) at 500°C, Lundin and Richarz (1995) for ageing between 480 and 650°C up to 10,000 hours and Hipplesley and Druce (1983). Their conclusions are similar: phosphorous segregates at particle (Carbides and Laves phases) / matrix interfaces and the segregation is confined to one atomic plane within the interface. The explanation given by Yuqing and McMahon (1987) is that phosphorous segregation is possible where carbon and chromium activities in solid solution are low, which means near $M_{23}C_6$ and Laves phase particles. Lundin et al (2000) considered that phosphorous segregation at matrix / $M_{23}C_6$ interface promotes heterogeneous Laves phase precipitation near $M_{23}C_6$ carbides. This hypothesis is confirmed by Suzuki et al (1986) also underlined the high interaction energy between phosphorous and molybdenum. In fact, phosphorous and sulphur segregate near the carbides and their segregation in grain boundaries is too limited to promote intergranular cracking.

4.2. Experiments

Ageing heat treatments were performed on P91 and T91 steels from 1,000 to 10,000 hours at 450°C and 550°C for the T91 steel and at 550°C and 625°C for the P91 steel. (The table of experiments is given in **appendix A - table A.G.1**). To evaluate metallurgical changes during tempering, the following works were performed:

1. Hardness measurements (HV 0.5, 50 hardness measurements per specimen).
2. Measurements of particles size and chemical composition after extraction on carbon replicas (The technique was introduced and described in **section D.I.2** and **appendix B.H**).
3. X-Ray diffraction as the precipitation of Laves phase induces a change in the matrix crystal lattice parameter due to the precipitation of Mo (The method has been introduced and successfully used by Brachet (1991) and Alamo et al (1996)).
4. TEM observations (Thin foil preparation is described in **appendix B.H**) with the collaboration of Dr. Y. de Carlan and Dr. L. Guetaz from the "Commissariat à l'Énergie Atomique".

Hardness measurements (see **figure A.I.16**) did not show any significant softening of the steels during ageing except for the P91 steel at 625°C as a drop of nearly 40 HV_{0.5} was found between the initial state and after 10,000 hours of ageing at 625°C.

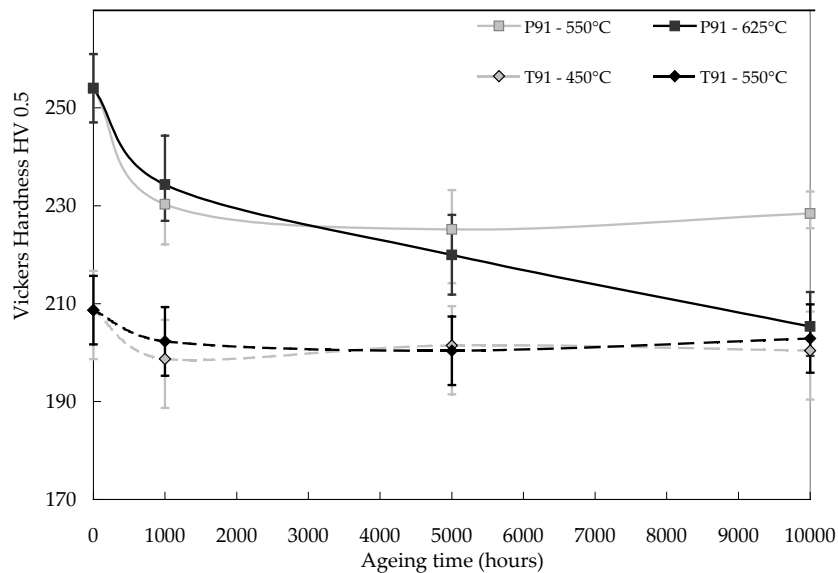


Figure A.I.16. Evolutions of Vickers Hardness during thermal ageing at 450°C and 550°C for T91 steel, 550°C and 625°C for P91 steel

4.3. Evolution of the precipitation state by SEM investigations

The evolution of the precipitation state was studied from SEM investigations performed on carbon extraction replicas. First, X-Ray energy dispersion spectroscopy analysis was performed to identify second phase particles. Results of particles identification showed that:

1. Laves phase appear after 1,000 hours of ageing both at 550°C and 625°C for the P91 steel and at 550°C for the T91 steel. No Laves phase was detected for ageing up to 10,000 hours at 450°C.
2. The enrichment of $M_{23}C_6$ carbides in Cr was observed during ageing at 550°C and 625°C which is consistent with Saroja et al (1993) who relates it to the difference in mobility of Fe and Cr atoms at high temperature.
3. From experimental measurements, presence of phosphorous mainly in Laves phase particles was detected for ageing up to 5,000 hours at 550°C and 625°C. This result is very interesting as dissolution of phosphorous near Laves phase particles ensure the absence of any grain boundary segregation.

Following the procedure described in **section A.I.2** but also in **appendix B.H**, the particles size were measured. The equivalent diameter d , which is the diameter of a circle equal in area to the measured area was used as the parameter for the characterisation of the particle size. An histogram of particle size distribution could then be plotted. This histogram must be carefully interpreted as three populations of precipitates are represented. However, as underlined by the representation of Dimmler et al (2004), the maximum of the histogram of size distribution gives a good approximation of $M_{23}C_6$ carbides average size (see **figure A.I.17**).

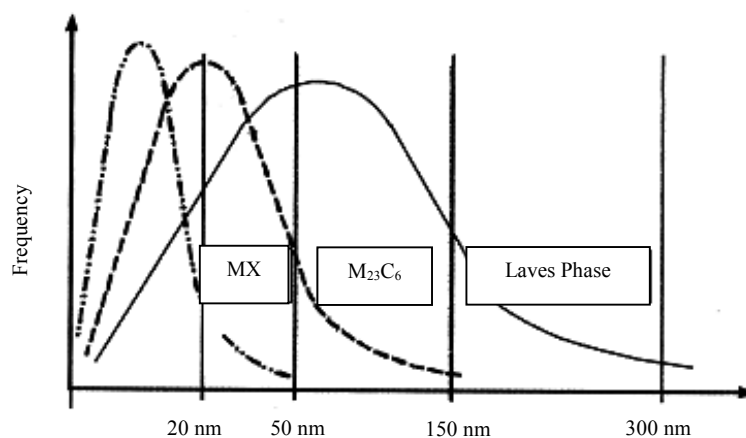


Figure A.I.17. Interpretation of histogram of second phase particle distribution (from Dimmler et al (2004) for a 9Cr1Mo-NbV steel)

It seems in particular difficult to separately assess the evolution of the size of MX (left part of the histogram) and Laves phase (right part of the histogram). Therefore, it was chosen to only consider the maximum of the distribution, which

corresponds, to the most important population of precipitates in the considered material: the $M_{23}C_6$ carbides. Results of the $M_{23}C_6$ particles size measurements are given in **figure A.I.17**.

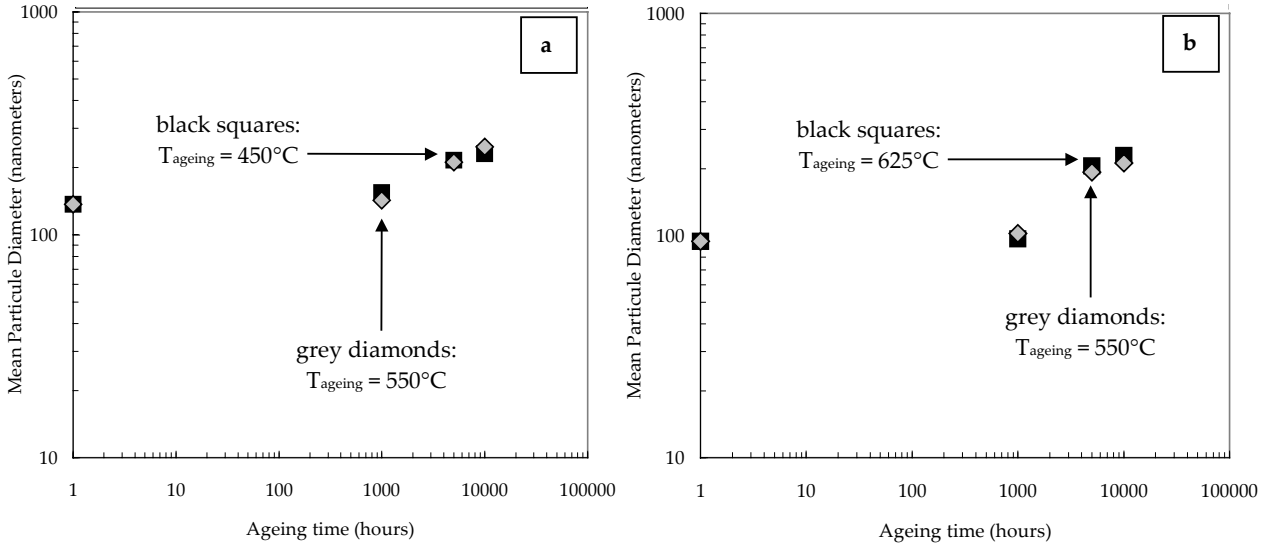


Figure A.I.18. Average particle size evolution during stress free thermal ageing at 450 and 550 °C for T91 steel and 550 and 625°C for P91 steel

Main conclusions about the results given in **figure A.I.18**. are:

1. The particle size did not significantly increase for ageing up to 1,000 hours.
2. $M_{23}C_6$ average size increased for ageing larger than 1,000 hours at 550°C and 625°C for P91 steel.

The evolution of the carbide size for ageing times larger than 1,000 hours was well described using the classical Lifshitz, Slyosov, Wagner (LSW) law of coarsening (Lifshitz and Slyosov (1961), Wagner (1961)):

$$r^3 - r_0^3 = K_d t \quad (\text{eq. A.I.20})$$

All results are reported in **table A.I.9**. For comparison, Hald and Straub (1998) gave $K_d = 1.5 \cdot 10^{-29} \text{ m}^3\text{s}^{-1}$ for ageing at 600°C. The average value of the $M_{23}C_6$ carbides in the initial state i.e. normalised and tempered material, $r_0 = d_0/2$, already given in **table A.I.3** is reported as it is used to fit **equation A.I.20**.

Steel	Ageing temperature	K_d
P91 ($r_0 = 48 \text{ nm}$)	550°C	$3.2 \cdot 10^{-29} \text{ m}^3\text{s}^{-1}$
	625°C	$4.2 \cdot 10^{-29} \text{ m}^3\text{s}^{-1}$
T91 ($r_0 = 68 \text{ nm}$)	450°C	$3.2 \cdot 10^{-29} \text{ m}^3\text{s}^{-1}$
	550°C	$4.7 \cdot 10^{-29} \text{ m}^3\text{s}^{-1}$

Table A.I.9. Evaluation of $M_{23}C_6$ coarsening kinetics during thermal ageing

The kinetics constant K_d at 550°C is higher for T91 steel than for P91 steel probably because the initial precipitation state is different. Indeed from the thermodynamical point of view (cf. the classical theory of nucleation), the growth rate of an existing precipitates is all the more fast that its initial size is large.

Following a technique introduced by Brachet (1991) and Alamo et al (1996), the occurrence of Laves phase precipitation was also confirmed by X-Ray diffraction measurements (see **figure A.I.19**). Indeed, it is assumed that Laves phase precipitation imply a decrease of the martensite lattice parameter due to a decrease in Mo content in the solid solution which is observable as the atomic number of Mo is quite high ($Z = 42$).

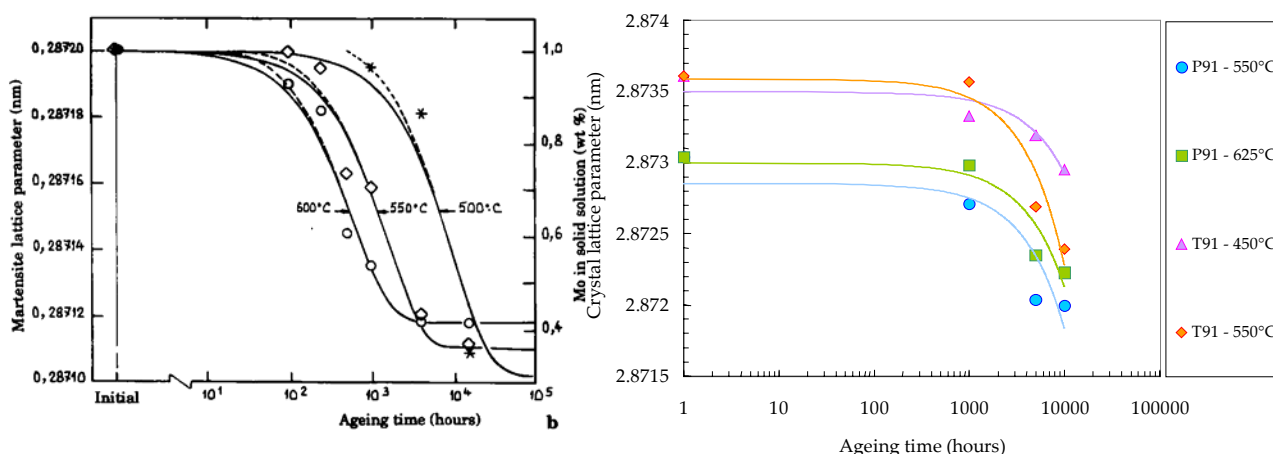

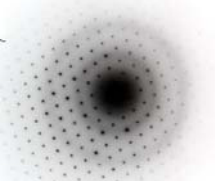
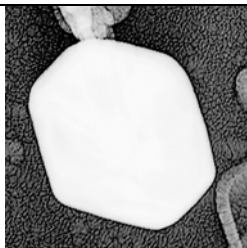
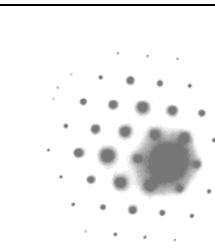


Figure A.I.19. Description of Laves phase precipitation using crystal lattice parameter measurements (X-Ray diffraction)
(a) Brachet (1991) – (b) Results of the present study

It is shown in **figure A.I.19** that the Laves phase precipitation starts after 1,000 hours of ageing for the P91 steel both at 550 and 625°C and for the T91 steel at 550°C. The crystal lattice parameter of the T91 steel slightly evolve at 450°C which shows that if Laves phase precipitation occurs, this phenomenon is very limited. In fact, the X-Ray diffraction measurements of **figure A.I.19** confirm the results of X-Ray EDS analysis on carbon extraction replica.

4.4. TEM investigations

TEM investigations were also performed to ensure the validity of the results previously given. First, all the precipitates were identified with performing EDS X-ray analysis. Those measurements gave information about precipitate type but one could not ensure their real nature. Therefore, using a TEM, diffraction patterns and corresponding EDS X-ray analysis of several precipitates were performed in order to associate one precipitate with its representative chemical composition evaluated by EDS X-ray analysis (Note that EDS X-ray analysis can not be used to determine carbon, oxygen and nitrogen contents). Diffraction patterns were compared to simulated patterns so as to determine the crystallography of precipitates. A free software developed by the EPFL available on the world-wide web: <http://cimewww.epfl.ch/> was used to simulate the diffraction patterns. The results of the study are reported in **table A.I.10**. They confirmed the validity of the phase identification from EDS X-ray analysis.

Type of precipitate	Dark field image of the precipitate and diffraction pattern (TEM investigations)	Chemical composition measured by EDS X-Ray analysis in the TEM														
Carbide $M_{23}C_6$	  (Zone axis [110]) ⇒ face centred cubic with $a = 1.05 - 1.15$ nm	$Cr_{23}C_6$ (Fe, Mo) <table border="1"> <thead> <tr> <th>Element</th> <th>wt %</th> </tr> </thead> <tbody> <tr> <td>Cr</td> <td>54-65</td> </tr> <tr> <td>Fe</td> <td>28-32</td> </tr> <tr> <td>Mo</td> <td>7-10</td> </tr> <tr> <td>Nb</td> <td>0-2</td> </tr> <tr> <td>V</td> <td>0-2</td> </tr> <tr> <td>Si</td> <td>2-4</td> </tr> </tbody> </table>	Element	wt %	Cr	54-65	Fe	28-32	Mo	7-10	Nb	0-2	V	0-2	Si	2-4
Element	wt %															
Cr	54-65															
Fe	28-32															
Mo	7-10															
Nb	0-2															
V	0-2															
Si	2-4															
Laves Phase Fe_2Mo + (V,Nb,Si)	  (Zone axis [111]) ⇒ hexagonal with $a = 0.47 - 0.48$, $c = 0.44 - 0.45$	Fe_2Mo (Cr,V,Nb,Si) <table border="1"> <thead> <tr> <th>Element</th> <th>wt %</th> </tr> </thead> <tbody> <tr> <td>Cr</td> <td>7-10</td> </tr> <tr> <td>Fe</td> <td>43-49</td> </tr> <tr> <td>Mo</td> <td>35-41</td> </tr> <tr> <td>Nb</td> <td>0.2-3</td> </tr> <tr> <td>V</td> <td>0.3-1</td> </tr> <tr> <td>Si</td> <td>4-8</td> </tr> </tbody> </table>	Element	wt %	Cr	7-10	Fe	43-49	Mo	35-41	Nb	0.2-3	V	0.3-1	Si	4-8
Element	wt %															
Cr	7-10															
Fe	43-49															
Mo	35-41															
Nb	0.2-3															
V	0.3-1															
Si	4-8															

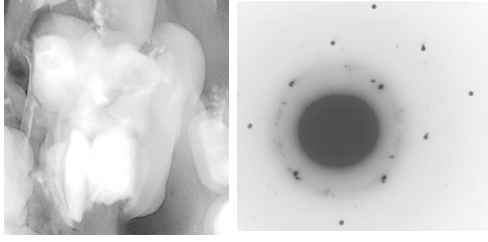
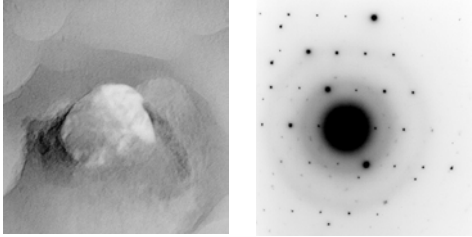
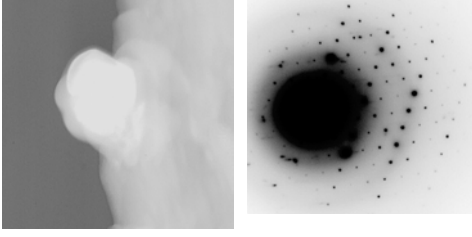
Type of precipitate	Dark field image of the precipitate and diffraction pattern (TEM investigations)	Chemical composition measured by EDS X-Ray analysis in the TEM														
Laves Phase (Fe,Cr) ₂ Mo + (V,Nb,Si)	 <p>100 nm</p> <p>⇒ hexagonal with $a = 0.47 - 0.48$; $c = 0.44 - 0.45$</p>	(Fe,Cr) ₂ Mo (V,Nb,Si) <table border="1"> <thead> <tr> <th>Element</th> <th>wt %</th> </tr> </thead> <tbody> <tr> <td>Cr</td> <td>30-35</td> </tr> <tr> <td>Fe</td> <td>30-35</td> </tr> <tr> <td>Mo</td> <td>30-35</td> </tr> <tr> <td>Nb</td> <td>1-2</td> </tr> <tr> <td>V</td> <td>1-2</td> </tr> <tr> <td>Si</td> <td>4-8</td> </tr> </tbody> </table>	Element	wt %	Cr	30-35	Fe	30-35	Mo	30-35	Nb	1-2	V	1-2	Si	4-8
Element	wt %															
Cr	30-35															
Fe	30-35															
Mo	30-35															
Nb	1-2															
V	1-2															
Si	4-8															
V(N,C)	 <p>50 nm</p> <p>(Zone axis [111]) ⇒ indexed as face centred cubic $a = 0.4 - 0.5$ nm</p>	V(N,C) - NaCl type crystallographic structure <table border="1"> <thead> <tr> <th>Element</th> <th>wt %</th> </tr> </thead> <tbody> <tr> <td>Cr</td> <td>8-10</td> </tr> <tr> <td>Fe</td> <td>0-1</td> </tr> <tr> <td>Mo</td> <td>0-1</td> </tr> <tr> <td>Nb</td> <td>10-15</td> </tr> <tr> <td>V</td> <td>70-80</td> </tr> <tr> <td>Si</td> <td>0-1</td> </tr> </tbody> </table>	Element	wt %	Cr	8-10	Fe	0-1	Mo	0-1	Nb	10-15	V	70-80	Si	0-1
Element	wt %															
Cr	8-10															
Fe	0-1															
Mo	0-1															
Nb	10-15															
V	70-80															
Si	0-1															
Nb (N,C)	 <p>100 nm</p> <p>(Zone axis [110]) ⇒ indexed as face centred cubic $a = 0.4 - 0.5$ nm</p>	Nb (N,C) - NaCl type crystallographic structure <table border="1"> <thead> <tr> <th>Element</th> <th>wt %</th> </tr> </thead> <tbody> <tr> <td>Cr</td> <td>5-10</td> </tr> <tr> <td>Fe</td> <td>2-5</td> </tr> <tr> <td>Mo</td> <td>10-15</td> </tr> <tr> <td>Nb</td> <td>55-65</td> </tr> <tr> <td>V</td> <td>10-15</td> </tr> <tr> <td>Si</td> <td>0-1</td> </tr> </tbody> </table>	Element	wt %	Cr	5-10	Fe	2-5	Mo	10-15	Nb	55-65	V	10-15	Si	0-1
Element	wt %															
Cr	5-10															
Fe	2-5															
Mo	10-15															
Nb	55-65															
V	10-15															
Si	0-1															

Table A.I.10. Identification of the correspondence between the crystal structure of precipitate and its chemical composition by TEM investigations

TEM investigations show that $M_{23}C_6$ carbides exhibit various shapes: penny or spherical. Moreover, it was suggested, considering the shape of precipitates, that only a few of them are coherent with the matrix but majority is either non coherent or semi-coherent with the matrix. It was also found that MX particles were mainly spherical, very few elongated MX precipitates were observed. It will be shown in **Part B** that this point may be very important as the shape of the strengthened MX precipitates strongly determine the material creep strength. As this work was out of the scope of the present study, orientation relationship between precipitates and the martensite matrix were not investigated.

TEM micrographs and EBSD analysis were performed on the P91 steel after 10,000 hours of ageing at 550 and 625°C (see **figure A.I.20**).

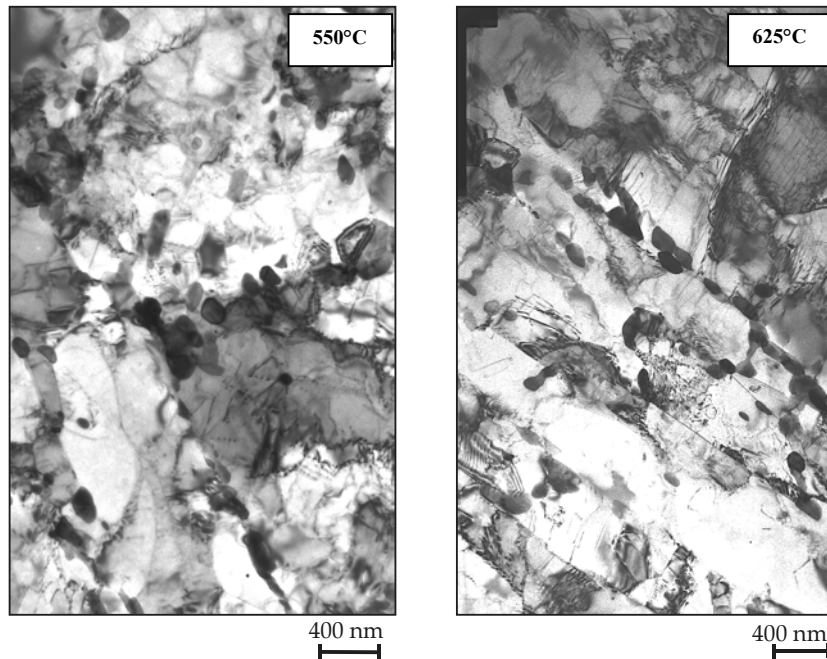


Figure A.I.20. Bright fields micrographs of specimens aged for 10,000 hours at 550°C and 625°C (P91 steel)

The conclusions of these observations are qualitative. The two TEM micrographs of the aged materials (figure A.I.20) must be compared to the initial state (figure A.II.10). The two main differences that can be underlined are:

1. The dislocation density obviously decreased during thermal ageing.
2. The lath morphology is somewhat broken in the aged material with the formation of subgrains within the laths.

It can also be noticed that the TEM observations allow to confirm the validity of the particles size measurements made after SEM investigations on carbon extraction replicas.

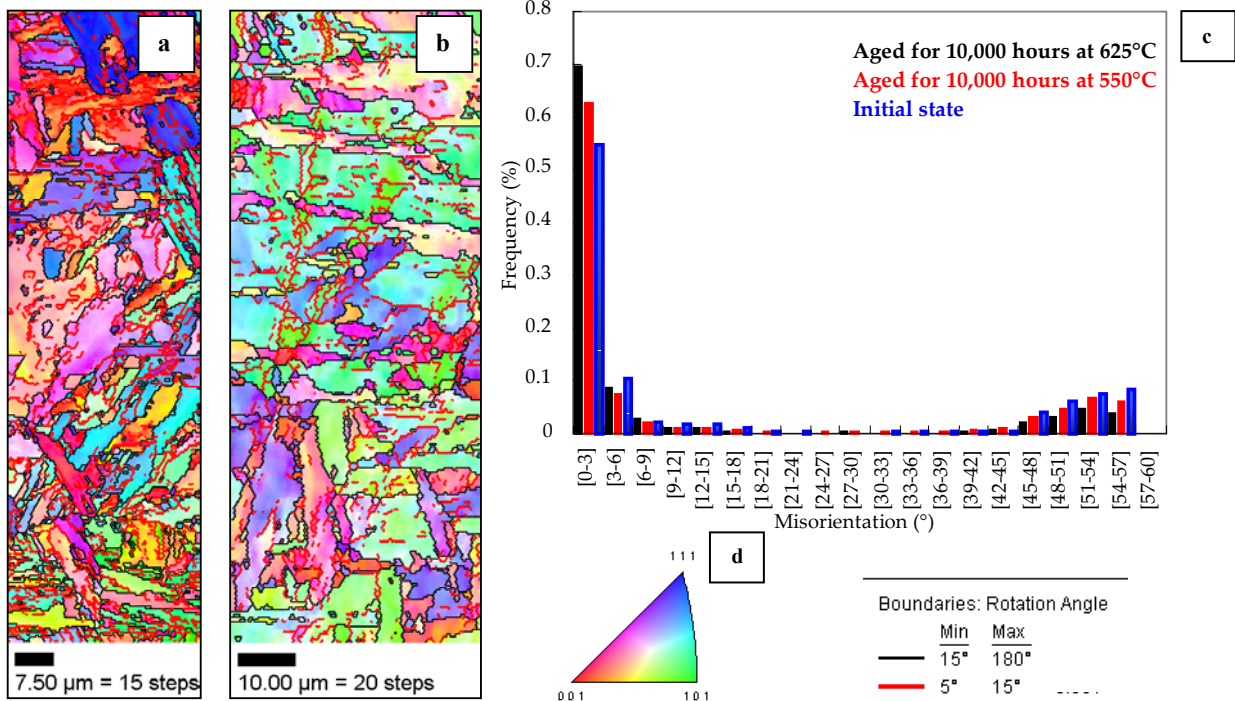


Figure A.I.21. EBSD maps of P91 specimens aged for 10,000 hours at (a) 550°C, (b) 625°C, (c) Misorientation angle histogram (between neighbouring grains) and (d) colour key

The EBSD maps of figure A.I.21 confirmed the TEM observations on a larger scale i.e. the formation of low angle boundaries which correspond to subgrain boundaries within the laths. By comparison with the initial state the fraction of

low angle boundaries ($< 6^\circ$) increases during ageing. Note that the tendency is the opposite to that observed for the material deformed at high temperature (see histogram of **figure A.I.21** by comparison with that given in **figure A.I.13**). In fact, these EBSD analysis on aged materials show that in stress free ageing conditions, both at 550°C and 625°C, the recovery of the initial microstructure proceeds.

4.5. Effect of thermal ageing on tensile properties at 625°C

Tensile tests were performed on P91 steel specimens aged for 10,000 hours both at 550°C and 625°C. The tensile tests were carried out at 625°C. The mechanical properties deduced from these tests are given in **table A.I.11**.

Ageing conditions	Initial strain rate	$R_p^{0.2}$	Uniform elongation	R_m	Final elongation	Reduction of area
550°C – 10,000 hours	10^{-2} s^{-1}	310 MPa	1.3 %	330 MPa	16.9 %	67.7 %
550°C – 10,000 hours	10^{-3} s^{-1}	280 MPa	1.1 %	290 MPa	18.4 %	76.9 %
550°C – 10,000 hours	10^{-4} s^{-1}	235 MPa	1.0 %	245 MPa	20.0 %	77.2 %
550°C – 10,000 hours	10^{-5} s^{-1}	190 MPa	1.5 %	200 MPa	16.8 %	75.2 %
625°C – 10,000 hours	10^{-2} s^{-1}	310 MPa	1.5 %	330 MPa	17.8 %	73.9 %
625°C – 10,000 hours	10^{-3} s^{-1}	270 MPa	0.9 %	280 MPa	16.5 %	78.5 %
625°C – 10,000 hours	10^{-4} s^{-1}	225 MPa	0.8 %	235 MPa	16.1 %	79.6 %
625°C – 10,000 hours	10^{-5} s^{-1}	185 MPa	1.5 %	195 MPa	15.2 %	79.7 %

Table A.I.11. Results of tensile tests at 625°C carried out on aged specimens

The effect of ageing on mechanical properties deduced from the comparison of **table A.I.6.** and **table A.I.12** are as follows :

1. The effects of ageing at 550°C and 625°C are very similar.
2. A decrease in the 0.2% proof stress and the tensile strength of 20 – 30 MPa is observed for all strain rates.
3. The values of the uniform and final elongation are not affected by thermal ageing. Metallographic investigations also revealed the recrystallisation of the initial lath martensite and the absence of any significant damage in fractured specimens outside the area very close to the fracture surface as already observed for the material in the initial state.
4. As can be shown in **figure A.I.22**, the aged materials also exhibit a significant and positive strain rate sensitivity of the mechanical properties.

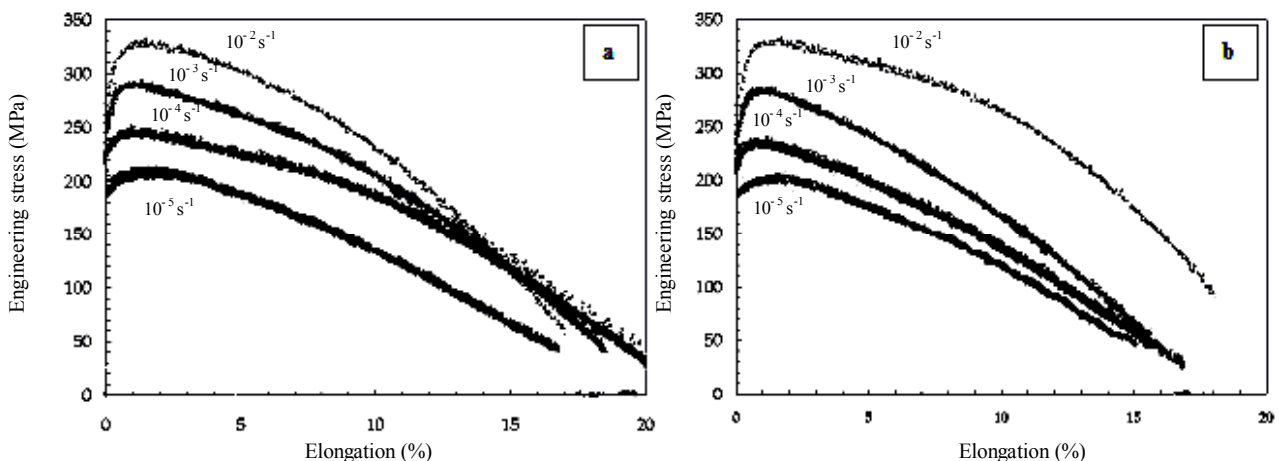


Figure A.I.22. Tensile tests at 625°C on aged P91 steel (a) after 10,000 hours at 550°C – (b) after 10,000 hours at 625°C

5. Environmental effects

The study was not concerned with environmental effects. However, some points about oxidation of P/T91 steels may be given. Laverde et al (2004) studied oxidation due to steam at 575, 600 and 650°C. They found that the oxidation proceeds by the formation of three distinct layers respectively constituted by $(\text{Fe,Cr})_3\text{O}_4$, Fe_3O_4 and Fe_2O_3 . These results are consistent with those given by Tokei et al (2000) and Greef et al (2000). Ishitsuka et al (2004) studied the influence of silicon content on oxidation in steam environment. They found that Si promotes the formation of a SiO_2 protective film and of a Fe_2SiO_4 protective layer especially for temperatures larger than 650°C. They also show a strong dependence of

the oxidation behaviour with temperature (see figure A.I.23). A transition region for temperature between 600°C and 650°C, corresponding to the formation of the FeO oxide, is observed. In this region, 9Cr1Mo-NbV steels exhibits a higher sensitivity to oxidation (see figure A.I.23 where a strong dependence of oxidation kinetics to temperature is observed). Oxidation kinetics can be described by parabolic laws of the form:

$$\Delta w^2 = k_p t \quad (\text{eq. A.I.21})$$

where Δw is the mass gain due to oxidation and k_p depends on temperature following a classical Arrhenius representation. The evolution of k_p but also the oxide type are given between 500 and 700°C by Ishitsuka et al (2004) in figure A.I.23.

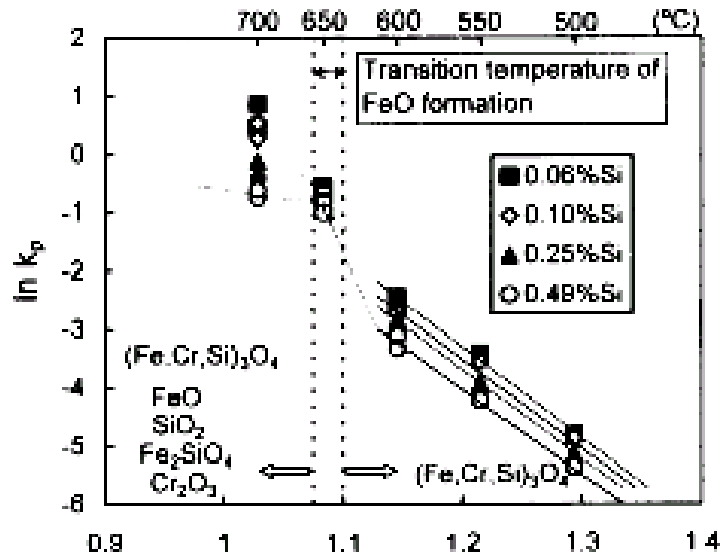


Figure A.I.23. Evolution of oxidation kinetics and chemical composition of oxides between 500 and 750°C from Ishitsuka et al (2004)

However if the addition of Si may increase steam oxidation resistance, Si is also a δ -ferrite former element and it can affect the material ductility. Zurek et al (2004) also evidenced an anomalous dependence of the oxidation kinetics during steam oxidation in the temperature range between 600°C and 650°C. They found that the protective Cr rich oxide layer poorly formed in this temperature range and they related it to the temperature dependence of the diffusion kinetics of Cr and carbide dissolution. Concerning the oxidation sensitivity of 9Cr-1Mo steels, the work of Ennis et al (2002) suggests that an air environment has little effect on 9Cr1Mo-NbV steels. The representation of figure A.I.24 shows that mass gain due to oxidation at 650°C is negligible up to 3,500 hours.

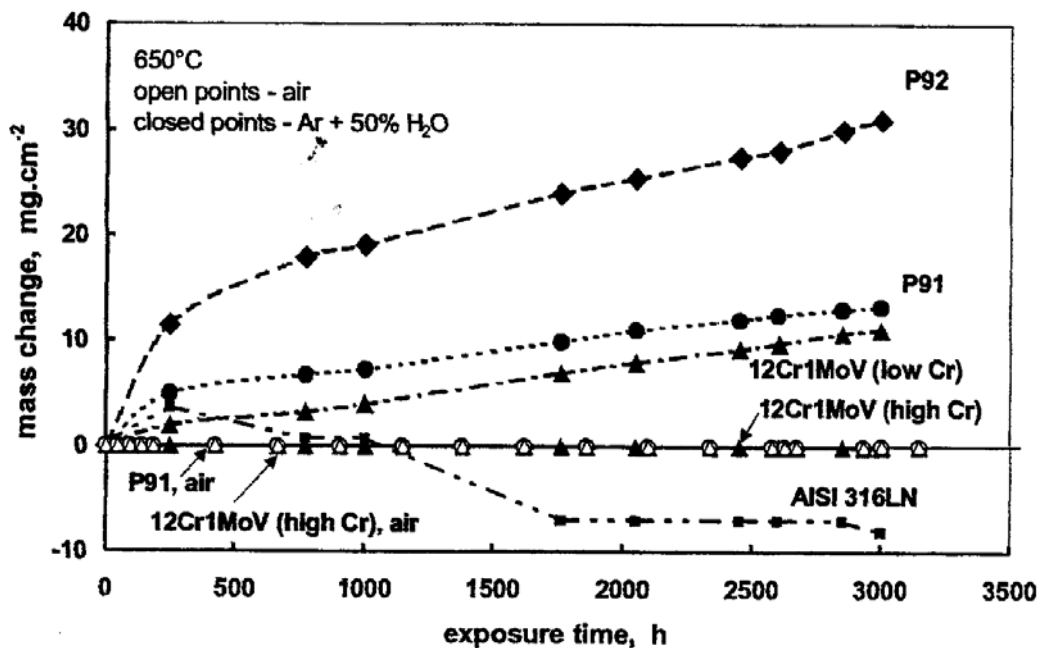


Figure A.I.24. Mass change due to oxidation by air and water exposures from Ennis et al (2002)

The influence of oxidation on kinetics of creep and fatigue crack initiation and propagation was already studied (environmentally assisted cracking). Experiences of the use of chromium ferritic steels for piping in power plants up to 50,000 hours under high temperature steam corrosion environment are reported by Yukitoshi et al (1982) for a 9Cr-2Mo steel. Their analysis showed that the material is not sensitive to corrosion and no damage due to corrosion was evidenced. However, at 550°C, Ogata and Yamamoto (1996 and 1997) found higher kinetics of fatigue crack growth in air than in vacuum at least for initial crack length lower than 1 mm.

However, corrosion obviously does not affect the material creep strength and especially its sensitivity to intergranular cracking. It is currently assumed that corrosion induces a decrease in components wall thickness. Therefore, to account for oxidation phenomena, the plots of the applied engineering stress versus the creep time to failure presented in **figure A.I.25**, which is extracted from Parrot and Shibli (2004), assumed a loss of wall thickness of 0.1 mm per year from each exposed surface.

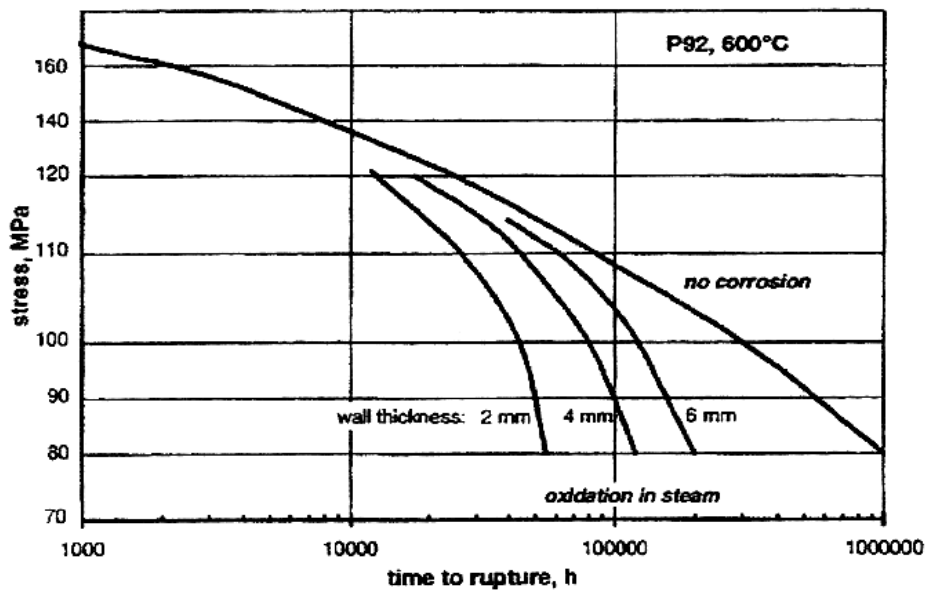


Figure A.I.25. Calculated effect of the stress corrosion on the stress rupture life of P92 tubes at 600°C (Quadackers and Ennis (19998) in Parrot and Shibli (2004))

6. Conclusions

The investigation of the present chapter allow to determine the metallurgical and general mechanical properties of the 9Cr1Mo-NbV steels as well as the effects of thermal ageing. The main conclusions are as follow:

1. The material microstructure resulting from normalising at 1050-1060°C, rapid cooling and high temperature tempering i.e. > 750°C is a lath martensite (0.5 – 2 µm in thickness) arranged in packets (20 – 50 µm in size) within the prior austenite grain (> 100 µm in size) and strengthened by mainly M₂₃C₆ carbides (> 100 nm in size) and MX particles (10 - 20 nm in size). The presence of M₂X precipitates was not evidenced and may probably be related to the high temperature tempering.
2. The material exhibits good high temperature tensile properties with a tensile strength of 350 MPa for a strain rate of 10⁻³ s⁻¹ at 625°C (For comparison, Tavassoli (1998) has reported a tensile strength of 150 MPa for the 316LN stainless steel). A positive strain rate effect is observed for temperatures larger than 450°C whereas the material is obviously sensitive to dynamic strain ageing (DSA) at lower temperatures. It was also shown that the recrystallisation of the initial lath microstructure occurs during tensile deformation between 450°C and 625°C.
3. The material microstructure and tensile properties are affected by thermal ageing between 450°C and 625°C. The lath martensite microstructure is recovered (decrease of the dislocation density and formation of subgrains). M₂₃C₆ carbides coarsen for ageing times larger than 1,000 hours. Laves phase precipitation occurs for ageing times larger than 1,000 hours and ageing temperatures larger than 450°C. Both the 0.2 % proof stress and the tensile strength are lowered by 20 - 30 MPa after 10,000 hours of ageing. Note also that the precipitation of a Z-phase which is a complex carbo-nitride is reported for an ageing time larger than 30,000 hours in the literature.
4. As phosphorous and sulphur are dissolved into M₂₃C₆ carbides and Laves phase, 9Cr1Mo-NbV steels are obviously not sensitive to this type of intergranular cracking.
5. Literature data evidence that oxidation phenomena in air conditions do not affect the material properties even for long term high temperature exposures. It is assumed that oxidation only leads to a reduction of the component wall

thickness but does not affect the material sensitivity to intergranular cracking. Therefore, in the present study the main part of mechanical tests will be carried out in laboratory atmosphere.

References

- Alamo A., Brachet J.C., Castaing A., Foucher C. (1996). Effects of the initial metallurgical condition on the microstructure and mechanical properties of 9Cr-1Mo and 9Cr-1MoNbV thermal aged steels. *Microstructures and mechanical properties of aging materials II* edited by P.K. Liaw. 121-134.
- Andrews K.W., Hughes H., Dyson D.J. (1972). Constitution diagrams for Cr-Mo-V steels. *Journal of the Iron and Steel Institute of Japan*. **May**. 337-345.
- Armas A.F., Petersen C., Schmitt R., Avalos M., Alvarez-Armas I. (2002). Mechanical and microstructural behaviour of isothermally and thermally fatigued ferritic/martensitic steels. *Journal of nuclear materials*. **307-311**. 509-513.
- Armas A.F., Avalos M., Alvarez-Armas I., Petersen C., Schmitt R. (1998). Dynamic strain ageing evidences during low cycle fatigue deformation in ferritic-martensitic stainless steels. *Journal of Nuclear Materials*. **258-263**. 1204-1208.
- Barcelo F., Brachet J.C. (1994). Quantification par analyse d'images de la taille de l'ancien grain austénitique d'aciers martensitiques 9Cr-1Mo. *La revue de métallurgie - CIT*. 255-265.
- Bestwick, Escaravage C. (1998). DCRC – Report n°11 – Design properties of modified 9Cr1MoVNb steel. *European Fast Breeder associates*. (Private communication).
- Bjarbo A., Hattestrand M. (2001). Complex carbide growth, dissolution and coarsening in a modified 12Pct chromium steel – an experimental and theoretical study. *Metallurgical and materials transactions*. **32A**. 19-27.
- Brachet J.C. (2004). Métallurgie des aciers martensitiques de base 9-12%Cr (Mo,W,V,Nb,Ta) - Effets des traitements thermiques (isothermes/anisothermes) sur les évolutions microstructurales. *Seminar – Centre des Matériaux – ENSMP*(in French).
- Brachet J.C. (1991). Alliages martensitiques 9Cr-1Mo: effet de l'addition de l'azote et du vanadium sur la microstructure, les transformations de phase et les propriétés mécaniques. *PhD Thesis Paris Sud Orsay University* (in French).
- Brinkman C.R., Gieseke B., Maziasz P.J. (1993). The influence of long term thermal aging on the microstructure and mechanical properties of modified 9Cr-1Mo steel. *Microstructures and mechanical properties of aging material* edited by P.K. Liaw - TMS publications. 107-115.
- Bush (2001). An introduction to the 9Cr1MoV alloys. *Valve Magazine*. **13(1)**.
- Caballero F.G., Capdevila C., Alvarez L.F., Garcia de Andres (2004). Thermoelectric power studies on a martensitic stainless steel. *Scripta materialia*. **50**. 1061-106.
- Caron R.N., Krauss G. (1972). The tempering of Fe-C martensite. *Metallurgical Transactions*. **3**. 2381-2389.
- Chandravathi K.S., Laha K., Bhanu Sankara rao K., Mannan S.L. (2001). Microstructure and tensile properties of modified 9Cr-1Mo steel (grade91). *Materials science and technology*. **17**. 559-565.
- Choudhary B.K., Bhanu Sankara Rao K., Mannan S.L., Kashyap B.P. (1999a). Influence of thermal ageing on tensile deformation and fracture behaviour of forged thick section 9Cr-1Mo ferritic steel. *Journal of Nuclear Materials*. **273**. 315-325.
- Choudhary B.K., Bhanu Sankara Rao K., Mannan S.L., Kashyap B.P. (1999b). Serrated Yielding in 9Cr-1Mo ferritic steel. *Materials Science Technology*. **15**. 791-797.
- Danon A., Servant C., Alamo A., Brachet J.C. (2003). Heterogeneous austenite grain growth in 9Cr martensitic steels: influence of heating rate and the austenitization temperature. *Materials science and engineering*. **A348**. 122-132.
- Dimmler G., Weinert P., Kozeschnik E., Cerjak H. (2004). Quantification of Laves phase in advanced 9-12%Cr steels using a standard SEM. *Materials Characterization*.
- Dronhofer A., Pesicka J., Dlouhy A., Eggeler G. (2003). On the nature of internal interfaces in tempered martensite ferritic steels. *Z. metallkd.94*. **5**. 511-519.
- Dutta B., Palmiere E.J., Sellars C.M. (2001). Modelling the kinetics of strain induced precipitation in Nb microalloyed steels. *Acta Materialia*. **49**. 785-794.
- Fougeres R. (1975). Etude de la microplasticité des martensites d'aciers au carbone par des essais de fluage au voisinage de la température ambiante. *PhD thesis. INSA Lyon* (In French).
- Garcia de Andres C., Bartolomé M.J., Capdevila C., San Martin D., Caballero F.G., Lopez V. (2001). Metallographic techniques for the determination of the austenite grain size in medium carbon microalloyed steels. *Materials characterization*. **46**. 389-398.
- Greef A.P., Law C.W., Swant H.C. (2000). The oxidation of industrial FeCrMo steel. *Corrosion science*. **42**. 1725-1740.
- Guetaz L., Millier J.P., Urvoy S. (2003). Mécanismes de déformation de l'acier martensitique EUROFER. Note Technique DTEN N°2002/128 - *Communication privée Commissariat à l'Energie Atomique*.
- Guttman D. (1974). Etude du revenu de la martensite dans des aciers faiblement alliés à 2% de Mn – Influence de l'antimoine. *PhD thesis – Université de Nancy – In French*.
- Hald J. and Straub S. (1998). Microstructural stability of 9-12%CrMo(W)VNbN steels. *Materials for advanced power engineering - 6th Liege Conference*. 155-169.

- Hippesley C.A., Druce S.G. (1983). The influence of phosphorous segregation to particle - matrix interfaces on ductile fracture in high strength steel. *Acta Metallurgica*. **32(11)**. 1861-1872.
- Hofer P., Cerjak H., Warbichler P. (2000). Quantification of precipitates in a 10% Cr steel using TEM and EFTEM. *Materials Science and Technology*. **16**. 1221-1225.
- Hofer P., Cerjak H. and Warbichler P. (1999). Quantification of the development of precipitates after exposure to service conditions in new 9-12%Cr steels demonstrated on G-X12CrMoWVNbN 10-1-1. *Praktische Metallography*. **36(9)**. 503-513.
- Ishitsuka T., Inoue Y., Ogawa H. (2004). Effect of silicon on the steam oxidation resistance of a 9%Cr heat resistant steel. *Oxidation of metals*. **61(1/2)**. 125-139.
- Iwanaga K., Tsuchiyama T. and Takaki S. (1998). Relationship between creep behavior and microstructure in martensitic heat resistant steel. *Tetsu Hagane*. **84(12)**. 60-65.
- Jaoul B. (1965). Etude de la plasticité et application aux métaux. *Dunod - Paris*. 297. (In French).
- Jakobova A., Vodarek V., Hennhofer K., Foldyna V. (1998). Microstructure and creep properties of P91 steel and weldments. *Materials for advanced power engineering - 6th Liege Conference*. 373-382.
- Jones W.B., Hills C.R., Polonis D.H. (1991). Microstructural evolution of modified 9Cr-1Mo steel. *Metallurgical transactions*. **22A**. 1049-1058.
- Kaneko K., Matsumara S., Sadataka A., Fujita K., Moon W.J., Ozaki S., Nishimura N., Tomokiyo Y. (2004). Characterization of carbides at different boundaries of 9Cr steel. *Materials science and engineering*. **A374**. 82-89.
- Kelly P.M. (1965). The martensite transformation in steels with low stacking fault energy. *Acta Metallurgica*. **13**. 635-646
- Clueh R.L. and Harries D.R. (2001). High chromium ferritic and martensitic steels for nuclear applications. *American Society for Testing Materials*
- Krauss G. (1999). Martensite in steels: strength and structure. *Materials Science Engineering*. **A273/275**. 40-57.
- Kurdjumov G., Sachs G. (1930). *Z phys*. **64**.325-343.
- Laverde D., Gomez-Acebo T., Castro F. (2004). Continuous and cyclic oxidation of T91 ferritic steel under steam. *Corrosion Science*. **46**. 613-631.
- Lifshitz I.M., Slyosov V.V. (1961). The kinetics of precipitation from supersaturated solid solution. *Journal of physics and chemistry of solids*. **19**. 35
- Lundin L.M. and Richarz B. (1995). Atom probe study of phosphorous segregation to the carbide matrix interface in an aged 9% chromium steel. *Applied Surface Science*. **87/88**. 194-199.
- Lundin L.M., Hattestrand M., Andren H.O. (2000). Redistribution of Elements During Ageing and Creep Testing of 9-12% Chromium Steels. *Proceedings of the 5th International Charles Parsons Turbine Conference*. 602-617.
- Maki T., Tsuzaki K., Tamura I. (1980). The morphology of microstructure composed of lath martensites " *Transactions of the I.S.I.J.* **20**. 207-213.
- Maruyama K., Sawada K., Koike J.I. (2001). Strengthening mechanisms of creep resistant tempered martensitic steel. *ISIJ international*. **41(6)**. 641-653.
- Masuyama K. (2001). History of power-plants and progress in heat resistant steels. *ISIJ international*. **41(6)**. 612-625.
- Massol E., Leclercq S. (2003). Comportement en fatigue et fluage de matériaux de turbines et de collecteurs thermiques – Etude bibliographique. *DEF HT-26/03/014/A* (Private communication).
- Materkowski J.P., Krauss G. (1979). *Metallurgical transactions*. **10A**. 1643.
- Menyhard M., McMahon C.J. (1989). On the effect of molybdenum in the embrittlement of phosphorous doped iron. *Acta metallurgica*. **37(8)**. 2287-2295.
- Mikami M., Tsuchiyama T., Takaki S. (2001). Isothermal transformation behavior in 12%Cr-0.3%C steel. *Testsu hagane*. **87(1)**. 49-54.
- Mohan R., Marschall C. (1998). Cracking instabilities in a low carbon steel susceptible to dynamic strain ageing. *Acta materialia*. **46(6)**. 1933-1948.
- Morito S., Tanaka H., Konishi R., Furuhashi T., Maki T. (2003). The morphology and crystallography of lath martensite in Fe-C alloys. *Acta materialia*. **51**. 1789-1799.
- Mujahid M., Quereshi M.I. and Ali M. (1999). Development of microstructure during heat treatment of high carbon Cr-Mo steel. *Materials science and technology*. **15**. 391-395.
- Nagesha A., Valson M. Kannan R., Bhanu Sankara Rao K., Mannan M.L. (2002). Influence of temperature on the low cycle fatigue behaviour of a mod. 9Cr1Mo ferritic steel. *International journal of fatigue*. **24**. 1285-1293.
- Nakajima T., Spigarelli S., Evangelista E., Endo T. (2003). Strain enhanced growth of precipitates during creep of T91. *Materials Transactions*. **44(9)**. 1802-1808.
- Noble F.W., Senior B.A., Etre B.L. (1990). The effect of phosphorous on the ductility of 9Cr-1Mo steels. *Acta metallurgica and materialia*. **38(5)**. 709-717.
- Ogata T., Yamamoto M. (1997). High temperature fatigue crack propagation property of 9Cr1Mo steel under vacuum and air conditions. *JSME International*. **40(3)**; 283-289.
- Ogata T., Yamamoto M. (1996). High temperature fatigue crack propagation property of 9Cr1Mo steel under vacuum and air conditions. *Localized damage IV ed. H. Nisitani – computational mechanics*.

- Okamura H., Ohtani R., Saito K., Kimura K., Ishii R., Fujiyama K., Hongo S., Iseki T., Uchida H. (1999). Basic investigation for life assessment technology of modified 9Cr-1Mo steel. *Nuclear engineering and design*. **193**. 243-254.
- Orr J., Burton D., Rasche C. (1993). Sensitivity of microstructure and mechanical properties of steel 91 to initial heat treatments. *Ironmaking and steelmaking*. **20(6)**. 415-423.
- Orr J. and DiFrancesco A. (1993). Effect of compositional variations on properties of steel 91. *Ironmaking and steelmaking*. **20(6)**. 424-430.
- Parameswaran P., Saroja S., Vijayalakshimi M., Raghunathan V.S. (1996). Decomposition modes of austenite in Cr-Mo ferritic steel. *Journal of nuclear materials*. **232**. 226-232.
- Parrot A., Shibli A. (2004). Performance du P91 et des autres aciers martensitiques à 9%Cr : Expérience industrielle et en laboratoire. *EdF report n°HT-26/02/006/A. In French (Private communication)*.
- Perhacova J., Grman D., Svoboda M., Patscheider J., Vyrostkova A., Janovec J. (2001). Microstructural aspects of phosphorous grain boundary segregation in low alloy steels. *Materials Letters*. **47**. 44-49.
- Pesicka J., Kozel R., Dronhofer A., Eggeler G. (2003). The evolution of dislocation density during heat treatment and creep of tempered martensite ferritic steels. *Acta materialia*. **51**. 4847-4862.
- Pickering F.B. (1997). Microstructural development and stability in high chromium ferritic power plant steels. *Editors A. Strang, D.J Gooch – The institute of materials – London*.
- Raghavan V. (1994). *C-Cr-Fe (Carbon-Chromium-Iron)*. **15(4)**. 418-419.
- Robson J.D., Bhadhesia H.K.D.H. (1997a). Modelling precipitation sequences in power plant steels - Kinetic Theory. *Materials Science Technology*. **13**. 631-639.
- Robson J.D., Bhadhesia H.K.D.H. (1997b). Modelling precipitation sequences in power plant steels - Application of kinetic Theory. *Materials Science Technology*. **13**. 640-644.
- Sandwick B.P.J. and Wayman C.M. (1983). Characteristics of lath martensite. *Metallurgical Transactions A*. **14A**. 809-824.
- Saroja S., Parameswaran P., Vijayalakshimi M., Raghunathan V.S. (1995). Prediction of microstructural states in Cr-Mo steels using phase evolution diagrams. *Acta Metallurgica Materiala*. **43(8)**. 2985-3000
- Saroja S., Vijayalakshimi M., Raghunathan V.S. (1993). Effect of prolonged exposures of 9Cr-1Mo-0.07C steel to elevated temperatures. *Materials Transactions JIM*. **34(10)**. 901-906.
- Sasaki T., Kobayashi K., Yamaura T., Kasuya T., Masuda T. (1991). Production and properties of seamless modified 9Cr-1Mo steel boiler tubes. *Kawasaki Steel Technical Report n°25*. 78-86.
- Sawada K., Taneike M., Kimura K. and Abe F. (2003). In situ observation of recovery of lath structure in 9% chromium creep resistant steels. *Materials Science and Technology*. **19**. 739-742.
- Schacht G., Richter R. (1998). Experiences with etching reagents to show former austenite grain boundaries in steels. *Praktische Metallography*. **35**. 385-393.
- Schaffernak B., Hofer P., Cerjak H. (2000). Description of the precipitation behaviour of advanced 9-12% Cr steels for power plant applications. *Proceedings of the 5th International Charles Parsons Turbine Conference*. 519-527.
- Schinkel J.W., Rademakers P.L.F., Drenth B.R., Scheepens C.P. (1984). Heat treatment, aging effects and microstructure of 12Pct Cr steels. *Journal of heat treating*. **3(3)**. 237-248.
- Schneider H. (1960). *Foundry trade journal*. **108(5)**. 563.
- Senior B.A. (1989). The precipitation of Laves phase in 9Cr1Mo steels. *Materials Science and engineering*. **A119**. L5-L9.
- Sevc P., Janovec J., Katana V. (1994). On kinetics of phosphorous segregation in Cr-mo-V low alloy steel. *Scripta metallurgica et materialia*. **31(12)**. 1673-1678.
- Shinoda T., Nakamura T. (1981). The effects of applied stress on the intergranular phosphorous segregation in a chromium steel. *Acta metallurgica*. **29**. 1631-1636.
- Shtansky D.V. (2000). Decomposition of martensite by discontinuous like precipitation reaction. *Acta materialia*. **48**. 969-983.
- Shtansky D.V., Inden G. (1997). Phase transformation in FeMoC and FeWC steels - I. The structural evolution during tempering at 700°C. *Acta materialia*. **45(7)**. 2861-2878.
- Sireesha M., Albert S.K., Sundaresan S. (2001). Microstructure and mechanical properties of weld fusion zones in modified 9Cr1Mo steel. *Journal of Material engineering and performances*. **10**. 320-330.
- Solignac P. (1994). Extraction et analyse des précipités A₃B dans une matrice base nickel. CRY/RE/94/44/MPS/AMG. *Private communication*.
- Soussan P. (2000). Etude du fluage des aciers 9Cr1Mo-NbV. *Rapport de stage de DEA. Centre des Matériaux - Ecole Nationale Supérieure des Mines de Paris*.
- Speich G.R. (1969). Tempering of low carbon martensite. *Transactions of the metallurgical society of AIME*. **245**. 2553-2564.
- Speich G.R. and Leslie (1962). Tempering of steel. *Metallurgical Transactions*. **3**. 1043-1054.
- Stocker Ch., Spiradek K., Zeiler G. (2002). Microstructural features influencing the creep properties of 9-12Cr steels focusing on Laves phase precipitation. *Materials for advanced power engineering - Proceedings of the 7th Liege conference*. **III.21**. 1459-1469.
- Suzuki S., Hanada R., Kimura H. (1986). Interaction between molybdenum and phosphorous in solid solutions and its effect on the precipitation process in Fe-Mo-P alloys. *Materials science and engineering*. **80**. 75-85.

Suzuki K., Kumai S., Toda Y., Kushima H., Kimura K. (2003). Two phase separation of primary MX carbonitride during tempering in creep resistant 9Cr1Mo-NbV steel. *ISIJ international*. **43(7)**. 1089-1094.

Taneike M., Sawada K., Abe F. (2004). Effect of carbon concentration on precipitation behavior of $M_{23}C_6$ carbides and MX carbonitrides in martensitic 9Cr steel during heat treatment. *Metallurgical transactions*. **35A**. 1255-1261.

Tavassoli A.A.F. (1998). Material design data for fusion reactors. *Journal of nuclear materials*. **258-263**. 85-96.

Thomson R.C. (2000). Characterization of carbides in steels using atom probe field ion microscopy. *Materials characterization*. **44**. 219-233.

Takei Z., Viehhaus H., Grabke H.J. (2000). Initial staged of oxidation of a 9CrMoV steel: role of segregation and martensite laths. *Applied surface science*. **165**. 23-33.

Van der Sschaeye A. (1992). Modified 9%Cr steel (Grade P91): low cycle and crack propagation rate of base material and welds at room and high temperature. *Proceedings of the international conference on pressure vessel technology - Dusseldorf Germany*. 802-822.

Viswanathan R., Berasi M., Tanzosh J., Thaxton T. (1990). Ligament cracking and the use of modified 9Cr-1Mo alloy steel (P91) for boiler headers. *New alloys for pressure vessels and piping* edited by M. Prager. 97-103.

Vitek J.M. and Klueh R.L. (1983). Precipitation reactions during the heat treatment of ferritic steels. *Metallurgical Transactions*. **14A**. 1047-1056.

Vyrostova A., Kroupa A., Janovec J., Svoboda M. (1998). Carbide reactions and phase equilibria in low alloy Cr-Mo-V steels tempered at 773-993K. Part I: Experimental measurements. *Acta Materialia*. **46(1)**. 31-78.

Wagner C. (1961). Theorie der Alterung von Niederschlägen durch Umlösen. *Z. elektrochemie*. **65**. 581

Warreing J. (1994). A review of the mechanical and physical properties of modified 9CrMoNbV (Grade 91) steel. CEA/SRMA, N.T SRMA94-2013.

Welding Framatome (2003). Joint 9% Cr - 1Mo HTR INNO Dossier de fabrication du joint soudé MC/TS 1972. TFCW R 02.320. (Private communication).

Wu W., Hwu L.Y., Lin D.Y. and Lee J.L. (2000). The relationship between alloying elements and retained austenite in martensitic stainless steel welds. *Scripta materialia*. **42**. 1071-1076.

Yamada K., Igurashi M., Muneki S., Abe F. (2002). Effect of heat treatment on precipitation kinetics in high Cr ferritic steels. *ISIJ International*. **12(7)**. 779-784.

Yaguchi M., Takahashi Y. (1999a). A viscoplastic constitutive model incorporating dynamic strain aging effect during cyclic deformation conditions. *International journal of plasticity*. **16**. 241-262.

Yaguchi M., Takahashi Y. (1999b). Unified inelastic constitutive model for modified 9Cr-1Mo steel incorporating dynamic strain aging effect. *JSME*. **A42(1)**. 1-10.

Yoshida M., Takasugi T. (1997). Phase relation and microstructure of Nb-Cr-V and nb-Cr-Mo alloy systems. *Materials science and engineering*. **A224**. 69-76.

Yukitoshi T., Yoshikawa K., Daikoku T., Masuyama F. (1982). Experience of high chromium ferritic steel tubes in power plant. *Journal of materials for energy systems (ASM)*. **4(2)**. 89-109.

Yuqing W., McMahon C.J. (1987). Interaction of phosphorous, carbon, manganese and chromium in intergranular embrittlement of iron. *Materials Science Technology*. **3**. 207-216

Zhang W., Senior B.A., Noble F.W. (2000). Comparison of effects of aging on fracture of 9Cr1Mo and 2.25Cr1Mo steel. *Materials Science Technology*. **7**.

Zurek J., Wessel E., Niewolak L., Schmitz F., Kern T.U., Singheiser L., Quadackers W.J. (2004). Anomalous temperature dependence of oxidation kinetics during steam oxidation of ferritic steels in the temperature range 550-650°C. *Corrosion science*.

Chapter A.II. Weldments

1. Welding procedure

1.1. Geometry of the welds

The two weldments considered here, are:

1. The WJP91 weldment which consists in the butt welding of two pipes of 295 mm in maximum diameter and 55 mm in thickness (see **figure A.II.1b**).
2. The WJT91 weldment which consists in the welding of two plates of 150 mm in thickness (see **figure A.II.1a**).

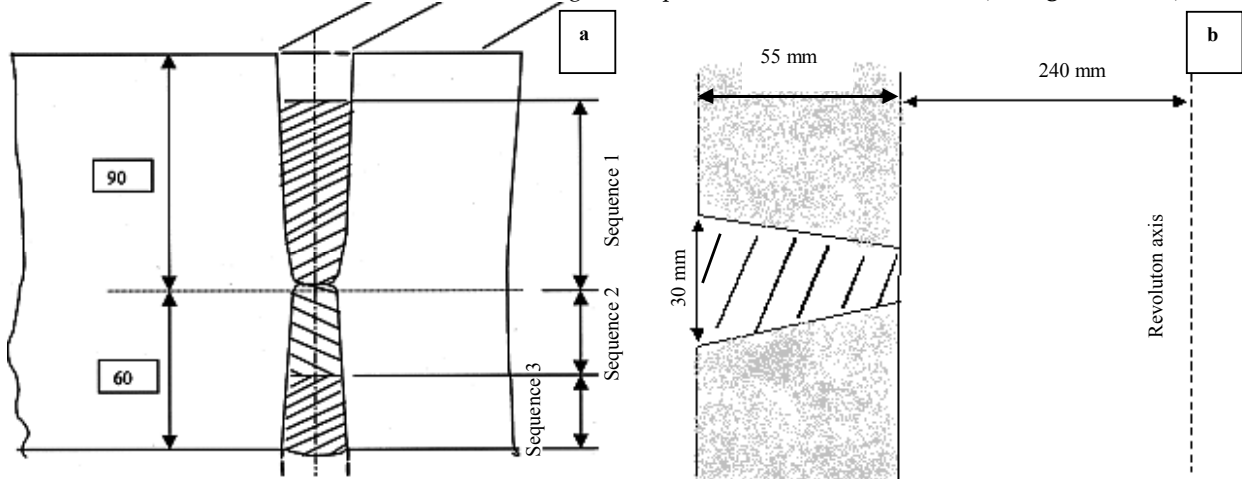


Figure A.II.1. Geometry of WJT91 (a) and WJP91 (b) weldments

1.2. Description of the welding procedures

In both cases, the **welding method is arc welding**. Consequently, details about this welding method will be given in the following (If one wants to have any details on all the welding methods please read Murry (2000) and Bonnet (2000)). Arc welding is currently use to weld high thickness components. The principle of arc welding is to produce an electrical arc between an electrode and elements to be welded. Two cases can be distinguished:

1. The electrode is made of weld metal surrounded by a protective slag which is vaporised in the arc plasma: this process is called metal inert gas (MIG).
2. The electrode is a non consumable electrode in tungsten whereas the weld metal is provided as a wire: this process is called tungsten inert gas (TIG).

To stabilise the electrical arc, the welding operation is often done under inert gas atmosphere (helium, argon): for example ARCAL 37 (70% helium et 30% argon) is used for the welding of the WJT91 weldment. The main characteristics of the welding procedure of the WJP91 and the WJT91 weldments are respectively reported in **table A.II.1** and **A.II.2**.

Run	Process	Wire diameter (mm)	Pre-heat temperature	Current (min/max)	Heat input energy	Post weld heat treatment
1	TIG	2.4	260°C	70 / 130 A	1296 Jmm ⁻¹ (Mean value)	760°C for 2 hours
2 - 3	MIG	3.2	200°C	90 / 135 A		
4 - 17	MIG	4.0	200°C	130 / 200 A		

Table A.II.1. Welding procedure for the WJP91 weldment (TIG and MIG welding)

Pre-heat temperature	Interpass temperature	Sequence 1 27 runs	Sequence 2 9 runs	Sequence 3 9 runs	Post weld heat treatment
150 – 225 °C	< 225 °C	$v_a = 1.8 \cdot 10^{-3} \text{ ms}^{-1}$ $E = 1700 \text{ Jmm}^{-1}$ 600 gh ⁻¹	$v_a = 1.75 \cdot 10^{-3} \text{ ms}^{-1}$ $E = 2150 \text{ Jmm}^{-1}$ 800 gh ⁻¹	$v_a = 1.8 \cdot 10^{-3} \text{ ms}^{-1}$ $E = 1700 \text{ Jmm}^{-1}$ 800 gh ⁻¹	750°C for 15 hours and 18 minutes

Table A.II.2. Welding procedure for the WJT91 weldment (TIG)

1.3. General properties of the welded joints

1.3.1. Sensitivity of weldments to solidification, hot, reheat and hydrogen cracking phenomena

There are different types of cracking that may appear due to the welding procedure:

1. Solidification cracking.
2. Hot cracking.
3. Reheat cracking.
4. Hydrogen cracking.

Solidification cracking occurs for metals which have a high thermal expansion coefficient which is obviously not the case for 9Cr1Mo-NbV steels. The average coefficient of linear expansion from room temperature to 700°C is $\alpha_m = 12.7 \cdot 10^{-6} \text{ s}^{-1}$ (see Warreing (1994)).

Hot cracking occurs where the solidus temperature is reached as a liquid film may be trapped between the solidification limit and the columnar grain. When films are unable to accommodate the tensile contraction strains, cracking occurs. Bailey and Jones (1978) were the first to study hot cracking susceptibility in ferritic steels. They proposed a criterion named unit crack susceptibility and depending on the chemical composition of the steel which is defined as:

$$\text{UCS} = 230.0C + 190.0S + 75.0P + 45.0\text{Nb} - 12.3\text{Si} - 5.4\text{Mn} - 1.0 \quad (\text{eq. A.II.1})$$

More generally, the austenite former elements are said to increase the hot cracking susceptibility and ferrite former elements are said to lower it. Barnes et al (2000) studied the effect of Nb, Mn and welding conditions on hot cracking. They found that for high Nb content, local segregation may lead to high local concentration of Nb, and a liquid film which is an Nb intermetallic phase very sensitive to cracking can formed (if no crack occur, this intermetallic phase is solidified in δ ferrite which is retained during cooling). On the contrary, Mn increases the resistance to hot cracking. From their study, Barnes et al (1998) also concluded that the welding parameters have little influence on the hot cracking susceptibility.

Reheat cracking may occurs for two reasons. The principal cause is that when heat treating susceptible steels, the grain interior becomes strengthened by carbide precipitation, forcing the relaxation of residual stresses by creep deformation at the grain boundaries. The second factor of reheat cracking is the segregation of elements at grain boundaries. It is also called reverse temper embrittlement. To investigate the weldment sensibility to reheat cracking due to temper embrittlement, a step cooling which is a multi stages tempering treatment is often performed.

Finally, hydrogen cracking is possible if hydrogen is dissolved in the weld metal during the welding procedure. Indeed, when the austenite martensite transformation proceeds, the hydrogen solubility strongly decreases (from 5-10 cm³/100g of metal to 0-3 cm³/100g of metal) and it may leads to the formation of hydrogen bubbles.

1.3.2. Welding recommendations

Martensitic stainless steels are considered to be the most difficult of the stainless steel alloys to weld even if their good weldability is often praised. Therefore all parameters must be optimised to decrease susceptibility to cracking. Main criteria to ensure the weldment integrity are:

1. A rapid arc displacement rate, i.e. between $10^{-3} - 10^{-2} \text{ s}^{-1}$ is suggested by Yajiang et al (2002).
2. Limitations of phosphorous, sulphur and hydrogen contents because P and S elements segregate and weld metal is very sensitive to hydrogen cracking during solidification (Recommendations from the « National Certified Pipe Welding Bureau » (1999)).
3. Limitations of Mn (i.e. < 0.4 wt%) and Nb (i.e. < 0.05 wt%) contents that induce great sensibility to solidification cracking (Barnes (1998)). Note however that the addition of Mn is necessary to prevent sulphur segregation by forming MnS particles.
4. Not too high welding energy as cooling parameter $\Delta t_{800 \rightarrow 500}$ must never exceed 31 seconds to ensure martensite transformation during cooling (Brozda and Zeman (1996)).
5. A minimum post weld heat treatment of 3 hours at 750°C is recommended to eliminate residual stresses evaluated to 28 MPa by Brozda and Zeman (1996), and especially to ensure good toughness properties for the fresh martensite. This temperature of 750°C is also depicted as the optimum to give the best fracture toughness properties by Bhaduri et al (1997).
6. Beres et al (2001) have defined acceptable values for preheat and intermediate temperatures as:
 $T_{\text{pre-heat}} = (Ms - 90) \pm 10^\circ\text{C} \approx 290^\circ\text{C} \pm 10^\circ\text{C}$ $T_{\text{intermediate}} = (Ms - 190) \pm 10^\circ\text{C} \approx 190^\circ\text{C} \pm 10^\circ\text{C}$
7. Yajiang et al (2002) recommended an heat input between 850 Jmm⁻¹ and 1170 Jmm⁻¹ for the TIG welding technique and between 1330 Jmm⁻¹ and 2100 Jmm⁻¹ for the MIG welding technique.

The weld metal composition and thermal treatments are optimised to reach the specified values of Charpy impact toughness (with locating the notch in the weld metal) and tensile properties. The objectives are KCV > 41 J at 20°C for thermal power plants and 45 J for the future fast breeder reactor. The study of Viswanathan et al (1990) showed that a minimum PWHT of 1 hour at 760°C is necessary to reach this goal (see **figure A.II.2**). Niederhoff et al (1991) have recommended 4 hours at 750°C. Gosh et al (2004) also evidenced that the preheat temperature affect the impact toughness properties and recommended a preheat temperature lower than 250°C.

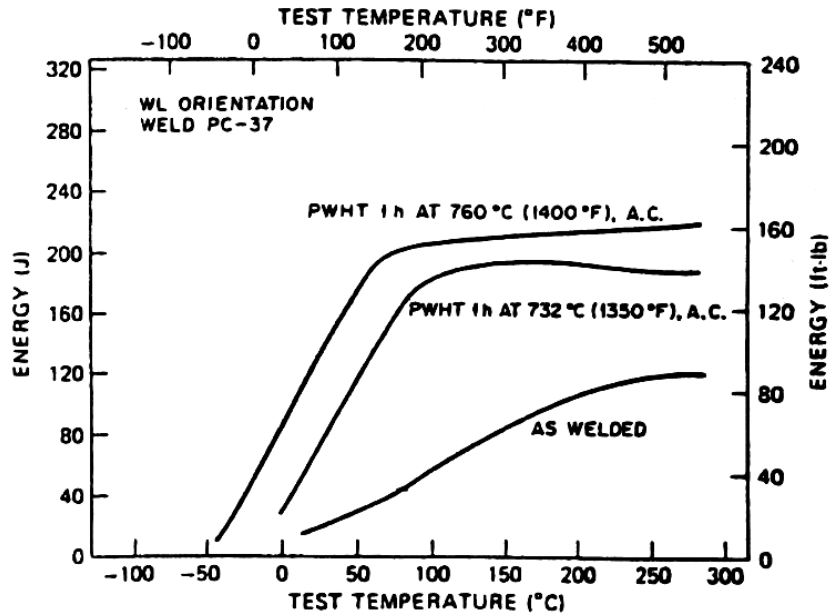


Figure A.II.2. Effect of the PWHT on Charpy impact energy from Viswanathan et al (1990)

When comparing the eight recommendations with the characteristics of the welding procedures for the WJP91 and the WJT91 weldments, it can be concluded that these recommendations are quite well respected. However, the preheat temperatures seem to be a little too low i.e. 200°C - 260°C and 150°C - 225°C in comparison with the recommended temperature of 300°C. The welding heat input energy of the WJT91 weldment seems also to be a little bit too high.

1.3.3 Residual stresses

In this study, attention was not focused on residual stresses induced by the welding procedure as their influence on the high temperature creep flow and damage behaviour is very limited. It is admitted that the residual stresses are largely relaxed during the PWHT at least for low and middle thickness components. There is however no deny that this point must require higher attention for high thickness components for which the homogeneity of the PWHT is not ensured.

2. Structure and properties of the weld metal

2.1. Microstructure and general mechanical properties of the weld metal

In the technology of welding 9Cr1Mo-NbV martensitic steels, the filler metals have nearly the same composition than the base metals. Some elements like Mn or Cu are added to improve the material weldability. In the ASME norms, three compositions of the filler metal depending on the welding technique which is used are proposed (see **figure A.II.3**).

Element	ASME SFA-5.28 (TIG)	ASME SFA-5.23 (MIG)	ASME SFA-5.5 (MIG)
C	0.07 – 0.13	0.07 – 0.13	0.08 – 0.13
Mn	1.25	1.25	1.25
P	0.01	0.01	0.01
S	0.01	0.01	0.01
Si	0.15 - 0.30	0.8	0.30
Cr	6.0 - 9.5	6.0 – 10.0	8.0 - 10.5
Mo	0.6 – 1.1	0.6 – 1.1	0.85 – 1.2
Ni	1.00	1.00	1.00
V	0.15 – 0.25	0.15 – 0.25	0.15 – 0.30
N	0.03 – 0.07	0.03 – 0.07	0.02 – 0.07
Nb	0.02 – 0.10	0.02 – 0.10	0.02 – 0.10
Al	0.04	0.04	0.04
Cu	0.2	/	0.25

Figure A.II.3. Composition of the filler metal (ASME recommendations)

The composition of the filler metals used to weld the two components studied here are given in **table A.II.3**.

	C	Si	Mn	P	S	Al	Cr	Cu	Mo	V	Ni	N	Nb
WMP91	0.091	0.37	0.41	0.028	0.013	0.07	8.44	0.04	0.92	0.24	0.27	0.038	/
WMT91	0.08	0.18	1.00	0.004	0.005	/	9.03	0.17	0.9	0.18	0.71	/	0.08

Table A.II.3. Chemical composition of the filler metals examined in the present study (wt%)

The main differences between the chemical composition of the two filler metals concern Cu and Mn whose contents are higher in the WMT91 weld metal than in the WMP91 weld metal. Note also that by comparison with the chemical compositions of the base metal, the Nb content is strictly controlled as it is detrimental to the toughness properties of the weld metal (see Dittrich et al (1994)).

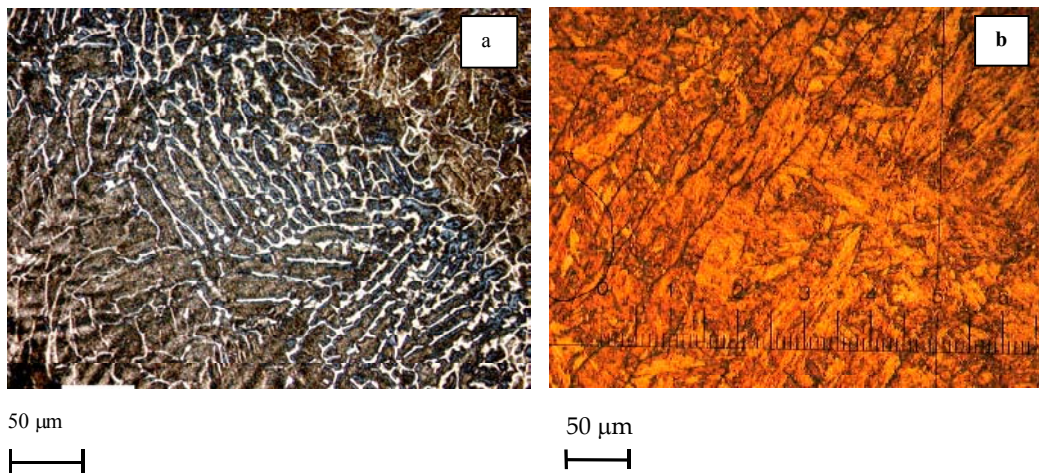


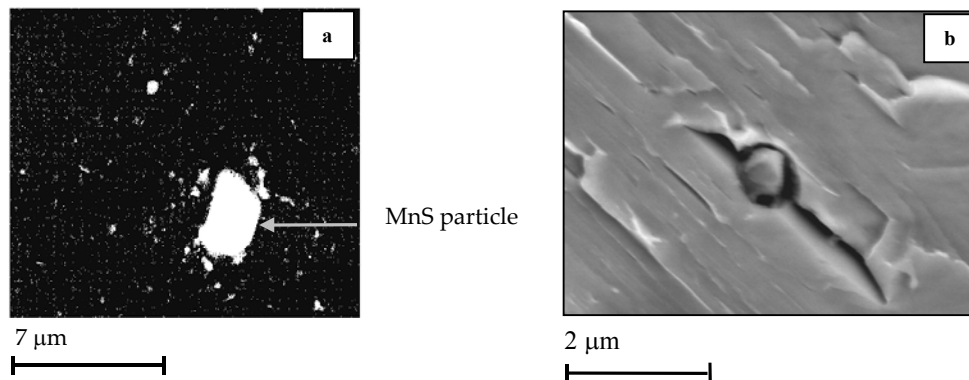
Figure A.II.4. Microstructure of the weld metals (a) dendritic structure before PWHT (b) Columnar grains elongated following the thermal gradient after PWHT

Before the PWHT (i.e. in the as welded state), the weld metal exhibits a dendritic structure of solidification (see **figure A.II.4a**). The phase which appears in white in **figure A.II.4a** is probably retained austenite. After the PWHT, the microstructure of the weld metal is a tempered martensitic microstructure (see **figure A.II.4b**) and the austenite evidenced in **figure A.II.4a** obviously transformed into martensite during cooling after PWHT. The austenite grain size is quite heterogeneous as shown in **figure A.II.4a** where small grains i.e. < 25 μm in size are observed. It was also observed that grain growth occurs along the thermal gradient due to the welding conditions. Therefore, many columnar grains are observed in the weld metal (see **figure A.II.4b**).

Two techniques were used to investigate the presence of MnS particles in the weld metals:

1. X-Ray dispersive energy spectroscopy (EDS) analysis was performed on carbon extraction replicas (see **figure A.II.5a**).
2. Specimens were fractured at low temperature i.e. -150°C as MnS particles are privileged sites for cleavage crack initiation (see **figure A.II.5b**).

The two types of investigation evidenced the presence of MnS particles in the weld metal whose size can go up to several microns as can be shown in **figure A.II.5**. These particles do probably not affect the material creep strength at high temperature but could be involved in low temperature rupture behaviour. Note also that the other extracted particles evidenced in **figure A.II.5a** were identified as M_{23}C_6 carbides which is consistent with the results of Andren et al (1995).



*Figure A.II.5. Extraction of a MnS particles on a carbon replica (SEM observation)
Initiation of a cleavage crack on a MnS particle at low temperature*

The presence of δ ferrite in the weld metal is reported by Andren et al (1995) up to 13 wt% for high Nb and V contents which is consistent with results of **figure A.I.2**. Balmforth and Lippold (2000) have also established a composition diagram which predicts weld deposit microstructure for a large variety of ferritic martensitic stainless steels. In the present study, the presence of δ ferrite was investigated by SEM and light optical investigations. No δ ferrite was evidenced.

The presence of retained austenite is reported by Wu et al (2000) who proposed a formula to calculate the amount of retained austenite depending on the M_s temperature:

$$\gamma(\%) = 36.412 - 0.126M_s \quad (\text{eq. A.II.2})$$

The relationship of **equation A.II.2** postulates that the microstructure in the as welded state is composed of 1% of retained austenite for $M_s = 280^{\circ}\text{C}$. As the martensite start temperature of 9Cr1Mo-NbV steels is largely higher than 300°C , it should be assumed that no austenite is retained after cooling. However, the presence of retained austenite in the as welded state was evidenced in the previous section so that the validity of the relationship of **equation A.II.2** is questionable.

Santella et al (2001) investigated the possible formation of austenite during post weld heat treatment (i.e. austenite reversion) as Mn and Ni contents in the weld metal are higher than in the base metal and established the following formula:

$$A_{c1} = 854.5 - 43.9(\text{Mn} + \text{Ni}) - 9(\text{Mn} + \text{Ni})^2 \quad (\text{eq. A.II.3})$$

which leads to $A_{c1} = 820^{\circ}\text{C}$ for WMP91 and 753°C for WMT91. It means that the formation of austenite is possible during the tempering of the WJT91 weldment. This point could not be experimentally investigated as the possibly formed austenite which lacks of carbon retransforms in martensite during cooling after PWHT and is very difficult to distinguish. However, it obviously does not affect the weldment creep strength.

2.2 Investigations of cracking in the WJP91 steel weld metal

9Cr1Mo-NbV steels are very little sensitive to solidification cracking as they exhibit a low thermal expansion coefficient. Hydrogen cracking is avoided as the welding operation is carried out under inert gas atmosphere and as the base metal is preheated before welding and also heated between welding runs.

Using **equation A.II.1**, the unit crack, i.e. the hot cracking susceptibility were calculated using the chemical composition of the filler metals as UCS = 17.7 and 14.6 respectively for the WJP91 and WJT91 weldments. Their value are quite low and even if the susceptibility of the WJT91 weldment to hot cracking is higher, the two UCS are nevertheless quite low.

The sensitivity of the weldment to reheat cracking was explored. Three points bending tests were carried out on the WJP91 weldment at -150°C both on the as welded conditions and after a step cooling treatment (with steps of 10 hours, 20 hours and 20 hours at respectively 625°C , 550°C and 500°C). The two tests gave similar results: a cleavage fracture surface was observed without any indication of intergranular cracking due to the segregation of phosphorous. As the WJT91 weldment contains smaller amounts of impurity elements such as P or S, it was assumed, without performing additional experiments, that it was also not sensitive to reheat cracking.

However, many defects were observed in the two weld components of the present study. Very large cracks (several mm in size) were especially observed in the WJP91 welded component at the fusion line as can be seen in figure A.II.6.



1 mm


Figure A.II.6. Macro-cracks in the WJP91 welded component at the fusion line

3. Microstructural characterisation of 9Cr-1MoNbV steel heat affected zone

3.1. Evidence of microstructural changes in the heat affected zone

The weldment is made of three main areas:

1. The weld metal which is deposited during the welding operation.
2. The heat affected zone is a zone where the microstructure of the base metal is affected by local heating due to the deposit of the weld metal in the liquid state (i.e. at its melting temperature).
3. The base metal.

In addition, the HAZ of weldments consists in various microstructural states (three mains) in a zone which is only 5 mm thick. Indeed, the welding procedure induces local heating of the base metal at temperatures ranging from 1400°C at the fusion line to 750°C in the so called heat affected zone (HAZ). Microstructural heterogeneity in the HAZ can be related to phase transformations.

In order to set the phase transformation points, dilatometric tests were performed on the base metal in the heating rate range between $0.5^{\circ}\text{C}\text{s}^{-1}$ and $20^{\circ}\text{C}\text{s}^{-1}$. Transformations temperatures were found to remain constant with $A_{c1} = 854^{\circ}\text{C}$ and $A_{c3} = 915^{\circ}\text{C}$ (see **table A.I.4**). These values are in good agreement with those calculated by Brachet (1991). The three main parts of the HAZ that are currently considered are:

1. The coarse grained heat affected zone (CGHAZ): $T_{\text{max}} \gg A_{c3}$, the austenite transformation is complete and austenite grain growth is promoted by elevated temperature. (Nearest zone from the fusion line).
2. The fine grained heat affected zone (FGHAZ): T_{max} is just above A_{c3} , the austenite transformation is nearly complete but austenite grain growth is limited.
3. The intercritical heat affected zone (ICHAZ): $A_{c1} < T_{\text{max}} < A_{c3}$, the martensite is partially transformed into austenite during the welding thermal cycle.

Note also that near the HAZ, for T_{max} just under A_{c1} , the martensite is over-tempered. The third domain i.e. the ICHAZ can also be divided into two sub-domains, as carbide dissolution, only occurs in the upper bound of the intercritical zone (**figure A.II.7**). Note that the solvus temperatures of $M_{23}C_6$ and MX particles are also reported on the representation of Igarashi et al (1998).

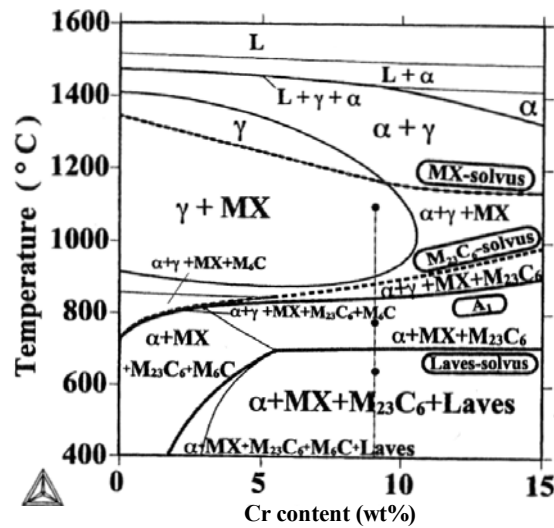


Figure A.II.7. Phase diagram given by Igarashi et al (1998) for chromium martensitic stainless steels

Finally, the occurrence of gradients in chemical compositions between the weld metal, the base metal and the HAZ. Some differences in chemical compositions due to the high temperature assisted diffusion from the HAZ to weld metal have been reported by Niederhoff et al (2003). In the present study, X-Ray dispersive wavelength analysis, using a Castaing electron microprobe, were carried out. It was found that wt% Cr, C and Mo were a little higher in the weld metal than in the HAZ but no massive depletion in a given region was observed. Therefore, mechanical properties in the weldment are obviously not affected by high temperature assisted diffusion. In fact, gradients of chemical composition are more likely to occur when the chemical composition of the weld metal is largely different from that of the base metal.

3.2. Effect of heating rate on phase transformation temperatures

The heating rates of weld thermal cycles are very high (approximately $100^{\circ}\text{C s}^{-1}$ – $200^{\circ}\text{C s}^{-1}$) and both A_{c1} and A_{c3} depend on it. Therefore, a study of the effect of the heating rate on the phase transformation was carried out. Experiments were carried out using a Gleeble 1500 thermal mechanical testing machine with recording diametral strain of smooth round specimens of 5 mm in diameter and 110 mm in length during the thermal cycle (see **appendix B.F.** for details about the testing machine). Therefore, both the A_{c1} and A_{c3} phase transformation points could be determined for various heating rates from 5°C s^{-1} to $220^{\circ}\text{C s}^{-1}$ (see **figure A.II.7**).

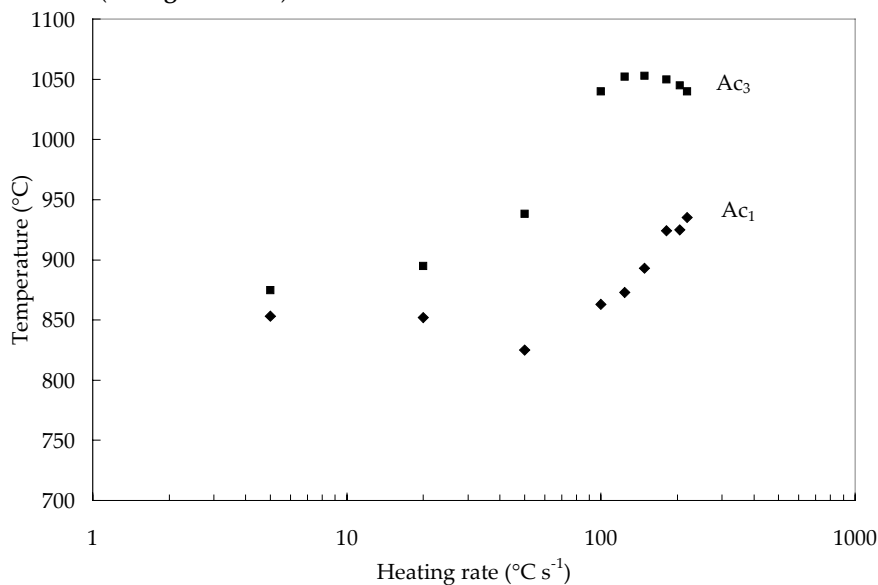


Figure A.II.8. A_{c1} and A_{c3} dependencies on heating rate for P91 steel

The effect of the heating rate has already been studied by Brachet (2004) and Murdoch et al (2001) for heating rates up to $100^{\circ}\text{C s}^{-1}$. An increase in the A_{c1} and A_{c3} temperatures was also observed but the enlargement of the intercritical domain is not reported. This phenomena is however not surprising as phase transformation and especially carbides dissolution are temperature but also time dependent phenomena.

Danon et al (2003) found an influence of the heating rate on the austenite grain growth for normalizing temperatures between 1000°C and 1100°C. At 1050°C, they found an abnormal coarsening of austenite grain for heating rates larger than 30°Cs⁻¹ (It also appears for lower heating rates when the normalising temperature is increased). They correlate this phenomenon to the absence of carbide dissolution and of MX particles at high heating rate. The importance of this effect is not assessed in the present study as in welding conditions, the annealing time at temperatures larger than A₃ are very short (typically < 1 min) and the growth of austenite grains is therefore limited. Moreover, SEM and light optical microscopy investigations did not evidenced abnormal austenite grain growth in the weldments. Note that the evolution of the precipitation state during high speed weld thermal cycle will be investigated in more details in **chapter C.III**.

3.3. Evidence of a soft zone area in the HAZ

Microstructural heterogeneity can be evidenced by hardness measurements and Moorthy et al (1997) have shown that the magnetic Barkhausen noise non destructive method is a very good technique to evaluate HAZ characteristics lengths. In the present study, Vicker's hardness measurements, which is the most commonly used technique (see Jakobova et al (1998), Cerjak and Schuster (1994), De Witte and Coussement (1991)) were carried out. The hardness profile obtained after PWHT shows a minimum in the heat affected zone 3 mm far from the fusion line (see **figure A.II.9**) which corresponds to the ICHAZ.

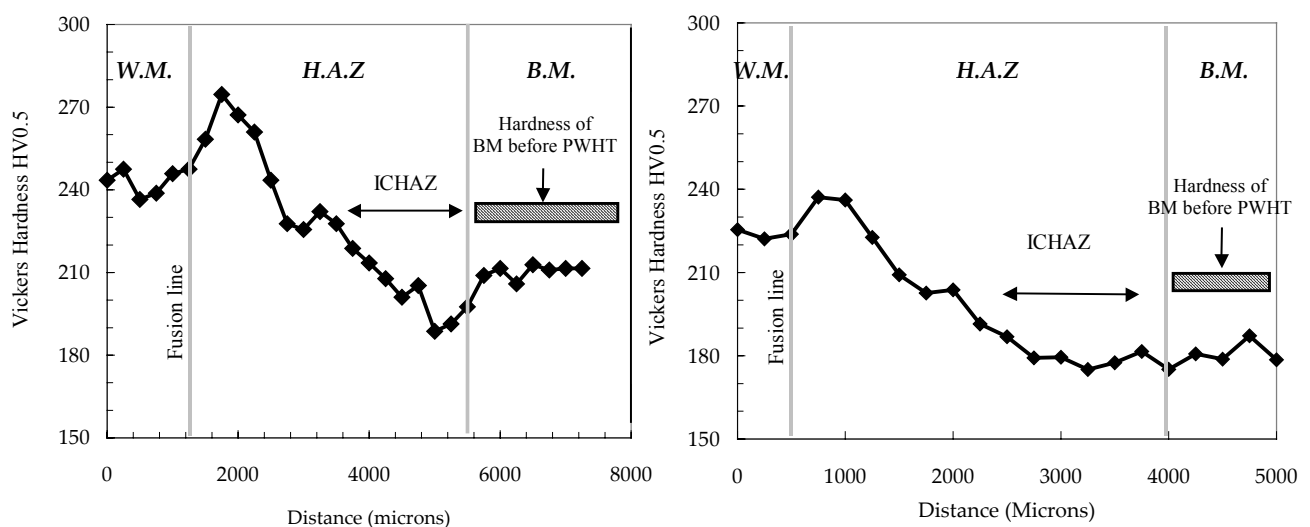


Figure A.II.9. Hardness profile in the WJP91 (left) and WJT91 (right) weldments

Note that, as two different heat input energy were used in the welding procedure of the WJT91 weldment, hardness profile were plotted in the three regions (i.e. for specimens located in sequence 1, sequence 2 and sequence 3 described in **figure A.II.1**). No difference was evidenced so that the hardness profile plotted in **figure A.II.9** is valid for the three welding sequences. It can be also notice that the hardness of the base metal is 10 - 20 points lower than that in the initial state (see **table A.I.3**) for both the WJP91 and the WJT91 weldment. In the case of the WJT91 weldment, this point is quite surprising as the metal was normally submitted to the PWHT. It can be concluded here, that the PWHT has a great influence on the value of hardness at room temperature but as it will be shown in **Part D**, that despite the difference in hardness between the base metal and the weld metal, the two materials exhibit similar creep flow properties.

4. Microstructure of the intercritical HAZ (ICHAZ)

4.1. TEM investigations

TEM investigations on thin foils clearly showed the microstructural differences between the base metal and the ICHAZ as it is shown in **figure A.II.10**. Carbon extraction replicas were also used to characterise the precipitation state in the ICHAZ.

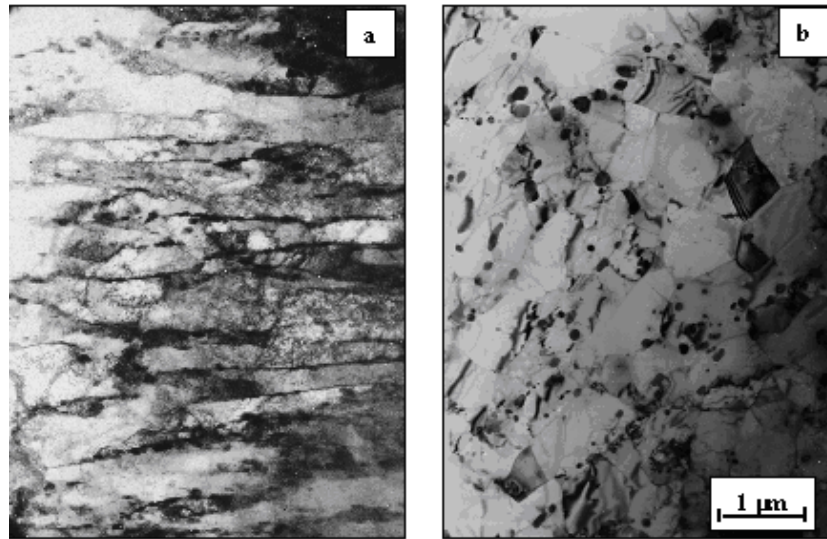


Figure A.II.10. TEM micrograph – a. Base Metal – b. ICHAZ (Y. De Carlan – CEA Saclay) i.e. 3.0 mm from the fusion line

The differences between the P91 base metal and the ICHAZ of the WJP91 weldment, evidenced by TEM and carbon extraction replicas investigations, can be summed up as follow:

1. The ICHAZ exhibits a lower dislocation density than the base metal.
2. Carbides coarsening occurs in the ICHAZ, the mean size of the $M_{23}C_6$ carbides reaches 200 nm in comparison with nearly 100 nm in base metal.
3. Lath morphology has completely disappeared in the ICHAZ which exhibits a totally recovered equiaxed microstructure with no more evidences of a lath morphology.
4. Solubility limits of MX particles which are higher than 1100°C (see **figure A.I.5**) ensure that these precipitates are obviously not dissolved during the weld thermal cycle both in the FGHAZ and in the ICHAZ so that the newly formed martensite is not strengthened by a dispersion of these precipitates during the PWHT. In the present study, the small size of MX particles did not allow to perform a systematic study of the precipitates during the PWHT. Nevertheless, non dissolved MX particles probably grow during the PWHT.

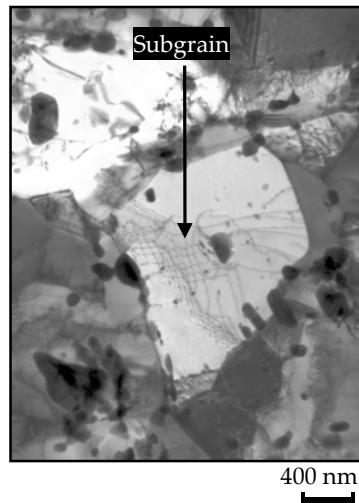


Figure A.II.11. Evidence of subgrain formation in the ICHAZ i.e. 3.0 mm from the fusion line

TEM investigations also showed the formation of subgrain (see arrow in **figure A.II.11**) at the interior of small grain whose size may be lower than 1 μm (see also Hald and Lund (1993), Yajiang et al (2002)).

4.2. EBSD Investigations

EBSD maps were performed both on the base metal and the intercritical heat affected zone so as to investigate microstructural states and study misorientation between grains. The results are given in **figure A.II.12** for the WJP91 weldment. Note that the same EBSD analysis was performed for the WJT91 weldment and give comparable results.

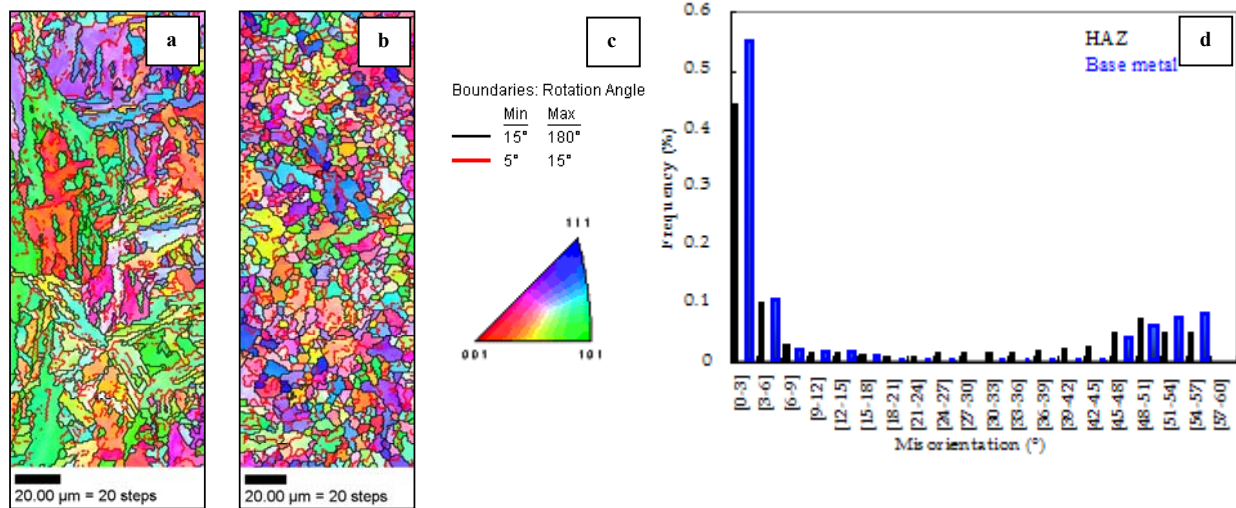


Figure A.II.12. EBSD maps in the WJP91 weldment: Comparison between (a) base metal and (b) ICHAZ, (c) colour key and (d) misorientation angle histogram (between neighbouring grains)

The two EBSD maps of respectively the base metal and the intercritical heat affected zone confirm differences between the two microstructural states. The boundaries of the small equiaxed grains are mainly high angle boundaries ($> 15^\circ$) as can be shown in **figure A.II.12b**. When looking at the misorientation histogram of **figure A.II.12d**, it can be shown that the fraction of low angle boundaries is lower in the ICHAZ than in the base metal. In fact, the observed differences are very similar to these observed between the base metal in the initial state and after tensile deformation (see **figure A.I.10**). Therefore, the evolution of the microstructure in the ICHAZ would be more a sort of recrystallization than recovery and the driving force of this metallurgical change is probably either the deformation induced by the martensitic transformation or residual stresses resulting from the welding operation.

It is also interesting to notice the difference between the size of the grains observed in the TEM micrograph in **figure A.II.11b**, i.e. $\approx 1 \mu\text{m}$, with that given by the EBSD map in **figure A.II.12b**, i.e. $\approx 5 - 10 \mu\text{m}$. These differences can be easily explained as TEM investigations and EBSD analysis give information at two different scales:

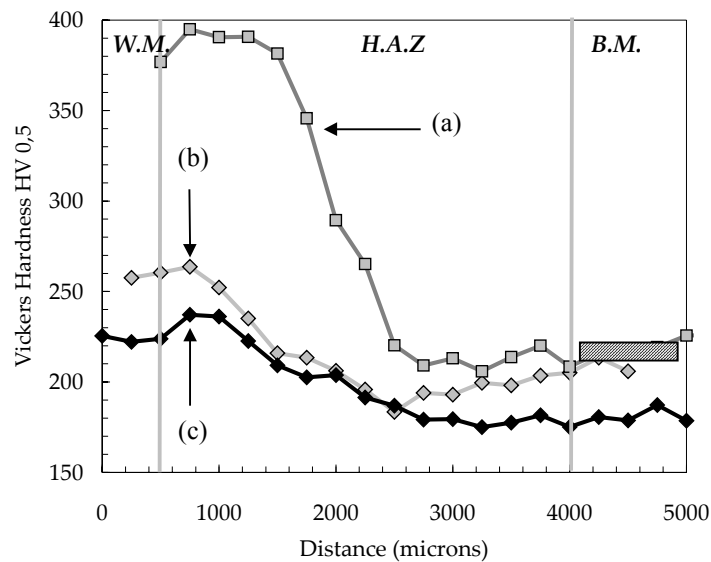
1. TEM investigations show the evolution of the recovery of the dislocations which modify the high temperature creep flow behaviour of the matrix (All boundaries including low angle boundaries are evidenced in TEM micrographs).
2. EBSD analysis show the modification of the interfaces and especially their possible sensitivity to high temperature intergranular cracking (High angle boundaries can be evidenced and the corresponding grain size can be determined as shown in **figure A.II.12b**).

In fact, one must keep in mind that the two means of investigations are very complementary but in terms of damage development the accurate observation scale is that of EBSD analysis with focusing attention on high angle boundaries.

4.3. Origin of the microstructural changes and resulting properties of the ICHAZ

The minimum in hardness is found especially for the WJP91 steel in the later part of the ICHAZ that is heated in the first part of the intercritical domain. In this region, the $\alpha \rightarrow \gamma$ phase transformation occurs but the carbide dissolution is largely incomplete as it mainly occurs in the upper bound of the intercritical domain. As a consequence, carbon is not put into the solid solution. The martensite which forms during rapid cooling is a very low carbon martensite and is consequently soft.

As massive lath recovery is observed over all the ICHAZ over a distance larger than 1.5 mm in the weldment, it is assumed that the PWHT plays a key role in the microstructural changes. The effect of the PWHT temperature was studied on the WJT91 weldment by comparing hardness profiles in the HAZ for three conditions: no tempering, a tempering of two hours at 760°C and a tempering of more than fifteen hours at 750°C (see **figure A.II.13**).



*Figure A.II.13. Profile of Vickers hardness in the HAZ of the WJ791
(a) No PWHT (b) a PWHT of 2 hours at 760°C (c) a PWHT of 15 hours and 18 minutes at 750°C*

The hardness profile in the as welded state (No PWHT) is very useful to determine the evolution of the $\alpha \rightarrow \gamma$ phase transformation in the HAZ. The representation of **figure A.II.13** also shows that the degree of softening of the HAZ strongly depends on the PWHT treatment as the most important softening is evidenced for the longest PWHT duration.

In fact two phenomena, which occur in the HAZ during weld thermal cycles, must be investigated:

1. The evolution of the precipitation state during the weld thermal cycle to which the properties of the newly formed martensite are obviously strongly linked.
2. The evolution of the microstructure of the HAZ during the PWHT.

These two points and the consequences of the corresponding microstructural changes on the HAZ creep strength will be investigated in more details in **chapter C.I**, **chapter C.II** and **chapter C.III**.

5. Tensile and toughness properties of weldments

5.1. Literature data

The literature data first concern measurements of dynamic fracture toughness by performing drop weight or impact tests on Charpy V-notched specimens. Moreover, those measurements were essentially carried out on the weld metal. Moitra et al (1999) performed drop weight tests on weldments in the temperature range between -25°C and -55°C . As they recorded the load time trace, they evidenced three main peaks corresponding to crack initiation successively in the CGHAZ, the FGHAZ and the ICHAZ. They could evaluate the toughness gradient in the HAZ and energies to crack initiation to 53 J in the CGHAZ, 85 J in the FGHAZ and 128 J in the ICHAZ.

The tensile properties of 9Cr1Mo-NbV steel weldment have also been evaluated from tensile tests on cross-welds specimens. The results given by Sturm et al (2002), Sireesha et al (2001), Letofsky et al (2000), Haarman et al (1999) Cerjak et al (1998) and Cerjak et al (1995) are reported in **table A.II.4**.

Reference	Weldment	PWHT	Test temperature	Initial strain rate	$R_p^{0.2}$	R_m	Reduction of area
Brozda and Zeman (1996)	9Cr1Mo-NbV	750°C /4h	20°C	Not given	490 MPa	662 MPa	71%
			450°C	Not given	388 MPa	477 MPa	76%
			550°C	Not given	280 MPa	331 MPa	92%
Letofsky et al (2000) & Cerjak et al (1998)	9Cr1Mo1W-NbV 12Cr1Mo1W-NbV	760°C /2h 730°C /12h	600°C	$10^{-5} s^{-1}$	310 MPa	300 MPa	90%
			600°C	$10^{-5} s^{-1}$	Not given	260 MPa	Not given
Cerjak et al (1995)	9Cr1Mo-NbV	760°C /2h	600°C	$10^{-5} s^{-1}$	Not given	260 MPa	Not given
Sireesha et al (2001)	9Cr1Mo-NbV	730°C /2h	20°C	$3 \cdot 10^{-4} s^{-1}$	873 MPa	960 MPa	52%
		760°C /6h	20°C	$3 \cdot 10^{-4} s^{-1}$	673 MPa	786 MPa	51%
Sturm et al (2002)	9Cr1Mo-NbV	760°C /2h	20°C	Not given	600 MPa	708 MPa	66%
			500°C	Not given	416 MPa	478 MPa	65%
			620°C	Not given	214 MPa	229 MPa	88%
Haarman et al (1999)	9Cr1Mo-NbV	760°C /2h	20°C	Not given	550 MPa	700 MPa	Not given
			500°C	Not given	380 MPa	440 MPa	Not given
			620°C	Not given	280 MPa	330 MPa	Not given
Coussement et al (1991)	9Cr1Mo-NbV	750°C /1h	20°C	Not given	523 MPa	687 MPa	73%
			200°C	Not given	478 MPa	611 MPa	77%
			600°C	Not given	310 MPa	324 MPa	91%
Coussement et al (1991)	9Cr1Mo-NbV	620-650°C /1h	20°C	Not given	652 MPa	768 MPa	76%
		750°C /1h	200°C	Not given	596 MPa	691 MPa	79%
			600°C	Not given	328 MPa	341 MPa	91%

Table A.II.4. Literature review of the tensile properties of chromium steel weldments

5.2. Experimental investigations of the tensile properties of the weldments

Tensile tests were carried out at 450°C and 550°C on the WJT91 weldment and at 625°C on the WJP91 weldment. The location of the specimens in weldments is illustrated in figure A.II.14. Note that the HAZ was positioned in the middle of the gauge length and that the three microstructural states i.e. the weld metal, the base metal and the heat affected zone were tested together.

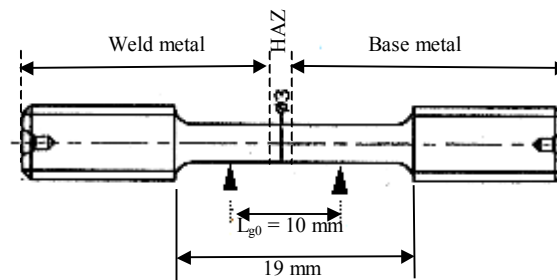


Figure A.II.14. Geometry of the smooth round tensile specimens

The elongation of the specimens was measured as:

$$\varepsilon = \frac{\Delta L_g}{L_{g0}} \quad (\text{eq. A.II.4})$$

where L_{g0} is the initial gauge length and ΔL_g is the actual elongation of the initial gauge length. The effect of the strain rate was explored at 450°C and 550°C. For tests on the WJP91 weldment the effect of the specimen location in the thickness of the welded joint was investigated. The main conclusions for the WJT91 weldment are:

1. A negative sensitivity to the strain rate is observed at 450°C.
2. The tensile strength and the 0.2% proof stress are between 30 MPa and 50 MPa lower than these of the base metal after the same PWHT.

The main conclusions for the WJP91 weldment are:

1. The upper welding pass is stronger than the preceding ones as $R_m = 315$ MPa in comparison with 295 MPa for the others. This phenomena may explained by the fact that except for the last welding pass, the material is over-tempered, and consequently softer, by the following welding runs.
2. Tensile strength and 0.2% proof stress are 30 MPa lower than these of the base metal.

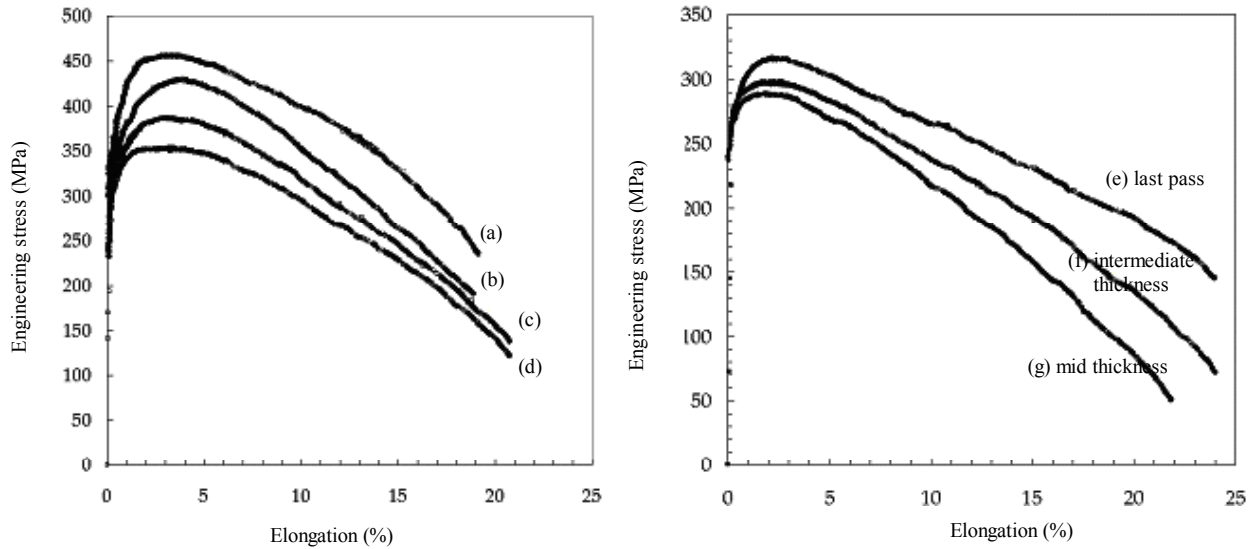


Figure A.II.15. Tensile curves for WJT91 - (a) 450°C - $10^{-3}s^{-1}$ (b) 450°C - $10^{-2}s^{-1}$ (c) 550°C - $10^{-2}s^{-1}$ (d) 550°C - $10^{-3}s^{-1}$ and for WJP91 at 625°C - $10^{-3} s^{-1}$ where (e)(f)(g) denote specimens machined from the last welding pass (e) to mid thickness (g)

The strain rate sensitivity was also explored at 625°C. The results of these tests are reported in table A.II.5 and figure A.II.16. It was evidenced that the tensile properties of the WJP91 weldment strongly depend on the strain rate. A decrease in the 0.2% proof stress and in the tensile strength, with decreasing the strain rate, as was also the case for the base metal, was evidenced.

Temperature	Initial strain rate	$R_p^{0.2}$	Uniform elongation	R_m	Final elongation	Reduction of area
625°C	$10^{-2} s^{-1}$	300 MPa	1.9 %	320 MPa	16.5	68.7%
625°C	$10^{-3} s^{-1}$	265 MPa	0.9 %	280 MPa	22.1	80.0%
625°C	$10^{-4} s^{-1}$	230 MPa	1.2 %	240 MPa	19.3	77.3%
625°C	$10^{-5} s^{-1}$	190 MPa	1.0 %	205 MPa	14.7	76.3%

Table A.II.5. Results of tensile tests at 625°C on the WJP91 weldment – Effect of the strain rate

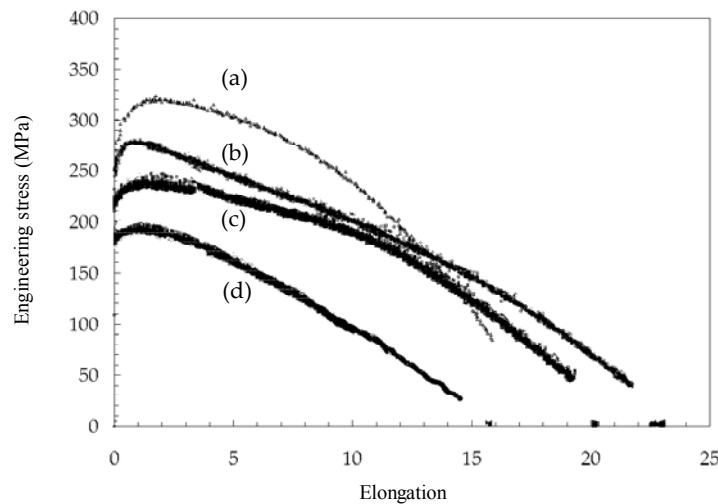


Figure A.II.16. Tensile curves for the WJP91: Investigations of strain rate effects (a) $10^{-2} s^{-1}$ (b) $10^{-3} s^{-1}$ (c) $10^{-4} s^{-1}$ (d) $10^{-5} s^{-1}$

Specimen failure occurs in the gauge length in the base metal but not far than 1 mm from the HAZ for all tensile tests, even for the lowest tensile strain rate (i.e. 10^{-5} s^{-1}), which is consistent with Sasaki et al (1991). Moreover, a higher ductility of the weldment than that of the base metal is evidenced. The same observation was made by Chandravati et al (2001). The final elongation of specimens reaches 20%. The final microstructure is also fully recovery with a grain size of few microns (see **figure A.II.17**).

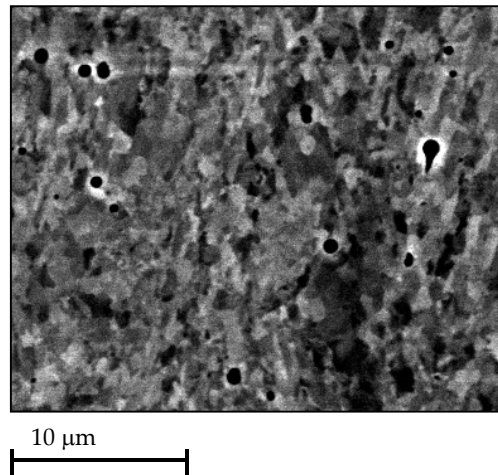


Figure A.II.17. SEM investigations in a cross section of the WJP91 weldment after tensile test and colloidal silica polishing

Contrary to the base metal, a high number of intragranular perfectly round voids were observed near the fracture area. SEM investigations have shown that these voids result from decohesion at matrix/particle, of mainly $M_{23}C_6$ carbide type, interfaces.

6. Effects of thermal ageing on P91 weldment at 550°C and 625°C

The effects of thermal ageing on WJP91 weldment were not extensively studied taking into account the complexity of the microstructure in the heat affected zone. However, Vickers hardness measurements were carried out to foresee the effects ageing on the properties of weldments. The corresponding hardness profiles after ageing at 550°C and 625°C are respectively plotted in **figure A.II.18a** and **A.II.18b**.

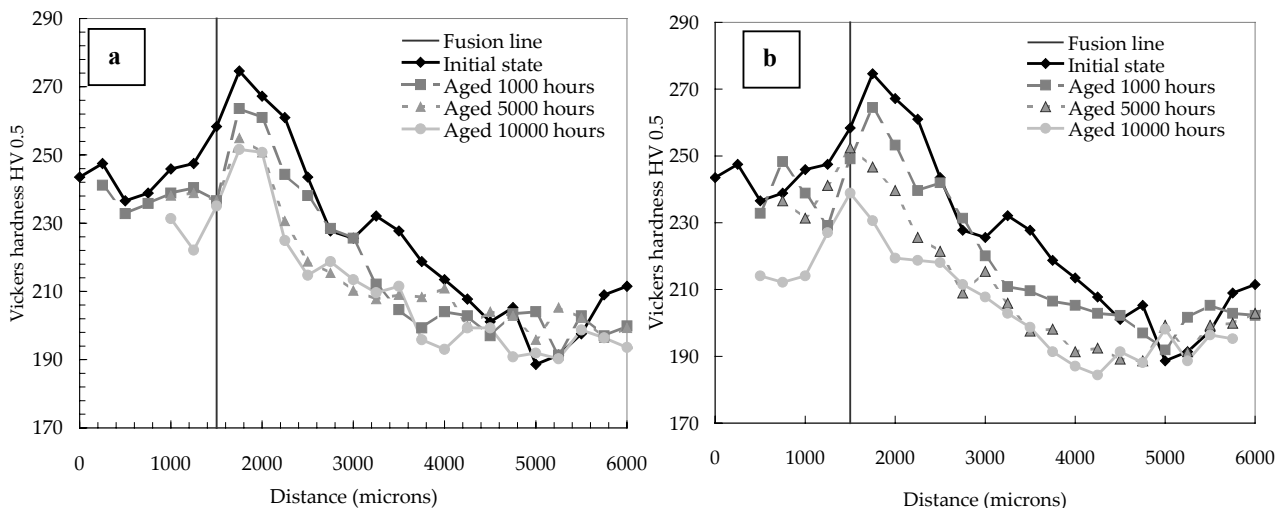


Figure A.II.18. Hardness profile for WJP91 weldment: Effect of thermal ageing at 550°C

The profiles of **figure A.II.18a** and **A.II.18b** evidence a further softening of the microstructure in the heat affected zone whereas the hardness of the double tempered base metal microstructure did not exhibit a significant reduction. Therefore, thermal ageing obviously affects the mechanical properties of the HAZ. SEM investigations also revealed the precipitation of Laves phase in all the weldment during thermal ageing. Note that the effects of thermal ageing in the ICHAZ will be explored in more details in **chapter C.III**.

7. Conclusions

The present chapter aimed at describing the welding properties of 9Cr1Mo-NbV steels and characterising the changes both in metallurgical and general mechanical properties due to the welding operation:

1. 9Cr1Mo-NbV steels exhibit a good weldability. For high thickness components, manual arc welding is the currently used joining method. The most commonly used filler metals have a chemical composition very closed to that of the base metal. The welding operation is followed by a high temperature i.e. > 750°C post weld heat treatment (PWHT) to release residual stresses, to temper the newly formed martensite and to optimise toughness properties of the weld metal.
2. The resulting weldment exhibits acceptable impact toughness and tensile properties even if it was shown that the tensile properties at 625°C are slightly lower (Both the 0.2 % proof stress and the tensile strength are reduced by 30 MPa to 50 MPa) than these of the base metal.
3. The main microstructural changes, due to thermal cycles experienced during the welding operation, are evidenced in the heat affected zone heated in the intercritical domain ($A_{c1} < T < A_{c3}$). This area exhibits a minimum of hardness. It could be related to a totally recovered microstructure having a low dislocation density and coarsen $M_{23}C_6$ carbide twice larger in size (typically 200 nm in diameter) than in the base metal.
4. As for the base metal, thermal ageing induces a softening of the weldment and the precipitation of Laves phase particles.

References

- Andren H.O., Cai G., Svensson L.E. (1995). Microstructure of heat resistant chromium steel weld metals. *Applied surface science*. **87/88**. 200-206.
- Bailey N., Jones S.B. (1978). The solidification cracking of ferritic steels during submerged arc welding. *Welding journal*. **57**. 217-231.
- Balmforth M.C. and Lippold J.C. (2000). A new ferritic martensitic stainless steel constitution diagram. *Welding research. Supplement*. 339s-345s.
- Barnes A.M. (2000). Solidification cracking susceptibility of modified 9Cr1Mo submerged arc weld metals: the influence of Mn and Nb. *Proceedings of the 5th International Charles Parsons Turbine Conference*. 407-430.
- Beres L., Balogh A., Irmer W. (2001). Welding of martensitic creep resistant steels. *Welding research. Supplement*. 339s-345s.
- Bhaduri A.K., Ray S.K., Rodriguez P. (1997). Optimising post weld heat treatment for alloy 800/(9Cr-1Mo) steel joints using toughness parameters for tensile tests. *Materials Science and technology*. **13**. 356-359.
- Bonnet C. (2000). Traitements thermiques associés au soudage des aciers. *Techniques de l'ingénieur – Traité Métallurgie*. **M1365**. 1-11.
- Brachet J.C. (1991). Alliages martensitiques 9Cr-1Mo: effet de l'addition de l'azote et du vanadium sur la microstructure, les transformations de phase et les propriétés mécaniques. *PhD Thesis Paris Sud Orsay University*.
- Brozda J., Zeman M. (1996). Weldability of 9Cr-1Mo-Nb, V P91 steel intended for service in the power industry. *Welding International*. **10(5)**. 370-380
- Danon A., Servant C., Alamo A., Brachet J.C. (2003). Heterogeneous austenite grain growth in 9Cr martensitic steels: influence of heating rate and the austenitization temperature. *Materials science and engineering*. **A348**. 122-132.
- Dittrich S., Gross V., Heuser H. (1994). Optimized and advanced P(T)91 filler metals. Second European conference on welding technology - EUROJOIN2. 415-425.
- Gosh P.K., Gupta P.C., Potluri N.B., Gupta Y. (2004). Influence of pre and post weld heating on weldability of modified 9Cr-1MoVNb steel plates under SMA and GTA welding processes. *ISIJ International*. **44(7)**. 1201-1210.
- Haarmann K., Vaillant J.C., Bendick W., Arbab A. (1999). The T/P91 book. *Vallourec and Mannesmann tubes*.
- Hald J., Lund E.M. (1993). TEM investigations in the HAZ in P91 steel (9Cr, 1Mo, Nb, V). *International conference of the joining of materials – Hebingor (Danemark)*.
- Igarashi M., Muneki S., Abe F. (1998). Microstructure control of martensite phase matrix in advanced ferritic steels for USC boilers to achieve long term stability. *Materials for advanced power engineering - 6th Liege Conference*. 637-646.
- Jakobova A., Vodarek V., Hennhofer K., Foldyna V. (1998). Microstructure and creep properties of P91 steel and weldments. *Materials for advanced power engineering - 6th Liege Conference*. 373-382.
- Clueh R.L. and Harries D.R. (2001). High chromium ferritic and martensitic steels for nuclear applications. *American Society for Testing Materials*
- Laha K., Chandravathi K.S., Bhanu Sankara Rao K. (2000). Microstructural Evaluation and creep deformation and rupture behavior of 9Cr-1Mo steel base metal, weld metal and weld joint. *Transactions of the Indian Institute of Metals*. **53(3)**. 217-221

- Letofsky E., Cerjak H., Warbichler P. (2000). The use of electron microscopic investigations to characterise the creep behaviour of welded joints in modern power stations materials. *Praktische Metallography*. **37(9)**. 509-520.
- Moitra A., Ray S.K., Mannan S.L. (1999). Determination of dynamic fracture toughness of heat affected zone of 9Cr1Mo steel from instrumented drop weight tests. *Materials science and technology*. **15**. 137-143.
- Moorhy V., Vaidyanathan, S., Laha K., Jayajumar T., Bhanu Sankara Rao K., Raj B. (1997). Evaluation of microstructures in 2.25Cr-1Mo and 9Cr-1Mo steel weldments using magnetic barkhausen noise. *Materials Science and Engineering*. **A231**. 98-104.
- Murry G. (2000). Soudage et soudabilité métallurgique des métaux. *Techniques de l'ingénieur – Traité Métallurgie*. **M715**. 1-35.
- Mythili R., Thomas Paul V., Saroja S., Vijalakshmi M., Raghunathan V.S. (2003). Microstructural modification due to reheating in multipass arc welds of 9Cr-1Mo steel. *Journal of nuclear materials*. **312**. 199-206.
- Niederhoff K., Wellnitz G., Zschau M. (1991). Experience with the fabricability of the creep resistant 9%Cr chromium steel X10CrMoVNb (P91). *ASME International power generation conference (San Diego)*. 1-8.
- Orr J., Burton D., Rasche C. (1993). Sensitivity of microstructure and mechanical properties of steel 91 to initial heat treatments. *Ironmaking and steelmaking*. **20(6)**. 415-423.
- Orr J. and DiFrancesco A. (1993). Effect of compositional variations on properties of steel 91. *Ironmaking and steelmaking*. **20(6)**. 424-430.
- Otoguro Y., Matsubara M., Itoh I., Nakazawa T. (2000). Creep rupture strength of heat affected zone on 9Cr heat resisting steels. *Nuclear engineering and design*. **196**. 51-61.
- Santella M.L., Swinden R.W., Reed R.W., Tanzosh J.M. (2001). Martensite formation in 9Cr-1Mo steel weld metal and its effect on creep behavior. *EPRI conference on 9Cr materials fabrication and joining technologies. Myrtle beach, SC USA*.
- Shiue R.K., Lan K.C., Chen C. (2000). Toughness and austenite stability of modified 9Cr-1Mo welds after tempering. *Materials science and engineering*. **A287**. 10-16.
- Sturm R., Jenko M., Ule B. (2002). A creep properties evaluation of P91 steel weldments using short term-testing. *Materiali in tehnologije*. **36(6)**. 319-324.
- Warreing J. (1994). A review of the mechanical and physical properties of modified 9CrMoNbV (Grade 91) steel. CEA/SRMA, N.T SRMA94-2013.
- Welding E.D.F. (2001). Validation expansion, standardisation of procedures for High Temperature Defect Assessment " BE-1702-HIDA (Private communication).
- Welding Framatome (2003). Joint 9% Cr - 1Mo HTR INNO Dossier de fabrication du joint soudé MC/TS 1972. TFCW R 02.320. (Private communication).
- Wu W., Hwu L.Y., Lin D.Y. and Lee J.L. (2000). The relationship between alloying elements and retained austenite in martensitic stainless steel welds. *Scripta materialia*. **42**. 1071-1076.
- Yajiang L., Juun W., Bing Z., Tao F. (2002). XRD and TEM investigations in the welding zone of 9Cr1Mo-V-Nb heat resisting steel. *Bulletin of materials science*. **25(3)**. 217-221.

Main Results of Part A

1. Base Metals

The base metals are low carbon chromium martensitic stainless steels of type 9Cr1Mo-NbV.

Matrix microstructure: Tempered lath martensite is arranged in packets within the prior austenite grain of 100 – 140 μm in size.

Precipitation state: The high tempering treatment results in the precipitation of mainly M_{23}C_6 carbides but also MX particles. These precipitates are located at all boundaries i.e. between packets, laths and prior austenite grains.

Mechanical properties: 9Cr1Mo-NbV steels have good high temperature mechanical properties. However, the tensile properties are very sensitive to the strain rate. Moreover, the very low value of the uniform elongation, especially at high temperature, evidenced a great sensitivity of the material to rapid softening. EBSD analysis revealed that the softening mechanism involved during high temperature tensile deformation is obviously the recrystallisation of the initial lath microstructure.

Effects of ageing on the microstructure: The thermal ageing modify the precipitation state as M_{23}C_6 carbides coarsening proceeds, Laves phases appear and the precipitation of a Z-phase which is said to strongly affect the mechanical properties, is reported for long term ageing i.e. larger than 30,000 hours. Moreover, the recovery of the initial lath microstructure occurs with the formation and the growth of subgrains within laths.

Effects of ageing on the general mechanical properties of the base metal: The 0.2% proof stress and the tensile strength are both affected by prior thermal ageing. The effects of ageing on creep flow and damage properties will be studied in **Part B** where the occurrence of dynamic recovery or recrystallisation assisted by creep deformation will be investigated.

2. Weldments

The weldments are made in 9Cr1Mo-NbV steels for which the weld metal that is currently used, exhibits nearly the same chemical composition than the base metal. The welding procedure is mainly submerged arc welding with relatively low input energy (1300 – 2200 Jmm^{-1}). The weldments are mainly studied after the post weld heat treatment.

Microstructure of the weld metal: The weld metal exhibits a lath martensite morphology just as the base metal. However, due to the thermal gradient, austenite grains are more frequently elongated than equiaxed and the presence of MnS particles was detected due to the higher sulphur content.

Effects of welding on the microstructure: The microstructure of the base metal is strongly modified due to local heating which lead to phase transformation in the heat affected zone. The heat affected zone may be divided into three main parts:

- The coarse grained heat affected zone (CGHAZ) - $T_{\text{peak}} \gg A_{c3}$.
- The fine grained heat affected zone (FGHAZ) - $T_{\text{peak}} \approx A_{c3}$.
- The intercritical heat affected zone (ICHAZ) - $A_{c1} < T_{\text{peak}} < A_{c3}$.

Metallurgical investigations in the ICHAZ especially revealed a minimum in hardness and a change in the initial lath martensite having a high dislocation density into a fully equiaxed grains microstructure containing few dislocations.

Effects of ageing on the mechanical properties of the weldments: As for the base metals, thermal ageing obviously affects the hardness and tensile properties of the weldments.

Part B

*Creep flow and damage mechanisms of 9Cr1Mo-NbV steel
at high temperature: Experiments and Modelling*

*(Etude expérimentale et modélisation du comportement, de l'endommagement et de la rupture en
fluage haute température de l'acier 9Cr1Mo-NbV)*

Introduction

In the first **chapter B.I**, after a short description of the principle of the creep test, the creep flow and damage mechanisms encountered in creep loading conditions are described. Attention is especially focused on the various ways to model creep flow and damage behaviour with or without coupling between creep flow and damage. As the present study is concerned with martensitic chromium stainless steels, results of previous studies on creep properties of 9Cr1Mo-NbV steels at high temperature are reminded.

The second part of the study (**chapter B.II**) deals with experimental investigations of creep flow and damage behaviour of the P91 steel at 625°C. The experimental database built for the HIDA project is described. Damage mechanisms are investigated by scanning electron microscope (SEM) investigations on polished cross-sections of the smooth round tested specimens. The main characteristics of creep flow and damage mechanisms are deduced from these creep results and observations. Quantification of creep damage is also performed by cross-sections SEM maps of damaged specimens followed by image analysis. The effect of prior thermal ageing on creep properties at 625°C is then explored.

The following part (**chapter B.III**) is dedicated to the formulation of a new creep model integrating multiple deformation and damage mechanisms. Experimental results on various kinds of specimen geometry are integrated in this chapter. This model was designed on the basis of the experimentally observed creep flow and damage mechanisms. It was written in the framework of the mechanics of porous media. The model formulation is first described. Then, the identification procedure and the resulting model parameters are given. A first validation of the model is made by comparison of the model predictions with the porosity ratio experimentally observed but also by comparison with literature data. The model is then successfully extrapolated to the temperature range between 600°C and 650°C.

To further validate the model (**chapter B.IV**), it is tested on several other cases as creep tests on plate notched (PNC), and compact tension (CT) specimens. The predictions of the model in terms of creep time to failure, of the location of damage nucleation, and of the direction of the crack propagation are investigated and compared with experimental results.

A locally coupled version of the model is also proposed in **chapter B.V**. The resulting equations, representing the development of creep damage, were integrated as a post-processor to mechanical FE calculations at the Centre des Matériaux but also at the CEA Cadarache by Y. Lejeail. A failure criterion is proposed and the predictions given by the post-process are compared with the results given by the fully coupled model.

Finally, an experimental study of creep flow and damage behaviour of the T91 steel at 450°C and 550°C is presented in **chapter B.VI**. It concerns creep tests on smooth round tensile bars. It is shown that the model can be used to represent creep flow and damage behaviour at 550°C. The extrapolation to lower temperature (i.e. 450°C) is also questioned.

Contents

Chapter B.I. State of the art.

Chapter B.II. Experimental investigations of creep mechanisms and cavitation processes in P91 steel at 625°C (Smooth round specimens).

Chapter B.III. Modelling creep mechanical and damage behaviour of the P91 steel at 625°C: “Creep failure model of a tempered martensitic stainless steel integrating multiple deformation and damage mechanisms”. V. Gaffard, J. Besson, A.F. Gourgues-Lorenzon. *Submitted to International Journal of Fracture in September 2004.*

Chapter B.IV. Validation of the model: Ability of the model to represent creep tests on CT and plate notched specimens.

Chapter B.V. Formulation and use of a locally coupled version of the model.

Chapter B.VI. Creep flow and damage behaviour of the T91 steel at 450°C and 550°C.

Chapter B.I. State of the art

1. Creep of metals

1.1. Description of the creep test

Creep test consists in applying a constant stress to the material and monitoring the strain of the specimen during time. At high temperature, creep curves exhibit three main stages:

1. Primary creep which corresponds to material hardening following the loading of the specimen.
2. Secondary creep which corresponds to steady state creep regime (The creep strain rate remains constant).
3. Tertiary creep which corresponds to an acceleration of creep strain due to softening, damage or cross section reduction.

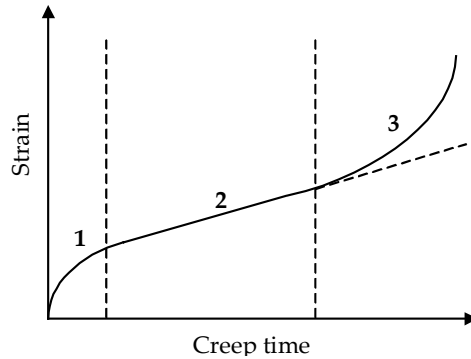


Figure B.I.1. Typical creep curves (Strain vs time)

1.2 Creep mechanisms

The following review of creep mechanisms is inspired by the works of Garofalo (1966) and Poirier (1985). Three main mechanisms can be distinguished to explain how the creep strain proceeds at high temperature:

1. Dislocation climb or cross-slip.
2. Diffusion or Harper-Dorn creep.
3. Grain boundary sliding (GBS).

At high stress levels, creep deformation mainly proceeds by dislocation glide and climb. Dislocations glide in slip planes (preferentially in slip planes suitably aligned to the applied stress) when the resolved shear stress exceeds a critical value. This stress is called the "Peierls stress" and is given by:

$$\sigma_{\text{Peierls}} = \frac{2\mu}{K} \exp\left(\frac{4\pi\zeta}{b}\right) \quad (\text{eq. B.I.1})$$

where, μ is the elastic shear modulus.

b is the length of the Burgers vector.

K is a constant depending on the dislocation type.

ζ is the dislocation core (a region where the crystalline order is defective).

A dislocation does not always glide freely and may be stopped by obstacles. Several configurations are possible. First, dislocation can be pinned by second phase particles which is often the case in alloyed steel. The dislocation pinned at its extremities bows out under stress and may emit dislocation loops. Those pinned dislocations which emit dislocation loops are known as Frank-Read sources. This is the main mechanism of dislocation creation during deformation of crystals. Frank-Read sources are activated when the Peach-Kohler force:

$$\tau_c = \frac{\mu b}{L} \quad (\text{eq. B.I.2})$$

is reached (with L the distance between pinning points). Second, dislocations may entangle or cut through each other leading to the formation of jogs on the dislocation line. Third, when arriving at a highly misorientated grain boundary or a precipitate, dislocation line is stopped and it may lead to a dislocation pile-up. The stress to which the obstacle is submitted is equal to $n\tau$ where n is the number of dislocations in the pile-up. When the dislocation glide is stopped and the Peierls stress is not reached, the dislocation movement may proceed by climb. The dislocation climb throughout an obstacle (particles, boundary ...) is possible thanks to the vacancies or jogs migration along the dislocation line. Creep strain rate is related to the dislocation glide by the Orowan's equation:

$$\dot{\epsilon} = \rho b v \quad (\text{eq. B.I.3})$$

where, ρ is the density of mobile dislocations and v is the average velocity of dislocations for which Weertman (1957) proposed the following expression in the case of solid solution strengthened alloy:

$$v = A\sigma^2 b^2 L \quad (\text{eq. B.I.4})$$

where L is the length of the dislocation pile up and A is a material constant.

The high stress creep level is often designated by "power-law" creep as steady state strain rate can be represented by a simple Norton power-law:

$$\dot{\varepsilon}_{ss} = B\sigma^n \quad (\text{eq. B.I.5})$$

The Norton power-law is consistent with the development of Weertman (1955), Nabarro (1967) and Spingarn et al (1979). All the three extensively studied steady state creep regime controlled by dislocation creep. Weertman (1957) determined the steady state creep strain rate in the case of lattice diffusion controlled creep:

$$\dot{\varepsilon}_L = \alpha_L \frac{Gb}{kT} D_L \left(\frac{\sigma}{G} \right)^3 \quad (\text{eq. B.I.6})$$

where D_L is the lattice diffusion coefficient and $\alpha_L \approx 1.0$.

Same development were made by Nabarro (1967) for core diffusion controlled creep leading to:

$$\dot{\varepsilon}_c = \alpha_c \frac{Gb}{kT} D_c \left(\frac{\sigma}{G} \right)^5 \quad (\text{eq. B.I.7})$$

where D_c is the core diffusion coefficient and $\alpha_c \approx 0.02$.

From many experimental studies, especially for creep at intermediate temperatures ($0.3 - 0.5 T_m$) and activation energy measurements, it was finally evidenced that both core and lattice diffusion control steady state creep strain rate. Therefore, Spingarn et al (1979) proposed a unified model with defining an effective diffusion coefficient:

$$\dot{\varepsilon}_L = A \frac{Gb}{kT} \left(D_L + \beta \left(\frac{\sigma}{G} \right)^2 D_c \right) \left(\frac{\sigma}{G} \right)^3 \quad (\text{eq. B.I.8})$$

where A and β are material constants and the effective diffusivity:

$$D_e = \left(D_L + \beta \left(\frac{\sigma}{G} \right)^2 D_c \right) \quad (\text{eq. B.I.9})$$

Senkov et al (1998) developed a model for steady state creep when strain is due to dislocation slip within grains. They also took into account the migration of grain boundaries. They found the resulting expression for steady state creep strain rate:

$$\dot{\varepsilon} = \dot{\varepsilon}_0 \left(\frac{\sigma}{G} \right)^4 \exp \left(- \frac{Q_0 - \gamma\sigma}{kT} \right) \quad (\text{eq. B.I.10})$$

where Q_0 is an activation energy and γ is the surface energy of the grain boundary. From all these works, one should deduce that **a Norton power-law may well represents power-law creep by dislocation climb or cross-slip with values of the exponent n ranging from 3.0 to 5.0.**

More original models were for example developed by Rosler and Artz (1990) who considered a creep deformation mechanism controlled by the thermal activation of dislocation detachment from second phase particles:

$$\dot{\varepsilon} = \dot{\varepsilon}_0 \exp \left(- \frac{Gb^2 r \left[(1-k) \left(1 - \frac{\sigma}{\sigma_d} \right) \right]^{3/2}}{kT} \right) \quad (\text{eq. B.I.11})$$

where r is the characteristic dimension of second phase particles, k is a material parameter representing the interaction between dislocation and second phase particles and σ_d is the stress needed for dislocation detachment from second phase particles. All the model presented in the previous paragraphs allow to represent only the steady state creep regime. Some authors like Sellars and Teggart (1966) or Robinson (1978) chose to represent both the primary and the steady state creep regimes with a single model. The formulation of Sellars and Teggart (1966) is based on the Zener and Hollomon (1944) parameter Z :

$$Z = \dot{\varepsilon} \exp \left(\frac{Q}{RT} \right) \quad (\text{eq. B.I.12})$$

where Q is an activation energy and Z is given by Sellars and Teggart (1966) as:

$$Z = A(\sinh(\alpha\sigma))^n \quad (\text{eq. B.I.13})$$

where A and α are model parameters so that:

$$\dot{\varepsilon} = A(\sinh(\alpha\sigma))^n \exp \left(- \frac{Q}{RT} \right) \quad (\text{eq. B.I.14})$$

The model proposed by Robinson (1978), which is used in Eggeler et al (1994), is expressed in the case of isotropic hardening as:

$$\dot{\sigma} = D(\dot{\varepsilon} - \dot{\varepsilon}_p) \quad (\text{eq. B.I.15})$$

where $\dot{\varepsilon}$ is the total strain rate and $\dot{\varepsilon}_p$ is the plastic strain rate.

$$\dot{\varepsilon}_p = A \left(\frac{s : s}{2K} - 1 \right)^n \frac{s}{\sqrt{s : s / 2}} \quad (\text{eq. B.I.16})$$

where s is the deviatoric stress, A is a model parameter and K is the isotropic hardening given by:

$$\dot{K} = \left(s : \dot{\varepsilon}_p \right) W_p \exp\left(-\frac{W_p}{W_0}\right) \quad (\text{eq. B.I.17})$$

where W_p is the plastic strain work and W_0 is a model parameter.

At low stress level, creep strain rate may also be represented by a Norton power-law with a theoretical exponent $n = 1$:

$\dot{\varepsilon}_{ss} = B\sigma$ even if it was already experimentally observed that n may vary between 1 and 2.

The first existing deformation mechanism at low stresses is the diffusion of atoms and vacancies. The applied stress generates an excess of vacancies at grain boundaries normal to the loading direction and a depletion along other boundaries which experience compressive stresses. To reach equilibrium, a vacancy flux occurs from boundaries experiencing tensile stresses to boundaries experiencing compressive stresses. The concentration of vacancies at grain boundaries is given by:

$$C_1 = C_0 \exp\left(\frac{\sigma b^3}{kT}\right) \quad (\text{eq. B.I.18})$$

Diffusion may occur through the lattice or along the grain boundaries. The two corresponding diffusional creep rates which directly depend on σ are respectively given by Herring (1950) and Nabarro (1967), (**equation B.I.19**), and Coble (1963), (**equation B.I.20**):

$$\dot{\varepsilon} = \frac{\alpha \Omega D_g}{kT d^2} \sigma \quad (\text{eq. B.I.19})$$

$$\dot{\varepsilon} = \frac{\beta \Omega \delta D_b}{kT d^3} \sigma \quad (\text{eq. B.I.20})$$

where, D_g is the diffusion coefficient in the grains, D_b is the grain boundary diffusion coefficient.

The two formulations only differ in the grain size dependence of the strain rate. It follows that Coble creep especially predominates in materials which have a small grain size. Harper and Dorn (1957) proved the existence of a third creep mechanism at low stresses as they measured creep strain rates, for pure aluminium, three times higher than those predicted by earlier theories of Herring, Nabarro and Coble.

In addition, at low stresses and high temperature, grain boundary sliding (GBS) often occurs in creep conditions especially in the diffusion creep regime. The review of Gifkins (1994) gives very interesting information about GBS. In the diffusion creep regime, GBS strongly depends on the grain boundary orientation because of the evolution of the vacancy flux previously described. Two GBS processes at low stresses, called Rachinger sliding and Lifshitz sliding, must be distinguished. Lifshitz considered GBS as an accommodation process of deformation by diffusion to maintain deformed grains neighbouring whereas Rachinger considered that GBS affects grains neighbouring. The GBS at low stresses is also often associated to cavity nucleation by ledge (ledges are formed by slip bands during creep) or particle (local stress at particle interface) mechanisms. The review of Gifkins (1994) also pointed out that GBS can occur during power-law creep. In this case, it is controlled by dislocation climb like the overall creep deformation. The sliding of a particular grain boundary is driven by the resolved shear stress on it. As pointed out by Langdon (2000), it is very difficult to determine which creep mechanism prevails at low stresses. Only microscale analysis of grain deformation or dislocation density measurements may give arguments for a choice. Gifkins et al (1975) have also shown that the contribution of GBS to the overall creep strain depends on the method used to define the strain due to grain boundary sliding. Finally, Raj and Ashby (1972) and Horsewell (1978) evidenced that the sliding rate is strongly slowed down by the presence of hard precipitates.

Ashby and Frost (1982), summed up very clearly, the changes in deformation mechanisms with designing mechanisms maps for numbers of materials. The general formulation of a deformation mechanisms map is given in **figure B.I.2**. It gives stress, strain rate and temperature dependence of deformation mechanisms and softening processes with respect to both the normalised stress σ/G and the ratio T/T_{melting} .

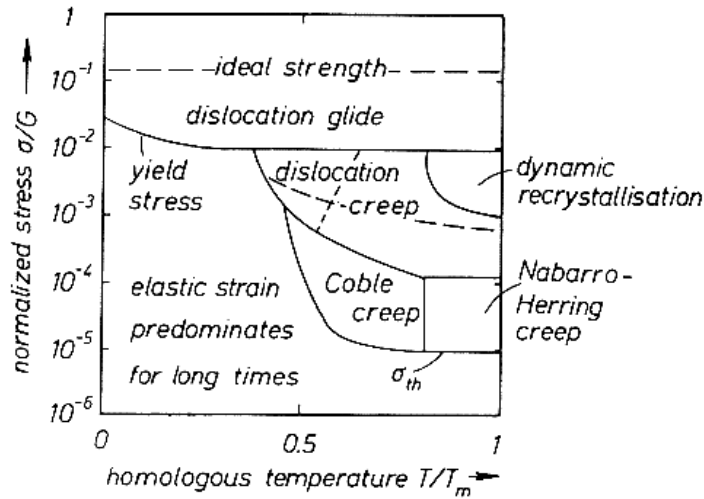


Figure B.I.2. Sketch of a deformation mechanism map (extracted from Riedel (1987))

To conclude, all the theoretical work concerned with the evaluation of the steady state creep strain rate corresponding to various physical mechanism showed that steady state creep can be represented by a Norton power-law of **equation B.I.5** with:

1. An exponent $n > 3.0$ for dislocation creep (high stress).
2. An exponent $n = 1$ (and sometimes $1 < n < 2$) for diffusion creep (low stress).

1.3. Creep cavitation processes

The following review of creep cavitation processes is inspired by the work of Kassner and Hayes (2003), Blum (2001), Riedel (1987) and Evans (1984). Two main types of voids are currently considered: the w-type (wedge crack) and the r-type (round void). The cavitation process can be divided into three main stages: the nucleation, the growth and the coalescence which are successively treated in the following.

1.3.1. Cavity nucleation

Nucleation mechanisms are not well determined. However, many observations give arguments to state that nucleation mainly occurs at grain boundaries. Vacancy condensation (studied by Raj (1977)), dislocation pile-ups (Zener-Stroh mechanism), grain boundary sliding are the most widespread nucleation mechanisms involved in classical theories (see **figure B.I.3**).

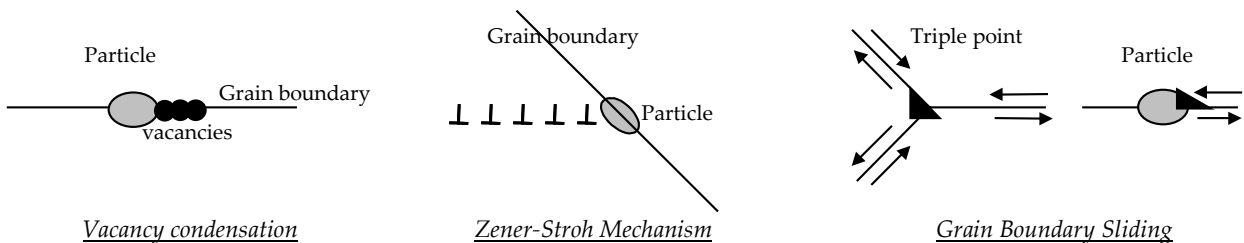


Figure B.I.3 Configurations for nucleation of creep cavities

In all cases, the nucleation is largely promoted in stress concentration areas like grain boundary triple points or second phase particles in alloy steels. For example, the presence of second phase particles at grain boundaries favours dislocations pile-up and the Zener-Stroh mechanism is often observed in alloy steels.

The first descriptions of cavity nucleation were mainly performed by considering thermodynamic principles as the nucleation phenomenon is thermally activated. Following the theory developed by Cahn and Hilliard (1956), the nucleation of a cavity results from the competition between the energy needed to create the cavity and the dissipation of energy which accompany the cavity nucleation. The variation in free energy corresponding to the nucleation of a cavity of radius R with neglecting the variation of the elastic energy due to the cavity nucleation is:

$$\Delta G = 4\pi R^2 \gamma - \sigma \frac{4}{3} \pi R^3 \quad (\text{eq. B.I.21})$$

where, γ is the surface energy of the cavity, R is the radius of the cavity and σ the applied stress. Cavity nucleation can occur provided an energy barrier is overridden which corresponds to $\frac{\partial \Delta G}{\partial R} = 0$. From this criterion a critical cavity

radius, r^* , and the Gibbs free energy corresponding to a cavity of radius r^* , ΔG^* , can be determined.

$$r^* = \frac{2\gamma}{\sigma} \text{ and } \Delta G^* = \frac{16\pi}{3} \frac{\gamma^3}{\sigma^2} \quad (\text{eq. B.I.22})$$

Same calculations can be made for cavity nucleation at grain boundary and leads to:

$$r^* = \frac{2(\gamma - \gamma_j / 4)}{\sigma} \quad (\text{eq. B.I.23})$$

where, γ_j is the surface energy of the grain boundary. As the critical radius is lowered (compare **equation B.I.22** and **equation B.I.23**), there is evidence that nucleation of new cavities is promoted at grain boundary but also at particle/matrix interface. Practically, calculated critical nuclei size range from 2 to 5 nm. However these approaches give not a good representation of the reality. Raj (1997) showed that an incubation time is required to form a critical cluster and experiments confirmed that the critical radius calculated by thermodynamic calculations does not correspond to the real one.

To integrate the kinetics of creep cavity nucleation into creep damage model, more simple phenomenological laws integrating the effects of creep strain and/or of the stress triaxiality ratio, have been fitted on experimental results. It is usually shown that creep cavitation is a continuous process as the density of creep cavity increases with strain (Yu and Hong (1989)). Many experimental studies have been concerned with evaluating effects of creep mechanical behaviour on cavity nucleation. The synthesis of Guttman (1982) relates the works of McLean (1981) and Argon et al (1980). McLean (1981) evidence the effect of the stress triaxiality ratio on nucleation kinetics with performing a counting of creep cavity on a Nimonic 80 alloy creep tested on round notched specimens. Same conclusions are given by Myers et al (1987) for a steel of type 1Cr-0.5Mo. The corresponding nucleation kinetics is written as:

$$\dot{f}_n = A \left(\frac{\sigma_1}{\sigma} \right)^2 \dot{\epsilon} \quad (\text{eq. B.I.24})$$

However, Argon et al (1980), Dyson (1983), Sundurarajan (1985) and Davanas and Solomon (1990) have found a dependence of nucleation kinetics on the equivalent stress which would lead to:

$$\dot{f}_n = A_d \dot{\epsilon} \quad (\text{eq. B.I.25})$$

Eggeler (1989) also showed for a 12% Cr steel a dependency of the nucleation kinetics to the overall strain rate. The same conclusions were given by Wu and Sandström (1995a) for the same alloy. All their creep tests were, however, carried out on smooth round specimens, for which the maximum stress triaxiality ratio does not exceed 1/3. In addition, in a synthesis published by Wu and Sandstrom (1995b), it is shown that the principal stress may also have a key role in the damage nucleation process. In fact, the best recommendation is to chose a nucleation law after having experimentally identified the accurate mechanical parameters with varying the stress triaxiality ratio.

1.3.2. Cavity growth

Once cavity nucleation has occurred, the following stage consist in the growth of the cavity. The cavity growth may proceed from matrix flow (High stress creep regime) or diffusion at grain boundaries (Low stress creep regime). The growth kinetics of a cavity of R in radius, was studied by Rice and Tracey (1969) in the high stress creep regime (i.e. viscoplasticity) and Hull and Rimmer (1959) in the low stress creep regime.

$$\text{The model of Rice and Tracey (1969) gives: } \frac{dR}{Rdt} = \alpha \dot{\epsilon} \exp \left(\frac{\sigma_m}{\sigma_{eq}} \right) \quad (\text{eq. B.I.26})$$

$$\text{The model of Hull and Rimmer (1959) gives: } \frac{dR}{dt} = \frac{D_{gb} \delta}{kT} \frac{\sigma_m \Omega}{LR} \quad (\text{eq. B.I.27})$$

where L is the intercavity spacing, δ is the thickness of the grain boundary, D_{gb} is the grain boundary diffusivity. Rice (1979), Edward and Ashby (1979) and Needleman and Rice (1980) determine a diffusion length parameter:

$$\Lambda_{gb} = \left(\frac{\Omega \delta D_{gb} \sigma}{kT \dot{\epsilon}} \right)^{1/3} \quad (\text{eq. B.I.28})$$

$$\Lambda_1 = \left(\frac{\Omega \delta D_1 \sigma}{kT \dot{\epsilon}} \right)^{1/2} \quad (\text{eq. B.I.29})$$

where D_L is the lattice diffusivity, Λ_{gb} and Λ_l respectively represent the diffusion length parameter for grain boundary "gb" and lattice "l" diffusion. It is usually assumed that the cavity growth is controlled by diffusion when its radius r is largely lower than the diffusion length parameter Λ_{gb} or Λ_l .

Coupled cavity growth can also occur when $\Lambda + r < \frac{\lambda}{2}$ with λ the intervoid spacing. This last case is the most commonly encountered situation. Therefore, the necessity to consider coupled influences of matrix flow and diffusion at grain boundaries on cavity growth was assumed by many authors such as Tvergaard (1984), Onck and Van der Giessen (1997) and Michel (2004). The representation of **figure B.I.4** sums up the influences of the two processes on cavity growth.

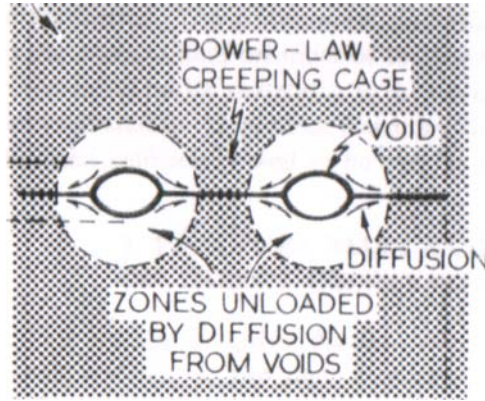


Figure B.I.4. Coupled diffusion and power law creep cavity growth (Extracted from Ashby et al (1979))

The creep cavity growth is consequently driven by two mechanisms in the steady state creep and a general expression depending on the cavity shape is given by Tvergaard (1984):

$$\dot{v} = \dot{v}_1 + \dot{v}_2 \quad (\text{eq. B.I.30})$$

$$\text{with, } \dot{v}_1 = 4\pi D \frac{\sigma_n - (1-f)\sigma_s}{\ln\left(\frac{1}{f}\right) - \frac{(3-f)(1-f)}{2}} \quad (\text{Hull and Rimmer like's formulation}). \quad (\text{eq. B.I.31})$$

σ_n : principal stress

σ_s : shear stress

D : grain boundary diffusivity

f : porosity ratio

$$\text{and, } \dot{v}_2 = 2\pi \dot{\epsilon}_e a^3 h(\psi) \left[\alpha_n \frac{\sigma_n}{\sigma_e} + \beta_n \right]^n \quad \left[\frac{\sigma_n}{\sigma_e} > 1 \right] \quad (\text{eq. B.I.32})$$

$$\dot{v}_2 = 2\pi \dot{\epsilon}_e a^3 h(\psi) \left[\alpha_n + \beta_n \right]^n \frac{\sigma_n}{\sigma_e} \quad \left[\frac{\sigma_n}{\sigma_e} < 1 \right]$$

$h(\psi)$ is a geometrical function depending on cavity shape. It can be noted in **equation B.I.25** that the expression of the viscoplastic cavity growth rate depends on the stress triaxiality ratio ($\frac{\sigma_n}{\sigma_e}$ in **equation B.I.32**). In a very detailed study,

Van der Giessen et al (1995) have suggested that the diffusional cavity growth rate should also depend on the stress triaxiality ratio. Then, as suggested by Hancock (1976), in the tertiary creep regime, the void growth mainly occurs by strain at the surface of the void.

The real situation may be even more complex and the occurrence of constraining effect on diffusion cavity growth was especially first pointed out by Dyson (1976). The origins of these constraining effects can be quite different and constrained cavity growth generally results from two situations:

1. Cavity nucleation is heterogeneous in creeping materials as grain boundaries being misoriented from 45° from the load axis where found to be more sensitive to creep cavitation. If the material surrounding a cavitated facet is rigid, the excess volume of the cavities could not be accommodated and cavity growth would come to as standstill. On the other hand, if the surrounding is relatively soft, the accommodation process occurs readily and the rate of cavity growth is controlled by diffusive transport. The effect describe above is purely geometric and is the most commonly reported phenomena leading to constraint cavity growth.

- Grain boundaries do not act as perfect vacancy sources, due to the presence of intergranular precipitates for example or damage development, so that the vacancy flux is not necessarily ensured and the kinetics of cavity growth is slowed down.

The first developments of creep failure models related to the constrained cavity growth, proposed by Dyson (1979), were inspired by the experimental observations of Goods and Nix (1978), Dyson and Rodgers (1974) and Pavinich and Raj (1977). Goods and Nix (1978) introduced vapour water bubbles in pure silver and measure the creep growth of these cavities during creep. They especially evidenced that the exponent relating the creep time to failure and the applied engineering stress was not unity but between 3.0 and 4.0. The work of Dyson and Rodgers (1974) was slightly different as they introduced cavities by a pre-straining and annealing treatment. They found as Pavinich and Raj (1977) that the creep time to failure was related to stress with the same exponent than that relating creep strain rate and stress. The works of both Dyson and Rodgers (1974) and Pavinich and Raj (1977) showed that cavity growth rates were reduced below those given by vacancy diffusion controlled growth and Dyson (1979) explained this tendency by microstructural and geometrical constraints effects.

Chokshi (1987) proposed a model to describe the constrained cavity growth in the diffusional creep regime. The strain rates in the uncavitated ("uc") and cavitated ("c") regions are respectively given by:

$$\dot{\epsilon}_{ur} = \frac{\dot{Z}}{d} + \frac{ADGb}{kT} \left(\frac{b}{d}\right)^p \left(\frac{\sigma_1}{G}\right)^n \quad (\text{eq. B.I.33})$$

$$\dot{\epsilon}_{cr} = \frac{ADGb}{kT} \left(\frac{b}{d}\right)^p \left(\frac{\sigma_{eq}}{G}\right)^n \quad (\text{eq. B.I.34})$$

where \dot{Z} is the opening rate of the cavitated boundaries given by a Hull and Rimmer's like formulation, σ_1 is the stress normal to the grain boundary, σ_{eq} is the equivalent stress, D is the diffusion coefficient, d is the grain size, b is the Burgers vector and G is the shear modulus. The compatibility of deformation between cavitated and uncavitated regions leads to:

$$\dot{\epsilon}_{cr} = \dot{\epsilon}_{ur} \quad (\text{eq. B.I.35})$$

The evolution of cavity growth and whether it is or not constrained can be summed up by the representation proposed by Miller and Langdon (1980) in **figure B.I.5**.

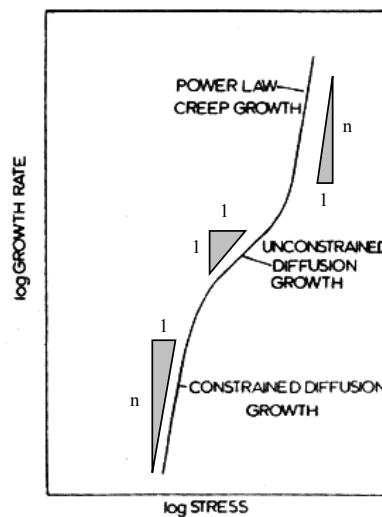


Figure B.I.5. Summary of cavity growth regimes from Miller and Langdon (1980)

Note that Beere (1980) pointed out that in the transition stress range between power-law creep cavity growth and unconstrained diffusion cavity growth, a coupling between the two cavity growth mechanisms exists. One can also be interested in correlating the evolution of the cavity growth kinetics with the evolution of the creep flow mechanism. Chokshi (1987) showed that creep cavitation and deformation processes are strongly linked. As it is shown from experimental results on copper in **figure B.I.6**, the change in the creep flow mechanism leads to a change in the cavity growth kinetics.

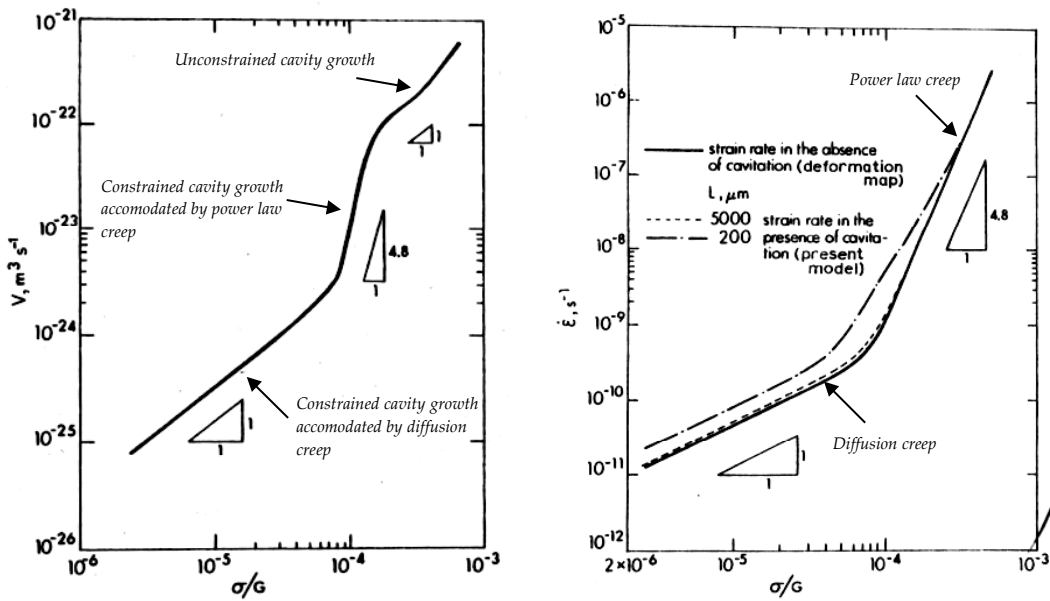


Figure B.I.6. Effect of a change in the creep deformation mechanism on the cavity growth rate, from Chokshi (1987)

An evaluation of the transition stress from unconstrained diffusion to constrained cavity growth is also proposed by Chokshi (1987) as:

$$\frac{\sigma}{G} = \left\{ \frac{8\pi\Omega\delta D_{gb}\alpha}{A\lambda^2 dbD} \left(\frac{d}{b} \right)^p \right\}^{\frac{1}{n-1}} \quad (\text{eq. B.I.36})$$

The theories of constrained cavity growth are supported by experimental results which are not of easy interpretation and probably neglect some aspects of the high temperature creep damage behaviour:

1. On the one hand, the interpretation of experiments of Goods and Nix (1978) should require more attention. They introduced a large amount of H₂O bubbles (nearly a volume fraction of 10%) and it is especially shown that bubbles provoke very premature failures. A steady state creep regime is, for example, not necessarily reached before the onset of fracture. On the other hand, Dyson and Rodgers (1974) introduced cavities by a pre-straining treatment that obviously modify the diffusion creep flow behaviour.
2. The models of constrained cavity growth neglect that grain boundary diffusion may act as an accommodation process to damage development. All models take into account a single mechanism of accommodation i.e. grain deformation so that at low stresses constraining is likely to occur as grains very little deform.
3. Theories of constrained cavity growth consider only one mechanism of cavity growth.

1.3.3. Cavity coalescence

The creep coalescence is the last step of the cavitation process that leads to failure. The coalescence behaviour depends on the type of creep cavity. When the cavity growth proceeds by matrix flow, the coalescence starts early due to plastic instability of inter-voids spaces and the final rupture is ductile. But when the cavity growth is intergranular, the coalescence stage starts later as cavity growth may even proceed until only fine ligaments remain between cavities. More generally, the usual way to consider cavity coalescence is to see it as an increase of the cavity growth rate due to the localisation of deformation in the intervoid spacing.

1.4. Recovery and dynamic recrystallization in creep conditions

One of the most observed microstructural change during creep is the formation of misoriented subgrains (polygonisation) separated by dislocations walls. Indeed, subgrain boundaries are a low energy configuration for an excess of dislocations especially in the case of non uniform deformation of polycrystal. For materials having one family of slip systems, walls form normal to the slip plane and the resulting subgrains are elongated. In the case of many cubic polycrystals, a second slip system is activated leading to the formation of dislocation walls in two directions and the resulting microstructure is equiaxed. In the steady state creep regime, subgrain size is proportional to $1/\sigma$.

Ashby et al (1979) and Gandhi et Ashby (1979) also published fracture mechanism maps from low to high temperature. The general formulation of a fracture map is presented in **figure B.I.7**.

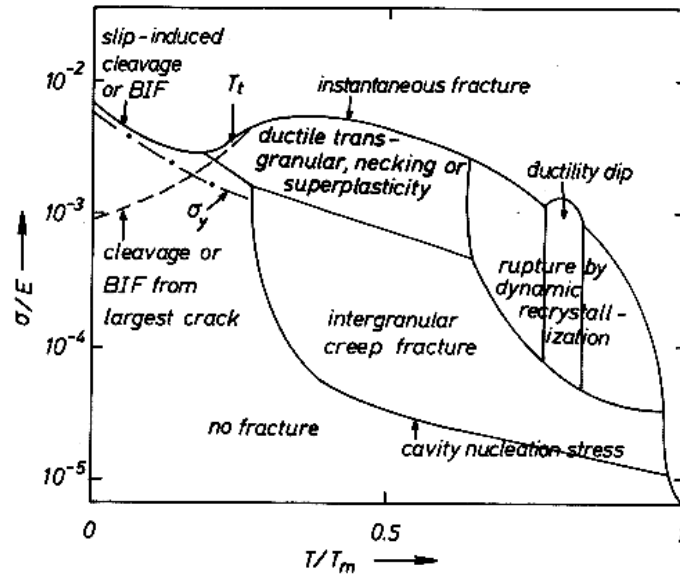


Figure B.I.7. Sketch of a fracture mechanism map (extracted from Riedel (1987))

To sum up, three main fracture modes under creep loading conditions can be encountered (see figure B.I.8):

1. Brittle fracture induced by transgranular cracking.
2. Transgranular or power-law creep rupture
3. Rupture due to dynamic recrystallisation

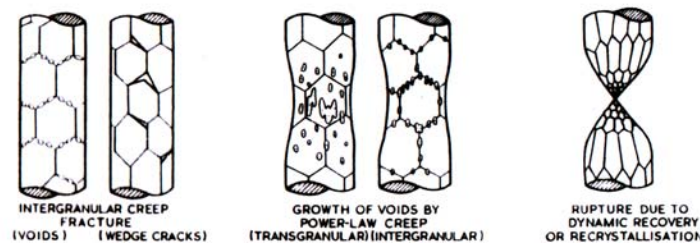


Figure B.I.8. Fracture modes at low and high temperatures from Ashby et al (1979a)

1.5. Phenomenological prediction of creep time to failure

Predictions of creep failure are mainly based on phenomenological formulae which do not take into account explicitly the type of rupture. These relationships are based on experimentally calculated values of steady state creep strain rates and times to failure. Monkman-Grant (1956) and Larson-Miller (1952) were the first to design failure predictive parameters. The Monkman-Grant (1956) parameter is expressed as:

$$C_{MG} = \dot{\epsilon}_{ss}^m t_f \quad (\text{eq. B.I.37})$$

where t_f is the time to failure and $\dot{\epsilon}_{ss}$ the steady state strain rate. Values of C_{MG} and m are evaluated from experimental results by plotting $\dot{\epsilon}_{ss}$ versus $1/t_f$. These values of C_{MG} and m remain relatively unchanged when varying temperature in a not too large domain. Note that a generalisation of the Monkman-Grant formalism was proposed by Phaniraj et al (2003). The Larson-Miller (1952) parameter is given by:

$$P_{LM}(\sigma) = [C + \log(t_f)] \frac{T}{1000} \quad (\text{eq. B.I.38})$$

where, C is a constant and T is the absolute temperature in Kelvin. The value of C is first set (20 – 30 is the commonly used range of values for chromium steels) and the dependence of P_{LM} upon stress is fitted using a linear or polynomial representation.

A less used parameter was established as the Sherby-Dorn parameter:

$$\theta(\sigma) = t_f \exp\left(-\frac{Q}{RT}\right) \quad (\text{eq. B.I.39})$$

where Q is an activation energy, R is the gas constant and $\theta(\sigma)$ is an empirical function of stress. This parameter is supposed to be valid in a quite large temperature domain.

One should notice that these models are very useful provided long term creep behaviour is clearly identified. **In general, these models supposed that both the creep flow and damage behaviour of the material do not change from short to long term creep.** Predictions may consequently be wrong if the material exhibits changes in creep mechanisms for long term creep exposures. Therefore, extrapolations to longer times and different temperatures than those covered experimentally are highly questionable.

2. Models for creep flow and damage behaviour

2.1. Models for describing creep flow

The easiest way to represent the material creep flow is to use a simple Norton law as introduced in **section 1.2**. However, this representation just allows to describe uniaxial steady state creep regime. More complex formulations, like the Robinson formulation, must be used to represent primary stage, to be integrated in three dimensional finite element calculations and to account for triaxiality effects. In the present study, material constitutive equations were written in the framework of Lemaitre and Chaboche so that the corresponding formulations of constitutive equations will be described in the following.

2.1.1. General fomulation of constitutive equations for viscoplastic materials in the framework of Lemaitre and Chaboche (1990)

A thermodynamic approach developed in France by Lemaitre and Chaboche (1990) since the 80's, is used at the Ecole des Mines de Paris to determine the constitutive equations of materials. The main principles of the approach are reminded here.

The overall strain is described as the summation between an elastic and an inelastic contribution:

$$\varepsilon = \varepsilon_e + \varepsilon_{in} \quad (\text{eq. B.I.40})$$

The same decomposition is made for the free energy:

$$\Psi = \Psi_e(\varepsilon_e, T) + \Psi_p(\alpha, r, m_k, T) \quad (\text{eq. B.I.41})$$

where α is the internal variable associated to kinematic hardening, r is the internal variable associated to isotropic hardening and m_k are the other internal variables that can be used to describe other phenomena (damage, dislocation behaviour, ageing, ...).

The stress tensor is given by:

$$\sigma = \rho \frac{\partial \Psi}{\partial \varepsilon_e} = C : \varepsilon_e \quad (\text{eq. B.I.42})$$

where C is the fourth order stiffness tensor.

$R = \rho \frac{\partial \Psi}{\partial r}$ and $X = \rho \frac{\partial \Psi}{\partial \alpha}$ are the thermodynamic variables associated with respectively isotropic and kinematic hardening and $M_k = \rho \frac{\partial \Psi}{\partial m_k}$ the thermodynamic variables associated with the other internal variables, m_k .

The Clausius-Duhem inequality leads to:

$$\sigma : \dot{\varepsilon}_p - R \dot{p} - X : \dot{\alpha} - \rho \frac{\partial \Psi}{\partial m_k} \dot{m}_k - \frac{1}{T} \vec{q} \text{grad} T \geq 0 \quad (\text{eq. B.I.43})$$

as the isotropic hardening can be describes by the cumulated plastic strain:

$$p = \int_0^t \left(\frac{2}{3} \dot{\varepsilon}_p(t) : \dot{\varepsilon}_p(t) \right) dt \quad (\text{eq. B.I.44})$$

Intrinsic and thermal dissipation are supposed to be uncoupled and consequently must both verify the Clausius-Duhem inequality which leads to:

$$\phi = \sigma : \dot{\varepsilon}_p - R \dot{p} - X : \dot{\alpha} - \rho \frac{\partial \Psi}{\partial m_k} \dot{m}_k \geq 0 \quad \text{and} \quad -\frac{1}{T} \vec{q} \text{grad} T \geq 0 \quad (\text{eq. B.I.45})$$

Unlike the case of plasticity, a simple dissipation potential: $\phi^*(\sigma, X, R, M_k; T, \alpha, r, m_k)$ is necessary to describe flow rules. And the evolutions of each of the variables are given by the normality rule:

$$\dot{\varepsilon}_p = \frac{\partial \phi^*}{\partial \sigma}; \dot{\alpha} = \frac{\partial \phi^*}{\partial X}; \dot{r} = \frac{\partial \phi^*}{\partial R}; \dot{m}_k = \frac{\partial \phi^*}{\partial M_k} \quad (\text{eq. B.I.46})$$

The dissipation potential must verify $\phi \geq \phi^* \geq 0$ to account for the second principle of thermodynamics.

If recovery effects have to be integrated to constitutive law the dissipation potential is written:

$$\phi = \Omega_p + \Omega_r \quad (\text{eq. B.I.47})$$

$$\text{with} \quad \Omega_p = \Omega_p(J(\sigma - X) - R - k, X, R, M_k; T, \alpha, r, m_k) \quad (\text{eq. B.I.48})$$

$$\Omega_r = \Omega_r(X, R, M_k; T, \alpha, r, m_k) \quad (\text{eq. B.I.49})$$

For viscoplastic materials the most commonly used form of Ω_p is that of a Norton power-law.

2.1.2. Formulation of constitutive equations to describe creep flow in the case of isotropic hardening

The general formulation for constitutive equations described in the previous sections simplified to the case of isotropic hardening are given here in the case of the absence of any recovery effects. The dissipation potential is written as:

$$\phi = \Omega_p (J(\sigma) - R - k; T, \dot{\epsilon}) \quad (\text{eq. B.I.50})$$

where $J(\sigma) \approx J_2(\sigma) = \sigma_{\text{eq}} = \left(\frac{3}{2} \mathbf{s} : \mathbf{s}\right)^{1/2}$ where σ_{eq} is the equivalent von Mises stress and \mathbf{s} is the deviatoric part of the stress tensor. Applying the normality rule, it follows:

$$\dot{\epsilon}_p = \frac{\partial \Omega_p}{\partial \sigma} = \frac{3}{2} \frac{\partial \Omega_p}{\partial \sigma_{\text{eq}}} \frac{\mathbf{s}}{\sigma_{\text{eq}}} = \frac{3}{2} \dot{\mathbf{p}} \frac{\mathbf{s}}{\sigma_{\text{eq}}} \quad \text{and} \quad \dot{\mathbf{r}} = \dot{\mathbf{p}} \quad (\text{eq. B.I.51})$$

The viscoplastic potential is defined following a generalisation of the Norton power-law with one of the two equations:

$$\Omega_p = \frac{K}{n+1} \left(\frac{\sigma_{\text{eq}} - R - k}{K} \right)^{n+1} \quad \text{for additive hardening} \quad (\text{eq. B.I.52})$$

$$\Omega_p = \frac{K}{n+1} \left(\frac{\sigma_{\text{eq}} - R - k}{K} \right)^{n+1} \dot{\mathbf{p}}^n \quad \text{for multiplicative hardening} \quad (\text{eq. B.I.53})$$

where n , K , k and η are materials parameters. The two formulations are not linked with specific physical mechanism of hardening. Therefore, the formulation of **equation B.I.53** i.e. with a multiplicative formulation of the hardening law is generally chosen as it is easier to fit.

2.1.3. Microstructurally based models

The idea of these models is to describe creep flow throughout the dislocation behaviour. Such a work has been performed by Dimmler et al (2002) and Weinert (2002) to describe creep flow of a 9Cr1Mo-NbV steel. This model can be more generally applied to alloy steels as it is based on the description by Orowan of the interaction between dislocations and particles. The creep strain rate is given by:

$$\dot{\epsilon} = A(S)(\sigma - \sigma_i)^n \quad (\text{eq. B.I.54})$$

where the inner stress: $\sigma_i = M(\tau_{\text{disl}} + \tau_{\text{part}})$ with M the Taylor factor. There are two contributions to the inner stress. τ_{disl} represents the work hardening due to dislocation motion and τ_{part} represents work hardening due to the interaction between dislocations and precipitates.

$$\tau_{\text{disl}} = \alpha G b \sqrt{\rho_{f,\infty}} \quad (\text{eq. B.I.55})$$

where, G is the shear modulus, b is the Burgers vector and $\rho_{f,\infty}$ is the steady state density of mobile dislocations that is

given by $\rho_{f,\infty} = \frac{1}{3.9} \left(\frac{\sigma}{Gb} \right)^2$ with σ the applied stress.

$$\tau_{\text{part}} = C \frac{Gb \sqrt{f_v}}{r_{\text{part}}} \ln \left(\frac{2r_{\text{part}}}{r_0} \right) \quad (\text{eq. B.I.56})$$

where f_v is the volume fraction of precipitates, r_{part} the precipitate average radius and r_0 the cutoff radius of dislocations ($\approx 30b$). One should notice that τ_{part} remains constant when the precipitation state do not change. In the diffusional creep regime σ_i is constant and equal to 0 which is equivalent to Harper-Dorn, Hull and Rimmer and Coble assumptions.

Dimmler et al (2002) and Weinert (2002) successfully used their model to represent high temperature creep flow behaviour of 9Cr1Mo-NbV steels. This type of model is often appreciate by metallurgists as they are based on a very fine description of the physical creep mechanisms at the scale of the microstructure. However, such models only exist under an uniaxial form and cannot be used in finite element modelling for structure design for example. In addition, it is not so easy to experimentally determine such quantities as the density of mobile dislocations.

2.2. Uncoupled damage models

Those models have been developed in the framework of the local approach to fracture. They are based on the determination of an incremental damage law starting from finite element calculations of creep stress and strain fields using the constitutive equation of the damage free material. This method was used at the Ecole des Mines de Paris by Yoshida (1985), Piques (1989), and Bouche (2001). The calibration of these models is based on experimental

measurements of damage. The experimentally fitted damage law strongly depends on the choice of the quantity representative of damage. For the three above mentioned studies, damage mainly proceeds as intergranular cracking so that the total length of cavitated boundaries was chosen as the damage parameter. The damage law was of the form:

$$df = A \langle \sigma_1 \rangle^\alpha \varepsilon_{eq}^\beta d\varepsilon_{eq} \quad (\text{eq. B.I.57})$$

where σ_1 is the principal stress, A , α and β are material parameters. Failure occurs for a critical damage $f = f_c$. Based on the assumption that the model of **equation B.I.57** failed in predicting long term creep damage behaviour for the 316LN stainless steel, Michel (2004) proposed an improvement of this model with introducing two cavity growth rates respectively corresponding to high and low stress creep regimes:

$$df = V_g d\varepsilon_{eq} + \frac{3}{2} f \sinh\left(\frac{3}{2} \frac{\sigma_m}{\sigma_{eq}}\right) d\varepsilon_{eq} + A \langle \sigma_1 \rangle dt \quad (\text{eq. B.I.58})$$

where V_g and A are material parameters. $V_g d\varepsilon_{eq}$ represents cavity nucleation, $\frac{3}{2} f \sinh\left(\frac{3}{2} \frac{\sigma_m}{\sigma_{eq}}\right) d\varepsilon_{eq}$ represents cavity growth due to the creep strain of the matrix following the description of Rice and Tracey and $A \langle \sigma_1 \rangle dt$ accounts for long term creep damage due to grain boundary diffusion. The proposed failure criterion is based on the detection of the

matrix deconsolidation i.e. the material creep failure occurs for $\frac{\partial \sigma_{eq}\left(\varepsilon_{eq}^f, \dot{\varepsilon}_{eq}^f, f_c\right)}{\partial \varepsilon_f} = 0$ where,

$$\sigma_{eq}\left(\varepsilon_{eq}^f, \dot{\varepsilon}_{eq}^f, f\right) = \frac{\sigma_{eq}\left(\varepsilon_{eq}^f, \dot{\varepsilon}_{eq}^f\right)}{1-f} \quad (\text{eq. B.I.59})$$

ε_{eq}^f and $\dot{\varepsilon}_{eq}^f$ are respectively the strain and the strain rate at the onset of fracture.

The model of Michel (2004) was successfully used to predict the long term creep damage behaviour of the 316LN austenitic stainless steel but the combination of strain and time dependent phenomena is criticisable. It would be better if the long term creep damage contribution depends on the related creep deformation mechanism i.e. grain boundary diffusion.

Auzoux (2004), who studied the effect of prior strain hardening on the high temperature intergranular creep cracking of austenitic stainless steels, proposed another formulation to take into account that:

1. Damage initiation is not continuous.
2. The stress triaxiality ratio affects damage evolution.
3. Prior strain hardening enhances the development of damage.

$$df = A \left(1 - B \exp\left(\frac{\varepsilon_{ph}}{\varepsilon_0}\right)^r\right) (1 + mf) \exp\left(q \frac{\sigma_1}{\sigma_{eq}}\right) d\varepsilon_{eq} \quad (\text{eq. B.I.60})$$

where ε_{ph} is the strain due to prior hardening and A , B , m and q are materials parameters.

These three models are quite interesting but due to the absence of any coupling with the creep strain, they are little adapted to the modelling of creep crack growth. More generally, in the case of complex loading conditions for which the damage development may involve complex stress and creep strain redistributions, the use of a model coupling creep flow and damage behaviour is necessary.

2.3. Models coupling creep flow and damage behaviour

2.3.1. Phenomenological constitutive damage model

Phenomenological constitutive damage models can be included in the framework of the continuum damage mechanics which was defined by Kachanov (1957). The idea was to take into account damage evolution by introducing an effective stress σ^* that is given in the uniaxial case by:

$$\sigma^* = \frac{\sigma_{eq}}{1-D} \quad (\text{eq. B.I.61})$$

where D represents the effect of damage on the mechanical response of the material, i.e. damage development induces a decrease of the loading section. The evolution of damage is given by:

$$\dot{D} = \left[\frac{\sigma_{eq}}{A_0(1-D)} \right]^\eta \quad (\text{eq. B.I.62})$$

where A_0 is the initial loading section and η is a model parameter.

In the first developments of the theory, rupture was associated with $D = 1$, but the necessity to consider a critical damage value, D_c , soon appeared as rupture obviously occurs before all the material is damaged. A rupture criterion was later associated:

$$t_c = \frac{1 - (1 - D_c)^{\eta+1}}{r + 1} \left(\frac{\sigma_{eq}}{A_0} \right)^{-\eta} \quad (\text{eq. B.I.63})$$

Rabotnov (1969) assumed that damage also affects creep deformation with integrating the effective stress to a Norton power law so that:

$$\dot{\varepsilon} = A \frac{\sigma_{eq}^n}{(1-D)^m} \quad (\text{eq. B.I.64})$$

Micromechanical models derived from the continuum damage mechanics have also been designed in the framework of the local approach to fracture with integrating experimental damage quantification in their identification procedure. A very interesting review is given by Eggeler (1991) who especially showed that the scale of the experimental measurements of damage must be carefully chosen to be in accordance with the physical mechanisms represented by the model. This is obviously one of the key points of the local approach to fracture.

Recent advances in the application of the continuum damage mechanics to creep flow and damage are due to Hayhurst (1995). The damage evolution model newly proposed allows to represent cavity growth due to both matrix viscoplasticity and grain boundary diffusion. Two damage contributions were added to the creep constitutive law:

1. ω_1 is linked to creep crack initiation and growth at grain boundaries.
2. ω_2 is linked to cavity growth in the matrix.

The formulation of the model is:

$$\dot{\varepsilon} = A \frac{1}{(1-\omega_1)(1-\omega_2)^n} \sinh(B\sigma_{eq}) \quad (\text{eq. B.I.65})$$

$$\text{with, } \dot{\omega}_1 = CA \frac{1-\omega_1}{(1-\omega_2)^n} \sinh(B\sigma_{eq}) \quad (\text{eq. B.I.66})$$

$$\text{and, } \dot{\omega}_2 = DA \frac{1}{(1-\omega_1)(1-\omega_2)^n} \sinh(B\sigma_{eq}) \quad (\text{eq. B.I.67})$$

where A, B, C and D are material parameters

The concept of the effective stress was also the basis of the work first performed by Lemaitre and Chaboche (1985) later continued by Zyczkowski (2000) and Lemaitre and Desmorat (2004) who integrated damage in the thermodynamic description introduced in **section 2.1**. The free energy is affected by damage so that:

$$\Psi = \Psi_e(\varepsilon_e, y, T) + \Psi_p(\alpha, r, m_k, T) \quad (\text{eq. B.I.68})$$

where D is the scalar variable representing damage.

The thermodynamic force associated to the damage variable is:

$$Y = -\rho \frac{\partial \Psi}{\partial D} \quad (\text{eq. B.I.69})$$

It is assumed that dissipation of deformation and damage processes are independent from each other. Therefore, the Clausius-Duhem inequality is written as:

$$\phi_1 = \sigma : \dot{\varepsilon}_p - R \dot{p} - X : \dot{\alpha} - \rho \frac{\partial \Psi}{\partial m_k} \dot{m}_k \geq 0 \quad \text{and} \quad \phi_2 = Y \dot{D} \geq 0 \quad (\text{eq. B.I.70})$$

Following the normality rule, the evolution law of damage is given by:

$$\dot{D} = -\frac{\partial \phi_2}{\partial Y} \quad (\text{eq. B.I.71})$$

so that:

$$\dot{D} = \left(\frac{Y}{S} \right)^s \dot{p} \quad (\text{eq. B.I.72})$$

where S and s are damage parameters and:

$$Y = \frac{1}{2} \underline{\underline{\varepsilon}}^e : \underline{\underline{E}} : \underline{\underline{\varepsilon}}^e = \frac{R_v}{2E} \frac{\sigma_{eq}^2}{(1-D)^2} = \frac{R_v}{2E} \sigma_{eq}^{*2} \quad (\text{eq. B.I.73})$$

with:

$$R_v = \frac{2}{3}(1+\nu) + 3(1-2\nu) \left(\frac{\sigma_m}{\sigma_{eq}} \right)^2 \quad (\text{eq. B.I.74})$$

where ν is the Poisson's ratio, σ_m is the hydrostatic stress and σ_{eq} is the von Mises equivalent stress.

Such a work have been recently extended by Bellenger and Bussy (2001) to model creep damage evolution. They introduced the damage scalar variable:

$$X = \frac{D}{1-D} \quad (\text{eq. B.I.75})$$

They expressed the Helmholtz free energy per unit volume:

$$\Psi = \Psi_e(\underline{\underline{\varepsilon}}_e, X) + \Psi_p(p) + \Psi_x(X) \quad (\text{eq. B.I.76})$$

where Ψ_e integrates the effect of damage on the elastic response and Ψ_x is the free energy induced by the damage development.

The thermodynamic conjugate force Y to X is given by:

$$Y = \rho \frac{\partial \Psi_e}{\partial X} + \rho \frac{\partial \Psi_x}{\partial X} = -\frac{1}{2(1+X)} \text{tr}(\underline{\underline{\varepsilon}}_e : \underline{\underline{E}} : \underline{\underline{\varepsilon}}_e) + Z(X) \quad (\text{eq. B.I.77})$$

1. For brittle and combined ductile brittle fracture: $Z(X) = q(1 - \exp(-cX))$

2. For ductile failure: $Z(X) = \frac{\ln(1+X)}{A}$

The model developed in the framework of the continuum damage mechanics by Lemaitre and Chaboche (1985) and Lemaitre and Desmorat (2004) has more physical basis than the formulation of Hayhurst (1995) as the model is designed in a thermodynamic framework. The damage evolution is calculated from the evaluation of the elastic strain energy release and it is proposed to experimentally determine the damage evolution law by performing unloading during the tests to measure the loss of stiffness:

$$D = 1 - \frac{E^*}{E} \quad (\text{eq. B.I.78})$$

where E^* is the effective Young's modulus and D is the actual value of damage. Measurements of E^* in high temperature creep conditions is however not so easy. Moreover, phenomenological models do also not allow to represent the three stages of creep damage development.

2.3.2. Micromechanically based damage models

Much work has been performed in the framework of continuum mechanics of porous media to model ductile failure. Gurson (1977), and later Tvergaard and Needleman (1984), Lemaitre (1985), Rousselier (1987), Gologanu and Leblond (1993) and Zhang et al (2000) designed coupled models where softening due to cavity growth is introduced in the constitutive equations. First formulation of those models was proposed by Gurson (1977) who derived the equation of the yield surface from the analysis of a spherical pore in a perfect rigid matrix (i.e. plasticity):

$$\phi = \frac{\sigma_{eq}^2}{\sigma_m^{*2}} + 2f \cosh\left(\frac{\sigma_{kk}}{2\sigma_m^*}\right) - 1 - f^2 = 0 \quad (\text{eq. B.I.79})$$

where σ_{kk} is the trace of the stress tensor, σ_{eq} is the von Mises equivalent stress and σ_m^* is the effective stress which is determined by solving **equation B.I.79**.

The evolution of the porosity ratio is given by the mass conservation and the void nucleation:

$$\dot{f} = (1-f)\text{trace } \underline{\underline{\varepsilon}}_p + \dot{f}_n \quad (\text{eq. B.I.80})$$

where the strain rate tensor $\underline{\underline{\varepsilon}}_p$ is given by:

$$\underline{\underline{\varepsilon}}_p = \dot{p} \frac{\partial \phi}{\partial \underline{\underline{\sigma}}} \quad (\text{eq. B.I.81})$$

with \dot{p} the plastic multiplier and \dot{f}_n is the void nucleation rate as:

$$\dot{f}_n = A_n \dot{p} \quad (\text{eq. B.I.82})$$

where A_n is a material dependent function. A Gaussian shape is proposed for A_n by Chu and Needleman (1980) whereas Besson et al (2000) preferred a constant rate representation. Note also that Chu and Needleman (1980) also proposed a stress controlled nucleation kinetics that is, however, little used:

$$\dot{f}_n = H\dot{p} + C_n \dot{\sigma}_{kk} \quad (\text{eq. B.I.83})$$

The authors who followed Gurson (1977) have introduced improvements of this initial formulation to be applied to more complex situations (see Pineau and Besson (2000)). Tvergaard and Needleman (1984) introduced an effective porosity f^* to represent the abrupt increase in porosity ratio due to void coalescence.

$$\phi = \frac{\sigma_{eq}^2}{\sigma_m^{*2}} + 2q_1 f^* \cosh\left(\frac{q_2}{2} \frac{\sigma_{kk}}{\sigma_m^*}\right) - 1 - q_1^2 f^{*2} = 0 \quad (\text{eq. B.I.84})$$

q_1 and q_2 are material parameters which accounts for void growth. These two parameters were calibrated to respectively 1.5 and 1.0 by Koplick and Needleman (1988). Faleskog et al (1998) proposed different values of q_1 and q_2 depending on the hardening exponent and the ratio E/σ_0 of the material. The evolution of the effective porosity f^* is given by:

$$f^* = \begin{cases} f & \text{if } f < f_c \\ f_c + \delta(f - f_c) & \text{otherwise} \end{cases} \quad (\text{eq. B.I.85})$$

where f_c is the critical porosity at the onset of void coalescence (the values of δ currently found in the literature range from 3 to 8 and these of f_c are generally set to 0.1). This coalescence law introduced by Tvergaard and Needleman (1984) has largely been discussed by Zhang et al (2000) and Pardoen and Hutchinson (2000). Both underlined that this formulation may give poor results for high stress triaxiality ratio as the crack initiation and growth strongly depend on the value of f_c . Benzerga (2003) showed that the value of δ also strongly depends on the stress triaxiality ratio. Zhang et al (2000) consider that f_c should no longer be a material constant and that a description of coalescence derived from Thomason's (1985) description would be better. Thomason (1985) analysis is based on the description of the evolution of plasticity around voids due to their growth. It assumes that when cavities grow, the reduction of the inter void ligament leads to a localisation of the deformation. Brown and Embury (1973) have evaluated the intervoid distance leading to plastic localisation as:

$$X = 2\sqrt{R_x + R_y} \quad (\text{eq. B.I.86})$$

where R_x and R_y are the two axis of the ellipsoidal void, so that $X = 2R$ for round voids of radius R .

The representation of **figure B.I.9** evidences the transition between diffuse and localised plastic flow. The Gurson model is well adapted to represent the diffusive flow only until the strain is localised.

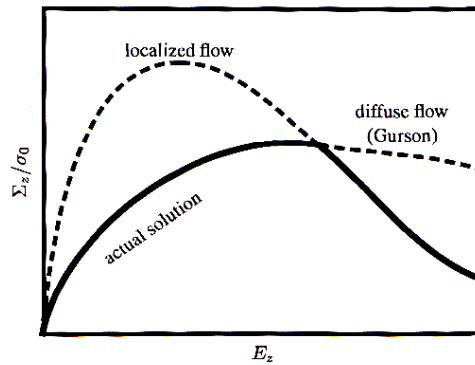


Figure B.I.9. Transition between the diffusive flow and the localized flow in the inter-void spacing (extracted from Berdin et al (2004))

Thomason (1985) determined a stress σ_z^{loc} corresponding to the onset of the cavity coalescence.

$$\frac{\sigma_z^{loc}}{\sigma_0} = \left[1 - \left(\frac{R_x}{X} \right)^2 \right] + \left[\alpha \left(\frac{R_z}{X - R_x} \right)^{-2} + \beta \left(\frac{R_x}{X} \right)^{-1/2} \right] \quad (\text{eq. B.I.87})$$

This criterion has been recently modified by Pardoen and Hutchinson (2000), Benzerga (2000) and Ragab (2004). The great interest of the proposed description of coalescence is that it is derived from calculated mechanical instabilities and two model parameters of little physical significance f_c and δ are eliminated. Note however, that for convenience, f^* is commonly used.

The Gurson model was also extended to the case of ellipsoidal cavities by Gologanu et al (1993, 1994) as cavity growth is especially not isotropic at low stress triaxiality levels. The pioneering work on growth of ellipsoidal cavities can be attributed to Budiansky et al (1982). Gologanu et al (1993 and 1994) introduced the void parameter g which represents an effective porosity ratio with transforming ellipsoidal cavities into voids of radius equal to the focal distance. The model is written in Gologanu (1997) as:

$$\phi = \frac{F_1}{\sigma_m^2} \|\underline{S} - \eta \sigma_H^g \underline{X}\| + F_2 \cosh\left(\kappa \frac{\sigma_H^g}{\sigma_m}\right) + F_3 = 0 \quad (\text{eq. B.I.88})$$

with $F_1 = C$, $F_2 = 2q(g+1)(g+f)$ and $F_3 = -(g+1)^2 - q^2(g+f)^2$, \underline{X} is the strain tensor defined in a basis related to the cavity axis and σ_H^g is a generalized hydrostatic stress. The evolution of the cavity shape is given by:

$$\dot{S} = \frac{3}{2} (1 + h_s h_f h_\tau) \dot{E}_z^p + h_{sf} \dot{E}_{kk}^p \quad (\text{eq. B.I.89})$$

where, \dot{E}_z^p is the deviatoric strain rate tensor, \dot{E}_{kk}^p is the hydrostatic part of the strain rate tensor, h_{sf} is a function of f and S , h_s is a function of S , h_f is a function of f and h_τ is a function of the stress triaxiality ratio. The main interest of the model of Gologanu et al (1993 and 1994) is to take into account the anisotropy of cavity growth which can be especially very interesting in the case of high temperature creep where cavities are generally elongated following the grain boundaries. The use of the complex formalism proposed by Gologanu et al (1993 and 1994) can however be questioned taking into account that a large distribution of cavity shape is encountered in deforming materials.

Finally, Leblond et al (1994) proposed a generalisation of the Gurson model to materials deforming at high temperature, i.e. whose flow behaviour is represented by a Norton power-law (i.e. creep flow is represented by **equation B.I.5**), as:

$$\phi = \frac{\sigma_{eq}^2}{\sigma^*{}^2} + fq_1 \left[h_m \left(q_2 \frac{1}{2} \frac{\sigma_{kk}}{\sigma^*} \right) + \left(\frac{1-m}{1+m} \right) \frac{1}{h_m \left(q_2 \frac{1}{2} \frac{\sigma_{kk}}{\sigma^*} \right)} \right] - 1 - q_1^2 \left(\frac{1-m}{1+m} \right) f^2 \quad (\text{eq. B.I.90})$$

m is the strain hardening coefficient defined by $m = 1/n$ where n is the apparent Norton power-law exponent, q_1 and q_2 are the classical parameters of the Gurson model and $h_m(x)$ is given by:

$$h_m(x) = \left[1 + mx^{(1+m)} \right]^{1/m} \quad (\text{eq. B.I.91})$$

Note that when $m = 0$ i.e. pure plasticity, the model reduces to the original formulation of Gurson. This model has been studied by Klocker and Tvergaard (2000 and 2003) who showed that when increasing m both cavity growth kinetics and the onset of cavity coalescence are delayed.

2.3.3. Other approaches under current development

A new method called the θ -method has been introduced by Evans and Wilshire (1985) and has been recently developed by Eberle and Jones (2003a and 2003b). It consists in using short term creep experimental data at several stresses and temperatures to determine the following expression:

$$\varepsilon = \theta_1(1 - \exp(-\theta_2 t)) + \theta_3(\exp(\theta_4 t) - 1) \quad (\text{eq. B.I.92})$$

where θ_i are stress and temperature dependent parameters whose dependence is fitted as $\ln(\theta_i) = a_i + b_i T + c_i \sigma + d_i \sigma T$ and strain to failure is represented by $\ln(\varepsilon_f) = a + bT + c\sigma + d\sigma T$. For a combination (σ, T) **equation B.I.92** give the possibility to calculate $\varepsilon(t)$, $\varepsilon(f)$ and consequently t_f . The future of such formalisms is obviously without any outlets as physical mechanisms are not taken into account leading to the formulation of non usable models as that proposed by Goswami (2004). These models are, in fact, only curve fitting.

A new trend, largely more interesting, is to perform aggregates calculations like Onck and Van der Giessen (1997) or Diard (2001). The materials microstructure and in particular grain and grain boundaries are meshed. Such representation are very interesting as they allow to represent the effect of the grain boundary orientation in comparison with the loading axis. As the stress normal to the grain boundary can be evaluated, it especially allows to represent the phenomena predicted by the constrained cavity growth models. Grain boundaries are supposed to slide in a newtonian viscous manner with the velocity:

$$\dot{\gamma} = w \frac{\tau}{\eta} \quad (\text{eq. B.I.93})$$

where w is the thickness of the boundary, τ is the shear stress and η is the grain boundary viscosity which depends on grain boundary diffusion). Grains deformed due to elasticity and power-law creep following the constitutive equation established by Crossman and Ashby (1975) as:

$$\dot{\varepsilon} = \dot{\varepsilon}_0 \left(f \frac{\sigma^*}{\sigma_0} \right)^n \quad (\text{eq. B.I.94})$$

where $\dot{\varepsilon}_0$, n and σ_0 are material parameters. f^* is a strain enhancement factor depending on the microstructure and σ^* is the effective stress.

Damage accumulation can also be described as nucleation at grain boundary followed by growth both by grain boundary diffusion and grains viscoplastic deformation. The kinetics of cavity nucleation at grain boundary is given by:

$$\dot{N} = F_n \left(\frac{\sigma_n}{\sigma_0} \right)^2 \dot{\varepsilon} \quad (\text{eq. B.I.95})$$

where σ_n is the stress normal to the grain boundary

The cavity growth is expressed as the summation of two cavity growth rates (see **equation (B.I.21)**) with \dot{v}_1 and \dot{v}_2 being formulated with the same variables than in **equations (B.I.23)** and **(B.I.24)** but f is given by:

$$f = \max \left(\left(\frac{a}{b} \right)^2, \left(\frac{a}{a + 1.5L} \right)^2 \right) \quad (\text{eq. B.I.96})$$

where a is the major axis of the cavity, b is the inter-cavity spacing and L is a length parameter defined following the formulation of Needleman and Rice (1980) of **equation B.I.21**.

The resulting cavity growth rate is expressed as:

$$\dot{a} = \frac{\dot{v}}{4\pi a^2 h(\psi)} \quad (\text{eq. B.I.97})$$

where a is the major axis of the cavity and $h(\psi)$ is a function describing the cavity shape.

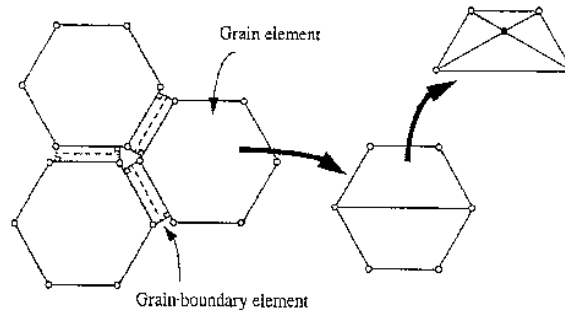


Figure B.I.10. Example of a mesh used for aggregates calculations (extracted from Onck and Van der Giessen (1997))

While the microstructure is more finely described and especially the grain boundary sliding can be represented, aggregates calculations are very time consuming yet.

2.4. Summary of the different damage models

The main characteristics of the predictive failure criterion and damage model are summarised in the following four **tables B.I.1, B.I.2, B.I.3 and B.I.4** where both advantage and inconvenient of the methods are given.

References	Model characteristics	Hypothesis	Formulation	Advantage	Inconvenient
Larson & Miller (1952)	Phenomenological prediction of creep lifetime		$P_{LM}(\sigma) = [C + \log(t_f)] \frac{T}{1000}$ with $P_{LM}(\sigma) = A\sigma + B$ A, B, C are model parameters	1.Easy to fit 2.Valid also when varying the temperature	1.Only valid for uniaxial loading conditions. 2.The validity of the relationship out of the domain experimentally investigated is not ensured.
Monkman & Grant (1956)	Phenomenological prediction of creep lifetime	The material "ductility" remains unchanged	$C_{MG} = \epsilon_{ss}^m t_f$ $C_{MG}, m \text{ are model parameters}$ $\epsilon_{ss} \text{ is the steady state strain rate}$	1.Easy to fit	1.Only valid for uniaxial loading conditions. 2.Need both creep flow and fracture data The validity of the relationship out of the domain experimentally investigated is not ensured.
Orr, Sherby & Dorn (1954)	Phenomenological prediction of creep lifetime		$\theta(\sigma) = t_f \exp\left(-\frac{Q}{RT}\right)$ with $\theta(\sigma) = A\sigma + B$ A, B are model parameters, Q is an activation energy	1.Easy to fit 2.Valid also when varying the temperature	1.Only valid for uniaxial loading conditions. 2.The validity of the relationship out of the domain experimentally investigated is not ensured.

Table B.I.1. Lifetime predictive parameters

References	Model characteristics	Hypothesis	Damage evolution	Failure criterion	Advantage	Inconvenient
Piques (1989)	1.Local approach to fracture	Damage development is promoted by both the principal stress Σ and the creep strain	$df = A \langle \sigma_1 \rangle^\alpha \epsilon_{eq}^\beta d\epsilon_{vp}$ $f = \text{porosity}$ $\sigma_1 \text{ is the principal stress}$ $A, \alpha, \beta \text{ are model parameters}$	Critical porosity f_c	1.Few material parameters 2.Easy to use in post treatment of mechanical FE calculations.	1.Fails in predicting the long term creep damage behaviour 2.The three stages of damage evolution i.e. initiation, growth and coalescence are not explicitly represented. 3.No coupling with the mechanical behaviour.
Michel (2004)	1.Local approach to fracture 2.No coupling with the mechanical behaviour	Damage development is promoted by both the matrix deformation (Rice-Tracey) and the grain boundary diffusion.	$df = V_g d\epsilon_{eq} + \frac{3}{2} f \sinh\left(\frac{3}{2} \frac{\sigma_m}{\sigma_{eq}}\right) d\epsilon_{eq} + A \langle \sigma_1 \rangle dt$ $f = \text{porosity}$ $\sigma_1 \text{ is the principal stress}$ $\sigma_m \text{ is the hydrostatic stress}$ $\sigma_{eq} \text{ is the von Mises equivalent stress}$	Critical porosity f_c or Material deconsolidation $\frac{\partial \sigma_{eq}}{\partial \epsilon_t} \left(\epsilon_{eq}^f, \epsilon_{eq}^f, f_c \right) = 0$	1.Few material parameters: A, V_g 2.Easy to use in post treatment of mechanical FE calculations. 3.Both cavity nucleation and cavity growth are represented 4.Succeeds in predicting long term creep lifetime	1.No coupling with the mechanical behaviour. 2.Both strain and time dependent formulation.
Auzoux (2004)	1.Local approach to fracture 2.No coupling with the mechanical behaviour	The effect of prior strain hardening is taken into account	$df = A \left(1 - B \exp\left(\frac{\epsilon_{ph}}{\epsilon_0}\right)^r \right) (1 + mf) \exp\left(\frac{\sigma_1}{\sigma_{eq}}\right) d\epsilon_{eq}$ $\sigma_1 \text{ is the principal stress}$ $\sigma_{eq} \text{ is the von Mises equivalent stress}$ $A, B \text{ \& } m \text{ are model parameters}$ $\epsilon_{ph} \text{ is the strain due to prior hardening}$	Critical porosity f_c	1.Few material parameters 2.Easy to use in post treatment of mechanical FE calculations.	1.The three stages of damage evolution i.e. initiation, growth and coalescence are not explicitly represented. 2.No coupling with the mechanical behaviour.

Table B.I.2. Uncoupled models developed in the framework of the local approach to fracture

References	Model characteristics	Hypothesis	Constitutive equations	Damage evolution			Advantage	Inconvenient	
				Nucleation	Growth	Coalescence Failure			
Kachanov (1957) Rabotnov (1969)	Pioneering work of the continuum damage mechanics		$\dot{\varepsilon} = A \frac{\sigma_{eq}^n}{(1-D)^m}$	$\dot{D} = \left[\frac{\sigma_{eq}^n}{A_0(1-D)} \right]^r$			D = 1	Coupling with the mechanical behaviour	1.The coupling with mechanical is purely phenomenological 2. This first model of continuum damage mechanics was only uniaxial.
Hayhurst (1995)	1.Continuum damage mechanics (Kachanov/Rabotnov) 2.Damage is coupled with the mechanical behaviour		$\dot{\varepsilon} = A \frac{1}{(1-\omega_1)(1-\omega_2)^n} \sinh(B\sigma_{eq})$	$\dot{\omega}_1 = CA \frac{1-\omega_1}{(1-\omega_2)^n} \sinh(B\sigma_{eq})$ $\dot{\omega}_2 = DA \frac{1}{(1-\omega_1)(1-\omega_2)^n} \sinh(B\sigma_{eq})$ A, B, C are materials parameters	Critical damage D _c		1.Both cavity growth due to matrix viscoplasticity (ω_2) and grain boundary diffusion (ω_1) are represented 2.Coupling with the mechanical behaviour	1.No representation of cavity nucleation 2.The coupling with mechanical is purely phenomenological	
Lemaitre & Chaboche (1985) Lemaitre & Desmorat (2004)	1.Continuum damage mechanics (Kachanov/Rabotnov) 2.Damage is coupled with the mechanical behaviour		$\dot{\varepsilon} = \left(\frac{\sigma^*}{K} \right)^n \quad \sigma^* = \frac{\sigma}{1-D}$	$\dot{D} = \left(\frac{Y}{S} \right)^p \dot{p}$ $Y = \frac{1}{2} \varepsilon^e : E : \varepsilon^e = \frac{R_v}{2E} \frac{\sigma_{eq}^2}{(1-D)^2} = \frac{R_v}{2E} \sigma^{*2}$ $R_v = \frac{2}{3}(1+\nu) + 3(1-2\nu) \left(\frac{\sigma_{kk}}{\sigma_{eq}} \right)^2$ E = Young's modulus ν = Poisson's ratio σ_{kk} = principal stress σ_{eq} = von Mises equivalent stress	Critical damage D _c		1.Coupling with the mechanical behaviour with respect to thermodynamical principles. 2.The damage evolution law can be fitted on experimental measurements of the evolution of the Young's modulus	1.No representation of cavity nucleation 2.The measurement of the evolution of the Young's modulus is not easy in high temperature creep conditions	

Table B.I.3. Coupled models developed in the framework of the continuum damage mechanics

References	Model characteristics	Hypothesis	Constitutive equations	Damage evolution			Advantage	Inconvenient
				Nucleation	Growth	Coalescence / Failure		
Tvergaard Needleman (1984) GTN model	1.Micromechanical model 2.Development of the Gurson model	1.Isotropic growth of a perfectly round cavity in a perfect rigid matrix. 2.Cavity growth and nucleation is given by mass conservation.	$\dot{\epsilon}_p = \dot{p} \frac{\partial \phi}{\partial \underline{\sigma}}$ The effective stress is defined by: $\phi = \frac{\sigma_{eq}^2}{\sigma_m^2} + 2q_1 f^* \cosh\left(\frac{q_2 \sigma_{kk}}{2 \sigma_m}\right) - 1 - q_1^2 f^{*2} = 0$ q_1, q_2 are model parameters f^* is the effective porosity σ_{kk} is the hydrostatic stress σ_{eq} is the von Mises equivalent stress	$\dot{f}_n = A_n \dot{p}$ $\dot{f}_n = H\dot{p} + C_n \sigma_{kk}$ Chu and Needleman (1980)	$\dot{f} = (1 - f)\text{trace } \dot{\epsilon}_p + \dot{f}_n$	$f^* = \begin{cases} f & \text{if } f < f_c \\ f_c & \text{if } f \geq f_c \end{cases}$ f_c and δ are material parameters. or Thomason (1985) description of coalescence	1.Coupling with the mechanical behaviour. 2.Nucleation, growth and coalescence are represented.	1.Strictly valid only for a perfect rigid matrix. 2.The calibration of model parameters would require void and unit cells calculations.
Gologanu et al (1993 and 1994)	1.Micromechanical model 2.Development of the Gurson model	1.Anisotropic growth of a cavity in a perfect rigid matrix. 2.Cavity growth and nucleation is given by mass conservation.	$\dot{\epsilon}_p = \dot{p} \frac{\partial \phi}{\partial \underline{\sigma}}$ The effective stress is defined by: $\phi = \frac{F_1}{\sigma_m^2} \left\ \underline{s} - \eta \sigma_{kk}^g \underline{X} \right\ + F_2 \cosh\left(\kappa \frac{\sigma_{kk}^g}{\sigma_m}\right) + F_3 = 0$ $F_1 = C$ $F_2 = 2q(g+1)(g+f)$ $F_3 = -(g+1)^2 - q^2(g+f)^2$ G, C, κ, η are model parameters \underline{X} is the strain tensor in a basis related to the cavity axis	$\dot{f}_n = A_n \dot{p}$ $\dot{f}_n = H\dot{p} + C_n \sigma_{kk}$ Chu and Needleman (1980)	$\dot{f} = (1 - f)\text{trace } \dot{\epsilon}_p$ and the evolution of the cavity shape is: $\dot{S} = \frac{3}{2}(1 + h_1 h_2 h_3) E_p + h_d E_{kk}^p$	$f^* = \begin{cases} f & \text{if } f < f_c \\ f_c & \text{if } f \geq f_c \end{cases}$ f_c and δ are material parameters. or Thomason (1985) description of coalescence	1.Coupling with the mechanical behaviour. 2.Nucleation, growth and coalescence are represented. 3.The anisotropy of cavity growth is taken into account	1.Complex identification 2.Integration of a nucleation law is not easy. 3.The calibration of model parameters would require void and unit cells calculations. 4.All cavities have the same shape.
Lebond Perrin Suquet (1994) LPS model	1.Micromechanical model 2.Generalisation of the Gurson model to high temperature deformation behaviour	1.The steady creep strain rate is described by the Norton law: $\dot{\epsilon}_{ssp} = B\sigma$	$\dot{\epsilon}_p = \dot{p} \frac{\partial \phi}{\partial \underline{\sigma}}$, The effective stress is defined by: $\phi = \frac{\sigma_{eq}^2}{\sigma^{*2}} + fq_1 \left[h_m \left(q_2 \frac{1}{2} \frac{\sigma_{kk}}{\sigma^*} \right) + \left(\frac{1-m}{1+m} \right) \frac{1}{h_m \left(q_2 \frac{1}{2} \frac{\sigma_{kk}}{\sigma^*} \right)} \right] q_2$ $-1 - q_1^2 \left(\frac{1-m}{1+m} \right) f^2 = 0$ with $h_m = \left[1 + m \left(\frac{1-m}{1+m} \right)^{1/m} \right]^{1/m}$ q_2 are model parameters σ_{kk} is the hydrostatic stress σ_{eq} is the von Mises equivalent stress	$\dot{f}_n = A_n \dot{p}$ $\dot{f}_n = H\dot{p} + C_n \sigma_{kk}$ Chu and Needleman (1980)	$\dot{f} = (1 - f)\text{trace } \dot{\epsilon}_{vp} + \dot{f}_n$	$f^* = \begin{cases} f & \text{if } f < f_c \\ f_c & \text{if } f \geq f_c \end{cases}$ f_c and δ are material parameters. or Thomason (1985) description of coalescence	1.Coupling with the mechanical behaviour. 2.Nucleation, growth and coalescence are represented. 3. Generalization of the GTN model to high temperature deformation	1.The calibration of model parameters would require void and unit cells calculations
Onck & Van der Giessen (1997)	1.Polycrystalline aggregates	1.The grain boundaries are represented and supposed to slide in a viscous manner 2. Grain are represented by hexagones.	$\dot{\epsilon}_p = \dot{p} \frac{\partial \phi}{\partial \underline{\sigma}}$ The strain of grains is given by: $\dot{\epsilon} = \dot{\epsilon}_0 \left(f^* \frac{\sigma^*}{\sigma_0} \right)^n$ Crossman, Ashby (1975) The grain boundary viscous Newtonian flow is expressed as: $\dot{\gamma} = w \frac{\tau}{\eta}$ (Ashby (1972))	$\dot{N} = F_n (\sigma_n / \sigma_0)$ σ_n is the stress normal to the grain boundary	$\dot{a} = \frac{\dot{v}}{4\pi a^2 h(\psi)}$ $\dot{v} = \dot{v}_1 + \dot{v}_2$ where v_1 and v_2 are respectively the cavity growth by matrix deformation and grain boundary diffusion		1.The two cavity growth mechanisms are represented 2.Grain boundary sliding and grain size effects can be taken into account.	1.Calculations are very time consuming. 2.The thickness of the grain boundary are really larger than the real thickness.

Table B.I.4. Micromechanical coupled models developed in the framework of the mechanics of porous media and polycrystalline calculations

3. Creep flow and failure properties of 9Cr1Mo-NbV steels near 625°C

There are a number of experimental data available, mainly from creep tests on smooth round specimens, on creep flow of 9Cr1Mo-NbV steels which is in particular well documented in the French RCCMR (1993) database for several temperatures between 350°C and 650°C. However, the majority of these data concern material creep in the high stress regime where strain is accommodated by dislocation climb and few experimental data are available in the low stress creep range where strain is accommodated by diffusion (creep times up to 40,000 hours). All results about creep flow properties near 625°C are summed up in **figure B.I.11**.

One can distinguished two regions at 625°C:

1. A power-law creep region corresponding to stresses between 80 MPa and 150 MPa where the Norton exponent $n = 8$ without taking into account any internal stress (Note also that Ennis (2001) considered two power-law creep regimes with $n = 15$ for the highest stresses).
2. A diffusion creep region where the Norton exponent $n = 1$.

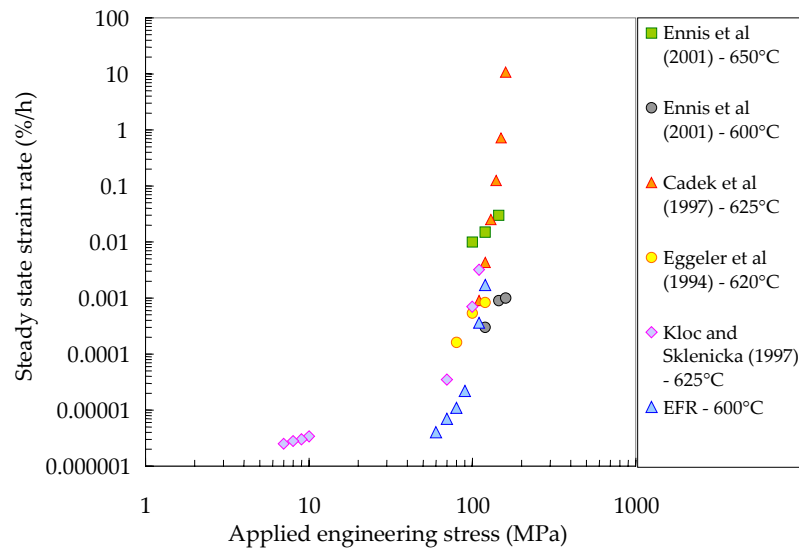


Figure B.I.11. Steady state creep strain rate versus stress near 625°C (experimental data)

The transition stress between the two creep regimes can be set to about 70 MPa. The high stress creep regime is characterised by a high value of the Norton power-law exponent. Many studies were concerned with determining the creep mechanism at high stresses. Cadek et al (1997) postulated that creep was controlled by interaction between dislocations and second phase particles but unsuccessfully tried to use the Rosler-Artz model associated with this mechanism. Some authors, like Foldyna et al (1984) were in favour of a creep rate controlled by dislocation climb around particles following the Orowan mechanism. Sklenicka et al (2003), Polcik et al (1999) and Orlova et al (1998) who performed extensive metallographic studies considered that dislocation rearrangement and subgrain formation are the creep controlling processes and concluded that the role of the dislocation substructure quickly overrides the strengthening effect of the precipitates.

The diffusion creep region is not easy to explore as it corresponds to very low creep strain rates. Steady state creep strain rates could be measured by Kloc and Sklenicka (1997) who performed creep tests on helicoidal spring specimens which is a technique introduced by Burton and Greenwood (1970). The results are confirmed in Kloc and Sklenicka (2004). The creep mechanism in the low stress regime is not yet determined. Only creep tests on 9Cr1Mo-NbV steels with various microstructure characteristics (various grain sizes for example) would provide useful information about it. However, Sklenicka et al (2003) considered that grain boundary sliding is largely inhibited by the presence of grain boundary precipitates.

Primary (I) and steady state (II) creep strain models proposed in the French code RCC-MR (1993) for 9Cr1Mo-NbV steels in the high stress creep regime are: $\dot{\epsilon}_I = C_1 \sigma^{n_1} t^{n_2}$ and $\dot{\epsilon}_{II} = C \sigma^n$ ($\dot{\epsilon}$ in %h⁻¹, σ in MPa and t in h) and the values of corresponding parameters at 450°C, 550°C and 600°C are reported in **table B.I.5**.

Temperature (°C)	C ₁ (%h ⁻¹ ·n ² MPa ⁻ⁿ)	n ₁	n ₂	C (%h ⁻¹ MPa ⁻ⁿ)	n
450 °C	1.30 ·10 ⁻¹⁴	5.0	0.30	2.35 ·10 ⁻²⁹	9.74
550 °C	2.08 ·10 ⁻¹⁰	3.8	0.34	1.1 ·10 ⁻²²	8.25
600 °C	2.46 ·10 ⁻⁸	3.2	0.36	6.16 ·10 ⁻²⁰	7.63

Table B.I.5. Model parameters for creep flow of 9Cr1Mo-NbV steels from RCC-MR (1993)

A single master curve, established from creep tests in the temperature range from 575°C to 650°C, is also proposed by Spigarelli et al (1997) as to represent the steady state creep strain rate in the power-law creep region:

$$\dot{\epsilon}_{ss} = A \left(\frac{\sigma}{E(T)} \right)^n \exp\left(-\frac{Q}{RT} \right) \quad (\text{eq. B.I.98})$$

where E, is the Young's modulus, R is the gas constant, A is a material parameter and the Norton exponent, n, is temperature dependent:

$$n = \frac{60698 \pm 5789K}{T(K)} + 57.7 \pm 6.55 \quad (\text{eq. B.I.99})$$

and Q is the apparent activation energy whose average value was evaluated to 719 kJmol⁻¹.

The creep flow behaviour of 9Cr1Mo-NbV steels at high temperature is also characterised by a very short steady state creep regime as the tertiary creep regime takes more than one third of the total testing time at least in the high stress creep regime. It is consequently assumed that the description of the tertiary creep regime is necessary to predict creep life of 9Cr1Mo-NbV steels.

All data concerning dependence of time to failure upon stress are given in **figure B.I.10**. Experimental results do not exceed 30,000 hours of creep time: results of longer creep exposures from RCC-MR are extrapolated data using a Larson-Miller predictive method.

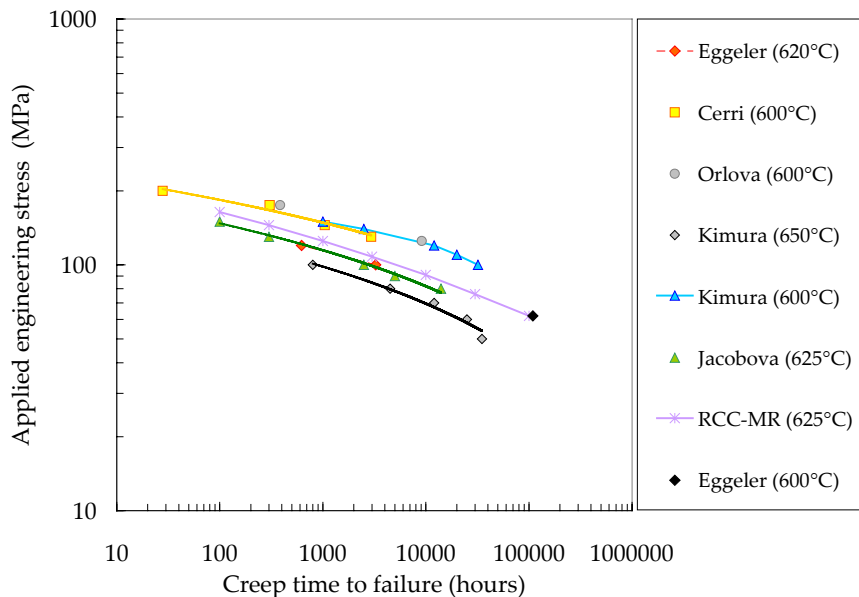


Figure B.I.12. Stress versus creep time to failure near 625°C

No change in the damage mechanism is observed up to 30,000 hours of creep between 600°C and 650°C. However, the long-term experimental result of Kimura et al (1998) at 650°C suggest that premature failure could occur for longer creep exposures. This transition in the creep life evolution may be related to the transition in creep flow mechanism, as **figure B.I.12** shows that it occurs near 50 MPa at 650°C which corresponds to the beginning of the diffusion creep regime described by Kloc and Sklenicka (1997). Unfortunately, no deformation mechanism map is available for 9Cr1Mo-NbV steels.

4. Metallurgical changes during high temperature creep of grade 91 steels

In materials description part, evidences of complexity of martensitic stainless steel microstructure was raised. Large amount of alloying elements are embedded in precipitation phenomena. Moreover, initial lath martensite microstructure containing a high dislocation density (Evaluated to 7.5·10⁻¹⁴ m² by Ennis (2000)) is strongly modified under stress effects.

During creep stages microstructural changes occur in terms of dislocation arrangement, recovery or recrystallization and particle nucleation, growth and coarsening.

4.1. Second phase particles and their effect on creep properties

Main conclusions of the effect of creep on the precipitation behaviour in 9Cr1Mo-NbV steels are summarised in **table B.I.6** considering from extended works on the subject.

Precipitates	Nucleation conditions	Precipitation zone	Growth and coalescence	Effect on Creep
$M_{23}C_6 - (Cr_{16}Fe_6Mo)C_6$ Fcc – a = 1.066 nm	Tempering, ageing and creep ageing conditions	At prior austenite, packet and lath boundaries	Coarsening is promoted by creep	Lose their pinning effect on dislocation leading to lath recovery
Z-phase - (CrVNb)N tetragonal – a = 0.286 nm c = 0.739 nm	Long term creep ageing conditions (larger than 30,000 hours)	At prior austenite, grain boundaries		At the expense of MX and $M_{23}C_6$ precipitates which leads to a loss of creep strength
Laves phase Fe_2Mo hexagonal – a = 0.474 nm c = 0.773 nm	Ageing and creep ageing conditions	At prior austenite, packet and lath boundaries	Coarsening is promoted by creep	Diminishes molybdenum solid solution strengthening
$M_{23}C_6 - (Cr)(VNb)$ Hexagonal a = 0.478 nm – c = 0.446 nm	Tempering, ageing and creep ageing conditions	At lath boundaries and within laths	Slow coarsening	Stabilise lath boundaries retarding recovery
M_6X	Long term ageing and creep ageing conditions	At prior austenite, packet and lath boundaries	Dissolve $M_{23}C_6$ particles. High coarsening rate	Lower precipitation strengthening
MX (NbC, NbN, VN, VC) fcc – a = 0.444 nm	Tempering, ageing and creep ageing conditions	At lath boundaries and within laths	Slow coarsening	Stabilise lath boundaries retarding recovery

Table B.I.6. Second phase particles in chromium stainless steels: precipitation characteristics and effects on creep properties (Synthesis of Foldyna et al (2001) Yamada et al (2001), Polcik et al (1999), Sawada et al (1999), Jakobova (1998), Parameswaran et al (1996), Senior (1989), Hosoi et al (1986), Grobner and Hagel (1980))

Some precision can be also given about second phases precipitation:

1. $M_{23}C_6$ carbides precipitation is nearly complete after tempering at 750°C or 760°C as was shown in **figure A.I.7** following the work of Parameswaran et al (1996). Only coarsening occurs during ageing and stress ageing conditions. This is confirmed by Nakajima et al (2003) who described $M_{23}C_6$ coarsening by an empirical law depending on the applied engineering stress.
2. Laves phase precipitation is heterogeneous as nuclei are $M_{23}C_6$ carbides, and precipitation kinetics of this phase is promoted by higher contents of silicon and phosphorous (Lundin et al (2000) and Senior (1989)).
3. MX and $M_{23}C_6$ coalescence starts after 6,000 hours of ageing under 125 MPa and 9,000 hours of ageing under 110 MPa at 600°C.

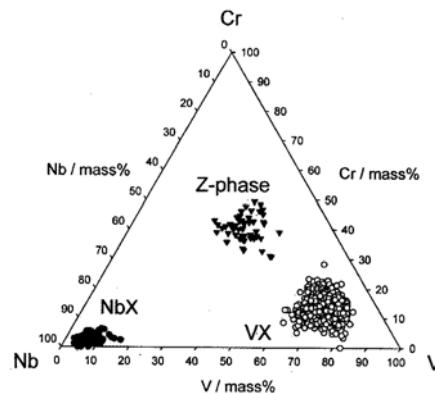


Figure B.I.13. Chemical composition of M in MX and Z-phase precipitates from Susuki et al (2003)

The precipitation state strongly determines the material creep strength. The role of the $M_{23}C_6$ carbides is very significant and three important features are described by Eggeler (1989):

1. Carbides prevent the moving of subgrain boundary.
2. Carbides impede reactions between free dislocations.
3. Carbides pin subgrain boundary dislocations, which diminishes the interface controlled diffusion creep.

Thus, carbides retard recovery process and prevent the material from intergranular cavitation due to diffusion. However, as underlined by Nakajima et al (2003), Hattestrand and Andren (2001) and Cerri et al (1998), creep promotes carbide coarsening and consequently leads to a deterioration of their pinning effect and diffusion retardation efficiency. Indeed, $M_{23}C_6$ carbide tend to coarsen as the solubility of their main constituents, Fe and Cr, is quite large in the ferrite matrix.

Laves phase precipitation is also said to lower the creep strength. Indeed, molybdenum has a solid solution strengthening effect that is lost after Laves phase precipitation (Sawada et al (1999)). Therefore, molybdenum is currently replaced by tungsten as the kinetic of W rich Laves phase precipitation is slower than that of Mo rich Laves phase. According to Stocker et al (2002), the Laves phase fraction remain constant after 4,000 hours at 600°C. In fact, a stable Laves phase distribution is obtained even in stress free thermal ageing conditions for times higher than 10,000 hours. Note also that Ishii et al (1998) drew completely contradictory conclusions as they considered that the presence of Laves phase at prior austenite grain and martensite lath contribute to creep strength.

The effects of MX and M_2X particles has been studied by many authors like Fujita and Takahashi (1978), Tokuno et al (1991a and 1991b), and Kasl and Kasha (1998). All show how MX and M_2X act as strong obstacles to dislocation glide. Tokuno et al (1991b) also studied the effect of their shape and concluded that complex shaped particles are more effective obstacles than spherical ones because local climb is less likely to occur. Yamada et al (2002) and Hamada et al (1995) showed that the precipitation of complex penny shape Nb(C,N) and V(C,N) particles allows to pin dislocation and to retard recovery of the microstructure. The strengthening effect of MX and M_2X particles is all the more interesting as these precipitates are mainly composed of niobium and vanadium whose solubility is quite small in the ferrite matrix i.e. creep little affects the strengthening properties of MX and M_2X particles. Finally, Williams et al (1981) showed that secondary precipitation of M_2X often occurs after long time creep exposure for temperatures below 525°C.

The loss of creep strength properties after long term creep is always attributed to the formation of the Z-phase which is a complex carbo-nitride precipitate. Its appearance is reported after 7,700 hours (75 MPa) of creep at 650°C by Gotz and Blum (2003). Suzuki et al (2003) have reported the appearance of Z-Phase after 5,000 hours at 650°C and 20,000 hours at 600°C. They evidenced Z-phase precipitates of a few hundred nanometers in size containing in mass percents: 20-30% V, 30-40% Cr, 15-20% Nb, 5-10 % Fe and Si (see figure B.I.13). They concluded that the Z-phase formed at the expense of the fine MX precipitates.

Considering the strong link between the precipitation state and the material creep resistance, it is of great interest to investigate the kinetics of all phenomena. The evolution of each of the four precipitates populations is well described by Kimura et al (2000) in figure B.I.14a.

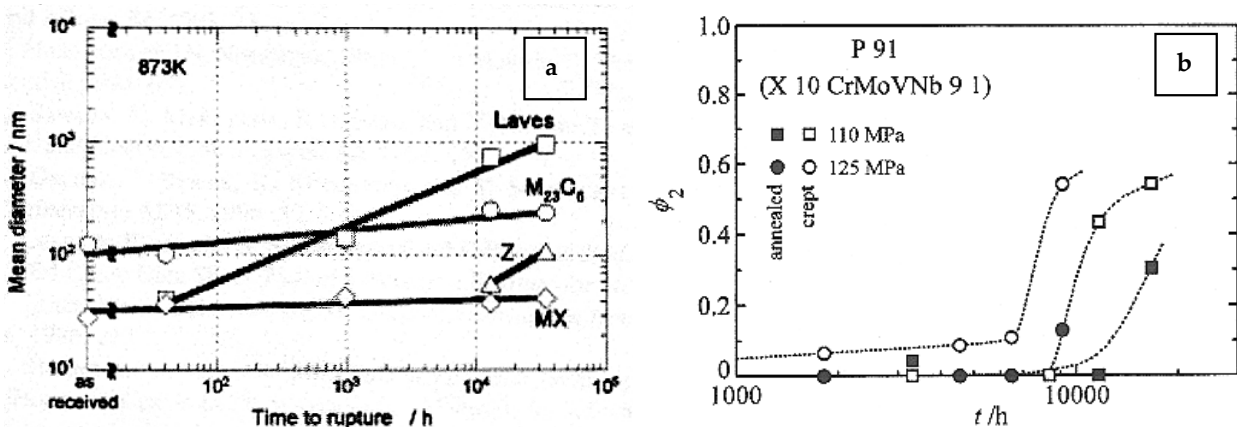


Figure B.I.14. Evolution of the size of second phase particles during creep at 600°C from (a) Kimura et al (2000) and (b) Polcik et al (1999)

Nakajima et al (2003) described particles growth kinetics during creep exposure at high temperature by a coarsening law as:

$$r^3 - r_0^3 = Kt \quad (\text{eq. B.I.100})$$

and showed that K depends on the effective diffusivity D_{eff} as pipe and lattice diffusion both control the coarsening kinetics.

The effective diffusivity is given by:

$$D_{\text{eff}} = D_L + (2LC_0\varepsilon/b)D_P \quad (\text{eq. B.I.101})$$

where ε is the tensile creep strain, C_0 is the average solute concentration, D_L is the diffusivity by lattice diffusion,

$D_L = D_{0L} \exp\left(-\frac{Q_L}{RT}\right)$ and D_P is the diffusivity by pipe diffusion and $D_P = A_P D_{0P} \exp\left(-\frac{0.6Q_L}{RT}\right)$ with $A_P D_{0P} = 10^{-24}$

m^4s^{-1} . The numerical values are given in **table B.I.8**.

Element	D_{0L} for lattice diffusivity	Q_L Activation energy for lattice diffusivity
Cr	$8.52 \cdot 10^{-4}$	251 kJmol ⁻¹
Mo	$4.6 \cdot 10^{-3}$	285 kJmol ⁻¹
V	$0.25 \cdot 10^{-4}$	264 kJmol ⁻¹
Nb	$5.3 \cdot 10^{-2}$	344 kJmol ⁻¹

Table B.I.8. Data needed to calculate diffusivity of species

The effective diffusivity can only be calculated provided the diffusion species controlling the coarsening kinetics is determined. In the case of $M_{23}C_6$, Mo is the controlling specie and V is the controlling specie for MX particles. From experimental investigations on particles of type MX and $M_{23}C_6$, Nakajima et al (2003) concluded that $K = D_{\text{eff}}$ well represents coarsening under creep loading conditions up to 30,000 hours. Finally, it is shown in **figure B.I.14b** that the applied engineering stress σ promotes particles coarsening as the kinetics of coarsening is higher in creep ageing conditions than in stress free ageing conditions.

The importance of second phase particles is very important as they locally induce very high stress concentrations and are very often preferential sites for cavity nucleation. Many studies have shown that creep cavities in tempered martensitic steels mainly initiate at particle matrix interfaces because of the high local stress concentrations.

4.2. Softening effects

As tertiary creep starts very early and takes more than one third of the creep time at high temperature, softening phenomena are obviously of great importance. In fact, chromium stainless steels are very sensitive to softening effects that can be related to the precipitation behaviour. Two main types of softening mechanisms can be released:

1. In cyclic loading and tensile conditions continuous softening is observed by Nagesha et al (2002) and Armas et al (1998). In this strain rate domain one can describe softening process as recrystallisation even if majority of authors prefer considering this as recovery process. For example, Tsuchiyama et al (2001) have observed that recrystallization may occur for high dislocation density (up to 2.10^{15} m^{-2}) in ultra low carbon steel (0.006 wt% C) where carbides spacing is higher than 10^{-7} m .
2. For long term creep exposure, extensive lath recovery occurs whose driving force should only be diffusion at grain boundary. Many authors agree this point.

Cerri et al (1998), Orlova et al (1997) showed that lath recovery occurs during creep. Recovery consists in subgrain formation and growth. Two subgrain growth kinetics equation under constant applied load are proposed:

$$\dot{d} = K'b \left(\frac{\sigma}{E}\right)^p \quad (\text{eq. B.I.102})$$

with d = subgrain size, b = Burgers vector and σ = maximal principal stress.

$$\log\left(\frac{d}{d_{\text{ST}}}\right) = \log\left(\frac{d_0}{d_{\text{ST}}}\right) \exp\left(-\frac{\varepsilon}{k}\right) \quad (\text{eq. B.I.103})$$

with d = subgrain size, d_0 = initial subgrain size, d_{ST} = subgrain size during the steady state creep.

The evolution of the material microstructure can be summarised by the representation of Iwanaga et al (1998) in **figure B.I.15**. The initial microstructural state is a lath martensite with a high dislocation density. As creep deformation proceeds, carbide coarsening occurs which enable boundary to move. Grain boundary and dislocation motion leads to the recovery of the martensite microstructure with large carbide particles.

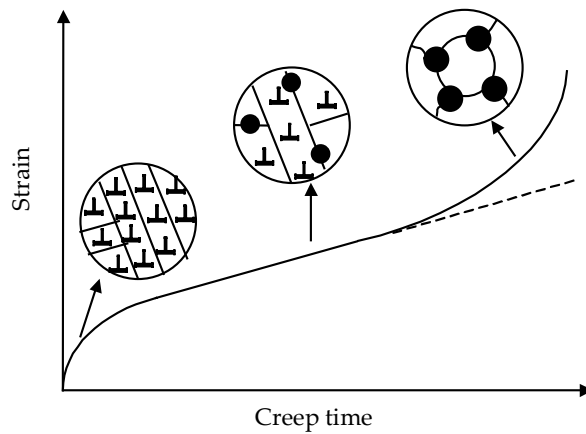


Figure B.I.15. Evolution of the microstructure during creep deformation from Iwanaga et al (1998)

4.3. Development of new chromium martensitic stainless steels

The development of new chromium stainless steel is currently largely studied with two goals:

1. Increase material strength under creep and fatigue conditions: This is the aim of 911, 92, 12%Cr, Pd or B reinforced materials and new oxide dispersion strengthened (ODS) alloys.
2. Reduce the effect of irradiation by replacing Nb, V and W element by low activation energy elements.

Grade 92 and 911 (9Cr-2W and 9Cr-1Mo-1W) steels have led to a substantial increase in creep strength as point out by several authors: Abe (2001), Hong (2001), Sawada et al (1999), Ennis et al (1997) and Abe and Nakazawa (1992). W has the same effect of Mo but precipitation of Laves phase of type Fe_2W and Fe_7W_6 is retarded in creep ageing conditions compared to $(Fe,Cr)_2Mo$ precipitation. Addition of W element must however be controlled as for higher contents than 2.7 wt% this element promotes formation of damaging δ ferrite. (Abe and Nakasawa (1992) and Ryu, Yu and Ku (2000)).

Recently, Taneike et al (2003) have developed a new generation of 9% chromium stainless steels based on the assumption that MX precipitates are the main lath structure stabilising particles. They designed an alloy with a fine dispersion of MX precipitates (5 - 10 nm) with a specific heat treatment (30 minutes at 1100°C followed by 1 hour at 800°C). Another great interest is that MX particle coalescence is very slow in creep ageing conditions (Particle size was found to be 20nm – 30 nm after 10,000 hours of creep at 650°C). As a consequence, the designed alloy has greater creep properties than grade 91 and 92 steels (see **figure B.I.16**).

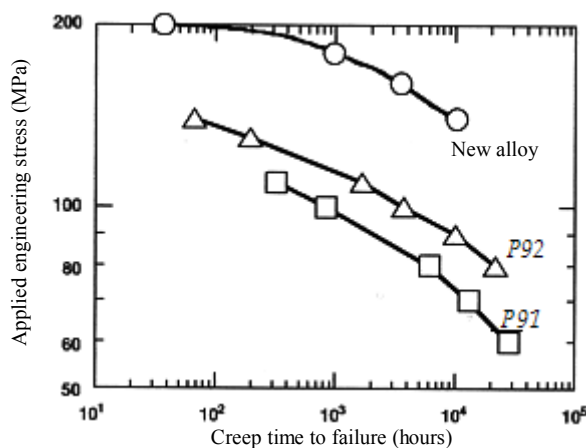


Figure B.I.16. Comparison of creep strength at 650°C of grade 91 and 92 and the new alloy steel proposed by Taneike et al (2003)

The effects of the addition of several alloying elements such as palladium or boron have been studied. Palladium added 9Cr1Mo steels exhibit a higher creep strength due to the formation of a α'' ordered phase ($FePdL_{10}$) and Okada et al (2002) show that the addition of Re in those steels delayed the growth of Laves phase and $M_{23}C_6$ carbides. They also evidenced that the addition of Ru, Os, Ir, Au and Pt improved creep strength. Abe et al (2004), Spiradek-hahn et al (2001), Azuma et al (2001), Muraki et al (2001), Kimura et al (2001) and Gustafson and Agren (2001) also showed that boron and cobalt stabilise the lath martensite microstructure of 9Cr steels and retard the onset of the acceleration of creep

deformation. As MX particles are the best creep strengthening precipitates, the effect of increasing the N content to form more MX precipitates was investigated by Sawada et al (2004). They showed that the N content cannot be largely increase as when it exceeds 0.05 wt%, Cr₂N precipitates form. These Cr₂N precipitates rapidly coarsen during creep exposure and little contribute to the material creep strengthening. It is also shown by Tamura et al (2003) that excess precipitation of MX weakens the grain boundaries.

The development of ODS steels started in the sixties but the high anisotropy of the material that results from the fabrication process delayed their commercial used during a long period. As underlined by Klueh et al (2002), main developments in Europe concern the EUROFER ODS which is fabricated by the powder compaction method. The EUROFER ODS is a martensitic stainless steel mechanically alloyed with a Y₂O₃ powder. In parallel, a 12%Cr Y₂O₃ reinforced steels is being developed in Japan. However, the anisotropy of mechanical properties remains very high.

In addition to efforts in increasing the creep strength, other efforts have to be made to replace high activation elements like Mo, W, Nb, V by low activation elements like Ca, Ta ... to use chromium stainless steels for nuclear applications (see Vanderschaaf et al (2000), Brachet et al (2000) and Brachet et al (1999)).

5. Conclusions

The creep flow and damage behaviour of tempered chromium martensitic stainless steels have been largely studied especially at 600°C and 650°C which were the chosen temperatures for the COST European programs. The main parts of literature data concern the high stress creep flow behaviour as only the work of Kloc and Sklenicka (1997) was concerned with low stress creep flow properties. Creep tests were mainly performed on smooth round specimens and the creep damage mechanisms were little investigated. Moreover, the impact of the change of creep flow at low stress on the long term creep lifetime has never been taken into account for predictions. However there is no deny that the literature contains thorough studies of the effect of second phase particles on creep that clearly show that carbides coarsening and Laves phase particles precipitation are detrimental for creep properties.

References

- Abe F., Horiuchi T., Taneike M., Sawada K. (2004). Stabilization of martensitic microstructure in advanced 9cr steel during creep at high temperature. *Materials science and engineering*. **A378**. 299-303.
- Abe F. (2003). Effect of quenching, tempering and cold rolling on creep deformation behavior of a tempered martensitic 9Cr-1W steel. *Metallurgical and materials transactions A*. **34A**. 913-923.
- Abe F., Horiuchi T., Sawada K. (2003). High temperature annealing for maximization of dissolved boron in creep resistant martensitic 9Cr steel. *Materials Science Forum*. **426-432**. 1393-1398.
- Abe F. (2001) Creep rates and strengthening mechanisms in tungsten strengthened 9Cr steels. *Materials science and engineering*. **A319-321**. 770-773.
- Abe F., Nakazawa S. (1992). The effect of tungsten on creep behavior of tempered martensitic 9Cr steels. *Metallurgical transactions A*. **23A**. 3025-3034.
- Anderson P.M., Rice J.R. (1985). Constrained creep cavitation of grain boundary facets. *Acta metallurgica*. **33(3)**. 409-422.
- Argon A.S., Chen I.W., Law C.W. (1980). Intergranular cavitation in creep : theory and experiments. 46-81.
- Armas A.F., Petersen C., Schmitt R., Avalos M., Alvarez Armas I. (2002). Mechanical and microstructural behaviour of isothermally and thermally fatigued ferritic martensitic stainless steels. *Journal of nuclear materials*. **307-311**. 509-513.
- Ashby M.F., Gandhi C. and Taplin D.M.R. (1979). Fracture mechanism maps and their construction for F.C.C. metals and alloys. *Acta metallurgica*. **27**. 699-729.
- Ashby M.F. (1972). Boundary defects and atomistic aspects of boundary sliding and diffusional creep. *Surface science*. **31**. 498-542.
- Azuma T., Miki K., Tanaka Y. (2001). Effect of boron on microstructural change during creep deformation in 12%Cr heat resistant steel. *3rd EPRI conference on Advances in materials technology for fossil power plants - university of Swansea (United Kingdom)*. 177-185.
- Beere W. (1980a). Models for constrained cavity growth in polycrystals. *Acta metallurgica*. **28**. 143-150.
- Beere W. (1980b). Inhibition of intergranular cavity growth in precipitate hardened materials. *Journal of materials science*. **15**. 657-669.
- Bellenger E., Bussy P. (2001). « Phenomenological modeling and numerical simulation of different modes of creep damage evolution. *International Journal of Solids and Structures*. **38**. 577-604.
- Benzerga A.A. (2002). Micromechanics of coalescence in ductile fracture. *Journal of the mechanics and physics of solids*. **50**. 1331-1362.
- Besson J., Devilliers Guerville L., Pineau A. (2000). Modelling of scatter and size effect in ductile fracture: Application to thermal embrittlement of duplex stainless steels. *Engineering fracture mechanics*. **67(2)**. 169-190.

- Berdin C., Besson J., Bugat S., Desmorat R., Feyel F., Forest S., Lorentz E., Maire E., Pardoën T., Pineau A., Tanguy B. (2004). Local approach to fracture. *Les presses de l'école des Mines edited by J. Besson (written as a course for the summer school « MEALOR »)*. 221-264.
- Blum W. (2001). Creep of crystalline materials: experimental basis mechanisms and models. *Material science and engineering*. **A319-321**. 8-15.
- Brachet J.C., Lombard V., Alamo A. (1999). Studies of phase transformations occurring in conventional, low activation (LA) and oxide dispersion strengthened (ODS) 7-11%Cr (Mo,W,V,Nb,Ta) martensitic steels. *Proceedings of PTM'99 - Kyoto - Japan*.
- Brachet J.C., Averty X., Lamagnero P., Alamo A., Rozenblum F., Raquet O., Bertin J.L. (2001). Behavior of different austenitic steels, conventional, reduced activation (RA) and ODS chromium rich ferritic martensitic steels under neutron irradiation in PWR environment. *Effects of radiation on materials 20th symposium ASTM STP/405*.
- Budiansky B., Hutchinson J., Slutsky S. (1982). Void growth and collapse in viscous solids. *Mechanics of solids*. Hokins H. and Sewell M. editors. The Rodney Hill 60th anniversary volume. Pergamon press.
- Burton B. and Greenwood G.W. (1970). The contribution of grain boundary diffusion to creep at low stresses. *Metal Science Journal*. **4**.
- Cadek J., Sustek V., Pahutova M. (1997). An analysis of a set of creep data for a 9Cr-1Mo-0.2V steel. *Materials Science and Engineering*. **A225**. 22-28
- Cerri E., Evangelista E., Spigarelli S., Bianchi P. (1998). Evolution of microstructure in a modified 9Cr-1Mo steel during short term creep. *Materials Science and Engineering*. **A245**. 285-292.
- Chen J.W., Argon A.S. (1981). Diffusive growth of grain boundary cavities. *Acta metallurgica*. **29**. 1759-1768.
- Chokshi (1987). Analysis of constrained cavity growth during high temperature creep deformation. *Materials science and technology*. **3**.
- Chu C., Needleman A. (1980). Void nucleation effects in biaxially stretched sheets. *Journal of engineering material technology*. **102**. 249-256.
- Coble R.L. (1963). A model for boundary-diffusion controlled creep in polycrystalline materials. *Journal of applied physics*. **34**. 1679-1682.
- Crossman F.W., Ashby M.F. (1975). The non uniform flow of polycrystals by grain boundary sliding accommodated by power-law creep. *Acta metallurgica*. **23**. 425-440.
- Davanas K. and Solomon A.A. (1990). Theory of intergranular creep cavity nucleation growth and interaction. *Acta metallurgica and materialia*. **38(10)**. 1905-1916.
- Diard O. (2001). Un exemple de couplage, comportement – endommagement – environnement, dans les polycristaux. Application à l'interaction pastille-gaine. *PhD thesis of the Ecole Nationale Supérieure des Mines de Paris (In French)*.
- Dimmler G., Weinert P., Cerjak H. (2002). Investigations and analysis of the stationary creep behaviour of 9-12% chromium ferritic martensitic steels. *Materials for advanced power engineering - Proceedings of the 7th Liège conference, Forschungszentrum Julich. Editors Lecomte-Beckers, Carton, Schuber and Ennis (Editors)*. **II**. 1539-1549.
- Dyson B.F., Rodgers M.J. (1974). Prestrain, cavitation and creep ductility. *Metal science*. **8**. 261-266.
- Dyson B.F. (1976). Constraints on diffusional cavity growth rates. *Metal Science*. 349-353.
- Dyson B.F. (1979). Constrained cavity growth, its use in quantifying recent creep fracture results. *Canadian metallurgical quarterly*. **18**. 31-38.
- Dyson B.F. (1983). Continuous cavity nucleation and creep fracture. *Scripta metallurgica*. **17**. 31-37.
- Eberle N. and Jones F.L. (2003a). Creep deformation in a modified 9Cr-1Mo steel - θ projection approach to prediction of creep properties. *Materials Science and Technology*. **19**. 214-218.
- Eberle N. and Jones F.L. (2003b). Creep deformation in modified 9Cr-1Mo steel – dynamical systems approach to prediction of creep properties. *Materials Science and Technology*. **19**. 365-371.
- Edward G.H. and Ashby M.F. (1979). Intergranular fracture during power-law creep. *Acta Metallurgica*. **27**. 1505-1518.
- Eggeler G. (1989). The effect of long term creep on particle coarsening in tempered martensite ferritic steels. *Acta Metallurgica*, **37(12)**, 3225-3234.
- Eggeler G., Earthmann J.C., Nilsvang N., Ilschner B. (1989b). Microstructural study of creep rupture in a 12%Cr ferritic steel. *Acta metallurgica*. **37(1)**. 49-60.
- Eggeler G. (1991). Microstructural parameters for creep damage quantification. *Acta Metallurgica et Materialia*. **39(2)**. 221-231.
- Eggeler G., Tato W., Jemmely P. et al (1992). Creep rupture of circular notched P91 specimens: influence of heat treatment and notch geometry. *Scripta Metallurgica et Materialia*. **27**. 1091-1096.
- Eggeler G., Ramteke A., Coleman M., Chew B., Peter G., Burblies A., Hald J., Jefferey C., Rantala J., DeWitte M., Mohrmann R. (1994). Analysis of creep in a welded 'P91' pressure vessel. *International journal of pressure vessels and piping*. **60**. 237-257.
- Ennis P.J. (2002). Recent advances in creep resistant steels for power plant applications. *OMMI*. **1(1)**.
- Ennis P.J., Zielinska-Lipiec A., Wachter O., Czyrska-Filemonowicz (1997). Microstructural stability and creep rupture strength of the martensitic steel P92 for advanced power plant. *Acta materialia*. **45(12)**. 4901-4907.

- Ennis P.J., Zielinska-Lipiec A., Wachter O., Czyska-Filemonowicz (2000). Quantitative microscopy and creep strength of 9% chromium steels for advanced power stations. *Proceedings of the 5th International Charles Parsons Turbine Conference*. 498-507.
- Evans H.E. (1984). Mechanisms of creep fracture. *Elsevier applied science – London*.
- Evans R.W. and Wilshire B. (1985). Creep of metals and alloys. *The institute of metals – London*.
- European Fast Reactor Associates – EFR (1998).
- Faleskog J., Gao X., Fong Shih C. (1998). Cell model for non linear fracture analysis. I. Micromechanics calibration. *International journal of fracture*. **89**. 355-373.
- Foldyna V., Jacobova A., Rimán R., Genple A. (1984). Effect of dispersed phase on creep resistance of 9Cr-1Mo (V) steel. *Creep fracture of engineering materials and structures - Swansea - Pineridge press*. 685-695.
- Gandhi C. and Ashby M.F. (1979). Fracture mechanism maps for materials which cleave: F.C.C., B.C.C. and H.C.P. metals and ceramics. *Acta metallurgica*. **27**. 1565-1602.
- Garofalo F. (1966). Fundamentals of creep and creep rupture in metals. *Macmillan series in materials science*. London.
- Gifkins R.C. (1994). Grain boundary participation in high temperature deformation: an historical review. *Materials Characterization*. **32**. 59-77.
- Gifkins R.C., Langdon T.G., McLean D. (1975). Grain boundary sliding and axial strain during diffusional creep. *Metal science*. **9**. 141-144.
- Goods S.H., Nix W.D. (1978). The kinetics of cavity growth and creep fracture in silver containing implanted grain boundary cavities. *Acta metallurgica*. **26**. 739-752.
- Gologanu M., Leblond J., Devaux J. (1993). Approximate models for ductile metals containing non spherical voids- case of axisymmetric prolate ellipsoidal cavities. *Journal of mechanics and physics of solids*. **41(11)**. 1723-1754.
- Gologanu M., Leblond J., Devaux J. (1994). Approximate models for ductile metals containing non spherical voids- case of axisymmetric oblate ellipsoidal cavities. *Journal of engineering material technology*. **116**. 290-297.
- Gologanu M. (1997). Etude de quelques problèmes de rupture ductile des métaux. *PhD thesis - Université Paris VI. In French*.
- Goswami T. (2004). Development of generic creep fatigue life prediction models. *Materials and design*. **25**. 277-288.
- Gotz G., Blum W. (2003). Influence of thermal history on precipitation of hardening phases in tempered martensite 10%Cr-steel X12CrMoWVNbN 10-1-1. *Materials science and engineering*. **A348**. 201-207.
- Großner P.J. and Hagel W.C. (1980). The effect of molybdenum on high-temperature properties of 9%Cr steels. *Metallurgical transactions*. **11A(4)**. 633-642.
- Guttman M. (1982). Mécanismes microscopiques de la germination et de la croissance des cavités et des fissures intergranulaires dans les métaux et alliages à haute température sous sollicitation cyclique. *Private communication*.
- Gustafson A., Agren J. (2001). Possible effect of Co on coarsening of $M_{23}C_6$ carbide and Orowan stress in a 9%Cr steel. *ISIJ International*. **41(4)**. 356-360.
- Hancock J.W. (1976). Creep cavitation without a vacancy flux. *Metal science*. 319-325.
- Harper J.G., Dorn J.E. (1957). Viscous creep of aluminium near its melting temperature. *Acta Metallurgica*. **5**. 654
- Hayhurst D.R. (1995). High-temperature design and life assessment of structures using continuum damage mechanics - *Creep and Fatigue: Design and Life Assessment at High Temperature in Mechanical Engineering Publications Ltd.* (UK), 399-410.
- Herring C. (1950). Diffusional viscosity of a polycrystalline solid. *Journal of applied physics*. **21**. 437-445
- Hong S.G., Lee W.B., Park C.G. (2001). The effects of tungsten addition on the microstructural stability of 9Cr-Mo steels. *Journal of nuclear materials*. **288**. 202-207.
- Horsewell A. (1978). The sliding of grain boundaries containing particles during diffusional creep. *Scripta metallurgica*. **13**. 21-25.
- Hull D., Rimmer D.E. (1959). The growth of grain boundary voids under stress. *Philosophical Magazine*. **4(42)**. 673-687.
- Jacobova A., Vodarek V., Hennhofer K., Foldyna V. (1998). Microstructure and creep properties of P91 steel and weldments. *Materials for advanced power engineering - 6th Liege Conference*. 373-382.
- Kasl J., Kasha V. (1998). Microstructural investigations of advanced creep resistant 10% Cr steel. *Materials for advanced power engineering - 6th Liege Conference*.
- Kassner M.E. and Hayes T.A. (2003) Creep cavitation in metals. *International Journal of Plasticity*. **19**. To be published.
- Kimura K., Suzuki K., Toda Y., Kushima H., Abe F. (2002). Precipitation of Z-phase and degradation behaviour of mod. 9Cr-1Mo steel. *Materials for advanced power engineering 2002 edited by Lecomte-Beckers J.* **II.21**. 1171-1180.
- Kimura K., Seki K., Toda Y., Abe F. (2001). Development of high strength 15Cr ferritic creep resistant steel with addition of tungsten and cobalt. *ISIJ International*. **41**. S121-S125.
- Kimura K., Kushima H., Abe F. (2000). Heterogeneous change in microstructure and degradation behaviour of 9Cr1Mo-NbV steel during long term creep. *Key engineering materials*. **171-174**. 483-494.
- Kimura K., Kushima H., Abe F., Yagi K. (1997). Inherent creep strength properties of ferritic steels. *Materials Science and engineering*. **A234-236**. 1079-1082.
- Kloc L., Sklenicka V. (2004). Confirmation of low stress creep regime in 9%Cr chromium steel by stress change experiments. *Materials science and engineering A*. To be published.

- Kloc L., Sklenicka V. (1997). Transition from power law to viscous creep behavior of P91 type heat treated steel. *Materials Science Engineering*. **A234-236**. 962-965.
- Kloc L., Sklenicka V., Ventruha J. (2001). Comparison of low stress creep properties of ferritic and austenitic creep resistant steels. *Materials Science and Engineering*. **A319-321**. 774-778.
- Klueh R.L., Gelles D.S., Jitsukava S. Kimura A., Odette G.R., Vanderschaaf B., Vidrova M. (2002). Ferritic/martensitic steels – overview of recent results. *Journal of nuclear materials*. **307-311**. 455-465.
- Koplick J. and Needleman A. (1988). Void growth and coalescence in porous plastic solids. *International journal of solids and structures*. **24(8)**. 835-853.
- Kubon Z., Foldyna V., Hajduk D., Simecek D. (2000). Creep and relaxation properties of 9-12% Cr steels. *Proceedings of the 5th International Charles Parsons Turbine Conference*. 485-497.
- Langdon T.G. (2000). Identifying creep mechanisms at low stresses. *Materials Science and Engineering*. **A283**. 266-273.
- Larson F.R. and Miller J. (1952). A time-temperature relationship for rupture and creep stresses, *Transactions of the ASME*. **74**. 765-775.
- Lemaitre J., Chaboche J.L. (1990). *Mechanics of solids materials*. Cambridge university press.
- Lemaitre J., Desmorat R. (2004). *Engineering damage mechanics: Ductile, creep, fatigue and brittle failures*. Springer verlag.
- Lundin L.M., Hattestrand M., Andren H.O. (2000). Redistribution of Elements During Ageing and Creep Testing of 9-12% Chromium Steels. *Proceedings of the 5th International Charles Parsons Turbine Conference*. 602-617.
- Maruyama K., Sawada K., Koita J., Sato H., Yagi K. (1997). Examination of deformation mechanism map in 2.25Cr1Mo steel by creep tests at strain rates 10^{-11} - 10^{-6} s⁻¹. *Materials science and engineering*. **A224**. 166-172.
- McLean D. (1981). Damage accumulation in creep. *Annales de Chimie Françaises*. **6**. 124-139.
- Michel B. (2004). Formulation of a new intergranular creep damage model for austenitic stainless steels. *Nuclear Engineering and Design*. **227(2)**. 161-174.
- Miller D.A., Langdon T.G. (1980). Independent and sequential cavity growth mechanisms. *Scripta metallurgica*. **14**. 143-148.
- Monkman F.C. and Grant N.J. (1956). An empirical relationship between rupture life and minimum creep rate in creep-rupture tests, *Proceedings of the ASTM*, **56**, 593-620.
- Muraki T., Hasegawa Y., Tamehiro H., Ohgami M., Maruyama N., Mikami M. (2001). Creep strengthening mechanism of boron containing 9-12% chromium heat resistant steel. *3rd EPRI conference on Advances in materials technology for fossil power plants - university of Swansea (United Kingdom)*. 437-446.
- Myers M.R., Pilkington R., Needham N.G. (1987). Cavity nucleation and growth in a 1%Cr-0.5%Mo steel. *Materials Science and Engineering*. **95(2)**. 81-91.
- Nabarro F.R.N. (1967). Steady state diffusional creep. *Philosophical magazine*. **16**. 231-237.
- Nagesha A., Valsan M., Kannan R., Bhanu Sankara Rao K., Mannan L. (2002). Influence of temperature on the low cycle fatigue behaviour of a modified 9Cr-1Mo ferritic steel. *International journal of fatigue*. **24**. 1285-1293.
- Nakajima T., Spigarelli S., Evangelista E., Endo T. (2003). Strain enhanced growth of precipitates during creep of T91. *Materials Transactions*. **44(9)**. 1802-1808.
- Ohta S., Saori M. (1986). Mechanism of void formation on grain boundary during creep of high carbon stainless steels. *Supplement to transactions of the Japan institute of metals*. 765-772.
- Okada H., Muneki S., Yamada K., Okubo H., Igarashi M., Abe F. (2002). Effects of alloying elements on creep properties of 9Cr-3.3W-0.5Pd-V,Nb,N,B steels. *ISIJ International*. **42(10)**. 1169-1174.
- Onck P. and Van der Giessen E. (1998). Micromechanics of creep fracture: simulation of intergranular crack growth. *Computational material science*. **13**. 90-102.
- Onck P. and Van der Giessen E. (1997). Microstructurally based modelling of intergranular creep fracture using grain elements. *Mechanics of Materials*. **26**. 109-126.
- Onck P. and Van der Giessen E. (1995). Void growth due to creep and grain boundary diffusion at high triaxialities. *Journal of mechanics and physics of solids*. **43(1)**. 123-165.
- Orlova A., Bursik J., Kucharova K., Sklenicka V. (1998). Microstructural development during high temperature creep of a 9% Cr steel. *Materials Science Engineering*. **A245**. 39-46.
- Orr R.L., Sherby O.D., Dorn J.E. (1954). *Transactions of the ASME*. **46**. 113.
- Parameswaran P., Saroja S., Vijayalakshimi M., Raghunathan V.S. (1996). Decomposition modes of austenite in Cr-Mo ferritic steel. *Journal of nuclear materials*. **232**. 226-232.
- Pardoën T., Hutchinson J. (2000). An extended model for void growth and coalescence. *Journal of mechanics and physics of solids*. **48(12)**. 2467-2512.
- Park J.S., Kim S.J., Lee C.S. (2001). Effect of W addition on the low cycle fatigue behaviour of high Cr ferritic steels. *Materials science and engineering*. **A298**. 127-136.
- Pavinich W., Raj R. (1977). Fracture at elevated temperature. *Metallurgical transactions*. **8A**. 1917-1933.
- Pineau A., Besson J. (2000). Some new trends in modeling ductile rupture of structural alloys. *Colloque Lemaitre*.

- Piques R. (1986). Mécanique et mécanismes de l'amorçage et de la propagation de fissures en viscoplasticité dans un acier austénitique inoxydable – PhD Thesis – Ecole nationale Supérieure des Mines de Paris.
- Polcik P., Sailer T., Blum W., Straub S., Bursik J., Orlova J. (1999). On the microstructural development of the tempered martensitic Cr steel P91 during long term creep: a comparison of data. *Materials Science Engineering*. **A260**. 252-259.
- Poirier J.P. (1985). Creep of crystals, high temperature deformation processes in metals, ceramics and minerals. *Cambridge university press*.
- Prunier V., Gampe U., Nikbin K., Shibli I.A. (1998). HIDA activity on P91 steel. *Creep and fatigue crack growth in high temperature plant*. HIDA Conference - CEA Saclay - France.
- Ragab A.R. (2004). A model for ductile fracture based on internal necking of spheroidal voids. *Acta materialia*. **52**. 3997-4009.
- Raj R. (1978). Nucleation of cavities at second phase particles in grain boundaries. *Acta metallurgica*. **26**. 995-1006.
- Raj R., Ashby M.F. (1975). Intergranular fracture at elevated temperature. *Acta metallurgica*. **23**. 653-66.
- Raj R., Ashby M.F. (1972). Grain boundary sliding and the effects of particles on its rate. *Metallurgical transactions*. **3**. 1937-1943.
- RCCMR (1993). RCCMR French design code modified in 2000. DMC253.
- Rice J. and Tracey D. (1969). On the ductile enlargement of voids in triaxial stress fields. *Journal of mechanics and physics of solids*. **17**. 201-217.
- Riedel H. (1987). Fracture at high temperatures. *Materials research and engineering – Springer Verlag*.
- Robinson D.N. (1978). A unified creep plasticity model for structural materials at high temperature. *ORNL report / TM-5969*.
- Rosler J., Artz E. (1990). A new model based creep equation for dispersion strengthened materials. *Acta metallurgica et materialia*. **38(4)**. 671-683.
- Sawada K., Taneike M., Kimura K., Abe F. (2004). Effect of nitrogen content on microstructural aspects and creep behavior in extremely low carbon 9Cr heat resistant steel. *ISIJ International*. **44(7)**. 1243-1249.
- Sawada K., Takeda M., Maruyama K., Ishii R., Yamada M., Nagae Y., Komine R. (1999). Effect of W on recovery of lath structure during creep of high chromium martensitic steels. *Materials science and engineering*. **A267**. 19-25.
- Sklenicka V., Kucharova K., Svoboda M., Kloc L., Bursik J., Kroupa A. (2003). Long term creep behavior of 9-12%Cr power plant steels. *Materials Characterization*. **51**. 35-48.
- Sellars C.M., Teggart W.J.M. (196). Relationship between strength and structure in deformation at elevated temperatures. *Mem. Sci. Rev. Met.* **63(9)**. 731- 745.
- Senior B.A. (1989). The precipitation of Laves phase in 9Cr-1mo steel. *Materials Science Engineering*. **A119**. L5-L9
- Senkov O.N., Jonas J.J., Froes F.H. (1998). Steady state flow controlled by the velocity of grain boundary migration. *Materials Science and Engineering*. **A255**. 49-53.
- Spigarelli S., Kloc L., Bontempi P. (1997). Analysis of creep curves in a 9Cr1Mo modified steel by means of simple constitutive equations. *Scripta materialia*. **37(4)**. 399-404.
- Spingarn J.R., Barnett D.M., Nix W.D. (1979). Theoretical descriptions of climb controlled steady state creep at high and intermediate temperatures. *Acta metallurgica*. **27**. 1549-1561.
- Spiradek Hahn K., Nowakowski P., Zeiler G. (2001). Boron added 9%Cr steels for forged components in advanced power plants. *3rd EPRI conference on Advances in materials technology for fossil power plants - university of Swansea (United Kingdom)*. 165-175.
- Sundurarajan G. (1985). Continuous cavity nucleation and creep ductility. *Scripta metallurgica*. **10**. 1141-1146.
- Suzuki K., Kumai S., Kushima H., Kimura K. and Abe F. (2003). Precipitation of Z-Phase and precipitation sequence during creep deformation of mod. 9Cr-1Mo steel. *Tetsu Hagane*. **89(6)**. 69-76.
- Tamura M., Sakasegawa H., Kohyama A., Esaka H., Shinozuka K. (2003). Effect of MX particles on creep strength of ferritic steels. *Journal of nuclear materials*. **321**. 288-293.
- Taneike M., Abe F., Sawada K. (2003). Creep strengthening of steel at high temperatures using nano sized carbonitride dispersions. *Letters to nature*. **424**. 294-296.
- Taneike M., Sawada K., Abe F. (2002). Development of high strength 9Cr steel by combination of fine MX-Type nitrides and NO carbide. *Materials for advanced power engineering edited by Lecomte-Beckers J., Carton M., Schubert F. and Ennis P.J.* 1379-1384.
- Taro M., Yasushi H., Hiroshi T., Masahiro O., Naoki M., Masato M. (2003). Creep strengthening mechanism of boron containing chromium heat resistant steel. 437-446.
- Thomason P.F. (1985). Three dimensional model for the plastic limit loads at incipient failure of the intervoid matrix in ductile porous solids. *Acta Metallurgica*. **33(6)**. 1379-1389.
- Tokuno K., Hamada K., Uenori R., Takeda T., Itoh K. (1991a). Role of a complex carbonitride of niobium and vanadium in creep strength of 9Cr ferritic steels. *Scripta metallurgica et materialia*. **25**. 1763-1768.
- Tokuno K., Hamada K., Uenori R., Takeda T., Itoh K. (1991b). A complex carbonitride of niobium and vanadium in 9Cr ferritic steels. *Scripta metallurgica et materialia*. **25**. 871-876.

- Tsuchiyama T., Myamoto T., Takaki S. (2001). Recrystallisation of lath martensite with bulge nucleation and growth mechanism. *ISIJ International*. **41(9)**. 1047-1052.
- Tsukasa A., Kazuhiro M., Yasuhiko T. (2001). Effect of boron on microstructural change during creep deformation in 12%Cr heat resistant steel. *3rd EPRI conference on Advances in materials technology for fossil power plants - university of Swansea (United Kingdom)*. 177-185.
- Tvergaard V. (1984). On the creep constrained diffusive cavitation of grain boundary facets. *Journal of Mechanics and Physics of Solids*. **32(5)**. 373-393.
- Van der Giessen E., Vanderburg M.W.D., Needleman A., Tvergaard V. (1995). Void growth due to creep and grain boundary diffusion at high triaxialities. *Journal of mechanics and physics of solids*. **43(1)**. 23-165.
- Van der Schaaf B., Gelles D.S., Jisukawa S., Kimura A., Klueh R.L., Moslang A., Odette g.r. (2000). Progress and critical issues of reduced activation ferritic /martenitic steel development. *Journal of nuclear materials*. **283-287**. 52-59.
- Weinert P. (2002). Microstructural physically based creep modelling of 9-12% Cr steels. *Materials for advanced power engineering - Proceedings of the 7th Liège conference, Forschungszentrum Julich. Editors Lecomte-Beckers, Carton, Schuber and Ennis (Editors)*. **II**. 1211-1221.
- Williams K.R., Findler R.S., Askins M.C. (1981). The effect of secondary precipitation on the creep strength of 9Cr1Mo steel. *Creep and Fracture of Engineering materials and structures edited by B. Wilshire and D.R.J. Owen*. 475-487.
- Wu R., Sandström R. (1995a). Creep cavity nucleation and growth in 12Cr-Mo-V steel. *Materials science and technology*. **11**. 579-588.
- Wu R., Sandström R. (1995b). Strain dependence of creep cavity nucleation in low alloys and 12%Cr steel. *Materials science and technology*. **12**. 405-415.
- Yamada K., Igarashi M., Muneki S., Abe F. (2002). Effect of heat treatment on precipitation kinetics in high Cr ferritic steels. *ISIJ international*. **12(7)**. 779-784.
- Yamada K., Igarashi M., Muneki S., Abe F. (2001). Creep properties affected by morphology of MX in high Cr ferritic steels. *ISIJ International*. **41**. Supplement S116-S120.
- Yamada K., Igarashi M., Muneki S., Abe F. (2001). Creep properties affected by morphology of MX in high Cr ferritic steels. *Advances in materials technology for fossil power plants – Edited by Viswanathan R*. 125-131.
- Yu J., Hong S.H. (1989). Micromechanisms of creep crack growth. *Scripta metallurgica*. **23**. 957-962.
- Zener C., Hollomon J.H. (1944). Plastic flow and rupture of metals. *Transactions of the ASME*. **33**. 163-244.
- Zhang Z.L., Thaulow C., Odegaard J. (2000). A complete Gurson model approach for ductile fracture. *Engineering fracture mechanics*. **67**. 155-168.
- Zyczkowski M. (2000). Creep damage evolution equations expressed in terms of dissipated power. *International journal of mechanical science*. **42**. 755-769.

Chapter B.II. Experimental investigations of creep mechanisms and cavitation processes in P91 steel at 625°C (Smooth round specimens)

In the present study, the testing temperature was set to 625°C as this temperature was chosen for the HIDA project (see Prunier et al (1998) and Jayet-Gendrot (1999)). In the present chapter, attention will be focused on determining the creep deformation and damage mechanisms of the P91 steel at 625°C from only the results creep tests on smooth round specimens.

1. Overview of creep experiments at 625°C

An experimental database was built to investigate creep flow and damage behaviour of the P91 steel at 625°C. First, creep tests on smooth round tensile bars were carried out to determine the creep flow properties (**figure B.II.1**). Most tests were carried out until specimen failure. An additional test, with the load varying with steps was performed in order to investigate the creep flow behaviour at relatively low stress increasing then decreasing stress from 60 MPa to 120 MPa. The results of experiments are respectively reported in **appendix A, table A.A.4** and **table A.A.5**.

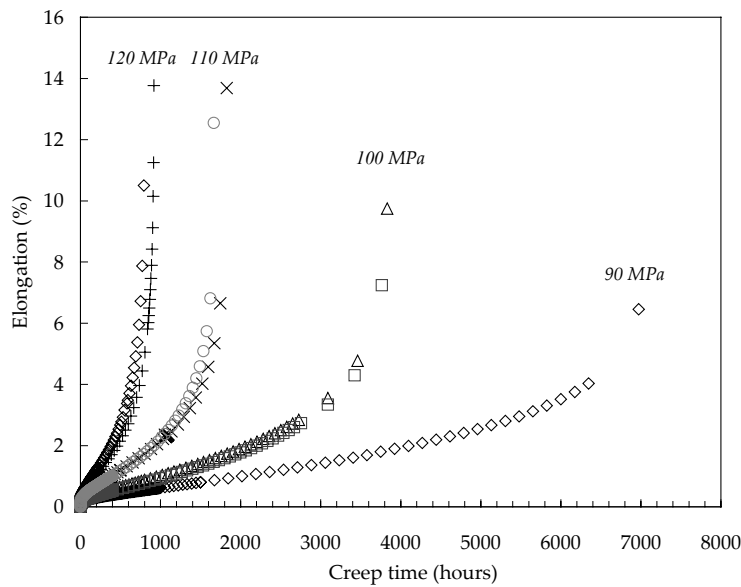


Figure B.II.1. Creep curves for tests on SC specimens

The elongation of creep specimens was calculated as:

$$\varepsilon = \frac{\Delta L_g}{L_{g0}} \tag{eq. B.II.1}$$

where ΔL_g is the actual elongation of the initial gauge length and L_{g0} is the initial gauge length i.e. 36 mm.

The steady state creep strain rates are plotted in **figure B.II.2** from which a Norton power-law with no threshold stress could be determined as:

$$\dot{\varepsilon}_{ss} = B\sigma^n \tag{eq. B.II.2}$$

where B and n are model parameters fitted from experimental data as $n = 8.1$ and $B = 3.03 \cdot 10^{-22} \text{ h}^{-1}\text{MPa}^{-8.1}$. This value of the Norton power-law exponent suggests a dislocation creep deformation mechanism. Note that in the domain experimentally investigated (creep tests up to 7,000 hours) no change in the Norton exponent was observed even if the multiple load level tests obviously confirmed a transition stress near 70 MPa.

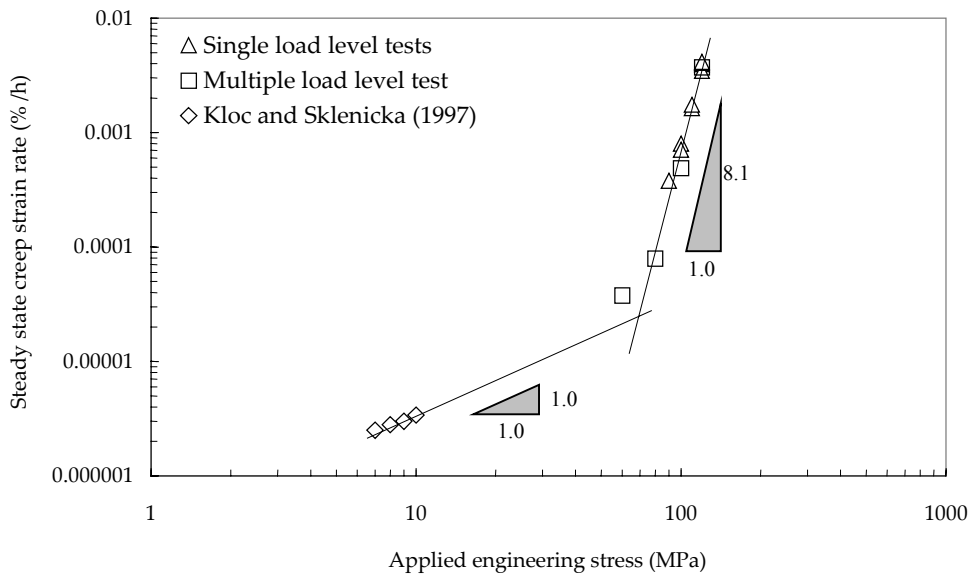


Figure B.II.2. Steady state strain rate versus applied engineering stress for SC specimens

In figure B.II.3, creep time to failure are related to the steady state strain rate as stated by the Monkman-Grant (1956) MG relationship:

$$\epsilon_{ss}^m t_r = C_{MG} \quad (\text{eq. B.II.3})$$

where m and C_{MG} are model parameters. It was fitted as $m = 0.94$ and $C_{MG} = 0.058 \text{ h}^{-0.06}$. Assuming that both creep flow and damage mechanisms up to 10,000 hours are the same than these encountered during long term creep exposure i.e. 100,000 hours, the MG fit estimates that the P91 steel reaches a 100,000 hours creep lifetime for an applied engineering stress of 65 MPa. Please remind that this extrapolation is supported by a strong hypothesis in terms of long term creep damage mechanisms and that the MG relationship is not valid in multiaxial loading conditions i.e. for stress triaxiality ratios larger than 1/3.

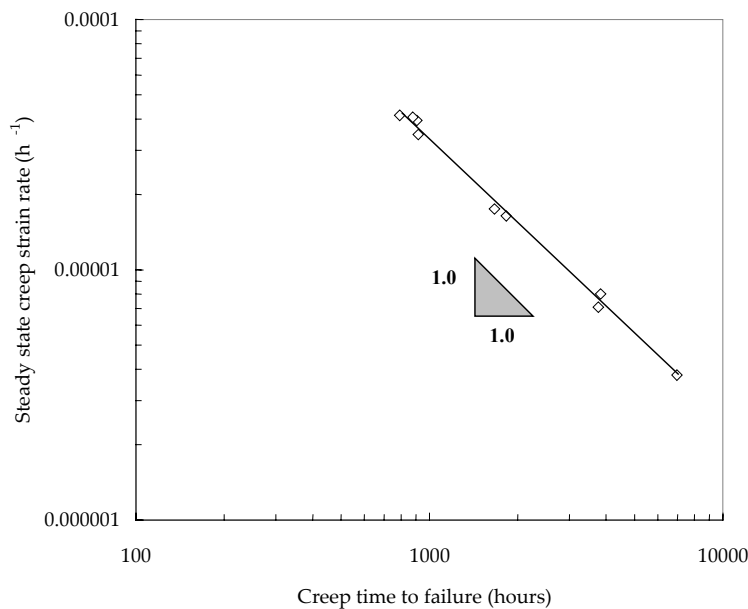


Figure B.II.3. Monkman grant plot for creep tests on SC specimens

2. Creep mechanisms at 625°C

2.1. The primary creep

Primary creep generally corresponds to an increase in the dislocation density. This material hardening must be related to thermally activated phenomena, as creep tests are usually carried out at applied engineering stresses lower than the 0.2% proof stress generally measured at high strain rates (270 MPa for a strain rate of 10^{-3} s^{-1}).

For 9Cr1Mo-NbV steels, the primary creep regime occurs within very small strain intervals which means that the material hardening in the early stages of creep deformation is very limited. Pesicka et al (2003) who performed measurements of the evolution of dislocation density during creep show that there is no significant increase in the dislocation density during primary creep. Their conclusion is that a steady state dislocation density is reached for very low strain levels but other microstructural events occur. They evoke a load transfer from hard to soft regions as subgrains resulting both from high temperature tempering and then from creep exhibit lower dislocation densities than lath microstructure areas. As pointed out by Eggeler (1989), very high primary creep rates (typically 10^3 h^{-1}) are evidenced because of the initial high dislocation density but their decrease is very rapid as dislocations are pinned by carbides and the dislocation production is very limited. Sawada et al (1997) determined the following expression giving the dislocation density within laths:

$$\rho = 0.3075 \left(\frac{\sigma}{G} \right)^2 \left(\frac{1}{b} \right)^2 \quad (\text{eq. B.II.4})$$

in m^{-2} where the shear modulus G is equal to $-48T(\text{K}) + 103572$ in MPa and b is the Burgers vector equal to $a/2 \langle 111 \rangle = 2.5 \cdot 10^{-10} \text{ m}$ for the P91 steel, so that at 625°C :

$$\rho = 1.35 \cdot 10^9 \sigma^2 \quad (\text{eq. B.II.5})$$

No study of the origin of dislocation production during the creep of 9Cr1Mo-NbV steels was found in the literature. Therefore, the mechanisms of dislocation production and the reasons why this production is rapidly stopped are not well known yet.

2.2. Importance of the tertiary creep regime

The ratio, time at the end of the steady state creep regime over creep time to failure is plotted versus creep time to failure. This representation (see **figure B.II.4**) shows that the tertiary creep regime represents more than 65 % of the creep lifetime at 625°C and $\sigma = 120 \text{ MPa}$ and near 80 % of the creep lifetime at 625°C and $\sigma = 90 \text{ MPa}$. This result suggests that the steady state creep strain rate is not a sufficient data to describe properly creep failure properties of 9Cr1Mo-NbV steels. A more detailed analysis and description of creep softening and cavitation processes is then necessary to predict creep life of these materials at 625°C .

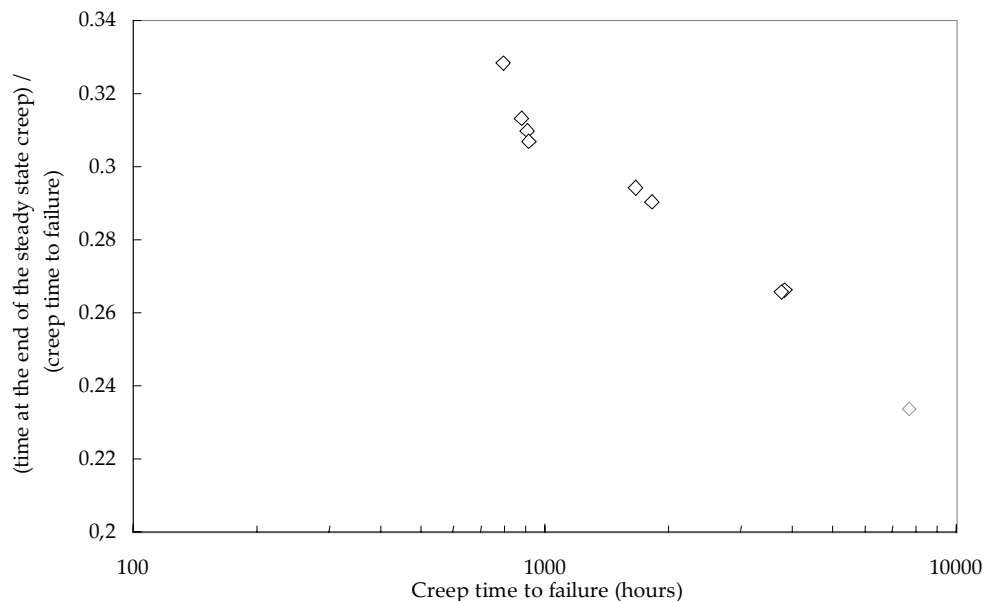


Figure B.II.4. Importance of the tertiary creep regimes

3. Creep softening behaviour

3.1. Effect of stress and time on the evolution of the precipitation state

Hattestrand and Andren (2001) have experimentally shown that coarsening of second phase particle is strongly accelerated under creep ageing conditions. Such a conclusion was also previously given by Eggeler (1989) who gave the following arguments to explain why kinetics of coarsening is higher than in stress free ageing conditions:

1. The applied stress promotes diffusion of the chemical species from boundaries parallel to the applied stress to these perpendicular to it.
2. The higher dislocation density in subgrain boundaries induces higher diffusion kinetics.

3. Dislocations that are pinned during primary creep, then remain sessile and constitute additional diffusion paths.

The evolution of average particle size in stress free ageing and creep ageing conditions is given in **figure B.II.5**. These measurements show that the applied engineering stress accelerates carbide coarsening at 625°C for applied engineering stresses up to 90 MPa. For longer ageing times (> 10,000 hours), carbide size is rather independent of the applied or not applied engineering stress. TEM investigations also showed that both particle coarsening and lath recovery occur.

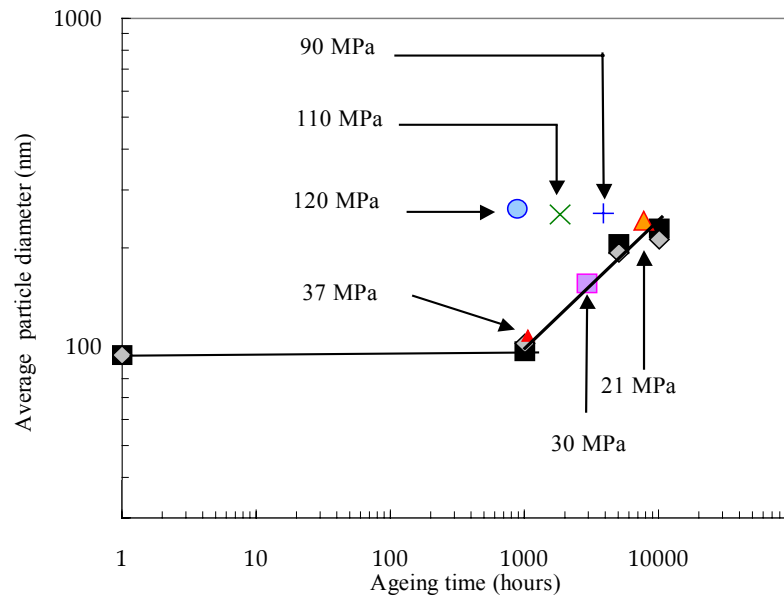


Figure B.II.5. Evolution of the particle mean size: Comparison between thermal ageing at 550 and 625°C (line) and creep ageing conditions at 625°C

Figure B.II.5 shows that the increase in the particle mean diameter is accelerated by applying a load. It also shows that for stress under 90 MPa, the evolution of the mean particles size is nearly the same than under only thermal ageing conditions.

3.2. Softening behaviour

Kadoya et al (1997) have concluded that the intrinsic mechanism of tertiary creep is dislocation strain softening which is proportional to the accumulated creep strain. Yoshida et al (2001) used TEM and EBSD to study the evolution of microstructure during creep. The main results of their study are:

1. The formation of subgrains at the interior of laths is observed with no change in lath boundary misorientation (i.e. low angle misorientation <math>< 5^\circ</math>).
2. The migration of packets boundaries is reported. In the as tempered state, there is a majority of neighbouring grains with $\langle 110 \rangle$ and $\langle 111 \rangle$ common axis (which corresponds to packet boundaries) and this number significantly decreases during creep.

The onset of accelerating creep stage occurs at early stage of creep deformation and at lower stresses the tertiary creep starts for lower strain. One explanation given by Kimura et al (2000) is that softening is heterogeneous. It leads to an instability and the tertiary stage starts earlier. From **figure B.II.6a**, one can typically deduced that creep softening starts for $\epsilon > 1 - 2\%$.

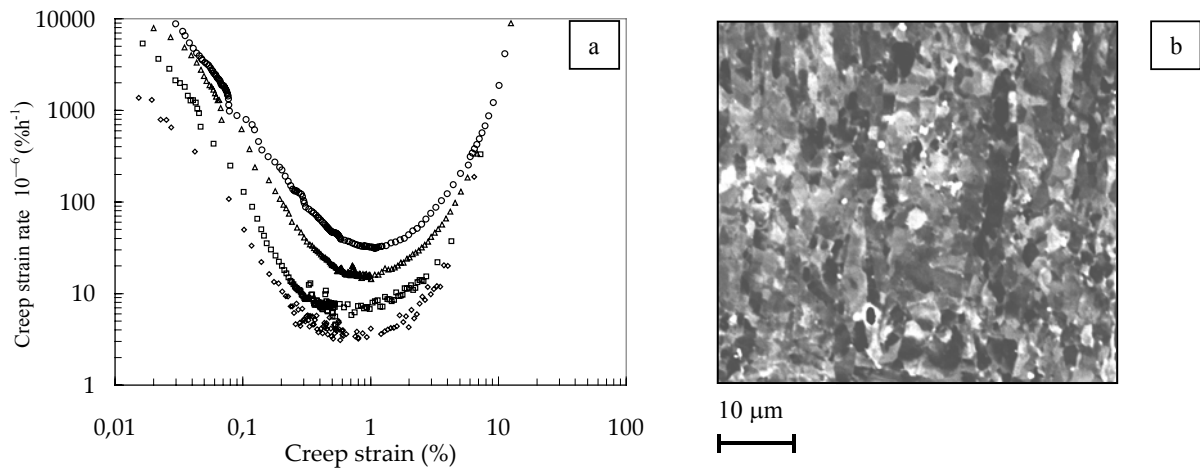


Figure B.II.6. Evidences of material softening (a) and lath martensite recovery (b) during creep at 625°C

The material softening evidenced in **figure B.II.6a** can be related to a recovery or a recrystallisation of the initial lath martensite microstructure as observed in **figure B.II.6b**. Another point evidenced in **figure B.II.6a** is that the material softening occurs for lower strain when the applied engineering stress decreases. Moreover, the elongation at the onset of material softening is about 1% which is consistent with the uniform elongation before the onset of material softening measured during tensile tests (see **table A.I.6**).

In fact, two types of material softening can be found in 9Cr1Mo-NbV steels:

1. Strain assisted softening, as more recovery is observed in the necking regions than in the other areas at high stress levels
2. Time assisted softening, as the recovery of the lath martensite also occurs in stress free ageing conditions (see **Part A, section I.4.4.**) and was also observed for long term creep exposure. The example of the SC specimen submitted to long term creep exposure (7,000 hours) is very representative. The EBSD map of **figure B.II.7a** evidences a modification of the initial lath martensite microstructure. As shown by the misorientation angle histogram of **figure B.II.7c**, there is an increase of the fraction of high angle boundaries.

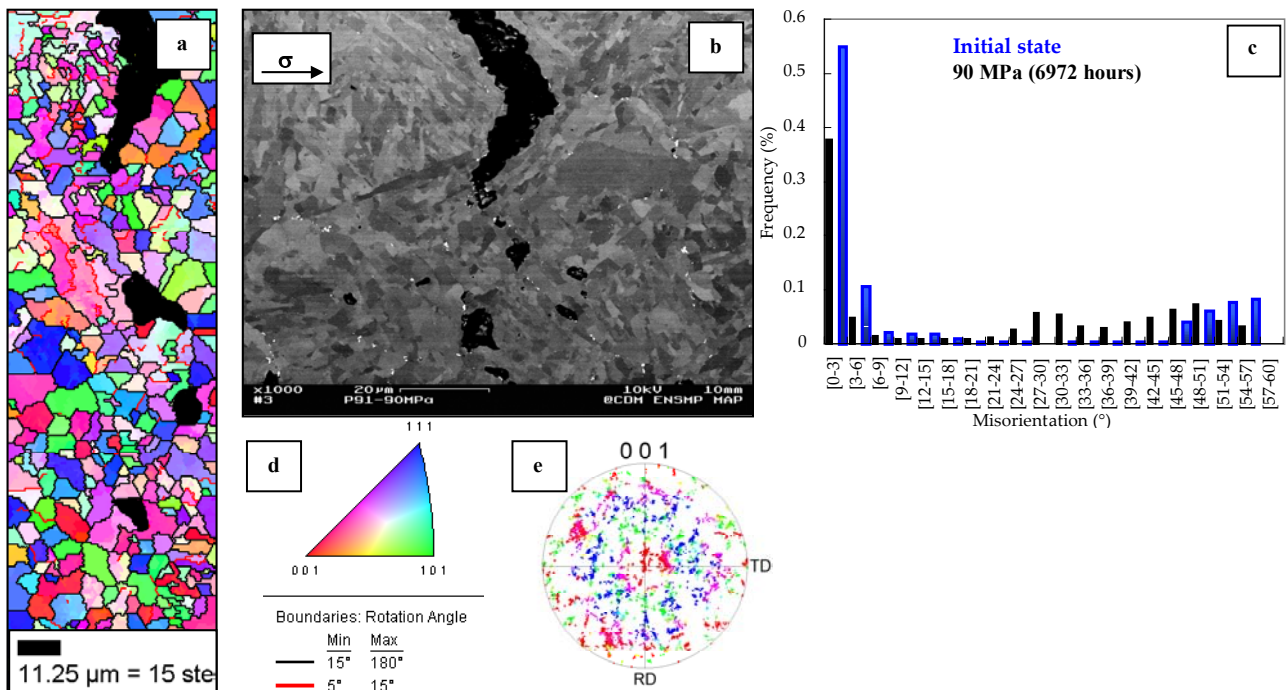


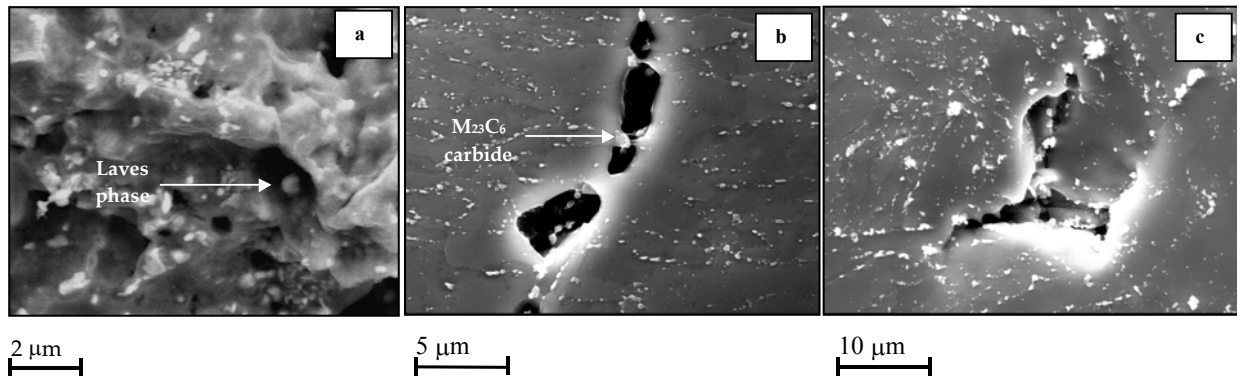
Figure B.II.7. Time dependent softening of the P91 steel during creep at 625°C

(a) EBSD map (b) SEM image (almost the same area than in (a)), (c) Misorientation angle histogram (between neighbouring grains) (d) color key and (e) {001} pole figure

4. Creep damage behaviour

4.1. Initiation

Carbon extraction replicas were taken from fracture surfaces and analysed in the SEM (see **figure B.II.8a**). In addition, SEM investigations were performed in specimens polished cross-sections (see **figure B.II.8b** and **B.II.8c**). Laves phase and carbides were observed, both on the fracture surface and near the cavities in polished cross-sections, which give arguments to state that nucleation preferentially occurred at second phase particles. These observations confirmed these of Stocker et al (2002) and Senior (1989). It is also shown in **figure B.II.8c** that triple points are privileged sites for cavity nucleation.



*Figure B.II.8. Mechanisms of cavity nucleation: At second phase particles and triple points
(a) carbon extraction replica (b) and (c) polished cross-sections*

From experimental observations, it was deduced that the stress concentrations at particle matrix interface likely promote cavity nucleation. Therefore, it is of great interest to determine which mechanical parameters govern cavity nucleation. The first analysis was performed by Eshelby (1961) who determined the value of the internal stress near an inclusion. In principle the cavity formation occurs when the elastic energy released from the particle by interfacial separation is equal to the surface energy .

$$\sigma = \Sigma + \frac{2}{3} \mu \varepsilon_{eq} \quad (\text{eq. B.II.6.})$$

where μ is the elastic shear modulus, ε_{eq} is the von Mises equivalent viscoplastic strain and Σ is the principal stress. Following this analysis, Beremin (1981) proposed that cavity nucleation occurs for a critical value of the local stress, σ_d , given by:

$$\sigma_d = \Sigma + k(\sigma_{eq} - \sigma_{el}) \quad (\text{eq. B.II.7.})$$

where σ_{eq} is the equivalent von Mises stress, σ_{el} is the yield stress and k is a factor depending on the shape of the second phase particle. Huez et al (1998) show that the analysis of Beremin (1981) is not valid for high stress triaxiality ratio. In fact, it can be assumed that the cavity nucleation can only be represented by the combined effects of the stress triaxiality ratio and the equivalent stress (i.e. the equivalent viscoplastic strain).

4.2. Location of creep cavities

The EBSD technique was used to determine the location of creep cavities. Let focus on how EBSD information was used. Martensitic and bainitic transformations have been extensively studied by Kurdjumov and Sachs and Nishiyama and Wassermann. They determined 24 orientations relationships between martensite and the parent austenite. EBSD patterns of grains set on both sides of a cavity were analysed (in other words, two pairs of three Euler angles $\varphi_1, \phi, \varphi_2$). A simple Matcad® application was then used to determine if one of the 24 KS-KS relationships is matched. The results can be interpreted as follows:

1. If no KS-KS relationships is matched (i.e. deviation larger than $7^\circ - 8^\circ$ from one of the KS-KS relationship) and the misorientation between grains is high: the cavity is located at a prior austenite grain boundary.
2. If a KS-KS relationship is matched (i.e. deviation lower than $7^\circ - 8^\circ$ from one of the KS-KS relationship) and the misorientation between grains is high: the cavity is located at a packet boundary.
3. If a KS-KS relationships is matched and the misorientation between grains is low: the cavity is located at a lath boundary or subgrain.
4. If no grain boundary is evidenced, the cavity is considered to be intragranular.

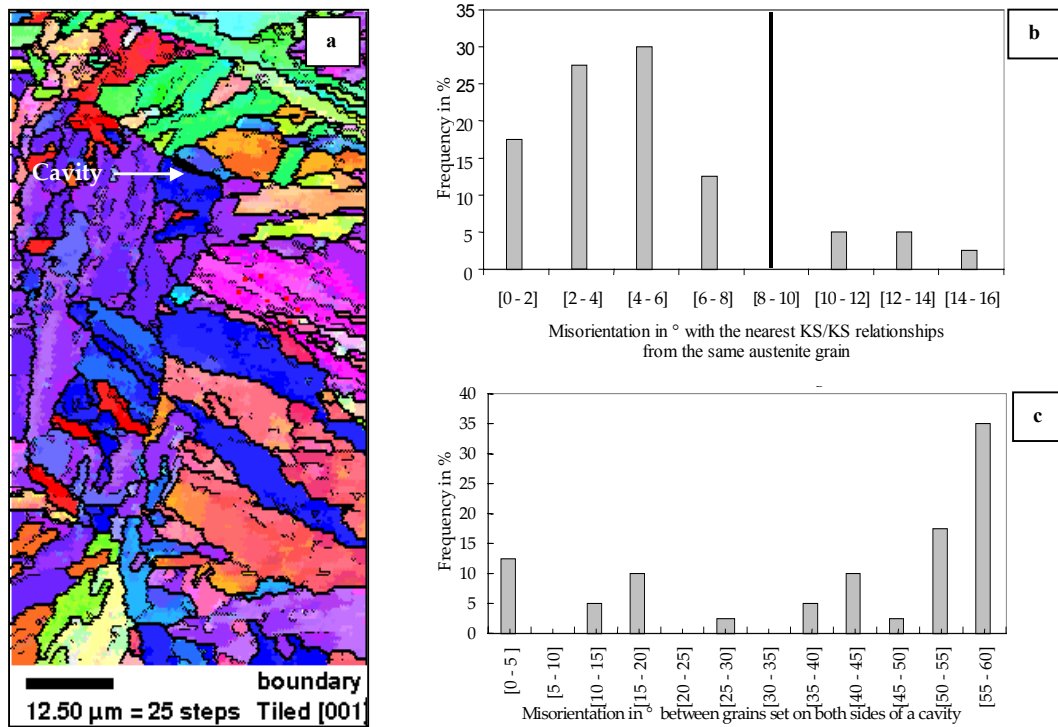


Figure B.II.9 EBSD study of creep cavity location in the P91 steel after creep (Example)

The example of an EBSD map is given in **figure B.II.9a**. In addition EBSD analysis was used to determine the orientation relationships between grains set on both side of the cavity. From the study of about one hundred cavities, the histogram of misorientations between grains sets on both sides of the cavity, could be plotted in **figure B.II.9c**. The misorientations with the nearest KS/KS relationships from the same austenite grain were also plotted.

The interpretation of these histograms was done using the four points given before. First, it is evidenced in **figure B.II.9c** that more than 80% of the creep cavities formed at high angle boundaries. In addition, the KSKS orientation relationships between grains in the neighbouring of cavities are matched for 85% of the cavities (see **figure B.II.9b**). Therefore, it can be concluded that 85% of the cavities are located at packet or prior austenite grain boundaries (with the majority at packet boundaries) and 15% at lath boundaries. The conclusion of this study is that each type of grain is concerned even if the majority of cavities is located at high angle packet boundaries inside the former austenite grain.

4.3. Cavity growth

It is very difficult to study quantitatively the evolution of the cavity size during the high temperature creep deformation process. However, SEM investigations in cross-sections, with focusing attention on the cavity shape, give useful information to determine the cavity growth mechanisms.

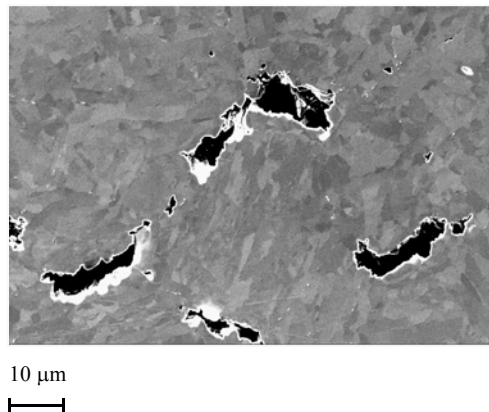


Figure B.II.10. Cavity observed in a polish cross sections after colloidal silica polishing (SC specimen - 100 MPa - 3800 hours)

For the shorter creep tests (< 1,000 hours), creep cavities exhibit a round shape far from the fracture surface and an elongated shape along the loading axis due to high level of matrix deformation encountered near the fracture surface.

When increasing the creep time, as shown in **figure B.II.10**, the creep cavities exhibit a more elongated shape perpendicular to the loading axis. The cavities in **figure B.II.10** are nevertheless not really “crack like” and their growth is also promoted by matrix deformation. In fact, the situation is that of coupled cavity growth. More generally, from the observations of cavity shapes in the cross sections of all creep tested specimens, it was concluded that both matrix deformation and diffusion at grain boundaries promote cavity growth.

4.4. Quantification of the porosity ratio

Measurements of porosity ratios were carried out on smooth round creep tested specimens. It consists of imaging scan, using a SEM with backscattered electron channelling contrast of SC specimens cross-sections after colloidal silica polishing. Each map was constituted of nearly 300 images taken at a magnification of 400. The minimum cavity size that can be observed using this technique was about 1 μm in diameter. Image analysis was then performed using Matlab® image processing toolbox in which an image processing treatment was implemented. Operations on images consists in several dilatation and erosion operations followed by measurements of the cavity morphology (see **appendix B.G** for detail).

The aim of the measurements was:

1. To determine porosity ratios so as to compare them with calculations in the following of the study.
2. To determine if a change of the effect of both the principal stress and the cumulated viscoplastic strain on damage kinetics occurs.

In the local approach to fracture, the question of the pertinence of the damage quantity to measure experimentally is always asked. Piques (1986), who studied the high temperature creep of an austenitic stainless steel chose the length of cracked boundary. In this study, the surface of the cavity which surrounds a cavity was chosen as the reliable damage parameter as the creep model of the present study was written in the framework of the mechanics of porous media (see **chapter B.III** in the following). The way damage surface ratio was determined is illustrated in **figure B.II.11** in fractured SC specimens cross-sections.

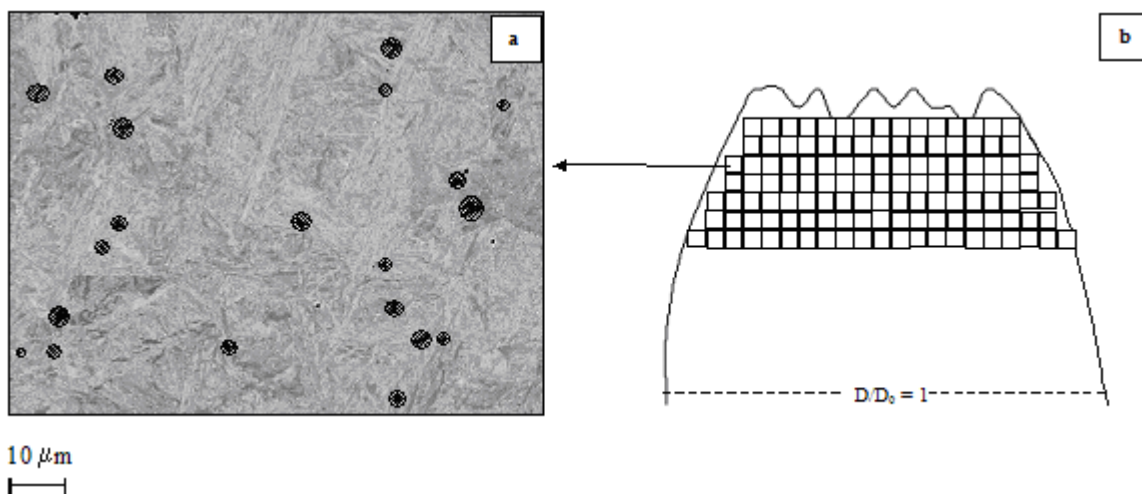


Figure B.II.11. Counting method to give experimental results on porosity ratio to be compared with calculations (a) SEM micrograph and (b) map in SC fractured specimens cross-sections

From the image analysis procedure the following characteristics of each observed cavity was determined:

1. Its surface (S).
2. Its orientation compared to the loading axis as it was often shown that intergranular cavities nucleate and grow on boundaries with a deviation of 45° from the loading axis.
3. The major axis (M) of the circumscribed ellipse from which the area corresponding to the sphere, of M in diameter, surrounding the cavity was calculated.

The cavities in fractured SC specimens appeared to be mainly oriented following the loading direction as they mainly developed in the necking area. Damage quantification was then mainly used to evaluate cavity nucleation and growth kinetics. The best way to evaluate the cavity nucleation kinetics is to count the evolution of the number of cavities.

Cavity growth can be evaluated as the evolution of the porosity ratio. Such measurements were done by image analysis in the minimum cross-sections of the SC specimens after creep failure (see figure B.II.12a and B.II.12b). The average number of cavities is calculated on field of 214*286 μm .

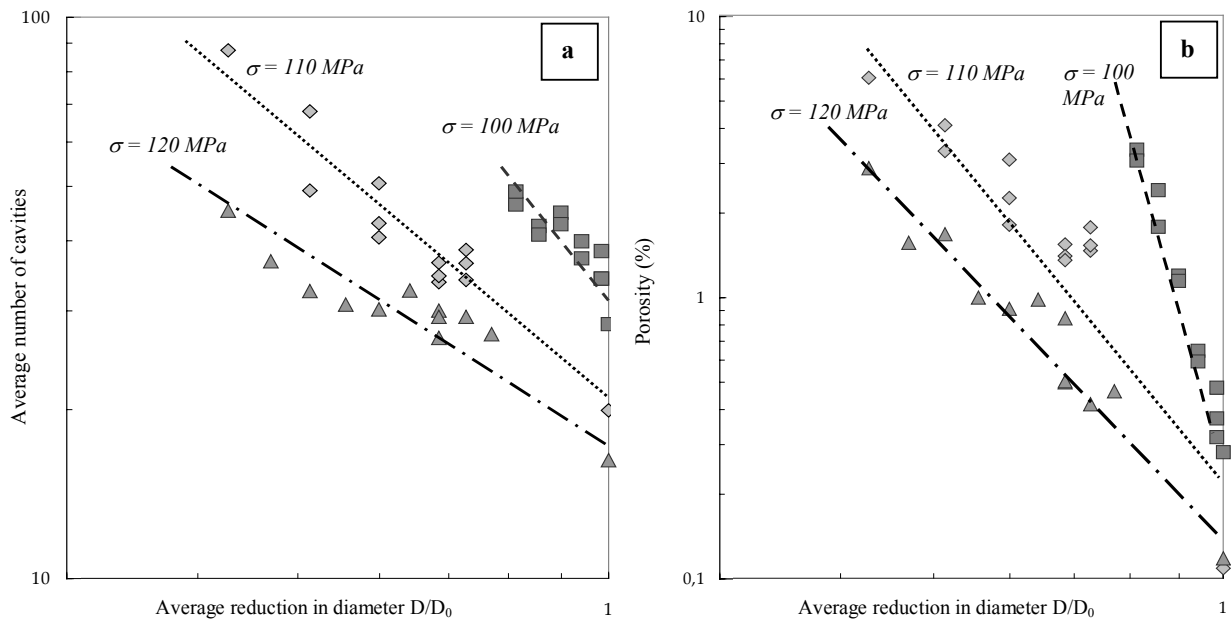


Figure B.II.12. Evolution of the number of cavities (a) and of the porosity ratio (b) versus specimen necking

The interpretation of those measurements is not so easy. Indeed, damage mainly developed in the necking area so that both the strain and the stress triaxiality ratio are increased. Therefore, it is obviously very hazardous to fit a model involving only the strain rate, as the porosity ratio also depends on the applied engineering stress.

More suitable evolution laws should take the effect of the stress triaxiality into account. In addition, one of the most important point of the plots of **figure B.II.12a** and **B.II.12b** is that the damage mechanisms evolve from high to low stresses levels as the slopes of the linear fits between, cavity number or porosity ratio, and the average reduction of specimen diameter, increase when decreasing the applied engineering stress.

The main conclusions of the measurements of damage are as follows:

1. Both the creep strain and the stress triaxiality ratio play a key role in cavity nucleation and growth.
2. Damage measurements allow to determine the rupture location in various final specimen geometry and for various stress levels.
3. The measurements showed that damage mechanisms obviously changed when decreasing the applied engineering stress (i.e. the respective role of the creep strain and the stress triaxiality ratio on damage development evolve).
4. In the framework of the local approach to fracture, the suitable experimental damage measurement depends on the formulation of the model chosen to represent the evolution of damage. Further developments will be given in **section 3.5** in **chapter B.III**).

4.5. Cavity coalescence and specimen failure

The cavity coalescence is the very late stage of the creep failure so that it is hardly observable. It is, however, very interesting to use the results of damage quantification to evaluate the porosity ratio just behind the fracture surface as it gives the critical porosity: f_c at the onset of the creep failure. It can be shown in **figure B.II.13** that f_c is nearly equal to 0.1.

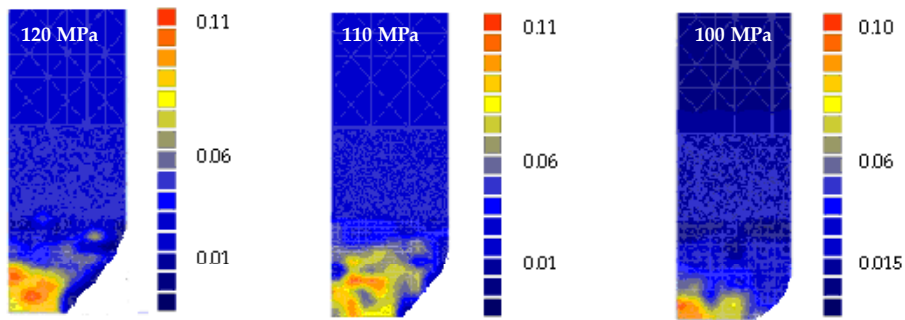


Figure B.II.13. Quantification of damage in cross sections of fractured SC specimens

In the stress domain experimentally investigated, the large deformation encountered at the fracture stage lead to the ductile failure of all the specimens (see **figure B.II.14**). However, the extensive oxidation of the specimens tested in air prevent from observations at a more finer scale. For better understanding of creep fracture behaviour, creep tests on plate notched specimens under vacuum (10^{-3} Pa) were added to the experimental database. The results of these tests are given in **chapter B.III**.

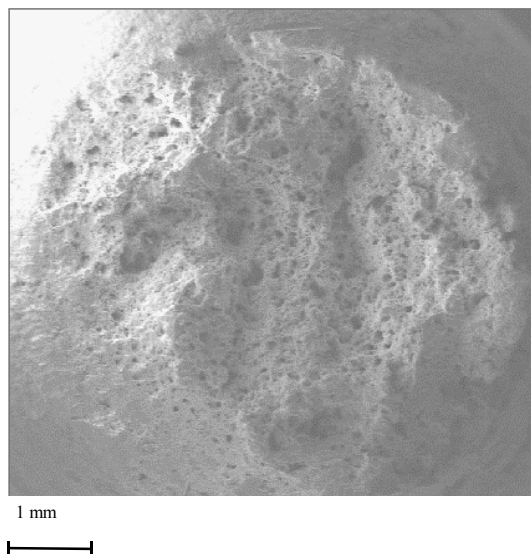


Figure B.II.14. Fracture surface of a creep fractured SC specimen (120 MPa – 1,000 hours)

The evolution of SC specimens reduction of area was also plotted in **figure B.II.15**. For comparison, the level of the reduction of area for tensile tests is indicated on the plot. It is shown that the reduction area of the SC specimens largely decrease with creep exposure. This evolution, already evidenced in a number of high temperature creeping materials as the austenitic stainless steels, confirm the change in damage mechanisms at low stress. It can be deduced that intergranular crack growth become the dominating damage mechanism for creep exposures longer than 10,000 hours.

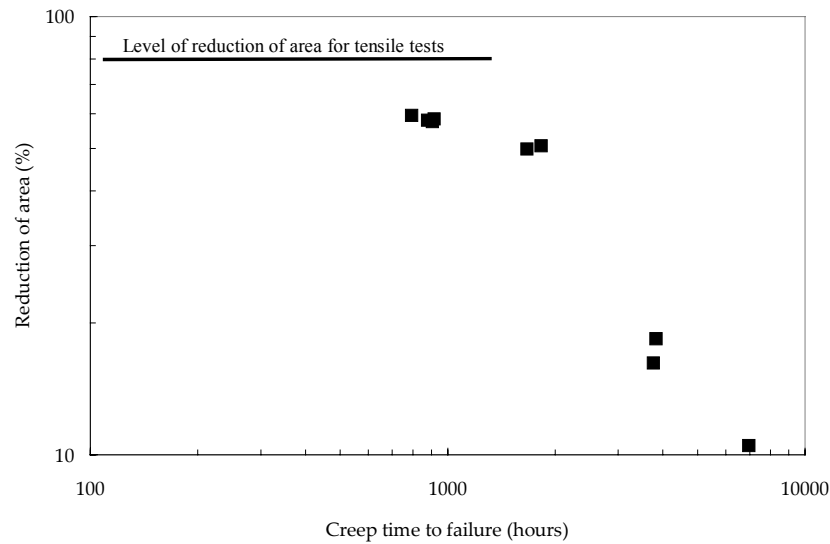


Figure B.II.15. Evolution of the reduction of area of SC specimens versus the creep time to failure

5. Effects of ageing on creep strength

5.1. Literature results

Few studies concerning the effects of ageing on creep properties have been found in the literature. The corresponding results are reported in **table B.II.1**.

Author	Ageing conditions	Creep conditions	Creep time to failure	
			Aged	Non Aged
Vilhelmsen (1996)	10,000 hours - 600°C	580°C - 180MPa	130 hours	780 hours
Brinkman (1993)	50,000 – 75000 hours 482 – 649°C	<i>No numerical results are given – Creep times to failure for aged material are under minimum values for non aged material</i>		
Sklenicka et al (2003)	10,000 hours 650°C	600°C - 120 MPa	3,500 hours	15,000 hours
		600°C - 150 MPa	170 hours	920 hours

Table B.II.1. Effects of ageing on creep properties

Literature results show that ageing reduces by more than four times the material creep lifetime at high temperature. Unfortunately, neither metallurgical explanations nor micrographs of the creep tested specimens are given.

5.2. Experiments

Creep tests were carried out at 625°C up to fracture on smooth round specimens of aged P91 material for two ageing temperatures: 550°C and 625°C and three ageing times: 1,000 - 5,000 and 10,000 hours. Details about experimental results are given in **appendix A. table A.A.13**. In the limited time of the PhD, only two creep tests could have been carried out. The corresponding creep curves are given in **figure B.II.16** where the experimental scatter-band for the non aged base metal was also plotted. It shows that both the steady state creep strain rates and the creep strength of the aged material are largely lower than these of the non aged material.

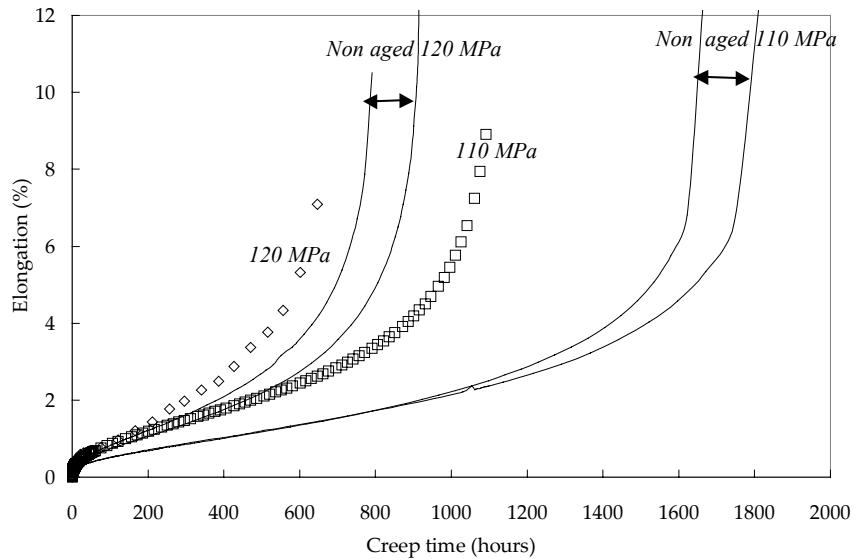


Figure B.II.16. Creep curves for creep tests on SC specimen: aged specimens (symbols) and experimental scatter band for non aged specimens (lines)

5.3. Influence of ageing on creep flow and fracture behaviour

Comparison between creep flow of non aged and aged specimens leads to the following conclusions:

1. Steady state strain rates are higher for aged material but not as much as found by Sklenicka et al (2003). Steady state strain rate is approximately 50% higher than for non aged material (see **figure B.II.17a**).
2. Creep curves of the aged specimens exhibit a very short secondary creep stage and the acceleration of creep strain starts for a critical strain lower than for the non aged specimen (see **figure B.II.17b**).

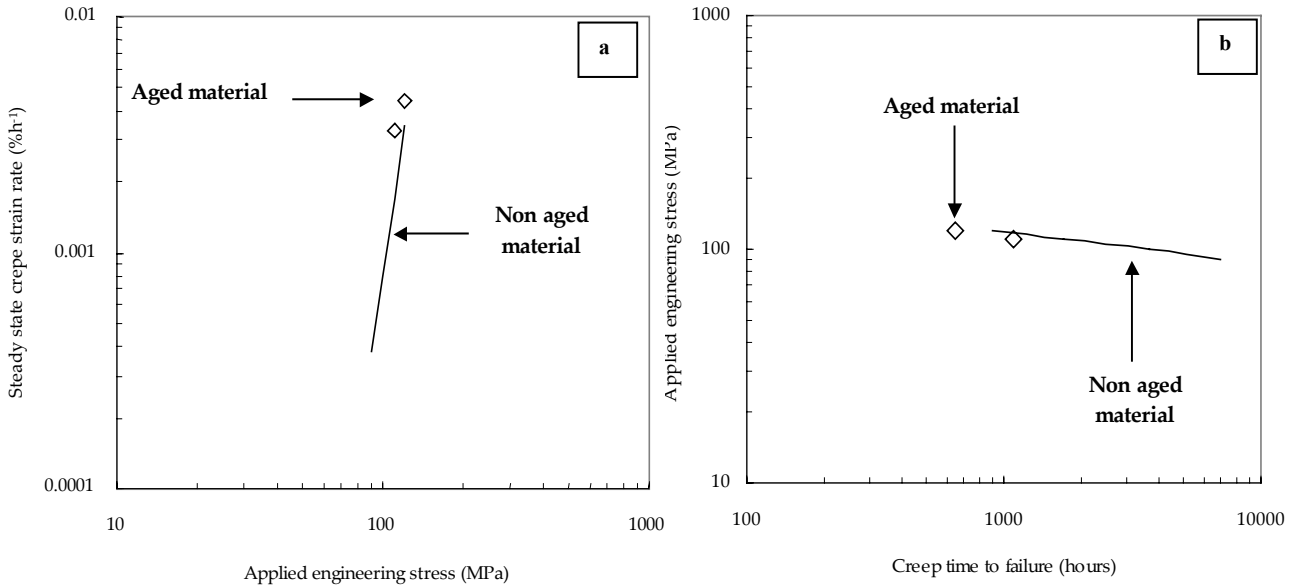


Figure B.II.17. Comparison between aged and non aged material (a) steady state strain rate versus applied engineering stress (b) Applied engineering stress versus time to failure

The results given in **Part A** have shown that $M_{23}C_6$ carbides coarsening and Laves phase precipitation occur during thermal ageing. Carbides coarsening is obviously responsible for the earlier starts of tertiary stage. It confirms the key role of carbides in the material microstructural stability for the non aged material.

5.4. Influence of ageing on creep damage behaviour

SEM investigations evidenced, as for the non aged base metal, that extensive recovery of the initial lath microstructure occurs especially in the necking area.

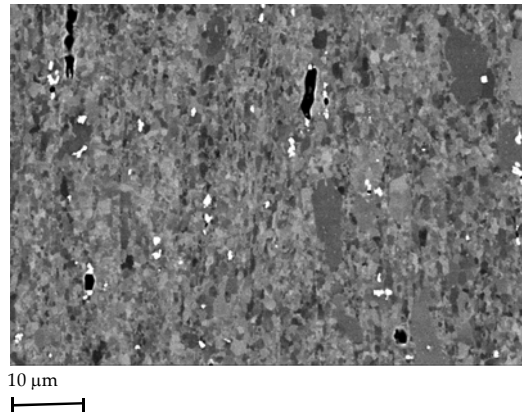


Figure B.II.17. Polished cross sections (colloidal silica) of creep tested (120 MPa and 650 hours) base metal aged 10000 hours at 625°C

Damage mechanisms are also the same than these encountered in the non aged base metal. Moreover, SEM investigations revealed how important, carbide coarsening and Laves phase precipitation during ageing are. The micrograph of **figure B.II.17** shows that large second phase particles (white dots in **figure B.II.17**) are privileged sites for cavity nucleation.

6. Conclusions: Design requirements for a model able to represent high temperature creep flow and damage mechanisms in 9Cr1Mo-NbV steels

From the synthesis of literature data and the experimental results of the present study an accurate model requires:

1. To represent several, at least two, creep deformation and damage mechanisms: one to represent the dislocation creep and the other the diffusion creep regime (see Kloc and Sklenicka (1997) and Kloc and Sklenicka (2004)).
2. To represent the material softening during creep as carbide coarsening and decrease in the initially high dislocation density both promote lath martensite recovery and the acceleration of creep strain rate of the tertiary creep regime.
3. To integrate the three classical stages of the creep damage development:
 - Nucleation which obviously depends on both the creep strain and the stress triaxiality ratio.
 - Cavity growth which proceeds under the coupled influence of the matrix deformation and the grain boundary diffusion
 - Coalescence which corresponds to a localisation of the creep deformation in the intervoid spacing once a critical porosity ratio is reached. A critical porosity $f_c = 0.1$ at the onset of cavity coalescence was experimentally determined.
4. The integration of experimental data given by creep tests on various kind of notched specimens geometry as the stress triaxiality ratio obviously plays a key role in the damage evolution.

All these elements will be taken into account in the **chapter B.III** where both the formulation and the identification of the corresponding model will be described.

References

- Beremin F. (1981). Cavity formation from inclusions in ductile fracture. *Metallurgical transactions*. **12A**. 723-731.
- Besson J. (2001). Eprouvettes axisymétriques entaillées. *Essais mécaniques et lois de comportement - Hermes - Paris*. 319-351 (in French).
- Eggeler G. (1989). The effect of long term creep on particle coarsening in tempered martensite ferritic steels. *Acta metallurgica*. **37(12)**. 3225-3234.
- Ennis P.J. (2002). Recent advances in creep resistant steels for power plant applications. *OMMI (Review on the internet)*. **1(1)**.
- Eshelby J. (1961). *Progress in solids mechanics*. Amsterdam North Holland.
- Hattestrand M., Andren H.O. (2001). Influence of strain on precipitation reactions during creep of an advanced 9% chromium steel. *Acta Materialia*, **49(12)**, 2123-2128.

- Huez J., Feaugas X., Helbat A., Guillot Y., Clavel M. (1998). Damage process in commercially pure alpha titanium without (Ti40) and with (Ti40-4) hydrides. *Metallurgical and materials transactions*. **29A**. 1615-1625.
- Jayet-Gendrot S. (1999). Uniaxial creep properties of P9 materials at 625°C (base metal and weld). *HIDA 1702/PMB/57*.
- Kadoya Y., Nishimura N., Dyson B.F. and McLean M. (1997). Origins of tertiary creep in high chromium steels. *Creep and Fracture of Engineering Materials and Structures*. Ed. J.C. Earthman and F.A. Mohamed. The Minerals, Metals and Materials Society, Warrendale, PA. 343-352.
- Kloc L., Sklenicka V. (2004). Confirmation of low stress creep regime in 9%Cr chromium steel by stress change experiments. *Materials science and engineering A*. To be published.
- Kloc L., Sklenicka V. (1997). Transition from power law to viscous creep behavior of P91 type heat treated steel. *Materials Science Engineering*. **A234-236**. 962-965.
- Nakashima H., Terada D., Yoshida F., Hayakawa H. and Abe H. (2001). EBSD analysis of modified 9Cr-1Mo of modified 9Cr-Mo martensitic steel. *ISIJ International*. **41**. Supplement S97-S100.
- Pesicka J., Kuzel R., Dronhofer A., Eggeler G. (2003). The evolution of dislocation density during heat treatment and creep of tempered martensite ferritic steels. *Acta Materialia*. **51**. 4847-4862.
- Piques R. (1989). Mécanique et mécanismes de l'amorçage et de la propagation de fissures en viscoplasticité dans un acier austénitique inoxydable. *PhD Thesis – Ecole Nationale Supérieure des Mines de Paris, Paris, France* (in French).
- Prunier V., Gampe U., Nikbin K., Shibli I.A. (1998). HIDA activity on P91 steel. *Creep and fatigue crack growth in high temperature plant*. HIDA Conference - CEA Saclay - France.
- Sawada K., Taneike M., Kimura K, Abe F. (2003). In situ observation of recovery of lath structure in 9% chromium creep resistant steel. *Materials Science and Technology*. **19(6)**. 739-742.
- Sawada K., Maruyama K., Komine R., Nagae Y. (1997). Microstructural changes during creep and life assessment of Mod.9Cr-1Mo steel. *Tetsu-to-Hagane (Journal of the Iron and Steel Institute of Japan)*. **83(7)**. 466-471.
- Senior B.A. (1989). The precipitation of Laves phase in 9Cr – 1Mo steels. *Materials Science and Engineering*. **A119**. L5-L9.
- Sklenicka V., Kucharova K., Svoboda M., Kloc L., Busik J., Kroupa A. (2003). Long term creep behaviour of 9-12%Cr power plant steels. *Materials Characterization*. **51**. 35-48.
- Stocker Ch., Spiradek K., Zeiler G. (2002). Microstructural features influencing the creep properties of 9-12%Cr steels focusing on Laves phase precipitation. *Materials for advanced power engineering – Proceedings of the 7th Liège conference*. **III(21)**. 1459-1469.
- Yoshida F., Terada D., Nakashima H., Abe H., Hayakawa H., Zaefferer S. (2001). Microstructure change during creep deformation of modified 9Cr-1Mo steel. *Advances in materials technology for fossil power plants edited by R. Viswanathan*. 143-151.

Chapter B.III. Modelling creep mechanical and damage behaviour of the P91 steel at 625°C

The present chapter was written as an article submitted to international journal of fracture in September 2004. It deals with experiments and modelling of creep flow and damage behaviour of 9Cr1Mo-NbV steels at 625°C. At the end of the present chapter, some improvements of the model formulation suggested during the ECF15 conference are investigated.

Creep failure model of a tempered martensitic stainless steel integrating multiple deformation and damage mechanisms

V. Gaffard, J. Besson, A.F. Gourgues-Lorenzon

*Ecole Nationale Supérieure des Mines de Paris (E.N.S.M.P.) - Centre des Matériaux
UMR CNRS 7633 BP 87, 91003 Evry Cedex France (corresponding author: jacques.besson@ensmp.fr)*

Abstract

A new model considering both deformation and damage evolution under multiple viscoplastic mechanisms is used to represent high temperature creep deformation and damage of a martensitic stainless steel in a wide range of load levels. First, an experimental database is built to characterise both creep flow and damage behaviour using tests on various kinds of specimens. The parameters of the model are fitted to the results and to literature data for long term creep exposure. An attempt is made to use the model to predict creep time to failure up to 10⁵ hours.

Keywords: *9Cr1Mo-NbV martensitic stainless steel – High temperature creep flow and damage – Creep time to failure – Finite Element Modelling*

1. Introduction

Tempered martensitic stainless steels of type 9Cr1Mo-NbV (P/T91) have been recently developed for the boiler and turbine of supercritical and ultra supercritical power plants. These steels exhibit very complex high temperature creep cavitation processes with coupled influences of creep strain, material softening (Tsuchiyama et al (2001)) and ageing (e.g. Klueh and Harries (2001)). Moreover, despite a high level of ductility, premature failure is observed for long term creep exposures (e.g. Kimura et al (2000)) and might be related to a change in creep flow and damage mechanisms.

As for many materials, in 9Cr1Mo-NbV steels several creep flow regimes can be distinguished (e.g. Frost and Ashby (1982)) as a function of stress and temperature, from high stress deformation controlled by cross-slip or dislocation climb to low stress deformation controlled by grain boundary diffusion. These creep flow regimes may also be involved in various creep damage mechanisms. Therefore, describing creep flow and damage behaviour in a wide range of stresses implies to take various flow and damage mechanisms into account.

Up to now, several attempts have been made to take coupling between several creep flow and damage mechanisms into account. Lemaitre (1985) and Hayhurst (1995) developed models coupling a single deformation process with damage mechanisms in the framework of the continuum damage mechanics introduced by Kachanov (1958) and Rabotnov (1969). Bellenger and Bussy (2001) designed a viscoplastic model where tertiary creep is described using a scalar damage variable, whose evolution law depends on the fracture mode (intergranular or ductile). Needleman and Rice (1980), Tvergaard (1984a), Onck and Van der Giessen (1997) and Michel (2004) incorporated coupled influences of grain boundary diffusion and power-law creep into cavity growth rate description based on works by Hull-Rimmer (1959) and Rice and Tracey (1976). In the case of martensitic stainless steels, Weinert (2002) designed a microstructurally based creep model where creep flow takes into account microstructural changes such as dislocation recovery, and subgrain nucleation and growth. This evolution is coupled with a contribution of intragranular damage in the framework of the continuum damage mechanics. The ability of this model to represent creep flow and damage behaviour from high to low stress is, however, not established.

To the authors' knowledge, no attempt has been made to simultaneously take into account coupled influences of several viscoplastic flow and of several damage mechanisms in a single model.

This study aims at building and testing such a model in the case of a typical P91 martensitic stainless steel, for which interactions between dislocation creep and diffusion creep, as well as extensive creep cavitation and softening have been evidenced for experimentally reachable lifetimes. In this study, the model is developed in the framework of the continuum mechanics of porous media allowing coupling interactions between various damage and deformation mechanisms from low to high stress levels.

2. Material and experimental procedures

2.1. Material

The chemical composition of the steel used in this study is shown in **table B.III.1**. The material was supplied as a pipe of 295 mm in outer diameter and 55 mm in thickness. This pipe was austenitized at 1065°C for one hour, cooled and then tempered at 765°C for two hours. The resulting microstructure (**figure B.III.1**) is lath martensite arranged in packets (30 - 40 μm in size) within prior austenite grains (100 μm in mean size). TEM investigations showed a high dislocation density and the precipitation of many carbides of mainly M₂₃C₆ type, where M = Cr (size up to 100 nm), located at grain and packet boundaries, and finer MX precipitates (10 - 20 nm in size), where M = V or Nb and X = C or N, distributed both within laths and at lath boundaries.

C	Si	Mn	P	S	Al	Cr	Ni	Mo	V	Nb	N
0.09	0.31	0.41	0.014	0.005	0.016	8.56	0.26	0.92	0.21	0.065	0.042

Table B.III.1. Chemical composition of the steel studied in wt %

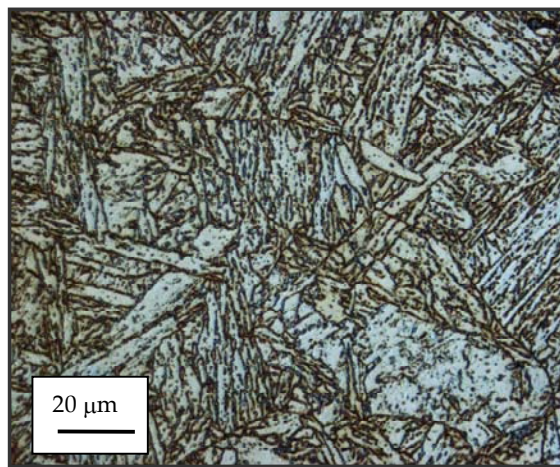


Figure B.III.1. Light optical micrograph of the P91 steel (Villela etching)

All specimens were cut along the longitudinal axis of the pipe. All experiments were carried out at 625°C (898 K).

2.2 Tensile tests

Tensile tests on smooth bars with a gauge length of 19 mm and a diameter of 3 mm were performed to accurately describe the loading and primary creep stages at high stress levels and the final rupture stage of all creep experiments. Tests were performed at initial strain rates ranging from 10⁻³ s⁻¹ to 10⁻² s⁻¹, representative of the specimen strain rate during the loading and final tertiary stages in the creep tests. Some other tests were also performed at lower strain rates (10⁻⁴ and 10⁻⁵ s⁻¹) to investigate the strain rate sensitivity of the material.

2.3. Creep tests (625°C)

Creep tests were performed on four types of axisymmetric specimens: smooth round tensile bars (SC) with a gauge length of 36 mm and a gauge diameter of 5 mm, which are part of the HIDA project (Prunier et al (1998) and Jayet-Gendrot (1999)); round U-notched bars (NC1.2 and NC4.0), which have a maximum diameter of 13 mm, a minimum diameter of 6 mm and a notch radius of 1.2 and 4.0 mm respectively, and round V-notched bars (NC0.25), which have a maximum diameter of 23 mm, a minimum diameter of 14 mm and a 45° V-notch with a radius of 0.25 mm. Elongation of NC0.25, 1.2 and 4.0 specimens was measured between points located on both sides of the notched area with gauge lengths of respectively 10, 20 and 20 mm.

Creep tests on SC specimens were carried out to determine material creep flow properties in uniaxial loading conditions. In addition, damage nucleation and growth are largely influenced by the stress state, in particular by the stress triaxiality ratio, τ , which is locally defined as the ratio $\frac{1}{3} \frac{\sigma_m}{\sigma_{eq}}$ where σ_m is the local hydrostatic stress and σ_{eq} is the local equivalent von Mises stress. Therefore, creep notched NC0.25 (which allowed for stable crack propagation), NC1.2, and NC4.0

specimens were used to investigate the effect of the stress triaxiality ratio as they allow to set it to various desired values in the minimum cross section of the specimens. The maximum values of τ , in the area of minimum section, at the end of the loading stage, were respectively 1.1, 1.3 and 1.8. These types of creep specimen geometry were introduced by Hayhurst et al (1977a) who studied the effect of various notched bar geometry on stress and strain fields. Moreover, NC1.2 and NC4.0 specimens were machined with respectively three and two widely separated notches along the gauge area, in order to investigate damage mechanisms. This allowed metallographic study of longitudinal cross sections of non-broken notches, which were assumed to be representative of the damage state at the onset of the tertiary stage (Piques (1989)).

Tensile creep tests were carried out at 625°C under constant applied load in controlled laboratory atmosphere (20°C ± 2°C and 50% relative humidity). The load was applied using dead weights for SC specimens and using an electrical mechanical testing machine for NC specimens. The temperature was monitored using three thermocouples spot welded onto the specimen surface. The temperature gradient between top and bottom ends of the specimen did not exceed 2°C. The elongation measured using linear variable differential transducers was continuously recorded with a sensitivity of 1 µm.

3. Experimental results

3.1. Tensile properties

At temperatures higher than 500°C, deformation of 9Cr-1MoNbV steel is rate sensitive due to metallurgical changes and viscosity effects (Yaguchi and Takahashi, (2000)). For the values of strain rate experimentally investigated, a significant strain rate effect could be observed between 10^{-5} s^{-1} and 10^{-3} s^{-1} (The tensile strength was more than 140 MPa lower at 10^{-5} s^{-1} than at 10^{-3} s^{-1}) but tensile properties were nearly the same for strain rates ranging from 10^{-3} to 10^{-2} s^{-1} (see **table B.III.2**). In this range, the following mean properties at 625°C were deduced: 0.2% proof stress = 340 MPa, and tensile strength = 360 MPa. Tensile curves exhibited a very little homogeneous elongation before the onset of necking ($\approx 1\%$), as the initial high dislocation density and the small grain size (lath width) lead to a rapid saturation of the dislocation density followed by dislocation cross-slip and climb (Guetaz et al (2003)). Tensile tests performed at 450°C and 550°C show that the recovery process is all the more facilitated as the test temperature is high (Elongation before the onset of necking are respectively of 2% to 3% at 550°C and 4% to 5% at 450°C – see **table B.III.3**).

Temperature	Strain rate	0.2% proof stress	Uniform elongation	R _m
625°C	$5 \cdot 10^{-2} \text{ s}^{-1}$	360 MPa	2.5 %	380 MPa
625°C	10^{-2} s^{-1}	345 MPa	0.9 %	360 MPa
625°C	10^{-3} s^{-1}	320 MPa	0.8 %	350 MPa
625°C	10^{-4} s^{-1}	245 MPa	0.7 %	250 MPa
625°C	10^{-5} s^{-1}	190 MPa	1.1 %	210 MPa

Table B.III.2. Tensile properties at 625°C : Effect of the strain rate

Temperature	Strain rate	0.2% proof stress	Uniform elongation	R _m
625°C	10^{-3} s^{-1}	320 MPa	0.8 %	350 MPa
550°C	10^{-3} s^{-1}	390 MPa	2.6 %	435 MPa
450°C	10^{-3} s^{-1}	450 MPa	4.9 %	550 MPa

Table B.III.3. Comparison of tensile properties at 450, 550 and 625°C

The material ductility is very high so that final longitudinal elongation exceeds 15 %. Final reduction of area of specimens was up to 70% and from metallographic investigations, one could observe that recovery took place during tensile tests as the initial lath structure was replaced by small equiaxed grains. No significant volume damage could be detected except very close to the fracture surface. The microstructural changes during tensile tests indicate that strain softening effects have to be taken into account in the model for this range of strain rates.

3.2. Creep flow properties

For SC specimens, the initial values of the applied engineering stresses (load divided by the initial area of the minimum section) range from 90 MPa to 120 MPa and corresponding times to failure range from 800 hours to 7,000 hours (**figure B.III.2**). Creep flow curves of P91 steels exhibited very short primary and short secondary creep stages. Tertiary creep was found to be the main part of the creep time at least for the highest stress levels (> 100MPa, see **figure B.III.2**).

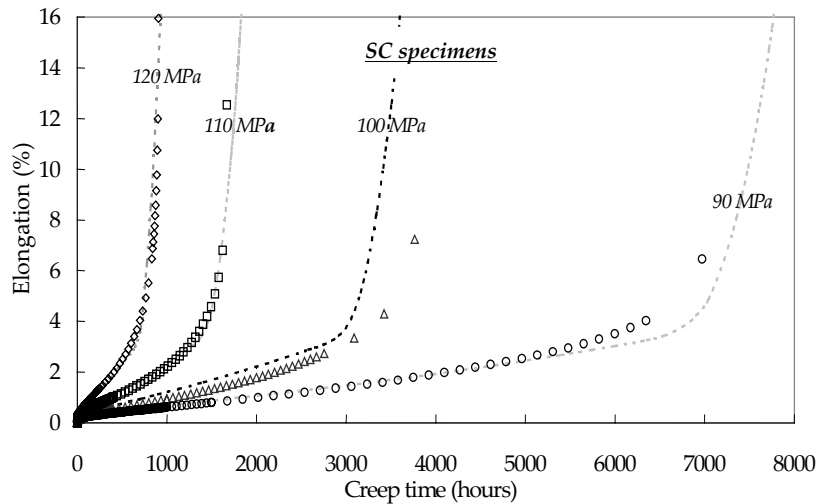


Figure B.III.2. Comparisons of experimental (symbols) and calculated (lines) creep curves for creep tests on SC specimens

In order to investigate the secondary stage creep behaviour, a test with load levels varying with steps (60 – 80 – 100 – 120 MPa) was performed on a smooth round tensile bar. Increasing, then decreasing load levels allowed to check for the absence of any history effect and of significant damage in these specimens, so that only the mechanical behaviour was considered, at least up to the onset of the tertiary stage.

Steady state creep strain rate versus stress was compared for SC specimens with a standard Norton law with no threshold stress:

$$\dot{\epsilon}_{ss} = B\sigma^n \quad (\text{eq. B.III.1})$$

where B and n are model parameters. The curves obtained with both single load and multiple load levels tests are similar (see figure B.III.3). Power-law coefficient n was fitted to these data leading to a value of 8.0. To describe creep flow in the low stress regime, data from Kloc and Sklenicka (1997) who carried out creep tests on helicoidal spring specimens machined in another type of P91 steel (having nearly the same chemical composition and normalising treatment of 1h at 1060°C followed by a tempering of 2 hours at 750°C) were then added to the database. One can note that creep strain rates at high stresses from Kloc and Sklenicka (1997) well agree with the results of the present study. Results of figure B.III.3 suggest that at high stresses, the deformation mechanism is dominated by dislocation cross-slip or climb, while for stresses below 70 MPa it is dominated by grain boundary diffusion. In the following, the “high stress creep regime” will refer to stresses higher than 70MPa and the “low stress” creep regime to stresses lower than 70 MPa.

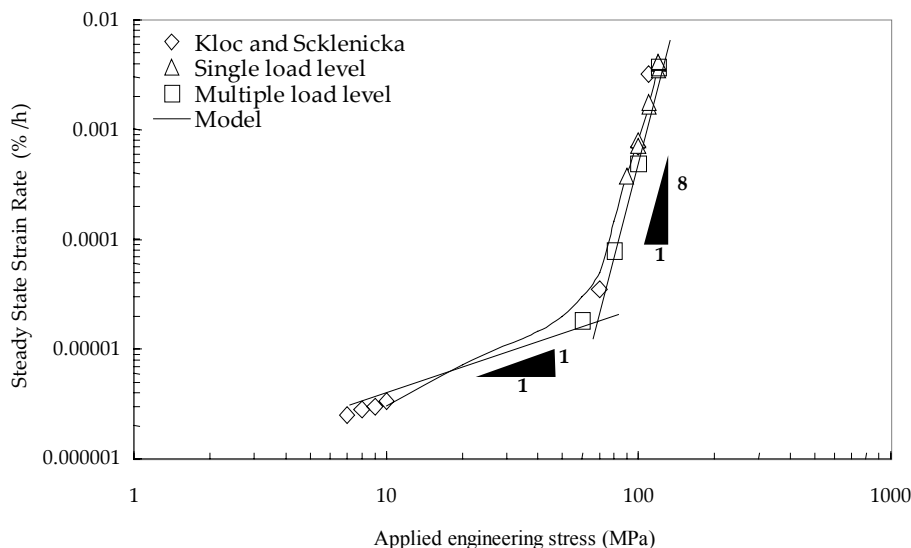


Figure B.III.3. Steady state strain rate versus stress at 625°C: Experimental results with SC specimens and literature results

Creep tests carried out on NC0.25, NC1.2 and NC4.0 specimens and resulting lifetimes are listed in table B.III.4. Creep curves for NC1.2 and NC0.25 specimens are shown respectively in figure B.III.4 and figure B.III.5. In contrast to SC specimens, secondary creep dominates in the lifetime for all tests, as the strain softening effect is constrained in the notch. Moreover, a significant notch strengthening effect, also observed by Wasmer et al (2002), is evidenced by comparing both secondary creep rate and lifetime with those of SC specimens.

Geometry	Number of specimens	Range of nominal applied stress	Creep times to failure
NC4.0	5	100 MPa – 175 MPa	100 hours – 8,000 hours
NC1.2	8	150 MPa – 218 MPa	200 hours– 3,000 hours
NC0.25	4	160 MPa - 250 MPa	30 hours – 1,400 hours

Table B.III.4. Characteristics of creep tests on NC specimens

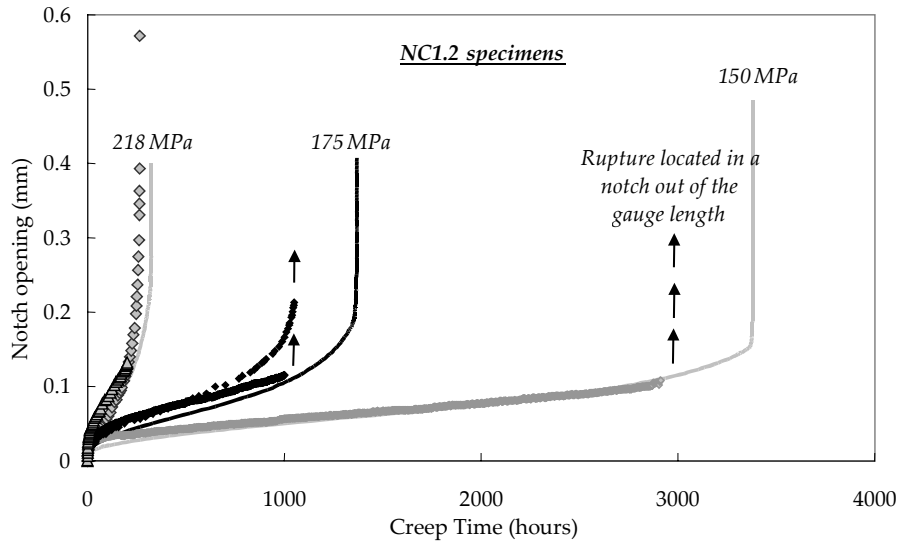


Figure B.III.4. Experimental (symbols) and calculated (lines) creep curves for creep tests on NC1.2 specimens

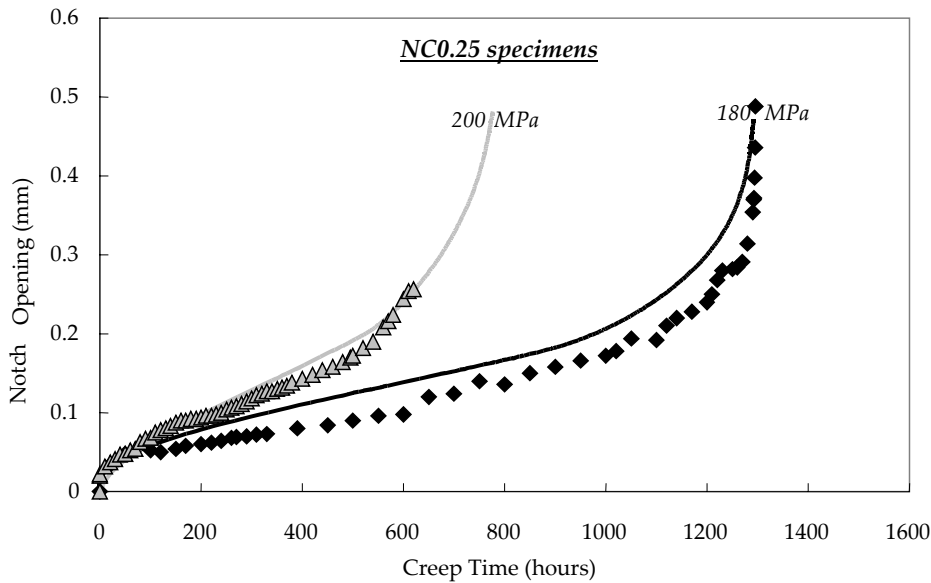


Figure B.III.5. Experimental (symbols) and calculated (lines) creep curves for creep tests on NC0.25 specimens

3.3. Creep fracture properties

The Monkman-Grant (MG) (1956) relationship states that the time to rupture of creeping materials depends on the steady state strain rate:

$$\dot{\epsilon}_s^m t_R = C_{MG} \quad (\text{eq. B.III.2})$$

where $\dot{\epsilon}_s$ is the steady state strain rate and t_R the time to rupture. In the investigated range of stresses, a unique relationship was fitted with $m = 0.94$ and $C_{MG} = 5.8 \cdot 10^{-2} \text{ h}^{0.06}$ (with $\dot{\epsilon}_s$ in h^{-1} and t_R in h). However, extrapolation using this formula might be hazardous because the MG constant, C_{MG} , depends on the creep regime and does not take into account a possible loss of ductility. This point will be more clearly explored in the following in section 4.5.

Larson-Miller (LM) (1952) also introduced a predictive parameter:

$$P_{LM} = \left[20 + \log(t_R) \right] \frac{T(K)}{1000} = f(\sigma) \quad (\text{eq. B.III.3})$$

P_{LM} stress dependence was evaluated as $P_{LM} = -0.028\sigma + 24$ from experimental results on SC specimens (i.e. in the high stress creep regime) where σ is in MPa, t_R is in hours and T is in Kelvin. In **figure B.III.6**, experimental results are well reproduced using this well known LM parameter. However, long term creep data at 650°C from Kimura et al (2000) and at 600°C from Eggeler et al (1989b), who carried out creep tests longer than 30,000 hours, show a change in the damage mechanism for longer failure times leading to premature failure in comparison with LM predictions, as shown in **figure B.III.6**.

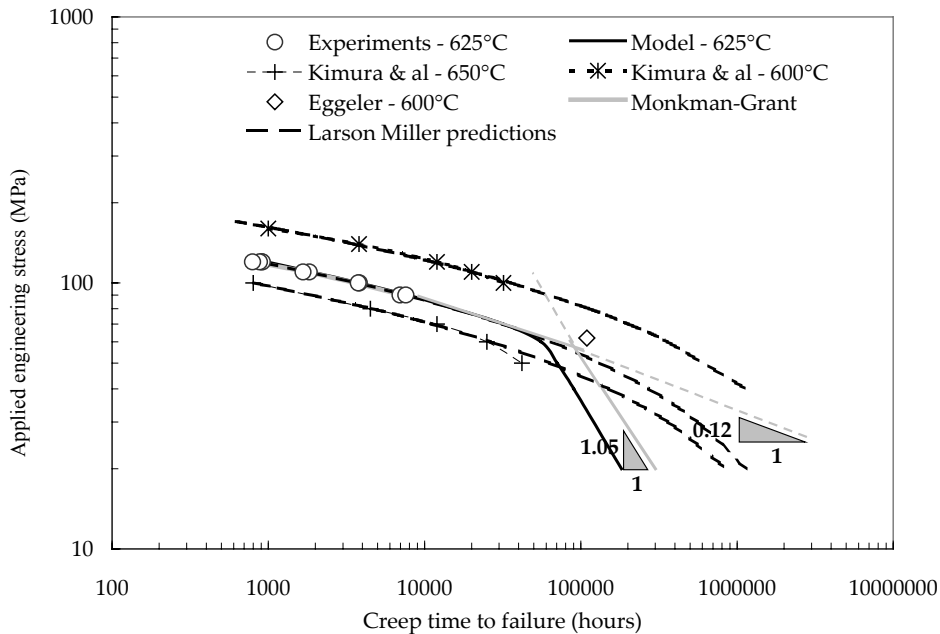


Figure B.III.6. Stress versus time to failure for SC specimens

The same plot for experimental results on SC and all NC specimens allows to investigate the effect of the notch on the material creep strength (see **figure B.III.7**). The creep behaviour of notched bars has been widely studied by Hayhurst et al (1977b). The effect of the notch on the stress and strain state is as follows (Besson (2001a), Al-Faddagh et al (1982)). Due to the notch geometry, the mean stress triaxiality ratio is increased, so that for the same average equivalent strain rate (i.e. the same average von Mises equivalent stress), the notched specimen can sustain a higher load. Stress and strain redistribution also occur. Stress and strain are maximum at the notch root after the initial loading stage, which is mainly elastic. As deformation proceeds, the location of the stress maximum shifts towards the centre of the notched area. This redistribution process is affected both by the specimen geometry and material constitutive equations. However, increasing the stress triaxiality ratio also leads to higher damage kinetics, so that the strengthening effect may be lost for low ductility materials (Yue et al (2002) and Othman et al (1994)) or for very severe notches.

Results of **figure B.III.7** show that, for the investigated P91 steel, the notch has a strengthening effect from notch radii ranging from 4.0 mm to 1.2 mm because this material has a high ductility level. Same conclusions are given by Eggeler (1992). On the other hand, there is no difference in the lifetime between NC1.2 and NC0.25 specimens, although the maximum stress triaxiality ratio is much higher in the later specimen. This indicates a loss in ductility for values of τ higher than about 1.8. This notch weakening effect has already been observed by Eggeler (1992), especially at low stresses.

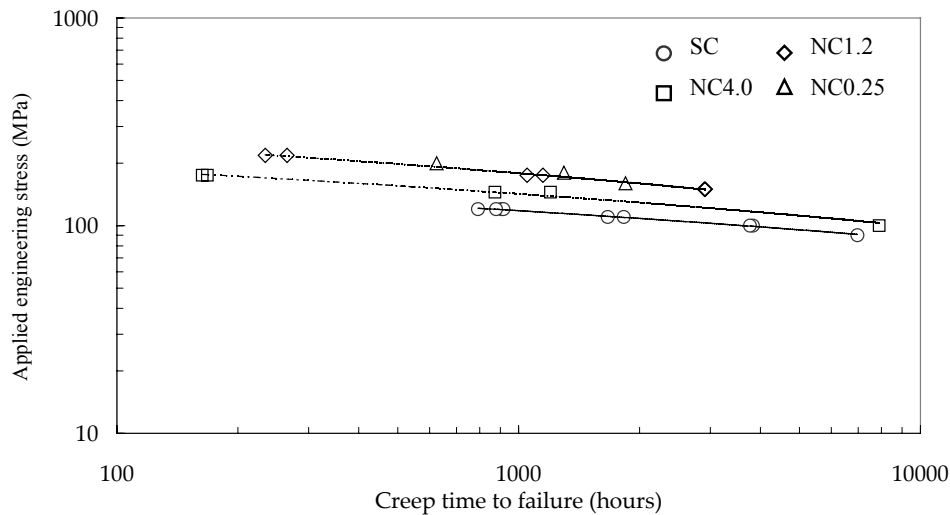


Figure B.III.7. Stress versus time to failure: Experimental results on SC and NC specimens

3.4. Ageing and softening effects

Metallurgical changes of the initial lath martensite microstructure occur under creep conditions. They are partly dominated by the effect of creep strain but time dependent phenomena also play a role as pointed out by Kadoya et al (1997). Two main evolutions of the initial precipitation state were experimentally observed: coarsening of carbides (mainly $M_{23}C_6$) and precipitation of Laves phase. The precipitation of a Z-phase, which is a complex carbide nitride is also reported by Suzuki et al (2003) and Kimura et al (2002) for longer tests durations (longer than 30,000 hours at 625°C). Carbide coarsening and precipitation of the Z-phase might be related to lath recovery as they lead to a decrease in the dislocation pinning effect of carbides and MX particles (Iwanaga et al (1998)). The process of lath martensite recovery is usually described as subgrain nucleation and growth, where the kinetics of subgrain growth which can be well represented by $\dot{d} = A\sigma^{-p}$, where d is the subgrain size and σ the principal stress (Orlova et al (1998) and Polcik et al (1999)). In addition, Laves phase precipitation induces a loss of solid solution strengthening effect of molybdenum and affects the material creep strength (Stocker et al (2002) and Senior (1989)).

Metallurgical changes were investigated here both during furnace thermal ageing and in creep ageing conditions at 625°C. Average precipitate size measurements were carried out for stress free and creep aged material (out of the necking zone of all SC specimens, i.e from 90 MPa to 120 MPa) at 625°C. Carbon extraction replicas were examined by scanning electron microscopy (SEM) using a field emission gun SEM and the distribution of particle size was quantitatively evaluated using image analysis. Carbide coarsening is accelerated under applied load, which is consistent with Hattestrand and Andren (2001), Nakajima et al (2003), Cerri et al (1998), Eggeler (1989) and Engberg et al (1984). For long term ageing (more than 10,000 hours), stress no longer influences the coarsening kinetics and the final average size of the carbides is about 250 nm both with and without applied stress. Moreover, X-Ray diffraction analysis of replicas confirmed that the precipitation of Laves phase particles had occurred during ageing.

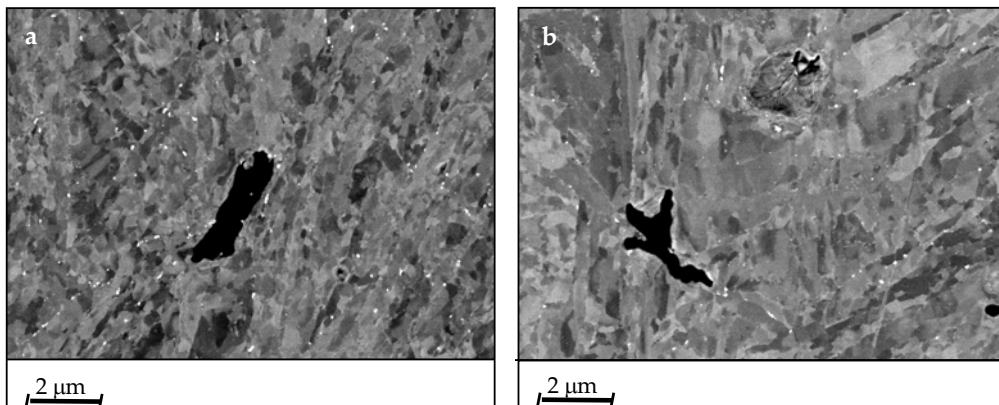


Figure B.III.8. Extensive recovery of martensite for creep test at 175MPa (900 hours) on NC1.2 specimen occurs near the notch (a) but not in the bulk (b), Colloidal silica polishing – SEM (BSE) observations on longitudinal cross-sections of crept specimens. White dots indicate Laves phase precipitates

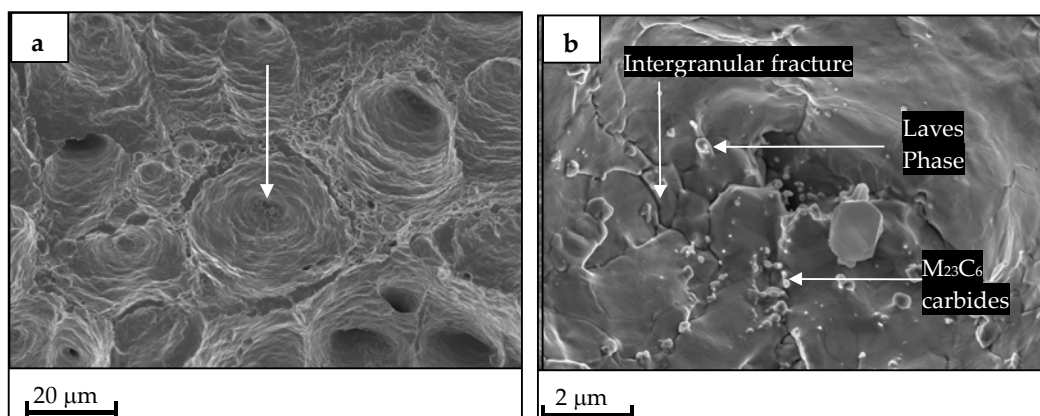
To investigate the microstructural evolution of the martensite matrix, longitudinal cross-sections of all specimens were polished using colloidal silica and were examined with backscattered electron (BSE) channelling contrast in the SEM. Recovery of the martensite phase was observed in the necking area for SC specimens and near the notch in short term creep tests on NC1.2 specimens (**figure B.III.8**), indicating that softening effects are strain controlled but also require a high stress level. Long term creep exposure also led to lath recovery, since SEM investigations on NC1.2 specimens show that lath recovery occurred both near the notch and at the centre of specimens for long time tests ($\approx 3,000$ hours). Lath recovery, which starts locally during the tempering treatment (see Sawada (2003)) was frequently observed after thermal ageing up to 10,000 hours by TEM investigations, which confirms that the softening process may be time controlled at lower stresses.

All metallurgical changes previously described are of great importance in martensitic stainless steels because they strongly affect creep properties, leading to a loss in creep strength (Sklenicka et al (2003)). Vilhensen (1996), Brinkman et al (1993) and Brachet (1991) also show that prior thermal ageing leads to a strong decrease in the material tensile and creep strength, which give arguments about the importance of ageing effects on creep flow and failure properties. Therefore, these effects will be taken into account in the constitutive equations of the model (see **section 5.1**).

3.5. Damage evolution and fracture mode

All fracture surfaces of creep specimens were investigated with SEM. All specimens, tested in laboratory air, exhibited a ductile fracture surface with dimples of $20\ \mu\text{m}$ in size. Fracture surfaces could not be observed at a finer scale because of extensive oxidation phenomena. However, by considering the complex microstructure of the steel investigated, the fracture mode had to be examined at the scale of the lath size. To do this, three additional creep tests were carried out on flat, double edge notched specimens at 625°C under high vacuum (10^{-3} Pa) in order to obtain a fracture surface free from oxidation. The applied stress was set from 120 MPa to 170 MPa and the fracture times ranged from 10 hours to 1,800 hours.

The fracture mode was also ductile with a dimple size of about $20 - 30\ \mu\text{m}$ (**figure B.III.9a**). However, when looking closer inside dimples, intergranular fracture at subgrain boundaries (size of 2 to $5\ \mu\text{m}$, resulting from lath recovery), was detected (see **figure B.III.9b**). The fracture mode of the steel could then be called “intergranular then ductile”, as fracture starts from intergranular cavitation at grain and subgrain boundaries and then develops by growth and coalescence of cavities in a ductile manner. The concept of “constrained cavity growth” introduced by Dyson (1976) is often applied to tempered martensitic stainless steels (Eggeler (1989)) but the present study obviously demonstrates that in the investigated experimental conditions, cavity growth is rather assisted than hindered by matrix viscoplasticity.



*Figure B.III.9. Fracture surface of a creep specimen tested under vacuum (120MPa – 1,800 hours)
- SEM observations (a) .General view (b). closer view into the dimple (arrow in (a))*

Damage mechanisms were also investigated by SEM on longitudinal cross sections in the area of minimum diameter. Even in the absence of recovery, creep cavities frequently nucleate at grain boundaries due to stress concentrations at second phase particles (mainly M_{23}C_6 carbides and Laves phases) or triple junctions (arrow in **figure B.III.10b**). Note that all boundary types (i.e. between laths, packets and prior austenite grains) are concerned. Cavities in **figure B.III.10b** seem to be of the “wedge crack” type but when looking at them closely, they appear to form by coarsening of several small round voids as underlined by Kassner and Hayes (2003). It can then be stated that nucleation of micrometer-sized cavities is the main damaging mechanism and that cavity growth does not dominate. This mechanism can also be related to the early coarsening of small cavities, which have nucleated at interlath boundaries, that is also often observed (**figure B.III.10a**).

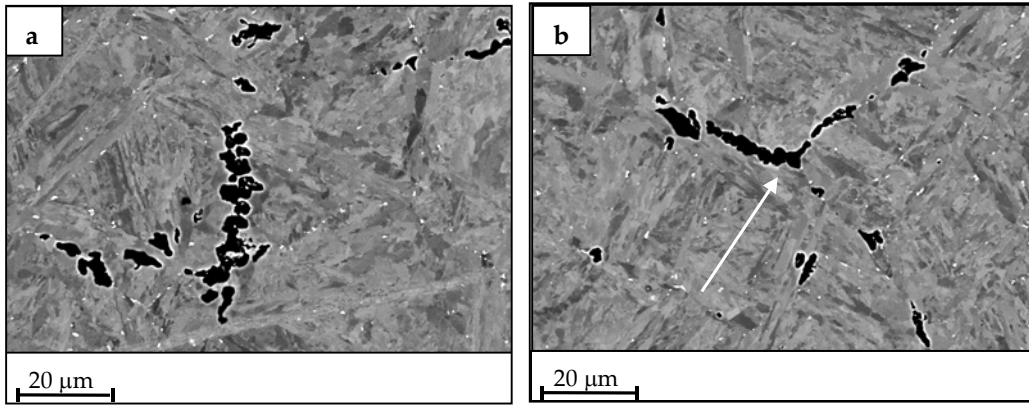


Figure B.III.10. Cavity growth and coalescence at boundaries (NC1.2 – 150 MPa – 3,000 hours) Longitudinal cross sections, SEM-BSE observations after colloidal silica polishing

To get quantitative data on damage location, image analysis was carried out on cross-sections of both fractured smooth specimens and notched specimens in the non fractured notch. Detailed maps of the damaged area were taken with a SEM in the BSE electron imaging mode with a magnification of 400. The minimum cavity size that could be observed with this method was about 1 μm . The area fraction of cavities was calculated and cavity morphology was also analysed. To use these data in the model presented in the next section, elongated cavities were converted into spheres having the same diameter as the maximum cavity length, according to the procedure commonly used for ductile fracture modelling (Besson et al (2000) and Pardoen et al (1998)).

The area fraction of cavities was also measured on several NC specimens and especially in the non fractured notch of NC1.2 specimens. The representation of **figure B.III.11** was deduced from these measurements. It gives the location of the rupture area as a ratio x/R (where x is the distance between the specimen axis and the area where failure initiates and R the minimum radius of the specimen in the deformed state) versus the creep time to failure for all specimens. In the less severely notched specimens, extensive stress redistribution induces damage near the specimen axis. On the other hand, in the NC0.25 specimens, damage occurs near the notch root due to the high severity of the notch.

Finally, microfractographic cross-sections analysis on SC specimens revealed that cavitation mainly occurred in the neck area and the area fraction of cavities was found to be less than 0.3 % out of the neck area. This strongly suggests that necking is triggered by plastic softening, and not by damage.

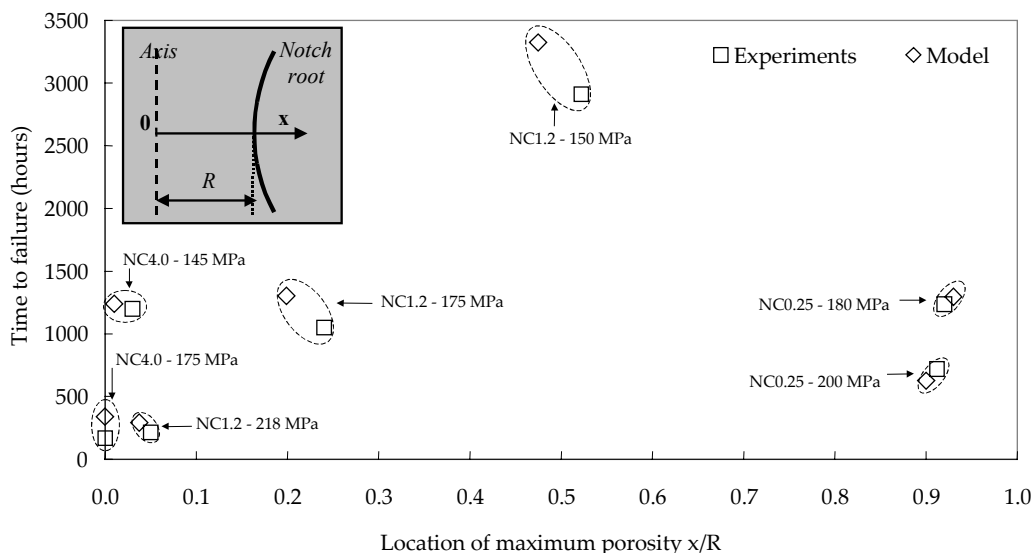


Figure B.III.11. Location of the most damaged area at the onset of the rupture for NC1.2 and NC0.25 specimens. Comparison between model predictions and experimental observations

4. Modelling creep flow and damage up to failure

4.1. Model for the undamaged material

Contesti and Cailletaud (1989) have already introduced a double inelastic deformation model after the first attempt of Pugh (1978). In the present study, three viscoplastic deformation mechanisms are considered following classical descriptions of creep flow mechanisms. The first one accounts for loading and final rupture stages (quasi plastic flow regime (i.e rate dependent plasticity - subscript "qp"). The second one accounts for power law creep (viscoplastic creep regime – subscript "vp"). The third one accounts for the low stress grain boundary diffusion creep (diffusional creep regime – subscript "d").

An additive decomposition of the contribution of each mechanism is assumed. The strain rate tensor, $\dot{\underline{\varepsilon}}$, can be expressed as:

$$\dot{\underline{\varepsilon}} = \dot{\underline{\varepsilon}}_e + \dot{\underline{\varepsilon}}_{qp} + \dot{\underline{\varepsilon}}_{vp} + \dot{\underline{\varepsilon}}_d \quad (\text{eq. B.III.4})$$

where $\dot{\underline{\varepsilon}}_e$ is the elastic strain rate tensor. The elastic strain tensor is related to the stress tensor by Hooke's law: $\underline{\sigma} = \underline{\underline{C}} : \underline{\varepsilon}_e$ where $\underline{\underline{C}}$ is the fourth order stiffness tensor. For each mechanism (m = qp, vp or d) a yield surface, ϕ_m , is defined as:

$$\phi_m = \sigma_m^* - R_m \quad (\text{eq. B.III.5})$$

R_m is the flow stress. It depends on the flow mechanism. σ_m^* is a scalar effective stress, which corresponds to the von Mises equivalent stress in the case of the damage free material. Non elastic deformation occurs by 'm' mechanism when $\phi_m > 0$. The corresponding strain rate tensor is given by the normality rule as follows:

$$\dot{\underline{\varepsilon}}_m = \dot{p}_m \frac{\partial \phi_m}{\partial \underline{\sigma}} \quad (\text{eq. B.III.6})$$

The plastic multiplier, \dot{p}_m , is assumed to be given by a Norton power-law:

$$\dot{p}_m = \left\langle \frac{\phi_m}{K_m} \right\rangle^{n_m} \quad (\text{eq. B.III.7})$$

The cumulated viscoplastic strain is defined as the time integral of $\dot{p}_m : p_m(t) = \int_0^t \dot{p}_m dt$

The flow stress, R_m , is expressed as a function of an effective viscoplastic strain, \bar{p}_m , which accounts for cross hardening between the various deformation regimes:

$$\bar{p}_m = \sum_{m'} H_{mm'}^p p_{m'} \quad (\text{eq. B.III.8})$$

where $H_{mm'}^p$ are the cross-hardening coefficients.

4.2. Model for the damaged material

The previous model was extended to incorporate damage following the procedure detailed in (Besson and Guillemer-Neel (2003) and Besson et al (2001b)). A new definition of the effective stress, σ_m^* , must be used. It depends on damage, which is represented by the void volume fraction, f . In the following, the same definition is used for σ_m^* for all deformation mechanisms for the sake of simplicity. It is defined using the Gurson-Tvergaard-Needleman (GTN) model (1984b) extended to strain rate dependent materials (Needleman and Tvergaard (1991)) as:

$$\frac{\sigma_{eq}^2}{\sigma_m^{*2}} + 2q_1 f^* \cosh\left(\frac{q_2}{2} \frac{\sigma_{kk}}{\sigma_m^*}\right) - 1 - q_1^2 f^{*2} = 0 \quad (\text{eq. B.III.9})$$

where σ_{eq} is the von Mises equivalent stress and σ_{kk} is the trace of the stress tensor. q_1 and q_2 are model coefficients which are assumed to be constant. f^* is a function of porosity, which is designed to account for the coalescence of cavities at the onset of the creep failure following the pioneering work of Tvergaard (1989) (see section 4.4. for details). The definition of σ_m^* is implicit and equation (6) must be solved numerically to obtain its value. Using this definition of σ_m^* , equations (2), (4) and (5) remain unchanged. The strain rate tensor is expressed as:

$$\dot{\underline{\varepsilon}}_m = (1 - f_t) \dot{p}_m \frac{\partial \phi_m}{\partial \underline{\sigma}} \quad (\text{eq. B.III.10})$$

where f_t is the total porosity so that,

$$\dot{\underline{\epsilon}}_m : \underline{\sigma} = (1 - f_t) \dot{p}_m \underline{\sigma}_m^* \quad (\text{eq. B.III.11})$$

which expresses the fact that the macroscopic plastic work (left handside) is equal to the microscopic plastic work (right handside). The evolution of porosity is obtained by expressing the mass conservation modified to account for the nucleation of new voids so that:

$$\dot{f}_m = (1 - f_t) \sum_m \text{trace}(\dot{\underline{\epsilon}}_m) + \dot{f}_n = (1 - f_t)^2 \sum_m \dot{p}_m \text{trace} \left(\frac{\partial \phi_m}{\partial \underline{\sigma}} \right) + \dot{f}_n \quad (\text{eq. B.III.12})$$

where \dot{f}_n is the void nucleation rate. It is assumed that each mechanism can contribute to nucleation. Consequently, \dot{f}_n is expressed as a sum of individual contributions: $\dot{f}_n = \sum_m \dot{f}_{nm}$.

Dependencies of creep cavity nucleation on stress and strain are not well understood yet. Dyson (1983) and Hayhurst et al (1983) developed models of strain rate dependent continuous cavity nucleation. Many measurements were performed by Wu and Sandstrom (1995) for a 12%Cr steel and led to the conclusion that the nucleation kinetics is controlled only by strain. They confirmed this result in Wu and Sandstrom (1996) where a review of more than ten other works concerning 2%Cr and 12%Cr steels is added and supports their conclusions (see also Eggeler et al (1989b)). However, creep cavity measurements were only carried out on smooth creep specimens, for which the stress state is uniaxial and uniform. Other authors like Myers et al (1987), who performed cavity measurements on both smooth and notched specimens (i.e. multiaxial strain state), and McLean (1981), concluded in favour of a stress dependence of the cavity nucleation. Experimental results, and especially the location of rupture in NC specimens (see **figure B.III.11**), also showed that nucleation depends on the stress state.

In the following, each contribution to the overall nucleation kinetics will be expressed as:

$$\dot{f}_{nm} = \left(A_m + B_m \left(\frac{1}{3} \frac{\sigma_m}{\sigma_{eq}} \right)^{\alpha_m} \right) \dot{p}_m \quad (\text{eq. B.III.13})$$

A_m , B_m and α_m are adjustable parameters. Nucleation is therefore strain controlled; however, the nucleation rate also depends on the stress triaxiality ratio. This expression differs from the stress controlled nucleation law developed in Chu and Needleman (1980) or Herding and Kuhn (1996)).

In the model, a coupling is assumed between the contributions to damage resulting from each of the three mechanisms. It allows a cavity, which has nucleated by a given mechanism, to grow under the effect of any other mechanism. This description of cavity growth is consistent with the work of Tvergaard (1984a) and Michel (2004).

In terms of damage evolution the model outputs are, for each mechanism, the porosity due to nucleation: f_{nqp} , f_{nvp} and f_{nd} , and the porosity due to growth: f_{gqp} , f_{gvp} and f_{gd} . The total porosity is given by the summation of these six quantities.

4.3. Numerical procedures

The model was implemented in the finite element software Zébulon (Besson and Foerch (1997)). A fully implicit integration scheme was used to integrate the material constitutive equations, which allows the calculation of the consistent tangent matrix (Simo and Taylor (1985)). The method is derived from the one detailed in Besson et al (2001b), modified to deal with an arbitrary number of deformation mechanisms. Finite strains were treated using co-rotational reference frames (Besson et al (2001c)). The material was considered to be broken when f^* was greater than $\frac{1}{q_1} - \epsilon$,

where $\frac{1}{q_1}$ is the theoretical value for f^* at fracture and ϵ is taken equal to 0.01. As soon as the material was considered as

broken, its behaviour was replaced by an elastic behaviour with a very low stiffness (Young's modulus: $E_b = 1$ MPa). A similar technique was used in Liu et al (1994) showing convergence of the results for sufficiently low values of the Young's modulus E_b . Gauss points where these conditions are met are referred to as "broken Gauss points". In regions where damage develops, eight-node axisymmetric elements with reduced integration (ie. 4 Gauss points) were used. Elements containing two broken Gauss points were automatically removed by checking this condition after each time increment.

A two dimensional axisymmetrical mesh was chosen. The mesh size and mesh design play an important role in calculations involving crack initiation and propagation (Rousselier (1987); Tvergaard and Needleman (1984b); Xia and al. (1995)). Due to the softening of the material, the mesh size influences the fracture energy and it is often argued that this quantity should be adjusted on experiments involving stable crack growth in order to fit the crack energy (Gullerud et al. (2000); Rousselier (1987)). The mesh size is then interpreted as some microstructural characteristic length (e.g. a multiple of the interparticle spacing or grain size). In the following, the elements in the region where damage was expected to develop were quadratic squares (with reduced integration) whose edge size is equal to 100 μm . This element size was

found appropriate to model NC0.25 specimens, in which stable crack growth occurs. For SC specimens, a small geometrical defect was introduced to trigger necking at the centre of the gauge area.

5. Model Identification

5.1. Flow rules

Considering the high number of parameters in the model, the identification procedure was carefully defined. It was based on FE calculations for all specimens including SC specimens as, for high deformation rates, part of the creep tertiary stage are due to structure effects.

From experimental creep tests on SC specimens, the creep flow behaviour in quasi plastic and viscoplastic creep regimes was first determined. Based on experimental evidence that damage does not occur in SC specimens before the onset of necking, the corresponding model parameters were identified without accounting for coupling between damage and viscoplastic flow (i.e. using the model described in section 4.1). Therefore, to start with, only creep flow parameters were determined (see **sections 1 to 7** in **table B.III.5**).

Yield stress parameters were fitted by taking into account experimental observations of material softening in the quasi plastic and viscoplastic creep regimes. In the following, R_{om} , Q_{m1} and Q_{m2} ($m = qp, vp$) are constants having temperature-dependent positive values and \bar{p}_m is the effective plastic strain.

In the quasi-plastic regime the yield stress was defined as:

$$R_{qp}(\bar{p}_{qp}) = R_{oqp} + Q_{qp1}(1 - \exp(-b_{qp1} \bar{p}_{qp})) - Q_{qp2}(1 - \exp(-b_{qp2} \bar{p}_{qp})) \quad (\text{eq. B.III.14})$$

where $R_{oqp} + Q_{qp1}(1 - \exp(-b_{qp1} \bar{p}_{qp}))$ accounts for material hardening and $-Q_{qp2}(1 - \exp(-b_{qp2} \bar{p}_{qp}))$ accounts for material softening associated with the recovery of the microstructure observed for tensile specimens. All these parameters and the Norton law coefficients associated with the quasi plastic regime were fitted to experimental tensile curves in the strain rate range from $10^{-3}s^{-1}$ to $10^{-2}s^{-1}$. This allows to well describe the rate dependent plasticity of the material.

The yield stress associated with the viscoplastic creep mechanism was designed in the same way as for the quasi plastic mechanism:

$$R_{vp}(\bar{p}_{vp}) = R_{ovp} + Q_{vp1}(1 - \exp(-b_{vp1} \bar{p}_{vp})) - \left\{ Q_{vp2}(1 - \exp(-b_{vp2}(\bar{p}_{vp} - p_c))) \right\} \quad (\bar{p}_{vp} > p_c) \quad (\text{eq. B.III.15})$$

where $R_{ovp} + Q_{vp1}(1 - \exp(-b_{vp1} \bar{p}_{vp}))$ represents material hardening in the first steps of creep deformation and $-Q_{vp2}(1 - \exp(-b_{vp2}(\bar{p}_{vp} - p_c)))$ is the softening function added to account for ageing and softening phenomena described in **section 3.4**, which are only effective for a local equivalent viscoplastic strain higher than $p_c = 0.03$. This critical strain, p_c , corresponding to the onset of softening effects was set because the influence of softening on creep flow properties should only appear after dislocation rearrangement and annihilation override dislocation multiplication.

For the diffusional mechanism, the yield stress function was set to:

$$R_d(\bar{p}_d) = 0 \quad (\text{eq. B.III.16})$$

It was assumed that grain boundary diffusion does not involve any significant hardening of the material. The parameters of the Norton law which give the value of the plastic multiplier \dot{p}_d (i.e. K_d and n_d) were calculated from literature data as explained in **section 3.2**.

Cross-hardening between deformation mechanisms was defined throughout the interaction matrix, $H_{mm'}^p$:

$$H_{mm'}^p = \begin{bmatrix} H_{11} & H_{12} & H_{13} \\ H_{21} & H_{22} & H_{23} \\ H_{31} & H_{32} & H_{33} \end{bmatrix} = \begin{bmatrix} 1 & 1 & 0 \\ 1 & 1 & 0 \\ 0 & 0 & 1 \end{bmatrix} \quad (1 \text{ for } m=qp, 2 \text{ for } m=vp \text{ and } 3 \text{ for } m=d) \quad (\text{eq. B.III.17})$$

Setting H_{31} , H_{32} , H_{13} , and H_{23} to zero can easily be admitted, as the viscous mechanism does not strongly depend on plasticity and power-law creep regimes. The interaction between plasticity and power law creep is more difficult to assess. On the other hand, the primary creep stage depends on work hardening during the loading stage, therefore a strong coupling between plasticity and primary creep regimes was assumed with $H_{21}^p = H_{12}^p = 1$.

1.Young's modulus	E	145 GPa
2.Poisson's ratio	ν	0.3
3.Quasi plastic hardening at 625°C	R_{0qp} Q_{qp1} b_{qp1} Q_{qp2} b_{qp2}	173 MPa 128 MPa 400 80 MPa 7.3
4.Viscoplastic hardening at 625°C	R_{0vp} Q_{vp1} b_{vp1} Q_{vp2} b_{vp2} p_c	0 MPa 40 MPa 569 40 MPa 75 0.03
5.Quasi plastic flow rule at 625°C	K_{qp} n_{qp}	$112 \text{ MPah}^{1/n_{qp}}$ 5.0
6.Viscoplastic flow rule at 625°C	K_{vp} n_{vp}	$542 \text{ MPah}^{1/n_{vp}}$ 5.4
7.Diffusion flow rule at 625°C	K_d n_d	$0.33 \cdot 10^9 \text{ MPah}^{1/n_d}$ 1.0
8.GTN model	q_1 q_2 f_c δ_c <i>Nucleation by the viscoplastic mechanism</i> A_{vp} B_{vp} α_{vp} <i>Nucleation by the diffusional mechanism</i> A_d B_d α_d	1.5 1.0 0.1 6.0 0.01 0.15 2.0 12 15 2.0

Table B.III.5. Model parameters

5.2. Damage behaviour

Referring to McLean (1981) and Myers (1987), the dependence of the nucleation rate on stress triaxiality, i.e. α_{vp} and α_d in **equation B.III.10**, were set to 2.0. The parameters which describe the kinetics of nucleation were finally identified by assuming that the model output is a volume fraction of porosity. Therefore, the effect of carbide coarsening (i.e. their increase in size but decrease in number) on nucleation was not taken into account, as the overall fraction of carbides was shown to remain nearly constant during the tests, in accordance with the results of Kadoya et al (1997) and Anderson et al (2003).

The tertiary creep stage in SC specimens is mostly due to softening effects, as damage was only observed after specimen necking. Necking induces an increase in the stress triaxiality but strain effects are dominant. Therefore, the strain controlled damage parameters A_{vp} and A_d were determined to reach the porosity ratios and times to failure experimentally measured in SC specimens.

Creep tests on NC specimens were used to determine the influence of the stress triaxiality ratio on nucleation kinetics: parameters B_{vp} and B_d . The three notch radii investigated (4.0 mm, 1.2 mm and 0.25 mm) allow various distributions of the stress triaxiality ratio in the ligament. In particular, the experimentally measured rupture area (see **figure B.III.11**) show that these variations in mechanical fields strongly affect rupture location. Therefore, creep data on NC0.25, NC1.2 and NC4.0 specimens could be used to identify respective contributions of the stress triaxiality and equivalent viscoplastic strain to nucleation.

Cavity growth is determined by parameters q_1 and q_2 . They were set to their classical values: $q_1 = 1.5$ and $q_2 = 1.0$. This set of values was originally determined to adjust models of plasticity to micromechanical unit cell calculations (Tvergaard (1982), Koplík and Needleman (1988), Faleskog et al (1998)). In the present model, the effects induced by viscoplasticity are more complex. However, the study is not concerned with a precise determination of q_1 and q_2 , as it would require extensive unit cell calculations, and as the main damage process is nucleation.

Attention was finally focused on the description of cavity coalescence even if this step of the creep damage evolution traditionally received little attention. It was stated that the coarsening behaviour strongly depends on the damage

mechanism. When cavity growth mainly proceeds by the matrix deformation, coalescence starts for a relatively low fraction of porosity: classically for $f_c = 0.1 - 0.15$ (Koplik, Needleman, 1988).

Therefore, for “qp” and “vp” mechanisms the coarsening laws were written as:

$$\dot{f}^* = f_t + \delta_c (f_{nm} + f_{gm} - f_{cm}) \quad \text{if } (f_{gm} + f_{nm}) > f_{cm} \quad (\text{eq. B.III.18})$$

$$\dot{f}^* = f_t \quad \text{if } (f_{gm} + f_{nm}) < f_{cm} \quad (\text{eq. B.III.19})$$

Values of f_c and δ_c were set to respectively 0.1 and 6.0. This formulation means that coalescence starts provided cavity growth is promoted by matrix viscoplasticity. For the “d” mechanism, no coalescence law was used, as for $n = 1$ the stability of the material prevents void coalescence (Ashby et al (1979)). The resulting set of model parameters is given in **section 8** of **table B.III.5**.

6. Model validation and application

6.1. Model validation

The validation strategy first consisted in making sure that the model well describes all creep flow curves and satisfactorily predicts times to failure. Then, the ability of the model to predict right damage location was also analysed. Finally, using results from Kloc and Sklenicka (1997) and Kimura et al (2000), the ability of the model to describe a change in the flow mechanism and long term premature failure was investigated.

Figure B.III.3 shows that the model well predicts the change in creep flow regime from high to low stress level in accordance with experimental results and results from Kloc and Sklenicka (1997). **Figures B.III.2, B.III.4** and **B.III.5** show very good agreement between experimental and FE calculated creep curves for all kinds of specimen geometry.

To be applied to the design of components, the model had to be able to predict damage behaviour in the case of high level of stress triaxiality. One way to do this is to predict right damage localisation for NC specimens. Predicted and experimental rupture zones are in very good agreement for NC1.2 and NC0.25 specimens (**figure B.III.11**).

In addition, relative contributions of each of the porosity terms were evaluated using the model for NC1.2 specimens and some NC1.4 (145MPa) and NC0.25 (180MPa) specimens. The results are given in **table B.III.6** with the ratio between viscoplastic and diffusional contributions.

	f_{nvp}	f_{nd}	f_{gvp}	f_{gd}	f_{nvp}/f_{nd}	f_{gv}/f_{gd}
NC1.2 – 218 MPa	0.058	0.0054	0.026	0.00001	10.7	2600
NC1.2 – 175 MPa	0.055	0.018	0.028	0.000048	3.05	583
NC1.2 – 150 MPa	0.041	0.042	0.03	0.000162	0.97	185
NC4.0 – 145 MPa	0.042	0.012	0.042	0.000046	3.5	913
NC0.25 - 180 MPa	0.053	0.018	0.035	0.000056	2.9	625

Table B.III.6. Damage contributions in the first square element where the total porosity ratio exceeds 0.1

Looking at the decomposition of porosity contributions to the overall damage is very interesting. Cavity nucleation both proceeds by matrix viscoplasticity and diffusion at grain boundaries. Cavity growth is only promoted by grain deformation and in the later stage of creep life: at the onset of creep rupture, nucleation and growth equally contribute to damage, but calculations showed that nucleation is the dominating mechanism up to high deformation levels. This is consistent with the observation of a dominant influence of nucleation (see **figure B.III.10a** and **B.III.10b**), and of intergranular cavitation triggered by matrix viscoplasticity (see **figure B.III.9a** and **B.III.9b**). A change in the relative influences of diffusional and viscoplastic contributions to the overall porosity is also evidenced for NC1.2 specimens. It gives arguments to state that notch should promote change in deformation and damage mechanisms for shorter tests duration than for smooth specimens.

A comparison between measured and calculated porosity surface ratios (see **section 3.5**) was also performed. Good agreement was found between measured and calculated porosity ratios for fractured SC specimens and non fractured NC1.2 specimens.

6.2. Model application

First, single volume element calculations for various constant stress triaxiality ratios: $\tau = 1/3, 1.3, 1.8$ and 2.5 were performed to investigate the relative contributions to the overall porosity ratio (**figure B.III.12**). For all values of τ , a transition is observed near $\sigma_{eq} = 70$ MPa. Below this transition stress, the damage is mainly promoted by the diffusional mechanism. It is also interesting to notice that cavitation due to grain boundary diffusion only proceeds by nucleation, as the cavity growth process is very limited. Another point is that the relative proportions of nucleation and growth due to the matrix viscoplasticity increase with the stress triaxiality ratio. These calculations also allowed to plot the time to

failure versus σ_{eq} for the four values of τ . Even if no experimental evidence is given in the present study (see **figure B.III.7**), the results of **figure B.III.13** show that creep tests on notched specimens may lead to observe the transition in the creep time to failure - stress dependence for more easily reachable experimental times (i.e. for less than 10,000 hours on NC0.25 specimens, for example). Such effects have already been experimentally observed by Yoshida (1985) and Piques (1989) and are supported by the theoretical work of Sham and Needleman (1983) and Van der Giessen et al (1995), who show the influence of the stress triaxiality ratio on damage accumulation.

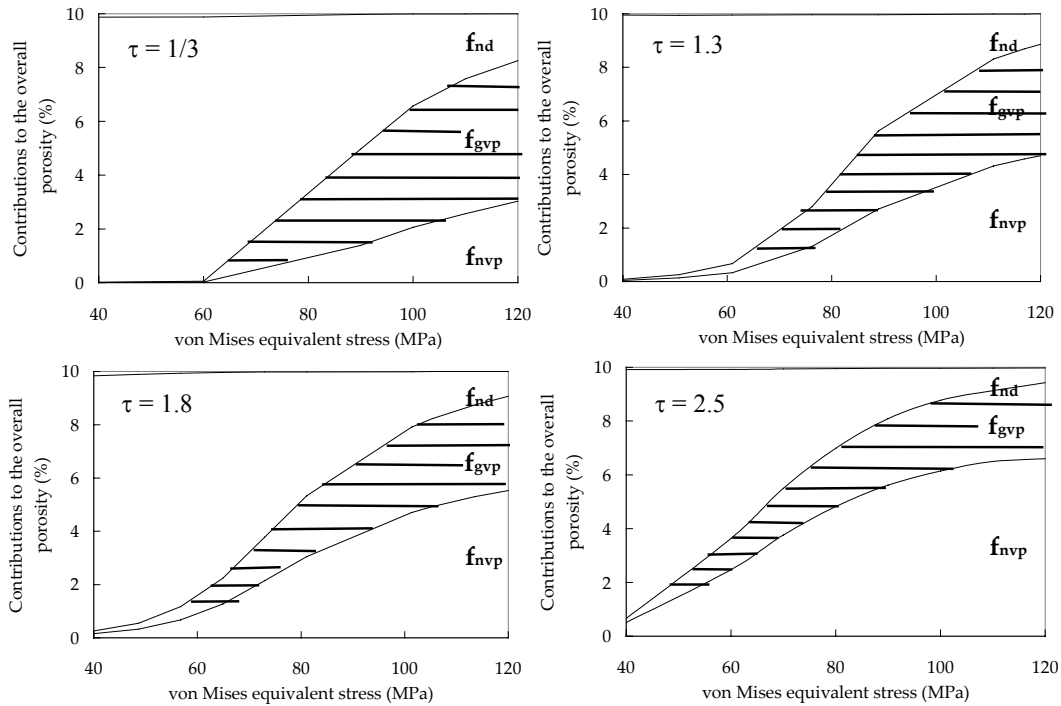


Figure B.III.12. Contributions to the overall porosity at the onset of creep failure (i.e. $f_t = 10\%$): single volume element calculations for various stress triaxiality ratios (a) $\tau = 1/3$, (b) $\tau = 1.3$, (c) $\tau = 1.8$, and (d) $\tau = 2.5$

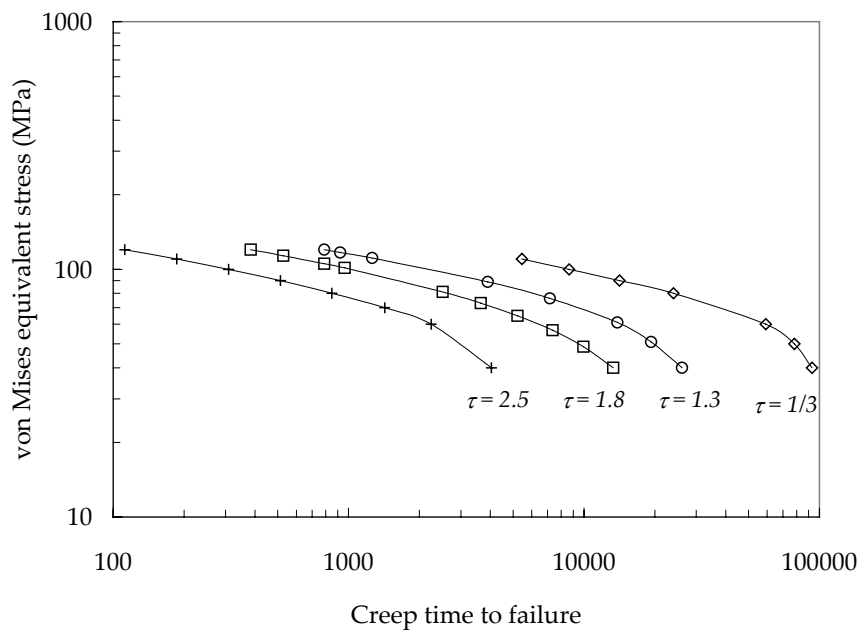


Figure B.III.13. von Mises equivalent stress versus creep time to failure: Single elements calculations for various stress triaxiality ratios

From a practical point of view, a comparison of the model with the MG formalism was made. In fact, one could state that the change in the time to failure dependence to the applied stress is only due to a change in the creep flow mechanism around 70 MPa and that the material ductility remains actually “constant”. To investigate this point, and using the steady state creep strain rates calculated by the model for the damage free material, the MG relationship given in **section 3.3** was used to predict creep time to failure from high to low stress. The comparison between the model and the MG

predictions (see **figure B.III.6**) evidenced poor agreement, as the transition is delayed to higher creep times using the MG formalism: predicted creep lifetimes are twice higher than those given by the model in the low stress creep regime. This shows that the model takes into account a loss in the intrinsic material ductility, due to the contribution of the diffusional mechanism to damage accumulation. The model could then be applied, for example, to work-hardened austenitic stainless steels for which no change in the material creep flow mechanism is observed whereas a decrease in ductility is evidenced (Piques (1989) and Michel (2004)). The third damaging deformation mechanism may only contribute to damage accumulation and not significantly to the macroscopic strain. This is in fact the idea supported by the work of Michel (2004) but without coupling between flow and damage behaviour.

Finally, NC0.25 specimens allowed for stable crack propagation and using the resistivity technique, the creep crack initiation and propagation could be monitored. The crack length (in mm) was deduced from resistivity measurements using the correlation previously established by Hourlier (1982) for the same specimen geometry. As FE calculations were performed on square elements of 100 μm in size, the time to crack initiation was defined experimentally as the time to reach a propagation of the crack over 100 μm and numerically as the time for which the first square element breaks in FE calculations. The ability of the model to predict the time to crack initiation which corresponds to 75% of the overall lifetime in NC0.25 specimens was ensured.

6.3. Ability of the model to represent experimental literature results at 600 and 650°C

The model was used to evaluate creep time to failure corresponding to the experimental data of Kimura et al (2002). In the high stress creep regime, steady state creep strain rates were deduced from the experimental database of Kimura et al (2000) and used to modify the value of K_{vp} to fit experimental steady state strain rates at 600°C and 650°C. In the low stress creep regime, Kloc and Sklenicka (1997) suggested that the activation energy E_a is nearly equal to the activation energy for pipe diffusion in α -iron (i.e. 174 kJmol^{-1} from Frost and Ashby (1982)). Spigarelli et al (1997) reported an activation energy of 160 kJ/mol in the low stress creep regime. Here,

$$\frac{1}{K_d} \propto \frac{\beta}{T} \exp\left(\frac{-E_a}{RT}\right) \quad (\text{eq. B.III.20})$$

where β is material parameter and from $K_d(625^\circ\text{C})$, $K_d(650^\circ\text{C})$ and $K_d(600^\circ\text{C})$ could be respectively evaluated with $E_a=174\text{kJmol}^{-1}$. The set of values for K_{vp} and K_d at 600°C and 650°C is given in **table B.III.7**. All other parameters were assumed to remain unchanged.

	600°C	650°C
K_{vp}	860 $\text{MPah}^{-1/n_{vp}}$	400 $\text{MPah}^{-1/n_{vp}}$
K_d	0.63 $\cdot 10^9 \text{MPah}^{-1/n_d}$	0.18 $\cdot 10^9 \text{MPah}^{-1/n_d}$

Table B.III.7. Transposition of the model from 625°C to 600°C and 650°C

Comparisons between the model predictions and the results of Kimura et al (2000) is given in **figure B.III.14**. The result of a long term creep test on a 12%Cr steel from Eggeler (1989b) is also plotted in **figure B.III.14**. The model well reproduces their results even if it may be too conservative at 600°C and 650°C.

The authors want to prevent readers from the use of the model at higher temperatures than 650°C. This could only be done provided it made sure that the A_{c1} temperature (start of austenitic transformation) is not locally reached (In C, Cr, Mo depleted zones i.e. near carbides for example). Indeed, this would induce local formation of austenite and might dramatically reduce the creep strength of the material. Same precautions must be taken at lower temperatures as dynamic strain ageing occurs under 500°C in 9Cr1Mo-NbV steels (see Yaguchi and Takahashi (2000)).

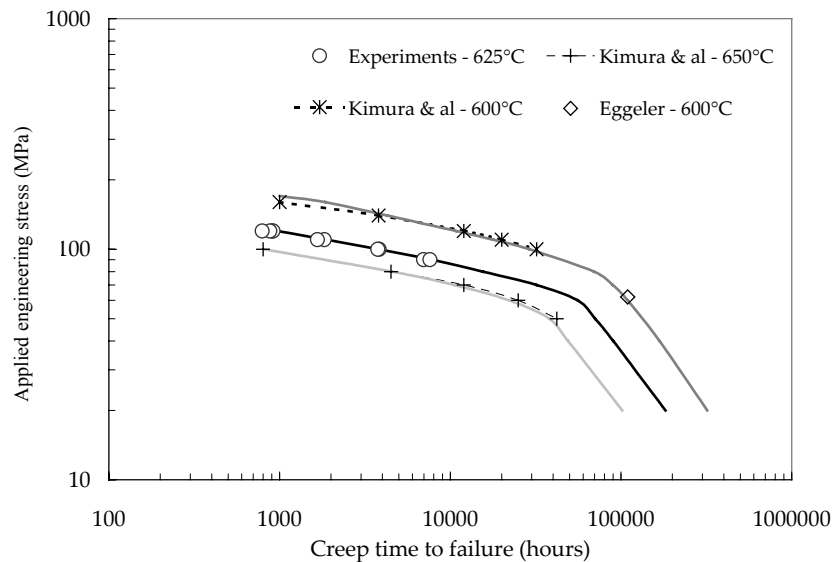


Figure B.III.14. Use of the model to predict creep time to failure at 600 and 650°C: Comparison between model (lines) and experiments from Kimura et al (2002)

Conclusions

The main results of this work are as follows:

1. Creep tests at 625°C (898°K) on various specimens geometry of a tempered P91 type martensitic stainless steel allowed to get a large database on the material creep flow properties in the high stress creep regime. In addition, literature results were added to the database to describe the low stress creep regime.
2. Long term ageing and detailed investigations of all crept specimens led to the following conclusions:
 - Creep ageing and long term stress free ageing led to carbide coarsening and recovery of lath martensite by subgrain formation and growth.
 - The new subgrains are very sensitive to boundary cracking and frequently initiate creep failure.
3. A model including constitutive equations to represent all creep mechanisms and a coupling between flow and damage contributions was built in the framework of continuum damage mechanics of porous media. Constitutive equations take softening effects into account. All damage steps i.e. cavity nucleation, growth and coarsening and their dependence to the stress triaxiality and the equivalent viscoplastic strain are modelled. The resulting model well reproduces the experimental results from high to low stresses and predicts long term premature failure.
4. Creep tests on notched specimens may lead to premature failure for shorter tests duration than on SC specimens (< 10,000 hours).

Acknowledgements

Financial and technical support from Electricité de France (EdF), Framatome and Le Commissariat à l'Énergie Atomique (CEA) is acknowledged. Thanks are due to Professor André Pineau (ENSMP) for fruitful discussions and to Dr. R. Piques (ENSMP) who largely contributed to the birth of this research project. Special thanks are also due to B. Brugier (Framatome); Y. Rousseleau and G. Lindet (EdF); Dr. Y. De Carlan and Dr. L. Guetaz (CEA); M. Rousselot, F. Grillon, J. Valy, A. Naslot, O. Adam, J.L. Ajzenberg, G. Cassas, J.P. Etourneau, J. Gibier, J. Labrousse and C. Meurin (Centre des Matériaux, ENSMP) for their priceless assistance.

References

- Al-faddagh K.D., Fenner R.T., Webster G.A. (1982). Steady state distributions in circumferentially notched bars subjected to creep. *Journal of strain analysis*. 17(3). 123-132.
- Anderson P., Bellgardt T., Jones F.L. (2003). Creep deformation in a modified 9Cr-1Mo steel. *Materials Science and Technology*. **19**, 207-213.

- Ashby M.F., Gandhi C. and Taplin D.M.R. (1979) Fracture mechanism maps and their construction for fcc metals and alloys. *Acta metallurgica*. **27**. 699-729.
- Bellenger E., Bussy P. (2001). Phenomenological modeling and numerical simulation of different modes of creep damage evolution. *International Journal of Solids and Structures*. **38**. 577-604.
- Besson J., Guillemer-Neel C. (2003). An extension of the Green and Gurson models to kinematic hardening, *Mechanics of materials*, **35**, 1-18.
- Besson J. (2001a). Eprouvettes axisymétriques entaillées. *Essais mécaniques et lois de comportement - Hermes - Paris*. 319-351 (in French).
- Besson J., Cailletaud G., Chaboche J.L., Forest S. (2001b). Mécanique non linéaire des matériaux. *Hermes – Paris* (in French).
- Besson J., Steglich D., Brocks W. (2001c). Modeling of crack growth in round bars and plane strain specimens. *International Journal of Solids and Structures*, **38 (46-47)**, 8259-8284.
- Besson J., Devillers-Guerville L., Pineau A. (2000). Modeling of scatter and size effect in ductile fracture. Application to thermal embrittlement of duplex stainless steels. *Engineering Fracture Mechanics*. **67(2)**. 169-190.
- Besson J., Foerch R. (1997). Large scale object-oriented finite element code design. *Computer Methods in Applied Mechanics and Engineering*. **142**. 165-187.
- Brachet J.C. (1991). Alliages martensitiques 9Cr-1Mo: Effets de l'addition de l'azote, du niobium et du vanadium sur la microstructure, les transformations de phases et les propriétés mécaniques. *PhD Thesis – University of Paris Sud Orsay* (in French).
- Brinkman C.R., Gieseke B., Maziasz P.J. (1993). The influence of long thermal aging on the microstructure and mechanical properties. *Microstructure and mechanical properties of aging materials – The Minerals, Metals and Materials Society*. 107-115.
- Cadek J., Sustek V., Pahutova M. (1997). An analysis of a set of creep data for a 9Cr-1Mo-0.2V steel. *Materials Science and Engineering*. **A225**. 22-28
- Cerri E., Evangelista E., Spigarelli S., Bianchi P. (1998). Evolution of microstructure in a modified 9Cr-1Mo steel during short term creep. *Materials Science and Engineering*. **A245**. 285-292.
- Chu C.C., Needleman A. (1980). Voids nucleation effects in biaxially stretched sheets. *Journal of Engineering Materials and Technology*. **102**. 249-256.
- Contesti E., Cailletaud G. (1989). Description of creep plasticity interaction with non unified constitutive equations: Application to an austenitic stainless steel. *Nuclear Engineering and Design*. **116**. 265-280.
- Dyson B.F. (1983). Continuous cavity nucleation and creep fracture. *Scripta Metallurgica*. **17**. 31-37.
- Dyson B.F. (1976). Constraints on diffusional cavity growth rates. *Metal Science*. **10, October**. 349-353.
- Eggeler G., Tato W., Jemmely P. et al (1992). Creep rupture of circular notched P91 specimens: influence of heat treatment and notch geometry. *Scripta Metallurgica et Materialia*. **27**. 1091-1096.
- Eggeler G. (1989). The effect of long term creep on particle coarsening in tempered martensite ferritic steels. *Acta Metallurgica*, **37(12)**, 3225-3234.
- Eggeler G., Earthman J.C., Nilsvang N., Ilschner B. (1989b). Microstructural study of creep rupture in a 12% chromium ferritic steel. *Acta Metallurgica*. **37(1)**. 49-60.
- Engberg G., Karlsson S., Von Walden E. (1984). An interpretation of tertiary creep in 12%Cr steel at 550°C. *Creep and fracture of engineering materials and structures*, ed. B. Wilshire, D.R.J. Owen, Swansea 1-6 April. Pineridge Press. 697-709.
- Ennis P.J., Czyrska-Filemonowicz A. (2002). Recent advances in creep resistant steels for power plant applications. *OMMI*. **1(1)**. 1-27.
- Faleskog J., Gao X., Fong Shih C. (1998). Cell model for nonlinear fracture analysis. I. micromechanics calibration. *International Journal of Fracture*. **89**. 355-373.
- Frost H.J., Ashby M.F. (1982). Deformation-mechanism maps: The plasticity and creep of metals and ceramics. Oxford, Pergamon Press.
- Guetaz L., Millier J.P., Urvoy S. (2003). Mécanismes de déformation de l'acier martensitique Eurofer. *Private communication*.
- Gullerud A.S., Gao X., Dodds Jr.R. and Haj-Ali R. (2000). Simulation of ductile crack growth using computational cells: numerical aspects. *Engineering Fracture Mechanics*. **66**. 65-92
- Gurson A.L. (1977). Continuum theory of ductile rupture by void nucleation and growth : Part 1 – Yield criteria and flow rules for porous ductile media. *Journal of Engineering Materials and Technology*. **99**, 2-15.
- Hattestrand M., Andren H.O. (2001). Influence of strain on precipitation reactions during creep of an advanced 9% chromium steel. *Acta Materialia*, **49(12)**, 2123-2128.
- Hayhurst D.R., Leckie F.A. and Henderson J.T. (1977a). Design of notched bars for creep rupture testing under tri-axial stresses. *International Journal of Mechanical Sciences*. **19(3)**. 147-159.
- Hayhurst D.R., Henderson J.T. (1977b). Creep stress redistribution in notched bars. *International Journal of Mechanical Sciences*. **19(3)**. 133-146.

- Hayhurst D.R. (1995). High-temperature design and life assessment of structures using continuum damage mechanics - *Creep and Fatigue: Design and Life Assessment at High Temperature in Mechanical Engineering Publications Ltd.* (UK), 399-410.
- Hayhurst D.R., Trampczynski W.A., Leckie F.A. (1983). On the role of cavity nucleation in creep deformation and fracture. *Acta Metallurgica*. **31(10)**. 1537-1542.
- Herding U., Kuhn G. (1996). A field boundary element formulation of damage mechanics. *Engineering Analysis with Boundary Elements*. **18(2)**. 137-147.
- Hourlier F. (1982). Propagation de fissures de fatigue sous sollicitations polymodales. *PhD Thesis – Ecole Nationale Supérieure des Mines de Paris, Paris, France.*(in French).
- Hull D., Rimmer D.E. (1959).The growth of grain boundary voids under stress. *Philosophical Magazine*. **4(42)**. 673-687.
- Iwanaga K., Tsuchiyama T., Takaki S. (1998). Relationship between creep behavior and microstructure in martensitic heat resistant steel. *Tetsu-to-Hagané (Journal of the iron and steel institute of Japan)*. **84(12)**. 896-901.
- Jayet-Gendrot S. (1999). Uniaxial creep properties of P9 materials at 625°C (base metal and weld). *HIDA 1702/PMB/57*.
- Kachanov L.M. (1958). Time of the rupture process under creep conditions. *Isv. Akad. Nauk. SSR. Otd Tekh. Nauk*. **8**. 26-31.
- Kadoya Y., Nishimura N., Dyson B.F. and McLean M. (1997). Origins of tertiary creep in high chromium steels. *Creep and Fracture of Engineering Materials and Structures*. Ed. J.C.Earthman and F.A. Mohamed. The Minerals, Metals and Materials Society, Warrendale, PA. 343-352.
- Kassner M.E. and Hayes T.A. (2003). Creep cavitation in metals. *International Journal of Plasticity*. **19(10)**. 1715-1748.
- Kimura K., Suzuki K., Toda Y., Kushima H., Abe F. (2002) Precipitation of a Z-Phase and degradation behaviour of modified 9Cr-1Mo steel, *Materials for advanced power engineering – Proceedings of the 7th Liège conference, Forschungszentrum Julich, Lecomte-Beckers, Carton, Schuber and Ennis (Editors)*. **II(21)**. 1171-1180.
- Kimura K., Kushima H., Abe F. (2000). Heterogeneous changes in microstructure and degradation behaviour of 9Cr-1Mo-V-Nb steel during long term creep. *Key Engineering Materials*. **171-174**. 483-490.
- Kloc L., Sklenicka V. (1997). Transition from power-law to viscous creep behaviour of P-91 type heat resistant steel. *Materials Science and Engineering*. **A234-236**. 962-965.
- Clueh R.L., Harries D.R. (2001). High-chromium ferritic and martensitic steels for nuclear applications. *Book - American Society for Testing Materials*.
- Koplik J., Needleman A. (1988). Void growth and coalescence in porous plastic solids. *International Journal of Solids and Structures*. **24(8)**. 835-853.
- Kushima H., Kimura K., Abe F. (2002) Long term creep strength prediction of high Cr ferritic resistant steels. *Materials for advanced power engineering – Proceedings of the 7th Liège conference, Forschungszentrum Julich, Lecomte-Beckers, Carton, Schuber and Ennis (Editors)*. **III(21)**. 1581-1590.
- Larson F.R. and Miller J. (1952). A time–temperature relationship for rupture and creep stresses, *Transactions of the ASME*. **74**. 765-775
- Lemaitre J. (1985). A continuum damage mechanics model for ductile fracture. *Journal of Engineering Materials and Technology*. **107**. 83-89.
- Liu Y., Murakami S., Kanagawa Y. (1994). Mesh dependence and stress singularity in finite element analysis of creep crack growth by continuum damage mechanics approach. *European Journal of Mechanics*. **13A(3)**. 395-417.
- McLean D. (1981). Damage accumulation in creep. *Annales de chimie*. **6**.124-139.
- Michel B. (2004). Formulation of a new intergranular creep damage model for austenitic stainless steels. *Nuclear Engineering and Design*. **227(2)**. 161-174.
- Monkman F.C. and Grant N.J. (1956). An empirical relationship between rupture life and minimum creep rate in creep-rupture tests, *Proceedings of the ASTM*, **56**, 593-620.
- Myers M.R., Pilkington R. , Needham N.G. (1987). Cavity nucleation and growth in a 1%Cr-0.5%Mo steel. *Materials Science and Engineering*. **95(2)**. 81-91.
- Nakajima T., Spigarelli S., Evangelista E., Endo T. (2003). Strain enhanced growth of precipitates during creep of T91. *Materials Transactions JIM*. **44(9)**. 1802-1808.
- Needleman A., Tvergaard V. (1991). An analysis of dynamic, ductile crack growth in a double edge cracked specimen. *International Journal of Fracture*. **49**. 41-67.
- Needleman A., Rice J.R. (1980). Overview n°9 - Plastic creep flow effects in the diffusive cavitation of grain boundaries. *Acta Metallurgica*. **28(10)**. 1315-1332.
- Onck P., Van der Giessen E. (1997). Microstructurally based modelling of intergranular creep fracture using grain elements. *Mechanics of Materials*. **26(2)**. 109-126.
- Orlova A., Bursik J., Kucharova K., Sklenicka V. (1998). Microstructural development during high temperature creep of 9%Cr steel . *Materials Science and Engineering*. **A245**, 39-48.
- Othman A.M., Dyson B.F., Hayhurst D.R. and Lin J. (1994). Continuum damage mechanics modelling of circumferentially notched tension bars undergoing tertiary creep with physically based constitutive equations. *Acta Metallurgica et Materialia*. **42(3)**. 597-611.
- Pardo T., Doghri I., Delannay F. (1998). Experimental and numerical comparison of void growth models and void coalescence criteria for the prediction of ductile fracture in copper bars. *Acta Materialia*. **46(2)**. 541-552.

- Piques R., Molinié E., Pineau A. (1991). Comparison between two assessment methods for defects in the creep range. *Fatigue and fracture of engineering materials and structures*. **14(9)**. 871-885
- Piques R. (1989). Mécanique et mécanismes de l'amorçage et de la propagation de fissures en viscoplasticité dans un acier austénitique inoxydable. *PhD Thesis – Ecole Nationale Supérieure des Mines de Paris, Paris, France* (in French).
- Polcik P., Sailer T., Blum W., Straub S., Bursik J., Orlova A. (1999). On the microstructural development of the tempered martensitic Cr-steel P91 during long term creep – a comparison of data. *Materials Science and Engineering*. **A260**. 252-259.
- Prunier V., Gampe U., Nikbin K., Shibli I.A. (1998). HIDA activity on P91 steel. *Creep and fatigue crack growth in high temperature plant*. HIDA Conference - CEA Saclay - France.
- Pugh C.E. (1978). On establishing constitutive equations for use in design of high temperature fast reactor structure. *Nuclear Engineering and Design*. **51**. 23-27
- Rabotnov Y.N. (1969). Creep problems in structural members. *North-Holland, Amsterdam*.
- Rice J.R, Tracey D.R. (1969). On the ductile enlargement of voids in triaxial stress fields. *Journal of the Mechanics and Physics of Solids*. **17(3)**. 201-217.
- Rousselier G. (1987). Ductile fracture models and their potential in local approach of fracture. *Nuclear Engineering and Design*. **105**. 97-111.
- Sawada K., Taneike M., Kimura K, Abe F. (2003). In situ observation of recovery of lath structure in 9% chromium creep resistant steel. *Materials Science and Technology*. **19(6)**. 739-742.
- Sawada K., Takeda M., Maruyama K., Ishii R., Yamada M., Nagae Y., Komine R. (1999). Effect of W recovery of lath structure during creep of high chromium martensitic steels. *Materials Science and Engineering*. **A267**. 19-25.
- Senior B.A. (1989). The precipitation of Laves phase in 9Cr – 1Mo steels. *Materials Science and Engineering*. **A119**. L5-L9.
- Sham T. L., Needleman A. (1983). Effects of triaxial stressing on creep cavitation of grain boundaries. *Acta Metallurgica*. **31(6)**. 919-926.
- Simo J.C, Taylor R.L. (1985). Consistent tangent operators for rate-independent elastoplasticity. *Computer Methods in Applied Mechanics Engineering*. **48(1)**. 101-118.
- Sklenicka V., Kucharova K., Svoboda M., Kloc L., Bursik J., Kroupa A. (2003). Long term creep behavior of 9-12% Cr power plant steels. *Materials characterization*. **51(1)**. 35-48.
- Spigarelli S., Kloc L., Bontempi P. (1997). Analysis of creep curves in a modified 9Cr-1Mo modified steel by means of simple constitutive equations. *Scripta Materialia*. **37(4)**. 399-404.
- Stocker Ch., Spiradek K., Zeiler G. (2002). Microstructural features influencing the creep properties of 9-12%Cr steels focusing on Laves phase precipitation. *Materials for advanced power engineering – Proceedings of the 7th Liège conference*. **III(21)**.1459-1469.
- Suzuki K., Kumai S., Kushima H. et al (2003). Precipitation of Z-phase and precipitation sequence during creep deformation of modified 9Cr-1Mo Steel . *Tetsu-to-Hagané (Journal of the Iron and Steel Institute of Japan)*. **89(6)**. 691-698.
- Tsuchiyama T., Miyamoto T., Takaki S. (2001). Recrystallisation of lath martensite with bulge nucleation and growth mechanism. *ISIJ International*. **41(9)**. 1047-1052.
- Tvergaard V., Needleman A. (1984a). On the creep constrained diffusive cavitation of grain boundary facets. *Journal of the Mechanics and Physics of Solids*. **32(5)**. 373-393.
- Tvergaard V., Needleman A. (1984b). Analysis of the cup cone fracture in a round tensile bar. *Acta Metallurgica*. **32(1)**. 157-169.
- Tvergaard V. (1989). Material failure by void growth to coalescence. *Advances in Applied Mechanics*. **27**. 83-151.
- Tvergaard V. (1982). Ductile fracture by nucleation between larger voids. *Journal of the Mechanics and Physics of Solids*. **30**. 265-286.
- Van der Giessen E., Van der Burg M.W.D., Needleman A., Tvergaard V. (1995). Void growth due to creep and grain boundary diffusion at high triaxialities. *Journal of the Mechanics and Physics of Solids*. **43(1)**. 123-165.
- Vilhensen T. (1996). Creep failure of modified 9Cr steel weldments. *PhD Thesis of the University of London and for the Imperial College, London*.
- Wasmer K., Biglari F., Nikbin K. M. (2002). Multiaxial failure behaviour in advanced steels at elevated temperatures. *Proceedings of the ECF 14 Conference - Cracovie*. 553-562.
- Weinert P. (2002). Microstructural physically based creep modelling of 9-12% Cr steels. *Materials for advanced power engineering – Proceedings of the 7th Liège conference, Forschungszentrum Julich, Lecomte-Beckers, Carton, Schubert and Ennis (Editors)*. **II**. 1211-1221.
- Wu R. and Sandstrom R. (1996). Strain dependence of creep cavity nucleation in low alloy and 12%Cr steels. *Materials Science and Technology*. **12(5)**. 405-415.
- Wu R. and Sandstrom R. (1995). Creep cavity nucleation and growth in 12Cr-Mo-V steel. *Materials Science and Technology*. **11(6)**. 579-588.
- Xia L., Shih C.F., Hutchinson J. W. (1995). A computational approach to ductile crack growth under large scale yielding conditions. *Journal of the Mechanics and Physics of Solids*. **43(3)**. 389-413.
- Yaguchi M., Takahashi Y. (2000). A viscoplastic constitutive model incorporating dynamic strain aging effect during cyclic deformation conditions. *International Journal of Plasticity*. **16**. 241-262.

Yoshida M. (1985). Endommagement intergranulaire de fluage dans un acier inoxydable 17Cr-12Ni – Etude quantitative – Rôle de la multiaxialité des contraintes. *PhD Thesis – Ecole Nationale Supérieure des Mines de Paris, Paris, France* (in French).

Yue Z.F., Lu Z.Z., Wang X.M. (2002). A numerical study of damage development and creep life in circular notched specimens during creep. *Materials at high temperature*. **19(3)**. 147-152.

Supplement B.III.S1. Improvement of the model

1. Relevance of the Gurson model to represent cavity growth for materials deforming at elevated temperature

In **chapter B.III** attention was mainly focused on the integration of multiple coupled flow and damage mechanisms into a single model. As a matter of fact, the formulation of the Gurson model, a priori strictly valid in the case of pure plasticity, was chosen. However, this use of the Gurson model to describe cavity growth for materials deforming at high temperature has already been criticised. So on the model of the present study during the 15th European conference on fracture where it was first presented. Therefore, it was necessary to investigate the relevance of the model as written in **chapter B.III** to represent cavity growth for a material deforming at high temperature.

The overall stress potential for a viscoplastic material containing spherical voids and deforming under high temperature conditions was determined by Leblond – Perrin – Suquet (LPS) (1994) as the so called “m-dependent porous material model” which was written:

$$\phi_m(\sigma, f^*) = A\sigma^* \frac{m}{m+1} \left(\frac{\Lambda_m(\sigma, f^*)}{\sigma^*} \right)^{\frac{m+1}{m}} \quad (\text{eq. B.III.S1.1})$$

where, σ^* is the effective stress equal to the von Mises equivalent stress for the undamaged material and the model parameters A and m, which is the strain hardening coefficient, are given by the Norton power-law which is written as:

$$\dot{\epsilon}_{ss} = A\sigma_{eq}^{\frac{1}{m}} \quad (\text{eq. B.III.S1.2})$$

where σ_{eq} is the equivalent stress. Moreover in **equation B.III.S1.1**, Λ_m is given by:

$$\Lambda_m = \frac{\sigma_{eq}^2}{\sigma^{*2}} + fq_1 \left[h_m \left(q_2 \frac{1}{2} \frac{\sigma_{kk}}{\sigma^*} \right) + \left(\frac{1-m}{1+m} \right) \frac{1}{h_m \left(q_2 \frac{1}{2} \frac{\sigma_{kk}}{\sigma^*} \right)} \right] - 1 - q_1^2 \left(\frac{1-m}{1+m} \right) f^2 \quad (\text{eq. B.III.S1.3})$$

q_1 and q_2 are the classical parameters of the Gurson model and h_m is given by:

$$h_m(x) = \left[1 + mx^{(1+m)} \right]^{1/m} \quad (\text{eq. B.III.S1.4})$$

A reduced form of the stress potential can be used as:

$$\phi = \frac{\sigma_{eq}^2}{\sigma^{*2}} + fq_1 \left[h_m \left(q_2 \frac{1}{2} \frac{\sigma_{kk}}{\sigma^*} \right) + \left(\frac{1-m}{1+m} \right) \frac{1}{h_m \left(q_2 \frac{1}{2} \frac{\sigma_{kk}}{\sigma^*} \right)} \right] - 1 - q_1^2 \left(\frac{1-m}{1+m} \right) f^2 \quad (\text{eq. B.III.S1.5})$$

One can note that when $m \rightarrow 0$ (i.e. pure plasticity), the stress potential is reduced to the Gurson-Tvergaard-Needleman (1984) GTN model as:

$$\lim_{m \rightarrow 0} (h_m(x)) = \lim_{m \rightarrow 0} \left(\left[1 + mx^{(1+m)} \right]^{1/m} + \left(\frac{1-m}{1+m} \right) \frac{1}{h_m(x)} \right) \rightarrow \cosh(x) \quad (\text{eq. B.III.S1.6})$$

In the case of diffusion creep the strain hardening coefficient $m = 1$ so that:

$$\lim_{m \rightarrow 1} (h_m(x)) = \lim_{m \rightarrow 1} \left(\left[1 + mx^{(1+m)} \right]^{1/m} + \left(\frac{1-m}{1+m} \right) \frac{1}{h_m(x)} \right) \rightarrow 1 + x^2 \quad (\text{eq. B.III.S1.7})$$

so that the stress potential can be reduced to the following expression:

$$\phi = \sigma_{eq}^2 + fq_1 \left(q_2 \frac{1}{2} \right)^2 \sigma_{kk} + \sigma^{*2} (fq_1 - 1) \quad (\text{eq. B.III.S1.8})$$

One can recognised in **equation B.III.S1.8**, a potential of the elliptic form (see Green (1972)).

Therefore, to describe more accurately the cavity growth in the high temperature creep regime, it would be necessary to use the potential of **equation B.III.S1.5** to describe the cavity growth assisted by the power-law creep and to use the potential of **equation B.III.S1.8** to describe the cavity growth assisted by grain boundary diffusion.

The model of Leblond et al (1994) has been recently studied by Klocker and Tvergaard (2000 and 2003) who especially performed void cells calculations and compare it to the classical Gurson model (i.e. $m \rightarrow 0$). They focused their attention on the effect of m on cavity growth and coalescence. In Klocker and Tvergaard (2000), they showed that the strain rate hardening coefficient m has a significant influence on void growth and coalescence as high values of m reduces the cavity growth rate and delay the onset of coalescence. They evidenced little deviations between the porous model and

the void cells calculations that they attribute to a bad description of the strain localisation because the cavities remain no more spherical. Therefore, they performed the same work in Klocker and Tvergaard (2003) with including modifications, inspired by the works of Gologanu et al (1994 and 1995), in the model of Leblond et al (1994) to account for effect of ellipsoidal cavities on stress localization. They found a better agreement with void cell calculations.

The work of Klocker and Tvergaard (2000) can be criticised as they used the concept of the effective porosity of the GTN model to describe the cavity coalescence. The effective porosity is a material parameter whose value especially takes the viscosity of the material into account. Therefore, the benefits from the use of the potential proposed by Perrin et al (1994) which provides a more accurate description of strain localisation in the intervoid spacing is lost. However, there is no deny that if one wants to use the Thomason's (1985) description of coalescence, the use of the exact potential proposed by Perrin et al (1994) is obviously necessary.

Note also that Faleskog et al (1998) have shown that the effect of material hardening can be taken into account in the Gurson model provided a relevant calibration of the values of q_1 and q_2 is performed by void cells calculations. In fact, the description of cavity growth and coalescence using the GTN model formulation are dependent of q_1 , q_2 , f_c , δ and the mesh size. These parameters can be considered as material parameters taking into account the material viscosity so that provided they are accurately calibrated, the initial Gurson model formulation can probably also be used to describe void growth in high temperature deformation condition.

2. Comparison with the model of the present study

2.1. Modifications of the model

In the case of the present study, the strain hardening parameter m was determined from the value of the apparent Norton power-law exponent that is equal to 8.0 (i.e. $m = 0.125$) and the resulting expression of the **equation B.III.S1.5** was used to describe the cavity growth in the power-law creep regime.

In the case of the low stress diffusion creep regime (i.e. $m = 1$), the potential of **equation B.III.S1.8** was used. It was rewritten so that the elliptic potential could be easily recognised:

$$\phi = \frac{1}{(1 - fq_1)} \sigma_{eq}^2 + \frac{fq_1 q_2^2}{4(1 - fq_1)} \sigma_{kk} - \sigma^*{}^2 \quad (\text{eq. B.III.S1.9})$$

The fitted parameters of the first model, given in **table B.III.5**, were used so as to compare the two model formulations.

2.2 Single volume element calculations

Single volume element calculations were performed for various stress triaxiality ratios i.e. $\tau = 1/3, 1.1, 1.3$ and 1.8 corresponding to the stress triaxiality ratios encountered in the notched specimens experimentally tested. It allows to plot the evolution of porosity contributions as in **figure B.III.12** and the evolution of the creep time to failure versus the von Mises equivalent stress as in **figure B.III.13**. The corresponding results are plotted in **figures B.III.S1.1** and **B.III.S1.2** where the results given by the model presented in **chapter B.III** are also plotted.

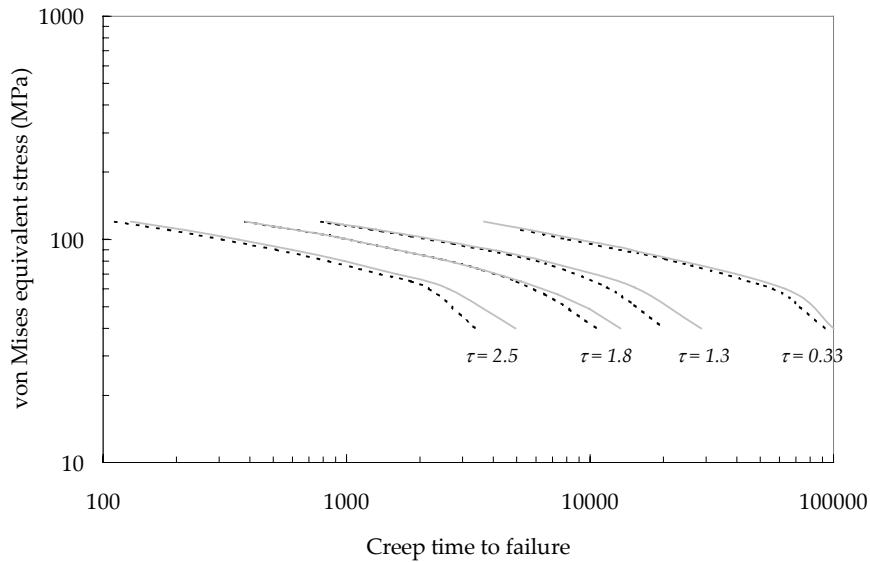


Figure B.III.S1.1. von Mises equivalent stress versus creep time to failure:

Single elements calculations for various stress triaxiality ratios (black interrupted lines = GTN model and grey lines = LPS model)

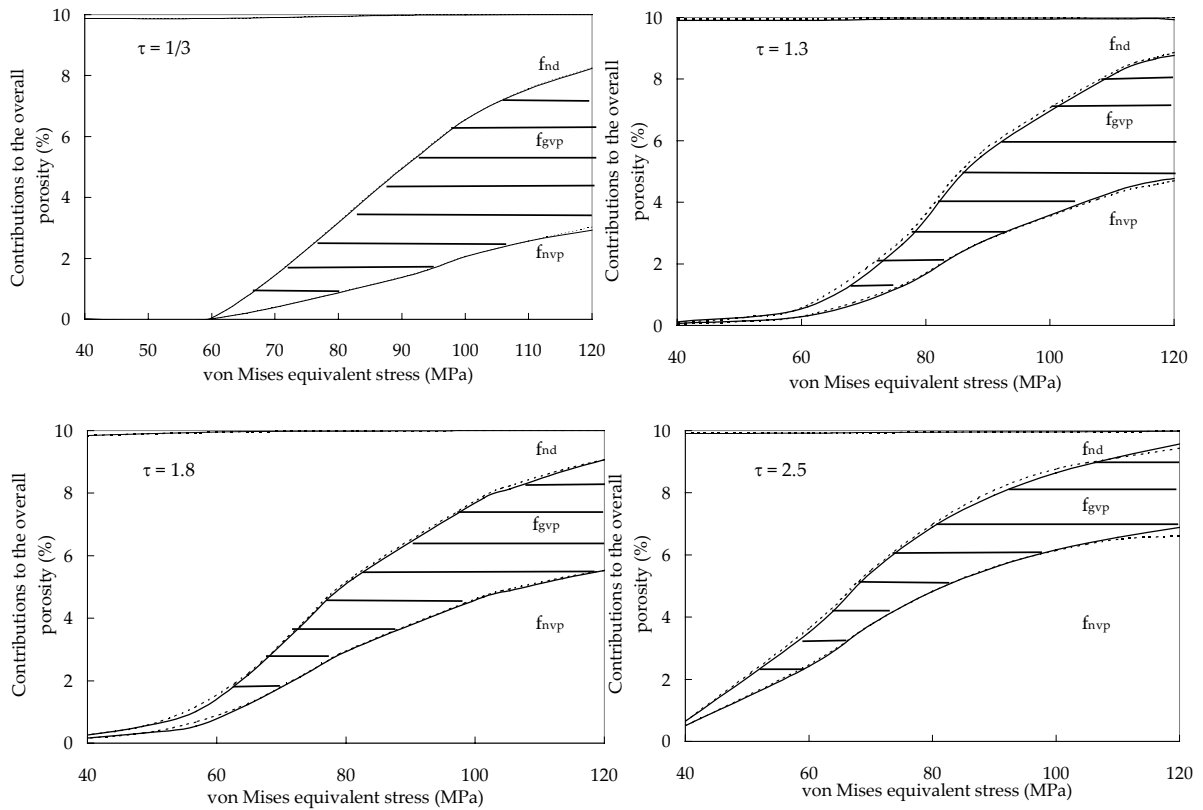


Figure B.III.S1.2. Contributions to the overall porosity at the onset of creep failure (i.e. $f_i = 0.1$): Single element calculations for various stress triaxiality ratio $\tau = 1/3$, $\tau = 1.3$, $\tau = 1.8$ and $\tau = 2.5$ (black interrupted lines = first model and grey lines = new model)

The following conclusions can be drawn from the comparison of the two models:

1. The evolution of the creep damage (i.e. nucleation and growth) is little affected in both the low and high stress creep regime.
2. Predicted creep lifetime are affected with using the new model especially in the low stress creep regime as the transition in creep damage mechanism is especially a little delayed (see figure B.III.S1.1).

2.3. Comparison of the two models for FE calculations on NC1.2 and NC0.25 specimens

The new proposed formulation of the model was also compared to the first model for creep notched specimens with radius of respectively 1.2 mm and 0.25 mm. The results are shown in **figures B.III.S1.3** and **B.III.S1.4** where the results of the first model are plotted in black lines and the results of the new model are plotted in grey lines.

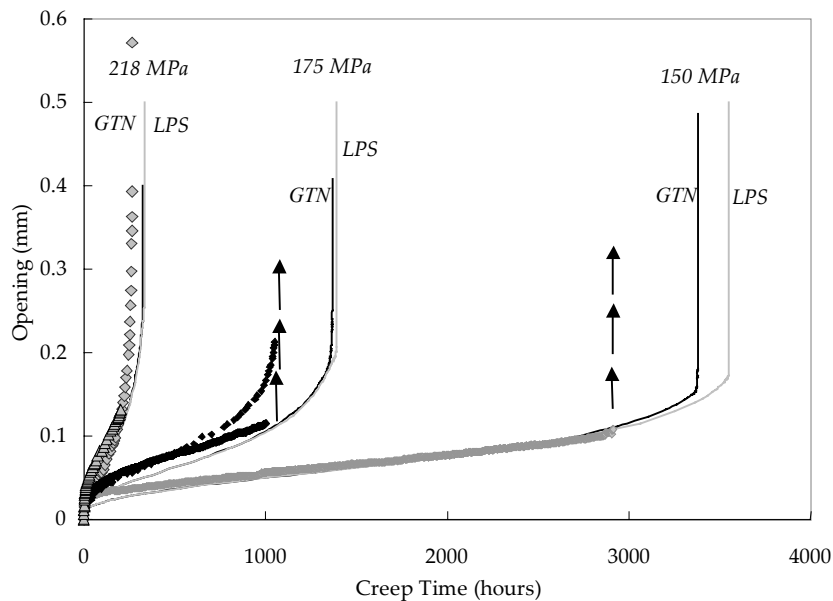


Figure B.III.S1.3. Experimental (symbols) and calculated (black lines for the first model and grey lines for the new model), creep curves for creep tests on NC1.2 specimens

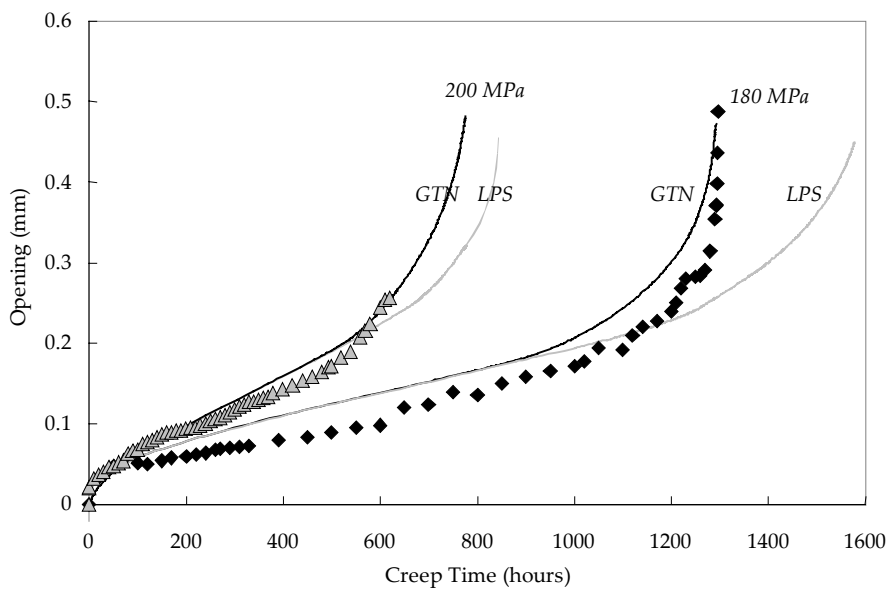


Figure B.III.S1.4. Experimental (symbols) and calculated (black lines for the first model and grey lines for the new model), creep curves for creep tests on NC0.25specimens

It can be evidenced that the cavity growth rate is decreased and the onset of coalescence is by consequence delayed with the new model which in accordance with the previous studies of Klocker and Tvergaard (2000 and 2003). This effect is all the more important than the stress triaxiality ratio is high. However, the curves predicted by using the new model are in quite good agreement with experimental results.

2.4. Comparison of the two models in terms of predictions of the creep lifetime

A comparison between the creep time to failure in SC and NC specimens predicted by using the GTN model and the LPS model is plotted in **figure B.III.S1.5**. It shows that the predictions given by the two models exhibit a quite good agreement for all kind of specimen geometry.

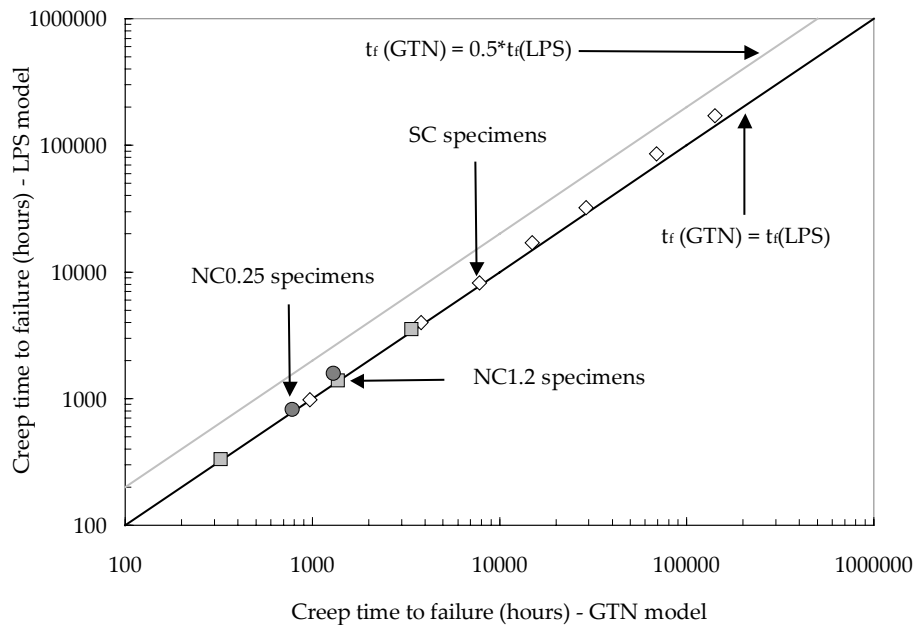


Figure B.III.S1.5. Creep time to failure given by the GTN model versus the creep time to failure given by the LPS model

To be in accordance with experimental data, the model integrating the description of cavity growth of the LPS model was refitted. As the predictions of the two models were quite similar in the high stress creep regime, it was chosen to fix the values of q_1 and q_2 , only the model parameters representing cavity nucleation in the low stress creep regime were refitted. It was found that for $A_d = 14.0$ and $B_d = 16.0$ the model integrating the description of cavity growth proposed by Leblond - Perrin - Suquet (1994), exhibit similar results than the model integrating the description of cavity growth proposed by Gurson - Tvergaard - Needleman (1984).

3. Conclusions

An improvement of the initial formulation of the multiple creep flow and damage model, which consist in using a description of cavity growth more adapted to viscoplasticity (i.e. LPS model rather than GTN model), was tested. Some differences were evidenced as the description of cavity growth by the LPS model leads to a short delay in the beginning of cavity coalescence especially in the low stress creep regime as already shown by void cells calculations in Klocker and Tvergaard (2000 and 2003). However, after a slight refit of the cavity nucleation model parameters in the low stress creep regime as $A_d = 14.0$ and $B_d = 16.0$, the results given by the two model formulation are very similar.

In the study of the base metal (in the present **Part B**), the initially proposed formulation of the model is conserved. Nevertheless, to ensure a description of cavity growth and coalescence more easily admitted for high temperature behaviour, the LPS model will be used in **Part C** and **Part D** of the present study.

References

- Gologanu M., Leblond J.B., Devaux J. (1995). Approximate models for ductile metals containing non spherical voids – Case of axisymmetric prolate ellipsoidal cavities. *Journal of mechanics and physics of solids*. **41(11)**. 1723-1754.
- Gologanu M., Leblond J.B., Devaux J. (1994). Approximate models for ductile metals containing non spherical voids – Case of axisymmetric oblate ellipsoidal cavities. *Journal of engineering materials and technology*. **116**. 291-297.
- Green R. (1972). A plasticity theory for porous solids. *International journal of mechanical sciences*. **14**. 215-224.
- Klocker H., Tvergaard V. (2000). Void growth and coalescence in metals deformed at elevated temperature. *International journal of fracture*. **106**. 259-276.
- Klocker H., Tvergaard V. (2003). Growth and coalescence of non-spherical voids in metals deformed at elevated temperature. *International journal of mechanical sciences*. **45**. 1283-1308.
- Leblond J.B., Perrin G., Suquet P. (1994). Exact results and approximate models for porous viscoplastic solids. *International journal of plasticity*. **10(3)**. 213-235.

Thomason P.F. (1985). Three dimensional model for the plastic limit loads at incipient failure of the intervoid matrix in ductile porous solids. *Acta Metallurgica*. **33(6)**. 1379-1389.

Tvergaard V., Needleman A. (1984). Analysis of the cup cone fracture in a round tensile bar. *Acta Metallurgica*. **32(1)**. 157-169.

Chapter B.IV. Use of the model to represent creep flow and damage behaviour for creep tests on CT and plate notched specimens

1. Experiments and results

Details about tests, experimental techniques and specimens geometry are given in *appendices A and B*.

1.1. Description of the tests

Creep tests on plate notched specimens (PNC) under vacuum of 10^{-3} Pa were also carried out. Those specimens have a gauge length of 3.8 mm, a minimum width of 5.6 mm and a minimum thickness of 2 mm. For those tests, load was applied using a mechanical electrical testing machine and elongation was continuously recorded. Temperature was monitored using one thermocouple spot welded on the specimen surface near the notch. The temperature gradient between bottom and top did not exceed 2°C . Moreover, grids in gold of a step of $20\ \mu\text{m}$ were engraved on specimens surface to investigate damage mechanisms and grain boundary sliding.

Two creep tests on compact tension specimens (CT), which were not pre-cracked, were also carried out. The minimum section of these specimens was $28 \times 10 = 280\ \text{mm}^2$. Notch radius was set to 0.25 mm in order to be consistent with tests on NC0.25 specimens.

1.2 Experimental results

For tests on PNC specimens stress holding values were from 170 MPa to 120 MPa and corresponding times to failure between 150 hours and 1,800 hours (results of these tests are also reported in **appendix A** in **table A.A.9**). The experimental curves are given in **figure B.IV.1**.

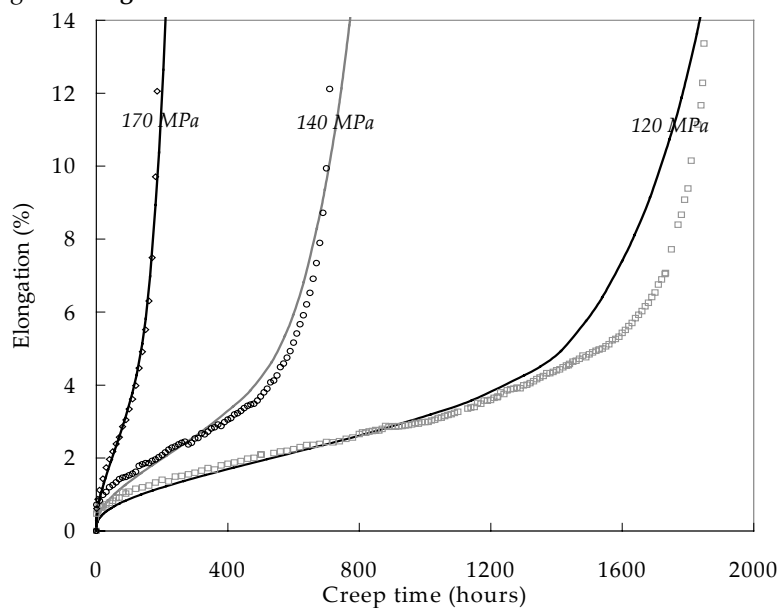


Figure B.IV.1. Creep tests on PNC specimens : Experimental (symbols) and simulated (lines) curves.

For tests on CT specimens, applied engineering stresses (load divided by the initial area of the minimum section) were of 30 MPa and 25 MPa and the corresponding creep times were respectively of 1,200 and 2,700 hours (results of these tests are also reported in **appendix A** in **table A.A.11**). Using the formulas established by Rice and Rosengreen (1968) and Hutchinson (1968), it corresponds to stress intensity factors at the crack front of $24.6\ \text{MPa}\text{m}^{1/2}$ for $\sigma = 30\ \text{MPa}$ and $20.5\ \text{MPa}\text{m}^{1/2}$ for $\sigma = 25\ \text{MPa}$ ($a/w = 0.3$). Creep curves are shown in **figure B.IV.3**. Note that due to a breakdown of the furnace the creep test carried out with an applied engineering stress of 25 MPa was interrupted and then restart after having repaired the furnace.

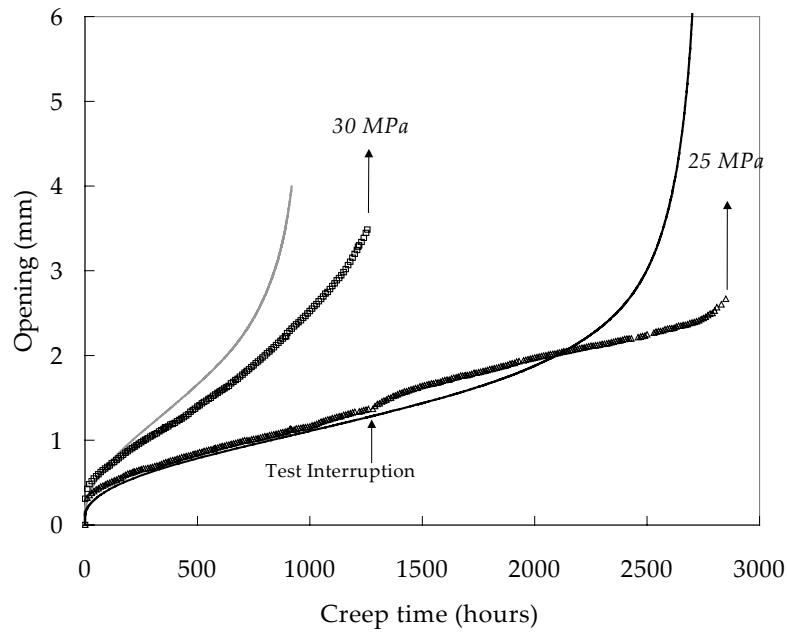


Figure B.IV.2. Creep tests on CT specimens : Experimental (symbols) and simulated (lines) curves

1.3. Interpretation of creep tests on CT specimens

Creep tests were interrupted before specimens failure. The specimens were then fractured by load controlled fatigue testing at room temperature. The frequency was set to 20 Hz, the maximum and minimum values of the applied engineering stress were respectively set to 40 MPa and 30 MPa with a triangular signal. The oxidation of the specimen surface allowed to determine the crack propagation area by optical observations. The two crack propagation area are shown in figure B.IV.3.

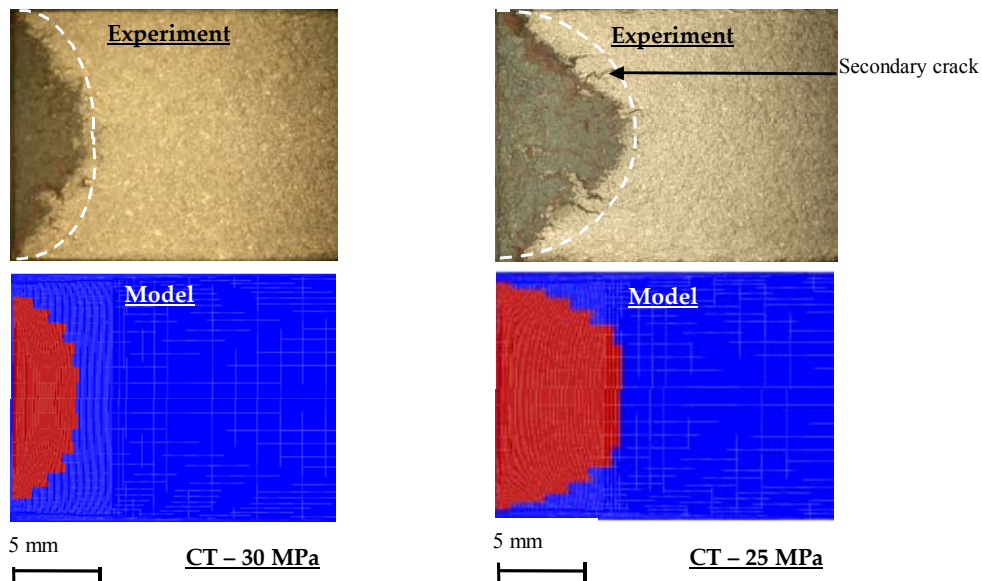


Figure B.IV.3. Optical micrograph of crack propagation areas for creep tests on CT specimens (a) 30 MPa and (b) 25 MPa and comparison with results of FE calculations

The crack propagation was investigated (see figure B.IV.4). It was larger at the centre of the specimen (tunnelling effect) as plane strain conditions (high stress triaxiality ratio) prevails at this location whereas, plane stress conditions (low stress triaxiality ratio) are met at the free surface. The electrical resistivity technique was used to determine the time to the crack initiation and to follow the crack propagation. However, due to the tunnelling effect, the time to crack initiation was hardly detectable using the electrical resistivity technique. It is assumed that the variation of resistivity due to the crack propagation only becomes measurable when the crack reaches the specimens edges so that the measured time to crack initiation are obviously an overestimation of the real one.

SEM investigations of damage at the centre of the specimens were performed on polished cross sections. First observations allows to determine the direction of the crack propagation at the centre of the specimen:

1. For $\sigma = 30$ MPa, the crack was found at 30° from the notch axis.
2. For $\sigma = 25$ MPa, the crack was found to follow the direction of the notch axis.

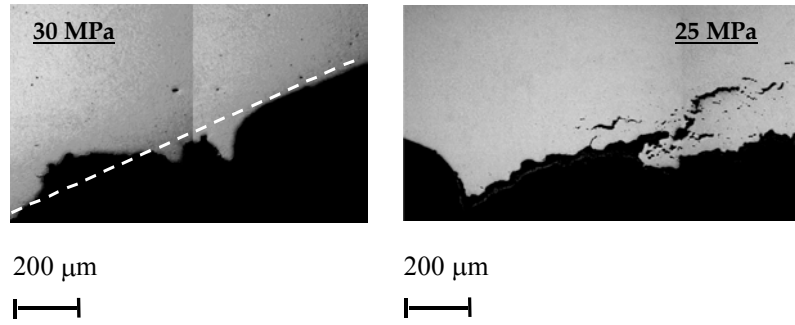


Figure B.IV.4. Direction of the crack propagation

2. Three dimensional FE calculations – Validation of the model

3D calculations were performed in all cases as the stress state is neither plane-stress nor plane-strain. As the mesh design plays a key role in calculations involving crack initiation and propagation, the mesh size of $100\mu\text{m}$ used for the model identification was chosen. Linear element with selective integration were used (see Hughes (1980)) to avoid high pressure variations into elements due to the incompressibility of the plastic strain. The specificity of these elements is that the interpolation matrix $[B]$, which allows to calculate the strain deformation from the nodes displacement, is divided into a dilatation and a deviatoric contribution. It follows that the volume variation of the element remains constant.

2.1. FE calculations for tensile tests on PNC specimens

As can be shown in **figure B.IV.5** the creep strain is maximum near the notch and the stress triaxiality ratio at the centre of the specimen. The comparison between experimental and calculated creep curves which is given in **figure B.IV.1** shows that the agreement between experiment and model prediction is quite satisfactorily.

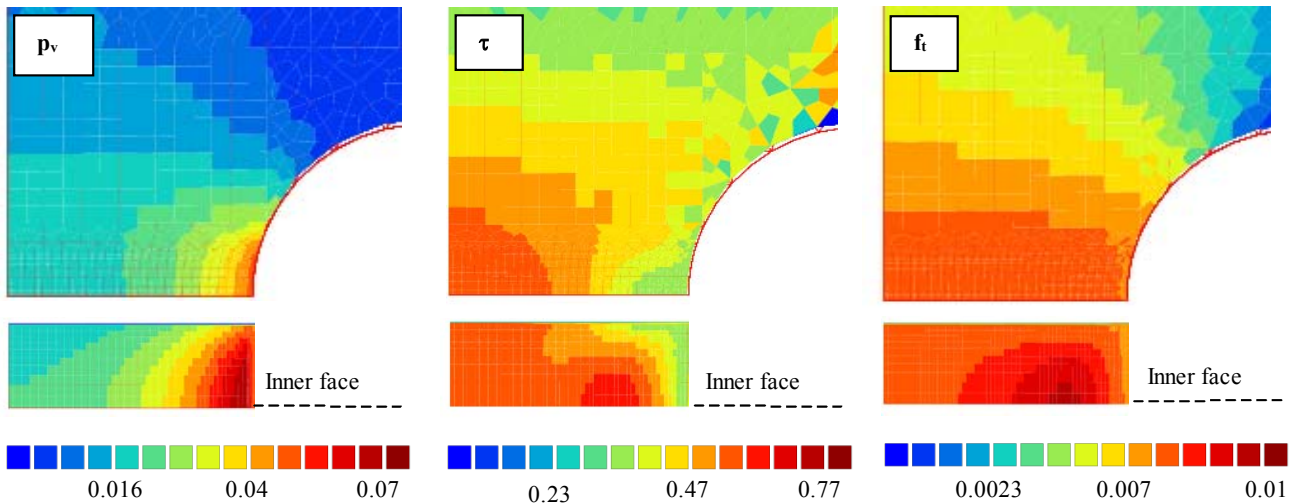


Figure B.IV.5. Results of FE calculations for PNC specimens

2.2. FE Calculations for Compact Tension (CT) creep tests

Attention was first focused on analysing the mechanical fields in the CT specimens. It was evidenced that the von Mises equivalent stress is maximum near the notch and near the free surface whereas the stress triaxiality ratio is maximum $500\mu\text{m}$ far from the notch and at the centre of the specimen (see the maps in **figure B.IV.6a** and **B.IV.6b**). Note also that the stress triaxiality ratio locally reaches the maximum value of 1.35 at the end of the loading stage.

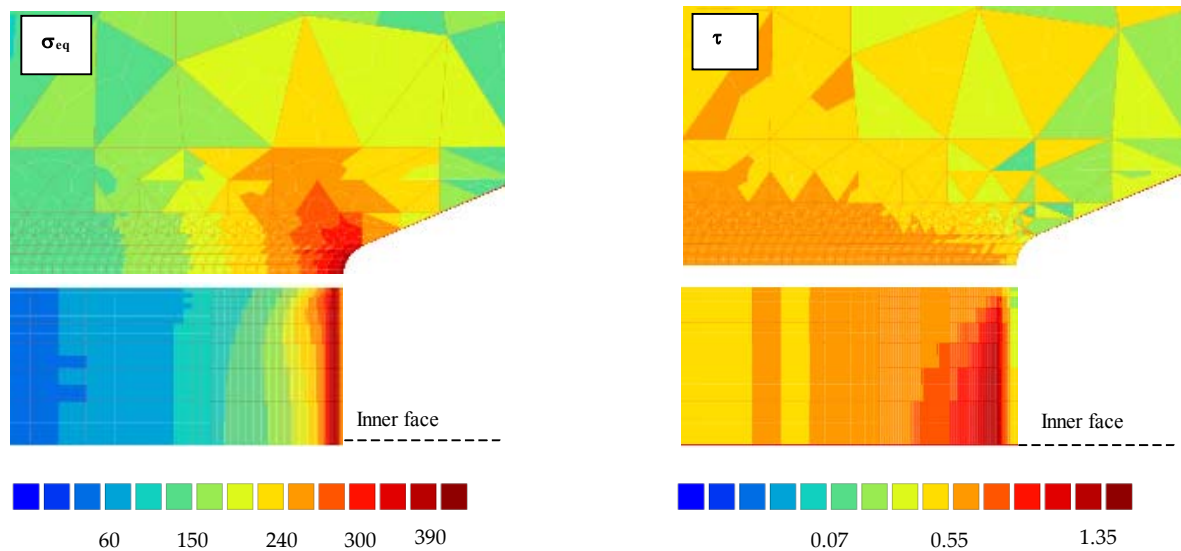


Figure B.IV.6. Fields of the equivalent von Mises stress and the stress triaxiality ratio at the end of the loading stage ($\sigma = 25$ MPa)

The evolution of the porosity in the CT specimen was investigated. It was shown that damage develops mainly 500 μm far from the notch and at the centre of the specimens where plane strain conditions are encountered (see figure B.IV.6). Then, the comparison of figure B.IV.3 evidences a very satisfactory agreement between the experimentally observed and calculated crack propagation areas even if the shape of the crack front is slightly different than that experimentally observed. For the comparison, calculations results were taken for the overall displacement given by the macroscopic curve at which creep tests were experimentally stopped.

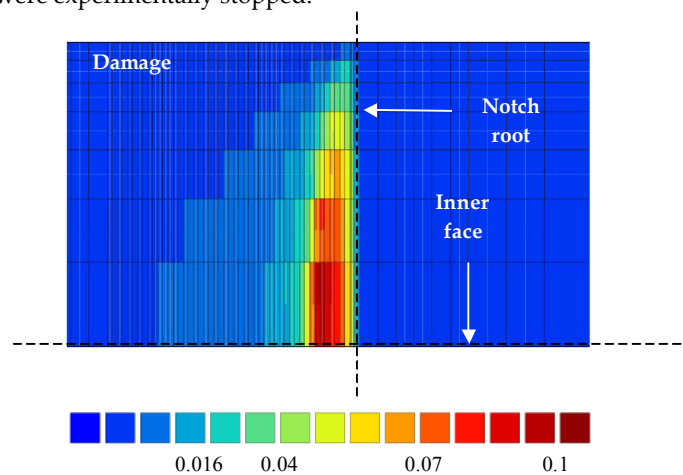


Figure B.IV.7. Location of damage development in CT specimens

2.3. Comparison of the results of the micromechanical model of the present study with the predictions of the global approach to fracture

As well as for low temperature fracture, master curves plotted in the framework of the rupture mechanics are currently used for designing purposes. Therefore, the main aspects of this approach usually called “the global approach to fracture” are reminded in the following. The accuracy of such methods with respect to the results of chapter B.III is also discussed.

2.3.1. Presentation of the global approach to fracture

The global approach to fracture is based on the description of the mechanical fields at the crack tip throughout a loading parameter whose expression depends on the creep flow behaviour:

1. If plasticity is confined the significant parameter is the intensity factor “K”.
2. If the plastic zone at the crack tip is wider, the relevant parameter is the Rice integral “J” (Rice (1968)) and the analytical expressions of the stress and strain fields at the crack tip are well described by the Hutchinson (1968), Rice and Rosengreen (1968) “HRR” expressions.

- In the high temperature creep regime, a viscoplastic zone develops at the crack tip inside the initial plastic zone. The accurate parameter C^* was introduced by Riedel and Rice (1980) with distinguishing C_h^* for the primary creep regime and C^* for the steady state creep regime.

During the creep test, the relevant loading parameter also depends on the creep time due to stress relaxation at the crack tip (see **figure B.IV.8**). Note also that Adachi et al (2004) have recently introduced the new Q^* parameter which is derived from the Q parameter in plasticity (O'Dowd and Shih (1991, 1992)) to represent creep crack growth in a CrMoV steel.

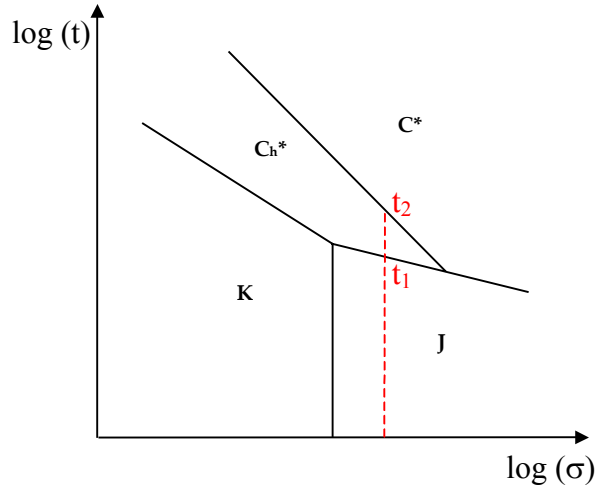


Figure B.IV.8. Fracture mechanics parameters

For the sake of completeness, the J-integral from which the expression of both C_h^* and C^* are derived is given. J is described by Rice (1968) as the energy release due to the propagation of a crack of length, a , as:

$$J = \int_0^P \frac{\partial \delta}{\partial a} dP \quad (\text{eq. B.IV.1})$$

where P is the applied load and δ is the crack opening.

The J-integral can also be defined as a contour integral around the crack tip:

$$J = \int_{\Gamma} w dy - \vec{T} \left(\frac{\partial \vec{u}}{\partial x} \right) ds \quad (\text{eq. B.IV.2})$$

where Γ is the contour around the crack tip, \vec{T} is the stress acting on the contour as $\vec{T} = \sigma \vec{n}$ with n the normal to the contour, \vec{u} is the displacement vector and w is given by:

$$w = \int \sigma_{ij} d\epsilon_{ij} \quad (\text{eq. B.IV.3})$$

Three main methods for calculating J , C_h^* and C^* can be distinguished (Note that J , C_h^* and C^* are calculated in a similar way except that the description of the material creep flow behaviour changes):

- The method proposed by Kumar et al (1981) which was integrated in the EPRI design code.
- The method proposed by Ainsworth (1984) which was integrated in the R5 procedure.
- The method of the Ecole des Mines de Paris (EMP) developed by Piques (1989).

As already shown by Pineau (1992) and in **figure B.IV.8**, all the creep stages can not be described with only one loading parameter as the relevant loading parameter is not the same for plasticity (J) primary (C_h^*) and secondary creep (C^*). Therefore, the description of fracture in the high temperature creep regime is often limited to the establishment of correlations between the loading parameter in the steady state creep regime, C^* , and both the time to the crack initiation T_i and the steady state crack propagation rate $\dot{\delta}$. Depending on the material behaviour either the creep time to the crack initiation or the steady state creep crack growth can be chosen as the relevant parameter. For example, it will be shown in the following that the creep time to the crack initiation is the longest stage for 9Cr1Mo-NbV steels so that it can be chosen as the relevant parameter and the steady state crack propagation stage can be neglected.

2.3.2. Use of the global approach of fracture to represent creep crack initiation and growth in the steady state creep regime

In the following, the developments of the EMP method will be used so that the expressions of C^* introduced by Piques (1989) are reminded. In the steady state creep regime, the creep strain rate can be described as:

$$\dot{\epsilon}_{vp,s} = \eta \sigma^{n_2} \quad (\text{eq. B.IV.4})$$

where n_2 and η are material parameters with $n_2 = 8.4$ and $\eta = 9.95 \cdot 10^{-23} \text{ h}^{-1} \text{MPa}^{-n_2}$. For CT specimen, the expression of C^* determined by Piques (1989) is:

$$C^* = \frac{2n_2 \alpha \eta P}{(n_2 + 1) B} \left(\frac{p}{m \left(\frac{a}{W} \right) B W} \right)^{n_2} \quad (\text{eq. B.IV.5})$$

where B is the specimen thickness, a is the crack length and W is the maximum distance of crack propagation (see **figure B.IV.9**). The function $m \left(\frac{a}{W} \right)$ is given by:

$$m \left(\frac{a}{W} \right) = \left[\left(1 + \frac{a/W}{q-1} \right)^2 + \frac{(1-a/W)^2}{q-1} \right]^{1/2} - \left(1 + \frac{a/w}{q-1} \right) \quad (\text{eq. B.IV.6})$$

where $q = 1.5876$ in the case of the plane strain hypothesis and $q = 2.0$ in the case of plane stress hypothesis.

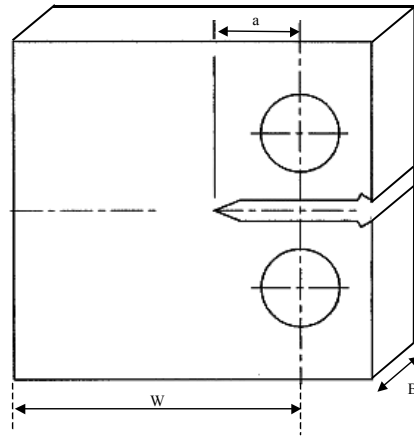


Figure B.IV.9. Geometry of CT specimens

For NC0.25 axisymmetric notched specimens, C^* is given by:

$$C^* = \left(\frac{n_2 - 1}{n_2 + 1} \right) \frac{P \eta}{2 \pi R} \left(\frac{P}{\pi R b} \right)^{n_2} \quad (\text{eq. B.IV.7})$$

where b and R are respectively the maximum and minimum radius of the specimen (see **figure B.IV.10**).

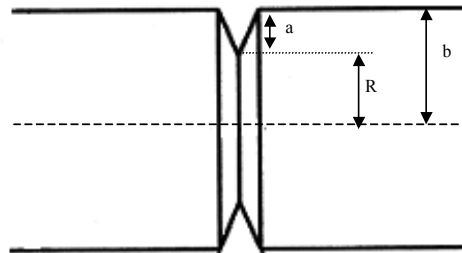


Figure B.IV.10. Geometry of NC0.25 specimens

The loading parameters could be calculated and correlated with the time to crack initiation (see **table B.IV.1**). It can first be noticed that the time to the crack initiation corresponds to 2/3 of the overall creep lifetime.

Geometry	P (N)	C* (plane strain)	C*(plane strain)	Ti (Experiments)	Ti (Calculations)
CT	8400	27.1	1.244	/	318 hours
CT	7000	4.88	0.224	1340 hours	828 hours
NC0.25	37500	22.32		410 hours	423 hours
NC0.25	30500	6.53		775 hours	733 hours
NC0.25	27500	2.16		1,250 hours	1,430 hours
NC0.25	24500	0.615		/	2,480 hours
NC0.25	21500	0.144		/	3,700 hours
NC0.25	18500	0.0253		/	5,150 hours

Table B.IV.1. The loading parameters C* and times to the crack initiation for CT specimens

A single representation of the evolution of the time to crack initiation versus C* was plotted using experimental data from NC0.25 and CT specimens (see figure B.IV.9). Note that the time to the crack initiation was hardly experimentally measured for CT specimens due to a tunnelling effect. The experimental creep time to the crack initiation reported for the CT specimen in figure B.IV.11, corresponds to the time for which the crack which initiated at the centre of the specimen, reaches the edges of the specimen.

For comparison and to validate the model presented in chapter B.III, the predictions of the model are also plotted. First, a correlation between Ti and C* was fitted as:

$$T_i = \lambda_1 \langle C^* \rangle^{-0.45} \quad (\text{eq. B.IV.8})$$

where λ_1 is a material parameter and C* is given by equation B.IV.4. Note that the fitted law is consistent with previous results of Tan et al (2001).

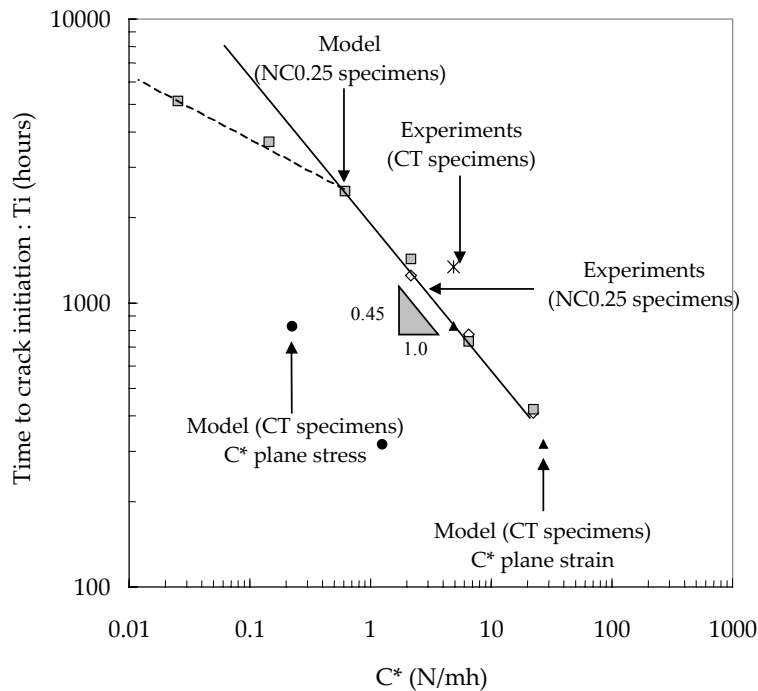


Figure B.IV.11. Correlation Ti-C* for creep tests on CT and NC0.25 specimens at 625°C

As the crack started from the centre of the specimens for CT specimens (i.e. where plane strain conditions are encountered), the representation of figure B.IV.11, shows that only a single correlation is necessary to represent the evolution of the time to the crack initiation for NC0.25 and CT specimens. It is also very interesting to see that the model well predicts creep crack initiation in NC0.25 specimens. Another interesting point is that the model predicts that the correlation given in equation B.IV.5 is no more valid for very low values of C*. This is very important as it corresponds to the premature rupture due to a change in deformation and damage mechanisms which was evidenced in chapter B.III. The global approach to fracture mechanics is not able to represent such a change unless correlations between C* and both the time to the crack initiation and the crack propagation rate are previously fitted in the diffusion low stress creep regime.

The steady state crack propagation rate were also experimentally measured for NC0.25 specimens as Hourlier (1982) determined a correlation between the crack length (in mm) and the resistivity measurements for this specimen geometry:

$$\frac{\phi_0}{\phi} = -0.5832 + 1.7497 \left(\frac{V}{V_0} \right)^{0.5} - 0.1644 \left(\frac{V}{V_0} \right) \quad (\text{eq. B.IV.9})$$

where, V and V_0 are respectively the current and initial resistivity and, ϕ and ϕ_0 are respectively the current and initial minimum diameter of the specimen. The actual crack length is given by:

$$a = \frac{\phi_0 - \phi}{2} \quad (\text{eq. B.IV.10})$$

A correlation between $\dot{\delta}_{\text{exp}}$ and C^* could then be determined (see **figure B.IV.12**):

$$\dot{\delta}_{\text{exp}} = \chi (C^*)^{0.4} \quad (\text{eq. B.IV.11})$$

where χ is a material parameter. This fit is consistent with the results of Shibli (2001). The evolution of the crack propagation was also deduced from FE calculations. It led to steady state crack propagation rate twice higher than those experimentally measured

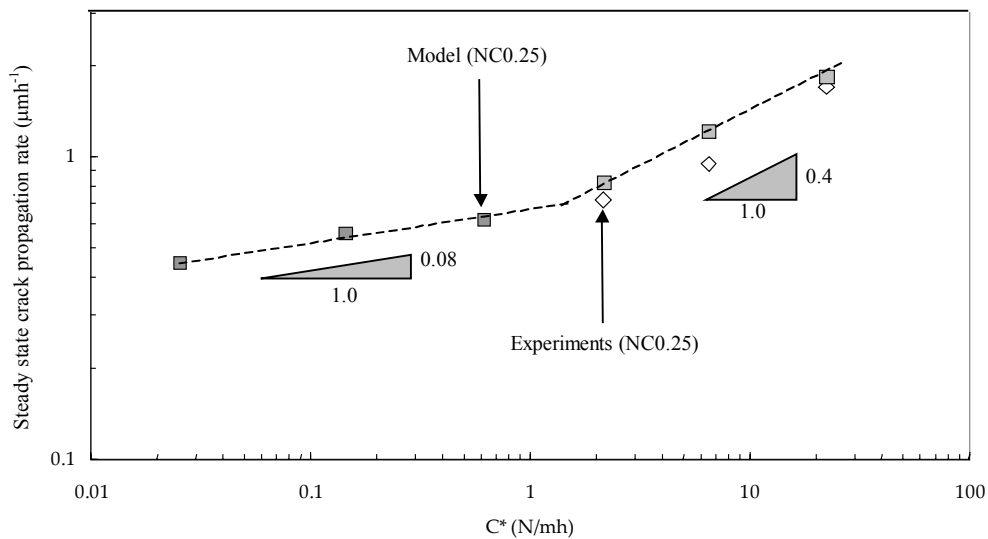


Figure B.IV.12. Steady state crack propagation rate versus the loading parameter C^ for stable crack propagation tests on NC0.25 specimens – Comparison between model and experiments*

The comparison of experimental data with the model of the present study shows a quite good agreement even if it is not as good as for the time to the crack initiation. In fact the crack propagation is very dependent on the coalescence law and especially on f_c . The coalescence law used in the model has largely been discussed by Zhang et al (2000) and Pardoen and Hutchinson (2000). Both underlined that this formulation may give bad results for high stress triaxialities as the crack initiation and growth strongly depend on the value of f_c . Zhang et al (2000) consider that f_c should be no longer a material parameter and a description of coalescence derived from that of Thomason (1985) is preferable. All the procedure to integrate the Thomason formalism is described in Zhang et al (2000) and Pardoen and Hutchinson (2000), and it would certainly be of great interest to integrate it to the model of the present study.

3. Conclusions

The ability of the model to represent creep flow and damage behaviour for CT and PNC specimens was shown. The model particularly succeeds in predicting creep crack growth in compact tension specimens.

The model also underlines the limits of the global approach to fracture which is supported by no real physical basis especially in terms of damage mechanisms. The master curves $T_i - C^*$ or $\dot{\delta} - C^*$ are especially not valid at low stresses. The great advantage of the model developed in the present study, in the framework of the local approach to fracture with introducing a strong coupling with the mechanical behaviour, is that it allows to continuously follow the evolution of a crack from its initiation to its steady state propagation until the specimen failure and from high stress to low stress.

References

- Adachi T., Yokobori A.T., Tabuchi M., Fuji A., Yokobori T., Nikbin K. (2004). The proposal of Q^* parameter and derivation of the law of creep crack growth life for a round bar specimen with a circular notch for CrMoV steel. *Materials at high temperature*. **21(2)**. 95-100.
- Ainsworth R.A (1984). The assesment of defects in structures of strain hardening material. *Engineering fracture mechanics*. **19(4)**. 633-642.
- Hourlier F. (1982). Propagation de fissures de fatigue sous sollicitations polymodales. *PhD Thesis – Ecole Nationale Supérieure des Mines de Paris, Paris, France*.
- Hughes T.J.R. (1980). Generalization of selective integration procedures to anisotropic and non linear media. *International journal of numerical methods and engineering*. **14**. 1413-1418.
- Hutchinson J. W. (1968). Singular behaviour at the end of a tensile crack in a hardening material. *Journal of mechanics and physics of solids*. **16**. 13-31.
- Kumar V., German M.D., Shih C.F. (1981). An engineering approach for elastic plastic fracture. *EPRI Report NP1931*.
- O'Dowd N.P., Shih C.F. (1991). Family of crack tip fields characterised by a triaxiality parameter I. Structure of fields. *Journal of the mechanics and physics of solids*. **39**. 898-1015.
- O'Dowd N.P., Shih C.F. (1992). Family of crack tip fields characterised by a triaxiality parameter II. Fracture applications. *Journal of the mechanics and physics of solids*. **40**. 939-963.
- Pardoën T., Hutchinson J. (2000). An extended model for void growth and coalescence. *Journal of mechanics and physics of solids*. **48(12)**. 2467-2512.
- Piques R. (1989). Mécanique et mécanismes de l'amorçage et de la propagation de fissures en viscoplasticité dans un acier austénitique inoxydable. *PhD Thesis – Ecole Nationale Supérieure des Mines de Paris, Paris, France (in French)*.
- Pineau A. (1992). Assessment procedures for defects in the creep range. *High Temperature structural design Larsson L.H. editor ESIS 12, Mechanical engineering publications*. 355-397.
- Rice J.R (1968). Path independant integral and the approximate analysis of strain concentration by notches and cracks. *Journal of applied mechanics*. **35**. 379-386.
- Rice J.R., Rosengreen G.F. (1968). Plane strain deformation near a crack tip in a power-law hardening material. *Journal of mechanics and physics of solids*. **16**. 1-12.
- Shibli I.A. (2001). Overview of the HIDA project. *International journal of pressure vessels and piping*. **78(11-12)**. 729-735.
- Simo J.C., Taylor R.L., Pister K.S. (1985). Variational and projections method for the volume constraint in the finite deformation elastoplasticity. *International journal of numerical methods and engineering*. **48**. 101-118.
- Tan M, Celard N.J.C., Nikbin K.M., Webster G.A. (2001). Comparison of creep crack initiation and growth in four steels tested in HIDA. *International Journal of Pressure Vessels and Piping*. **78**. 737-747.
- Thomason P.F. (1985). Three dimensional model for the plastic limit loads at incipient failure of the intervoid matrix in ductile porous solids. *Acta Metallurgica*. **33(6)**. 1379-1389.
- Zhang Z.L., Thaulow C., Odegaard J. (2000). A complete Gurson model approach for ductile fracture. *Engineering Fracture Mechanics* (2000). **67**. 155-168.

Chapter B.V. Formulation of a locally coupled version of the model

The transposition of the multiple damage and deformation mechanisms model in another FE software is not easy. Therefore, a simple model using the mechanical response of the undamaged material was developed in order to be used in a post processing treatment. The creep time to failure was determined using a local failure criteria. This version of the model was implemented as a post processor in Zebulon and in the FE software of the Commissariat à l'Energie Atomique, CASTEM by Lejeail and Pluyette (2004).

1. General formulation of the locally coupled model for the GTN model

The model is a simplification of the fully coupled model described in **chapter B.III** in which the cavity growth rate was derived from the Gurson formulation as already explained in Decamp et al (1997) and more recently in Ragab (2004). Damage analysis is carried out by a post-processor routine on elasto-viscoplastic calculations at every gauss point at every time increment. The data given by the elasto-viscoplastic calculations and used by the post-processor are:

1. The local matrix viscoplastic strain which is equal to the von Mises equivalent cumulated viscoplastic strain computed on the structure.
2. The ratio $\frac{\sigma_{kk}^*}{\sigma_m^*}$ used in the porous model which is taken equal to the total macroscopic stress triaxiality ratio.

Mathematical derivation are needed to compute the value of the total porosity, f_t . Note that in the locally coupled version the model, the acceleration factor δ_c (i.e. the effective porosity f^*) is not used.

The local material behaviour is described by the Gurson criterion as:

$$\phi_m = \frac{\sigma_{eq}^2}{\sigma_m^{*2}} + 2q_1 f_t \cosh\left(\frac{q_2}{2} \frac{\sigma_{kk}^*}{\sigma_m^*}\right) - 1 - q_1^2 f_t^2 \quad (\text{eq. B.V.1})$$

where σ_{eq} is the von Mises equivalent stress and σ_{kk} is the trace of the stress tensor. q_1 and q_2 are model coefficients which are assumed to be constant and σ_m^* is the flow stress of the matrix. The plastic strain rate tensor can be calculated assuming the normality rule:

$$\dot{\underline{\varepsilon}} = (1 - f_{tot}) \dot{\lambda} \left(\frac{\partial \phi_m}{\partial \underline{\sigma}} \right) \quad (\text{eq. B.V.2})$$

with in the case of isotropic hardening,

$$\frac{\partial \sigma_{eq}}{\partial \underline{\sigma}} = \frac{3}{2} \frac{\bar{s}}{\sigma_{eq}} \quad (\text{eq. B.V.3})$$

and,

$$\frac{\partial \sigma_m^*}{\partial \underline{\sigma}} = \frac{\partial \sigma_m^*}{\partial \sigma_m} \frac{\partial \sigma_m}{\partial \underline{\sigma}} + \frac{\partial \sigma_m^*}{\partial \sigma_{eq}} \frac{\partial \sigma_{eq}}{\partial \underline{\sigma}} = \frac{\partial \sigma_m^*}{\partial \sigma_m} \bar{1} + \frac{3}{2} \frac{\bar{s}}{\sigma_{eq}} \frac{\partial \sigma_m^*}{\partial \sigma_{eq}} \quad (\text{eq. B.V.4})$$

so that finally:

$$\dot{\underline{\varepsilon}} = (1 - f_{tot}) \dot{\lambda} \left(\frac{3\bar{s}}{\sigma_m^{*2}} + \frac{q_1 q_2 f_t}{\sigma_m^*} \sinh(x) \bar{1} \right) \quad (\text{eq. B.V.5})$$

where, \bar{s} is the deviatoric part of the stress tensor, f_t is the total porosity and:

$$x = \frac{3}{2} \frac{q_2 \sigma_m^*}{\sigma_m} \quad (\text{eq. B.V.6})$$

where σ_m^* will be taken as the von Mises equivalent stress for the non damaged material.

$\dot{\lambda}$ is the plastic multiplier that is calculated assuming that the macroscopic plastic dissipation is equal to the matrix dissipation:

$$\underline{\sigma} : \dot{\underline{\varepsilon}} = (1 - f_t) \dot{\varepsilon}_{eq} \sigma_m^* \quad (\text{eq. B.V.7})$$

so that,

$$\dot{\lambda} = \frac{\dot{\sigma}_m}{2 \left(\frac{\sigma_{eq}^2}{\sigma_m^2} + q_1 f_t x \sinh(x) \right)} \dot{\epsilon}_{eq} \quad (\text{eq. B.V.8})$$

The evolution of the porosity is given by the mass conservation and the nucleation of porosity. The evolution of porosity associated to the viscoplastic flow 'm' is :

$$\dot{f}_m = (1 - f_t) \text{trace}(\dot{\underline{\epsilon}}) + \dot{f}_{n,m} \quad (\text{eq. B.V.9})$$

with the nucleation kinetics (see **chapter B.III**):

$$\dot{f}_{n,m} = (A_m + B_m \tau^{\alpha_m}) \dot{\epsilon}_{eq} \quad (\text{eq. B.V.10})$$

where τ is the stress triaxiality ratio.

and the total porosity:

$$f_{tot} = \sum_m f_m \quad (\text{eq. B.V.11})$$

Assuming the yielding condition given by the Gurson-Tvergaard-Needleman model: $\phi=0$, the evolution of the porosity is given by:

$$\dot{f}_m = (1 - f_t) F(x, f_t) + \dot{f}_{n,m} \quad (\text{eq. B.V.12})$$

$$\text{with, } F(x, f_t) = \frac{3}{2} \frac{q_1 q_2 f_t (1 - f_t) \sinh(x)}{1 + q_1 f_t x \sinh(x) - 2q_1 \cosh(x) + q_1^2 f_t^2} \quad (\text{eq. B.V.13})$$

2. General formulation of the locally coupled model for the LPS model

The plastic strain rate tensor is calculated assuming the normality rule with using the potential of the LPS model (see **equation B.III.S1.5**) so that:

$$\dot{\underline{\epsilon}} = (1 - f_{tot}) \dot{\lambda} \left[\frac{3\bar{s}}{\sigma_m^2} + \frac{q_1 q_2 f_t}{\sigma_m} (1 + m) x^m (h_m(x))^{(1-m)} \left(\bar{1} - \frac{\bar{1}}{(h_m(x))^2} \right) \right] \quad (\text{eq. B.V.14})$$

$$\text{where, } h_m(x) = [1 + mx^{(1+m)}]^{1/m} \quad (\text{eq. B.V.15})$$

The plastic multiplier is now given by:

$$\dot{\lambda} = \frac{\dot{\sigma}_m}{2 \left[\frac{\sigma_{eq}^2}{\sigma_m^2} + q_1 f_t x (1 + m) x^m (h_m(x))^{(1-m)} \left(\bar{1} - \frac{\bar{1}}{(h_m(x))^2} \right) \right]} \dot{\epsilon}_{eq} \quad (\text{eq. B.V.16})$$

The evolution of the porosity is expressed as:

$$\dot{f}_m = (1 - f_t) F_2(x, f_t) + \dot{f}_{n,m} \quad (\text{eq. B.V.17})$$

with,

$$F_2(x, f_t) = \frac{3}{2} \frac{q_1 q_2 f_t (1 - f_t) (1 + m) x^m (h_m(x))^{(1-m)} \left(\bar{1} - \frac{\bar{1}}{(h_m(x))^2} \right)}{1 - q_1 f_t \left(h_m(x) + \frac{1-m}{1+m} \frac{1}{h_m(x)} \right) + q_1 f_t x (1 + m) x^m (h_m(x))^{(1-m)} \left(\bar{1} - \frac{\bar{1}}{(h_m(x))^2} \right) + q_1^2 f_t^2 \left(\frac{1-m}{1+m} \right)} \quad (\text{eq. B.V.18})$$

3. General formulation of the locally coupled model for the elliptic model

The plastic strain rate tensor is calculated assuming the normality rule with using the potential of the elliptic model (see **equation B.III.S1.9**) so that:

$$\dot{\underline{\epsilon}} = (1 - f_t) \dot{\lambda} \left(3\bar{s} \frac{1}{(1 - f_t q_1)} + \frac{f_t q_1 q_2^2}{4(1 - f_t q_1)} \bar{1} \right) \quad (\text{eq. B.V.19})$$

Therefore, the plastic multiplier is expressed as:

$$\dot{\lambda} = \frac{\dot{\sigma}_m^*}{2 \left(\frac{\sigma_{eq}^2}{\sigma_m^*} C + \sigma_m^* F \right)} \dot{\epsilon}_{eq} \quad (\text{eq. B.V.20})$$

where,

$$C = \frac{1}{(1 - f_t q_1)} \quad (\text{eq. B.V.21})$$

and,

$$F = \frac{f_{tot} q_1 q_2^2}{4(1 - f_t q_1)} \quad (\text{eq. B.V.22})$$

The evolution of the porosity is given by:

$$\dot{f}_m = (1 - f_t) F_3(x, f_t) + \dot{f}_{n,m} \quad (\text{eq. B.V.23})$$

with,

$$F_3(x, f_t) = \frac{F(1 - f_t)}{F(\sigma_m^* - \sigma_m) + \sigma_m^*} \quad (\text{eq. B.V.24})$$

4. Post calculations using the GTN model

4.1. Procedure

The method has consisted in performing FE calculations using constitutive equations for the non damaged material. Two creep flow models can be used. They are based on:

1. Two inelastic contributions to the strain rate tensor: $\dot{\epsilon} = \dot{\epsilon}_e + \dot{\epsilon}_{vp} + \dot{\epsilon}_d$. This model is referred as “model 2M” in the following.
2. Only one inelastic contribution to the strain rate tensor: $\dot{\epsilon} = \dot{\epsilon}_e + \dot{\epsilon}_{vp}$. This model is referred as “model 1M” in the following. This representation is proposed as models including two inelastic contributions are not available in all the finite elements codes.

Although, one inelastic contribution to the strain rate tensor is used for the model 1M, for the two models, the two damage mechanisms i.e. viscoplastic and diffusion, are considered. Using the relationship of **equations B.V.24** and **B.V.25**, the evolution of porosity were determined as:

1. For the model 2M

$$\begin{aligned} df_{n,vp} &= (A_{vp} + B_{vp} \tau^{\alpha_{vp}}) d\epsilon_{eq}^{vp} \\ df_{n,d} &= (A_d + B_d \tau^{\alpha_d}) d\epsilon_{eq}^d \\ df_{g,vp} &= (1 - f_{tot}) F(x, f_t) d\epsilon_{eq}^{vp} \\ df_{g,d} &= (1 - f_{tot}) F(x, f_t) d\epsilon_{eq}^d \end{aligned} \quad (\text{eq. B.V.25})$$

2. For the model 1M, the creep strain due to diffusion must be calculated in post-processor from elasto-viscoplastic calculations at every time increment so that,

$$\begin{aligned} df_{n,vp} &= (A_{vp} + B_{vp} \tau^{\alpha_{vp}}) d\epsilon_{eq}^{vp} \\ df_{n,d} &= (A_d + B_d \tau^{\alpha_d}) \frac{\sigma_{eq}}{K_d} \\ df_{g,vp} &= (1 - f_{tot}) F(x, f_t) d\epsilon_{eq}^{vp} \\ df_{g,d} &= (1 - f_{tot}) F(x, f_t) \frac{\sigma_{eq}}{K_d} \end{aligned} \quad (\text{eq. B.V.26})$$

The evolution of the total porosity was then described using **equations B.V.12** and **B.V.13**.

4.2. Failure criterion

Two failure criteria were tested:

1. A critical porosity f_c : failure occurs when f_t reaches f_c .
2. The material loses its hardening capacity which corresponds to $\frac{d\sigma}{d\varepsilon_{eq}} = 0$.

Note that the evolution of a crack cannot be followed with the locally coupled model. Therefore, the calculated creep time to failure will correspond to the time to the crack initiation for the NC0.25 specimens where stable crack growth occurs.

4.3. Results

The predictions of the locally coupled model using a critical porosity as the failure criterion are shown in **figure B.V.1** for NC1.2 and NC0.25 specimens. It shows that the best predictions are found for $f_c = 0.1$. The corresponding creep times to failure for NC1.2 specimens are overestimated with a factor lower than 2.0 but the times to the crack initiation are very well predicted for NC0.25 specimens. The predictions of the creep time to failure given by the hardening criterion $\frac{d\sigma}{d\varepsilon_{eq}} = 0$ are not shown as they were not satisfactory. In fact, material deconsolidation is detected when the critical strain p_c corresponding to the onset of softening is reached so that the creep lifetime is largely underestimated.

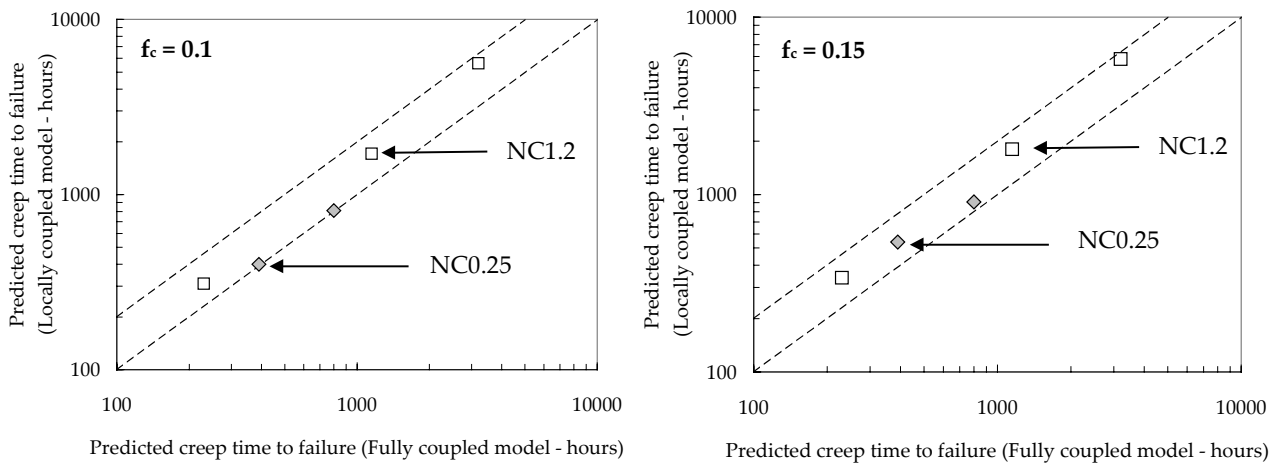


Figure B.V.1. Predictions of creep time to failure with the locally coupled model for NC1.2 and NC0.25 specimens

The results of the locally coupled model were also tested in terms of the rupture location especially in NC1.2 specimens as a shift was observed in the rupture location when decreasing the applied engineering stress (see **figure B.III.11**). The results of **figure B.V.2** show that the rupture location slightly shifts from the centre of the specimen to the notch root but the results are not as good as these given by the fully coupled model.

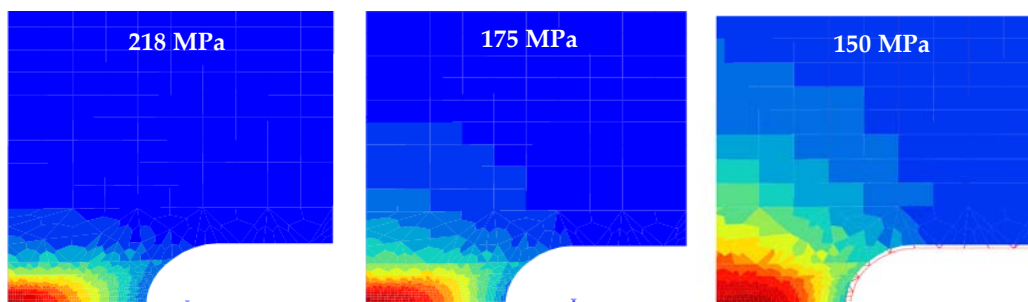


Figure B.V.2. Predictions of rupture location using the locally coupled model for NC1.2 specimens

Moreover, none of the failure criteria could be used to predict the creep time to failure of SC specimens as the rupture of SC specimens is more promoted by the material softening than by damage development. Therefore, it was assumed that specimens are failed when the critical strain $p_c = 0.03$ is reached. The corresponding results are plotted in **figure B.V.3**.

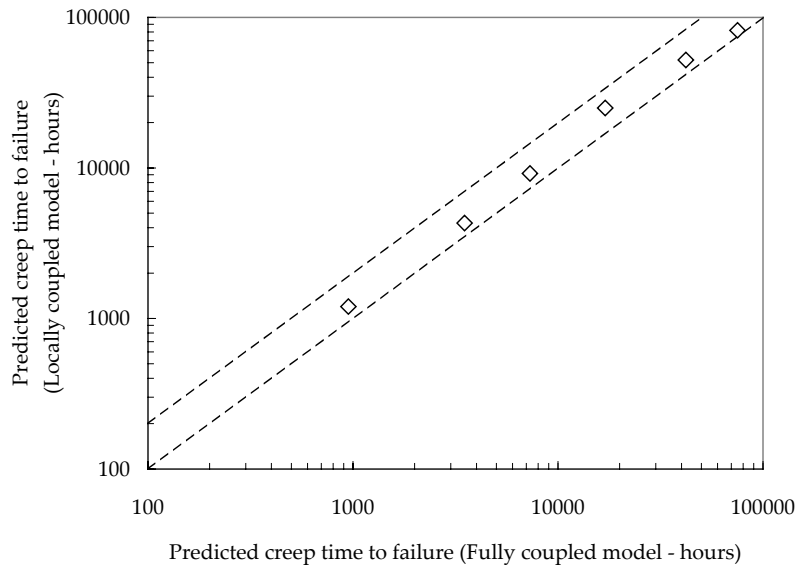


Figure B.V.3. Predictions of the creep time to failure with the locally coupled model for SC specimen

The main disadvantage of the locally coupled model is that it failed in predicting the right rupture location. Therefore, some efforts were performed to improve the locally coupled model. Cope (1965) described the local strain localisation due to damage. He introduces the localised strain:

$$\varepsilon_1 = \frac{\varepsilon}{\exp(-Kf)} \quad (\text{eq. B.V.26})$$

where K is a material parameter.

To take the effect of the stress triaxiality ratio, τ , into account, the expression of Cope (1965) was slightly modified leading to:

$$\varepsilon_1 = \frac{\tau^\alpha}{\exp(-Kf)} \varepsilon \quad (\text{eq. B.V.27})$$

For the sake of clarity, the results corresponding to the use of the modified Cope criterion are not shown. In fact the results were similar to these using a critical porosity and the predictions of the failure location were not really improved. It also confirmed that the coupling between creep flow and damage behaviour is necessary to well predict creep rupture location.

5. Conclusions about the use of a post process

The main conclusions of the study are:

1. A strong coupling exists between structural effects and damage development for SC specimens for high deformation rates (i.e. at high stresses). The use of the post processor is not necessary. Moreover, it is observed that the material nearly failed when softening effect occur. Therefore, the time for which the viscoplastic deformation reaches 3 % is a good estimation of the creep life in the high stress creep regime
2. For NC1.2 specimens the post process overestimates the creep lifetime with a factor of 2. It shows that the structure effect is very important for this specimen geometry.
3. For NC0.25 specimens, the locally coupled model can only be used to predict crack initiation. Very satisfactory results were found with the two versions of the post process and using a critical porosity $f_c = 0.1$.
4. A critical porosity fraction is a good rupture criterion. As softening occurs and because of the complex loading conditions, the hardening rate measurement did not give reliable information about creep failure.
5. The plastic strain localisation criterion derived from Cope (1965) gave good results in predicting creep time to failure but bad predictions in terms of rupture area for NC specimens.

In this work parameters which were fitted in **chapter B.III** for the coupled model were used. As the coupling between mechanics and damage is not ensured in the locally coupled model, it is assumed that a new identification of the model parameter should lead to better results especially in terms of the prediction of the failure location in notched specimens.

References

- Cope L.H. (1965). The mechanical properties of nuclear cermets. *Metallurgia*. **72(432)**. 165-177.
- Decamp K., Bauvineau L., Besson J., Pineau A. (1997). Size and geometry effects on ductile rupture of notched bars in a C-Mn steel: experiments and modelling. *International journal of fracture*. **88(1)**. 1-18.
- Lejeail Y., Pluyette E. (2004). Définition du programme d'essais pour la détermination de coefficients de joints soudés en acier T91 dans le domaine du fluage – Précalculs et influence de certains paramètres. Note technique CEA (*Private communication – In French*).
- Ragab A.R. (2004). Application of an extended void growth model with strain hardening and void shape evolution to ductile fracture under axisymmetric tension. *Engineering fracture mechanics*. **71**. 1515-1534.

Chapter B.VI. Creep flow and damage behaviour of the T91 steel at 450°C and 550°C

This part is dedicated to the analysis of creep flow and damage behaviour of the T91 steel at 450°C and 550°C. Some creep tests were carried out on SC specimens to determine creep flow properties of the T91 steel but also lead to the appraisal of creep cavitation and softening processes. The study is not as detailed as for the P91 steel at 625°C (no creep tests on NC specimens were carried out for example).

1. Experiments

Mechanical tests of type tensile and creep tests were carried out at 450°C and 550°C. Creep tests were performed only on smooth round tensile bars (SC) having a gauge length of 36 mm and a gauge diameter of 5 mm. These tests were carried out under constant applied load in controlled laboratory atmosphere ($20^{\circ}\text{C} \pm 2^{\circ}\text{C}$ and 50% relative humidity). The load was applied using dead weights. The temperature was monitored using three thermocouples spot welded onto the specimen surface. The temperature gradient between top and bottom ends of the specimen did not exceed 2°C . The elongation measured using linear variable differential transducers was continuously recorded with a sensitivity of $1\ \mu\text{m}$. The major difficulty of the study was the initial state of the material. A lot of defects as that presented in **figure B.VI.1** were found in the T91 sheet. These defects may have all the more a great impact on the creep response as their size may exceed $600\ \mu\text{m}$. The results of the creep tests given in the following section show that, due to these defects, a large experimental scatter-band was found especially for creep tests at 450°C

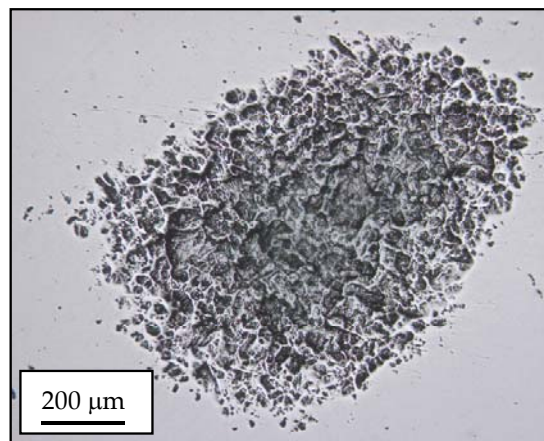


Figure B.VI.1. Defect in the T91 sheet in the initial state

2. Experimental results

The results of the tensile tests are given in **chapter A.I** so that they will not be reminded here. One must however keep in memory that 450°C is a temperature probably set near the domain where dynamic strain ageing occurs. Here, attention will be mainly focused on the results of creep tests.

For SC specimens, the initial values of the applied engineering stresses at 550°C (load divided by the initial area of the minimum section) range from 185 MPa to 215 MPa and corresponding times to failure range from 600 hours to 4,500 hours (**figure B.VI.2**). At 450°C, the initial values of the applied engineering stresses range from 385 MPa to 420 MPa and corresponding times to failure range from 100 hours to 3,200 hours (**figure B.VI.3**). All the experimental data are also reported in **appendix A table A.B.3** and **table A.B.4**.

As for the P91 steel, creep curves exhibit a very short primary creep regime at 450°C and 550°C. However, the secondary creep was found to be the longest stage of the creep deformation and tertiary creep were not as long as at 625°C. Many difficulties were found for creep tests at 450°C as the results were very dispersed especially at high stress level. This dispersion in experimental results can be attributed to the defects evidenced in the initial state (see **figure B.VI.1**).

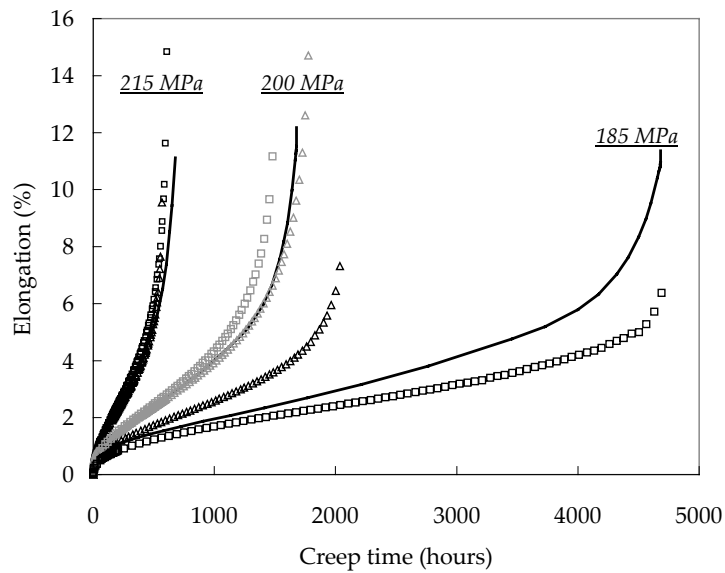


Figure B.VI.2. Comparison of experimental (symbols) and calculated (lines) creep curves for creep tests on T91 steel SC specimens at 550°C

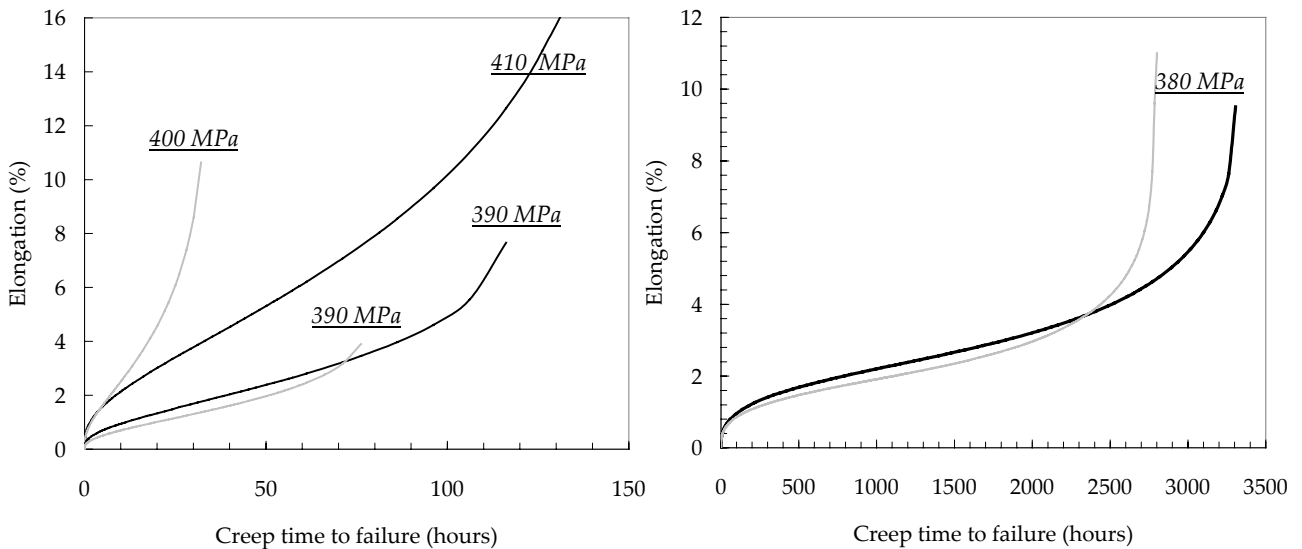
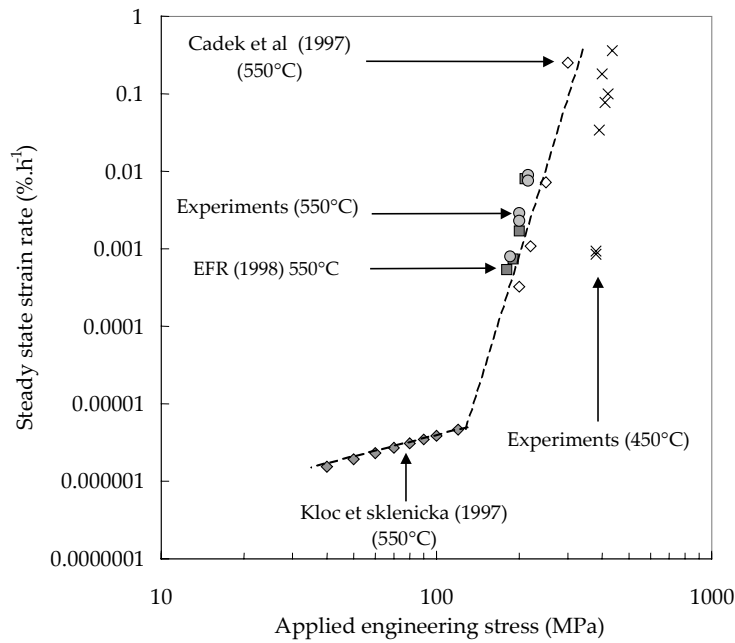


Figure B.VI.3. Experimental creep curves for creep tests on T91 steel SC specimens at 450°C

3. Creep mechanical and damage behaviour at 450°C and 550°C

3.1. Creep flow properties

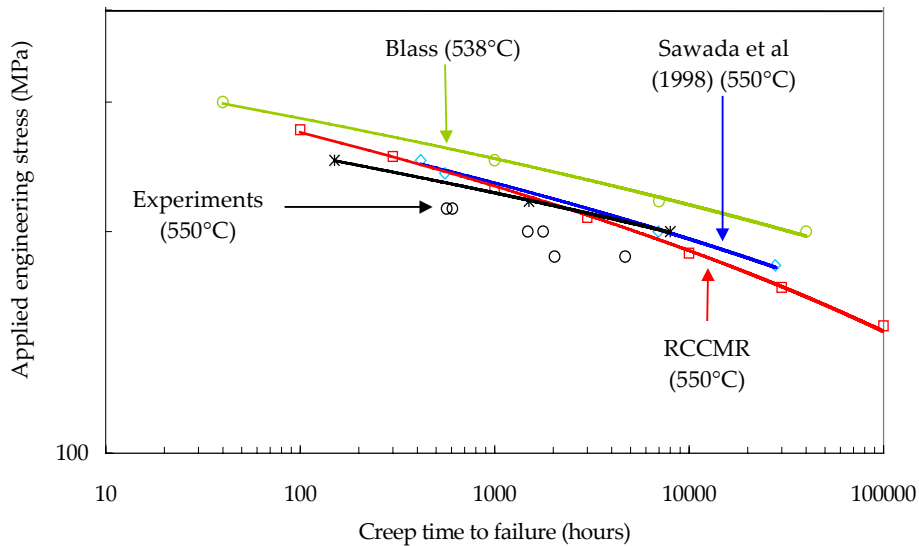
Experimental data and results found in the literature at 450°C and 550°C are shown in **figure B.VI.4**. All the creep tests of the present study were carried out in the high stress creep regime. **Exponents of the Norton power-law without considering any threshold stress are $n = 39.0$ and $n = 11.5$ at respectively 450°C and 550°C.** The results of creep tests at 550°C exhibit a quite good agreement with literature data at the same temperature. In addition, literature results from Kloc and Scklenicka (1997) which concerned creep data in the low stress creep regime ($n = 1.0$) were added to the database. All these data are plotted on the same representation in **figure B.VI.4**.



*Figure B.VI.4. Steady state strain rate versus stress at 450°C and 550°C :
Experimental results with SC specimens and literature results*

3.2. Creep failure properties

Literature results and results from the present study were plotted in the same graph for creep tests at 550°C (**figure B.VI.5**) and for creep tests at 450°C (**figure B.VI.6**). Very few data were found at 450°C as the 9Cr1Mo-NbV steels were essentially developed for high temperature ($\approx 600^\circ\text{C}$) applications. About this point, note that the RCCMR data at 450°C are not experimental results but extrapolated values from experiments at 550°C. As for the creep flow behaviour a satisfactory agreement was found between literature data and experimental results.



*Figure B.VI.5. Applied engineering stress versus creep time to failure for experiments
with SC specimens at 550°C and literature results*

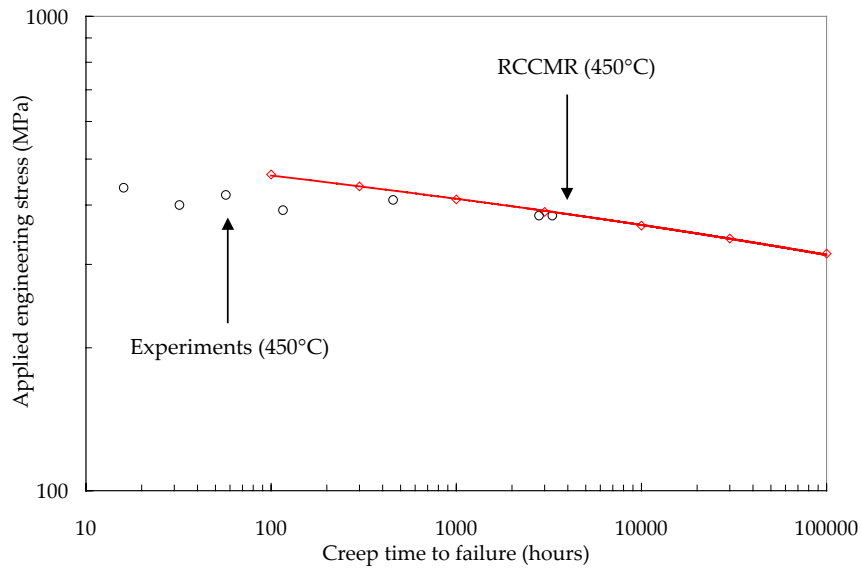


Figure B.VI.6. Applied engineering stress versus creep time to failure for experiments with SC specimens at 450°C and literature results

The experimental results were used to determine the classical creep lifetime predictive Monkman-Grant relationship. In the domain experimentally investigated, no change in damage mechanism was observed. It is especially very interesting to notice that a unique Monkman-Grant relationship could be determined to represent both creep tests results at 450°C, 550°C and 625°C (see **figure B.VI.7**). The MG relationship was written:

$$\dot{\epsilon}_s^m t_R = C_{MG} \quad (\text{eq. B.VI.1})$$

where $\dot{\epsilon}_s$ is the steady state creep strain rate in h^{-1} , t_R is the creep time to failure in h and the two materials parameters were fitted to $m = 1.0$ and $C_{MG} = 7.4 \cdot 10^{-2}$.

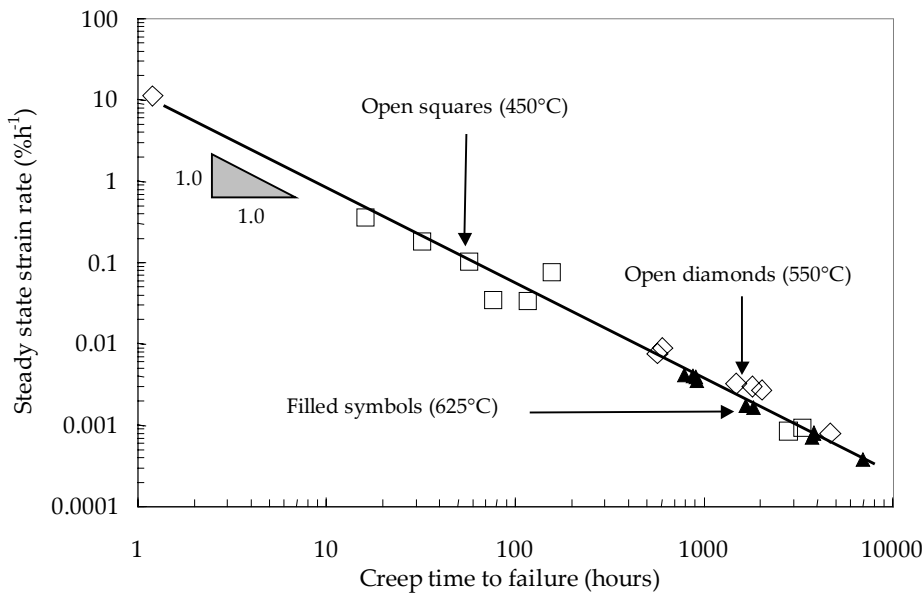
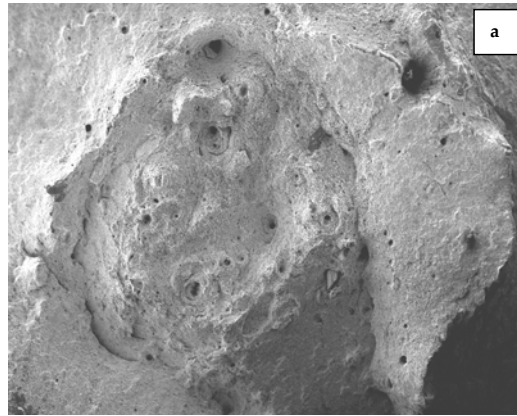


Figure B.VI.7. Monkman-Grant plots at 450 and 550°C

3.3. Damage characteristics and softening effects at 450°C and 550°C

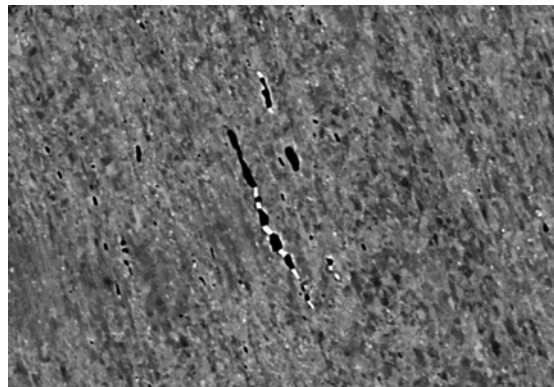
All creep tests were carried out in air atmosphere so that fine observations of the fracture surfaces were not possible. Both at 450°C and 550°C and for all the explored domain of applied engineering stresses, the specimens failed in a ductile manner. However, it was really interesting to notice the “cup cone” morphology of all the fracture surfaces (see **figure B.VI.8**) which evidences that fracture started from the centre of the specimen where the stress triaxiality ratio is the highest. It was also noticed that the specimens necking exceed 70% at the end of the test.



100 μm

*Figure B.VI.8. Example of a fracture surface of a creep specimen made in T91 steel – SEM observations
 ($T = 550^\circ\text{C} - \sigma = 185 \text{ MPa}$)*

To understand the damage mechanisms, cross sections of creep tested specimens were investigated in the FEG-SEM with the backscattered channelling (BSE) contrast, after polishing using colloidal silica. First, it was evidenced that softening largely promotes the tertiary creep stage both at 450°C and 550°C . It can be shown in **figure B.VI.9** that the initial lath martensite is totally recovered. This conclusion was also supported by Engberg et al (1984). The main effect of the temperature is that the softening starts for higher values of creep strain (typically higher than 3% at 550°C and higher than 4% at 450°C).



4 μm

*Figure B.VI.9. Cross-section of a creep tested specimen made in T91 steel (SEM-BSE investigation)
 ($T = 550^\circ\text{C} - \sigma = 185 \text{ MPa}$)*

The micrograph of **figure B.VI.9** also shows that cavity growth is very limited even in the later stage of creep fracture as a large amount of small cavities $< 1 \mu\text{m}$ in average diameter were detected. It is obviously the material softening which mainly triggers the specimen failures. It was also evidence that cavities mainly nucleate at the particle/matrix interface due to high stress concentrations. The situation shown in **figure B.VI.10a** is observed very often. In this case the large white precipitates are Laves phase particles but M_{23}C_6 carbides are also largely involved in the cavity nucleation process. About this point, if Laves phase precipitation was not observed after 10,000 hours of stress free ageing at 450°C , their presence was evidenced in creep ageing conditions.

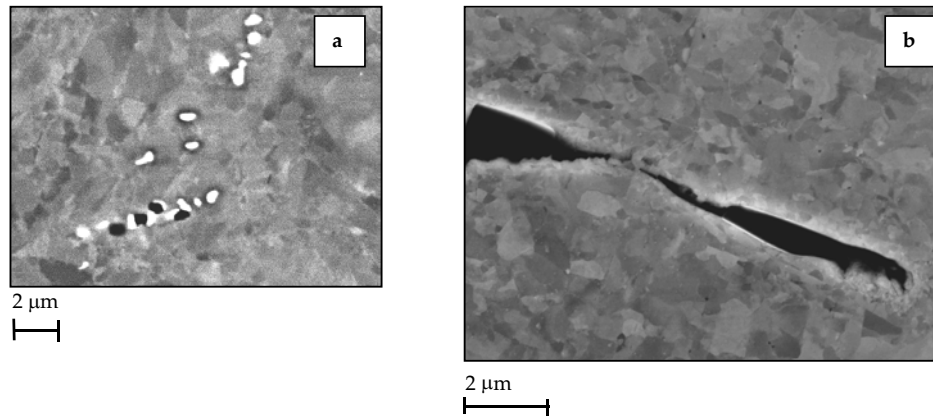


Figure B.VI.10. Creep damage behaviour of the T91 steel (a) Representative situation of the cavity nucleation process – (b) Intergranular fracture observed at 450°C

In terms of cavity growth mechanism, the morphology of the cavities observed at 550°C was the same than these observed at 625°C. However, SEM investigations in cross-sections of the specimens creep tested at 450°C, evidenced the presence of intergranular wedge cracks as can be shown in **figure B.VI.10b**. This type of damage is only observed at 450°C.

Finally note that there is very few literature data concerned with creep damage mechanisms under 550°C but these confirmed the observations of the present study. Williams et al (1981) studied creep behaviour of 9Cr1Mo steels in the temperature range 475°C - 550°C. Their investigations led to the conclusion that creep occurs almost by grain deformation processes as very few cavitation was observed. They also mentioned that the secondary precipitation of MX particles proceeds during long term creep (> 30,000 hours) and under 525°C. This secondary precipitation would result from the formation of solute atmospheres near mobile dislocations as dislocation annihilation during recovery creep leads to high solute concentration areas where precipitation is more likely to occur. This point needs more investigations as it indicates that the DSA may be a strengthening mechanism.

4. Application of the model to represent creep mechanical and damage behaviour at 450°C and 550°C

4.1. Creep flow activation energy

The aim of this part is to investigate the possibility to apply a simple activation energy criteria to evaluate creep flow properties at 450°C and 550°C from results at 625°C.

The thermal activation of creep can be represented by using a simple equation of type:

$$\dot{\epsilon} = A\sigma^n \exp\left[-\frac{Q}{k_b T}\right] \quad (\text{eq. B.VI.2})$$

where Q is the apparent activation energy. Moreover, this apparent activation energy strongly depends on stress, temperature and related creep mechanisms at the atomic scale. In the high stress creep regime, Jorge et al (2003), Cerri et al (1998), Cadek et al (1996) and Spigarelli et al (1997) have evaluated this activation energy in the temperature range between 550°C to 650°C. The method consists in performing creep tests at the same loading level with varying the temperature. The calculated values are very dispersed with $Q = 250\text{kJmol}^{-1} - 800\text{kJmol}^{-1}$ in the high stress creep regime. Anderson et al (2003) indicated that $Q = 796\text{kJmol}^{-1}$ when the Norton power-law exponent $n = 10 - 15$ and $Q = 216\text{kJmol}^{-1}$ when $n = 4$.

In fact, taking into account the high dispersion in activation energies in the high stress creep regime, it appears to be better to determine creep flow properties using experimental data.

The difficulty of using an activation energy may be summed up by the **figure B.VI.11**. From this representation, one should deduced that it is only possible to use an activation energy to evaluate creep flow properties in the low stress regime where the deformation is accommodated by grain boundary diffusion. Moreover, this energy is consistent with the activation energy for pipe diffusion in α Iron which is equal to 174kJmol^{-1} (Frost and Ashby (1982)). This procedure will be used to determine creep flow properties in the low stress creep regime at both 450°C and 550°C.

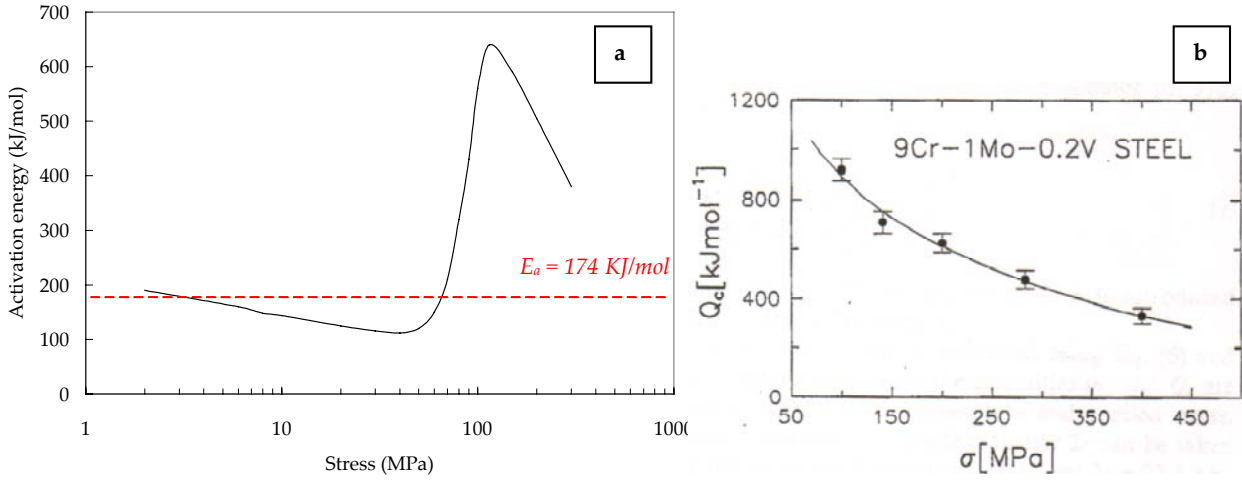


Figure B.VI.11. Stress dependence of the creep activation energy for a P91 steel between 923 and 1023 K from Kloc and Sklenicka (1997) and from Cadek et al (1997)

4.2. Determination of a creep model at 550°C

The same model formulation as that used for the P91 steel at 625°C (see **chapter B.III**) was preserved with using the LPS model to describe cavity growth. As the experimentally measured apparent Norton power-law exponent is equal to 11.5, the strain hardening parameter was calculated as $m = 0.089$.

4.2.1. Creep flow constitutive equations

For the sake of clarity, the creep flow constitutive equations are reminded. The quasi-plastic flow constitutive equation is given by:

$$\dot{p}_{qp} = \left\langle \frac{\sigma_m^* - R_{qp}}{K_{qp}} \right\rangle^{n_{qp}} \quad (\text{eq. B.VI.3})$$

$$\text{with } R_{qp}(p_{qp}) = R_{oqp} + Q_{qp1}(1 - \exp(-b_{qp1}p_{qp})) - Q_{qp2}(1 - \exp(-b_{qp2}p_{qp})) \quad (\text{eq. B.VI.4})$$

where, n_{qp} , K_{qp} , Q_{qp1} , Q_{qp2} , b_{qp1} and b_{qp2} are model parameters. The viscoplastic creep flow was described as:

$$\dot{p}_{vp} = \left\langle \frac{\sigma_m^* - R_{vp}}{K_{vp}} \right\rangle^{n_{vp}} \quad (\text{eq. B.VI.5})$$

$$\text{with } R_{vp}(p_{vp}) = R_{ovp} + Q_{vp1}(1 - \exp(-b_{vp1}p_{vp})) - Q_{vp2}(1 - \exp(-b_{vp2}(p_{vp} - p_c))) \text{ for } p_{vp} > p_c \quad (\text{eq. B.VI.6})$$

where, n_{vp} , K_{vp} , Q_{vp1} , Q_{vp2} , b_{vp1} and b_{vp2} are model parameters. In the low stress creep regime, the creep flow behaviour was represented by:

$$\dot{p}_d = \left\langle \frac{\sigma_m^*}{K_d} \right\rangle^{n_d} \quad (\text{eq. B.VI.7})$$

where n_d and K_d are model parameters whose values were set to the values extracted from the results of Kloc and Sklenicka (1997) (see **section 7** of **table B.VI.1**).

4.2.2. Model identification

The model parameters corresponding to the quasi-plastic contribution were fitted using the tensile tests at 550°C whose results were given in **chapter A.I**. For the identification of the viscoplastic flow rule, Q_{vp1} was set to 80 MPa and values of K_{vp} and n_{vp} were fitted on experimentally measured steady state strain rates. Then, the value of b_{vp1} was fitted so as to represent the primary creep stage. The model parameters p_c , Q_{vp2} and b_{vp2} which describe the material softening were determined to fit the tertiary creep stage. The value of p_c was set to 0.04 as it was evidenced that the tertiary stage started for larger strain than at 625°C. The resulting model parameters are given in the first seven sections of **table B.VI.1**.

The fitted values of damage parameters (i.e. A_{vp} , B_{vp} , A_d , B_d , α_{vp} , α_d) were unchanged in comparison with the model fitted to experimental data at 625°C as no changes in damage processes were evidenced.

1.Young's modulus	E	163 GPa
2.Poisson's ratio	ν	0.3
3.Quasi plastic hardening	R_{0qp} Q_{qp1} b_{qp1} Q_{qp2} b_{qp2}	280 MPa 220 MPa 45 400 MPa 8
4.Viscoplastic hardening	R_{0vp} Q_{vp1} b_{vp1} Q_{vp2} b_{vp2} p_c	0 MPa 100 MPa 224 35 MPa 25 0.05
5.Quasi plastic flow rule at 550°C	K_{qp} n_{qp}	1.0 5.0
6.Viscoplastic flow rule at 550°C	K_{vp} n_{vp}	$460 \text{ MPa h}^{-1/n_{qp}}$ 7.14
7.Diffusion flow rule at 550°C	K_d n_d	$2.53 \cdot 10^9 \text{ MPa h}^{-1/n_d}$ 1.0
8. LPS model	q_1 q_2 f_c δ_c <i>Strain hardening coefficients</i> m_{qp} m_{vp} m_d <i>Nucleation by the viscoplastic mechanism</i> A_{vp} B_{vp} α_v <i>Nucleation by the diffusional mechanism</i> A_d B_d α_d	1.5 1.0 0.1 6.0 1.0 0.087 0.0 0.01 0.15 2.0 14.0 16.0 2.0

Table B.VI.1. Model parameters at 550°C

4.2.3. Evaluation of the creep flow and failure properties – Validation of the model

Steady state strain rates versus applied engineering stress (**figure B.VI.12**) and applied engineering stress versus time to failure (**figure B.VI.13**) plots were established from the results of calculations and compared to both literature data and the results of the experiments of the present study. A good agreement was found between the model and the experimental results in terms of steady state creep strain rate and creep time to failure. Moreover, **figure B.VI.2** shows that the macroscopic curves are satisfactorily described by the model.

However, the ability of the model to well represent creep flow and damage behaviour in the case of multiaxial loading conditions can not be ensured. To do so, it would be necessary to perform an equivalent experimental work as that carried out on the P91 steel at 625°C i.e. creep tests on various geometry of axisymmetric U-notched specimens but also on compact tension or other specimen geometry.

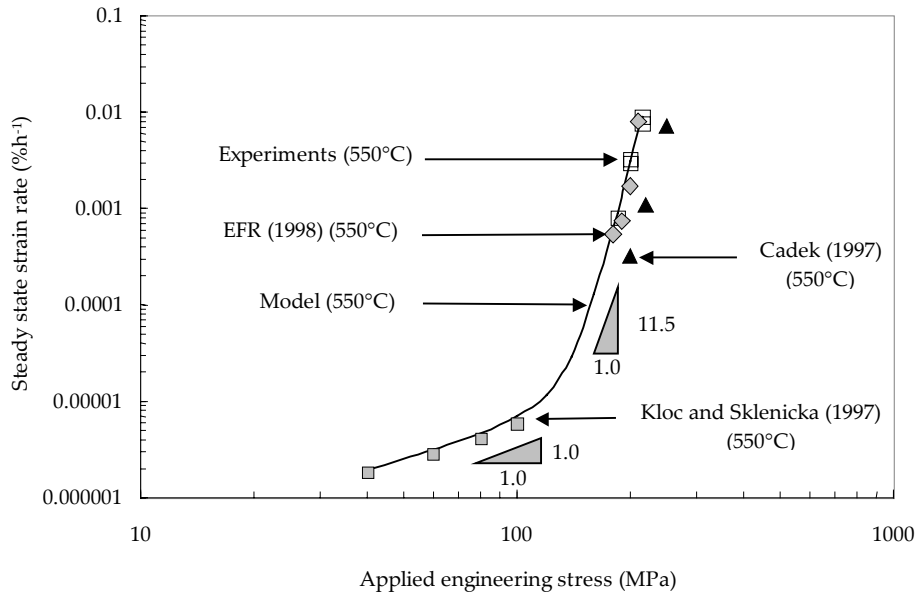


Figure B.VI.12. Steady state strain rate versus stress at 550°C: Experimental, model and literature results

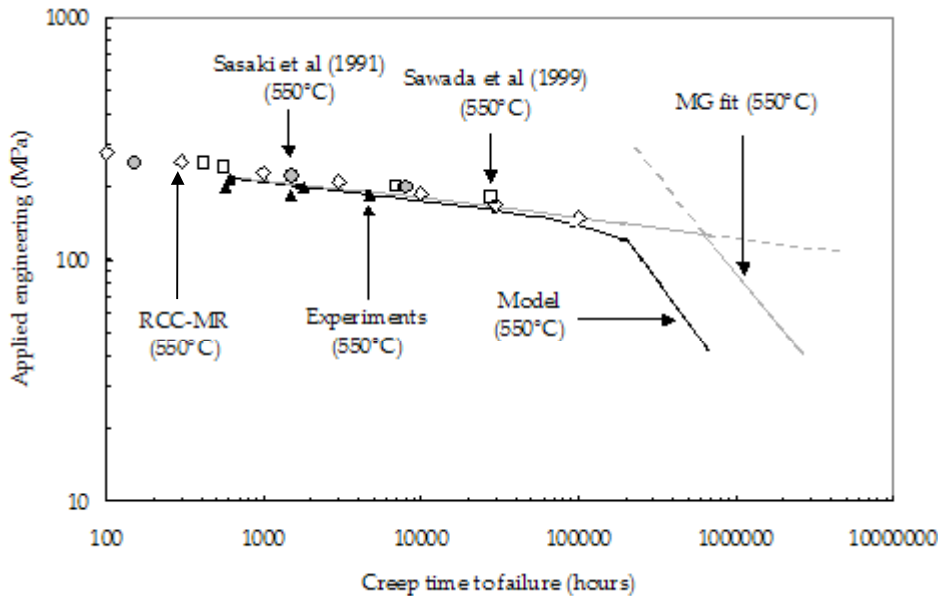


Figure B.VI.13. Stress versus time to failure for SC specimens at 550°C – Comparison with literature results and MG fit with the coefficients determined in the high stress creep regime

The results given by the model allowed to fit a suitable Monkman-Grant relationships in the low stress creep regime at 550°C with $m = 0.88$ and $C_{MG} = 0.098$.

4.3. Validity of the model transferability from 625°C to 450°C

The transferability of the model from 625°C to 450°C is obviously hardly possible. Indeed, at 450°C is a temperature close to the dynamic strain ageing (DSA) domain for the T91 steel. Creep flow and damage mechanisms may obviously not be the same than those encountered at 550°C and 625°C which was experimentally observed in **figure B.VI.10b**.

Few studies deal with the effect of the DSA on creep properties. Blum (2001), in a short review of creep mechanisms called back that DSA affects transition between primary and secondary creep stages as it corresponds to the sudden formation of solute clouds around the dislocations. The most important part of studies concerned with the dynamic strain ageing were mainly focused on its effect on the high temperature fatigue behaviour. However, even in the case of fatigue loading conditions, the influence of the DSA is not well understood. As shown by Qiang et al (1996) and Peng et al (2004), in austenitic stainless steels, the DSA can be a strengthening mechanism (i.e. if the material is pre-deformed in the DSA, it exhibits a higher fatigue strength). However, if no prior working in the DSA is carried out, Rodriguez (2000)

underlined that DSA may be an important damage mechanism especially for strain controlled fatigue. In creep loading conditions, the DSA can also be extremely damaging as it can provoke sudden bursts of strain. Indeed, clouds of solute atoms which form around dislocations, with reducing their mobility, leads to plastic instabilities. Finally, the experimental observations of the present study obviously suggest that grain boundaries are more sensitive to cracking in the DSA domain.

As the duration of the present study did not allow to perform enough experimental investigations, the following procedure is proposed to investigate the creep flow and damage behaviour at 450°C:

1. More creep tests on SC specimens must be carried out to determine creep flow in the high stress regime (In addition, a load varying test would give very useful information about creep flow properties).
2. In the low stress creep regime, the same procedure than these used at 550°C can be used (It leads to $K_d = 7.46 \cdot 10^{10} \text{ MPah}^{-1/n_d}$). It would certainly be better to determine K_d experimentally but the technique of the tests on helicoidal spring specimens requires a long experience in the domain.
3. Creep tests on NC1.2 and NC0.25 specimens are necessary to determine the effects of the stress triaxiality and the creep strain on cavity nucleation and growth. Moreover, it was previously shown that these tests give information about long term creep damage properties with not too much time consuming tests.

4.4. Taking into account the effect of the DSA in constitutive equations

The effects of the dynamic strain ageing are not included in the model. Another formulation of the model following those proposed by Yaguchi and Takahashi (1999, 2000, 2004a, 2004b) would be in better agreement with the physical deformation mechanisms related to the DSA. Their model, which is relatively complex, describes the negative strain rate sensitivity. It is based on an additive decomposition of the strain tensor:

$$\varepsilon = \varepsilon_e + \varepsilon_{in} \quad (\text{eq. B.VI.8})$$

The viscoplastic flow is given by:

$$\dot{\varepsilon}_{in} = \left\langle \frac{|\sigma - X| - \sigma_a}{D} \right\rangle^n \text{sgn}(\sigma - X) \quad (\text{eq. B.VI.9})$$

where X is the backstress described as:

$$\dot{X} = C(a\varepsilon_{in} - X\varepsilon_{in}) - YX^m \text{sgn}(X) \quad (\text{eq. B.VI.10})$$

and σ_a the isotropic hardening is described by :

$$\dot{\sigma}_a = b(\sigma_{as} - \sigma_a)\varepsilon_{in} \quad (\text{eq. B.VI.11})$$

where σ_{as} is the ageing stress defined by:

$$\sigma_{as} = A + B \log \left| \dot{\varepsilon}_{in} \right| \quad (\text{eq. B.VI.12})$$

where A and B are material constants.

The work of Yaguchi and Takahashi (1999) is especially very interesting as they proposed to determine experimentally both the back stress and the ageing stress from stepwise strain rate change tests. Note also that another model has recently been proposed by Graff et al (2004).

5. Conclusions

The following conclusions can be drawn from the experimental and numerical study of creep flow and damage behaviour of the T91 steel at 450°C and 550°C:

1. The initial experimental database constituted of creep test at 625°C was enlarged by creep tests 450°C and 550°C using a material of a different origin having nearly the same chemical composition but exhibiting a quite different tempering treatment.
2. The model integrating multiple deformation and damage mechanisms, introduced in the present study was successfully used to represent the high temperature creep flow and damage behaviour of the T91 steel at 550°C.
3. The use of the model at 450°C is not recommended by the authors as the model was not design to take into account physical mechanisms linked to the DSA. To do so, it would be necessary to integrate such constitutive equations as these proposed by Yaguchi and Takahashi (1999) in the model developed in the present study.
4. As the transition in creep mechanisms is not reached after 100,000 hours (see **figure B.VI.13**), the Monkman-Grant relationship, determined from results of short term creep tests (i.e. 1,000 – 3,000 hours), obviously gives good predictions of the material creep life up to 100,000 hours at 550°C and by deduction at 450°C.

References

- Bestwick , Escaravage C. (1998). Design properties of modified 9Cr1Mo VNb steel. *European fast breeder associates - Report B40151078C*.
- Blass J.J., Battiste R.L., O'Connor D.G. (1991). Reductions factors for creep strength and fatigue life of modified 9%Cr-1%Mo steel weldments. Confirmation by axial or torsional tests on tubular specimens with longitudinal or circumferential welds. *ASME pressure vessels and piping conference – San Diego 23-27*.
- Cadek J., Sustek V., Pahutova M. (1997). An analysis of a set of creep data for a 9Cr-1Mo-0.2V (P91 type steel). *Materials science and engineering*. **A225**. 22-28.
- Engberg G., Karlsson S., Von Walden E. (1984). An interpretation of tertiary creep in 12%Cr steel at 550°C. *Creep and fracture of engineering materials and structures*, ed. B. Wilshire, D.R.J. Owen, Swansea 1-6 April. Pineridge Press. 697-709.
- Graff S., Forest S., Strudel J.L., Prioul C., Pilvin P., Béchade J.L. (2004). Strain localization associated with static and dynamic strain ageing in notched specimens: experiments and finite elements simulations.
- Jorge A.M., Regone W., Balancin O. (2003). Effect of competing hardening and softening mechanisms on the flow stress curve modelling of ultra low carbon steel at high temperatures. *Journal of materials processing technology*. 142. 415-421.
- Kloc L., Sklenicka V., Ventruba J. (2001). Comparison of low stress creep properties of ferritic and austenitic creep resistant steels. *Materials Science and Engineering*. A319-321. 774-778.
- Peng K., Qian K., Chen W. (2004). Effect of dynamic strain ageing on high temperature properties of austenitic stainless steel. *Materials science and engineering*. **A379**. 372-377.
- Qiang K.W., Chen W., Peng K. (1996). Effects of dynamic strain ageing on high temperature fatigue properties of austenitic stainless steel. *Creep and fatigue: design and life assessment at high temperature. Mechanical engineering publications*.
- RCCMR (1993). RCCMR French design code modified in 2000. DMC253.
- Rodriguez P. (2000). Dynamic strain ageing: is it really adaming mechanism ? *Proceedings of the international symposium on materials ageing and life management*. Editors B. Raj, Bhanu Sankara Rao. Allied publishers limited, Chennai.
- Williams K.R., Findler R.S., Askins M.C. (1981). The effect of secondary precipitation on the creep strength of 9Cr1Mo steel. *Creep and Fracture of Engineering materials and structures edited by B. Wilshire and D.R.J. Owen*. 475-487.
- Yaguchi M., Takahashi Y. (1999). Unified inelastic constitutive model for modified 9Cr-1Mo steel incorporating dynamic strain ageing effect. *JSME international journal series A*. **42(1)**. 1–10.
- Yaguchi M., Takahashi Y. (2000). A viscoplastic constitutive model incorporating dynamic strain aging effect during cyclic deformation conditions. *International Journal of Plasticity*. **16**. 241-262.
- Yaguchi M. and Takahashi Y. (2004a). Ratchetting of viscoplastic material with cyclic softening, part 1: experiments on modified 9Cr-1Mo steel. *International Journal of Plasticity*. To be published.
- Yaguchi M. and Takahashi Y. (2004b).). Ratchetting of viscoplastic material with cyclic softening, part 2: application of constitutive models. *International Journal of Plasticity*. To be published.

Main Results of Part B

1. Creep flow and damage behaviour of 9Cr1Mo-NbV steels (P91 steel in the present study) at 625°C

Creep flow behaviour: Both a high stress creep regime where the deformation is accommodated by dislocation climb or cross-slip ($n > 4$) and a low stress creep regime where the deformation is accommodated by grain boundary diffusion ($n = 1$) were distinguished. The applied engineering stress corresponding to the transition between the two regimes was evaluated to 70 MPa.

Creep damage mechanisms: Cavity nucleation occurs at grain boundaries and more specifically at the interface between the matrix and second phase particles i.e. in stress concentration areas. The cavity growth is both promoted by diffusion at grain boundaries and the matrix viscoplasticity. The cavity coalescence which is the late stage of the damage development starts for low levels of volume cavitation i.e. $\approx 10\%$. Finally, it was evidenced that the material softening largely contributes to the acceleration of the creep strain and the specimen fracture.

2. Modelling creep flow and damage behaviour

Model formulation: The model was designed on the basis of experimental observations with assuming that three flow and damage mechanisms i.e. a quasi-plastic and two creep regimes respectively corresponding to high and low stresses, contribute to the overall deformation and to damage accumulation. An effort was made to ensure a coupling between the contributions of each of the three mechanisms to the overall creep flow and damage.

For each mechanism, the coupling between damage accumulation and the flow behaviour is described throughout the use of an effective stress following the description of Gurson, Tvergaard and Needleman. It was also proposed to improve the model formulation with a finer description of the effective stress using the development of Leblond, Perrin and Suquet (1994) for materials deforming at high temperature.

Identification of the model: The model was fitted to experimental data on various kind of U-notched and smooth axisymmetric specimen geometry.

Model validation: The model succeeded in predicting the rupture location in various kind of axisymmetric specimen geometry. It was also successfully used to represent crack growth in compact tension specimens and to predict creep lifetime of plate notched specimens.

Prediction of long term creep properties: The model especially predicts a decrease of the material creep strength in the low stress creep regime so that the criterion 10^5 hours of creep is respectively reached for $\sigma = 140$ MPa, 80 MPa, 40 MPa and 20 MPa at respectively 550°C, 600°C, 625°C and 650°C.

It is currently considered that the precipitation of a Z-phase is responsible for premature failure during long term creep exposure. Nevertheless, it is assumed in the present study that the change in creep flow and damage mechanism is responsible for premature failure during long term creep exposure.

Extrapolation of the model: It is shown both from literature data and creep results on the T91 steel at 550°C, that the model can be used in the temperature range between 550°C to 650°C. For lower temperatures, in its actual formulation, the model is not allowed to take into account the effect of the dynamic strain ageing. For higher temperatures, as the matrix may be locally depleted in alloys elements (near $M_{23}C_6$ carbides or Laves phase particles), the $\alpha \rightarrow \gamma$ phase transformation can locally occur leading to a strong modification of the material creep properties.

Part C

*Creep flow and damage mechanisms of 9Cr1Mo-NbV weldments
at high temperature. Experimental evaluation and modelling of creep flow and damage behaviour of
the weakest area of weldments*

*(Etude expérimentale et modélisation du comportement, de l'endommagement et de la rupture en
fluage haute température des joint soudés en acier 9Cr1Mo-NbV – Détermination des propriétés
intrinsèques de la ZAT faible)*

Introduction

This part of the PhD is dedicated to the study of high temperature creep flow and damage behaviour of the 9Cr1Mo-NbV steel weldments. It has already been evidenced in **Part A** that the welding operation leads to several microstructural changes in the so-called heat affected zone. These microstructural changes may affect the creep properties of the weldments. In this part, creep flow and damage mechanisms of the weldments are especially compared with these encountered in the base metal.

A review of literature results is first given. It concerns results of creep tests on weldments at high temperature. Details about both the importance and the origin of the loss of creep strength between the base metal and the weldment, but also creep rupture location in weldments are given. A first simple analysis is proposed to predict the weldment creep lifetime.

The next three parts are written in the form of self-contained project papers. Therefore, some information are sometimes recalled from one paper to another. In addition, at the end of **chapter C.II, C.III** and **C.IV**, some supplementary results are given.

The second part (**chapter C.II**) is dedicated to experimental results of creep tests on cross-weld specimens at 625°C. In the domain experimentally investigated, it is evidenced that creep rupture occurs in the ICHAZ with a reduction of a factor larger than 10 in the creep lifetime by comparison with the base metal. The loss of creep strength in the ICHAZ is attributed to its metallurgical properties. As a first step, a single one-dimensional model is proposed to assess the creep lifetime of weldment specimens. It allows to proceed a first useful evaluation of constraining effects in the weldment.

In the third part (**chapter C.III**), attention is focused on the definition of a procedure to design bulk specimens having the same microstructure as the weakest HAZ. To do so, a thermal model of heat dissipation, first introduced by Rosenthal (1941) and later modified by Rykalin (1957), is used to calculate the weld thermal cycles experienced by the base metal in various parts of the HAZ. The weld thermal cycles are then reproduced on base metal specimens and characterised in terms of metallurgical properties. Among them, that leading to the formation of a microstructure corresponding to the weakest HAZ, is chosen. Finally, an experimental database is built to determine creep flow and damage properties of this weakest microstructure. As this paper is mainly focused on the evaluation of metallurgical properties of the weakest HAZ, experimental results are not fully used to model creep flow and damage behaviour of the weakest HAZ. This is the scope of the following paper (**chapter C.IV**).

The improved formulation of the multiple deformation and damage mechanisms model introduced in **chapter B.III** is then used to represent creep flow and damage behaviour of the weakest ICHAZ. The fitted model succeeds in modelling the creep flow and damage behaviour of the weakest HAZ from high to low stresses (**chapter C.IV**) and for various kind of specimen geometry.

Contents

Chapter C.I. State of the art

Chapter C.II. Comparison between creep flow and damage behaviour of the P91 base metal and the WJP91 weldment at 625°C: “High temperature creep flow and damage properties of 9Cr1Mo-NbV steels: base metal and weldment” V. Gaffard, A.F. Gourgues-Lorenzon and J. Besson.

Chapter C.III. Creep flow and damage properties of the weakest area of the WJP91 weldment at 625°C: “High temperature creep flow and damage properties of the weakest area of 9Cr1Mo-NbV steel weldments”, V. Gaffard, A.F. Gourgues-Lorenzon and J. Besson.

Chapter C.IV. Modelling creep flow and damage behaviour of the weakest area of the WJP91 weldment: “Modelling high temperature creep flow and damage properties of the weakest area of 9Cr1Mo-NbV steel weldments”, V. Gaffard, J. Besson. and A.F. Gourgues-Lorenzon.

Chapter C.I. State of the art

1. Codification of creep failure in weldments

In the first part of the present work (**chapter A.II**), material heterogeneity in weldments has already been described. Three main parts: the base metal, the weld metal and the heat affected zone (HAZ) were distinguished. When performing creep tests at high temperature on weldments, creep rupture currently occurs in one of the following 4 zones sketched in **figure C.I.1**:

1. Rupture of type I is located in the weld metal.
2. Rupture of type II starts in the weld metal but end in the HAZ.
3. Rupture of type III starts from the HAZ near the fusion line and ends either in the base metal or near the fusion line.
4. Rupture of type IV is located in the HAZ near the base metal and runs parallel to the fusion line.

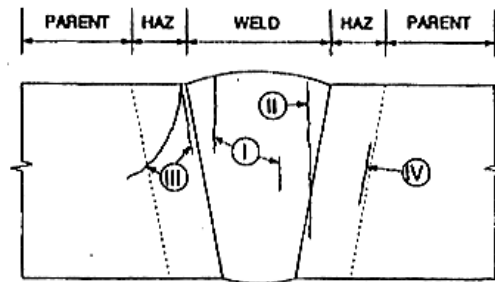


Figure C.I.1. Classification of rupture in weld components from Schuller et al (1974)

2. Rupture location when performing creep tests on 9Cr-1Mo-NbV steel weldments

Rupture location in 9Cr1Mo-NbV weldments depends on both the temperature and the stress level as it has already been noticed by Coussement and DeWitte (1995). Synthesis of experimental results from Spigarelli and Quadrini (2002), Laha et al (2000), Cerjak et al (1998), Kojima et al (1995), Cerjak and Schuster (1994), the sketch given by Coussement and De Witte (1995) and experimental data at 450°C, 550°C and 625°C are reported in **figure C.I.2**.

As weldment properties strongly depend on welding characteristics, all elements given by the authors about the creep tested welded components are given in **table C.I.1**.

Authors	Welding process	PWHT	Other given characteristics
Laha et al (2002)	MAW*	700°C – 1 h	/
Spigarelli and Quadrini (2002)	GTAW** – SMAW***	760°C – 8 h	/
Kojima et al (1995)	SMAW	740°C – 8 h	E = 3000 Jmm ⁻¹ – v _a = 0.3 ms ⁻¹
De Witte and Coussement (1991)	GTAW	760°C – 1h	/
Cerjak and Schuster (1994)	SMAW	760°C – 2h	E = 2500 Jmm ⁻¹

Table C.I.1. Welding characteristics of the tested weldments

**manual arc welding*

***gas tungsten arc welding*

****submerged metal arc welding*

Some precisions must be added for a better comprehension of **figure C.I.2**:

1. When rupture occurs in the HAZ, it always occurs in the ICHAZ parallel to the fusion line (i.e. type IV rupture).
2. When rupture occurs in the base metal, it always occurs near the HAZ and also parallel to the fusion line.

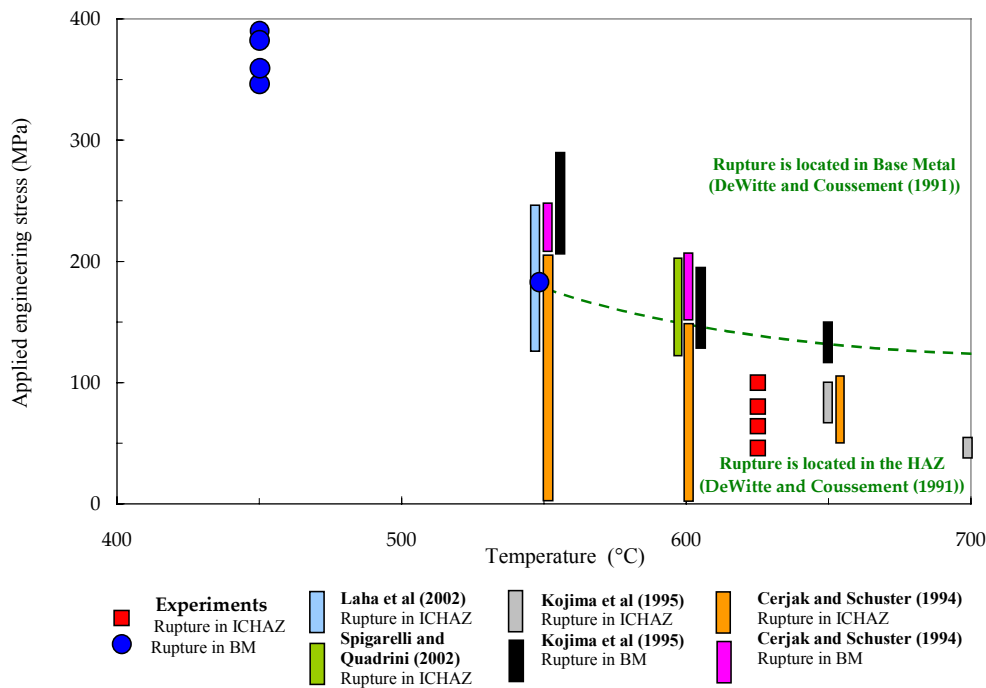


Figure C.I.2. Location of rupture in 9Cr1Mo-NbV weldments at high temperature

3. Comparison between the creep flow and damage properties of the base metal and the weldment

To characterise the effects of welding on mechanical and especially on creep properties, creep data of base metals and weldments are compared in **table C.I.2**. For the same applied engineering stress, the weldment fails ten times sooner than the base metal. Therefore, one should easily deduce that the welding operation strongly affects the creep strength of 9Cr1Mo-NbV steels. As the rupture is located in the ICHAZ, the microstructural changes in this area of the HAZ are obviously responsible for the loss of creep strength. Therefore, many studies were concerned with evaluating the creep flow and damage properties of the ICHAZ as reported in **section 5** in the following.

Temperature	Typical value for creep of weldments		Typical value for creep of base metal	
	Stress	Time to failure	Stress	Time to failure
575°C	200 MPa ^J	30 hours ^J	200 MPa ^J	300 hours ^J
	180 MPa ^J	100 hours ^J	160 MPa ^J	3,000 hours ^J
	120 MPa ^J	2,000 hours ^J	120 MPa ^J	20,000 hours ^J
	110 MPa ^J	9,000 hours ^J		
600°C	175 MPa ^{SQ}	25 hours ^{SQ}	130 MPa ^J	800 hours ^J
	120 MPa ^{CD}	700 hours ^{DC}	125 MPa ^O	7,518 hours ^O
	110 MPa ^{CD}	900 – 1,100 hours ^{DC}	120 MPa ^J	2,000 hours ^J
	108 MPa ^O	5,353 hours ^O	110 MPa ^J	7,000 hours ^J
	100 MPa ^{CD}	3,000 – 5,500 hours ^{DC}	100 MPa ^J	16,000 hours ^J
	70 MPa ^{CD}	10,000 – 11,500 hours ^{DC}		
625°C	100 MPa ^J	350 – 500 hours ^J	100 MPa ^J	2,500 hours ^J
	80 MPa ^J	2,300 hours ^J	90 MPa ^J	5,000 hours ^J
	60 MPa ^J	5,000 – 12,000 hours ^J	80 MPa ^J	14,000 hours ^J
650°C	100 MPa ^J	40 hours ^J	100 MPa ^J	200 hours ^J
	80 MPa ^J	150 hours ^J	80 MPa ^J	800 – 2,000 hours ^J
	70 MPa ^J	600 hours ^J	76 MPa ^O	6,015 hours ^O
	60 MPa ^J	1,200 hours ^J	70 MPa ^J	7,000 hours ^J
	50 MPa ^J	9,000 hours ^J	50 MPa ^J	27,000 hours ^J
	49 MPa ^O	7,595 hours ^O		

Table C.I.2. Creep of weldments: Synthesis of the works of^O Okamura et al (1999),^{SQ} Spigarelli and Quadri (2002),^{DC} De Witte and Coussement (1991),^J Jakobova et al (1998)

4. Studies of creep crack growth in the weldments

Some authors investigated the evolution of cracks in 9Cr1Mo-NbV steels weldments. Such a work is particularly difficult as microstructural heterogeneities may lead to a deviation of the crack. The most commonly used technique is to carry out creep tests with inserting cracks in the one of the three parts of the weldment i.e. the weld metal, the HAZ or the base metal as shown in **figure C.I.3**. It allows to determine a steady state crack propagation law for each part of the HAZ. It is also possible to perform tests with inserting cracks in the three zones so that the comparison between the various crack propagation rates is possible (see Gampe and Seliger (2001)).

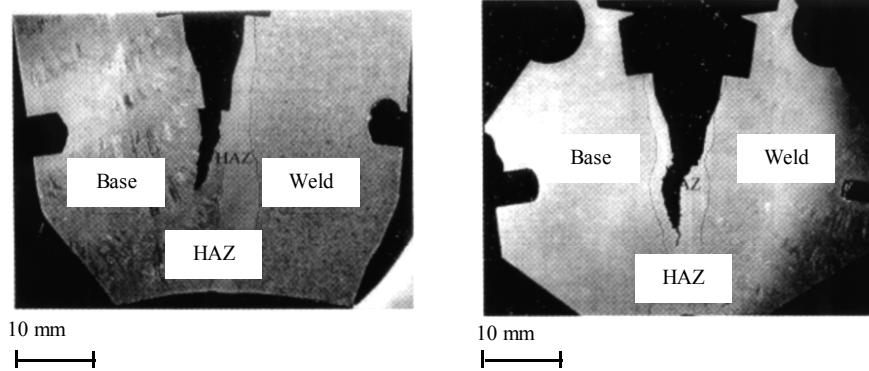


Figure C.I.3. Location of creep rupture in 9Cr1Mo-NbV weldments at high temperature (Extracted from Shibli and Mat Hamata (2001))

The steady state crack propagation can be expressed as:

$$\frac{da}{dt} = \beta(C^*)^\alpha \quad (\text{eq. C.I.1})$$

where β and α are materials parameters, C^* is the classical loading parameter used in the global approach to creep fracture (in $\text{Nm}^{-1}\text{h}^{-1}$) and da/dt is the crack propagation rate in mmh^{-1} . Note that C^* can be calculated provided the Norton power-law exponent of the material where the crack is located, is previously experimentally determined. The values of β and α at 625°C were determined by Shibli and Mat Hamata (2001) for both the base metal and the HAZ (see **table C.I.3**).

Material	Temperature	β	α
<i>Base Metal</i>	625°C	$6 \cdot 10^{-4}$	0.52
ZAT	625°C	$8 \cdot 10^{-4}$	0.57

Table C.I.3. Coefficients of the creep steady crack propagation equation C.I.1 calculated from the representation of Shibli and Mat Hamata (2001) given in figure C.I.4.

It is shown in **figure C.I.4** that the steady state crack propagation rate is substantially higher in the HAZ than in the base metal (These results are consistent with those of Maile et al (1998)). They confirm the lower creep lifetime evidenced by uniaxial creep data and the lower creep strength of the type IV region.

However, literature lacks from data concerning the creep time to the crack initiation. It was reminded in **chapter B.V** that the relative proportion of the two stages (i.e. initiation and growth) to the overall creep lifetime, strongly depends on the material ductility and that the time to the crack initiation was especially very long (obviously a longer stage than the crack propagation stage) in 9Cr1Mo-NbV steels.

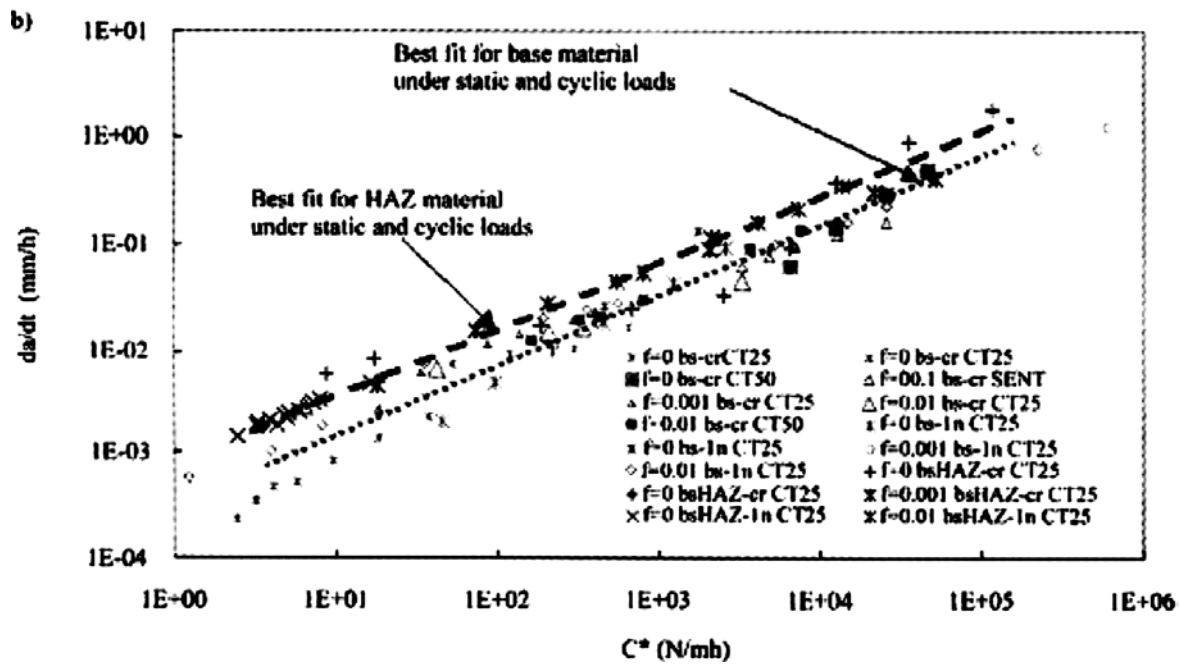


Figure C.I.4. Steady state crack propagation rates versus C^* (Extracted from Shibli et Mat Hamata (2001))

It is also shown in literature that for a better significance of creep crack propagation results, the pre-crack must be inserted in the HAZ (see Holdsworth (1998)) in 9Cr1Mo-NbV weldments. The use of miniaturised specimens, which would allow to study creep crack growth in various regions of the weldments, is also a field under investigation (see Tettamanti et al (1998)) even if no significant results have been published yet.

5. Modelling the microstructure of the weakest area in the weldment

In the weldments, the ICHAZ is a very narrow region (a few millimetres in thickness) so that it is desirable to reproduce the microstructure of the ICHAZ on bulk specimens to study its intrinsic creep properties. The thermal cycles representative of the ICHAZ used by various authors are reported in table C.I.4.

Source	T_{peak}	Heating rate	Cooling rate	PWHT
Hald and Lund (1993)	940°C	Not given	Not given	4.0 h - 774°C
Cerjak and Schuster (1994)	900 - 960°C	150°C s ⁻¹	$\Delta t_{800 \rightarrow 500} = 21$ s	12.0 h - 730°C
Eggeler (1994)	850 °C	Furnace (heating in 6 minutes and dwell of 5 minutes followed by air cooling)		12.0 h - 730°C
Tsuchida et al (1996)	900 °C	270°C s ⁻¹	$\Delta t_{800 \rightarrow 500} = 30$ s	8.5 h - 740°C
Otoguro et al (2000)	900 - 1100°C	Not given	$\Delta t_{800 \rightarrow 500} = 10$ s	1.0 h - 750°C
Letofsky et al (2000)	900 - 1000°C	Not given	Not given	2.0 h - 760°C
Matsui et al (2001)	920°C	4°C s ⁻¹	Not given	4.5 h - 740°C
Wu et al (2004)	850°C	Furnace (dwell of 20 minutes followed by air cooling)		2.0 h - 760°C

Table C.I.4. Thermal cycles chosen to reproduce the ICHAZ microstructure

Cerjak, Schuster (1994) considered that all cycles with peak temperatures between 900°C and 960°C were valids and made their final choice on hardness measurements. Moreover, Otoguro et al (2000) showed that the creep resistant microstructure depends on the applied engineering stress as for an applied engineering stress lower than 70 MPa the weakest simulated microstructure corresponds to $T_{\text{peak}} = 1000^\circ\text{C}$ and for an applied engineering stress larger than 70 MPa the weakest simulated microstructure corresponds to $T_{\text{peak}} = 1100^\circ\text{C}$. Matsui et al (2001) simulated two microstructures: the first corresponded to T_{peak} just above A_{c1} and the second to T_{peak} just below A_{c3} . The second specimen exhibited a largely recovered martensite structure with larger carbides and a lower creep strength which suggests that the weakest HAZ undergoes a welding thermal cycle in the upper bound of the intercritical domain.

Less widespread works like the one from Murdoch et al (2001) consider the necessity to perform heat treatments while applying a strain to obtain the right microstructure for the right temperature (i.e. just above A_{c1}). However, they also

found an equivalence between final microstructures obtained by strain added thermal treatment near A_{c1} and free thermal treatment near A_{c3} .

More information about metallurgical changes in the HAZ, and more specifically in the ICHAZ, will be given in **chapter C.III**. By way of introduction, the main features of the metallurgical state of the ICHAZ reported in the literature, and obviously responsible for the lower creep strength of the ICHAZ, are:

1. The $M_{23}C_6$ carbide size which is increased by a factor of 2 in comparison with that measured in the base metal due to carbide coarsening during the PWHT.
2. The dislocation density which is largely lower than in the base metal.
3. The initial lath microstructure which is replaced by a microstructure formed of low dislocation density equiaxed grains.

6. Creep results on simulated microstructures

Literature results of creep tests on simulated microstructures are summed up in **table C.I.5** and the dependence of the creep time to failure on the applied engineering stress for simulated microstructures is shown in **figure C.I.6**.

Authors	Simulated microstructure	Temperature	Load	Creep time
Cerjak and Schuster (1994)	$T_{peak} = 920^{\circ}C$ PWHT = 12 hours at $730^{\circ}C$	$550^{\circ}C$	250 MPa	200 hours
			230MPa	2,00 hours
			210 MPa	3,500 hours
			190 MPa	6,000 hours
Cerjak and Schuster (1994)	$T_{peak} = 920^{\circ}C$ PWHT = 12 hours at $730^{\circ}C$	$600^{\circ}C$	190 MPa	10 hours
			170 MPa	30 hours
Wu et al (2004)	$T_{peak} = 850^{\circ}C$ PWHT = 2 hours at $760^{\circ}C$	$600^{\circ}C$	180 MPa	65 hours
			150 MPa	605 hours
			130 MPa	3,220 hours
			110 MPa	12,500 hours
Eggeler et al (1994)	$T_{peak} = 850^{\circ}C$ PWHT = 12 hours at $730^{\circ}C$	$600^{\circ}C$	160 MPa	28 hours
			140 MPa	69 hours
			100 MPa	1,754 hours
Eggeler et al (1994)	$T_{peak} = 850^{\circ}C$ PWHT = 12 hours at $730^{\circ}C$	$620^{\circ}C$	140 MPa	18 hours
			120 MPa	53 hours
Tsuchida et al (1996)	$T_{peak} = 950^{\circ}C$ PWHT = 8.5 hour at $740^{\circ}C$	$625^{\circ}C$	100 MPa *	750 hours *
			70 MPa *	5,000 hours *
Otoguro et al (2000)	$T_{peak} = 900^{\circ}C$ PWHT = 1 hour at $750^{\circ}C$	$650^{\circ}C$	105 MPa	60 hours
			85 MPa	200 hours
			70 MPa *	1,000 hours *
			50 MPa *	10,000 hours *
Otoguro et al (2000)	$T_{peak} = 1100^{\circ}C$ PWHT = 1 hour at $750^{\circ}C$	$650^{\circ}C$	125 MPa	60 hours
			105 MPa	200 hours
			70 MPa *	1,000 hours *
			45 MPa *	10,000 hours *
Matsui et al (2001)	$T_{peak} = 920^{\circ}C$ PWHT = 4.5 hours at $740^{\circ}C$	$650^{\circ}C$	110 MPa	27.4 hours
			90 MPa	200 hours

Table C.I.5. Creep properties of simulated soft HAZ (results given by extrapolations)*

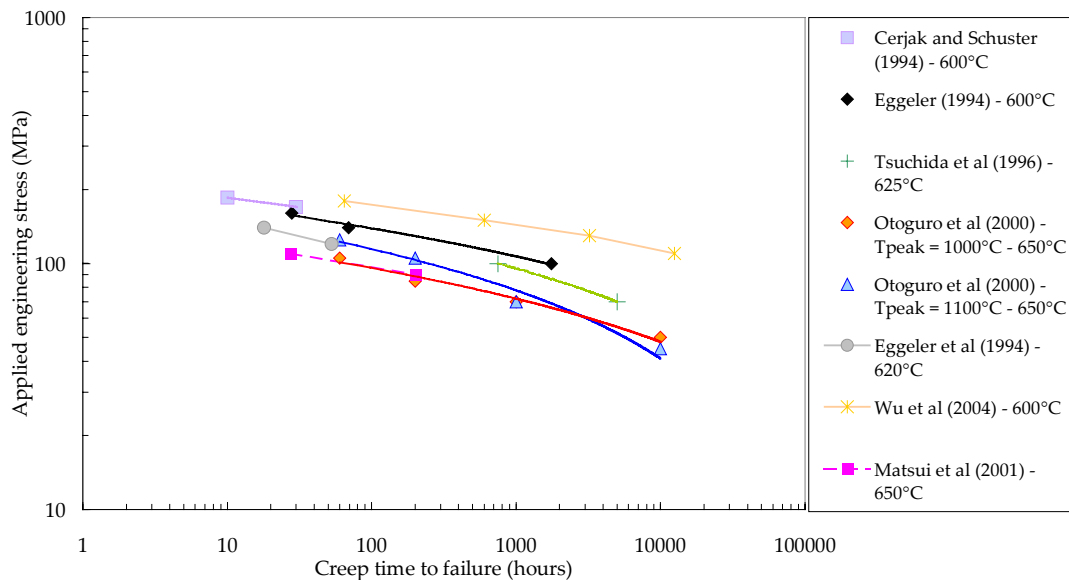


Figure C.I.6. Creep curves for creep tests on simulated ICHAZ microstructures

The results of **figure C.I.6** and **table C.I.5** show that the work of the different authors are in quite good agreement despite some differences in the weld thermal cycle they used. Therefore, it shows that there is a quite large degree of freedom in the choice of a thermal cycle representative of the ICHAZ provided the peak temperature, T_{peak} , of the welding heat treatment is set within the intercritical domain ($A_{c1} < T_{peak} < A_{c3}$).

7. Improving the creep properties of the weldments

Several ways have been explored to improve creep properties of weldments with the main guideline being the limitation of softening in the ICHAZ:

1. Sato and Tamura (1998) indicated that the only way to suppress softening in the ICHAZ is to perform a normalising and then a tempering treatment after welding. The resulting weldment would have the same creep properties than the base metal. However, this solution is not convenient for large industrial components that must be welded on field.
2. Kojima et al (1995) have tested the influence of a specific thermo-mechanical treatment on HAZ which was supposed to increase creep strength by changing the morphology of MX particles but they did not succeed in improving the creep strength of the weldment. The thermo-mechanical heat treatment increases the over-all hardness values including the maximum softening area but was not effective in increasing the creep rupture properties of welded joints.
3. De Witte and Coussement (1991) proposed an “half tempering” treatment which consists in tempering the base metal between 620°C and 650°C before welding to avoid complete precipitation of $M_{23}C_6$ carbides before welding and to form M_2X particles. The idea is that when performing the PWHT at 750°C - 760°C, the precipitation of $M_{23}C_6$ carbides will occur and the M_2X precipitates will transform in MX precipitates. The creep strength of the resulting weldment is significantly improved.
4. It is finally generally admitted that improving the creep strength of the base metal by changing the alloy composition (see end of **chapter B.I**) would also increase the creep strength of the weldments. Otoguro et al (2000) evidenced benefits from W addition. They also test the influence of the Nb/C ratio with the conclusion that it must be set so as NbC precipitates can dissolve during heating. However they found that boron addition which increase base metal creep strength, decreases weldments creep strength due to the precipitation of a damaging boron nitride. It is also evidenced that the reduction factor of the creep strength between the HAZ and the base metal does not change.

8. Conclusions

The synthesis of literature data about 9Cr1Mo-NbV weldment creep lifetime can be summed up as follow:

1. The location of the rupture depends on the temperature and the applied engineering stress as at low temperature and/or at high stress level rupture of weldments occurs in the base metal and at high temperature and/or low stress, the rupture is of type IV in the intercritical heat affected zone (ICHAZ).

- Whether the rupture is located in the base metal or in the ICHAZ, weldments have a creep strength lower than that of the base metal. This difference in creep rupture strength is more finely investigated in **chapter C.II**.

The metallurgical origin of the lower creep strength of the ICHAZ is largely investigated in the literature and will be more precisely detailed but also experimentally investigated in **chapter C.III**. Moreover, as literature data are only concerned with uniaxial creep data, the effect of the stress triaxiality ratio on the creep flow and damage behaviour of the weakest HAZ microstructure will be investigated in the present study (**chapter C.III** and **C.IV**). This experimental database allows to propose a model integrating and coupling multiple creep deformation and damage mechanisms for the weakest HAZ (**chapter C.IV**).

References

- Cerjak H., Letofsky E., Staubli M. (1998). The role of welding components made from advanced 9-12%Cr steels. *Materials for advanced power engineering - 6th Liege Conference*. 105-121.
- Cerjak H., Schuster F. (1994). Weldability and behaviour of weldings of new developed creep resistant 9-10% Cr steels. *Second conference on joining technology EUROJOIN2*. 157-167.
- DeWitte M., Coussement C. (1991). Creep properties of 12%Cr and improved 9%Cr weldments. *Materials at high temperature*. **9(4)**. 178-184.
- Dogan B., Petrovski B. (2001). Creep crack growth of high temperature weldments. *International journal of pressure vessels and piping*. **78**.
- Eggeler G., Rameke A., Coleman M., Chew B., Peter G., Burblies A., Hald J., Jefferey C., Rantal J., De Witte M., Mohrmann R. (1994). Analysis of creep in a welded 'P91' pressure vessel. *International journal of pressure vessels and piping*. **60**. 237-257.
- Escaravage C. (2002). Compte rendu de congrès, 28th MPA Seminar (State material testing institute of university of Stuttgart). *EVEDCR020516ECG/CPA. Private communication*.
- Gampe U., Seliger P. (2001). Creep crack growth testing of P91 and P22 pipe bends. *International journal of pressure vessels and piping*. **78**. 859-864.
- Hald J., Lund E.M. (1993). TEM investigations in the HAZ in P91 steel (9Cr, 1Mo, Nb, V). *International conference of the joining of materials – Hebingor (Danemark)*.
- Holdsworth S.R. (2001). Creep damage zone development in advanced 9%Cr steel weldments. *International journal of pressure vessels and piping*. **78**. 773-778.
- Kojima T., Hagashi K., Kajita T. (1995). HAZ softening and creep rupture strength of high Cr ferritic steel weldments. *ISIJ International*. **35(10)**. 1284-1290.
- Laha K., Chandravathi K.S., Bhanu Santara Ras K., Mannan S.L. (2000). Microstructural evolution, creep deformation and rupture behaviour of 9Cr1Mo steel base metal, weld metal and weld joint. *Transactions of the Indian Institute of metals*. **55(3)**. 217-221.
- Letofsky E., Cerjak H., Warbichler P. (2000). The use of electron microscopic investigations to characterise the creep behaviour of welded joints in modern power station materials. *Praktische Metallographie*. **37(9)**. 509-520.
- Maile K., Schellenberg G., Granacher J., Tramer M. (1998). Description of creep and creep fatigue crack growth in 1% and 9%Cr steels. *Materials at high temperature*. **15(2)**. 131-137.
- Matsui M., Tabuchi M., Watanabe T., Kubo K., Kinugawa J., Abe F. (2001). Degradation of creep strength in welded joint of 9%Cr steel. *ISIJ international*. **41**. s126-s130.
- Okamura H., Ohtani R., Saito K., Kimura K., Ishii R., Fujiyama K., Hongo S., Iseki T., Uchida H. (1999). Basic Investigation for life assessment technology of modified 9Cr-1Mo steel. *Nuclear Engineering and Design*. **193** (1999). 243-254.
- Otoguro Y., Matsubara M., Itoh I., Nakazawa T. (2000). Creep rupture strength of heat affected zone for 9Cr ferritic heat resisting steels. *Nuclear engineering and design*. **196**. 51-61.
- Sato T., Tamura K. (1998). Improvement of creep rupture strength of 9Cr1MoNbV welded joints by normalising and tempering after weld. *Materials for advanced power engineering - 6th Liege Conference*. 393-399.
- Schuller H.J., Hagn L., Woitschek A. (1974). *Maschinenschaden*. **47**. 1-13.
- Shibli I.A., Mat Hamata N. (2001). Creep crack growth in P22 and P91 welds – Overview from SOTA and HIDA projects. *International journal of pressure vessels and piping*. **78**. 785-793.
- Spigarelli S., Quadrini E. (2002). Analysis of the creep behaviour of a modified P91 (9Cr1Mo-NbV) welds. *Materials and design*. **23**. 547-552.
- Tettamanti S., Bicego V., Taylor N.G., Bregani F. (1998). Creep crack growth in materials for steel components: advanced modelling and miniaturised testing aspects. *Materials at high temperature*. **15(2)**. 51-55.
- Tsuchida Y., Okamoto K., Tokunaya Y. (1996). Study of creep rupture strength in heat affected zone of 9Cr-1Mo-V-N-Nb steel by welding thermal cycle simulation. *Welding international*. **10(6)**. 454-460.

Wu R., Sandstrom R., Seitisleam F. (2004). Influence of extra coarse grains on the creep properties of 9 percent CrMoV (P91) steel weldment. *Journal of engineering materials and technology*. **126**. 87-94.

Chapter C.II. Comparison between creep flow and damage behaviour of the P91 base metal and the WJP91 weldment at 625°C.

The present chapter was written as an article intended to be submitted to nuclear engineering and design. A study of metallurgical changes in weldments during creep exposure by means of electron backscattered diffraction (EBSD) analysis is also included at the end of the chapter.

High temperature creep flow and damage properties of 9Cr1Mo-NbV steels: base metal and weldment

V. Gaffard, A.F. Gourgues-Lorenzon, J. Besson

*Ecole Nationale Supérieure des Mines de Paris (E.N.S.M.P) - Centre des Matériaux
UMR CNRS 7633 BP 87, 91003 Evry Cedex France (corresponding author: anne-francoise.gourgues@ensmp.fr)*

Abstract

High temperature creep flow and damage properties of 9Cr1Mo-NbV steel and weldment are investigated in the present study. First, an experimental database is built to compare both creep flow and damage properties of the base metal and the weldment. Metallurgical investigations before and after creep tests revealed that the microstructural state is responsible for the lower creep strength in the weldment. A simple analysis based on the description of the steady state creep and the use of empirical lifetime prediction relationships is performed. It allows to predict the weldment creep lifetime without performing an extensive number of experiments.

1.Introduction

The need to reduce production costs and greenhouse gas effect emissions of power plants was recognised in the early 1980's. This objective can only be reached provided the efficiency of power plants is increased. Therefore, several research programs were launched in the United States (EPRI), in Japan and Europe (COST501 and 522) to develop materials for use at high temperature (up to 650°C) and pressure (up to 300 bars), essentially new chromium stainless steels. Among them, 9Cr1Mo-NbV steels are candidates as structural materials for boiler, turbines and steam lines of supercritical and ultra-supercritical power plants. More recently, it has also been envisaged to use them at lower temperatures (i.e. 450°C – 550°C) for the pressure vessels of nuclear power plants. 9Cr1Mo-NbV steels were chosen for their high resistance to oxidation, their good mechanical properties and their good weldability (high thermal conductivity and low thermal expansion coefficient). In the framework of the HIDA project (Shibli (2001)), creep experiments have been performed on both 9Cr1Mo-NbV steel and weldment at high temperature (Prunier et al (1998)). The present study gives complementary results to the database of the HIDA project. These results are compared to literature data (Kojima et al (1996), Jakobova et al (1998), Laha et al (2000), Spigarelli, Quadrini (2002)) and confirm the high sensitivity of 9Cr1Mo-NbV steel weldments to type IV cracking in the heat affected zone. In the literature, type IV cracking is analysed using a two steps methodology:

1. The heat affected zone (HAZ) creep properties are first investigated by microstructure simulation followed by mechanical testing (see Cerjak and Schuster (1994), Tsuchida et al (1996) and Ootoguro et al (2001)).
2. The creep response of the weldment is modelled using a multi-material representation: classically, a three materials representation is chosen: weld metal, simulated HAZ and base metal, to study the constraint effects with varying the values of geometry parameters such as the HAZ width or the angle between the load axis and the fusion line (see Chellapandi and Chetal (2000), Storesund and Tu (1995) and Eggeler (1994)).

In fact, type IV cracking is controlled by both constraint effects and the intrinsic creep strength of the weakest area of the weldment. The respective influences of, on the one hand, the constraint effects and, on the other hand, the creep damage properties of the HAZ, are of great importance and must be well understood before performing multi-material FE calculations. The aim of the present study is to show that detailed analysis of uniaxial creep data on weldments allows to evaluate creep properties mismatch and the resulting constraint effects. First, the physical creep damage mechanisms of the weldment of this steel are studied in details by means of metallurgical investigations. It especially allows to evaluate the intrinsic loss of ductility in the HAZ when comparing with creep damage mechanisms encountered in the base metal. Then, a simple uni-dimensional analysis of the problem (see also Spigarelli and Quadrini (2002)) is used to evaluate the creep properties of the HAZ. It allows to, then study the constraint effects by comparing bi-material FE calculations and measurements of local creep strains in cross-weld specimens. Finally, the investigations of the present

study allow to establish a simple model able to predict the creep lifetime of the weldment for design purposes. More generally, the conclusions of the analysis of the present paper can be used as a guideline for multi-material FE calculations.

2. Materials and experimental procedures

2.1. Materials

This study focuses on a circumferentially welded joint of two pipes of 295 mm in outer diameter and 55 mm in thickness. The welded area exhibits a V shape of 5 mm in width at the inner surface of the pipe and 25 mm at the outer surface of the pipe. The base metal and filler metals are 9Cr-1MoNbV steels whose chemical compositions are very close to each other (**table C.II.1**). Heat treatment of the base metal before welding consisted in a normalising treatment of one hour at 1065°C followed by a two hours tempering treatment at 765°C.

	C	Si	Mn	P	S	Al	Cr	Ni	Mo	V	Nb	N	Cu
Base Metal	0.09	0.31	0.41	0.014	0.005	0.016	8.56	0.26	0.92	0.21	0.065	0.042	/
Filler Metal	0.09	0.37	0.41	0.028	0.013	0.07	8.44	0.27	0.92	0.24	/	0.038	0.04

Table C.II.1. Chemical composition of base and filler metals used in this study (wt %)

The welding procedure was submerged metal arc welding with seventeen runs. To avoid solidification and reheat cracking, the heat input energy was set to values lower than 1300 Jmm⁻¹. To release residual stresses and temper freshly formed martensite, a post weld heat treatment (PWHT) of two hours at 760°C was performed on the welded pipe.

2.2. Metallurgical investigations

Microstructures were examined after PWHT by light optical and scanning electron microscope (SEM) investigations in a field emission gun SEM (Zeiss DSM 982). The electron backscattered diffraction (EBSD) analysis technique was also used in the FEG-SEM at 20 kV with the specimen tilted by 70° to determine crystallographic properties of the matrix. Carbon extraction replicas were analysed in the SEM to characterise the precipitation state in terms of particle size and chemical composition. The etching reagent for extraction was the Villela etchant (100 ml methanol, 1g picric acid and 5 ml hydrochloric acid). The particle size was determined as the equivalent diameter d_{eq} which corresponds to the diameter of a circle equal in area to the measured area of the particle. To do so, a public domain image analysis software Scion® was used. The chemical composition of precipitates was determined using X-Ray energy dispersive spectrometry. Thin foils of the material were also examined by transmission electron microscopy (TEM) after electrolytic thinning in a 45% butoxyethanol, 45% acetic acid and 10% perchloric acid solution at 0°C with a tension of 40 V.

2.3. Mechanical tests

Creep tensile tests were performed at 625°C (898 K) under constant applied load in controlled laboratory atmosphere (20°C – 50% relative humidity). The load was applied using dead weights. The temperature gradient between top and bottom ends of the specimen did not exceed 2°C. The elongation measured by linear variable differential transducers was continuously recorded with a sensitivity of 1 µm.

Specimens were machined from the welded joint described above along the transverse direction of the weld (i.e. along the pipe axis). Both creep tests on specimens containing only base metal (far from the welding area) and on cross-weld specimens with all microstructural states: weld metal, base metal and heat affected zone in the gauge area (see **figure C.II.1**), were performed. In weldment specimens, relative proportions of base and weld metals in the gauge area, and also the angle between the fusion line and the specimen axis, slightly vary with specimen location in the pipe thickness. Most creep specimens were smooth round tensile bars (SC specimens) with a gauge length of 36 mm and a gauge diameter of 5 mm. Part of these creep tests had already been carried out for the HIDA project (Prunier et al (1998), Jayet-Gendrot (1999)). The applied engineering stresses ranged from 90 MPa to 120 MPa and from 50 MPa to 100 MPa for respectively the base metal and the weldment.

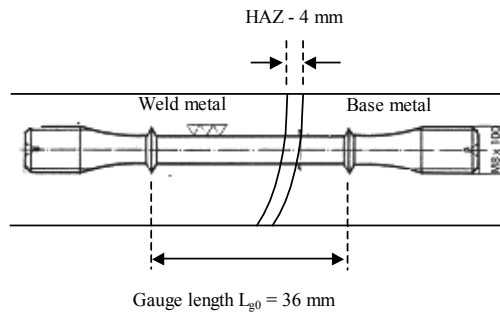


Figure C.II.1. Location of weldment specimens in the welded joint

To separately determine the steady state creep flow properties of the weld metal, an additional creep test with load levels varying with steps (60 – 80 – 100 – 120 MPa) was also carried out on a plate specimen having a gauge length of 20 mm and a thickness of 0.5 mm. This specimen was machined from the weldment in the largest welded area (i.e. near the outer surface of the pipe), so that all the gauge length was made of weld metal. Two complementary creep tests were also carried under high vacuum (10^{-3} Pa) on plate specimens made of base metal and weldment respectively to investigate fracture surfaces free from extensive oxidation. The applied engineering stresses were 120 MPa and 90 MPa for respectively base metal and cross-weld specimen. The corresponding creep times to failure for the base metal and the cross-weld specimen were respectively of 1,000 and 1,800 hours.

3. Results of microstructural characterisation

The base metal is a tempered martensitic stainless steel. Martensite exhibits a lath morphology (figure C.II.2b). Laths of close crystallographic orientation are gathered into packets within the prior austenite grain (100 μm in mean size). A number of M_{23}C_6 (mainly Cr_{23}C_6) carbides are located at both grain, packet and lath boundaries and MX precipitates ($\text{Nb}(\text{C},\text{N})$, $\text{V}(\text{N},\text{C})$) were also detected mainly at grain boundaries and within laths. The mean size of M_{23}C_6 carbide is $d_{\text{eq}} = 100$ nm. The TEM micrograph of figure C.II.2b also shows that the initial dislocation density is very high inside the lath martensite.

After the PWHT treatment, the weld metal exhibits a microstructure very similar to that of the base metal. The solidification substructure, commonly observed in the weld metal, was not observed as solid state austenite to martensite phase transformation occurs during cooling. However, a preferential growth of the austenite grain following the thermal gradient was evidenced (i.e. the austenite grain exhibited a columnar shape). The precipitation state is very similar to that of the base metal except that the presence of MnS particles resulting from the welding operation was also detected. Moreover, many defects and strongly softened regions (200 HV0.5) of few microns in thickness at interpass solidification fronts, were observed in the weld metal.

Major microstructural changes were evidenced in the HAZ as local heating of the base metal led to phase transformations. The welding thermal cycles experienced by the base metal in the HAZ are characterised by high speed heating rates ($100^\circ\text{C}\text{s}^{-1}$ - $200^\circ\text{C}\text{s}^{-1}$) and short annealing at the peak temperature (< 2 s). The HAZ is approximately a 4 mm - 5 mm long area (see figure C.II.2a) that is usually divided into three main areas from the weld to the base metal:

1. The coarse grained heat affected zone (CGHAZ) corresponds to maximum temperatures much higher than A_{c3} (i.e. much higher than 1050°C for a heating rate of $150^\circ\text{C}\text{s}^{-1}$). It exhibits a larger austenite grain size (180 μm – 200 μm in average) than the base metal.
2. The fine grained heat affected zone (FGHAZ) corresponds to a local maximum temperature just above A_{c3} . It exhibits a finer austenite grain size (50 μm – 60 μm in average) than the base metal.
3. The intercritical heat affected zone (ICHAZ) corresponds to local heating in the intercritical domain (i.e. between A_{c1} and A_{c3} where $A_{\text{c1}} \approx 930^\circ\text{C}$ for a heating rate of $150^\circ\text{C}\text{s}^{-1}$).

Near the HAZ, one can also distinguish the over-tempered base metal which corresponds to local heating at temperatures just below A_{c1} . The variations in the microstructural states are evidenced by the hardness profile plotted in figure C.II.2a with especially a strong drop of hardness in the ICHAZ. Such values for hardness and such a drop has already been reported for a large variety of 9Cr1Mo-NbV steels (Jakobova et al (1998), Cerjak and Schuster (1995), Eggeler et al (1994) and DeWitte and Couesment (1991).) Therefore, attention was focused on the properties of the ICHAZ microstructure. As shown in figure C.II.2c, this area exhibits a totally recovered microstructure and the initial martensite lath microstructure is replaced by an equiaxed one with grains of 5 μm – 10 μm in mean size (see also Letofsky et al (2000) and Hald and Lund (1993)). A lower dislocation density is also evidenced, whereas the average size d_{eq} of M_{23}C_6 carbides is larger than $d_{\text{eq}} = 200$ nm in this area i.e. twice the average size found in the base metal. In fact, dissolution of the initial M_{23}C_6 carbides only occurs in the upper bound of the intercritical domain (see Cerjak and

Schuster (1994)) so that over-ageing due to both the intercritical thermal cycle and the high tempering PWHT promote their coarsening in the ICHAZ. Moreover, the MX particles remain undissolved during heating so that the martensite, newly formed upon cooling, exhibits a lower microstructural stability than the base metal because of a decrease in both the strengthening and the grain boundary pinning effect of the second phase particles. Therefore, due to these metallurgical changes, one can foresee that the ICHAZ should exhibit a lower creep strength than the base metal. However, as constraint effects, due to microstructural inhomogeneity, may play a key role in the creep flow and damage behaviour of the welded joints, more detailed investigations were carried out as reported in the next section.

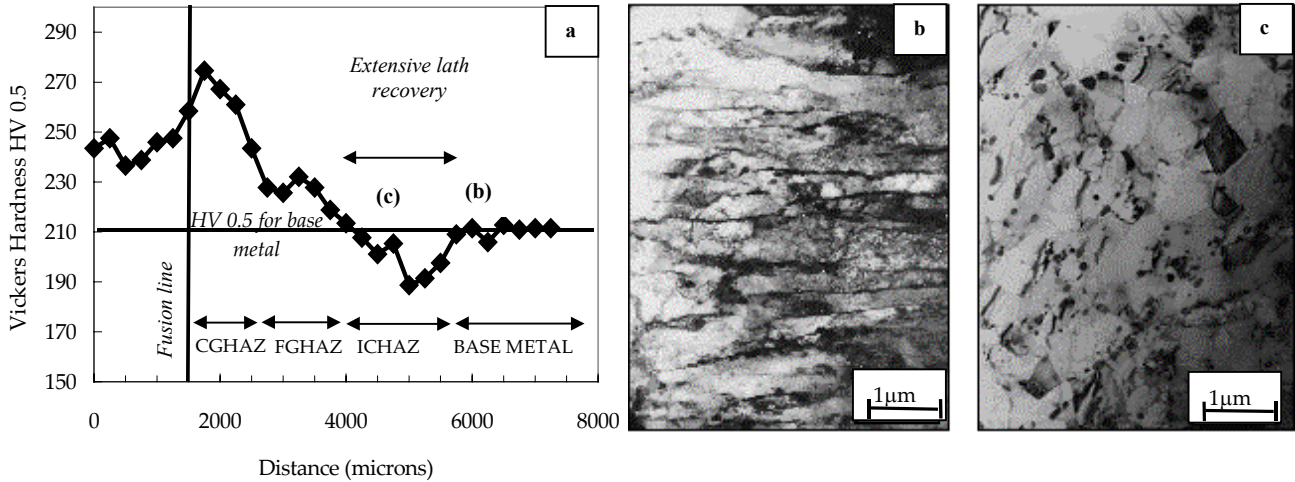


Figure C.II.2. Microstructural changes in the heat affected zone of the welded joint

(a) hardness profile (experimental scatter $\pm 5HV0.5$), (b) TEM observation of base metal and (c) TEM observation of the ICHAZ

4. Results of creep tests

4.1. Creep curves of the base metal

All creep experiments on the base metal are results of the HIDA project (Prunier et al (1998)). The creep curves are shown in figure C.II.3a. The 9Cr1Mo-NbV steel exhibits a very short primary creep stage. On the contrary, the tertiary creep stage is very long and represents two thirds of the overall creep life. Almost very short steady-state creep is observed.

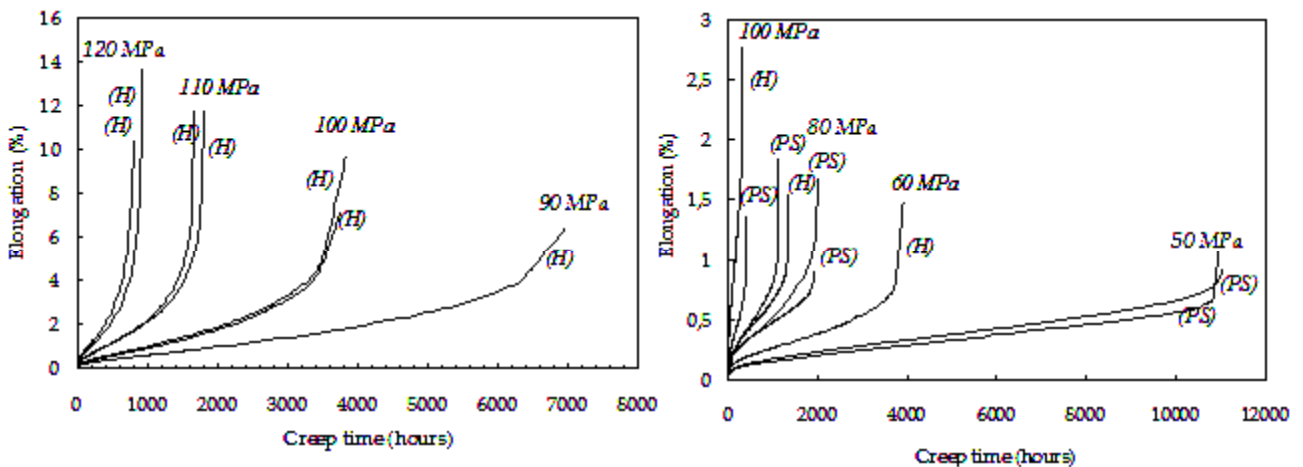


Figure C.II.3. Creep curves of the base metal and weldment specimens at 625°C

PS = present study and H = HIDA (Prunier et al (1998))

The elongation of the cross-weld specimens was determined as:

$$\varepsilon = \frac{\Delta L_g}{L_{g0}} \quad (\text{eq. C.II.1})$$

where $L_{g0} = 36 \text{ mm}$ is the initial gauge length (see figure C.II.1) and ΔL_g is the actual elongation of the gauge length.

The steady state strain rate, $\dot{\epsilon}_{ss}$ was represented using a Norton power-law (see **figure C.II.4**):

$$\dot{\epsilon}_{ss} = B\sigma^n \quad (\text{eq. C.II.2})$$

where σ is the applied engineering stress (see **table C.II.2** for values of B_{BM} and n_{BM}).

	B (h⁻¹MPa⁻ⁿ)	n
Base metal (BM) - Experiments	$B_{BM} = 3.03 \cdot 10^{-22}$	$n_{BM} = 8.1$
Weldment (W) - Experiments	$B_W = 2.08 \cdot 10^{-17}$	$n_W = 6.0$
HAZ – Calculated with $l_{HAZ} = 4$ mm	$B_{HAZ} = 3.23 \cdot 10^{-16}$	$n_{HAZ} = 5.8$

Table C.II. 2. Norton power-law parameters for base metal, weldment specimens and HAZ at 625°C

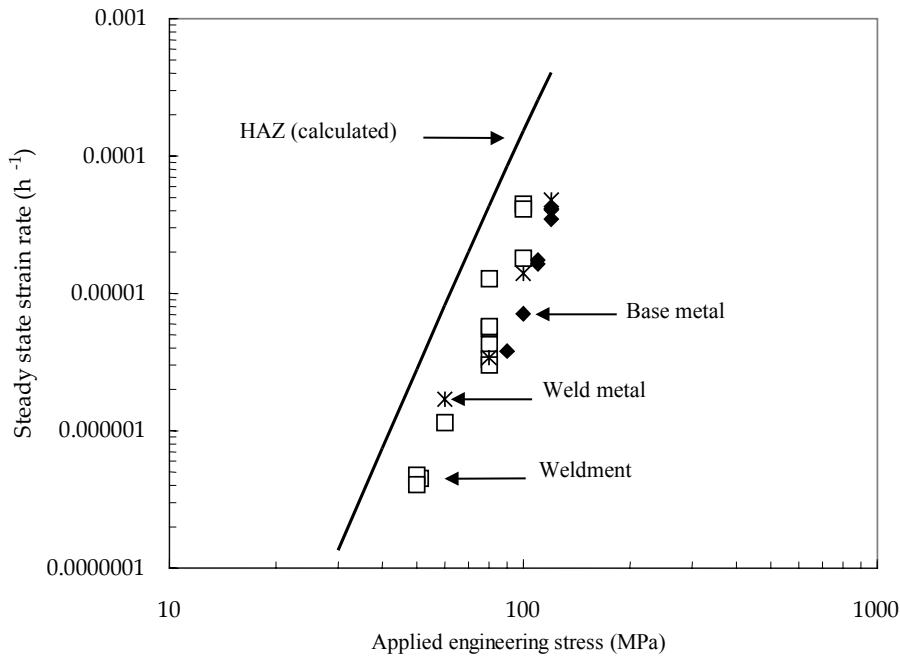


Figure C.II.4. Steady state creep strain rate versus nominal stress at 625°C

4.2. Creep curves of weldment specimens

Creep curves of tests on the weldment are shown in **figure C.II.3b**. Experimental data of the present study and literature results show very good agreement (see **figure C.II.5b**). For the highest stress levels (i.e. short test durations), an experimental scatter of the creep results is observed. A factor of three between minimum and maximum lifetimes for the same creep conditions is evidenced (especially for an applied engineering stress equal to 80 MPa). Specimens machined from upper welding runs appeared to have a lower creep strength than the other ones. This is probably due to the fact that in this area the newly formed martensite has not benefited from reheating due to the following welding runs, and also because the HAZ is thicker by about 1 mm in this area. However, this phenomenon, which is very marked at the highest stress levels, tends to disappear for longer test durations (10,000 hours - 50 MPa), where results do not depend on specimen location. The creep flow behaviour of the weldment, considered as an homogeneous material, was also represented by the Norton power-law (see **equation C.II.2**) with coefficients B_W and n_W given in **table C.II.2**.

The defects observed in the weld metal do not affect the creep strength of the weldment specimens. The creep fracture mode at 625°C was of type IV in all testing conditions i.e. in the ICHAZ parallel to the fusion line (Hyde and Tang (1998)). These results are consistent with literature data (Spigarelli and Quadri (2002), Laha et al (2000), Kojima et al (1995), Cerjak and Schuster (1994) and De Witte and Coussement (1991)). The literature database of **figure C.II.5a** also shows that the rupture location shifts from the HAZ to the base metal, but near the HAZ (i.e. in the over-tempered area), at high stresses, while remaining parallel to the fusion line. The transition stress between the two domains can be evaluated, from **figure C.II.5a**, to about 130 MPa at 625°C. Nevertheless, in all tests, the creep lifetime of the weldment is reduced with a factor of 12 compared to that of the base metal for the same applied engineering stress (i.e the applied engineering stress must be decreased by nearly 30% to reach the same creep time to failure than the base metal). The lower creep strength of the ICHAZ and its damage behaviour are obviously the key point determining the creep failure of the weldment from high to low stress and are investigated in more detail in the following.

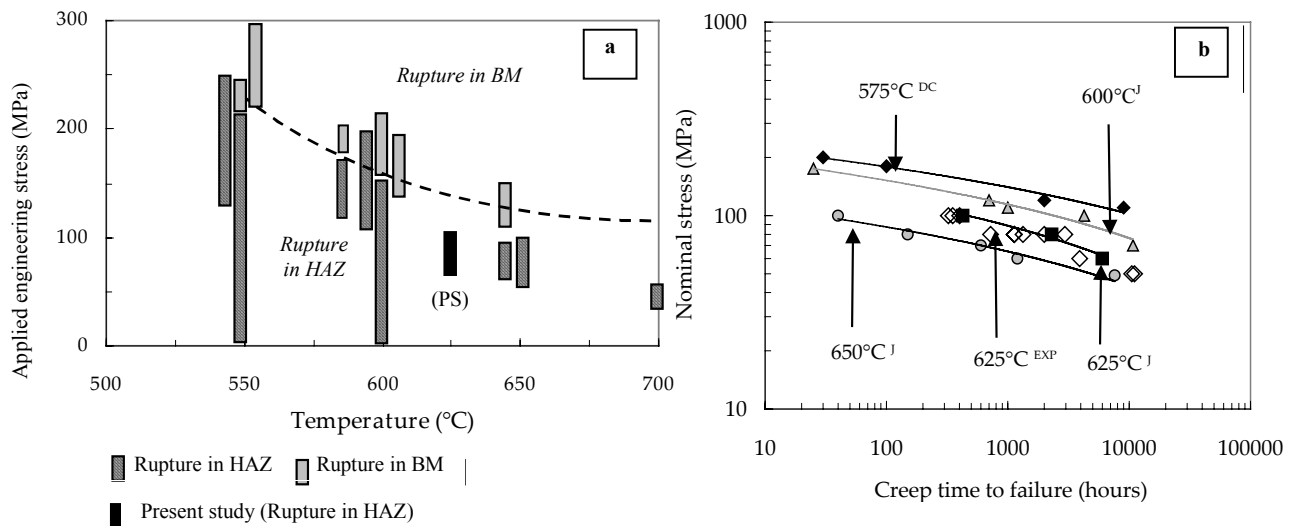


Figure C.II.5. (a) Rupture location in weldments (Synthesis from work by Spigarelli and Quadrini (2002), Laha et al (2000), Kojima et al (1995), Cerjak and Schuster (1994) and DeWitte and Coussement (1991) – (b) Creep rupture properties of weldments: Comparison between experiments (EXP) and literature results: J = Jakobova et al (1998) and DC = DeWitte and Coussement(1991).

4.3. Damage mechanisms in the base metal

SEM investigations of fracture surfaces showed that failure occurs in a ductile manner with dimples of 20 μm in size. Creep tests performed under vacuum to avoid oxidation, allowing for more detailed observations of the fracture surface, showed intergranular fracture inside the dimples (figure C.II.6a). Thus, ductile failure is the ultimate stage but does not control rupture. Additional investigations of cross-sections of the fractured creep specimens revealed the following key points of creep damage processes in the base metal at 625°C:

1. Cavities nucleate at grain boundaries, preferentially in stress concentration areas (near second phase particles or at triple junctions).
2. Cavity growth is assisted by grain deformation (see volume growth of cavities in figure C.II.7a) but also proceeds by coalescence of small intergranular cavities.
3. Recovery of the initial lath martensite microstructure (figure C.II.8b) triggers specimen necking, leading to ductile fracture for relatively low ($\approx 10\%$) volume fractions of cavities.

For long term creep exposure, time assisted softening of the microstructure (lath martensite recovery) is evidenced. This transformation of the initial lath martensite microstructure into small equiaxed, highly misoriented grains (compare figures C.II.8b and C.II.8d) obviously strongly affects long term creep fracture properties of the base metal.

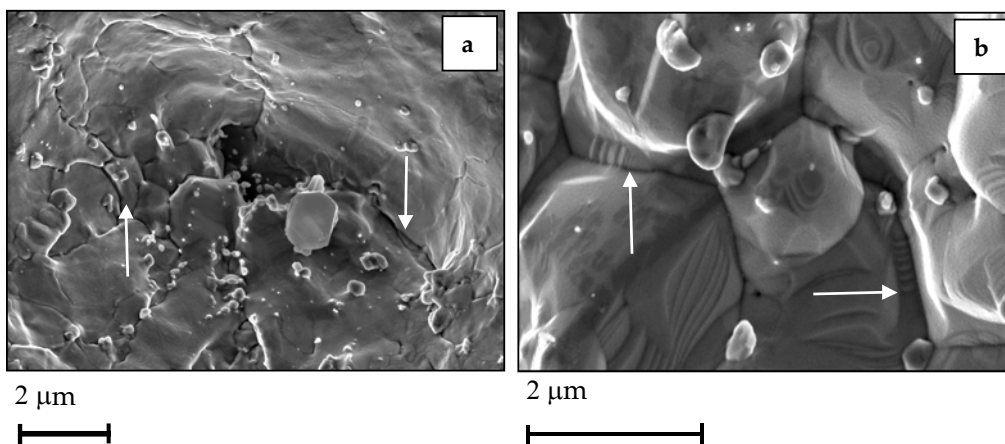


Figure C.II.6. Fracture surfaces of creep specimens tested under vacuum SEM observations (a) Base metal (120MPa – 1800 hours) – (b) Weldment (90 MPa – 950 hours) Arrows indicate secondary intergranular cracking between the grain boundary facets

4.4. *Damage mechanisms in the weldment*

SEM fractography of the weldment specimen creep tested under vacuum evidenced predominantly an intergranular fracture mode (**figure C.II.6b**). When comparing the fracture surface with that of the base metal specimen (**figure C.II.6a**), it appears that intergranular fracture is more prominent in the weldment than in the base metal. SEM investigations of cross-sections showed that, whatever the value of the applied engineering stress, rupture takes place in the ICHAZ, which has a fine grained, equiaxed microstructure. These observations are confirmed by EBSD analysis (see **figure C.II.8a** and **C.II.8c**) showing that creep fracture occurs in the equiaxed microstructure area. Moreover, the other parts of the weldment specimens are very little damaged (see also Li et al (2003)). Cavity nucleation occurs at grain boundaries and more precisely at triple points and at interfaces between the matrix and second phase particles. Large carbides of the initial microstructure and Laves phase particles ((Fe,Cr)₂Mo) formed during creep (larger than 300 nm in mean size) are preferential sites for cavity nucleation. The comparison with the dominating damage process in the base metal (see **figure C.II.7a**) shows that creep cavity growth is less assisted by grain deformation in the ICHAZ. The cavities exhibit a round shape in the base metal (**figure C.II.7a**) whereas they exhibit a more elongated “crack-like” shape in the weldment (see arrow in **figure C.II.7b**). The high misorientation between the small equiaxed grains also confirms the sensitivity of the ICHAZ microstructure to grain boundary cracking (see EBSD maps in **figure C.II.7a** and **C.II.7c**). Diffusion assisted cavity growth along the boundaries of small equiaxed grains (see **figure C.II.7b**) is thus probably the dominating damage mechanism in the weldment specimens.

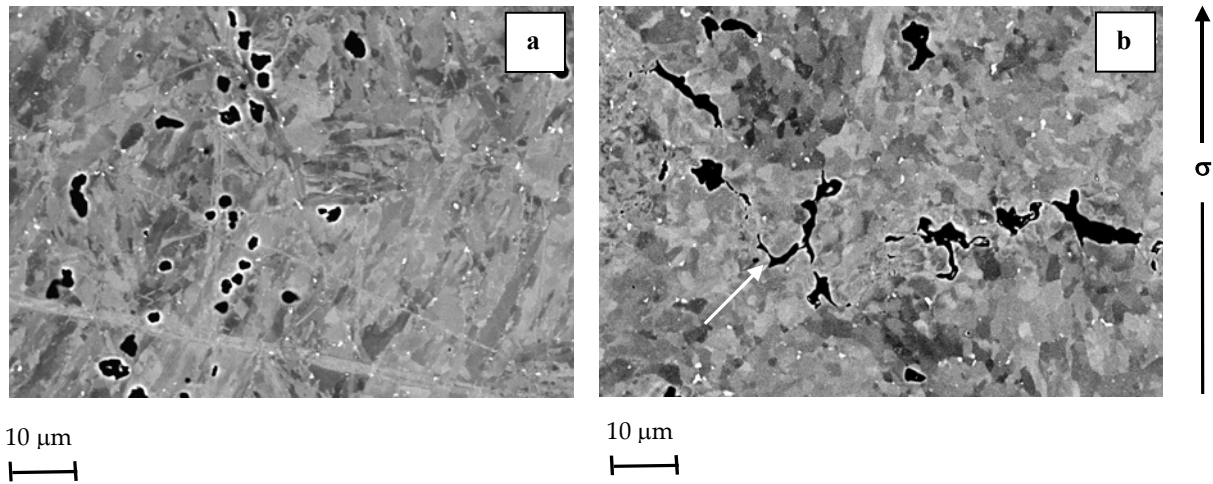


Figure C.II.7. Damage characteristics in (a) base metal and (b) weldments (backscattered electron SEM imaging after final polishing with colloidal silica)

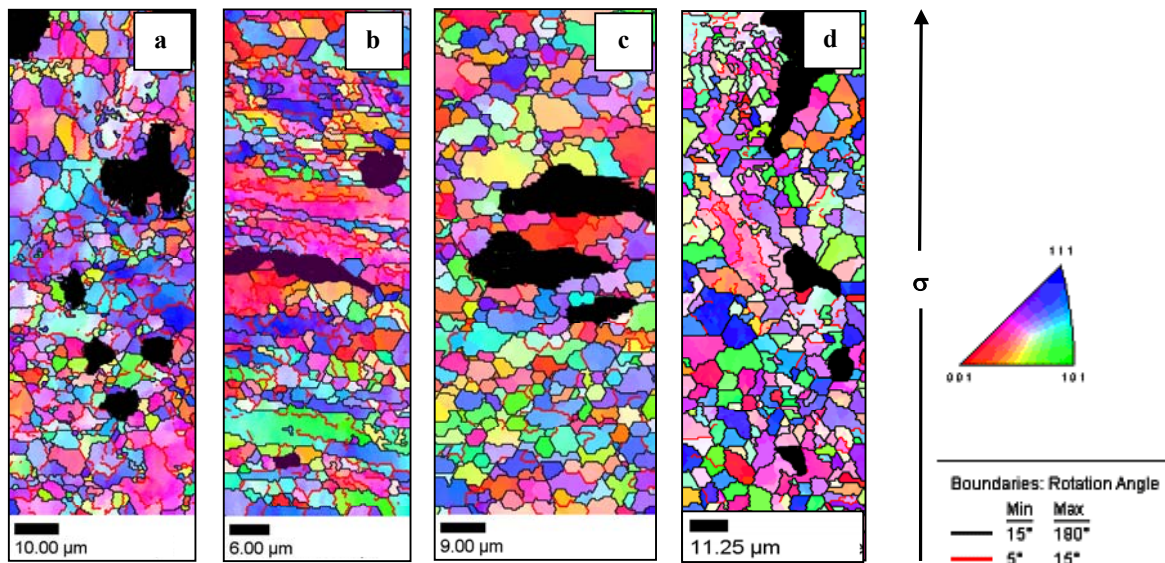


Figure C.II.8. EBSD maps in the rupture area for the weldment (a) 100 MPa – 300 hours and (c) 50 MPa – 10,000 hours) and the base metal (b) 120 MPa – 900 hours and (d) 90 MPa – 7,000 hours -Black lines delineate high angle boundaries (> 15°) - Grey lines delineate low angle boundaries (5 – 15°) - Cavities are in black colour

4.5. Reasons for loss of creep strength in the ICHAZ

Many arguments (including results of TEM investigations) are available to explain the loss of creep strength in the ICHAZ. Both the intercritical heat cycle and the PWHT are responsible for the loss of creep strength in the ICHAZ. First, the intercritical welding heat cycle strongly modifies the precipitation state, as the primary $M_{23}C_6$ carbides, but also the creep strengthening precipitates of type MX (Kojima et al (1995)) are not dissolved during this cycle. As they have already precipitated, $M_{23}C_6$ carbides coarsening occurs during the PWHT (as in Coussement and De Witte (1991)). The effect of the precipitation state is very important as a fine dispersion of $M_{23}C_6$ carbides and MX precipitates would delay ageing phenomena during tempering and high temperature creep (see also Spigarelli and Quadri (2002)). As summed up by Laha et al (2000), the poorer creep strength of the welded joint can be attributed to coarser carbides and to an equiaxed dislocations cell substructure in the recovered ICHAZ. A lower PWHT temperature would limit carbide coarsening and lath recovery but targeted fracture toughness properties of the weld metal would not be matched (Brozda and Zeman (1996)). Therefore, when possible (i.e. when components can be welded elsewhere than on site), the only way to improve the weldment creep strength would be to perform both normalising and tempering treatments after welding (Sato and Tamura (1998)). Note that such a procedure can be used for 9Cr1Mo-NbV weldments because base and weld metals have nearly the same chemical composition and thus the same microstructural evolution during heat treatments. De Witte and Coussement (1991) also proposed to perform a half tempering on the base metal (i.e. a tempering at 600 – 620°C) so that the $M_{23}C_6$, MX and $M_{2}X$ precipitates would only formed during the PWHT but such a procedure implies that all the welded pipe must be post weld heat treated.

5. Lifetime prediction of weldments

5.1. Short review of lifetime assessment methods

The purpose of this section is to propose a method for evaluating the creep strength of weldments from results of uniaxial tests on the base metal and the weldment. The first method proposed in 1987 (ASME Code case N-47), introduced a safety factor, S , defined by:

$$\sigma_w = S\sigma_{BM} \quad (\text{with } S = 2/3) \quad (\text{eq. C.II.3})$$

where σ_w is the engineering stress to be imposed to the weldment to reach the same creep time to failure as that of the base metal for an applied engineering stress equal to σ_{BM} . This approach does not take into account important factors such as the material or test temperature. Storesund and Tu (1996) proposed to evaluate the safety factor from experiments:

$$S = \left(\frac{t_w}{t_{BM}} \right)^{1/n_{BM}} \quad (\text{eq. C.II.4})$$

with t_w and t_{BM} respectively the creep time to failure of the weldment and of the base metal when performing creep tests at the same applied engineering stress. Both methods were applied to experimental data of the present study. They led to non conservative results, as predicted lifetimes were more than twice higher than those experimentally measured. Another approach, which requires detailed analysis, is based on the determination of creep flow and damage properties of each part of the HAZ (see Storesund and Tu (1995), Perrin and Hayhurst (1999), and Eggeler et al (1994)), with integrating the determined constitutive laws into multi-material finite element (FE) calculations. This method is time consuming in terms of both experiments, as a number of materials have to be taken into account to accurately represent the HAZ, and FE calculations. On the other hand, the main advantage of these models is to account for constraints effects between the various microstructures. In the present study, a more simple criterion is proposed to predict the lifetime of the weldment, at least for the design of structures not subjected to complex multiaxial loadings. It is also shown that useful conclusions concerning the constraining effect in the weldment can be drawn from uniaxial creep data.

5.2. Creep fracture properties of base metal and weldments

Classical empirical laws describing creep fracture properties were chosen in the present model. Relationships between the steady state creep strain rate and the creep time to failure were determined following the Monkman-Grant (1956) (MG) formalism:

$$\dot{\epsilon}_{ss} t_R^m = C_{MG} \quad (\text{eq. C.II.5})$$

where t_R is the creep time to failure, m and C_{MG} are model parameters. The Larson-Miller (1952) (LM) relationships were also determined as:

$$P_{LM} = [20 + \log(t_R)] \frac{T}{1000} = f(\sigma) \quad (\text{eq. C.II.6})$$

where $f(\sigma)$ is a linear relationship between the applied engineering stress σ and P_{LM} . $f(\sigma)$ is fitted to experimental data. The LM formulation is particularly relevant for weldments as the LM relationship is not sensitive to strain heterogeneity. Therefore, assuming that the creep time to failure of the weldment follows the weakest link theory, it can be deduced that the LM relationships give a good representation of the creep fracture behaviour of the HAZ. This hypothesis may largely be supported by the fact that only low damage levels are detected out of the HAZ area. The values of MG parameters and the LM correlation function, $f(\sigma)$, are given in **table C.II.3** for both base metal and weldment specimens and compared to experiments in **figure C.II.9**. Note that unique relationships were found at least in the lifetime range experimentally investigated.

	Larson - Miller	Monkman - Grant	
	$f(\sigma), \sigma$ in MPa	m	C_{MG}
Base metal (BM)	$-0.028 \sigma + 24$	0.94	$5.8 \cdot 10^{-2} h^{-0.06}$
Weldment (W)	$-0.026 \sigma + 22.9$	0.80	$3.8 \cdot 10^{-2} h^{-0.2}$
HAZ		0.88	$1.2 \cdot 10^{-1} h^{-0.12}$

Table C.II.3. Monkman-Grant parameters and Larson-Miller correlation for base metal, weldment specimens and HAZ (calculated from the model) at 625°C

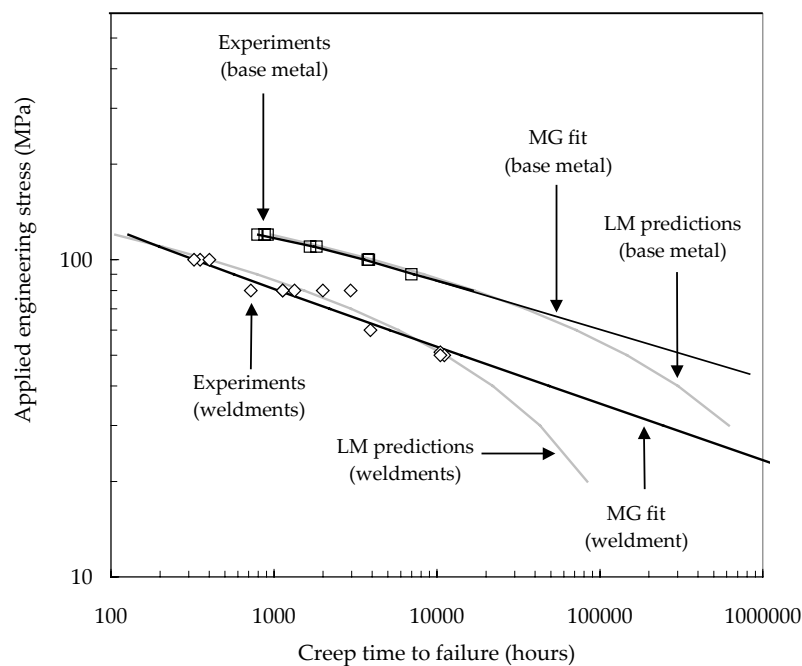


Figure C.II.9. Stress versus creep time to failure for the weldment and the base metal

5.3. Analysis of creep tests on weldment specimens – Derivation of the steady state creep properties of the HAZ

In the weldment specimens, the major part of the gauge area is made of base metal but it may be divided into three main parts: the weld metal, the HAZ and the base metal. The HAZ will be approximated to its weak area, namely, the ICHAZ. As the weld metal and the base metal exhibit similar steady state creep flow properties (see **figure C.II.4**), a bi-material representation was chosen. This simplification implies that the specimen location in the weldment is no longer essential provided the same amount of HAZ is tested. Following a decomposition of the strain rate already used by Spigarelli and Quadrini (2002), the overall steady state strain rate in the weldment, $\dot{\epsilon}_{ss}$, is expressed as:

$$l_{tot} \dot{\epsilon}_{ss} = l_{HAZ} \dot{\epsilon}_{ss,HAZ} + l_{BM} \dot{\epsilon}_{ss,BM} \quad (\text{eq. C.II.7})$$

where l_{tot} is equal to the total gauge length (i.e. 36 mm). Thus, the model does not take directly into account constraint effects in the weldment specimens. Nevertheless, due to creep properties mismatch, constraint effects obviously strongly depend on the length l_{HAZ} and more precisely on the ratio ϕ/l_{HAZ} where ϕ is the specimen diameter. A first approximation of l_{HAZ} was experimentally determined as the total width of the HAZ area i.e. 5 mm (see **figure C.II.2**). This length represents the highest acceptable value for l_{HAZ} . However, microstructural and mechanical properties are very heterogeneous in the HAZ, so that experimental measurements were made to more accurately determine the actual length of the deformed area in the HAZ. To do so, profiles of the thickness of the creep tested flat specimens were performed. They allowed to measure local strains (by measuring the specimen reduction in thickness) and by deduction

to set l_{HAZ} to 4 mm and l_{BM} to 32 mm (where $l_{BM} = l_{tot} - l_{HAZ}$). From **equation C.II.6**, and using the Norton power-laws determined for the base metal and the weldment, the creep flow behaviour of the HAZ could be derived. It was also modelled using a Norton power-law (plotted in **figure C.II.4**) whose coefficients, B_{HAZ} and n_{HAZ} , are given in **table C.II.2**.

5.4. Creep life prediction of weldments

The intrinsic creep flow behaviour of the HAZ being now estimated, and as failure in the weldment is due to the weakness of the HAZ, creep lifetimes experimentally measured for the weldment allow to fit a MG relationship for the HAZ. The corresponding values of parameters, $C_{MG,HAZ}$ and m_{HAZ} , are given in **table C.II.3**. MG fit for the HAZ, as well as results of experiments on both the base metal and the weldment at 625°C, are plotted in **figure C.II.10**. Using the steady state creep strain rate of the HAZ, MG predictions with coefficients fitted for the base metal were indistinguishable from these given by the MG predictions using coefficients fitted for the HAZ (see filled squares in **figure C.II.10**). This result must be considered with carefulness as differences in creep damage processes indicate a possible loss of ductility in the HAZ. In fact, the HAZ deformation is constrained by the lower creep strain rate of the base metal and the loading state is no longer uniaxial. A very simple way to explain this result is to consider that the lower creep strength of the HAZ is compensated by the constraining effect due to creep flow mismatch between the HAZ and the base metal. On the one hand, the HAZ exhibits a creep strength 30% lower than the base metal. On the other hand, Albert et al (2004) especially showed that the hydrostatic stress is largely increased in the HAZ leading to a decrease of nearly 30% of the von Mises equivalent stress for a given applied axial stress and when l_{HAZ} is nearly equal to the specimen diameter.

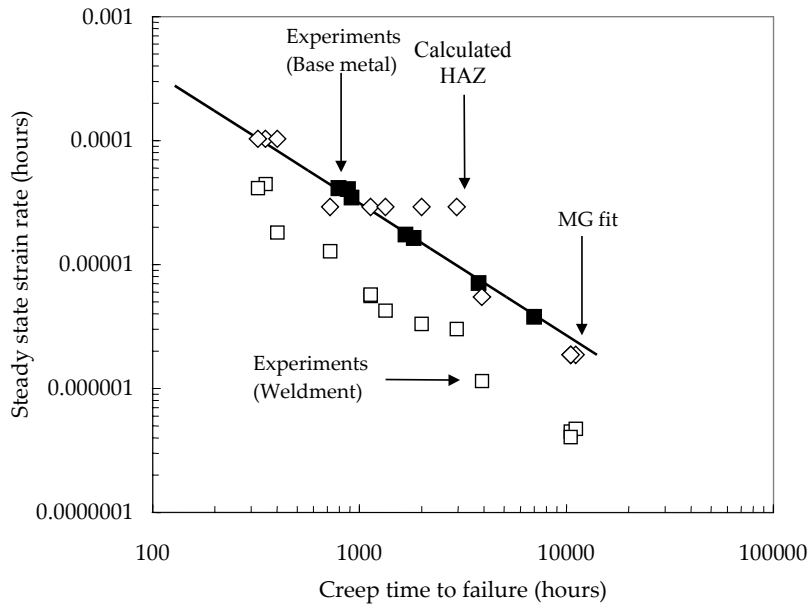


Figure C.II.10. Monkman-Grant plot for base metal (filled squares), weldment specimens (open squares) and calculated HAZ (open diamonds)

To address this point, the steady state creep strain rates of the HAZ were determined for two other values of l_{HAZ} i.e. 2 mm and 5 mm. The corresponding Norton power-law coefficients are given in **table C.II.4**. Monkman-Grant predictions are plotted in **figure C.II.11** using $C_{MG,BM}$ and m_{BM} . The differences between predictions for the three values of l_{HAZ} stay near the experimental scatter band. However, it shows that when the HAZ is less constrained i.e. for $l_{HAZ} = 5$ mm, the MG predictions are a little optimistic which also shows that the intrinsic ductility of the HAZ is probably higher than that of the base metal. It seems that for $l_{HAZ} = 4$ mm there is a compensation of the lower creep strength of the HAZ by the constraint effect for smooth round tensile bars, so that the lifetime parameters of the base metal can directly be used to evaluate the lifetime of weldments for this particular geometry and metallurgical properties of the HAZ in the welded joint.

	B (h⁻¹ MPa⁻ⁿ)	n
HAZ – Calculated with l_{HAZ} = 5 mm	2.15 10 ⁻¹⁶	5.8
HAZ – Calculated with l_{HAZ} = 2 mm	6.45 10 ⁻¹⁶	5.8

Table C.II.4. Norton power-law parameters for HAZ at 625°C

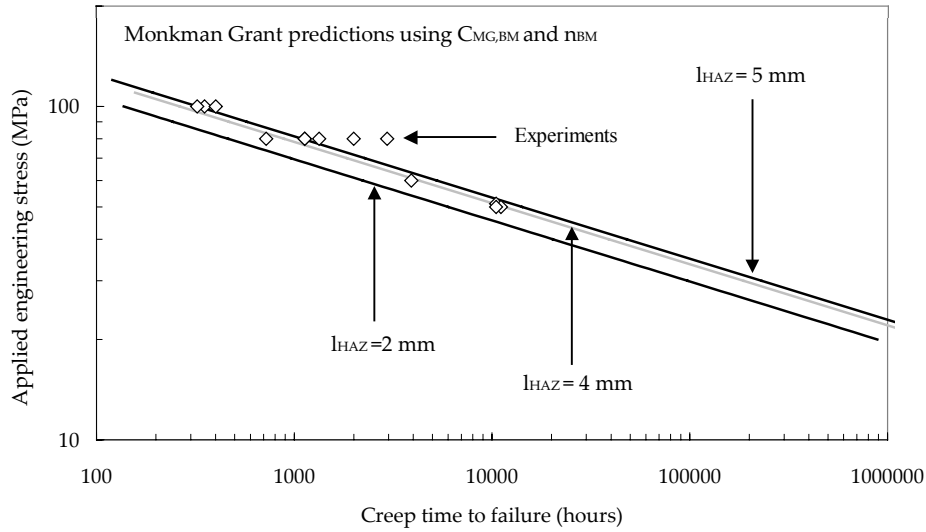


Figure C.II.11. Effect of l_{HAZ} on cross-weld specimens creep lifetime

5.5. Validation of the method

2D axisymmetric FE calculations using a bi-material representation were performed with the FE software Zebulon (Besson and Foerch (1997)). Taking into account symmetry relationships, a half of SC specimens was meshed with the HAZ representing 1 mm, 2 mm and 2.5 mm of the total gauge length equal to 18 mm. The HAZ area was finely meshed with quadratic squares (with reduced integration) of 100 μm in size. Norton power-law coefficients of **table C.II.2** were integrated to constitutive laws describing the creep flow properties of the base metal and the HAZ. The strain rate tensor was written as:

$$\dot{\underline{\underline{\epsilon}}} = \dot{\underline{\underline{\epsilon}}}_e + \dot{\underline{\underline{\epsilon}}}_{vp} \quad (\text{eq. C.II.8})$$

The elastic strain tensor $\underline{\underline{\epsilon}}_e$ is related to the stress tensor by Hooke's law: $\underline{\underline{\sigma}} = \underline{\underline{\underline{C}}} : \underline{\underline{\epsilon}}_e$ where $\underline{\underline{\underline{C}}}$ is the fourth order stiffness tensor. The Young's modulus was taken to 145 GPa and the Poisson ratio to 0.3. Large strain formulation was chosen to account for the evolution of the specimen geometry (e.g. necking). The non-elastic (viscoplastic) strain rate tensor is given by the normality rule:

$$\dot{\underline{\underline{\epsilon}}}_{vp} = \frac{3}{2} \dot{p} \frac{\underline{\underline{s}}}{\sigma_{eq}} \quad (\text{eq. C.II.9})$$

where $\underline{\underline{s}}$ is the stress deviator, σ_{eq} is the von Mises equivalent stress and the viscoplastic multiplier, \dot{p} , is assumed to be given by the Norton power-law:

$$\dot{p} = B \sigma_{eq}^n \quad (\text{eq. C.II.10})$$

The model parameters are given in **tables C.II.2** and **C.II.4** for the three investigated values of l_{HAZ} . Even if l_{HAZ} is much lower than the gauge length so that the influence of its value on the total elongation is probably low, the steady state creep strain rates of the weldments calculated for the three values of l_{HAZ} exhibits observable differences. It can be shown in **figure C.II.12**. that the calculated steady state creep strain rates with $l_{HAZ} = 4$ or 5 mm were in very good agreement with those experimentally measured on SC weldment specimens. On the contrary, for $l_{HAZ} = 2$ mm, they were twice lower than those experimentally measured due to a too high constraint effect. It was concluded that $l_{HAZ} = 4$ mm was a good approximation of the HAZ length and that there is a relatively high degree of freedom in the choice of l_{HAZ} as FE calculations also showed that the value of $l_{HAZ} = 5$ mm gives very similar results.

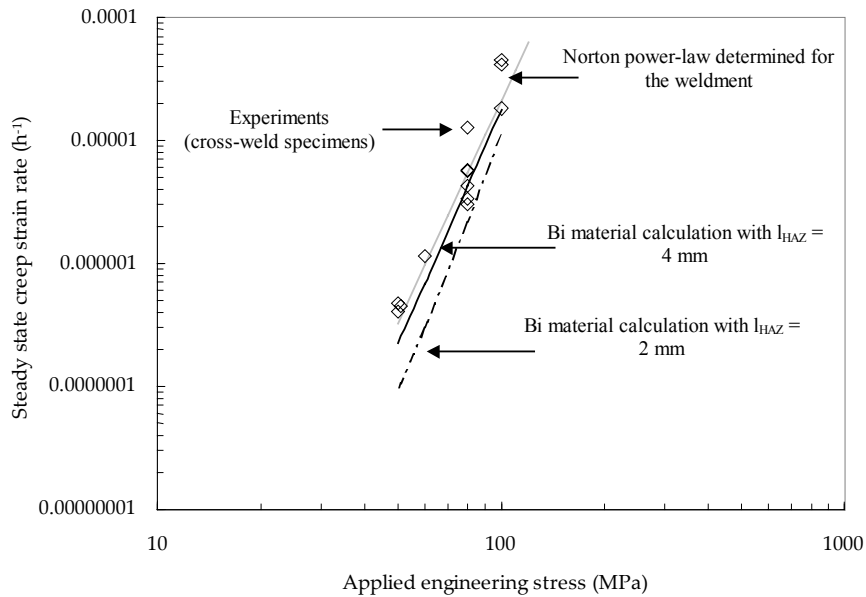


Figure C.II.12. Calculated steady state creep strain rates for cross-weld specimens bi-material calculations with two values of l_{HAZ} , respectively 4 mm and 2 mm

The validity of the value of the $l_{HAZ} = 4\text{mm}$ was also confirmed by the shape of the specimens at the onset of fracture even if the influence of damage is not taken into account in the model (see **figure C.II.13**). This value should be questioned as it was experimentally shown that the intercritical heat affected zone where type IV creep fracture occurs is a zone not larger than 2 mm. In fact, the present study shows that when a three material representation is chosen, the parameter l_{HAZ} must be fitted to account for the constraining effects. In the present case $l_{HAZ} = 2\text{mm}$ would lead to too strong constraining effects on the HAZ with respect to what is experimentally observed. For the fitted value of l_{HAZ} (i.e. 4 mm) the deformation in the HAZ is less constrained and the calculated strain gradients are in accordance with experimental observations. This result is also consistent with previous experimental measurements of strain accumulation by Laha et al (1990) for a 2.25CrMo weldment.

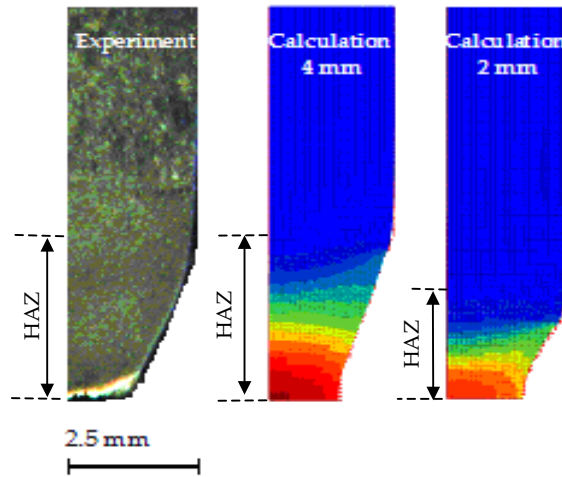


Figure C.II.13. Comparison of specimen creep deformation between experiment, and bi-material FE calculations with respectively $l_{HAZ} = 4$ and 2 mm (Applied engineering stress = 100 MPa)

The validity of the method and especially the compensation of the lower creep strength of the HAZ by structure effects for smooth round specimens was confirmed using literature data at 600°C. Eggeler et al (1994) reproduced HAZ microstructures and determined the intrinsic creep flow properties of the HAZ by performing creep tests on the simulated microstructure. Jakobova et al (1998) carried out creep tests on smooth round specimens made of weldments at 600°C with a material quite similar to that used by Eggeler et al (1994). The steady state creep flow properties, determined by Eggeler et al (1994) and given in **table C.II.5**, were introduced in the Monkman-Grant equation with the parameters of the base metal at 625°C ($C_{MG,BM}$ and m_{BM}). The resulting predictions, plotted in **figure C.II.14**, exhibit a good agreement with experimental results on weldments from Jakobova et al (1998).

	B (h⁻¹MPa⁻ⁿ)	N
HAZ	4.54 10 ⁻²¹	7.8

Table C.II.5. Creep flow properties of the HAZ at 600°C quoted from Eggeler et al (1994)

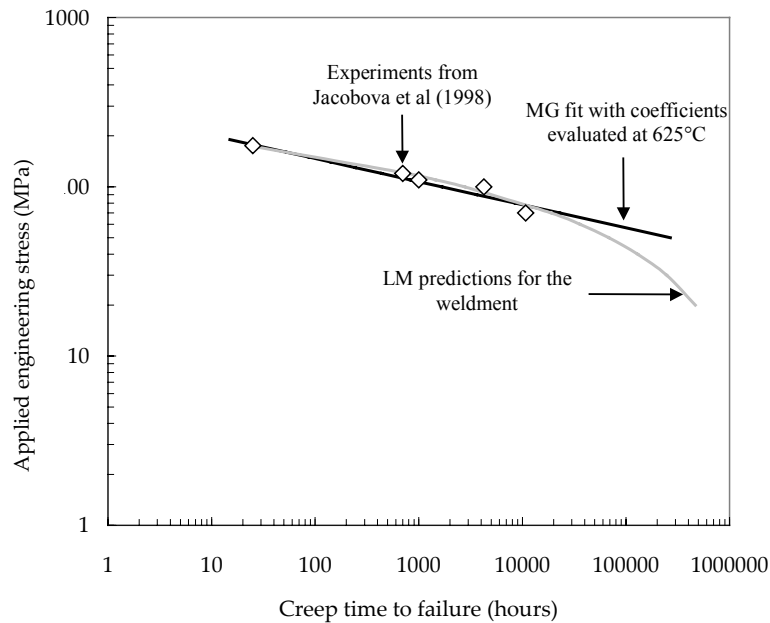


Figure C.II.14. Ability of the method to predict creep time to failure of weldments at 600°C from literature data

5.6. Quantitative investigation of constraint effects in the HAZ and structure effects on weldment creep lifetime

To study the constraint effects in the HAZ in a quantitative manner, the evolution of the stress triaxiality ratio, τ , which is defined as the ratio $\frac{1}{3} \frac{\sigma_m}{\sigma_{eq}}$ where σ_m is the hydrostatic stress and σ_{eq} the local equivalent von Mises stress, was derived from the results of FE calculations. The profiles of the evolution of τ from the HAZ to the base metal are plotted in **figure C.II.15** for an applied engineering stress equal to 60 MPa for the three investigated values of l_{HAZ} . First, these profiles show that the mismatch in creep properties between HAZ and base metal leads to an increase in the stress triaxiality ratio in the HAZ which locally reaches the value of 1.07 for $l_{HAZ} = 2$ mm. Therefore, the value of l_{HAZ} must be carefully determined as the loading state in weldment specimens strongly depends on it. Note also that as experimentally shown by Smith et al (2003), constraint in the HAZ also strongly influences cavity growth so that the damage kinetics also depends on the value of l_{HAZ} .

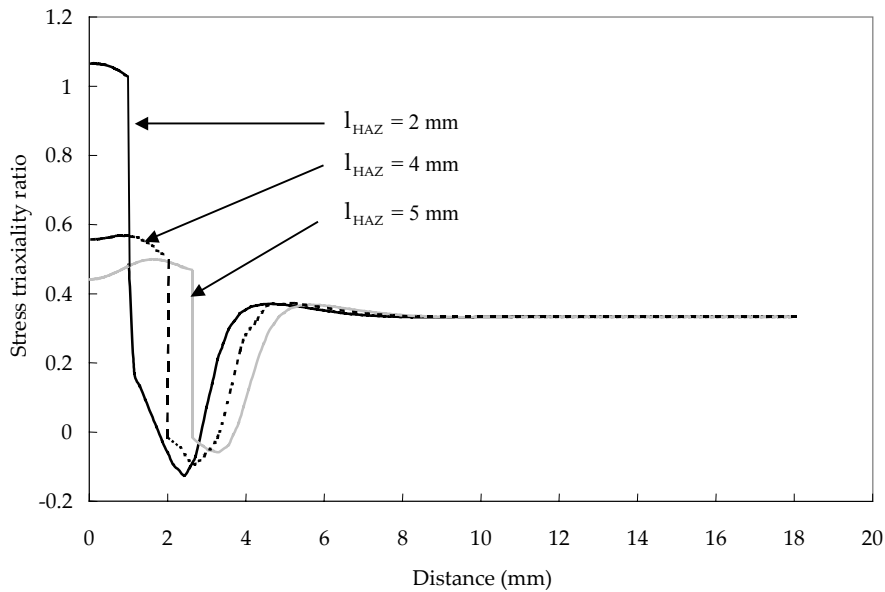


Figure C.II.15. Results given by bi-material FE calculations - Evolution of τ along the specimen axis with the distance to the symmetry plane for a local maximum viscoplastic strain equal to 1% for three values of l_{HAZ}

FE calculations were performed until structural effects (necking) lead to the specimen failure (i.e. instability due to reduction in diameter). The comparison between measured experimental creep lifetimes of the weldment and results from FE calculations in **figure C.II.16** evidence that the creep failure of the weldment is not only due to structural effects. As experimentally observed, damage accumulation is obviously responsible of weldment specimen failure. Thus it is necessary to take into account damage mechanisms in the FE calculations. Identification of creep damage behaviour of the HAZ is performed in **chapter C.III** and **chapter C.IV** but is beyond the scope of the present paper.

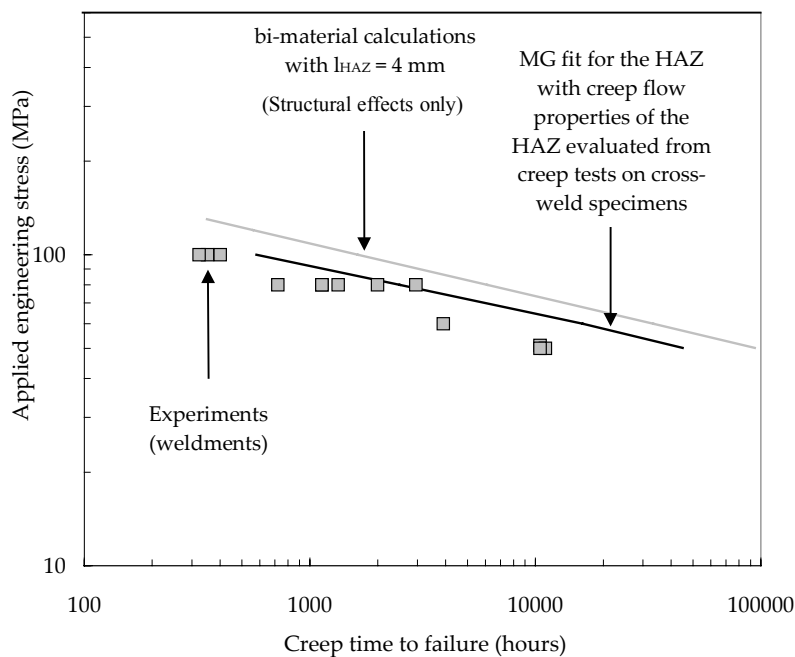


Figure C.II.16. Structure effect on creep lifetime of weldment specimens

6. Conclusions

In the present study, an experimental database of uniaxial creep tests on both 9Cr1Mo-NbV steel and weldment is built. Premature failure of type IV in the heat affected zone is observed in 9Cr1Mo-NbV steels weldments in comparison with the base metal. Metallurgical investigations have shown that the loss of creep strength can be attributed to microstructural changes such as carbide coarsening and extensive lath recovery that occur in the HAZ during welding. A simple one dimensional model is proposed to predict creep life of weldments. In this model, power law flow rules and Monkman-Grant life assessments, allow to predict creep lifetime of smooth round cross-weld specimens from the

knowledge of steady state creep flow properties of the base metal and the weldment, and creep fracture properties of the base metal. Bi material FE calculations without taking into account damage development gave useful information about constraints effects and especially allowed to determine the value of I_{HAZ} well representing constraining effect in 9Cr1Mo-NbV steel weldments. It was also shown that the lower creep strength of the HAZ can mainly be attributed to its creep flow properties whereas its intrinsic ductility is similar to that of the base metal (MG fit parameters of the HAZ and the base metal are similar).

Finally, although this method gives good predictions of weldments creep lifetime for smooth round specimens. More detailed analysis and multi-material FE calculations are, however, obviously necessary to predict creep lifetime of complex structures.

Acknowledgements

Financial and technical support from Electricité de France (EdF), Framatome and Le Commissariat à l'Energie Atomique (CEA) is acknowledged. Many thanks are due to Dr Y. De Carlan (CEA Saclay) for TEM observations.

References

- Brozda J., Zeman M., 1996. Weldability of 9Cr-1Mo-Nb, V P91 steel intended for service in the power industry. *Welding Int.*, 10(5), 370-380.
- Cerjak H. and Schuster F., 1994. Weldability and behaviour of weldings of new developed creep resistant 9 – 10% Cr steels. Second conference on joining technology EUROJOIN2. 157–167.
- DeWitte M., Coussement C., 1991. Creep properties of 12%Cr and improved 9%Cr weldments. *Mat. at high Temp.*, 9(4), 178-184.
- Eggeler G., Ramteke A., Coleman M., Chew B., Peter G., Burblies A., Hald J., Jefferey C., Rantala J., DeWitte M., Mohrmann R., 1994. Analysis of creep in a welded 'P91' pressure vessel. *Int. J. Pres. Ves. & Piping*, 60, 237-257.
- Gaffard V., Gourgues-Lorenzon A.F., Besson J., 2004. Creep failure model of a tempered martensitic stainless steel intergrating multiple deformation and damage mechanisms. *Submitted to Int. J. Fra.*
- Hald J., Lund E.M., 1993. TEM investigations in the HAZ in P91 steel (9Cr, 1Mo, Nb, V). *Int. conf. of the joining of mat. – Hebingor (Danemark)*.
- Hyde T.H. and Tang A. , 1998. Creep analysis and life assessment using cross-weld specimens. *International materials reviews*, 43(6), 221-243.
- Jakobova A., Vodarek V., Hennhofer K., Foldyna V., 1998. Microstructure and creep properties of P91 steel and weldments. *Mat. for adv. power eng.*, 8th Liege conf., 373-382.
- Jayet-Gendrot S. (1999). Uniaxial creep properties of P9 materials at 625°C (base metal and weld). *HIDA 1702/PMB/57*.
- Kojima T., Hagashi K., Kajita T., 1995. HAZ softening and creep rupture strength of high Cr ferritic steel weldments. *ISIJ Int.*, 35(10), 1284-1290.
- Laha K., Bhanu Sankara Rao K., Mannan L., 1990. Creep behaviour of a post weld heat treated 2.25Cr-1Mo ferritic steel base, weld metal and weldments, *Mat. Sci. and Eng. A*, 129, 183-195.
- Laha K., Chandravathi K.S., Bhanu Sankara Rao K., 2000. Microstructural evaluation and creep and rupture behaviour of 9Cr-1Mo steel base metal weld metal and weld joint. *Trans. Indian Inst. Met.* 53(3), 217-221.
- Larson F.R. and Miller J., 1952. A time-temperature relationship for rupture and creep stresses, *Transactions of the ASME*. 74. 765-775.
- Letofsky E., Cerjak H., Warbichler P., 2000. The use of light and electron microscopic investigations to characterise the creep behaviour of welded joints in modern power station materials. *Prakt. Metallogr.* 37(9), 509-521.
- Li D., Shinozaki K., Kuroki H., 2003. Stress strain analysis of creep deterioration heat affected weld zone in high Cr ferritic heat resistant steel. *Mat. Sci. Tech.*, 19, 1253–1260.
- Mannan S.L., Sastry D.H., 2000. Microstructural evaluation and creep deformation and rupture behaviour of 9Cr-1Mo steel base metal, weld metal and weld joint. *Trans. Indian Inst. Met.*, 53(3), 217-221.
- Monkman F.C. and Grant N.J., 1956. An empirical relationship between rupture life and minimum creep rate in creep-rupture tests, *Proceedings of the ASTM*, 56, 593-620.
- Okamura H., Ohtani R., Saito K., Kimura K., Ishii R., Fujiyama K., Hongo S., Iseki T., Uchida H., 1999. Basic investigation for life assessment technology of modified 9Cr-1Mo steel. *Nucl. Eng. Des.* 193, 243-254.
- Parker J.D. and Stratford G.C. (1996). Strain localization in creep testing of samples with heterogeneous microstructures. *Int. Jour. of Press. Vess. & Pip.* 68. 135-143.
- Perrin I.J. and Hayhurst D.R., 1999. Continuum damage mechanics analyses of type IV creep failure in ferritic cross weld specimens. *Int. Jour. Press. Vess. Pip.*, 76, 599-617.
- Prunier V., Gampe U., Nikbin K., Shibli I.A., 1998. HIDA activity on P91 steel. Creep and fatigue crack growth in high temperature plant – HIDA conference (CEA Saclay).

Sato T., Tamura K., Mitsuhata K, Ishura R. (1998). Improvement of creep rupture strength of 9Cr1MoNbV welded joints by normalising after weld Mat. For adv. power eng., 8th Liege conf., 393-399.

Shibli I.A., 2001. Overview of the HIDA project. Int. J. Press. Ves. & Piping, 78, 729-735.

Smith D.J., Walker N.S., Kimmins S.T. (2003). Type IV creep cavity accumulation and failure in steel welds. *International journal of pressure vessels and piping*. **80(9)**. 617-627.

Spigarelli S., Quadri E., 2002. Analysis of the creep behaviour of a modified P91 (9Cr1Mo-NbV) welds. Mat. and Des. , 23, 547-552.

Storesund J. and Tu S.T., 1995. Geometrical effects on creep in cross weld specimens. Int. J. Pres. Ves. & Pip., 62, 179-193.

Tu S.T., Segle P., Chong J.M., 1996. Strength design and life assessment of welded structures subjected to high temperature creep. Int. J. Pres. Ves. & Pip., 66, 171-186.

Vijayalakshmi M., Saroja S., Mythili R., Thomas Paul V., Raghunathan V.S., 2000. Mechanisms and kinetics of tempering in weldments of 9Cr-1Mo steel. J. of nuc. mat. , 279, 293-300.

Yajiang L., Juan W., Bing Z., Tao F., 2002. XRD and TEM analysis of microstructure in the welding zone of 9Cr-1Mo-V-Nb treated heat-resisting steel. Bull. Mater. Sci., 25(3), 213-217.

Supplement C.II.S1. Investigations of metallurgical changes in weldments during creep

1. EBSD analysis

The evolution of the microstructure in the weldments during creep was investigated by means of EBSD analysis. To do so, the EBSD maps presented in **figure C.II.8a** and **C.II.8b** were used. For the two maps, histogram of misorientation angle between neighbouring grains were plotted in **figure C.II.S1.1** and compared to the same histogram plotted for the heat affected zone in the initial state (see **figure A.II.12** in **chapter A.II**)

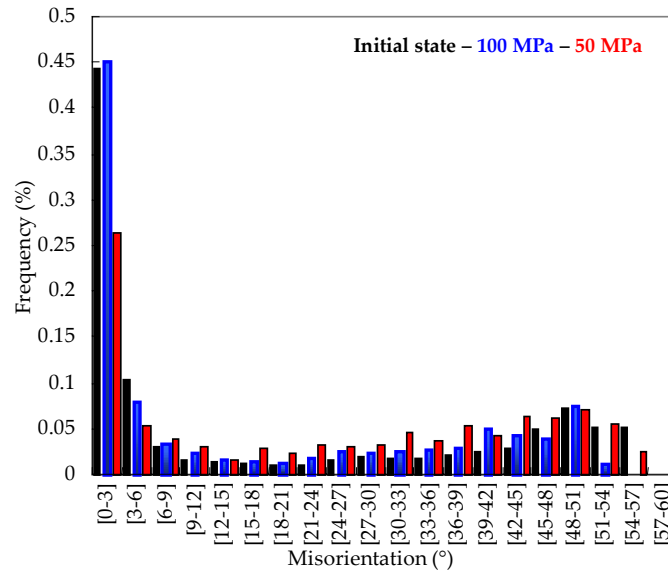


Figure C.II.S1.1. Histogram of misorientation angles (between neighbouring grains)

It is evidenced in **figure C.II.S1.1** that the histogram of misorientation angles slightly evolves during short term creep ($\sigma = 100$ MPa - 300 hours) whereas the evolution is more significant during long term creep (50 MPa - 10,000 hours). After long term creep exposure, the frequency of low angle boundaries largely decreases. The decrease in the frequency of low angle boundaries is not accompanied by the abrupt increase of the frequency of high angle boundary. As the increase in the misorientation angles is progressive, it shows that the evolution of the microstructure is probably recovery rather than recrystallisation.

2. SEM investigations

SEM investigations in polished cross-sections of cross-weld specimens evidenced a quite high fragility of the interfaces in the material. Due to extensive intergranular cracking, observations quasi-similar to fractography could be performed in specimens cross-sections. Such observations are reported in **figure C.II.S1.2** and **C.II.S1.3**. Note that the specimens were not etched before observations so that corrosion pits were not likely to occur.

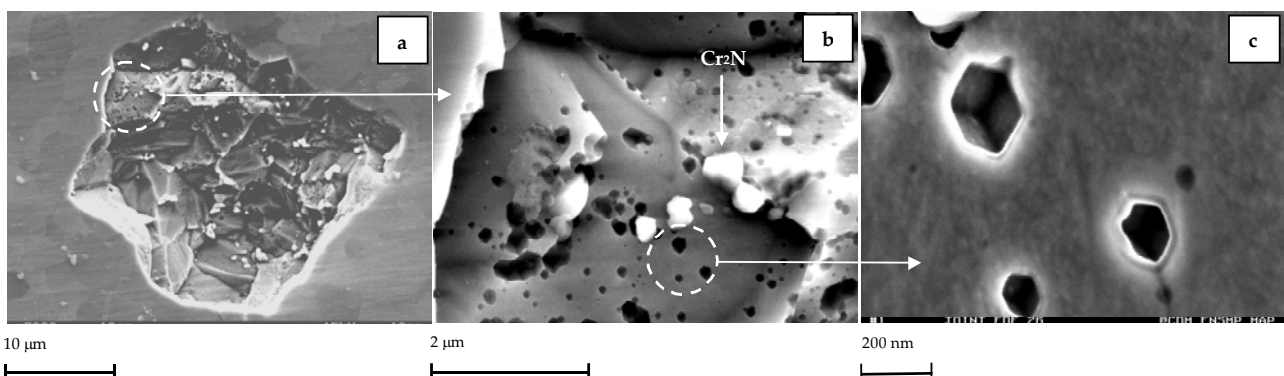


Figure C.II.S1.2. SEM investigations in cross-sections of SC cross-weld specimen ($\sigma = 50$ MPa)

In **figure C.II.S1.2**, three scales of investigations are presented. In **figure C.II.S1.2a**, facets due to intergranular cracking can be evidenced. **Figure C.II.S1.2b** is a closer view of **figure C.II.S1.2a** and **figure C.II.S1.2c** is a closer view of **figure C.II.S1.2b**. In **figure C.II.S1.2c**, the very first stage of damage development are evidenced. The quasi cubic shape of the newly formed cavities evidences that diffusion obviously plays a key role in the cavity nucleation process.

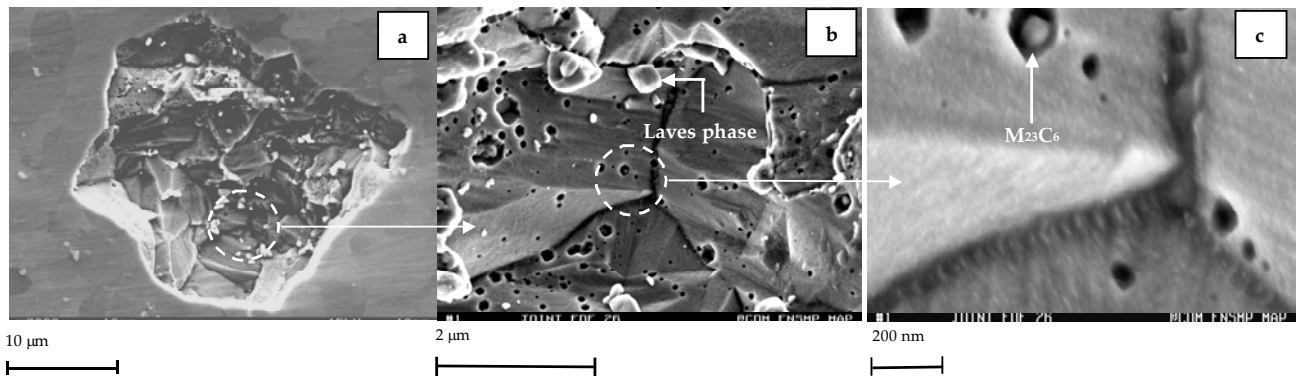


Figure C.II.S1.3. SEM investigations in cross-sections of SC cross-weld specimen ($\sigma = 50$ MPa)

It is finally confirmed in **figures C.II.S1.3b** and **C.II.S1.3c** that both Laves phase precipitation and $M_{23}C_6$ carbides are preferential sites for cavity nucleation. Note also that Cr_2N particles were detected in **figure C.II.S1.2b**.

Chapter C.III. Creep flow and damage properties of the weakest area of the WJP91 weldment at 625°C

In the present chapter, attention is focused on the metallurgical changes that occur in the heat affected zone (HAZ) during welding thermal cycles and on the simulation of the weakest HAZ microstructure. It was written as an article intended to be submitted to ISIJ International. In addition, some results of electron backscattering diffraction (EBSD) analysis as well as a study of ageing effects in the simulated intercritical heat affected zone (ICHAZ) are added at the end of the present chapter.

High temperature creep flow and damage properties of the weakest area of 9Cr1Mo-NbV steel weldments

V. Gaffard, A.F. Gourgues-Lorenzon, J. Besson

Ecole Nationale Supérieure des Mines de Paris (E.N.S.M.P) - Centre des Matériaux

UMR CNRS 7633 BP 87, 91003 Evry Cedex, France (corresponding author : anne-francoise.gourgues@ensmp.fr)

In the present study, creep flow and damage behaviour of P91 steel weldments are investigated. First, creep tests are carried out on both the base metal and the weldment. It is evidenced that creep failure of 9Cr1Mo-NbV weldments at high temperature occurs in the heat affected zone. The HAZ is characterised by microstructural heterogeneity over a distance that is not larger than 5 mm. Therefore, it is very difficult to determine creep flow and damage properties of the microstructure which governs creep failure of weldments. A method is developed to reproduce weld thermal cycles experienced in the HAZ on specimens made of base metal. The validity of this method is ensured by comparing several simulated and real microstructural states of the HAZ in terms of metallurgical properties. Among all the performed welding cycles, one corresponding to the microstructure which governs creep failure of weldments is chosen. Finally, creep flow and damage behaviour of this microstructure are identified with performing creep tests on various kinds of specimen geometry.

Keywords: 9Cr1Mo-NbV martensitic stainless steel; intercritical heat affected zone; Gleeble 1500 thermo-mechanical simulator; High temperature creep flow and damage.

1. Introduction

9Cr1Mo-NbV martensitic stainless steels have largely been studied during the last years. They are candidates as structural materials for supercritical and ultra-supercritical power plants. Their use as structural materials require to join components, usually by welding. 9Cr1Mo-NbV steels are said to exhibit suitable weldability (Klueh and Harries (2001)) due to a good thermal conductivity and a low thermal expansion coefficient but welding of them is quite difficult in the case of high thickness components. Therefore, low input energy levels, $< 2200 \text{ Jmm}^{-1}$, are generally required (see Brozda and Zeman (1996) and Yajiang et al (2002)). In addition, the welding operation leads to the modification of the base metal microstructure in the so called heat affected zone (HAZ). Thermal cycles experienced in the HAZ, which can be characterised by a peak temperature, T_{peak} , and a cooling rate between 800°C and 500°C , $\Delta t_{800 \rightarrow 500}$, locally lead to phase transformations so that the HAZ in these steels is classically divided into three main areas:

1. The coarse grained heat affected zone (CGHAZ) exhibits a higher former austenite (γ) grain size as $T_{\text{peak}} \gg A_{c3}$ promotes growth of the austenite grains, which is, however, controlled thanks to niobium and vanadium additions.
2. The fine grained heat affected zone (FGHAZ) exhibits a small former austenite grain size, as T_{peak} is just above A_{c3} .
3. The intercritical heat affected zone (ICHAZ) corresponds to $A_{c1} < T_{\text{peak}} < A_{c3}$. In this area, the $\alpha \rightarrow \gamma$ phase transformation partially proceeds during the thermal cycle.

Just near the HAZ, the over-tempered base metal area corresponds to T_{peak} just below A_{c1} which leads to an over-ageing of the base metal (see Jakobova et al (1998) and Okamura et al (1998)). These microstructural changes are of great importance as the creep strength of the weldment is lower than that of the base metal. This loss in creep strength is attributed to the HAZ where the type IV creep failure occurs. The identification of the HAZ area which governs the weldments creep failure has already been done by De Witte and Coussement (1991) who also proposed a fracture mechanism map where the evolution of damage mechanism in weldments from intragranular to intergranular fracture are represented. These results are to be confirmed by the present study. Type IV failure must be related to two phenomena:

1. There is obviously a weakness of the weldment linked to the lower creep strength of the HAZ: this is a material problem.

2. The microstructural heterogeneities obviously lead to complex loading state and constraint effects: this is a mechanical problem.

The present study is concerned with the first point i.e. determining the creep flow and damage properties of the weakest HAZ. To do so, special attention was focused on totally avoiding constraint effects due to microstructural heterogeneity. Indeed, it is interesting to study the constraint effects only once the properties of the weakest HAZ have been determined previously.

A method to represent several microstructural states of the HAZ with Gleeble thermal-mechanical simulations is first validate using various metallurgical investigations techniques. Then, a welding thermal cycle corresponding to the weakest HAZ is chosen. It allowed to machine various kinds of axisymmetric U-notched specimens geometry having the same microstructure as the weakest HAZ. All specimens were notched, allowing to localise loading in the microstructure under interest with controlled constraint effects due to the notch geometry only. This point is especially important as in previous studies (see Ootoguro et al (2000) and Tsuchida et al (1996)) uniaxial creep tests were carried out on smooth treated specimens so that several microstructures were tested at the same time and the loading state of the weakest HAZ was not known and not precisely controlled. In fact, such a procedure leads to little benefit in the comprehension of creep flow and damage behaviour of the weakest HAZ in comparison with information given by creep tests on cross-weld specimens. The key point of the present study is thus to determine the properties of the weakest HAZ with eliminating, as well as possible, the constraint effects due to the surrounding materials.

2. Material and experimental procedures

2.1. Materials

The study focuses on a circumferentially welded joint of two pipes of 295 mm in outer diameter and 55 mm in thickness exhibiting a V-shaped connection area. It was welded by submerged metal arc welding in seventeen runs. A post weld heat treatment (PWHT) of two hours at 760°C was performed after welding to release residual stresses. The base metal is a P91 tempered chromium martensitic stainless steel (see **table C.III.1** for chemical composition). Its microstructure consists in lath martensite packets with $M_{23}C_6$ (100 nm in mean size) and MX precipitates. Conventionally, the filler metal has nearly the same chemical composition as the base metal (see **table C.III.1**).

	C	Si	Mn	P	S	Al	Cr	Ni	Mo	V	Nb	N	Cu
Base Metal	0.09	0.31	0.41	0.014	0.005	0.016	8.56	0.26	0.92	0.21	0.065	0.042	/
Filler Metal	0.09	0.37	0.41	0.028	0.013	0.07	8.44	0.27	0.92	0.24	/	0.038	0.04

Table C.III.1. Chemical compositions of base and filler metals (wt%)

2.2. Simulation procedure of the welding thermal cycles

Weld thermal cycles were applied by using a Gleeble 1500 thermal-mechanical simulator which is capable of heating specimens by the Joule effect at very high heating rates corresponding to these encountered in welding conditions (i.e. $100^{\circ}\text{C s}^{-1} - 250^{\circ}\text{C s}^{-1}$). The specimen temperature is controlled by a thermocouple spot welded onto the specimen surface. Two types of round bars of respectively 5 mm and 12 mm in diameter were heat treated. Specimens of 5 mm in diameter were used to fit the weld thermal model and the 12 mm specimens were used to machined specimens for mechanical tests. For each of the two geometries, the closed-loop parameters of the Gleeble 1500 simulator were carefully adjusted in order to ensure an uncertainty smaller than 2°C for the value of T_{peak} and smaller than 1 s for the value of the cooling parameter $\Delta t_{800 \rightarrow 500}$. For specimens of 5 mm in diameter, phase transformations were continuously monitored using in-situ dilatometric measurements of the specimen diameter. To do so, heat treatments were performed under vacuum (10^{-3} Pa) to prevent from extensive oxidation of the specimen. Phase transformations monitoring is of highest importance, as both austenite start and end transformations temperatures (respectively A_{c1} and A_{c3}) and the properties of the austenite phase strongly depend on the heating rate (see also Danon et al (2003)). A preliminary study of the effects of the heating rate on A_{c1} and A_{c3} transformation points showed (**figure C.III.1**) that, when increasing the heating rate from 5°C s^{-1} to $200^{\circ}\text{C s}^{-1}$, the A_{c1} and A_{c3} temperatures increase by more than 150°C. Moreover, the temperature range of the intercritical domain (i.e. $A_{c3} - A_{c1}$) also increases from 25°C to 100°C. In the following, A_{c1} and A_{c3} temperatures are monitored according to the corresponding heating rate.

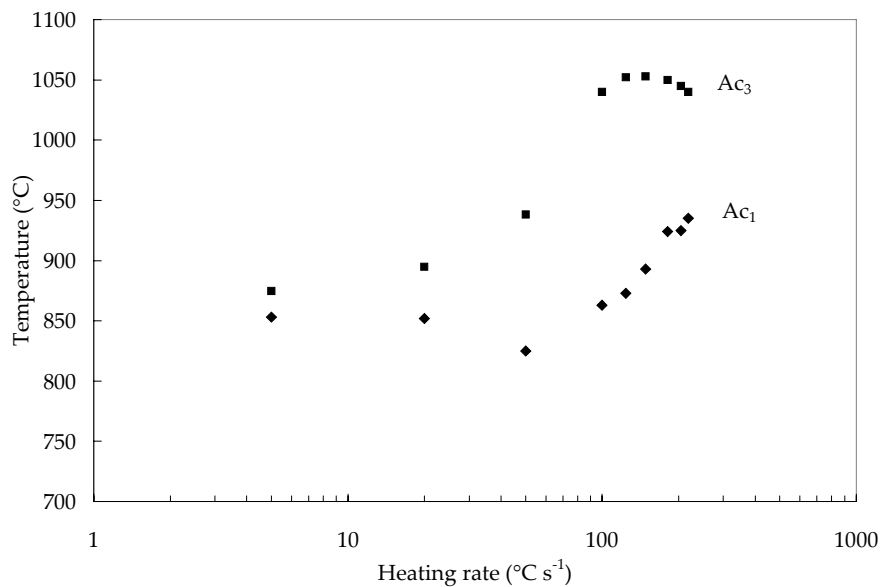


Figure C.III.1. Effect of the heating rates on A_{c1} and A_{c3} temperatures (dilatometry, the accuracy of the measured temperatures is $\pm 5^\circ\text{C}$)

2.3. Mechanical tests

Creep tests on cross-weld specimens were carried out on smooth round tensile bars (SC specimens) cut along the axial direction of the pipe with a gauge length of 36 mm and a gauge diameter of 5 mm. The cross-weld specimens were machined so that the base metal, the HAZ and the weld metal could be tested at the same time. These tests allowed to evaluate the difference between creep time to failure for the base metal and for the weldment and to determine the rupture location in weldments.

Creep tests were also carried out on simulated HAZ microstructures. To do so, the round bars of 12 mm in diameter were first treated in the Gleeble testing machine following the weld thermal cycle corresponding to the weakest HAZ (see **section 5.3**). Specimens were then given the actual PWHT i.e. 760°C for 2 hours.

It was evidenced from Vickers hardness measurements that, for the chosen operating conditions, the Gleeble heating treatment is homogenous only within a 7 mm wide area centred on the thermocouple position. Therefore, creep and tensile specimens were notched to localise stress and strain in the centre of the thermally treated area. Slightly U-notched specimens were machined to determine tensile and creep flow properties of the simulated HAZ. A tensile specimen (GTNT) was designed with a maximum diameter of 4 mm, a minimum diameter of 3 mm and a notch radius of 5 mm and a creep specimen (GTNC5.0) was designed with a maximum diameter of 6 mm, a minimum diameter of 3 mm and a notch radius of 5 mm. All creep tests on GTNC5.0 specimens were performed until failure except a complementary test with load varying with steps (50 MPa, 60 MPa and 70 MPa) which allowed to investigate creep flow properties in the low stress creep regime.

As the stress triaxiality ratio, which is defined as the ratio $\frac{1}{3} \frac{\sigma_m}{\sigma_{eq}}$ where σ_m is the local hydrostatic stress and σ_{eq} is the

local von Mises equivalent stress, may play a key role in damage mechanisms, two other types of round U-notched specimens (GTNC4.0, GTNC1.2) which have a maximum diameter of 6 mm, a minimum diameter of 3 mm and a notch radius of respectively, 4 mm and 1.2 mm, were designed. Finally, two types of round V-notched bars (GTNC0.25), which allow to obtain a stable crack propagation and to test the effect of a high triaxiality ratio, were also used. The first type (GTNC0.25-1) has a maximum diameter of 8 mm, a minimum diameter of 5 mm and a notch radius of 0.25 mm and the second type (GTNC0.25-2) has a maximum diameter of 8 mm, a minimum diameter of 4 mm and a notch radius of 0.25 mm.

All creep tests were carried out at 625°C (898K) for up to 5,000 hours under constant applied load in controlled laboratory atmosphere ($20^\circ\text{C} \pm 2^\circ\text{C}$ and 50% relative humidity). The load was applied using dead weights for SC specimens and using an electrical mechanical testing machine for GTNC specimens. The temperature was monitored using three thermocouples spot welded onto the specimen surface. The temperature gradient between top and bottom ends did not exceed 2°C. The total elongation was continuously measured by a linear variable transducer with a sensitivity of 1 μm .

2.4. Metallurgical investigations

Light optical observations after Vilella etching and scanning electron microscope (SEM) investigations using the backscattered electron (BSE) channelling contrast after colloidal silica polishing were carried out. The precipitation state was characterised using the carbon extraction replica technique to determine both the distribution size by image analysis and the chemical composition of precipitates using the X-Ray electron dispersive spectroscopy (EDS) analysis facility in a Zeiss DSM 982 SEM equipped with a field emission gun (FEG-SEM). Transmission electron microscopy (TEM) investigations were performed in a 200 kV JEOL 2000FX TEM. Thin foil preparation consisted in mechanical polishing followed by double jet electrolytic thinning. A 45% butoxyethanol, 45% acetic acid and 10% perchloric acid solution was used at 0°C under 40V. Electron backscatter diffraction (EBSD) analysis was conducted in the FEG-SEM at 20 kV with the specimen tilted by 70° after mechanical polishing using colloidal silica. It allows to quantitatively investigate the microstructural state and the evolution of grain boundary misorientations over large areas.

X-Ray diffraction data were collected at room temperature in the range of 96° - 126° (2 θ) by steps of 0.032° whereas the counting time was of 0.6 s per step. A diffractometer with CoK α radiation having a wavelength of 0.1788 nm and a Iron-K β filter was used. In addition an entry slit of 0.3° was added. X-Ray diffraction measurements were carried out with a linear detector of type Elphyse which was calibrated using silicon as the sample of reference.

3. Simulation of HAZ microstructures and determination of conditions to reproduce the weakest HAZ of the welded joints

First, a model, which allows to represent weld thermal cycle, is used for treating specimens in the Gleeble 1500 thermal-mechanical simulator. Then, the microstructural changes in the HAZ are investigated. To do so, specimens were treated with various weld thermal cycles which also allows, by comparison with real microstructures, to fit the thermal model parameters. Both results of creep tests on SC cross-weld specimens and metallurgical investigations were used to determine the weld thermal cycle corresponding to the weakest HAZ under high temperature creep loading conditions.

3.1. Modelling the welding thermal cycles

The calculations of weld thermal cycles were based on the Rosenthal (1941) model of thermal dissipation specifically designed for the case of arc welding and later simplified by Rykalin (1957). Note that the model is not allowed to represent the effects of multiple runs but was chosen for its easiness and assuming that for a given run, the following one only acts as a short term tempering treatment. As previously shown by Myhr and Grong (1990), a three dimensional formulation must be used because of the 55 mm thickness of the pipe. The model postulates that the heat input energy, due to the electrical arc, is mainly dissipated by conduction. The equation of heat dissipation is solved in a reference frame whose origin is the heat source:

$$T(t) - T_0 = \frac{Hv_a}{2\pi\Gamma r_a} \exp\left(-v_a \frac{\xi}{2k}\right) \exp\left(-v_a \frac{r_a}{2k}\right) \quad (\text{eq. C.III.1})$$

where T_0 is the preheat temperature, H is the heat input and $k = \Gamma/(\rho c)$ with Γ the thermal conductivity, ρ the density and c the specific heat. The following expressions:

$$\xi = x - v_a t, \quad r_a^2 = \xi^2 + y^2 + z^2 \quad (\text{eq. C.III.2})$$

where r_a and v_a are respectively the position of the arc and the arc displacement rate, allow to represent the arc displacement (i.e the evolution of the heat source position) during the welding procedure (see **figure C.III.2**). y is the distance between the heat source and the point in the HAZ which experiences the calculated welding thermal cycle. z remains also constant and represent the position of the heat source with respect to the specimen thickness. z was taken to 10 mm. The thermal cycle locally underwent by the base metal is finally described by:

$$T(t) - T_0 = \theta_1 \left(\frac{\Delta t_{T_2 \rightarrow T_1}}{t} \right) \exp\left(\frac{\Delta t_{T_2 \rightarrow T_1}}{et} \frac{\theta_1}{T_{\text{peak}} - T} \right) \quad \text{with} \quad \frac{1}{\theta_1} = \frac{1}{T_2 - T_0} - \frac{1}{T_1 - T_0} \quad (\text{eq. C.III.3})$$

where, $T_{\text{peak}} = T_0 + \frac{2}{\pi e} \frac{H}{\rho c r_a^2}$ is the peak temperature of the thermal cycle with $e = \ln(10)$, t the time and $\Delta t_{T_2 \rightarrow T_1}$, the

cooling parameter expressed as the time to cool the material from T_2 to T_1 . Note that the annealing time at T_{peak} is very short (typically < 2s). As is currently assumed, the values of T_2 and T_1 are taken as 800°C and 500°C respectively. The cooling parameter is given by:

$$\Delta t_{T_2 \rightarrow T_1} = \frac{H}{2\pi\Gamma} \frac{1}{\theta_1} \quad (\text{eq. C.III.4})$$

Therefore, the cooling parameter mainly depends on the heat input energy of the process and its value little depends on T_{peak} . In fact, most of the model parameters are material constants which were taken from Warreing (1994) and Haarmann et al (1999). The other parameters, namely, the arc displacement rate, the preheat temperature and the heat input energy (taking into account the efficiency of the process) are given by the process. Only one parameter had to be experimentally determined: the position of the heat source. It was very simply evaluated by microstructural observations of the weld metal, as the columnar solidification grains had grown along the direction of the thermal gradient. All parameters needed to calculate welding thermal cycles are gathered in **table C.III.2**. Note that the cooling parameter $\Delta t_{800 \rightarrow 500}$ does not exceed 31 s so that the martensite transformation occurs upon cooling with no formation of primary ferrite (see Brozda and Zeman (1996)).

Thermal conductivity	$\Gamma = 28 \text{ Wm}^{-1}\text{K}^{-1}$ (at 250°C)
Heat input energy	$H = 1296 \text{ Jmm}^{-1}$
Arc displacement rate	$v_a = 2.6 \cdot 10^{-3} \text{ ms}^{-1}$.
Preheat temperature	$T_0 = 250 \text{ }^\circ\text{C}$
Thickness of the component	$w = 55 \text{ mm}$
Cooling parameter	$\Delta t_{800 \rightarrow 500} = 16 \text{ s}$
Heat source position	4.5 mm from the fusion line

Table C.III.2. Physical constants and welding parameters for the thermal model

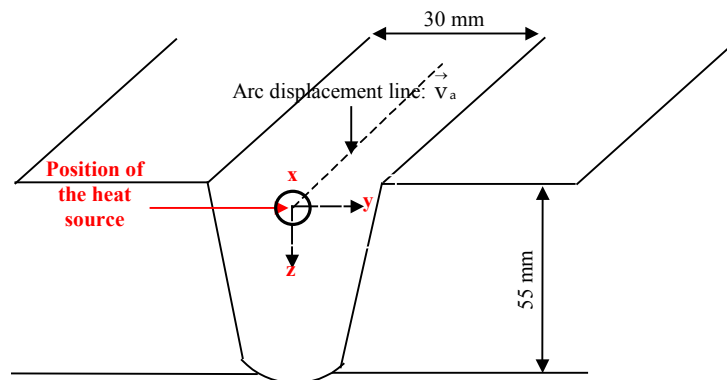


Figure C.III.2. Position of the heat source with respect to the weld geometry

3.2. Comparison between real and simulated HAZs

In the present study, the ability of the thermal model to be used to reproduce various microstructural states of the HAZ was investigated. Several treatments were calculated and then applied to round bars for various distances from the fusion line. The characteristics of the corresponding performed heat cycles are given in **table C.III.3**.

Distance from the fusion line	Peak temp.	Heating rate	Specificity
1.50 mm	1200°C	218°C s ⁻¹	$A_{c3} < T_{\text{peak}}$
2.00 mm	1128°C	204°C s ⁻¹	$A_{c3} < T_{\text{peak}}$
2.50 mm	1056°C	181°C s ⁻¹	$A_{c3} \approx T_{\text{peak}}$
3.00 mm	995°C	158°C s ⁻¹	$A_{c1} < T_{\text{peak}} < A_{c3}$
3.25 mm	986°C	155°C s ⁻¹	$A_{c1} < T_{\text{peak}} < A_{c3}$
3.50 mm	960°C	152°C s ⁻¹	$A_{c1} < T_{\text{peak}} < A_{c3}$
3.75 mm	936°C	148°C s ⁻¹	$A_{c1} < T_{\text{peak}} < A_{c3}$
4.00 mm	911°C	128°C s ⁻¹	$A_{c1} < T_{\text{peak}} < A_{c3}$
4.15 mm	885°C	126°C s ⁻¹	$A_{c1} < T_{\text{peak}} < A_{c3}$
4.20 mm	877°C	124°C s ⁻¹	$T_{\text{peak}} < A_{c1}$
4.50 mm	860°C	121°C s ⁻¹	$T_{\text{peak}} < A_{c1}$

Table C.III.3. Heat cycles performed

The domain of investigation allows to explore the effect of heating in the α , $\alpha + \gamma$ and γ temperature ranges. Simulated microstructures were then given the PWHT of 2 hours at 760°C for comparison with the actual welded joint. In fact, for each weld thermal cycle two specimens were treated and only one of two was submitted to the PWHT so that the properties of the simulated microstructures could be evaluated before and after PWHT. Vickers hardness measurements were carried out for both the weldment and the simulated microstructures after PWHT. It is shown in **figure C.III.3** that hardness values of the simulated and tempered microstructures are very close to the hardness profile in the tempered weldment. Therefore, it will be assumed that the parameter: “distance from the fusion line” can be used to choose the weld thermal cycle corresponding to the weakest HAZ.

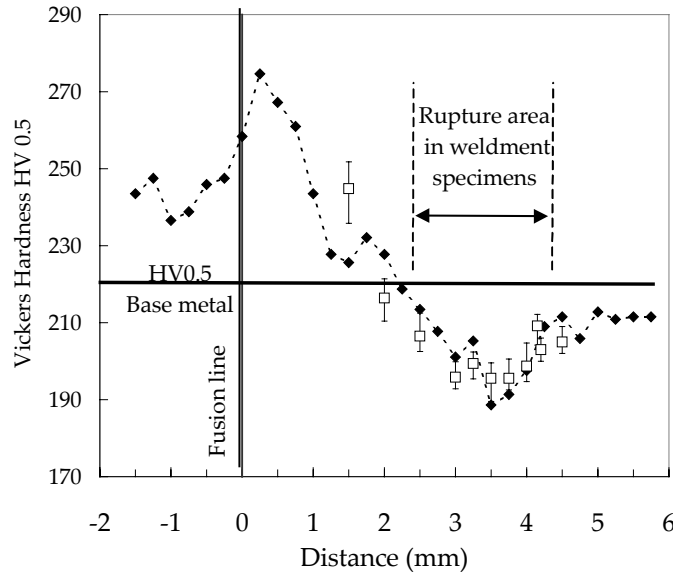


Figure C.III.3 Hardness comparison after PWHT: full symbols = welded joints and open symbols = simulated HAZ

3.2.1. Microstructure of the matrix after the simulated welding cycle

Attention was focused on the metallurgical properties of the simulated microstructures. To do so, the occurrence of phase transformation during heating and cooling was first investigated using the dilatometry results. The main characteristics of these dilation records are as follow:

1. Depending on the thermal cycle, the values of A_{c1} and A_{c3} were determined on the heating curves with an accuracy of $\pm 5^\circ\text{C}$.
2. Depending on the thermal cycle, the values of M_s can be detected on the cooling curves (**figures C.III.3** and **C.III.4**). In addition, non classically, two martensite start temperatures were observed leading to the definition of two M_s temperatures namely M_{s1} and M_{s2} . Note that such a phenomena has already been observed by Alvarez and Garcia (1995a and 1995b) in a 0.3C-13Cr steel and was related to the inhomogeneity in the austenite phase due to partial dissolution of carbides during heating (i.e. the matrix is locally depleted in carbon and chromium elements that are trapped in undissolved precipitates).

It was deduced from **table C.III.3** that among all the performed heat cycles, those with $885^\circ\text{C} < T_{\text{peak}} < 1056^\circ\text{C}$ correspond to intercritical annealing, which was confirmed by hardness measurements in the as welded conditions as shown in **figure C.III.6** where the hardness abruptly increase due to freshly formed martensite from transformed austenite. For a finer understanding of the phase transformations, a rule of mixtures was used to calculate the percentage of transformed martensite during heating and between the two martensite starts temperatures. The plots in **figure C.III.4** confirm that the $\alpha \rightarrow \gamma$ phase transformation occurs for weld thermal cycles with T_{peak} slightly below 900°C and is nearly complete for T_{peak} reaching 1100°C which is also in accordance with the plot of **figure C.III.3**. These results are also consistent with a previous study of Cerjak and Schuster (1994) who showed that 80% of the $\alpha \rightarrow \gamma$ phase transformation has proceeded for $T_{\text{peak}} = 920^\circ\text{C}$ with a comparable value of the heating rate (see **table C.III.3**). It is also shown in **figure C.III.4**. that the percentage of martensite transformation between M_{s1} and M_{s2} reaches a maximum value of 20% for T_{peak} around 1000°C .

Freshly formed and untransformed martensites could not be distinguished even in the as welded condition by SEM investigations so that dilatometric results could not be confirmed by direct observation. Note, however, that Kumar et al (2000 and 2002) have shown that ultrasonic measurements can be used to determine the evolution of the $\alpha \rightarrow \gamma$ phase transformation as the ultrasonic velocity decreases because of the increase in the volume fraction of martensite in the structure. The presence of retained austenite between the laths of martensite is reported by Shiue et al (2000), Moorthy et

al (1997) and Iwaga et al (1993) but it was not evidenced in the present study by neither SEM investigations nor X-Ray diffraction analysis.

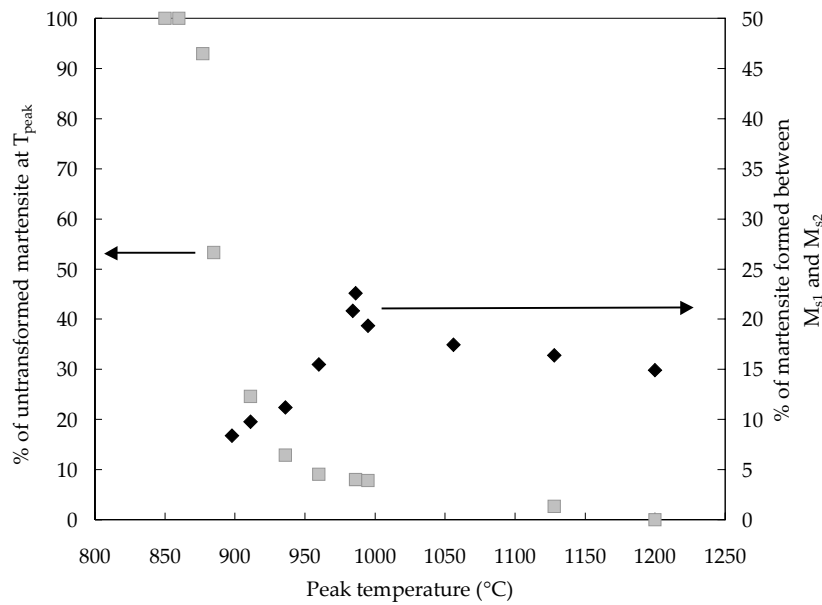


Figure C.III.4. Evolution of phase transformations (dilatometry)

The evolution of the martensite start transformation points M_{s1} and M_{s2} were also plotted versus the peak temperature of the weld thermal cycle in **figure C.III.5**. The increase in the value of M_s can be attributed to an easier nucleation (i.e. more austenite grain boundaries) but more probably to a lower carbon content in the solid solution. Brachet (1995) has previously established that:

$$\Delta M_s = K([C]_{ss} + [N]_{ss}) \quad (\text{eq. C.III.5})$$

with $K < 0$ and $[C]_{ss}$ and $[N]_{ss}$ the carbon and nitrogen contents in the solid solution. The experimental results of Taneike et al (2004) shows that when decreasing the carbon content from 0.16 to 0.002 wt% in a 9Cr3W steel, the martensite start temperature increases by 100°C. It is found here, that the maximum variation between M_{s1} and M_{s2} occurs for T_{peak} ≈ 990°C. It is also interesting to note that for T_{peak} = 1200°C the average value of M_s is nearly the same than that of the base metal. The shape of the M_s curves for T_{peak} in the intercritical domain are difficult to explain as on the one hand the α → γ phase transformation is only partial and, on the other hand, dissolution of M₂₃C₆ carbides is also partial. Thus, for a better understanding, the evolution of the precipitation state during welding thermal cycles was investigated.

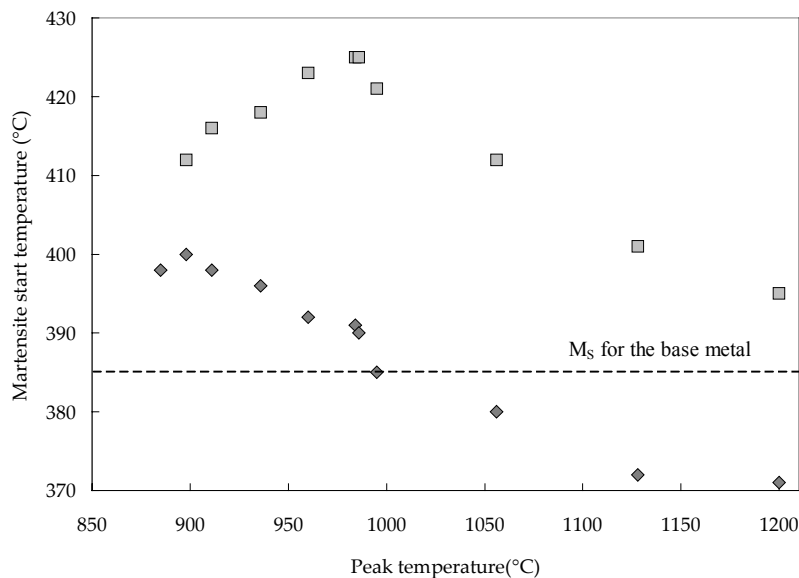


Figure C.III.5. Difference in the martensite start temperatures as a function of the thermal cycle

3.2.2. Evolution of precipitates during the simulated welding cycle

As mentioned in **section 2.1**, two main types of carbides, MX and $M_{23}C_6$ were detected in the initial state. In the present study, the evolution of MX (namely V(C,N) and Nb(C,N) respectively) precipitation states in the simulated and tempered microstructures was not investigated as it would require extensive TEM investigations. However, it can be assumed that in all the ICHAZ, primary MX stay during weld thermal cycles as their dissolution temperature is larger than 1100°C (see Orr and DiFrancesco (1993) and Ootoguro et al (2000)) and as **table C.III.3** shows that for intercritical heat treatments the peak temperature did not exceed the value of 1100°C whereas high heating rates also does not promote the dissolution of these precipitates. Therefore, it is possible that these MX precipitates grow or coarsen during the welding thermal cycle (see Kojima et al (1995)). Tsuchida et al (1996) also evidenced that the welding thermal cycle modify the morphology of MX precipitates from an elongated shape to a more spherical one, and that MX precipitates are no more coherent with the newly formed martensitic matrix. These two changes obviously strongly affect the thermal stability of the resulting microstructure and its creep strength.

Carbide dissolution during heating is not well explained. Several authors like Akbay et al (1994), Brachet et al (1991), Liu et al (1991) and Agren et al (1984) considered that the dissolution of $M_{23}C_6$ carbides only occurs after the main part of the $\alpha \rightarrow \gamma$ phase transformation has proceeded so that the intercritical domain can be divided into two parts. However, Shantsky and Inden (1997) have, for example, proposed a slightly different dissolution sequence for Fe-Cr-Mo steels with high C and Mo contents. In fact, the dissolution sequence of $M_{23}C_6$ carbides strongly depends on the chemical composition so that the occurrence of carbide dissolution with respect to the $\alpha \rightarrow \gamma$ phase transformation was investigated. To address this point, the hardness values of the simulated microstructures before PWHT were measured. They are plotted versus T_{peak} as recommended by Sanderson (1978) in **figure C.III.6**. The strong increase in the Vickers hardness observed for $T_{peak} = 900^\circ\text{C}$ shows that the $\alpha \rightarrow \gamma$ phase transformation occurs at that temperature. A small drop in hardness for $T_{peak} \approx 990^\circ\text{C}$ is also evidenced. Following the previous work of Sanderson, it can probably be related to the carbides dissolution but its interpretation is not easy (Note also that the drop in hardness does obviously not corresponds to the presence of retained austenite).

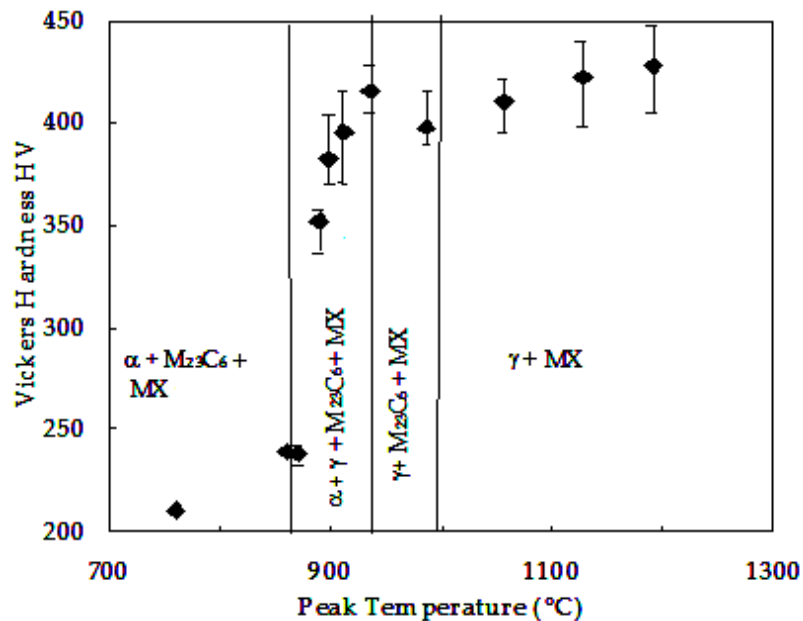


Figure C.III.6. Vickers hardness of simulated microstructures before PWHT

Therefore, complementary investigations were performed. First, X-Ray diffraction measurements allowed to determine the lattice parameters of the simulated microstructures in the as welded condition, and in particular the tetragonality of the martensite lattice. As shown by Cheng et al (1990) and Jack and Jack (1973), the matrix tetragonality strongly depends on the chemical composition of the matrix and especially on the carbon content in the solid solution. A classically used relationship was established as:

$$\frac{c}{a} = 1.000 + 0.045[C]_{ss} \quad (\text{eq. C.III.6})$$

where c and a are the martensite lattice parameters and $[C]_{ss}$ is the carbon content in the solid solution in wt%. As the lattice parameters, namely c and a , were determined from $\theta - 2\theta$ X-Ray diffraction analysis, the relationship of **equation C.III.6** could be used to calculate the carbon content in the solid solution. The carbon content in solid solution is plotted versus T_{peak} in **figure C.III.7**.

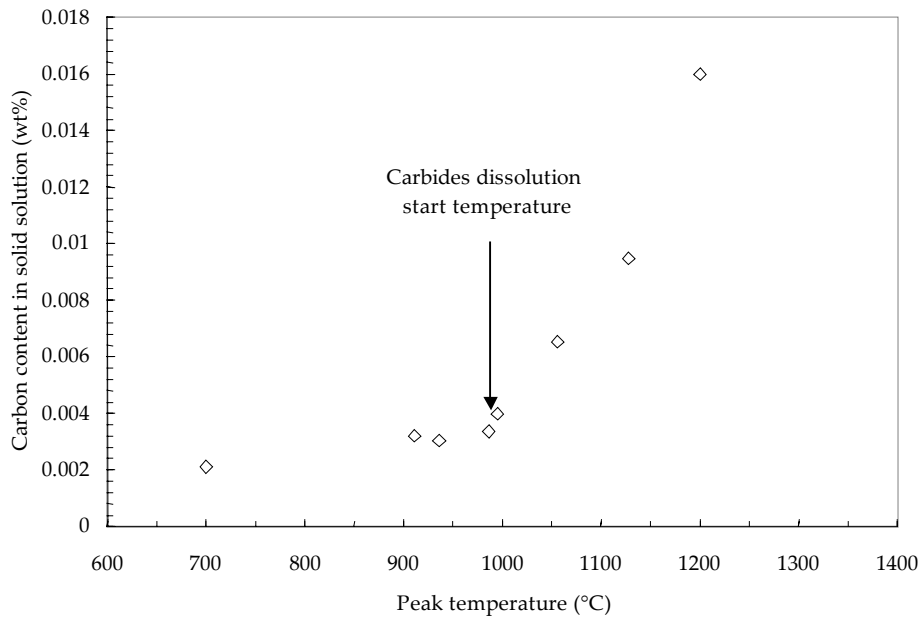


Figure C.III.7. Evaluation of the carbon content in solid solution at room temperature from X-Ray diffraction measurements

It is shown in **figure C.III.7** that in the initial state (i.e. the tempered base metal) the carbon content in solid solution is very low as almost all the carbon has precipitated in carbides. This value remains unchanged up to $T_{\text{peak}} = 1000^{\circ}\text{C}$ and then starts to increase rapidly. Therefore, it was assumed from these measurements that the dissolution of $M_{23}C_6$ carbides starts for peak temperature higher than 1000°C for the explored heating rates. One should also notice that even for $T_{\text{peak}} = 1200^{\circ}\text{C}$, the carbon content in the solid solution only reaches 0.016 wt% whereas the base metal contains 0.09 wt% of carbon. This point can be easily explained by the fast kinetics encountered during the weld thermal cycles and by carbon trapping in MX precipitates. Note also that these results are consistent with those of Bendick et al (1992) and Vijayalakshmi et al (1999).

All the investigations presented above lead to the following conclusions:

1. The weld thermal cycle whose peak temperature: $885^{\circ}\text{C} < T_{\text{peak}} < 1056^{\circ}\text{C}$ are intercritical treatments.
2. $M_{23}C_6$ carbides start to dissolve for $T_{\text{peak}} > 1000^{\circ}\text{C}$ and the martensite resulting from the $\gamma \rightarrow \alpha$ transformation after heating at $T_{\text{peak}} < 1000^{\circ}\text{C}$ exhibits a strong lack in carbon.
3. In the conditions of the weld thermal cycles, the MX carbides are obviously not dissolved at least for $T_{\text{peak}} < 1100^{\circ}\text{C}$ and probably little grow or coarsen.

3.2.3. Effects of the PWHT

It is now necessary to investigate whether the characteristics of the intercritically treated simulated microstructures, influence their evolution during the PWHT. Several studies concerned with the base metal have shown that the microstructural stability of 9Cr1Mo-NbV steels, especially under high temperature ageing and creep conditions, strongly depends on the pinning of dislocations and grain boundaries by a fine dispersion of carbides (see Nakajima et al (2003), Hattestrand and Andren (2001) and Cerri et al (1998), Tian et al (1991)). It has also been shown in Tsuchiyama et al (2001) that both a large carbide size and a low carbon content promote rapid softening of martensite during a high tempering treatment.

First, the hardness profile of **figure C.III.3** shows that in the CGHAZ (i.e. between 1 mm and 2 mm far from the fusion line), the hardness is relatively high (20 points higher than that of the base metal) as the precipitation of new strengthening carbides occurs during the PWHT. The yield strength of the martensite (locally equivalent to its hardness) is classically describes by a Norstrom law:

$$\sigma_y = \sigma_0 + \sigma_1 + k_y D^{-1/2} + k_s d^{-1/2} + \alpha Gb(\rho_0 + K(\%C)) \quad (\text{eq. C.III.7})$$

where σ_0 is associated to lattice friction, σ_1 is associated to solid solution strengthening, D is the packet size, d is the lath size, G is the shear modulus, b is the Burgers vector, ρ_0 is the dislocation density, $\%C$ is the carbon content in wt%, and k_y , k_s , and α are material constants. Therefore, from **equation C.III.7**, it can be deduced that the difference in hardness can be attributed to a lower grain size but also to the fact that the base metal is submitted to two tempering treatments (a tempering of 2 hours at 765°C and the PWHT of 2 hours at 760°C) whereas the CGHAZ is only submitted to the PWHT i.e. the carbon content in solid solution is lower in the base metal. On the contrary, in the ICHAZ (i.e. between 3 mm and

4 mm far from the fusion line), the hardness is lower by 20 points than that of the base metal which evidenced a softening of the material, attributed to the lath martensite recovery by Spigarelli and Quadrini (2002) and to the growth of precipitates by Kojima et al (1995). Moreover, Jakobova et al (1998) have shown that the growth of subgrains with low dislocation density (i.e. the lath recovery) is strongly related to the growth of $M_{23}C_6$ and MX carbides which no longer pinned the subgrain boundaries.

Therefore, SEM investigations were performed both on simulated and tempered microstructures. These observations confirmed that extensive lath recovery occurs during the PWHT for weld thermal cycles with a peak temperature ranging from 880°C to 1050°C i.e. for the intercritically treated microstructures. These observations are consistent with observations in corresponding zones of the real weldment. Note also that, the intercritical annealing has already been used by Guo et al (2000) to obtain an ultrafine grain size microstructure from lath martensite.

The evolution of the precipitation state was also investigated. Carbon extraction replicas were analysed for the simulated and tempered microstructures and the corresponding zones of the real weldment. The comparison of precipitate size distributions evidenced a difference of only 10 nm – 20 nm in the average $M_{23}C_6$ carbides size between simulated and real microstructures. The most interesting information given by these measurements was that the mean size of carbide after PWHT is larger than 200 nm in the ICHAZ, i.e. twice the size measured in the base metal. The evolution of $M_{23}C_6$ carbides population observed in the present study is consistent with the results given by Taneike et al (2004) who showed that when the carbon content is lowered, the $M_{23}C_6$ carbides exhibit a larger size and are less in number. It was also deduced that the extensive lath recovery probably results from a lack in carbon and the rapid coarsening of the $M_{23}C_6$ carbides non dissolved during the weld thermal cycle.

In addition, it was also evidenced that the PWHT temperature plays a key role in the martensite recovery. Basically, the PWHT is chosen to reach imposed values of fracture toughness for the weld metal. In the present study, a PWHT of two hours at 600°C was performed on several ICHAZ microstructures. In all cases, SEM investigations revealed that lath martensite was not softened during PWHT which was confirmed by values of hardness higher by 20 points in the ICHAZ than these measured after a PWHT of 2 hours at 760°C. Note that Shiue et al (2000) evidenced the same effect of the PWHT temperature on the final hardness but also that a high PWHT temperature leads to a lower toughness in the same microstructure.

3.3. Choice of a weld thermal cycle

Many authors (Hald and Lund (1993), Cerjak and Schuster (1994), Eggeler et al (1994), Tsuchida et al (1996), Ootoguro et al (2000), Letofsky et al (2000), Matsui et al (2001) and Wu et al (2004)) performed heat treatments in order to reproduce the weakest microstructure of the HAZ, using either a conventional furnace or a welding simulator. Most of the authors arbitrarily chose a thermal cycle corresponding to an intercritical treatment but Tsuchida et al (1996) and Ootoguro et al (2000) reproduced several microstructures and carried out high temperature creep tests to determine which one had the lowest creep strength. Typical thermal cycles used in literature are given in **table C.III.4**. Note that all these thermal treatments are intercritical ones. The necessity to impose a stress or strain during weld thermal cycle simulation to promote martensite softening during PWHT has already been addressed by Murdoch et al (2001), but the authors found that final microstructures obtained by a thermal treatment under stress near A_{c1} and a stress free thermal treatment near A_{c3} , respectively, are similar. There could possibly be an equivalence in the strain-temperature effect on the transformation kinetics but further investigations are needed to confirm this statement.

Source	Peak temperature	Heating rate	Cooling rate	PWHT
Hald and Lund (1993)	940°C	<i>Not given</i>	<i>Not given</i>	4.0 h – 774°C
Cerjak and Schuster (1994)	900 – 960°C	150°C s ⁻¹	$\Delta t_{800 \rightarrow 500} = 21$ s	12.0 h - 730°C
Eggeler et al (1994)	850 °C	<i>Furnace (heating in 6 minutes and dwell of 5 minutes followed by air cooling)</i>		12.0 h – 730°C
Tsuchida et al (1996)	900 °C	270°C s ⁻¹	$\Delta t_{800 \rightarrow 500} = 30$ s	8.5 h – 740°C
Ootoguro et al (2000)	900 – 1100°C	<i>Not given</i>	$\Delta t_{800 \rightarrow 500} = 10$ s	1.0 h – 750°C
Letofsky et al (2000)	900 – 1000°C	<i>Not given</i>	<i>Not given</i>	2.0 h – 760°C
Matsui et al (2001)	920°C	4°C s ⁻¹	<i>Not given</i>	4.5 h – 740°C
Wu et al (2004)	850°C	<i>Furnace (dwell of 20 minutes followed by air cooling)</i>		2.0 h – 760°C

Table C.III.4. Typical thermal treatments used to simulate microstructures of the weak HAZ

(Note that when heating and cooling rates are not given, thermal treatment are probably performed in conventional furnaces)

In the present study, the weld thermal cycle corresponding to the weakest HAZ was chosen using both a geometrical criterion (location of rupture in cross-weld specimens, characterised by its distance from the fusion line) as it was shown

in **section 3.2** that the thermal model well reproduces the corresponding zone in the real weldment, and metallurgical criteria.

First, creep tests on cross-weld SC specimens were carried out. The initial values of engineering stresses ranged respectively from 100 MPa to 50 MPa (corresponding to lifetimes from 300 hours to 10,000 hours) and from 120 MPa to 90 MPa (corresponding to lifetimes from 800 hours to 7,000 hours) for respectively the weldment and the base metal. Creep results of the present study are consistent with literature data given by Jakobova et al (1998). Note that for a given applied engineering stress $\sigma = 100$ MPa, creep failure occurs after 300 hours for weldments and after 3,500 hours for the base metal. More generally, the weldment creep lifetime is more than ten times lower than that of the base metal for the same applied engineering which corresponds to a reduction of the creep strength by 30%. SEM investigations of polished cross sections of weldment specimens evidenced that rupture occurs in the ICHAZ near the base metal (i.e. more than 2.5 mm far from the fusion line) parallel to the fusion line (type IV rupture, see **figure C.III.3**). Damage is mainly located in the ICHAZ (i.e. over a distance of 2 mm) but cavities are also detected in all the HAZ and in the over-tempered base metal. Similar observations are reported by Laha et al (2000), De Witte et al (1991) and Bendick et al (1992) in the temperature range from 575°C to 650°C. Therefore it is assumed that the thermal cycle corresponding to the weakest HAZ is characterised by a peak temperature: $885^{\circ}\text{C} < T_{\text{peak}} < 1060^{\circ}\text{C}$ (i.e. in the intercritical domain).

The choice of one of the intercritical cycles was based on metallurgical considerations. Second phase particles have a pinning effect on grain boundaries and dislocations. So, $M_{23}C_6$ carbide coarsening and changes in MX precipitation behaviour in the freshly formed martensite (see Bendick et al (1992) and Kojima et al (1995)) promote faster kinetics of creep recovery. Large carbides are also likely to be preferential sites for creep cavity nucleation as already evidenced for the base metal (see Eggeler (1989)). Taking into account the conclusions of **section 3.2** the weld thermal cycle was chosen as the cycle for which the $\alpha \rightarrow \gamma$ phase transformation is most completed while dissolution of $M_{23}C_6$ has not yet occurred during heating. The characteristics corresponding to this cycle are given in **table C.III.5**.

Peak temperature	Heating rate	Cooling rate	PWHT
986°C	155°Cs ⁻¹	$\Delta t_{800 \rightarrow 500} = 16 \text{ s } (\approx 19^{\circ}\text{Cs}^{-1})$	2 hours (760°C)

Table C.III. 5. Thermal cycle corresponding to the soft HAZ

The chosen weld thermal cycle exhibits a peak temperature of 986°C which is slightly larger than the values found in the literature and given in **table C.III.4**. Note, however, that Ootoguro et al (2000) showed that the weakest simulated microstructure was that with $T_{\text{peak}} = 900^{\circ}\text{C}$ for short term creep tests and that with $T_{\text{peak}} = 1000^{\circ}\text{C}$ for long term creep tests. Matsui et al (2001) also showed that the weld thermal cycle corresponding to the weakest HAZ exhibits a peak temperature just below A_{c3} .

3.4. Metallurgical validation of the chosen weld thermal cycle

The TEM comparison between simulated and real microstructures for the cycle with $T_{\text{peak}} = 986^{\circ}\text{C}$ is shown in **figure C.III.8**. It is observed that the two microstructures exhibit the same characteristics in terms of matrix morphology (i.e. low dislocation density small equiaxed grains) and precipitation state. These observations were also confirmed by EBSD analysis (see **figure C.III.9**). Note that the grain boundary misorientation distribution is dominated by low misorientation boundaries (i.e. $5^{\circ} - 15^{\circ}$). It is consistent with the occurrence of the lath recovery process during the PWHT. In the following section, attention will be focused on determining the creep flow and damage properties of this microstructure. Those mechanical tests will also allow to check that creep damage mechanisms are similar in actual and simulated HAZ microstructures.

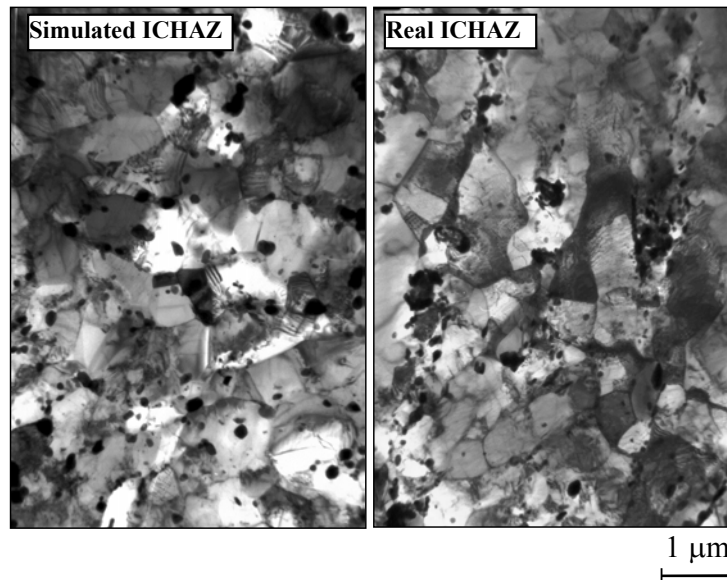


Figure C.III. 8. Thin foils TEM investigations: Comparison of real and simulated intercritical heat affected zone ($T_{peak} = 986^{\circ}\text{C}$) microstructures (bright field images)

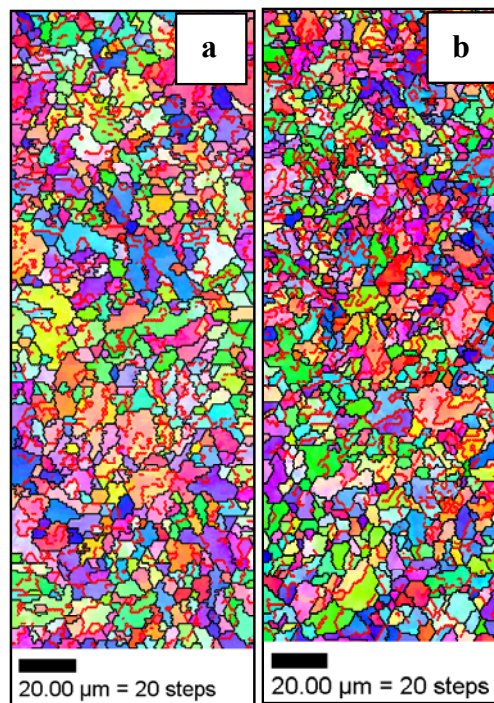


Figure C.III.9. EBSD investigations: Comparison between (a) real and (b) simulated intercritical heat affected zones ($T_{peak} = 986^{\circ}\text{C}$)

- Thick red lines for low angles boundaries ($5 - 15^{\circ}$)
- Thin black lines delineate high angle boundaries ($> 15^{\circ}$)

4. Tensile, creep flow and damage properties of the simulated ICHAZ microstructure at 625°C

4.1. Tensile properties at 625°C

Tensile curves show a strong strain rate effect on the tensile response. Non linear threshold stresses were evaluated to be 325 MPa at 5.10^{-3} s^{-1} , 280 MPa at 5.10^{-4} s^{-1} and 225 MPa at 5.10^{-5} s^{-1} . Maximum stress was evaluated to be 375 MPa at 5.10^{-3} s^{-1} , 330 MPa at 5.10^{-4} s^{-1} and 265 MPa at 5.10^{-5} s^{-1} . Curves also exhibited a very low homogeneous elongation ($< 1\%$) before the onset of the material softening. Cross-section SEM examinations of the specimens with BSE channelling contrast and EBSD analysis showed extensive recovery of the initially equiaxed microstructure with final highly misoriented grains of only a few hundreds of nanometers in mean size in the necking area. These results are similar to those obtained with the base metal (chapter B.III).

4.2. Creep flow properties at 625°C

Creep stress levels for GTNC5.0 specimens were set from 130 MPa to 70 MPa corresponding to creep lifetimes ranging between 150 hours and 3,500 hours. In addition, steady state creep strain rates at 50 MPa, 60 MPa, and 70 MPa were determined from the complementary test with load varying with steps. It is evidenced in **figure C.III.10** that the results of the creep test with load varying with steps and that of the creep test carried out at 70 MPa until the specimen failure are quasi indistinguishable.

Interpretation of all these tests is not straightforward as the notch induces multi-axial loading conditions. It requires inverse analysis by means of finite element calculations to determine the flow behaviour in a rigorous manner which is beyond the scope of this paper. However, the aim of the present study was to use simple representations to describe creep flow and damage behaviour of the ICHAZ. To do so, the concept of reference length, introduced by Yoshida (1985) and Piques (1989), was used. It was assumed that deformation only occurs in the notched area over a length: $l_{ref} \approx l_{notch}$ where $l_{notch} = 6$ mm for GTNC5.0 specimens. Therefore, steady state strain rates were evaluated with $\dot{\epsilon} = \frac{\Delta l}{l_{ref}}$ and are plotted versus the applied engineering stress in **figure C.III.10**. Two creep flow regimes can be identified with a transition value for a stress of about 80MPa. For both of them, creep flow behaviour in the steady state creep regime can be represented using a Norton power-law :

$$\dot{\epsilon}_{ss} = B\sigma^n \quad (\text{eq. C.III.8})$$

The values of coefficients B and n were determined both in the high and the low stress creep regimes:

1. For $\sigma > 70$ MPa, deformation probably proceeds by dislocation climb or cross-slip with $n = 9.5$ and $B = 2.13 \cdot 10^{-24} \text{ h}^{-1} \text{ MPa}^{-9.5}$.
2. for $\sigma < 70$ MPa, deformation probably proceeds by grain boundary diffusion with $n = 1.6$ and $B = 5.75 \cdot 10^{-9} \text{ h}^{-1} \text{ MPa}^{-1.6}$.

Note that in the two creep regimes, the steady state creep strain rates of the simulated ICHAZ are more than ten times higher than those encountered in the base metal (see Kloc and Sklenicka (1997) and **chapter B.III**).

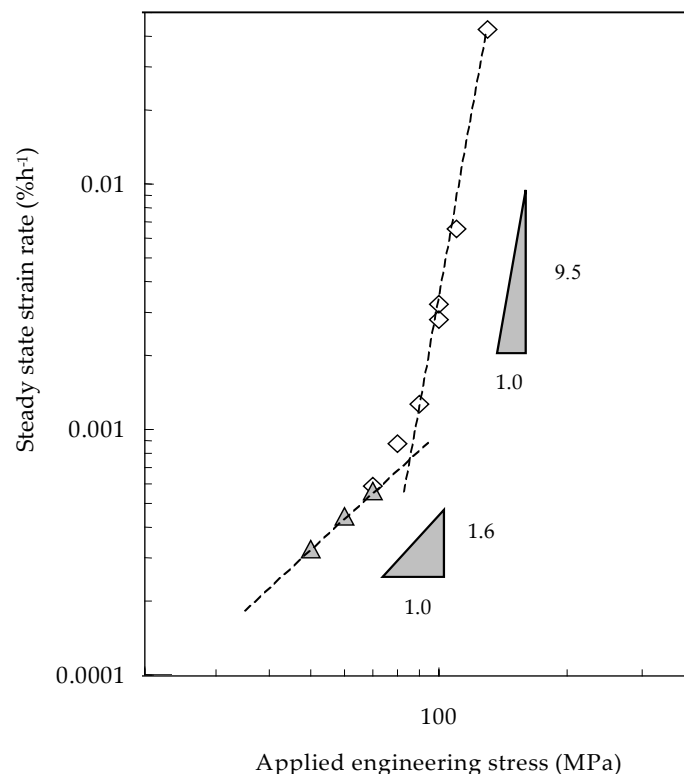


Figure C.III.10. Normalised steady state strain rate versus applied engineering stress (Open symbols = one test per load level, full symbols = multiple-steps test)

4.3. Creep fracture properties

It is evidenced in **figure C.III.11** that the experimental lifetime results of the present work are in good agreement with the previous works of Cerjak and Schuster (1994), Eggeler et al (1994), Tsuchida et al (1996), Ootoguro et al (2000), Matsui et al (2001) and Wu et al (2004). Literature data correspond to creep tests on smooth round specimens, which could explain that the results of the present study evidence a slightly better creep strength of the simulated HAZ due to the notch strengthening effect.

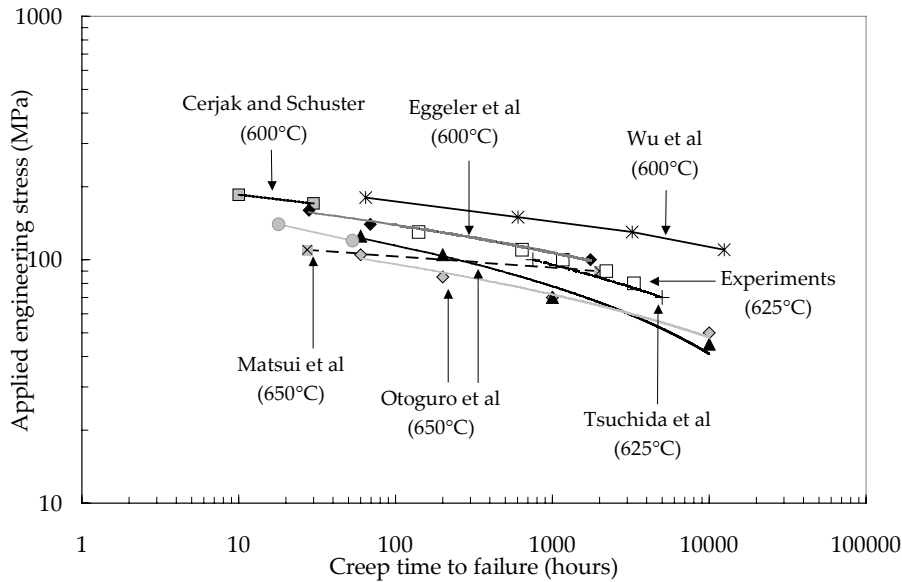


Figure C.III.11. Comparison of creep experiments on simulated ICHAZ at 625°C (GTNC5.0 specimens = open squares) with results from literature (smooth specimens)

To describe the creep fracture behaviour of the simulated ICHAZ, a Monkman-Grant (MG) relationship was used:

$$\dot{\epsilon}_{ss} t_R^m = C_{MG} \quad (\text{eq. C.III.9})$$

where m and C_{MG} are material parameters fitted in the high stress creep regime with $m = 0.8$ and $C_{MG} = 0.28 \text{ h}^{0.2}$ as no rupture data are available for the low stress creep regime. Using the concept of t_{ref} , it is shown (see **figure C.III.12**) that a unique MG fit can predict creep failure for all kinds of specimen geometry. It shows that the notch slightly affects the material ductility at least in the stress domain experimentally investigated. Assuming that the material ductility remains constant, the MG fit was plotted in both high and low stresses creep regimes (see **figure C.III.13**). Comparison with results on weldments (SC specimens) shows that predictions are in quite good agreement with experiments. MG predictions are a little optimistic in the high stress creep regime in comparison with tests on SC specimens (due to the notch strengthening effect) but are, on the contrary, conservative in the low stress creep regime. In fact, the notch has both a strengthening effect but it is also shown in Gaffard et al (2004) that it shifts the transition between high and low stress creep regimes towards shorter creep lifetimes.

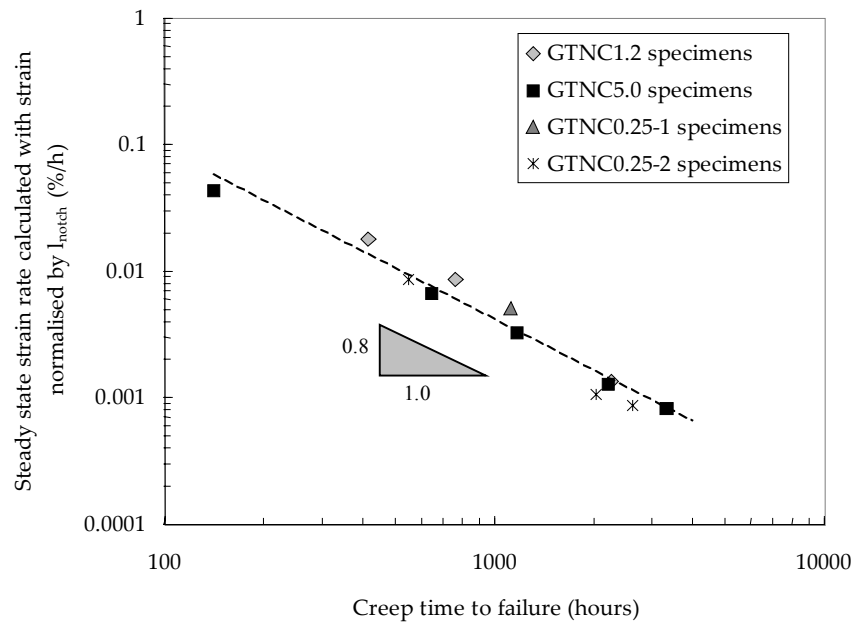


Figure C.III.12. Steady state strain rate versus time to failure for the simulated heat affected zone

The evolution of the creep time to failure with stress is plotted in **figure C.III.13** for all specimens. A notch strengthening effect is evidenced for notch radii ranging from 5.0 mm to 1.2 mm. Note, however, that the strengthening effect is more limited between GTNC1.2 and GTNC0.25 specimens. Therefore, the stress triaxiality ratio obviously plays a key role in the deformation and damage processes and in the creep lifetime behaviour.

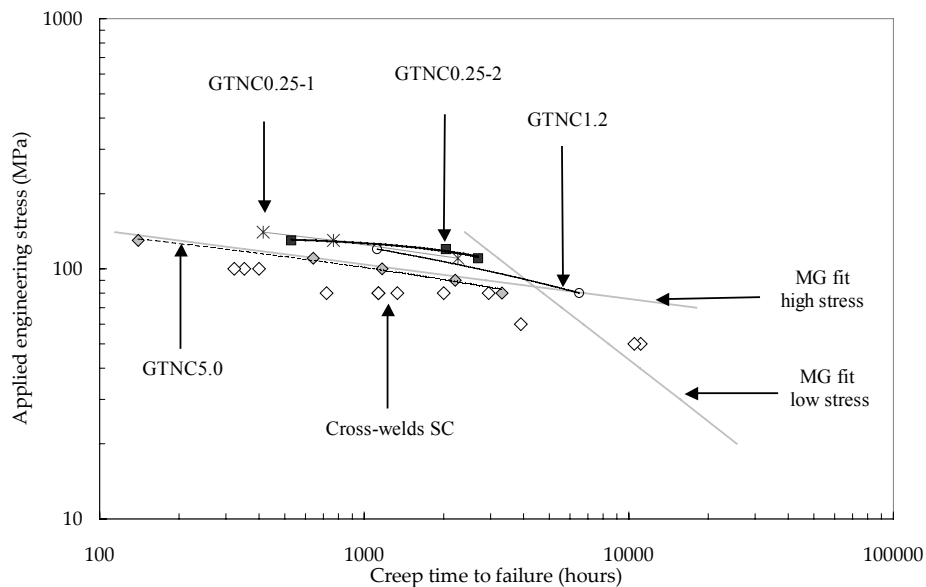


Figure C.III.13. Applied engineering stress versus creep time to failure for SC (cross-weld) and GTNC (simulated HAZ) specimen

4.4. Damage mechanisms

Cross-sections of creep fractured specimens (**figures C.III.14a and C.III.14b**) show that similar damage mechanisms are encountered in weldments and in the simulated ICHAZ. This is also confirmed by EBSD analysis (see **figures C.III.15a and C.III.15b**). The following conclusions about damage mechanisms both in weldments and in the simulated ICHAZ can be drawn:

1. Even if the initial microstructure is totally recovered, softening further occurs during creep tests. The comparison between EBSD maps in the initial state (**figure C.III.10a and C.III.10b**) and after creep exposure (**figure C.III.15a and C.III.15b**) shows that the ratio of high angle grain boundary increases during creep. It gives arguments to state that a softening of the initially recovered microstructure occurs (possibly recrystallisation).

2. Cavities nucleate at grain boundaries and especially at second phase particles. Observations of carbon extraction replicas and EDS analysis performed in the FEG-SEM revealed the presence of a number of Laves phases larger than 300 nm. In both real and simulated ICHAZ microstructures, these precipitates largely promote cavity nucleation.
3. It was shown by EBSD analysis that cavities mainly develop at high angle grain boundaries. Note about this point that EBSD allows to determine crystallographic damage characteristics with more ease and a better statistical significance than TEM observations.
4. The role of diffusion in cavity growth is very predominant which can be explained by a creep flow rate in the diffusion creep regime ten times faster in the simulated ICHAZ than in the base metal (see Gaffard et al (2004) for base metal creep flow properties).

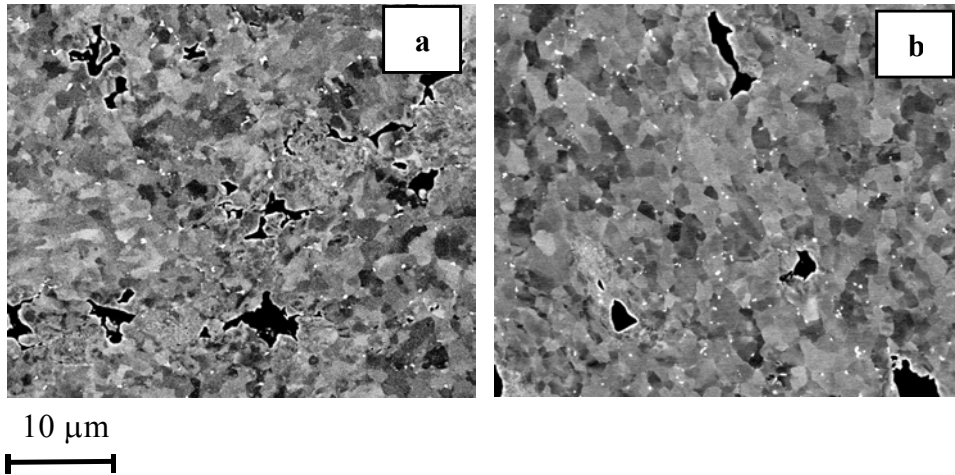


Figure C.III.14. Cross-sections SEM observations of damage in specimens (a) weldment (b) simulated HAZ (Cavities in black and loading direction along the vertical axis)

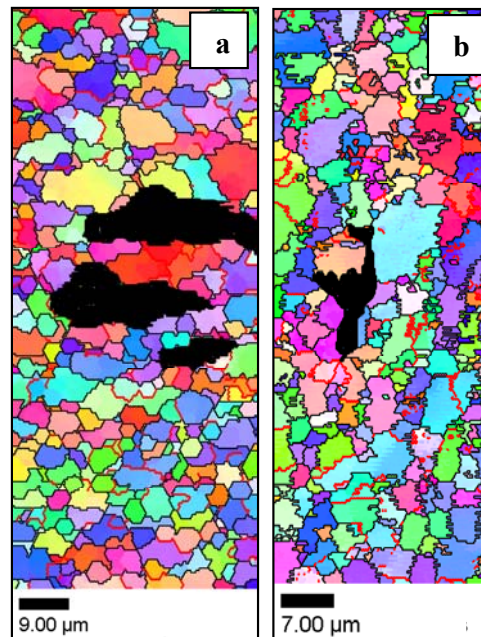


Figure C.III.15. EBSD maps of the damaged area of: (a) weldment (b) simulated HAZ specimens

- *Cavities are in black*
- *Thick red lines for low angles boundaries (5 – 15°)*
- *Thin black lines delineate high angle boundaries (> 15°)*

Both creep curves and damage investigations in notched simulated ICHAZ specimens are to be used to fit, using an inverse analysis approach analysis with finite elements simulations, a constitutive model coupling both creep flow and damage as already been done for the base metal (see Gaffard et al (2004)). This will be the subject of a forthcoming paper (**chapter C.IV**).

Conclusions

In the present study, attention was focused on determining the creep flow and damage properties of the weakest zone of 9Cr1Mo-NbV steel weldments using various kinds of specimen geometry and multi-scale metallurgical investigations. The following conclusions can be drawn:

1. 9Cr1Mo-NbV weldments exhibit a strong drop in creep strength in comparison with the base metal. This drop is attributed to the very low creep strength of the ICHAZ. It was based on a Rosenthal - Rykalin formalism whose model parameters are mainly physical constants or given by the welding procedure.
2. A thermal model was fitted and used to represent with satisfactory agreement various microstructural states of the HAZ. It corresponds to a thermal treatment in the upper bound of the intercritical domain near 990°C with a heating rate of 155°Cs⁻¹ and a cooling characterised by $\Delta t_{800 \rightarrow 500} = 16$ s which corresponds to a cooling rate of approximately 19°Cs⁻¹.
3. A weld thermal cycle leading to the formation of a microstructure having the same metallurgical and mechanical properties of the weakest HAZ was identified based on both metallurgical and mechanical investigations.
4. Mechanical tests show that the ICHAZ intrinsically exhibits a higher creep strain rate responsible for lower creep strength than the base metal.

Acknowledgements

Financial and technical support from Electricité de France (EdF), Framatome and Le Commissariat à l'Énergie Atomique (CEA) is acknowledged. Thanks are due to Dr L. Guetaz (CEA - Grenoble) for TEM investigations and to Mr D. Pachoutinsky for X-Ray diffraction measurements.

References

- Agren J., Vassilev G., 1984, *Materials science and engineering*, 64, 95-103.
- Albert S.K., Matsui M., Watanabe T., Hongo H., Kubo K., Tabuchi M., *ISIJ international* (2002), 42(12), 1497-1504.
- Akbay T., Reed R.C., Atkinson C., 1994, *Acta metallurgica and materialia*, 47, 1469-1478.
- Alvarez L.F. and Garcia C. *La revue de métallurgie CIT/SGM* (1995), 247-253.
- Alvarez L.F. and Garcia C. *La revue de métallurgie CIT/SGM* (1995), 1411-1416.
- Bendick W., Niederhoff K., Wellnitz G., Zschau M., Cerjak H., 3rd international conference on trends in welding research, Gatlinburg (1992) 587-591.
- Vijayalakshmi M., Saroja S., Raghunathan V. S. (1999) *Scripta Materialia*. 41(2), 149-152.
- Brachet J.C., *Journal de Physique IV - colloque C8* (1995), 5, C8-339.
- Brozda J., Zeman M., *Welding international* (1996), 10(5), 370-380.
- Chen L., Bottger A., de Keijser Th.H., Mittemeijer E.J., *Scripta metallurgica and materialia*, 24, 509-514.
- Cerjak H., Schuster F., *Conference on joining technology EUROJOIN2* (1994), 157-167.
- Cerjak H., Letofsky E., Schuster F., *Trends in welding research* (1995), proceedings of the 4th int. conference, Gatlinburg – Tennessee, ASM International, Metals Park OH.
- Danon A., Servant C., Alamo A., Brachet J.C. (2003). *Materials science and engineering*, A348, 122-132.
- DeWitte M., Coussement C., *Materials at high temperature* (1991), 9(4), 178-184.
- Eggeler G., Ramteke A., Coleman M., Burbliès A., Peter G., Hald J., Jefferey C., Rantala J., DeWitte M., Mohrmann R., *International journal of pressure vessels and piping* (1994), 60, 237-257.
- Gaffard V., Besson J., Gourgues-Lorenzon A.F., *International journal of fracture* (2004), submitted in september 2004.
- Guo Z., Sato K., Lee T.K., Morris J.W. (2000). *Ultrafine grained materials* edited by Mishra R.S., Semiatin, S.L.. The minerals, metals and materials society, Warrendale, PA.
- Haarmann K., Vailant J.C., Bendick W., Anbab A., *The T91/P91 book*. Vallourec et Mannesmann tubes (1999).
- Hald J., Lund E.M., *Int. Conf on the join. of mat., Hebingor – danemark* (1993), 317-324.
- Iwaga et al, *Journal of the iron and steel institute* (1998), 79(8), 996-1002.
- Jack D.H., Jack K.H., 1973, *Materials science and engineering*, 11, 1-8.
- Jakobova A., Vodarek V., Hennhofer K., Foldyna V., *Materials for advanced power engineering*, 8th Liege conf. (1998), 373-382.

Kojima T., Hagashi K., Kajita T., *ISIJ international* (1995), 35(10). 1284-1290.
 Kloc L., Sklenicka V., *Materials science and engineering* (1997), A234-236, 962-965.
 Kumar A., Jayakumar T., Raj B., *Philosophical Mag. A.* (2002), 80(1), 2469-2487.
 Kumar A., Laha K., Jayakumar T., Bhanu Sankara Rao K., Raj B., *Metall. and Mat. Trans. A.* (2002), 33(A), 1617-1626.
 Laha K., Chandravathi K.S., Bhanu Sankara Rao K., *Transactions of the indian institute of metals* (2000), 53(3), 217-221.
 Liu Z.K., Hoglund L., Jonsson B., Agren J., 1991, *Metall. Trans., A*, 22, 1753-1765.
 Matsui M., Tabuchi M., Watanabe T., Kubo K., Kinugawa J., Abe F., *ISIJ international* (2001), 41, s126-s130.
 Moorthy et al, *Materials science and engineering* (1997), A231, 98-104.
 Murdoch A.J., Allen D.J., Brown S.G.R., (2001), 1, 263-275.
 Myhr O.R., Grong O., *Acta metallurgica and materialia* (1990), 38(3), 449-460.
 Orr J., Di Francesco A., *Ironmaking and steelmaking* (1993), 20(6), 424-430.
 Otaguro Y., Matsubara M., Itoh I., Nakazawa T., *Nuclear engineering and design* (2000), 196, 51-61.
 Piques R., PhD Thesis, Ecole Nationale Supérieure des Mines de Paris, Paris, France (in French), (1989).
 Rosenthal D., *Welding journal* (1941), 20, 220s.
 Rykalin N.N., *Berechnung der Warmevorgänge beim Schweißen* (1957), Verlag technik, Berlin.
 Sanderson S.J, *Metal science* (1978), April. 220-222.
 Shantsky D.V., Inden G., *Acta materialia* (1997), 45(7), 2879-2895.
 Shiue et al, *Materials science and engineering* (2000), A287, 10-16.
 Spigarelli S., Quadri E., *Materials and design* (2002) 23, 547-552.
 Taneike M., Sawada K., Abe F., *Metallurgical transactions A* (2004) 35, 1255-1261.
 Tian S.L., Coussement C. DeWitte M., Shee M., *Int. j. of press. vess. & pip.* (1991). 46. 339
 Tsuchida Y., Okamoto K., Tokunaya Y. *Welding international* (1996), 10(6), 454-460.
 Tsuchiyama T., Miyamoto T., Takaki S. (2001). *ISIJ International*. 41(9). 1047-1052.
 Warreing J., CEA/SRMA, Internal report N.T SRMA94-2013 (1994).
 Wu R., Sandstrom R., Seitisleam F., *Journal of engineering materials and technology* (2004), 126, 87-94.
 Yoshida M., PhD Thesis, Ecole Nationale Supérieure des Mines de Paris, Paris, France (in French), (1985).

Supplement C.III.S1. Evolution of the simulated HAZ microstructure during tensile deformation: EBSD analysis

Electron backscattered diffraction (EBSD) analysis of the simulated HAZ microstructure after tensile deformation was not included in **chapter C.III**. However, such a work and especially a comparison between the initial state and after tensile deformation was performed for the base metal in **chapter A.I**. Therefore, the same work is carried out, here, for the simulated IHAZ. EBSD map in the necking area is presented in **figure C.III.S1.1a**. The histogram of angle misorientations between neighbouring grains was plotted in **figure C.III.S1.1c** were the same histogram for the simulated HAZ in the initial state is also plotted. It is evidenced that the amount of low angle misorientation grain boundaries largely decreases whereas two populations of high angle boundaries (i.e. 25° - 35° and 40° - 50°) increase. In addition, the final grain size does not exceed 1 μm. It can be concluded from EBSD analysis that recrystallisation of the initial microstructure obviously occurs in the simulated HAZ.

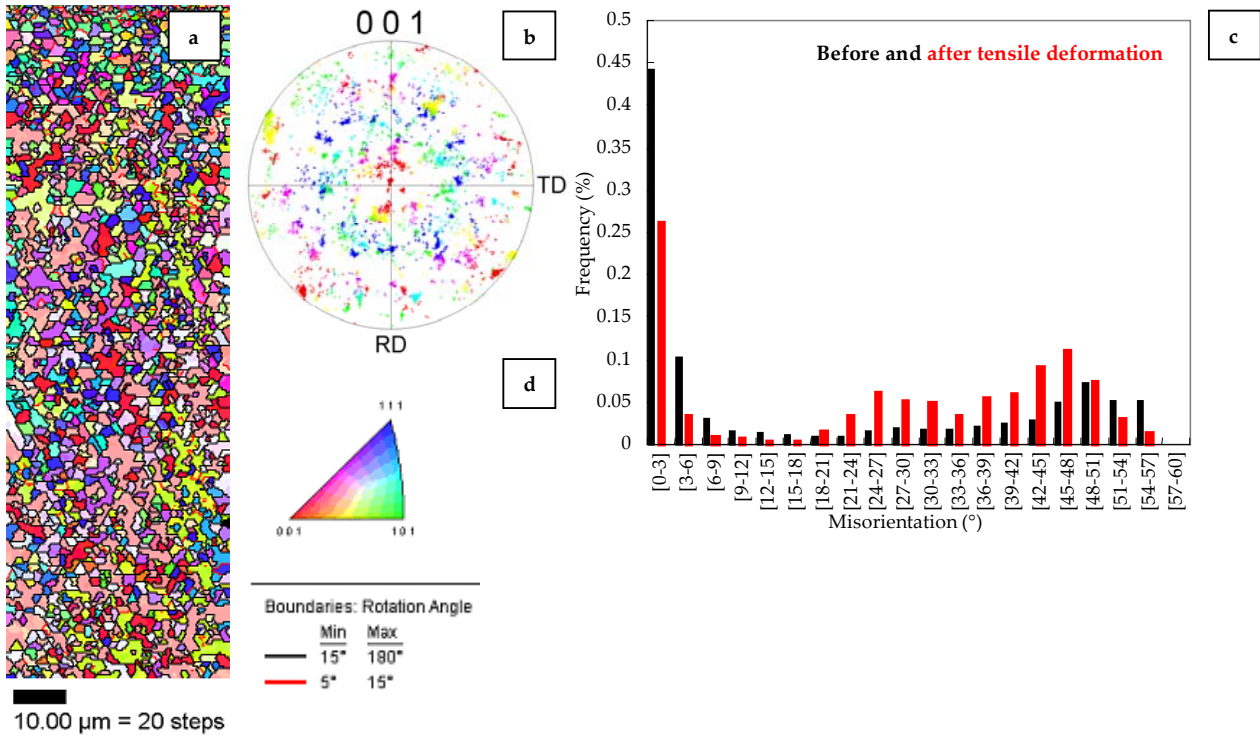


Figure C.III.S1.1. EBSD map (a) in the necking area after tensile test at 625°C (10^{-3} s^{-1}), (b) Misorientation angle histogram (between neighbouring grains - Comparison with the initial state), (c) {001} pole figure and (d) colour key

Supplement C.III.S2. Effect of ageing on the simulated HAZ

In **Part A** of the present study, the effects of thermal ageing on the WJP91 weldment were not investigated due to the too much important microstructural heterogeneities in the weldment. Now, as the weld thermal cycle representative of the weakest HAZ was determined, the effects of thermal ageing on this particular microstructure could be evaluated in detail. To do so, stress free thermal ageing treatments for 1,000 - 5,000 and 10,000 hours were carried out both at 550°C and 625°C which has already been done for the base metal (see **chapter A.I**). The significance of this study can be assumed as type IV failure in 9Cr1Mo-NbV weldments is also reported for long-term creep exposures (> 10,000 hours).

First, the hardness of the aged specimens was measured but no significant evolution could be noticed so that the results are not reported here. Then, carbon extraction replicas of the aged specimens were analysed in the FEG-SEM. It allows, after image analysis using the public domain software Scion®, to determine the evolution of the average particle size of $M_{23}C_6$ carbides following the procedure described in **chapter A.I**. This evolution is plotted versus the ageing time at both 550°C and 625°C in **figure C.III.S2.1**. For comparison, the average particle diameter measured for the base metal aged 10,000 hours at 625°C is added in the same figure. Note also that a semi-logarithmic scale was chosen for a better visualisation of the particle diameter evolution.

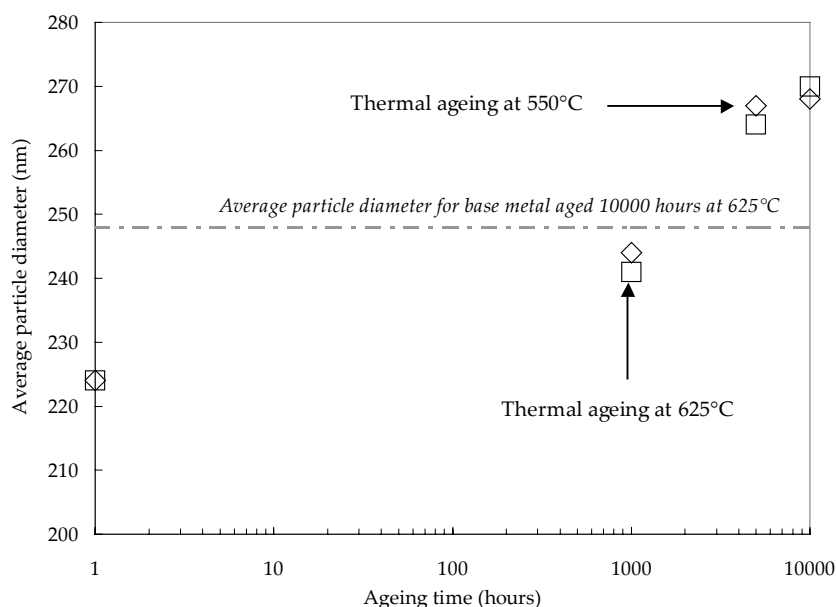
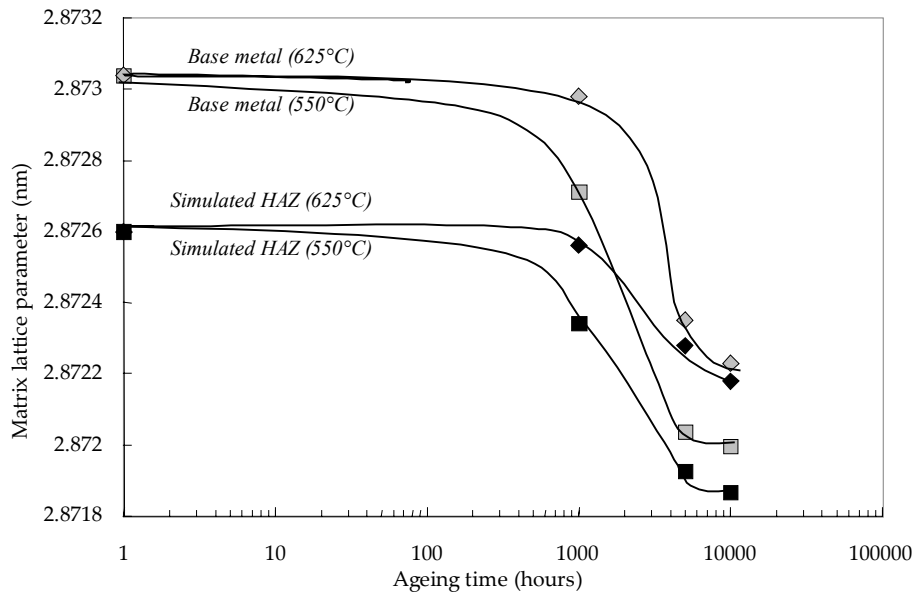


Figure C.III.S2.1. Evolution of the average particle size during thermal ageing at both 550°C and 625°C for the simulated HAZ

It is shown in **figure B.III.S2.1** that unlike for the base metal for which the average particle size increased from 100 nm to near 250 nm after 10,000 hours of ageing, the average particle size only slightly increases in the simulated HAZ. One can also note that the average particle size after 1,000 hours is nearly equal to that after 10,000 hours of ageing for the base metal. The present results confirm that the $M_{23}C_6$ carbides have obviously already coarsened in the initial state for the simulated HAZ (see also De Witte and Coussement (1991), Cerjak and Schuster (1994) and Spigarelli and Quadrini (2002)).

X-Ray energy dispersive spectroscopy (EDS) analysis were also performed to determine the chemical composition of the second phase particles. The results were equivalent to these given for the base metal. An enrichment of the $M_{23}C_6$ carbides in chromium was also evidenced during ageing and Laves phase precipitation was detected after 1,000 hours at 550°C and 5,000 hours at 625°C. Moreover, the occurrence of the Laves phase precipitation was evidenced from measurements of the crystal lattice parameter. The evolution of the martensite crystal lattice parameter versus the ageing time is plotted in **figure C.III.S2.2**. Note that the kinetics of Laves phase precipitation in the base metal and the simulated HAZ microstructure are very similar despite the difference in the matrix microstructure.



*Figure C.III.S2.2. Evidence of Laves phase precipitation using crystal lattice parameter measurements
Comparison between base metal and simulated HAZ*

Thus, one can consider that the simulated HAZ is something like an already aged material in its initial state so that the evolution of the average size of $M_{23}C_6$ carbides is very limited. However, the simulated HAZ is sensitive to the Laves phase precipitation in the same way as the base metal. Therefore, a degradation of the simulated HAZ microstructure in creep ageing conditions can be foreseen.

References

- Cerjak H., Schuster F. (1994). Weldability and behaviour of weldings of new developed creep resistant 9-10% Cr steels. *Second conference on joining technology EUROJOIN2*. 157-167.
- DeWitte M., Coussement C. (1991). Creep properties of 12%Cr and improved 9%Cr weldments. *Materials at high temperature*. **9**(4). 178-184.
- Spigarelli S., Quadri E. (2002). Analysis of the creep behaviour of a modified P91 (9Cr1Mo-NbV) welds. *Materials and design*. **23**. 547-552.

Chapter C.IV. Modelling creep flow and damage behaviour of the weakest area of the WJP91 weldment

The present chapter was written as an article intended to be submitted to engineering fracture mechanics. It deals with the identification of a creep model, integrating and coupling multiple deformation and damage mechanisms, for the simulated weakest heat affected zone. In addition, as a simple analysis was proposed in **chapter C.II**, a comparison between the two levels of analysis is performed at the end of the present chapter.

Modelling creep flow and damage behaviour of the weakest area of 9Cr1Mo-NbV steel weldments

V. Gaffard, J. Besson, A.F. Gourgues-Lorenzon

*Ecole Nationale Supérieure des Mines de Paris (E.N.S.M.P) - Centre des Matériaux
UMR CNRS 7633 BP 87, 91003 Evry Cedex France (corresponding author: jacques.besson@ensmp.fr)*

Abstract

A creep failure model integrating multiple deformation and damage mechanisms has been introduced in [1]. This model was successfully used to represent creep flow and damage behaviour of the 9Cr1Mo-NbV steel at high temperature. In the present study, the model formulation is improved to more accurately describe cavity growth in a material deforming under high temperature. To do so, the description of the effective stress proposed by Leblond et al (1994), in the case of high temperature deformation, is used. Here, an attempt is made to represent creep flow and damage behaviour of the weakest microstructure of 9Cr1Mo-NbV weldments, i.e. the intercritical heat affected zone (ICHAZ). First, the method used to design specimens having the same microstructure as the ICHAZ is described. Then, an experimental database containing both tensile and creep tests on various kinds of specimen geometry is built. It allows to determine creep flow and damage properties of the simulated ICHAZ. The parameters of the model are then fitted to experimental data and used to predict the long term creep behaviour of the ICHAZ.

Keywords: 9Cr1Mo-NbV weldments; High temperature creep flow and damage; Finite element modelling.

Introduction

9Cr1Mo-NbV steels have been developed to be used as structural components in thermal and nuclear power plants. Most in service problems involve welded components. A premature failure of type IV is especially observed in the heat affected zone (HAZ) of the weldment in comparison with the base metal [2][3][4] and [5]. This weakness under high temperature creep loading conditions is more precisely attributed to one part of the HAZ: the intercritical heat affected zone (ICHAZ) [6][7]&[8] which exhibits metallurgical and mechanical properties different from those of the base metal. To evaluate the weldment creep lifetime, the creep flow and damage properties of the weakest area must be first determined. Then, FE calculations must be performed to evaluate the effects of mismatch in creep flow properties between the materials which constitute the weldment. The present study is concerned with the first point i.e., determining the creep flow and damage properties of the weakest HAZ. To do so, a technique already used [8][9][10] and [11], consists in performing a thermal treatment of base metal specimens so that their microstructures become as much similar as possible to that of the ICHAZ found in the real weldment.

The method for designing specimens, which requires the use of an experimental facility capable of high heating rate, a Gleeble thermal-mechanical simulator in the present study, is rapidly reminded without giving extensive arguments for the choice of the weld thermal cycle as this point has already largely been addressed [8][9][10] and [11]. The resulting microstructure is described in detail and compared with that of the base metal.

In the present study, tensile and creep tests coupled with metallurgical investigations of damage mechanisms were used to fit the parameters of a creep model integrating multiple deformation and damage mechanisms [1], whose initial formulation is improved to better represent the effects of the high temperature deformation and especially strain hardening effects.

The present study particularly allows to propose a finer description of the cavity growth following the development of Leblond, Perrin and Suquet [21] as a generalization of the initial formulation of the Gurson model to high temperature creep deformation.

1. Materials and testing procedures

1.1. Materials

The material of the study is a tempered martensitic stainless steel whose chemical composition is given in **table C.IV.1**. It was supplied as a pipe of 295 mm in outer diameter and 55 mm in thickness. The pipe is normalised during 1 hour at 1065°C and then rapidly quenched so that martensite transformation occurs upon cooling. The normalisation is followed by a tempering of 2 hours at 765°C. The resulting microstructure is lath martensite arranged in packets within the prior austenite grain (100 µm in mean size) (see **figure C.IV.1a**). Precipitation of $M_{23}C_6$ carbides (100 nm in mean size at the end of the heat treatment) and MX particles (10 nm – 20 nm in mean size at the end of the heat treatment) occurs during tempering.

	C	Si	Mn	P	S	Al	Cr	Ni	Mo	V	Nb	N	Cu
Base Metal	0.09	0.31	0.41	0.014	0.005	0.016	8.56	0.26	0.92	0.21	0.065	0.042	/

Table C.IV.1. Chemical compositions of the base metal (wt%)

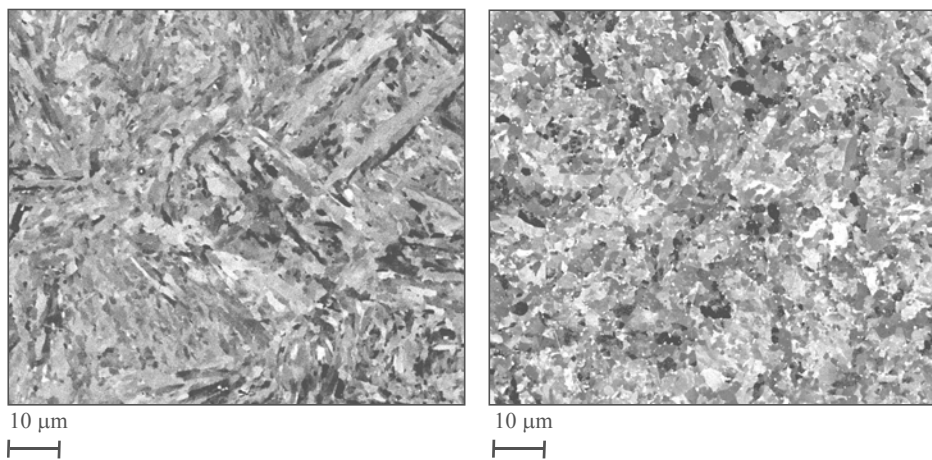


Figure C.IV.1 SEM(BSE) observations of the base metal before and after intercritical heat treatment (colloidal silica polishing)

1.2. Heat treatments

The weakest area of 9Cr1Mo-NbV steel weldments is located in the intercritical heat affected zone (ICHAZ) which experiences a weld thermal cycle with a peak temperature, T_{peak} , within the intercritical domain (i.e. $A_{c1} < T_{peak} < A_{c3}$). The weld thermal cycles can be calculated by a model of heat dissipation specifically designed by Rosenthal [11] for arc welding and later simplified by Rykalin [12]. Weld thermal cycles are characterised by high heating rates (between $100^{\circ}\text{Cs}^{-1}$ and $200^{\circ}\text{Cs}^{-1}$) and a cooling parameter $\Delta t_{800 \rightarrow 500}$ which is the time to cool the material from 800°C to 500°C, that are dependent both from the welding heat input energy and the material thermal properties. The characteristics of the weld thermal cycle corresponding to the weak ICHAZ are given in **table C.IV.2**. Details concerning the choice of the welding thermal cycle are given elsewhere (**chapter C.III**). A Gleeble 1500 thermal-mechanical simulator was used to reproduce high heating rate weld thermal cycle on bulk specimens. This treatment was followed by a tempering of two hours at 760°C which corresponds to the post weld heat treatment (PWHT) usually performed on weldments to release residual stresses and improve the weld metal ductility.

Peak temperature	Heating rate	Cooling rate	PWHT
986 °C	$155^{\circ}\text{Cs}^{-1}$	$\Delta t_{800 \rightarrow 500} = 16 \text{ s } (\approx 19^{\circ}\text{Cs}^{-1})$	2 hours (760°C)

Table C.IV.2. Thermal cycle corresponding to the weakestHAZ

The resulting microstructure exhibits several modifications by comparison with the base metal in the initial state. Scanning electron microscope (SEM) and transmission electron microscope (TEM) investigations, but also analysis of the precipitation state on carbon extraction replicas were performed. The main differences between the microstructure before (i.e. the tempered base metal) and after the intercritical treatment and PWHT are as follows:

1. Same types of second phase particles are found after the weld thermal treatment i.e. MX and $M_{23}C_6$ carbides but the size of $M_{23}C_6$ carbides after the weld heat treatment is found to be more than twice larger than the size of these carbides in the initial microstructure. Despite no experimental results can confirm it, MX particles probably grow or coarsen.
2. TEM investigations revealed a strong decrease in the dislocation density and a rearrangement of these dislocations into cells walls.
3. The initial lath martensite morphology is replaced by small equiaxed highly misoriented grains of $2\ \mu\text{m} - 5\ \mu\text{m}$ in mean size that probably results from lath martensite recovery during the high temperature PWHT (see **figure C.IV.1b**)

Transmission electron microscope, electron backscattered diffraction and carbon extraction replicas investigations, allowed to ensure a close similarity between the simulated HAZ and the corresponding area in the real weldment (see **chapter C.III**).

1.3. Mechanical testing

It was deduced from hardness measurements and metallurgical investigations that the weld heat treatment is homogeneous only within a 7 mm long area centred on the thermocouple position. Therefore, to test exclusively the microstructure of interest, creep and tensile specimens were designed from Gleeble treated blanks with adding a notch to localise strain in the simulated ICHAZ microstructure.

First, tensile tests were performed to determine the mechanical properties of the ICHAZ. To do so, a notched tensile specimen (GTNT) was designed with a maximum diameter, $2R_m$, of 4 mm, a gauge diameter, $2R_g$, of 3 mm, a notch radius, r , of 5 mm and a gauge length, L_g , of 10 mm (see **figure C.IV.2** for detail). These tests were performed at initial strain rates ranging from $10^{-4}\ \text{s}^{-1}$ to $10^{-2}\ \text{s}^{-1}$.

Then, to determine creep flow properties, creep tests were carried out on slightly U-notched creep specimens which have a maximum diameter of 6 mm, a gauge diameter of 3 mm, a notch radius of 5 mm and a gauge length of 20 mm (GTNC5.0 specimens). All creep tests on GTNC5.0 specimens were performed until failure except a complementary test with load varying with steps which consisted in determining steady state creep strain rates with increasing then decreasing load (the investigated applied engineering stresses were 50 MPa, 60 MPa and 70 MPa). This last test especially allowed to investigate creep flow properties in the low stress creep regime and to check the occurrence of history effects by comparing steady state creep strain rates measured during loading and unloading.

As the stress triaxiality ratio, which is defined as the ratio, $\tau = \frac{1}{3} \frac{\sigma_m}{\sigma_{eq}}$ where σ_m is the local hydrostatic stress and σ_{eq} is the

local von Mises equivalent stress, may play a key role in damage mechanisms, creep tests were performed on more severely notched specimens (GTNC4.0 and GTNC1.2 specimens) which have a maximum diameter of 6 mm, a gauge diameter of 3 mm, a gauge length of 20 mm and a notch radius of respectively 4 mm and 1.2 mm. Two types of round V-notched bars (GTNC0.25) which allows for stable crack propagation were also manufactured with a maximum diameter of 8 mm, a notch radius of 0.25 mm and a gauge length of 10 mm. The two types of GTNC0.25 specimens exhibit slightly different ratios, $a = r/R_g$ (where r is the notch radius and R_g the gauge radius), as this ratio may also modify stress redistributions in the area of minimum section. The GNC0.25-1 specimen has a gauge diameter of 5 mm which corresponds to $a = 0.05$ and the GTNC0.25-2 specimen has a gauge diameter of 4 mm which corresponds to $a = 0.0625$. For GTNC4.0, GTNC1.2, GTNC0.25-1 and GTNC0.25-2 specimens, the maximum value of the local stress triaxiality ratio at the end of the loading stage were respectively: 0.5, 0.85, 1.4 and 1.5. Note also that the maximum value of the local stress triaxiality ratio in GTNC5.0 specimens was 0.45.

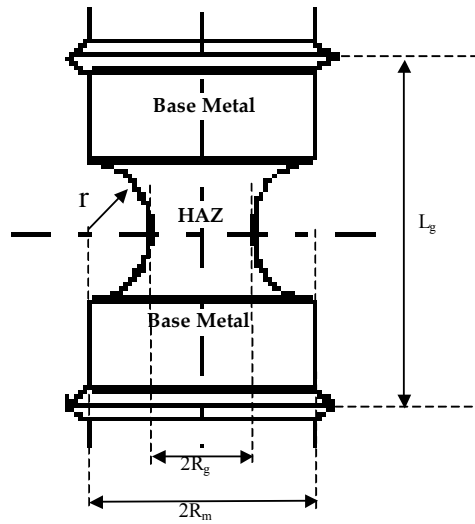


Figure C.IV.2. Geometry of U-notched creep specimens

All creep tests were carried out at 625°C (898K) under constant applied load in controlled laboratory atmosphere (20°C ± 2°C and 50% relative humidity). The load was applied using an electrical mechanical testing machine. The temperature was monitored using three thermocouples spot welded onto the specimen surface. The temperature gradient between top and bottom ends did not exceed 2°C. The elongation was continuously measured over the gauge length, L_g , by a linear variable transducer with a sensitivity of 1 μm .

2. Results of tensile and creep tests

2.1. Tensile properties

The mechanical properties, namely the 0.2% proof stress, the tensile strength or the uniform elongation before the onset of necking could not be directly deduced from experimental curves due to the effect of the notch. These properties will be evaluated by finite element (FE) calculations and inverse analysis in **section 5**. However, it can be noticed yet, that for the values experimentally investigated, the strain rate has a significant effect on the tensile response. Specimens also exhibit a final reduction of the minimum cross-section area larger than 80 % and the tensile curves evidence a strain assisted softening of the material. SEM investigations in specimens cross-sections after polishing with colloidal silica revealed a microstructure formed of fine equiaxed grains in the necking area, obviously resulting from the dynamic recovery of the initial microstructure as the grains remained equiaxed and their diameter did not exceed 1 μm i.e. four times lower in size than in the initial state.

2.2. Creep flow properties

For GTNC5.0, specimens the initial values of the applied engineering stresses range from 130 MPa to 80 MPa and corresponding creep times to failure from 300 hours to 3,500 hours (see **figure C.IV.3**). Creep flow curves exhibits short primary and secondary creep stages and the tertiary creep stage was found to be the main part of the test. For GTNC5.0 specimens, the average elongation rate was first calculated as:

$$\dot{\epsilon}_{ss} = \frac{\dot{L}_g}{L_{g^0}} \quad (\text{eq. C.IV.1})$$

where, L_{g^0} is the initial gauge length and \dot{L}_g is the elongation rate in the gauge length.

The evolution of the steady state average elongation rate versus the applied engineering stress is plotted in **figure C.IV.4** with adding the results of the load varying test with steps. Two main creep flow regimes can be distinguished:

1. The high stress creep regime for $\sigma > 70$ MPa, where creep deformation probably proceeds by dislocation slip or climb.
2. The low stress creep regime for $\sigma < 70$ MPa, where creep deformation probably proceeds by grain boundary diffusion.

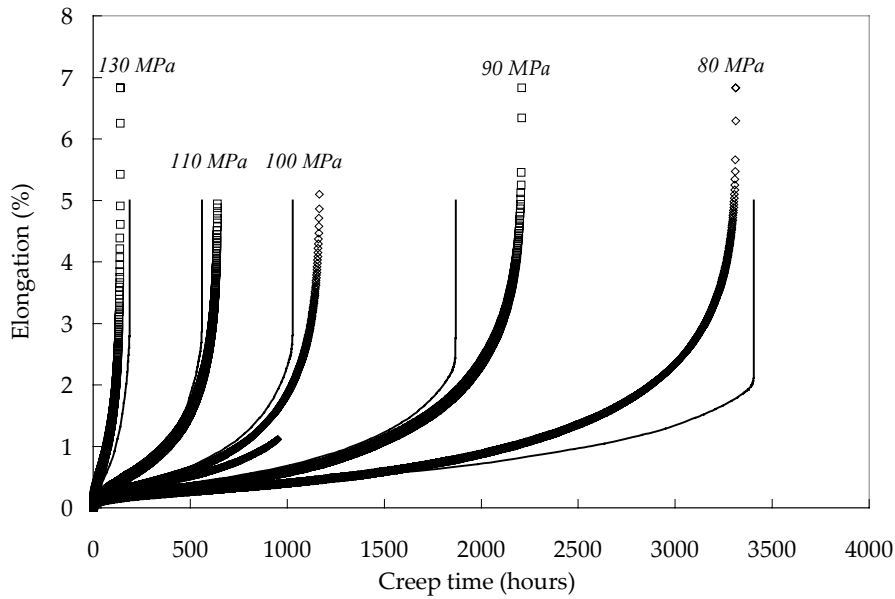


Figure C.IV.3. Comparison of experimental (symbols) and calculated (lines) creep curves for creep tests on GTNC5.0 specimens

Note that two creep flow regimes have already been distinguished [1] and [13] for the P91 base metal for which the transition stress was also equal to 70 MPa. The continuity between the results of the load varying test and other tests is also evidenced. Moreover, one can note in **figure C.IV.4** that for the load varying test, the average elongation rate measured during unloading steps at 50 MPa and 60 MPa were twice lower than those measured during loading. When looking at the creep curves, no creep primary stage was observed at 50 MPa and 60 MPa during loading, whereas some was observed at 70 MPa. The primary creep observed at 70 MPa may be related to a decrease in the mobile dislocation density and the decrease in the measured steady state creep strain rates during unloading steps at both 60 MPa and 50 MPa shows that it obviously plays a key role in the creep flow behaviour. It can also be evidenced in **figure C.IV.4** that the measured creep strain rate during unloading steps at 50 MPa and 60 MPa follows the same dependence to the applied engineering stress than in the high stress creep regime (i.e. the transition between high and low stress is delayed).

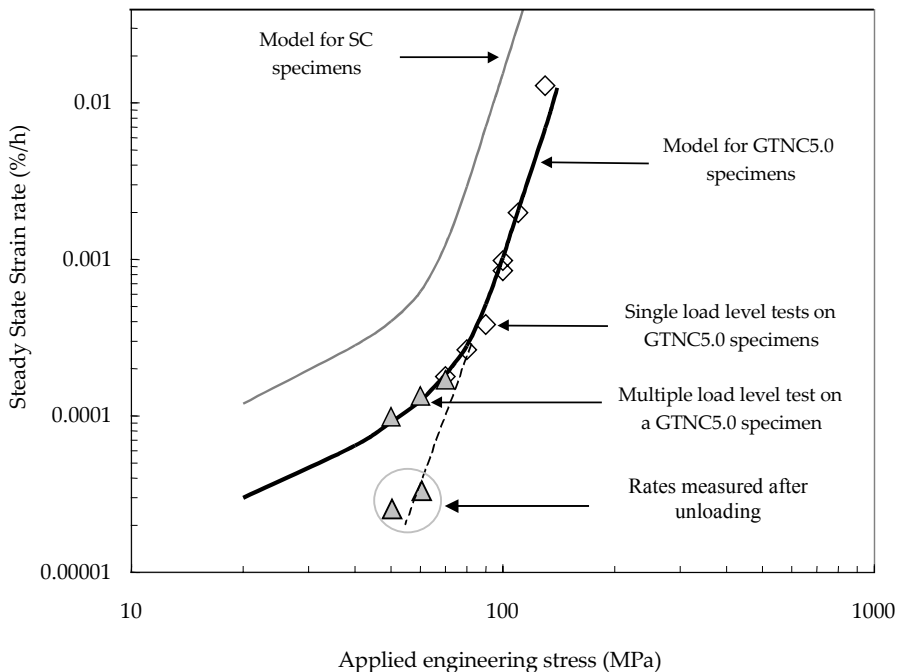


Figure C.IV.4. Steady state strain rates versus applied load for creep tests on GTNC5.0 specimen: Model (line) and experiments (symbols); and on SC specimens: Model (line).

Creep curves for GTNC4.0, GTNC1.2, GTNC0.25-1 specimens are given in **figure C.IV.5** and **figure C.IV.6**. These creep curves exhibit a slightly different shape than these of GTNC5.0 specimens. The secondary creep stage is the longest stage and the tertiary creep stage appears in the later stages of the creep lifetime. Indeed, in severely notched specimens the strain is constrained near the notch root so that it is the only region where softening occurs.

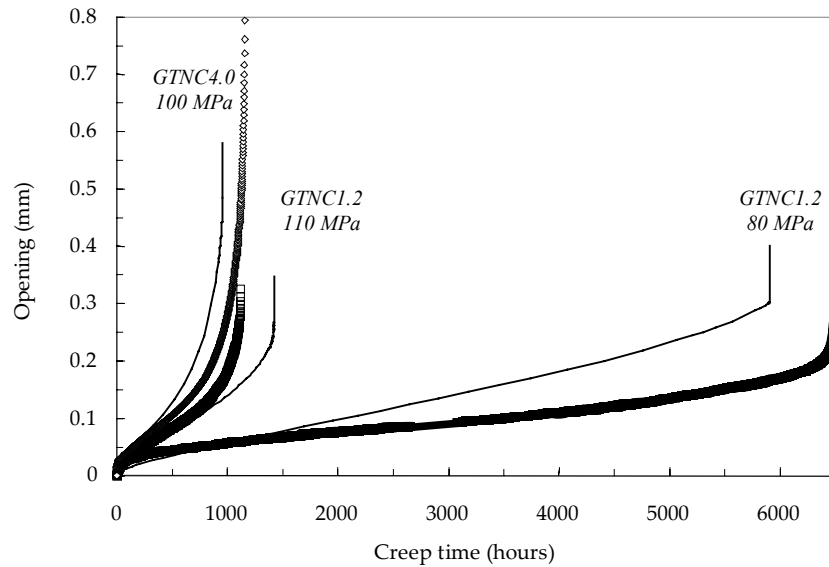


Figure C.IV.5. Comparisons of experimental (symbols) and calculated (lines) creep curves for creep tests on GTNC4.0 and GTNC1.2 specimens

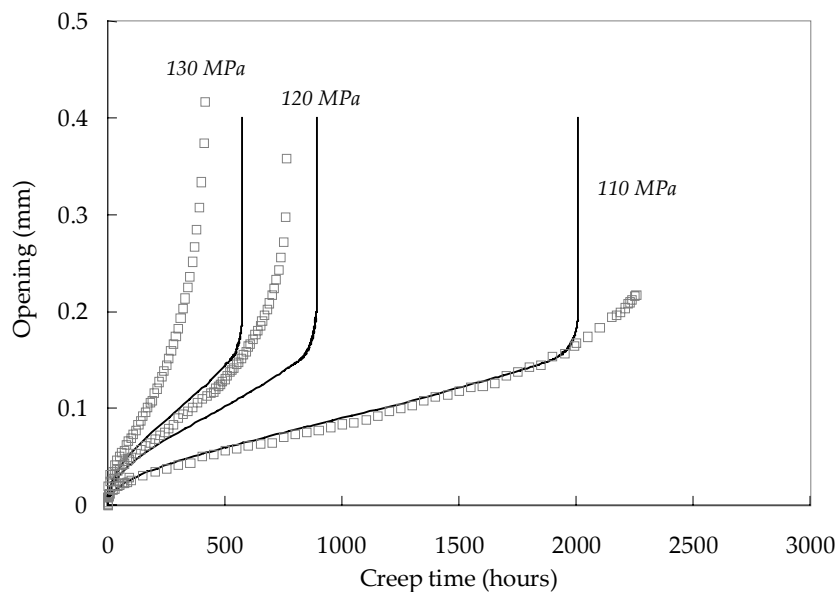


Figure C.IV.6. Comparisons of experimental (symbols) and calculated (lines) creep curves for creep tests on GTNC0.25-1 specimens

2.3. Creep fracture properties

Classical empirical relationship, for predictions of creep lifetime established by Monkman-Grant [14] and Larson-Miller [15] could not be, a priori, used as they are determined from uniaxial creep data. Nevertheless, the creep time to failure is plotted in **figure C.IV.7** for GTNC5.0, GTNC1.2, GTNC0.25-1 and GTNC0.25-2 specimens, as a function of the applied engineering stress. One can note that in the stress domain investigated, no change in damage mechanisms was evidenced. The representation of **figure C.IV.7** also shows that the notch has a small strengthening effect for notch radii from 5.0 mm to 1.2 mm while there is very little difference between GTNC1.2 and GTNC0.25 specimens despite the increase from 0.85 to 1.4 – 1.5 in the maximum initial stress triaxiality ratio.

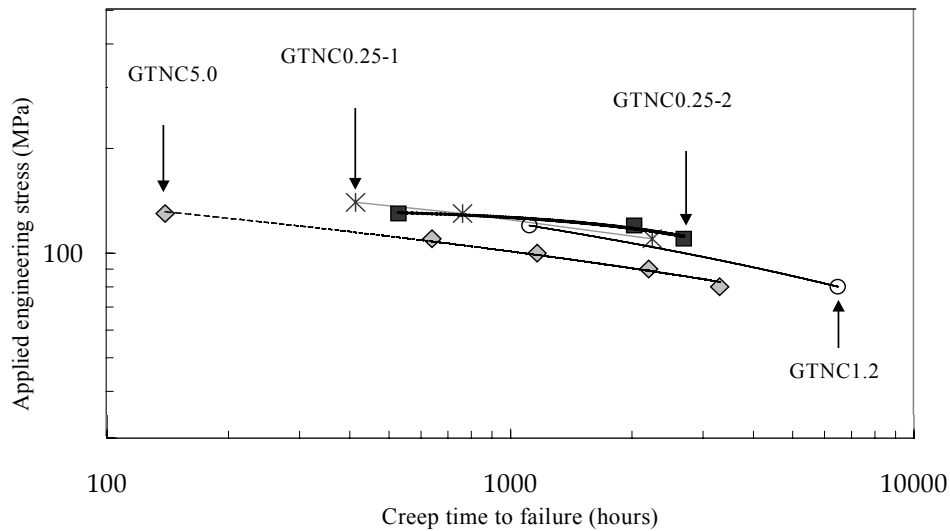


Figure C.IV.7. Applied engineering stress versus creep time to failure: Experimental results on GTNC specimens (effect of the notch geometry)

2.4. Creep damage mechanisms

All creep tested specimens failed in a ductile manner with a dimple size of 20 μm as for the base metal (see **chapter B.III**). The specimen surfaces were largely oxidised so that more detailed investigations could not be performed. Therefore, creep damage mechanisms were explored by SEM investigations in specimens cross-sections in the area of minimum diameter. As already observed in the base metal [1], cavities preferentially nucleate at grain boundaries near second phase particles and at triple points. Coarsened carbides particles initially present, and Laves phase particles, which appear during creep, both of few hundred nanometers in average size (white dots in **figure C.IV.8b**) are preferential sites for nucleation of new creep cavities. SEM investigations also revealed that damage is mainly intergranular as cavities are elongated along the grains boundaries and that only a low fraction of grain boundaries is affected by damage (see **figure C.IV.8b**). Note also that the creep damage mechanism experimentally observed are similar to those encountered in weldments [16][17] and [18].

Finally, the grain shape appear to remain equiaxed near the fracture surface despite the large experimentally measured necking of the specimens. It confirms that dynamic recovery or recrystallisation of the microstructure obviously occurs during creep which is consistent with the long creep tertiary stage observed on macroscopic curves. The macroscopic curves of **figure C.IV.3** also revealed that the tertiary creep starts for low values of the creep strain i.e. $\approx 1\%$ as it has already been observed for the base metal [1].

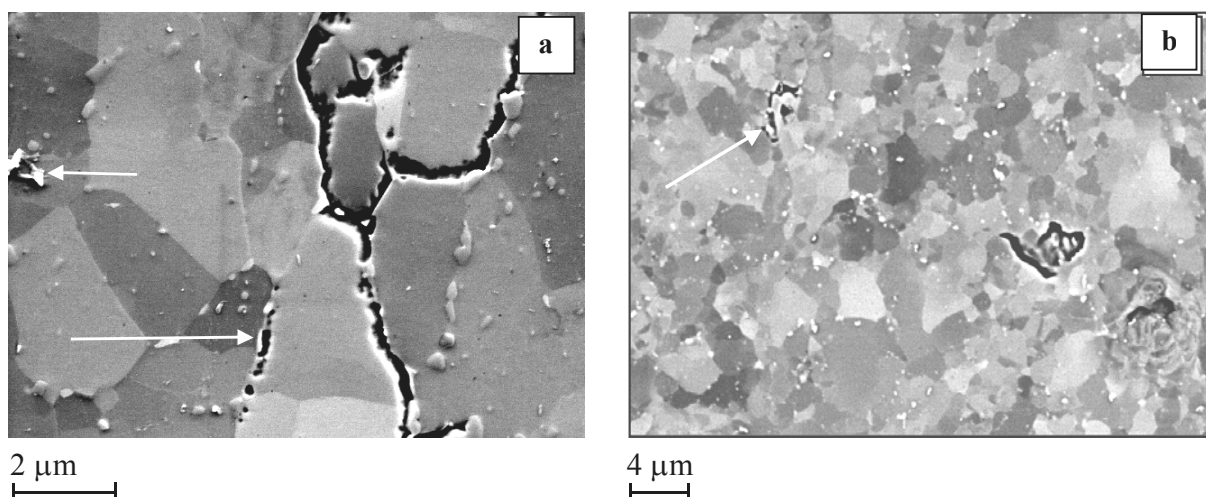


Figure C.IV.8. Cavity nucleation and growth at grain boundaries: Longitudinal cross section SEM (BSE) observations after colloidal silica polishing

3. Model formulation

The model was previously introduced in [1]. It consists in a three mechanisms damage model for viscoplastic materials based on an additive decomposition of the strain rate tensor. The first contribution to strain rate accounts for the quasi-plastic regime (subscript “qp”), the second one for power-law or viscoplastic creep (subscript “vp”) and the third one for grain boundary diffusion (“d”). In [1], attention was mainly focused on designing a fully coupled multiple mechanism model to take into account the changes in both deformation and damage mechanisms. Here, some improvements of the initial model formulation inspired by the model of Leblond, Perrin and Suquet [21] are integrated to more finely describe the high temperature cavity growth.

3.1. Description of creep flow in the damage free material

An additive decomposition was chosen and the resulting strain rate tensor, is given by:

$$\underline{\dot{\epsilon}} = \underline{\dot{\epsilon}}_e + \underline{\dot{\epsilon}}_{qp} + \underline{\dot{\epsilon}}_{vp} + \underline{\dot{\epsilon}}_d \quad (\text{eq. C.IV.2})$$

where $\underline{\dot{\epsilon}}_e$ is the elastic strain rate tensor, $\underline{\dot{\epsilon}}_{vp}$ accounts for power-law creep and $\underline{\dot{\epsilon}}_d$ accounts for low stress grain boundary diffusion creep. For each mechanism ($m = qp, vp, d$), a yield surface is defined as:

$$\phi_m = \sigma_m^* - R_m \quad (\text{eq. C.IV.3})$$

where, R_m is the flow stress and σ_m^* is an effective scalar stress which is equal to the von Mises stress, σ_{eq} , for the undamaged material. The strain rate tensor, $\underline{\dot{\epsilon}}_m$, is given by the normality rule:

$$\underline{\dot{\epsilon}}_m = \dot{p}_m \frac{\partial \phi_m}{\partial \underline{\sigma}} \quad (\text{eq. C.IV.4})$$

where the plastic multiplier \dot{p}_m is given by a Norton power-law:

$$\dot{p}_m = \left\langle \frac{\phi_m}{K_m} \right\rangle^{n_m} \quad (\text{eq. C.IV.5})$$

The flow stress terms, R_m are defined as a function of an effective plastic strain, \bar{p}_m , defined to take into account coupling between creep flow mechanisms. For a given mechanism, ‘ m' ’, the effective plastic strain was defined taking into account cross-hardening between deformation mechanisms, which were defined throughout the interaction matrix, $H_{mm'}^P$:

$$H_{mm'}^P = \begin{bmatrix} H_{11} & H_{12} & H_{13} \\ H_{21} & H_{22} & H_{23} \\ H_{31} & H_{32} & H_{33} \end{bmatrix} = \begin{bmatrix} 1 & 1 & 0 \\ 1 & 1 & 0 \\ 0 & 0 & 1 \end{bmatrix} \quad (\text{with indices 1 for } m = qp, 2 \text{ for } m = vp \text{ and 3 for } m = d) \quad (\text{eq. C.IV.6})$$

so that,

$$\bar{p}_m = H_{mm'}^P \begin{bmatrix} P_{qp} \\ P_{vp} \\ P_d \end{bmatrix} \quad (\text{eq. C.IV.7})$$

Note that the choice of the interaction matrix is justified in [1].

3.2. Coupling damage and creep flow

Coupling between creep flow and damage properties is based on the mechanics of porous media. In [1], the effective stress, σ_m^* depending on damage was defined following the description of the Gurson-Tvergaard-Needleman (GTN) model [20]. Here, it was supposed that a more accurate description of the cavity growth under high temperature deformation should be given by the formulation proposed by Leblond, Perrin and Suquet [21], which will be referred to as the LPS model in the following, and is expressed as:

$$\frac{\sigma_{eq}^2}{\sigma_m^{*2}} + f^* q_1 \left[h_m \left(q_2 \frac{1}{2} \frac{\sigma_{kk}^*}{\sigma_m^*} \right) + \left(\frac{1-m}{1+m} \right) \frac{1}{h_m \left(q_2 \frac{1}{2} \frac{\sigma_{kk}^*}{\sigma_m^*} \right)} \right] - 1 - q_1^2 \left(\frac{1-m}{1+m} \right) f^{*2} \stackrel{\text{def. } \sigma_m^*}{=} 0 \quad (\text{eq. C.IV.8})$$

where q_1 and q_2 are model parameters, m is the strain hardening coefficient equal to the inverse of the apparent Norton power-law exponent ($m = 1/n$), and f^* is a function of the total porosity, f_t , which is defined to account for cavity coalescence in the later stage of the material creep life (The expression of f^* is given in the following in **section 5**). The function $h_m(x)$ is given by:

$$h_m(x) = \left[1 + mx^{(1+m)} \right]^{1/m} \quad (\text{eq. C.IV.9})$$

One can note that for when $m \rightarrow 0$ (i.e. pure plasticity), the stress potential is reduced to the Gurson-Tvergaard-Needleman, [20] GTN model as:

$$\lim_{m \rightarrow 0} (h_m(x)) = \lim_{m \rightarrow 0} \left(h_m(x) + \left(\frac{1-m}{1+m} \right) \frac{1}{h_m(x)} \right) \rightarrow \cosh(x) \quad (\text{eq. C.IV.10})$$

In the quasi-plastic regime, this definition of σ_m^* given by Gurson-Tvergaard-Needleman [20] was kept whereas the expressions of σ_m^* were modified following **equation C.IV.5** in the viscoplastic and diffusion creep regimes.

In the case of diffusion creep the strain hardening coefficient $m \rightarrow 1$ so that:

$$\lim_{m \rightarrow 1} (h_m(x)) = \lim_{m \rightarrow 1} \left(h_m(x) + \left(\frac{1-m}{1+m} \right) \frac{1}{h_m(x)} \right) \rightarrow 1 + x^2 \quad (\text{eq. C.IV.11})$$

and when simplifying **equation C.IV.8**, the effective stress is now defined in the diffusion creep regime as:

$$\sigma_{eq}^2 + f^* q_1 \left(q_2 \frac{1}{2} \right)^2 \sigma_{kk} + \sigma_m^{*2} (f^* q_1 - 1) \stackrel{\text{def. } \sigma_m^*}{=} 0 \quad (\text{eq. C.IV.12})$$

Note that **equation C.IV.12** is quite similar to the elliptic model proposed in [22].

The strain rate tensor is modified to be:

$$\underline{\dot{\epsilon}}_m = (1 - f_t) \dot{p}_m \frac{\partial \phi_m}{\partial \underline{\sigma}} \quad (\text{eq. C.IV.13})$$

so that,

$$(1 - f_t) \dot{p}_m \sigma_m^* = \underline{\dot{\epsilon}}_m : \underline{\sigma} \quad (\text{eq. C.IV.14})$$

The evolution of porosity is expressed using mass conservation and by taking into account the nucleation of new voids [23]:

$$\dot{f} = (1 - f_t) \sum_m \text{trace}(\underline{\dot{\epsilon}}_m) + \dot{f}_n = (1 - f_t)^2 \sum_m \dot{p}_m \text{trace} \left(\frac{\partial \phi_m}{\partial \underline{\sigma}} \right) + \dot{f}_n \quad (\text{eq. C.IV.15})$$

with assuming that each mechanism contributes to nucleation, the nucleation kinetics was expressed as the sum of the individual contributions:

$$\dot{f}_n = \sum_m \dot{f}_{nm} \quad (\text{eq. C.IV.16})$$

As the stress triaxiality ratio may play a key role in the nucleation kinetics [24] and [25], for each mechanism, the kinetics of nucleation was described [1] by:

$$\dot{f}_{nm} = \left(A_m + B_m \left(\frac{1}{3} \frac{\sigma_m}{\sigma_{eq}} \right)^{\alpha_m} \right) \dot{p}_m \quad (\text{eq. C.IV.17})$$

where $\tau = \frac{1}{3} \frac{\sigma_m}{\sigma_{eq}}$ is the stress triaxiality ratio, A_m , B_m and α_m are adjustable parameters.

4. FE calculations procedure

The model was implemented in the finite element software Zebulon [26]. A fully implicit integration scheme was used to integrate the material constitutive equations, which allows the calculation of the consistent tangent matrix [27]. The method is derived from the one detailed in [28], modified to deal with an arbitrary number of deformation mechanisms. Finite strains were treated using co-rotational reference frames [29]. The material was considered to be broken when f^* was greater than $\frac{1}{q_1} - \varepsilon$, where $\frac{1}{q_1}$ is the theoretical value for f^* at fracture and ε is taken equal to 0.01. As soon as the material was considered as broken, its behaviour was replaced by an elastic behaviour with a very low stiffness (Young's modulus: $E_b = 1$ MPa). A similar technique was used [30] showing convergence of the results for sufficiently low values of the Young's modulus E_b . Gauss points where these conditions are met are referred to as "broken Gauss points". In regions where damage was expected to develop, eight-node axisymmetric elements with reduced integration (ie. 4 Gauss points) were used. Elements containing two broken Gauss points were automatically removed by checking this condition after each time increment.

A two dimensional axisymmetrical mesh was chosen. The mesh size and mesh design play an important role in calculations involving crack initiation and propagation [30][20] and [31]. Due to the softening of the material, the mesh size influences the fracture energy and it is often argued that this quantity should be adjusted on experiments involving stable crack growth in order to fit the crack energy [32] and [30]. The mesh size is then interpreted as some microstructural characteristic length (e.g. a multiple of the interparticle spacing or grain size). In the following, the elements in the region where damage was expected to develop were quadratic squares (with reduced integration) whose edge size is equal to 100 μm . This value of the element size was found appropriate in the case of the base metal [1], so that it was kept for this study.

5. Model identification

As the area where the Gleeble treatment is homogeneous was longer than the notched area but shorter than the gauge length of the creep specimens, FE calculations were performed using two materials i.e. HAZ and base metal (see **figure C.IV.9** for detail). The creep failure model of the base metal, integrating multiple deformation and damage mechanisms, were taken from [1] and the corresponding parameters, reported in **table C.IV.4**, were fixed during the identification procedure. The elastic properties of both the base metal and the simulated HAZ were taken as a Young's modulus of 145 GPa and a Poisson's ratio of 0.3.

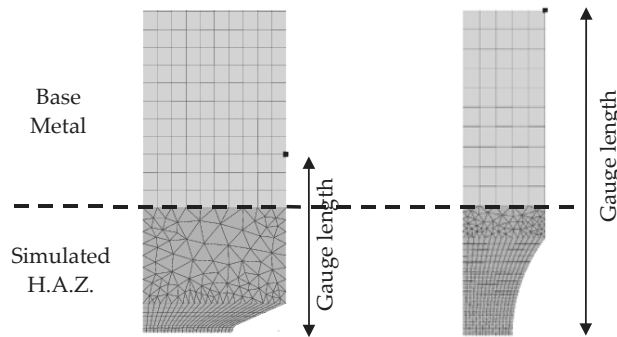


Figure C.IV.9. Representation of GTNC0.25 and GTNC5.0 specimens for FE calculations

First, the creep flow behaviour was determined from tensile creep tests in the quasi-plastic regime and from creep tests on GTNC5.0 specimens both in the viscoplastic and diffusion creep regimes. Based on experimental evidences that damage does not occur in GTNC5.0 specimens before the onset of necking, the model parameters could be identified without accounting for coupling between damage and viscoplastic flow. Therefore, the formulation of the model for the damage free material was used and the model parameters were fitted on primary and steady state creep regimes by inverse analysis [35].

Yield stress functions were fitted to represent, both the material hardening (positive term) and softening (negative term), in the quasi plastic and viscoplastic creep regime. In the quasi-plastic regime the yield stress was defined as:

$$R_{qp}(\bar{p}_{qp}) = R_{oqp} + Q_{qp1}(1 - \exp(-b_{qp1} \bar{p}_{qp})) - Q_{qp2}(1 - \exp(-b_{qp2} \bar{p}_{qp})) \quad (\text{eq. C.IV.18})$$

where R_{oqp} , Q_{qp1} , b_{qp1} , Q_{qp2} and b_{qp2} are model parameters having positive values. All these parameters and the Norton power-law coefficients associated with the quasi-plastic regime were fitted to experimental tensile curves in the strain rate range from 10^{-4} s^{-1} to 10^{-2} s^{-1} . This allows to well describe the rate dependent plasticity of the material. Mechanical properties of the simulated ICHAZ were derived from FE simulations performed on smooth round tensile bars in the strain rate domain ranging from 10^{-4} s^{-1} to 10^{-2} s^{-1} (see **table C.IV.3**).

Temperature	Strain rate	0.2 % proof stress	Uniform Elongation	R_m
625°C	10^{-2} s^{-1}	260 MPa	1.3 %	294 MPa
625°C	10^{-3} s^{-1}	230 MPa	1.3 %	261 MPa
625°C	10^{-4} s^{-1}	220 MPa	1.4 %	238 MPa

Table C.IV.3. Evaluation of tensile mechanical properties of the simulated ICHAZ from FE calculations

The results of **table C.IV.3** shows that the simulated HAZ exhibits a low homogeneous elongation, before the onset of material softening, but still higher than that of the base metal i.e. 1 % (see [1]). A significant strain rate effects can also be evidenced with a reduction of nearly 60 MPa of the tensile strength between 10^{-2} s^{-1} and 10^{-4} s^{-1} . Finally, the ratio of the 0.2% proof stress over the tensile strength is close to 1, as in the base metal, showing that work hardening is very limited.

The flow stress associated with the viscoplastic creep mechanism followed a similar formulation:

$$R_{vp}(\bar{p}_{vp}) = R_{ovp} + Q_{vp1}(1 - \exp(-b_{vp1}\bar{p}_{vp})) - \left\{ Q_{vp2}(1 - \exp(-b_{vp2}(\bar{p}_{vp} - p_c))) \right\} \quad (\bar{p}_{vp} > p_c) \quad (\text{eq. C.IV.19})$$

where R_{ovp} , Q_{vp1} , b_{vp1} , Q_{vp2} and b_{vp2} are constants having temperature-dependent positive values. Note that the softening function added to account for strain ageing and softening phenomena is only effective for a local equivalent viscoplastic strain higher than $p_c = 0.01$, as experimentally observed. Finally, for the diffusional mechanism, the yield stress function was set to:

$$R_d(\bar{p}_d) = 0 \quad (\text{eq. C.IV.20})$$

It was assumed that grain boundary diffusion does not involve any significant hardening of the material. The parameters of the Norton power-law which give the value of the plastic multiplier \dot{p}_d (i.e. K_d and n_d) were evaluated from experimental data on GTNC5.0 specimens in the low stress creep regime. The model parameters for the undamaged materials in both the viscoplastic and diffusion creep regimes are given in the first six sections of **table C.IV.4**.

Arguments for the choice of the matrix coefficients are given elsewhere [1]. The determined creep flow parameters (see **section 1 to 6** in **table C.IV.4**) were then integrated in the model with the coupling between creep flow and damage. As it has already been explained in [1], four damage parameters were set to their classical values: i.e. $q_1 = 1.5$, $q_2 = 1.0$, $\alpha_v = 2.0$ and $\alpha_d = 2.0$.

For the “qp” and “vp” mechanisms, the expression of f^* to account for cavity coalescence were expressed as:

$$f^* = f_t + \delta(f_{nm} + f_{gm} - f_{cm}) \quad \text{if } (f_{gm} + f_{nm}) > f_{cm} \quad (\text{eq. C.IV.21})$$

$$f^* = f_t \quad \text{if } (f_{gm} + f_{nm}) < f_{cm} \quad (\text{eq. C.IV.22})$$

This formulation means that coalescence starts provided cavity growth is promoted by the “qp” or the “vp” mechanism. For the “d” mechanism, no coalescence law was used (i.e. $f^* = f_t$), as for $n = 1$ the stability of the material prevents from void coalescence [36]. In fact, when the material is highly damaged, the effective stress is largely increased so that the rupture of the specimen is controlled either by the viscoplastic or by the quasi-plastic cavity growth. The phenomenon represented by the model, corresponds to the limit load failure experimentally observed.

The apparent exponent of the Norton power-law was determined as $n = 9.5$ (see **figure C.IV.4**) so that the strain hardening parameter of the LPS model, $m = 0.105$. Finally, the identification only concerned the four remaining damage parameters i.e. A_{vp} , B_{vp} , A_d and B_d . Creep tests on creep specimens exhibiting high stress triaxiality ratio allowed to fit B_{vp} and B_d whereas slightly notched GTNC5.0 specimens were used to fit A_{vp} and A_d . The resulting sets of model parameters are respectively given in **section 7** of **table C.IV.4**.

		ICHAZ	Base Metal
1. Quasi plastic hardening at 625°C	R_{0qp} Q_{qp1} b_{qp1} Q_{qp2} b_{qp2}	145 MPa 30 MPa 50 25 MPa 10	173 MPa 128 MPa 400 80 MPa 7.3
2. Viscoplastic hardening at 625°C	R_{0vp} Q_{vp1} b_{vp1} Q_{vp2} b_{vp2} p_c	0 MPa 40 MPa 200 20 MPa 10 0.01	0 MPa 40 MPa 569 40 MPa 75 0.03
3. Diffusion hardening at 625°C	R_{0vp}	0 MPa	0 MPa
4. Quasi plastic strain rate effect at 625°C	K_{qp} n_{qp}	240 MPa $h^{-1/n_{qp}}$ 8.6	112 MPa $h^{-1/n_{qp}}$ 5.0
5. Viscoplastic strain rate at 625°C	K_{vp} n_{vp}	395 MPa $h^{-1/n_{vp}}$ 4.95	542 MPa $h^{-1/n_{vp}}$ 5.38
6. Diffusion strain rate at 625°C	K_d n_d	0.020 $\cdot 10^9$ MPa h^{-1/n_d} 1.0	0.33 $\cdot 10^9$ MPa h^{-1/n_d} 1.0
7. LPS model	q_1 q_2 f_c δ_c	1.5 1.0 0.1 6.0	1.5 1.0 0.1 6.0

Strain hardening coefficients	m_{qp}	0.0	0.0
	m_{vp}	0.125	0.105
	m_d	1.0	1.0
Nucleation by the viscoplastic mechanism	A_{vp1}	0.01	0.05
	A_{vp2}	0.15	0.4
	α_v	2.0	2.0
Nucleation by the diffusional mechanism	A_{d1}	12.0	5
	A_{d2}	15.0	0.5
	α_d	2.0	2.0

Table C.IV.4. Model parameters for the base metal and the simulated weakest HAZ

6. Model validation and discussion

6.1. Validation

All the experimental database was used to fit the model parameters so that experimental and calculated creep curves for GTNC5.0, GTNC1.2 and GTNC0.25 specimens exhibit good agreement (see **figures C.IV.3** and **C.IV.4**) even if the model does not represent very well the creep response of GTNC0.25 specimens at high stress which might be related to heterogeneities in microstructural changes at the crack tip.

The steady state creep strain rates calculated by the model also show satisfactory agreement with experiments in the two creep regimes (see **figure C.IV.3**). Then, the model was validated in terms of predictions of damage evolution and creep fracture properties. First, the model predictions in terms of creep lifetime exhibit very good agreement with experimental results (see **figure C.IV.10**). Note that FE simulations were performed on smooth round specimen geometry (SC) having a gauge diameter of 5 mm and a gauge length of 36 mm to determine the uniaxial creep fracture behaviour of the simulated HAZ. The results of these simulations are also plotted in **figure C.IV.10**.

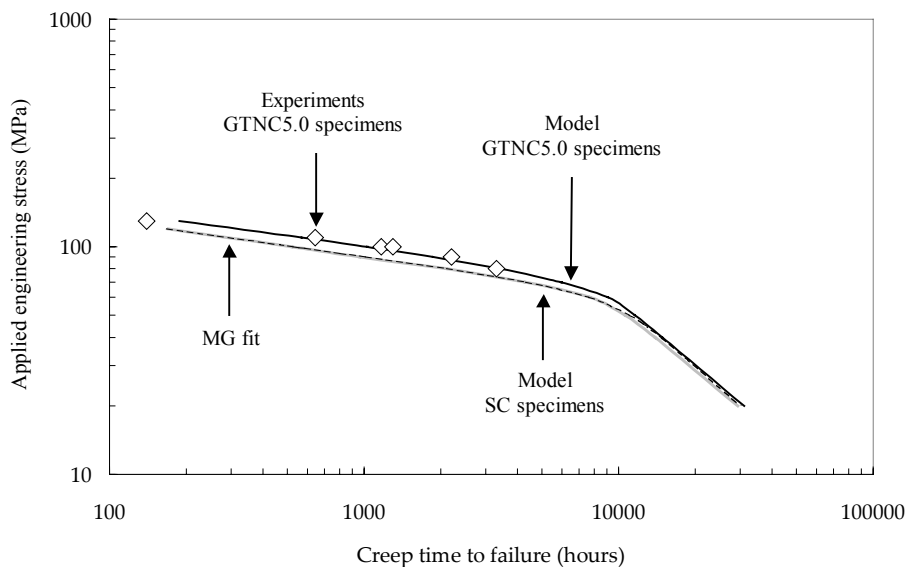


Figure C.IV.10. Stress versus time to failure for GTNC5.0 specimens: Model (line) and experiments (symbols) and SC specimens: Model (line) and MG fit (filled squares symbols)

The calculated locations of creep rupture exhibited also good agreement with experimental observations for GTNC5.0, GTNC1.2, GNTC0.2-1 and GTNC0.25-2 specimens as plotted in **figure C.IV.11**. It is also interesting to notice the shift of the damage location from the centre of the specimen to the notch. This tendency experimentally observed and well reproduced by FE calculations evidences the existence of the two creep damage mechanisms. The diffusion creep regime (i.e. $n = 1$), no stress redistribution occurs in the notched specimens so that the rupture is more likely to occur near the notch, whereas in the viscoplastic creep regime (i.e. $n > 4$), the stresses are redistributed and the rupture is more likely to occur at the centre of the specimen. Therefore, the shift in the rupture location reveals the growing contribution of diffusion to the damage development and the creep failure.

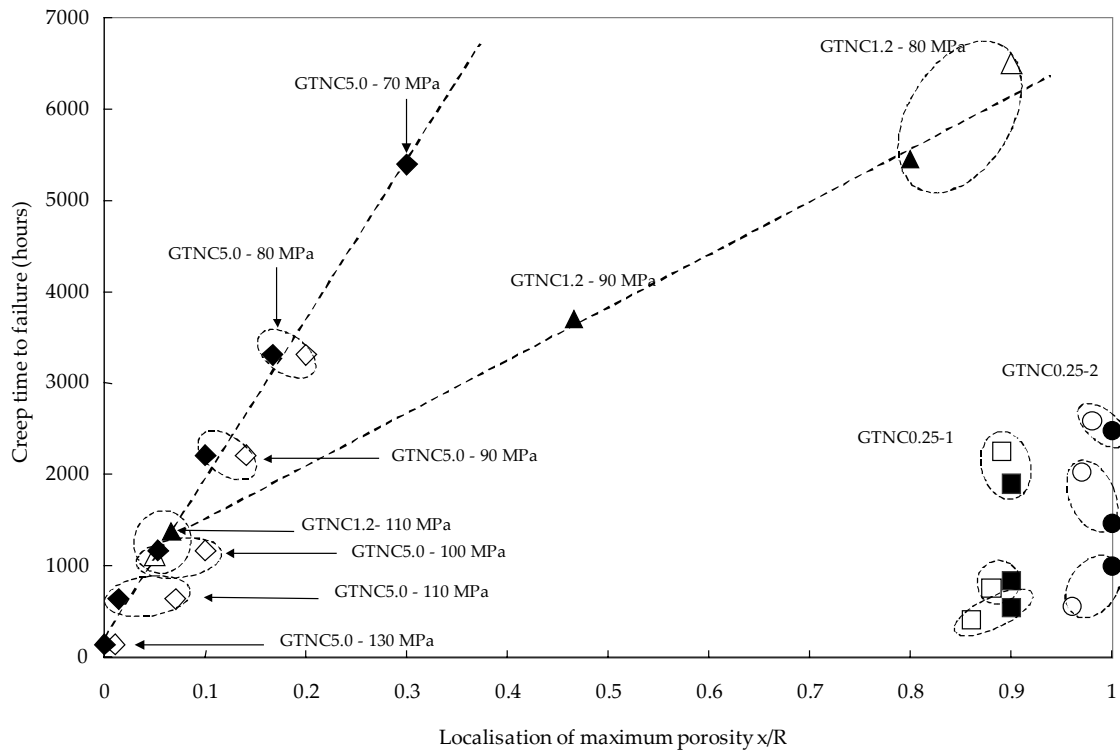


Figure C.IV.11. Location of the most damaged area at onset of the rupture for GTNC5.0, GTNC1.2, GTNC0.25-1, and GTNC0.25-2 specimens - Comparison between model predictions (filled symbols) and experimental observations (open symbols)

6.2. Discussion and use of the model

6.2.1. Consistency of the creep flow properties with earlier theories of diffusion creep

To confirm the validity of creep flow parameters of the ICHAZ, the consistency between K_d for the base metal and the simulated ICHAZ was investigated. In the diffusion creep regime, K_d is power-law dependent of the grain size with exponent of 2 in the case of Herring-Nabarro creep (intragranular diffusion) [37] and 3 in the case of Coble creep (intergranular diffusion) [38]. Therefore K_d can be more generally expressed as:

$$\frac{1}{K_d} \propto \alpha \frac{\exp(-E_a / RT)}{D^n} \quad (\text{eq. C.IV.23})$$

where E_a is the activation energy, D is the grain size, α is a temperature dependent material constant, T is the temperature in K and $R = 8.32 \text{ Jmol}^{-1}\text{K}^{-1}$. n is equal to 2 for Herring-Nabarro creep and 3 for Coble creep.

It was shown in [1] that the activation energy, E_a , in the low stress creep regime is consistent with the pipe diffusion energy. Therefore, the Coble creep diffusion mechanism is obviously the dominating mechanism. The main problem is to determine the representative grain sizes especially for the base metal whose lath martensite microstructure is very complex. The ICHAZ exhibits a microstructure of small equiaxed grains. The size of grains having high angle boundaries ($> 15^\circ$) was evaluated to $4 \mu\text{m} - 8 \mu\text{m}$ (see **chapter A.I**).

In the base metal, laths of same crystallographic orientations are gathered in packets [39] and [42] so that low misorientation lath boundaries are not great obstacles to creep flow. This is not the case for the boundaries between the highly misoriented packets. Therefore, the packet size whose average size is $20 \mu\text{m} - 30 \mu\text{m}$ is obviously the relevant grain size for diffusion in the base metal. In this range of grain sizes values and with the knowledge of K_d for the base metal ($K_d = 0.33 \cdot 10^9 \text{ MPah}^{-1}$), the value of the material constant α could be calculated.

Then, the minimum and maximum values of K_d in the simulated HAZ, were determined and are reported in **table C.IV.5**.

	Base metal, $\phi = 20 \mu\text{m} - 30 \mu\text{m}$	HAZ, $\phi = 4 \mu\text{m} - 8 \mu\text{m}$ Herring Nabarro predictions	HAZ, $\phi = 4 \mu\text{m} - 8 \mu\text{m}$ Coble predictions	Present study (model)
K_a	$0.33 \cdot 10^9 \text{ MPah}^{-1}$	$0.0058 \cdot 10^9 - 0.0528 \cdot 10^9 \text{ MPah}^{-1}$	$0.00078 \cdot 10^9 - 0.0211 \cdot 10^9 \text{ MPah}^{-1}$	$0.02 \cdot 10^9 \text{ MPah}^{-1}$

Table C.IV.5. Evaluation of K_a for the simulated ICHAZ using the value determined for the base metal and the expressions of steady state creep strain rates given by Herring-Nabarro and Coble

In fact, results of **table C.IV.5** show that the value of K_a experimentally determined is consistent with the two classical theories of creep diffusion. To conclude whether the diffusion mechanism is of Herring-Nabarro or Coble type two arguments can be given:

1. Herring-Nabarro creep currently occurs for higher temperature (i.e. $T/T_{\text{melting}} > 0.7$ which corresponds for the steel of the present study to $T > 900^\circ\text{C}$).
2. The activation energy is that of pipe diffusion (i.e. intergranular diffusion that is favoured in materials exhibiting small grains and so on a large number of grain boundaries).

For these reasons, the dominating diffusion creep mechanisms is probably Coble creep.

6.2.2. Evaluation of a Monkman-Grant relationship – Comparison with the model of the present study

The model fitted for the ICHAZ allowed to perform FE calculations for smooth round homogeneous specimens made of simulated HAZ. From the results of these calculations, a Monkman-Grant (MG) relationship could be determined in the high stress creep regime:

$$\dot{\epsilon}_{ss}^m t_R = C_{MG} \quad (\text{eq. C.IV.24})$$

with $m = 0.8$ and $C_{MG} = 0.28 \text{ h}^{0.2}$ (with $\dot{\epsilon}_s$ in h^{-1} and t_R in h).

The value of C_{MG} for the base metal is $C_{MG} = 0.058 \cdot 10^{-2} \text{ h}^{0.06}$. For an easier comparison, the MG relationship was fitted for the simulated HAZ using the same MG exponent $m = 0.94$ as for the base metal leads to $C_{MG} = 0.11 \text{ h}^{0.06}$. It shows that even if the creep strength of the simulated HAZ is lower than that of the base metal, its intrinsic ductility is higher. It seems that the simulated HAZ has a kind of super-plastic behaviour as despite very high level of creep strain, it exhibits a good ductility. Thus, the premature failure observed by comparison with results on base metal is essentially due to its much higher creep strain rate and not to an increase in damage rate (i.e. to its much lower resistance to creep flow).

Moreover, if one assumes that the material ductility remains constant from high to low stress (i.e. the MG parameters keep the same values in the low stress creep regime), there, from calculated steady state strain rates, MG predictions can be calculated and plotted in **figure C.IV.10** for SC specimens. The results are quasi indistinguishable from those given by the coupled model. Note that for the base metal [1], the material exhibited a lower ductility at low stresses than at high stresses (i.e. the MG predictions in the low stress creep regimes were optimistic in comparison with the model).

6.2.3. Single volume element calculations

As for the base metal [1], single volume element calculations were performed for four values of the stress triaxiality ratio: i.e. $\tau = 1/3, 0.85, 1.5$ and 2.5 . Representation of **figure C.IV.12** allows to determine the transition stress which correspond to a change in the main driving force for damage development. It was chosen to plot the results versus the von Mises equivalent stress to which the principal stress, σ_1 is related by:

$$\sigma_1 = \sigma_{eq} \left(\tau + \frac{2}{3} \right) \quad (\text{eq. C.IV.25})$$

where σ_{eq} is the von Mises equivalent stress and τ is the stress triaxiality ratio.

One can note that for $\tau = 0.85$, the transition occurs for $\sigma_{eq} = 70 \text{ MPa}$, i.e. $\sigma_1 = 105 \text{ MPa}$. Therefore, when comparing **figures C.IV.12** and **C.IV.11**, the shift in the creep rupture location in the minimum section of GTNC1.2 specimens can be attributed to a change in the dominating damage mechanism. As also shown in **figure C.IV.13**, when further increasing the stress triaxiality ratio, the transition in the damage mechanism is observed for shorter test durations.

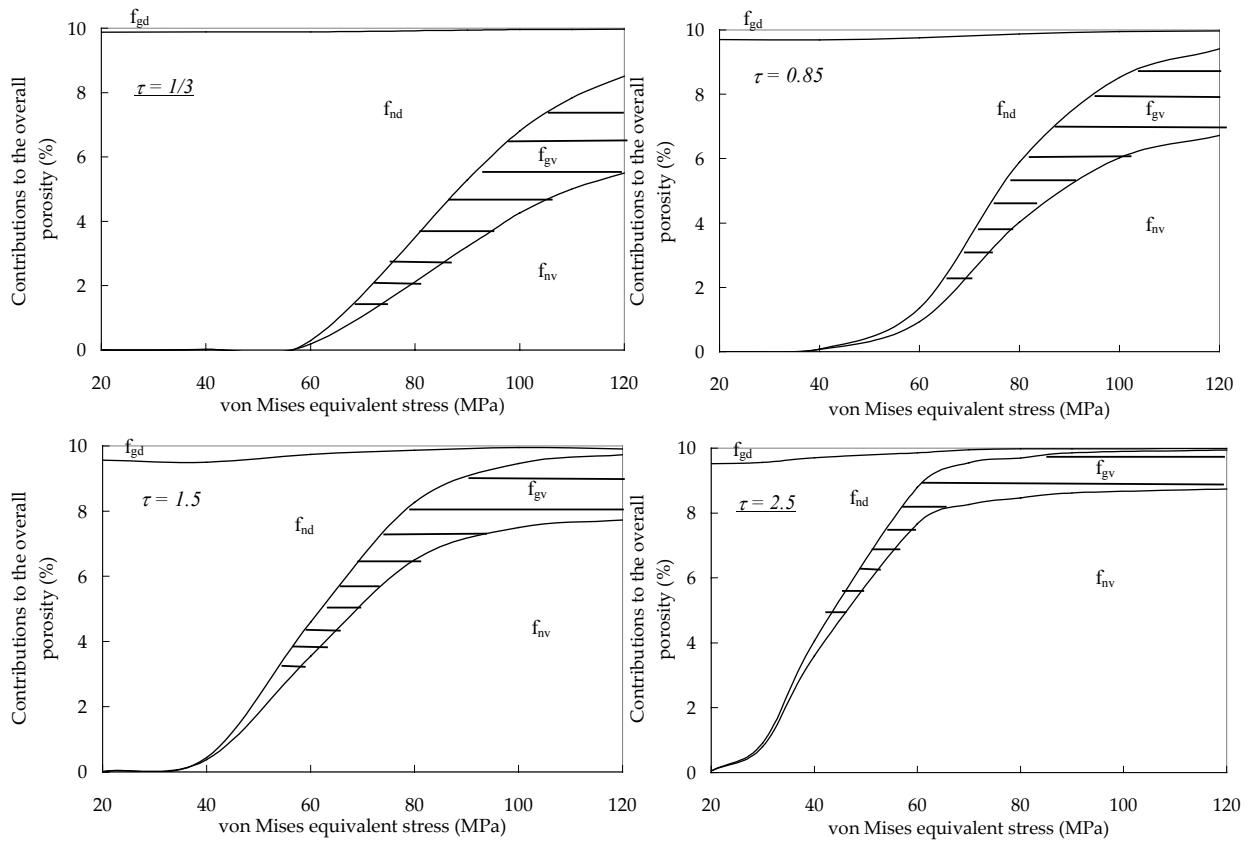


Figure C.IV.12. Contributions to the overall porosity at the onset of creep failure (i.e. $f_i = 10\%$): Volume element calculations for various values of the stress triaxiality ratio

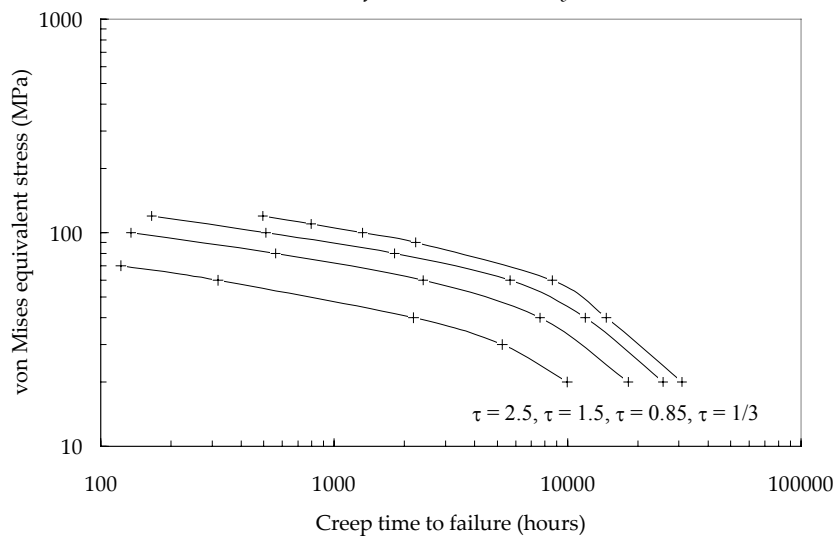


Figure C.IV.13. von Mises equivalent stress versus creep time to failure: volume element calculations for various values of the stress triaxiality ratio

6.2.4. Discussion of the two material hypothesis used for FE calculations

The necessity to perform FE calculations with two materials was also explored. To do so, FE calculations were done assuming an homogeneous material and using the model determined for the simulated HAZ in the previous section. Results were compared to two materials (base metal [1] and simulated HAZ) FE calculations on GTNC5.0 specimens showing that the base metal obviously inhibits the HAZ deformation especially in the low stress creep regime. For calculations with two materials the steady state creep strain rate is lower by a factor of two in the low stress creep regime by comparison with FE calculations with a single material. However, the calculated creep lifetimes are almost undistinguishable. Indeed, both creep strain and the stress triaxiality ratio promote damage and, even if the strain of the HAZ is little constrained, the increase in the stress triaxiality ratio leads to similar damage kinetics for calculations with

either one or two materials. The same work was performed for NC1.2 and NC0.25 specimens and shows that there are no differences between both the calculated creep flow and creep time to failure using a single or a two material representation.

6.2.5. Extrapolation of the model in a larger temperature range

The extrapolation of the model was successfully performed for the base metal in [1]. If the damage mechanisms are the same, then the model damage parameters can be kept unchanged in a larger temperature domain than that experimentally investigated ($\pm 50^\circ\text{C}$ around 625°C). Consequently, only creep flow properties need to be determined. In the high stress creep regime, they are difficult to assess especially because the occurrence of softening effects must be carefully studied. Therefore, it is recommended to perform creep tests to determine creep flow properties in the high stress creep regime. In the low stress creep regime, creep flow properties can be evaluated with the formalism which has already been used for the base metal [1] as it was evidenced that:

$$\frac{1}{K_d} \propto \frac{\beta}{T} \exp\left(\frac{-E_a}{RT}\right) \tag{eq. C.IV.24}$$

where E_a is the activation energy for pipe diffusion in α -iron evaluated to 174 kJmol^{-1} [41] and from the present study β could be evaluated to $5.84 \cdot 10^9 \text{ MPah}^{-1}$.

To test the possibility to extrapolate the model, the experimental results given in [8] at 600°C and 640°C were used. The microstructure simulated in [8] exhibits a good agreement in terms of carbide size and microstructure with that of the present study. The PWHT used in [8] is longer than that of the present study (12 hours) but at lower temperature (730°C) and the final hardness measured in the ICHAZ is very close to that measured in the present study. Therefore, it was assumed that the results given in [8] could be used in the present study.

In the viscoplastic creep regime, the value of n_{vp} was not changed i.e. $n_{vp} = 4.95$ and the values of K_{vp} were fitted to represent the experimentally measured steady state strain rates reported in [8], whereas the values of K_d were calculated from **equation C.IV.23**. The corresponding values of the model parameters are reported in **table C.IV.6**.

Temperature	K_{vp}	K_d
600°C	$480 \text{ MPa h}^{-1/n_{vp}}$	$0.038 \cdot 10^9 \text{ MPa h}^{-1}$
640°C	$295 \text{ MPa h}^{-1/n_{vp}}$	$0.014 \cdot 10^9 \text{ MPa h}^{-1}$

Table C.IV.6. Values of K_{vp} and K_d at 600 and 640°C

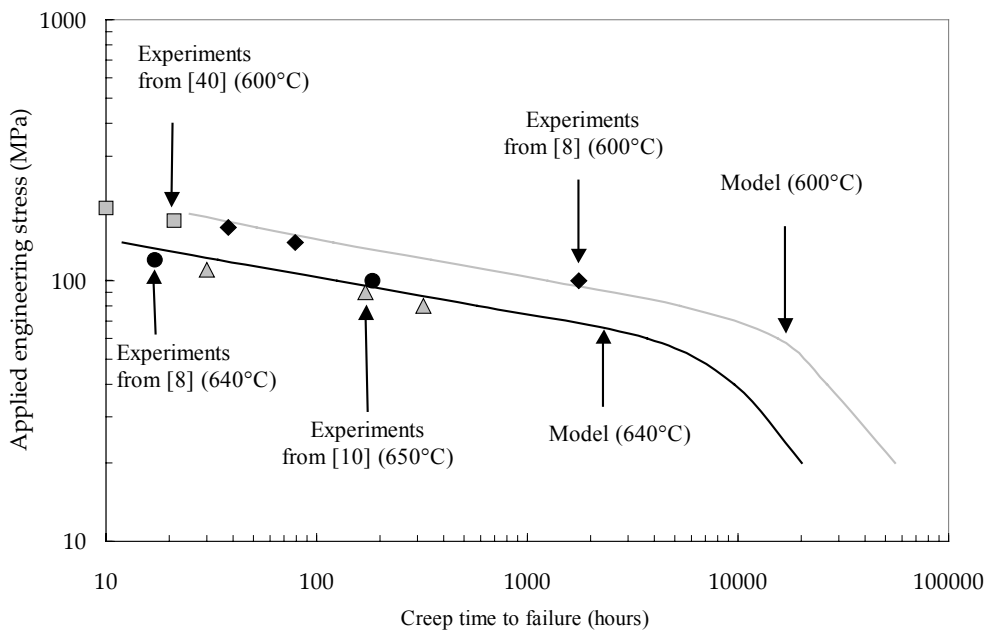


Figure C.IV.14. Use of the model to predict creep time to failure at 600 and 640°C
Comparison between model (lines) and experiments from [8], [10] and [42]

It is evidenced in **figure C.IV.14**, where creep rupture data for the simulated HAZ from [10] and [40] were added, that the model can readily be used to model the creep response of the simulated HAZ, at least, within the temperature range

between 600°C and 650°C. However, as already suggested for the base metal in [1] the ability of the model to represent creep flow and damage behaviour of the simulated HAZ is ensured only from 600°C to 650°C. Indeed, dynamic strain ageing probably occurs for temperatures lower than 450°C and the formation of austenite near carbon and chromium depleted areas (i.e. $M_{23}C_6$ carbide) is possible for temperatures larger than 650°C. The extrapolation of the model to the temperature range between 500°C - 600°C is probably possible but the absence of any experimental data in this temperature domain do not allow to assess this point.

Conclusions

The main results of the present study are as follows:

1. The microstructure of the weakest HAZ, i.e. the ICHAZ, of 9Cr1Mo-NbV steels under creep loading conditions at high temperature, was reproduced on notched creep specimens.
2. Creep tests on various kinds of specimen geometry allowed to build an experimental database on creep properties of the weakest HAZ and to determine its creep flow and damage behaviour. They evidenced that if the creep flow rate of the weakest HAZ is ten times higher than that of the base metal, its intrinsic ductility is not lower.
3. Metallurgical investigations in cross-sections of creep tested specimens led to the following conclusions:
 - Large carbides and Laves phase both promote cavity nucleation at grain boundaries.
 - Cavity growth follows the boundaries of small equiaxed grains and is only little assisted by bulk grain deformation.
 - Softening of the initial microstructure is promoted by creep strain.
4. The model introduced in [1] was improved to take into account high temperature strain hardening effects and was successfully used to represent creep flow and damage behaviour of the weakest HAZ.

Acknowledgements

Financial and technical support from Electricité de France (EdF), Framatome and Le Commissariat à l'Énergie Atomique (CEA) is acknowledged.

References

- [1] Gaffard V., Besson J., Gourgues-Lorenzon A.F., Creep failure model of a tempered martensitic stainless steel integrating multiple deformation and damage mechanisms. *Int. Journ. of fract.*, 2004
- [2] Spigarelli S., Quadrini E., Analysis of the creep behaviour of modified P91 (9Cr-1Mo-NbV) welds, *Materials and design*, 2002, 23, 547-552.
- [3] Okamura H., Ohtani R., Saito K., Kimura K., Ishii R., Fujiyama K., Hogo S., Iseki T., Uchida H., Basic investigation for life assessment technology of modified 9Cr-1Mo steel, *Nucl. eng. and des.*, 1999, 193, 243-254.
- [4] Jakobova A., Vodarek V., Hennhofer K., Foldyna V., Microstructure and creep properties of P91 steel weldments, *Mat. for adv. power eng.*, 8th Liege conf., 1998, 373-382.
- [5] Coussement C., De Backer T., DeWitte M., Verelst L., Internal pressure creep testing on welded components of modified 9Cr and 12Cr steel, *EUROJOIN 2*, Second european conference on joining technology, 1994, 461-479.
- [6] Kojima T., Hayashi K., Kajita Y., HAZ softening and creep rupture strength of high Cr ferritic steel weldments, *ISIJ int.*, 1995, 35(10), 1284-1290.
- [7] Cerjak H. and Schuster F., Weldability and behaviour of weldings of new developed creep resistant 9 – 10% Cr steels. Second conference on joining technology *EUROJOIN2*, 1994, 157 – 167.
- [8] Eggeler G., Ramteke A., Coleman M., Burbli A., Peter G., Hald J., Jefferey C., Rantala J., DeWitte M., Mohrmann R., Analysis of creep in a welded P91 pressure vessel, *Int. J. of press. ves. and piping*, 1994, 60, 237-257.
- [9] Tsuchida Y., Okamoto K., Tokunaga Y., Study of creep rupture strength in heat affected zone of 9Cr-1Mo-V-Nb-N steel by welding thermal cycle simulation, *Weld. int.*, 1996, 10(6), 454-460.
- [10] Otaguro Y., Matsubara M., Itoh I. and Nakazawa T., Creep rupture strength of heat affected zone for 9Cr ferritic heat resisting steels, *Nuc. eng. and des.*, 2000, 196, 51-61.
- [11] Rosenthal D., *Welding journal*, 1957, 20, 220s
- [12] Rykalin N.N., *Berechnung der Warmevorgänge beim Schweißen*, Verlag Technik, Berlin, 1957.
- [13] Kloc L., Sklenicka V., Ventruba J., Comparison of low stress creep properties of ferritic and austenitic creep resistant steels, *Mat. sci. eng.*, 2001, A319-321, 774-778.
- [14] Monkman F.C., Grant N.J., An empirical relationship between rupture life and minimum creep rate in creep rupture tests, *Proceedings of the ASTM*, 1956, 56, 593 – 620
- [15] Larson F.R. and Miller J., A time-dependent relationship for rupture and creep stresses, *Transactions of the ASME*, 1952, 74, 765-775.

- [16] DeWitte M. and Coussement C., Creep properties of 12%Cr and improved 9%Cr weldments, *Mat. High. Temp.*, 1991, 9(4), 179-184.
- [17] Letofsky E., Cerjak H., Warbichler P., The use of light and electron microscopic investigations to characterise the creep behaviour of welded joints in modern power station materials, *Prakt. Metallogr.*, 2000, 37, 509-521.
- [18] Coussement C., De Witte M., Behaviour of 12%Cr and improved 9%Cr weldments impact on the occurrence of type IV cracking in service, *JOINING/WELDING 2000*, 1991, 189-201.
- [19] Tsuchiyama T., Miyamoto T., Takaki S., Recrystallisation of lath martensite with bulge nucleation and growth mechanism. *ISIJ Int.*, 2001, 41(9), 1047-1052.
- [20] Tvergaard V., Needleman A., Analysis of the cup cone fracture in a round tensile bar, *Acta met.*, 1984, 32(1), 157-169.
- [21] Leblond J.B., Perrin G., Suquet P. Exact results and approximate models for porous viscoplastic solids, *Int. jour. of plast.*, 1994, 10(3), 213-235.
- [22] Green R. A plasticity theory for porous solids, *Int. jour. of mech. sci.*, 1972, 14, 215-224.
- [23] Chu C., Needleman A., Void nucleation effect in biaxially stretched sheets, *Jour. of eng. mater. techn.*, 1980, 102, 249-256.
- [24] McLean D., Damage accumulation in creep, *Annales de chimie*, 1981, 6, 124-139.
- [25] Myers M.R., Pilkington R., Needham N.G., Cavity nucleation and growth in a 1%Cr-0.5%Mo steels, *Mater. sci. and eng.*, 95(2), 81-91.
- [26] Besson J., Foerch R., Large scale object-oriented finite element code design. *Comp. methods in applied mec. and eng.*, 1997, 142, 165-187.
- [27] Simo J.C, Taylor R.L., Consistent tangent operators for rate-independent elastoplasticity, *Comp. meth. in appl. mech. eng.*, 1985, 48(1), 101-118.
- [28] Besson J., Cailletaud G., Chaboche J.L., Forest S., *Mécanique non linéaire des matériaux*, Hermes – Paris (in French), 2001.
- [29] Liu Y., Murakami S., Kanagawa Y., Mesh dependence and stress singularity in finite element analysis of creep crack growth by continuum damage mechanics approach, *Eur. Jour. of Mech.*, 1994, 13A(3), 395-417.
- [30] Rousselier G., Ductile fracture models and their potential in local approach of fracture. *Nucl. eng. and des.*, 1987, 105, 97-111.
- [31] Xia L., Shih C.F., Hutchinson J. W., A computational approach to ductile crack growth under large scale yielding conditions, *Jour. of the Mech. and Ph. of Sol.*, 1995, 43(3), 389-413
- [32] Gullerud A.S., Gao X., Dodds Jr.R. and Haj-Ali R., Simulation of ductile crack growth using computational cells: numerical aspects, *Eng. fract. mech.*, 2000, 66, 65-92.
- [33] Tvergaard V., Ductile fracture by nucleation between larger voids, *Jour. of the mech. and phys. of sol.*, 1982, 30, 265-286.
- [34] Koplick J., Needleman A., Void growth and coalescence in porous plastic solids. *Int. journal. of solids and struct.*, 1988, 24(8), 835-853.
- [35] Cailletaud G., Pilvin P. (1994). Identification and inverse problems related to material behaviour. *Inverse problems in engineering mechanics edited by H.D. Bui and M. Tanaka*. 79-86.
- [36] Ashby M.F., Gandhi C. and Taplin D.M.R., Fracture mechanism maps and their construction for fcc metals and alloys. *Acta metallurgica*, 1979, 27, 699-729.
- [37] Nabarro F.R.N., Steady state diffusional creep, *Phil. mag.*, 1967, 16, 231-237.
- [38] Coble R.L., A model for boundary diffusion controlled creep in polycrystalline materials, *Jour. of appl. phys.*, 1963, 34, 1679-1682.
- [39] Maki T., Tsuzaki K., Tamura I., The morphology of microstructure composed of lath martensites in steels, *Trans. ISIJ*, 1980, 20, 207-214.
- [40] Cerjak H., Letofsky E., Schuster F. (1995). Heat affected zone and weld metal behaviour of modern 9-10% Cr steels. *Trends in welding research – Proceedings of the 4th international conference – Gatlinburg Tennessee*. 633-638.
- [41] Frost H.J, Ashby M.F., *Deformation-mechanism maps: The plasticity and creep of metals and ceramics*. Oxford, Pergamon Press, 1982.
- [42] Chilton J.M., Barton C.J., Speich G.R., Martensite transformation in low carbon steels, *Jour. of the iron and steel inst.*, 1970, 184-193.

Supplement C.IV.S1. Comparison between the HAZ properties evaluated from analysis of the creep of cross-weld specimens and from creep tests on the simulated microstructure

In the two previous sections, two methods were used to determine creep flow and fracture properties of the HAZ:

1. An evaluation of the HAZ properties was first deduced from a one dimensional analysis of creep tests on cross-weld specimens (i.e. using a Norton power-law representation for the creep flow and a Monkman-Grant representation for the predictions of creep fracture).
2. The HAZ creep flow properties were determined from creep tests on specifically designed specimens having the same microstructure as than the weakest HAZ.

Therefore, a comparison between the creep flow and fracture properties of the HAZ given by the two methods is of great interest. It is done here in terms of creep flow properties in **figure C.IV.S1.1** and in terms of creep fracture properties in **figure C.IV.S1.2**.

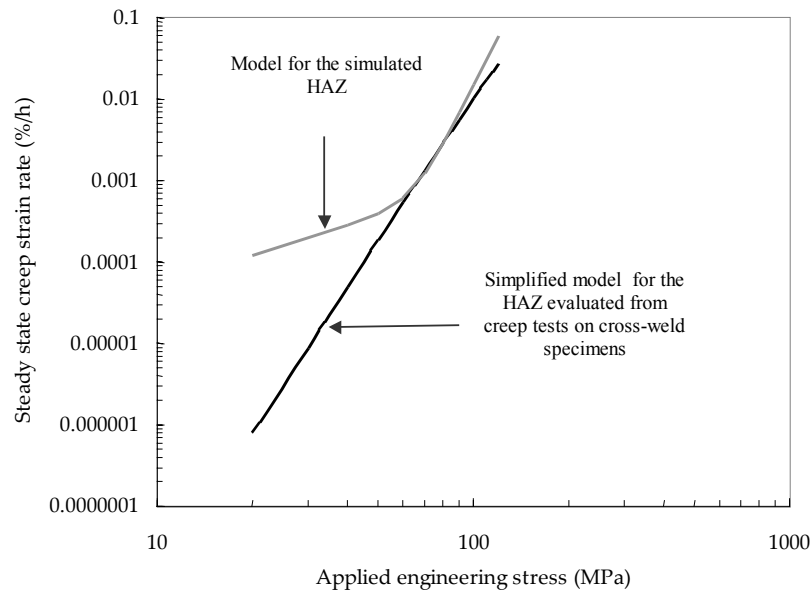


Figure C.IV.S1.1. Comparison of creep flow properties

The two plots in **figure C.IV.S1.1** exhibit very good agreement between the two predicted creep flow behaviour in the high stress creep regime. As creep tests were performed for creep durations not larger than 10,000 hours, the low stress creep regime could not be determined from creep experiments on cross-weld specimens so that the predictions of the simplified model exhibits poor agreement with the model determined for the simulated HAZ in the low stress creep regime. The same conclusions can be drawn from **figure C.IV.S1.2**, as creep tests on cross-weld specimens did not allow to investigate the transition in the damage mechanisms.

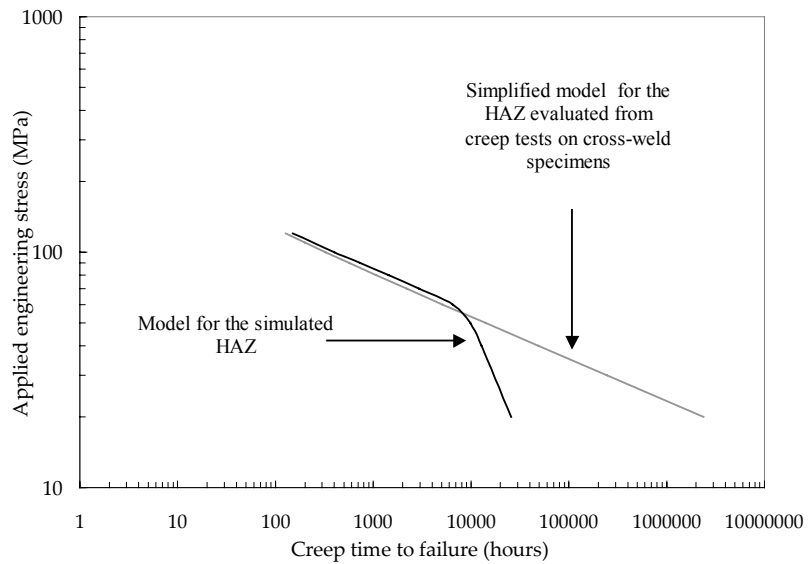


Figure C.III.S1.2. Comparison of creep fracture properties

To conclude about this point, the simplified model failed at predicting creep lifetime after the transition in the damage and creep flow mechanisms but longer creep tests durations should probably allow to evaluate creep flow and fracture properties of the HAZ in the low stress creep regime. However, such a creep rupture criterion can hardly be used to predict the creep lifetime of structures submitted to multiaxial loading conditions. Therefore, the identification of a coupled model after the reproduction of the simulated microstructure on bulk specimens is highly recommended.

Main results of Part C

1. Creep flow and damage behaviour of the WJP91 weldment at 625°C

Rupture: Rupture is of type IV i.e. in the heat affected zone and more precisely in the intercritical heat affected zone (ICHAZ) parallel to the fusion line.

Microstructure of the weakest HAZ i.e. the ICHAZ: It consists in fine equiaxed grains exhibiting a low dislocation density, $M_{23}C_6$ carbides of size twice larger than in the base metal i.e. 200 nm but also MX precipitates which probably slightly grow during the welding thermal cycle.

Damage mechanisms: Scanning electron microscope (SEM) investigations in cross-weld specimens cross-sections evidence that damage only develops in the HAZ and in the base metal near the HAZ. Second phase particles i.e. $M_{23}C_6$ carbides and Laves phases ((Fe,Cr)₂Mo) which appear during creep deformation are preferential sites for cavity nucleation. The cavity growth mainly proceeds following the grain boundaries and fracture occurs for higher level of damage than in the base metal.

Comparison with the base metal creep strength: Cross-weld specimens exhibit a reduction of 30% of the creep strength i.e. to reach the same creep lifetime, the applied engineering stress must be decreased by 30% for the cross-weld specimens in comparison with specimens made of only base metal.

2. Simulation of the weakest microstructure of the WJP91 weldment

Procedure: The simulation of welding microstructures requires the use of a high heating rates thermal simulator (a Gleeble 1500 simulator in the present study). A model of Rosenthal specifically developed to represent the weld thermal cycle in the case of manual arc welding and later improved by Rykalin was used. Model parameters are mainly physical constants or given by the process so that only one parameter must be fit from experimental observations i.e. the distance between the fusion line and the heat source.

Validation: The accuracy of the model to represent weld thermal cycle was evidenced by metallurgical investigations i.e. transmission electron microscope (TEM), electron backscattered diffraction (EBSD), carbon extraction replica and SEM.

Weld thermal cycle representative of the weakest HAZ: The main characteristics of the weld thermal cycle chosen to simulate the microstructure of the weakest HAZ on bulk specimens are reported in the table below.

Peak temperature	Heating rate	Cooling rate	PWHT
986°C	155°Cs ⁻¹	$\Delta t_{800 \rightarrow 500} = 16s (\approx 19^\circ Cs^{-1})$	2 hours (760°C)

Thermal cycle corresponding to the weakest HAZ

This specific weld thermal cycle was chosen as its microstructure corresponds to the one found where the creep failure of cross-welds specimens occurs but also because its metallurgical properties let foresee a lower creep strength.

2. Creep properties at 625°C of the weakest microstructure of the WJP91 weldment

Testing procedure: In order to avoid any constraining effects due to microstructural heterogeneities, the creep specimens were all notched to localise creep deformation in the thermal treated area.

Damage mechanisms: Metallurgical investigations revealed that damage mechanisms are the same than those encountered in cross-weld specimens which is a new argument to validate the choice of the weld thermal cycle. Creep tests on various kind of specimen geometry also showed that the stress triaxiality ratio plays a key role in damage development.

Creep flow and fracture properties: The creep model with coupled multiple deformation and damage mechanisms was improved to better represent high temperature strain rate effects and was successfully used to fit experimental data by inverse analysis. It allowed to determine uniaxial creep flow and damage properties of the weakest HAZ. The steady state creep strain rate is ten times higher in the weakest HAZ than in the base metal whereas the creep strength of the weakest HAZ is 30% lower than that of the base metal.

Part D

Modelling creep flow and damage behaviour of weldments

*(Modélisation du comportement, de l'endommagement et de la rupture en fluage des joints soudés
en acier 9Cr1Mo-NbV)*

Introduction

It was evidenced in **Part C** that the weldment exhibits a lower creep strength than the base metal. This loss of creep strength can be attributed to both the lower creep of the HAZ and constraint effects due to behaviour mismatch between materials in the weldment. In **Part C**, attention was only focused on the “material effect” i.e. on determining the creep flow and damage behaviour of the weakest area of the HAZ. The creep failure model integrating multiple deformation and damage mechanism introduced in **Part B** was improved and used to represent the high temperature creep flow and damage behaviour of the weakest HAZ.

The present part is concerned with evaluating the constraint effects. To start, a review of several previous work is made. These literature results are discussed because, as it has already been mentioned in **Part B**, in these studies, little attention was focused on integrating material data and fine understanding of creep deformation and damage behaviour of weldments. However, multi-material calculations literature data give useful information about the constraint effects due to both the specimen geometry and the different creep flow behaviours. Note that the main part of literature results concerned 0.5CrMoV, 1Cr0.5Mo and 2.25CrMo weldments but these weldments exhibit the same mechanical behaviour than 9Cr1Mo-NbV weldments with especially a great sensitivity to type IV creep fracture.

Then, the results of the present study presented in **Part B** and **Part C**, concerning respectively creep flow and damage behaviour of the base metal and the weakest HAZ at 625°C, are integrated in multi-materials FE calculations. For the sake of simplicity a three material approach is chosen, i.e. the cross-weld specimens are represented as the assembly of the weld metal, the weakest HAZ and the base metal. FE calculations are compared to experimental data on various kind of specimens geometry. A good agreement is found especially in terms of creep lifetime predictions. Therefore, it allows to study the role of microstructural heterogeneity and determine which constraining effects can be encountered in 9Cr1Mo-NbV weldments. A simplified method based on the peak rupture stress concept is proposed to evaluate creep lifetime of weldments. It requires only elast-viscoplastic calculations and post-processing calculations.

Complementary results about creep flow and damage behaviour of the WJT91 weldments are given. Following the same methodology than in **chapter B.VII**, the creep model of the HAZ determined at 625°C is transformed to represent the creep behaviour at 550°C. For the sake of simplicity, a two materials representation was chosen to model creep flow and damage behaviour of WJT91 weldments at 550°C.

Finally, to ensure the validity of the method, FE calculations are performed to represent several industrial cases. The possibility to use the results of the present study to predict weld components in service failure is especially shown. The model predictions especially exhibit a quite good agreement with predictive curves established from observed in-service creep failures.

Contents

Chapter D.I. State of the art.

Chapter D.II. Modelling coupled creep flow and damage behaviour of weldments: “Modelling high temperature creep flow and damage behaviour of a 9Cr1Mo-NbV weldments”.

Chapter D.III. Predictions of creep lifetime of cross-weld specimens by means of elasto-viscoplastic calculations and the use of a rupture criterion in post-calculation.

Chapter D.IV. Modelling creep flow and damage behaviour of the WJT91 weldment at 450°C and 550°C.

Chapter D.V. Use of the model to predict creep lifetime of welded components for industrial applications.

Chapter D.I. State of the art

As for the predictions of creep lifetime of structures, both methods developed in the framework of the global approach and the local approach to fracture have been applied. The main purpose is to assess the effects of material property differences and geometry on the stresses and strains.

1. Use of simple criteria for designing weld components

1.1. Introduction

The analysis of welded component integrity requires the evaluation of two effects:

1. The loss of creep strength due to metallurgical changes in the weldment with introducing a safety factor (This is the aim of the ASME Code case N-47). In the best case the values of this safety factor are fitted on experiments on cross-weld specimens.
2. The effect of welding on the loading state i.e. the multiaxiality introduced by microstructural heterogeneities. It is taken into account using analytical evaluation of stress and strain redistributions. The most commonly used method is to calculate a reference stress which takes into account both geometrical and mismatch effects.

1.2. Evaluation of the loss of creep strength due to material

As it has already been mentioned in **chapter C.II**, the first method proposed in 1987 (ASME Code case N-47), introduced a safety factor, S , defined by:

$$\sigma_w = S\sigma_{BM} \quad (\text{with } S = 2/3) \quad (\text{eq. D.I.1})$$

where σ_w is the engineering stress to apply to the weldment to reach the same creep time to failure as that of the base metal for an applied engineering stress equal to σ_{BM} . Note however that the value of the safety factor depends on the loading state. In the ASME code, four loadings categories are distinguished:

1. Category A = Normal service conditions.
2. Category B = Loading conditions in transient regimes due to system malfunctions.
3. Category C = Loadings corresponding to deviation of the normal conditions which require the system shutdown or repair.
4. Category D = loadings which strongly affects the integrity of the installation so that only the public health and the safety are considered.

As an amelioration of this criterion, Storesund and Tu (1996) proposed to evaluate the safety factor from experiments both on base metal and cross-weld specimens:

$$S = \left(\frac{t_w}{t_{BM}} \right)^{1/n_{BM}} \quad (\text{eq. D.I.2})$$

with t_w and t_{BM} respectively the creep time to failure of the weldment and of the base metal when performing creep tests at the same applied engineering stress, and n_{BM} is the Norton power-law exponent for the base metal.

1.3. Evaluation of the multiaxiality of the loading state

In the French design code RCC-MR, taking into account the presence of a weld is also based on the calculation of a reference stress whose value depends on the geometry of the component. This reference stress must verify:

$$\sigma_{ref} < nJ\alpha S \quad (\text{eq. D.I.3})$$

where S is the acceptable stress determined from experiments on the base metal and n, J and α are safety factors defined as:

1. n is a factor whose value depends on the geometry of the welded joint and non destructive control methods: $0.5 < n < 1.0$.
2. J is a coefficient depending on the weldment J_m, J_t or J_r .
3. α depends on the weld (example : for a level A weldment, $\alpha = 1$ and P_m must be lower than S_m).

The reference stress can be associated to the classification of stresses into two categories:

1. The primary stresses are the stress developed by loading conditions only to satisfy the law of equilibrium of external and internal forces and moments.
2. The secondary stresses are stresses developed due to geometrical effects or heterogeneities in materials properties.

The principles used by the R5 procedure to evaluate the structural integrity of a component are recalled by Budden (2003) and Patel (2001). A limit load reference stress is defined by:

$$\sigma_{ref} = \frac{P\sigma_y}{P_L(a, \sigma_y)} \quad (\text{eq. D.I.4})$$

where P is the applied engineering stress, σ_y is the yield stress and P_L is the rigid plastic limit load which is calculated for homogeneous component as:

$$P_L = \beta P \quad (\text{eq. D.I.5})$$

where β is a model parameter.

Then the rupture reference stress for ductile materials is given by:

$$\sigma_{ref}^R = [1 + 0.13(\chi - 1)]\sigma_{ref} \quad (\text{eq. D.I.6})$$

where χ is a stress concentration factor given by:

$$\chi = \frac{\sigma_e^{\max}}{\sigma_{ref}}$$

with σ_e^{\max} the maximum value of the equivalent stress calculated for an applied engineering stress equal to σ_{ref} .

When a creep crack which controls the component creep lifetime initially exists, the plastic limit load P_L is determined with taking into account the evolution of the crack. The creep crack growth is then given by:

$$\dot{a} = A(C^*)^q \quad (\text{eq. D.I.7})$$

where A and q are material parameters and the loading parameter C^* is given by:

$$C^* = K \frac{\dot{\epsilon}_{ref}}{\sigma_{ref}} \quad (\text{eq. D.I.8})$$

where K is the stress intensity factor and $\dot{\epsilon}_{ref}$ is the creep strain rate at the reference stress. The creep crack growth is then determined from experiments especially with performing creep tests on compact tension specimens. In the case of chromium steels weldments where rupture occurs in the type IV region, the creep crack growth is evaluated in the HAZ.

1.4. Examples of application

For a pipe under internal pressure, Coussement et al (1994) expressed the reference stress as:

$$\sigma_{wf} = \frac{\sqrt{3}}{2} \sigma_{ref} = \frac{\sqrt{3}}{2} \frac{P}{\ln(R_0 / R_i)} \quad (\text{eq. D.I.9})$$

where P is the internal pressure, R_0 is the outer radius and R_i is the inner radius and $\sqrt{3} / 2$ is the safety factor to account for materials mismatch effect. It is assumed that the reference stress is the stress which when applied to a component, results in the same rupture life as that of a uniformly loaded uniaxial creep specimen made of base metal.

Another example is given by Budden (1998) for a weld pipe under internal pressure. In the absence of any defect the reference stress is given by:

$$\sigma_{ref} = \frac{P\sigma_y}{P_L} = \frac{P}{\ln(R_0 / R_i)} \quad (\text{eq. D.I.10})$$

where R_0 and R_i are respectively the outer and inner radius of the pipe. In its approach Budden does not introduce a safety factor to account for materials mismatch effect. However, to account for stress redistributions due to material heterogeneity in the welded component, the reference stress of **equation D.I.10** is multiplied by a factor k having specific values for the HAZ, the base metal and the weld metal.

Then, uniaxial creep data are used to determine Monkman-Grant or Larson-Miller predictive relationships for the three materials. The reference stress calculated by **equation D.I.10** are then integrated to the predictive relationships to determine the corresponding creep lifetimes. The minimum of the three calculated creep lifetimes gives a prediction of the creep lifetime of the welded pipe. The method is also used in the presence of a defect with using **equation D.I.7** and **D.I.8**. A good agreement is found between predicted and calculated creep lifetime as the value of k is especially fitted to account for experimentally measured creep lifetime of the welded pipe.

1.5. Accuracy of these simple design criteria

The use of the criteria used in the designing codes seems to be dangerous for two reasons:

1. Extrapolation of uniaxial creep data are used. It was shown in the present study that such an extrapolation can be hazardous as a change in creep flow and damage mechanisms can occur.
2. The effect of welding is only taken into account with introducing safety factor that have no physical basis.
3. The multiaxiality of the loading is only taken into account by introducing corrective terms such as the k factor in the R5 procedure.

Moreover, specific formulations of the reference stress for each type of component geometry are required which are obviously not so easy to establish especially for complex structures geometry.

2. Description of the multi-material approach

Several authors: Hyde and al (2001), Perrin and Hayhurst (1999) and Eggeler (1994) used finite element calculations and a multi materials approach to model creep response of 2.25Cr1Mo and 9Cr1Mo-NbV weldments. They consider that weldments may be divided into three parts: the weld metal (WM), the heat affected zone (HAZ) and the base metal (BM) and they determine creep flow properties of each of the three zones with reducing HAZ to its softest part. Storesund and Tu (1995) performed a more detailed analysis by dividing HAZ into the CGHAZ and the ICHAZ.

This approach has several advantages. The first one, is that creep mechanical properties of each part of the welded component are determined and used. The second is that finite element calculations give the possibility to perform the analysis respecting the real geometry of the weld. As a matter of fact, using this method both heterogeneity and mismatch in creep properties and geometrical effects are taken into account and can be analysed. The inconvenient is that many time consuming experiments must be previously carried out so that a largely used method introduced by Perrin and Hayhurst (1996) consists in deducing creep properties of each constituents from those of the base metal.

2.1. Multi-materials calculations using only the creep flow behaviour

Some authors, like Chellapandi and Chetal (2000), performed multi material FE calculation using a two material representation (i.e. base and weld metal). They evidenced that the stress concentration factor is insignificant in 9Cr1Mo-NbV weldments which seems to be normal as the two materials exhibit similar creep flow properties. In fact, this representation is too much simplified especially to represent the type IV cracking. At least a three materials representation is necessary and the results presented in the following concern these types of representations.

2.1.1. Evaluation of the creep flow and damage properties of the materials

The best way to evaluate the creep flow and damage properties of each part of the weldment is to test each of them independently. However, such a work may be very time consuming in terms of creep experiments but also because the HAZ microstructures can only be tested provided they are previously simulated on massive specimens. Therefore, Wang and Hayhurst (1995) and then Perrin and Hayhurst (1996), proposed a method which allows to evaluate the weld and HAZ materials properties using the base metal as a reference and the values of a set of normalized material properties ratios (steady state creep strain rate, creep lifetime and failure strains). A data sheet was especially proposed for ferritic steels in Wang and Hayhurst (1993).

2.1.2. Difficulties in evaluating the effects of microstructural heterogeneity on stress and strain redistributions

The work of Vazda (1997) is interesting as it shows what one should not do. Vazda (1997) used FE calculations with a three material representation using the constitutive laws established by Eggeler et al (1994) for a 9Cr1Mo-NbV steel. The aim of his study was to evaluate the concentration effects in a circumferential weld especially when varying geometrical parameters as the weld angle or the HAZ width. For its study, Vazda (1997) defined concentration factors as the ratio between the maximum quantity in the welded pipe and the maximum of the same quantity in the same pipe made only of base metal. One of his conclusions is that the HAZ width has no effect on strain redistributions which is obviously wrong and Vazda (1997) would have found a better result if he had defined its concentration factor as the maximum quantity in the welded pipe and the maximum of the same quantity in the same pipe made only of HAZ. Indeed, one should easily admit that in the case of a hard/soft/hard weldment like 9Cr1Mo-NbV weldments, the more the HAZ width is small the more the creep strain is constrained. Therefore, the effects of microstructural heterogeneity on stress

and strain redistributions must be evaluated with referring to the initial properties of each of the constituents of the weldment.

2.1.3. Effect of the creep flow properties mismatch on mechanical fields

Stress redistributions in weldments have been investigated by Storesund and Tu (1995) in 0.5CrMoV, 1Cr0.5Mo and 2.25CrMo weldments which are hard/soft/hard weldments. They found that stress concentrations appear in the weld and base metals near the HAZ. More generally, the principal stress is maximum in the hardest material and the equivalent creep strain is maximum in the weakest material.

2.1.4. Geometric effects

Three geometric parameters may lead to constraint effects in the weldments:

1. The weld interface angle between the weld and the base metal i.e. the angle between the fusion line and the loading direction.
2. The width of the heat affected zone especially as the heat affected zone is the weakest area in CrMo steel weldments.
3. The specimen diameter and more specifically the ratio between the specimen diameter and the HAZ width.

Hyde et al (2001) largely studied the effect of the weld angle for an internally pressurised thick walled CrMoV pipe but also the effect of an additional axial load. They concluded that for the pipe under internal pressure, when increasing the weld angle larger than 15°, the time to failure is slightly increased. The effect of the weld angle is more important when the pipe is submitted to an additional axial load as the time to failure is increased by 10% in this case. The same conclusions are given by Craine and Newman (1996), Storesund and Tu (1996) and Law and Payten (1997). Even for 45° angles, the weld angle has little influence on the stress concentrations.

The value of the HAZ width is obviously an important parameter as the constraint effect strongly depends on it. However, Perrin and Hayhurst (1999) who performed calculations with the plane stress hypothesis have found that the width of the HAZ does not have a significant effect on the stress distributions but this result is probably strongly influenced by the plane stress hypothesis. The problem of the HAZ width was also explored by Law and Payten (1997) and Storesund and Tu (1996) but as they simultaneously vary both the HAZ width and the specimen diameter, it is very hard to conclude about the effect of the HAZ width from their studies.

The effect of the specimen diameter is particularly interesting as it gives useful information to interpret the results of experiments. Storesund and Tu (1995) studied the diameter effect by varying its value from 4 mm to 16 mm without changing the length of cross-weld specimens. They especially showed that stresses distributions strongly depend on the specimen diameter:

1. For a small specimen, the principal stress is maximum at the outer surface while for larger specimen the maximum of the principal stress shifts toward the inside of the specimen.
2. The value of the principal stress decreases with increasing the specimen diameter (i.e. the value of the specimen diameter has an equivalent effect than the HAZ width).

In fact, one can note that in the absence of any crack, the two geometrical effects: the HAZ width and the specimen diameter have the same influence on constraints in the weldment. Decreasing the HAZ width or the specimen diameter is equivalent. In fact, the relevant parameter to describe constraint effects is the ratio $l_{HAZ} / \phi_{specimen}$.

2.1.5. Use of FE creep flow calculations for designing purposes

The methods presented here are not strongly different from these introduced in **section 1** except that the reference stress is evaluated from multi-material FE calculations i.e. with taking into account the mismatch between materials creep flow properties.

Some authors considered that the multi-material method can be used without describing creep damage evolution in the whole weld component. For example, Storesund and Tu (1995) and more recently, Hyde et al (2001) proposed a simple method based on the knowledge of the steady state creep properties of the base metal, the weld metal and the heat affected zone. The idea is to perform FE calculations using only constitutive equations describing the steady state creep stage. They used post-processing calculations to determine a “peak rupture stress” to account for the effect of the multi-axial loading state on damage development. The “peak rupture stress” expressed as:

$$\sigma_{rs} = \alpha \sigma_1 + (1 - \alpha) \sigma_{eq} \quad (\text{eq. D.I.12})$$

where σ_1 is the principal stress and σ_{eq} the von Mises equivalent stress. The value of α has already been fitted to 0.43 by Browne et al (1982) for 0.5Cr0.5Mo and 2^{1/4}Cr1Mo weldments. The peak rupture stress is then reported on the plot σ versus time to failure of the material where this peak rupture stress is located (i.e. base or weld metal or heat affected zone) to evaluate the creep life of the weldment. If no experimental data are available, extrapolations using a Monkman-grant or a Larson-Miller empirical relationships are used.

2.2. Multi-materials calculations using coupled creep flow and damage behaviour

2.2.1. Presentation

The three materials representation is the most commonly used as creep flow model coupled deformation and damage behaviour require a large number of creep data. The creep models used for these studies by Hyde and Tang (1998), Tu et al (1996), Segle et al (1996), Perrin et al (2000), are models of the continuum damage mechanics generalised to the case of multiaxial loading in which the concept of the ‘‘peak rupture stress’’ is used. The constitutive multi-axial laws for describing the creep strain rate and the damage kinetics are respectively given by:

$$\frac{d\epsilon_{ij}}{dt} = \frac{3}{2} B \left(\frac{\sigma_{eq}}{1 - D} \right)^{n-1} \frac{S_{ij}}{1 - D} \quad (\text{eq.D.I.13})$$

$$\frac{dD}{dt} = A \frac{(\alpha \sigma_1 + (1 - \alpha) \sigma_{eq})^\nu}{(1 - D)^\phi} \quad (\text{eq.D.I.14})$$

where, σ_{eq} is the von Mises equivalent stress, S_{ij} is the deviatoric stress, σ_1 is the principal stress, χ , α , ϕ , n , A and B are material parameters, the value of α can be set to the commonly given value of 0.43. However, it is better to calibrate the value of α with comparing FE calculations and experiments (see Segle et al (1996)). Note also, that an analytical approach called the ‘‘skeletal point stress’’ is proposed by Hyde et al (1996). This approach was introduced by Krauss (1980) and is determined from creep tests on uniaxial and notched creep specimens. It is based on the existence of a point: ‘‘the skeletal point’’ where the stress remains unchanged both spatially and with time. This skeletal point is characterised by a skeletal von Mises stress σ_{eq}^* and a skeletal principal stress σ_1^* . The stress σ_{net} is defined as the nominal stress applied to the notched specimen and σ_{rep} is defined as the stress which when applied to an uniaxial specimen gives the same rupture time. Then, the three ratios: $\frac{\sigma_{eq}^*}{\sigma_{net}}$, $\frac{\sigma_1^*}{\sigma_{net}}$ and $\frac{\sigma_{rep}}{\sigma_{net}}$ are calculated.

If $\frac{\sigma_{rep}}{\sigma_{net}}$ is nearly equal to $\frac{\sigma_1^*}{\sigma_{net}}$ only the principal stress influences the creep failure, if $\frac{\sigma_{rep}}{\sigma_{net}}$ is nearly equal to $\frac{\sigma_{eq}^*}{\sigma_{net}}$ only the von Mises equivalent stress influences the creep failure and if $\frac{\sigma_{rep}}{\sigma_{net}}$ lies between $\frac{\sigma_{eq}^*}{\sigma_{net}}$ and $\frac{\sigma_1^*}{\sigma_{net}}$ both the principal stress and the von Mises equivalent stress influence the creep failure. The skeletal approach can especially be used to calibrate the value of α using the values of the three ratios. Note that one of the strong hypothesis of this approach is that the notch effect (i.e. the increase of the stress triaxiality ratio) is assumed to have a monotonic impact on the creep lifetime which is obviously not the case as shown for the base metal in the present study (see **chapter B.III**).

Finally, the creep time to failure associated to this approach is given, using a Monkman-Grant like relationship, by:

$$t_f = \frac{1}{A} (\alpha \sigma_1 + (1 - \alpha) \sigma_{eq})^\nu \quad (\text{eq.D.I.15})$$

The evaluation of the weldment creep lifetime consists in determining the lowest t_f of the constituents (i.e. t_f is calculated using the different values of the materials parameters A and ν). Several examples of application are given in Hyde and Sun (2002), Hyde et al (2000) and Hyde et al (1996) and this approach is also used to follow the creep crack growth (see Hyde et al (2001)).

Finally, less widespread works like that of Li et al (2003) used the Gurson - Tvergaard - Needleman (Tvergaard, Needleman (1984)) model to study the influence of mechanical mismatching on the failure of welded joints. Few information can be given as the results of their work are poorly described and illustrated.

2.2.2. Effect of creep flow and damage properties mismatch on lifetime predictions

Segle et al (1996) studied the influences of the mismatch in creep flow and damage properties of an assembly of three materials: a base metal, a HAZ that is the weakest area and a weld metal. Their study consists in varying the creep flow and damage properties of the weld metal. They evidenced that the rupture location shifts from inside the HAZ when the weld metal exhibits creep soft properties to the weld metal when the weld metal exhibits creep hard properties. However their results are largely influenced by the value of α as its value influences whether damage development is controlled by the principal stress or the creep strain. Therefore, there is a strong need to previously determine the

physical mechanisms responsible for damage in each part of the weldment before modelling creep flow and damage behaviour of the weldment.

3. Conclusions about literature data

Material mismatching obviously affects the stress and strain distributions in cross-weld specimens and the resulting multiaxial loading state obviously affects the kinetics of damage development. To account for the mismatch effect, the concept of the reference stress was introduced in single material FE calculations. Creep lifetime of welded components was then evaluated from uniaxial creep data on base metal.

Then, multi-material FE calculations were introduced allowing to directly account for constraint effect due to geometry and mismatch between materials creep flow properties. These multi-material FE calculations also allowed to study the influence of geometry (weld angle, width of the HAZ and specimen diameter) on constraint effects. In addition, the concept of the peak rupture stress was introduced to account for the effect of the multiaxial loading state on damage evolution and used in post-calculation procedure to predict welded component creep lifetime. Finally, for direct evaluation of welded component creep lifetime, models of continuum damage mechanics were used in multi material FE calculations to couple creep flow and damage behaviour.

There is no deny that multi-material FE calculations constituted a great evolution in the description of constraint effects in weldment except that creep properties of each constituents of the weldment were not systematically experimentally determined but deduced from that of the base metal. As a consequence, the results of the works presented before can largely be criticised as from the author point of view, material and constraint effects must be separately studied. It will be argued in the following that creep flow and damage properties of each constituents of the welded components must be previously determined. It is especially very important to determine whether damage development is controlled by the principal stress or the von Mises equivalent stress. Once and only once this work is done, multi-material FE modelling can be used to study constraint effects.

For the sake of clarity, the method proposed in the literature, and described before, are summed up in **table D.I.1**.

Experiments	Evaluation of creep fracture properties	Effect of welding and geometry on creep flow properties	Effect of welding on creep fracture properties	Integrity of the welded component	Remark
Base metal	Monkman-Grant (1956) relationship: $\dot{\epsilon}_{ss,BM} t_{R,BM}^m = C_{MG,BM}$ with $\dot{\epsilon}_{ss,BM} = B_{BM} \sigma^{n_{BM}}$ or Larson-Miller (1952) relationship: $P_{LM,BM} = (20 + \log(t_{R,BM})) \frac{T(K)}{1000}$ with $P_{LM,BM} = f_{BM}(\sigma)$	Definition of a reference stress σ_{ref} integrating the effect of both the mismatch in creep properties and the geometry.	Use of a safety factor $\sigma_w = S \sigma_{BM}$ with $S < 1$ so that $t_{R,BM}(\sigma_{BM}) = t_{R,w}(S \sigma_{BM})$	$t_{R,w} = t_{R,BM} \left(\frac{\sigma_w}{S} \right)$	No data concerning creep properties of weldment so that S is often largely conservative.
Base metal HAZ Weld metal	Monkman-Grant (1956) relationships: $\dot{\epsilon}_{ss,BM} t_{R,BM}^m = C_{MG,BM}$ with $\dot{\epsilon}_{ss,BM} = B_{BM} \sigma^{n_{BM}}$ $\dot{\epsilon}_{ss,HAZ} t_{R,HAZ}^m = C_{MG,HAZ}$ with $\dot{\epsilon}_{ss,HAZ} = B_{HAZ} \sigma^{n_{HAZ}}$ $\dot{\epsilon}_{ss,WM} t_{R,WM}^m = C_{MG,WM}$ with $\dot{\epsilon}_{ss,WM} = B_{WM} \sigma^{n_{WM}}$ or Larson-Miller (1952) relationships: $P_{LM,BM} = (20 + \log(t_{R,BM})) \frac{T(K)}{1000}$ with $P_{LM,BM} = f_{BM}(\sigma)$ $P_{LM,HAZ} = (20 + \log(t_{R,HAZ})) \frac{T(K)}{1000}$ with $P_{LM,HAZ} = f_{HAZ}(\sigma)$ $P_{LM,WM} = (20 + \log(t_{R,WM})) \frac{T(K)}{1000}$ with $P_{LM,WM} = f_{WM}(\sigma)$	Definition of a reference stress σ_{ref} integrating the effect of both the mismatch in creep properties and the geometry.	No criterion is necessary.	$t_{R,w} = \text{Min} \begin{pmatrix} t_{R,BM}(\sigma_{ref}) \\ t_{R,HAZ}(\sigma_{ref}) \\ t_{R,WM}(\sigma_{ref}) \end{pmatrix}$	The constraint effect on damage development is not taken into account.
Base metal HAZ Weld metal	Monkman-Grant (1956) relationships: $\dot{\epsilon}_{ss,BM} t_{R,BM}^m = C_{MG,BM}$ with $\dot{\epsilon}_{ss,BM} = B_{BM} \sigma^{n_{BM}}$ $\dot{\epsilon}_{ss,HAZ} t_{R,HAZ}^m = C_{MG,HAZ}$ with $\dot{\epsilon}_{ss,HAZ} = B_{HAZ} \sigma^{n_{HAZ}}$ $\dot{\epsilon}_{ss,WM} t_{R,WM}^m = C_{MG,WM}$ with $\dot{\epsilon}_{ss,WM} = B_{WM} \sigma^{n_{WM}}$ or Larson-Miller (1952) relationships: $P_{LM,BM} = (20 + \log(t_{R,BM})) \frac{T(K)}{1000}$ with $P_{LM,BM} = f_{BM}(\sigma)$ $P_{LM,HAZ} = (20 + \log(t_{R,HAZ})) \frac{T(K)}{1000}$ with $P_{LM,HAZ} = f_{HAZ}(\sigma)$ $P_{LM,WM} = (20 + \log(t_{R,WM})) \frac{T(K)}{1000}$ with $P_{LM,WM} = f_{WM}(\sigma)$	Multi-material finite element calculations	Introduction of a peak rupture stress to take into account the effect of the multiaxiality of the loading state on damage development and fracture properties: $\sigma_{rs} = \alpha \sigma_1 + (1-\alpha) \sigma_{eq}$ where σ_1 is the principal stress and σ_{eq} is the von Mises equivalent stress and $\alpha = 0.43$ for Cr-Mo weldments.	$t_{R,w} = \text{Min} \begin{pmatrix} t_{R,BM}(\sigma_{rs}) \\ t_{R,HAZ}(\sigma_{rs}) \\ t_{R,WM}(\sigma_{rs}) \end{pmatrix}$	The calibration of α has no physical basis. The maximum of the peak rupture stress does not necessarily occurs in the material which exhibits the worst creep strength which is not taken into account by numbers of authors.
Base metal Cross-weld	Continuum damage mechanics models (Note that as proposed by Perrin and Hayhurst (1996), creep constitutive equations for the HAZ and the weld metal are sometimes from these of the base metal)	Multi-material finite element calculations.	Multi-material finite element calculations.	Failure occurs when the classical criterion $D = D_c$ is reached in one of the materials	The creep damage properties of weld and base metal are not experimentally determined
Base metal HAZ Weld metal Cross-weld	Continuum damage mechanics models are fitted for the three materials	Multi-material finite element calculations.	Multi-material finite element calculations.	Failure occurs when the classical criterion $D = D_c$ is reached in one of the materials	

Table D.I.1. Methods to predict weldments creep lifetime

4. Finite element (FE) 2D axisymmetric calculations performed for the present study

From the author point of view, there is a strong lack of simple analysis of the effects of microstructural heterogeneity on stress and strain redistributions. To better understand the problem, it was chosen to perform simple FE 2D axisymmetric calculations for various possible situations without introducing any contribution of damage. The results presented above may appear to be obvious for mechanical engineers but this presentation seems to be necessary taking into account the absence of any clear conclusion in literature data.

4.1. Study of the effect of material heterogeneity

Three materials that will be called "hard", "soft1" and "soft2" were considered so that the steady state creep strain rate of the "soft1" material was five times larger than that of the "hard" material and two times larger than that of "soft2" material.

For each of the three materials, the strain rate tensor was written as:

$$\dot{\underline{\underline{\epsilon}}} = \dot{\underline{\underline{\epsilon}}}_e + \dot{\underline{\underline{\epsilon}}}_m \quad (\text{eq. D.I.16})$$

where m is the creep mechanism i.e. viscoplastic creep "vp" in the high stress creep regime and diffusion creep "d" in the low stress creep regime. The elastic strain tensor $\underline{\underline{\epsilon}}_e$ is related to the stress tensor by Hooke's law: $\underline{\underline{\sigma}} = \underline{\underline{C}} : \underline{\underline{\epsilon}}_e$ where $\underline{\underline{C}}$ is the fourth order stiffness tensor. The Young's modulus was taken to 145 GPa and the Poisson ratio to 0.3. The non-elastic (viscoplastic) strain rate tensor is given by the normality rule:

$$\dot{\underline{\underline{\epsilon}}}_m = \frac{3}{2} \dot{p}_m \frac{\underline{\underline{s}}}{\sigma_{eq}} \quad (\text{eq. D.I.17})$$

where s is the stress deviator, σ_{eq} is the von Mises equivalent stress and the viscoplastic multiplier, \dot{p}_m , is assumed to be given by a Norton power-law:

$$\dot{p}_m = \left\langle \frac{\sigma_{eq} - R_m}{K_m} \right\rangle^{n_m} \quad (\text{eq. D.I.18})$$

where n is the Norton exponent and K_m and R_m are material parameters respectively in MPa^{-n} and in MPa. The set of the chosen values of model parameters for the three materials is given in **table D.I.2**. Note also that, in both the low stress (diffusion controlled creep deformation) and high stress (dislocation controlled creep deformation) creep regimes, differences in steady state creep strain rates were increased by a factor of 2 from hard to soft1 and from soft1 to soft2 materials.

	High stress creep regime	Low stress creep regime
Hard	$K_{vp} = 600 \text{ MPah}^{-1/5}$ $R_{vp} = 10 \text{ MPa}$ $n_{vp} = 5.0$	$K_d = 1 \cdot 10^9 \text{ MPah}^{-1}$ $R_d = 0 \text{ MPa}$ $n_d = 1.0$
Soft1	$K_{vp} = 435 \text{ MPah}^{-1/5}$ $R_{vp} = 10 \text{ MPa}$ $n_{vp} = 5.0$	$K_d = 2 \cdot 10^8 \text{ MPah}^{-1}$ $R_d = 0 \text{ MPa}$ $n_d = 1.0$
Soft2	$K_{vp} = 378 \text{ MPah}^{-1/5}$ $R_{vp} = 10 \text{ MPa}$ $n_{vp} = 5.0$	$K_d = 1 \cdot 10^8 \text{ MPah}^{-1}$ $R_d = 0 \text{ MPa}$ $n_d = 1.0$

Table D.I.2. Model parameters

The situations illustrated in **figure D.I.1** were represented for 2D axisymmetric calculations. For comparison, single material calculations were performed for the three materials. The three areas were meshed with square 8 nodes elements (with reduced integration).

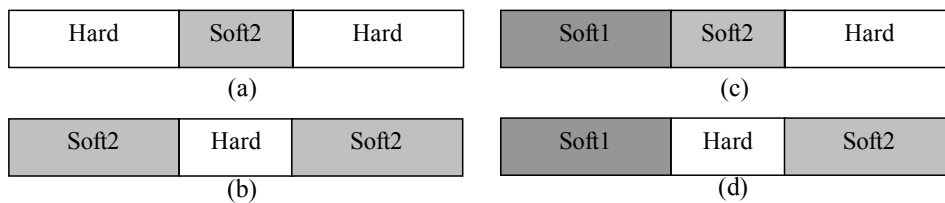


Figure D.I.1. Scheme of the four studied situations

To limit the calculation time, only one stress state per creep regime was studied (i.e. $\sigma_{nom} = 100 \text{ MPa}$ in the high stress creep regime and $\sigma_{nom} = 40 \text{ MPa}$ in the low stress creep regime). The effect of heterogeneity in materials creep flow behaviour was studied with a single 2D axisymmetric geometry having a minimum radius of 2.5 mm and a total length of 15 mm divided into three equal parts. Three mechanical parameters were studied:

1. The von Mises equivalent stress: σ_{eq} .
2. The cumulated creep strain: p_{vp} in the high stress creep regime and p_d in the low stress creep regime.
3. The stress triaxiality ratio: τ , which is locally defined as the ratio $\frac{1}{3} \frac{\sigma_m}{\sigma_{eq}}$ where σ_m is the local hydrostatic stress and σ_{eq} is the local equivalent von Mises stress.

Their evolution along the specimen axis were plotted for the same total specimen elongation of 1%, with comparing the four situations illustrated in **figure D.I.1**, both in the high stress and low stress creep regime respectively in **figure D.I.2** and **D.I.3**.

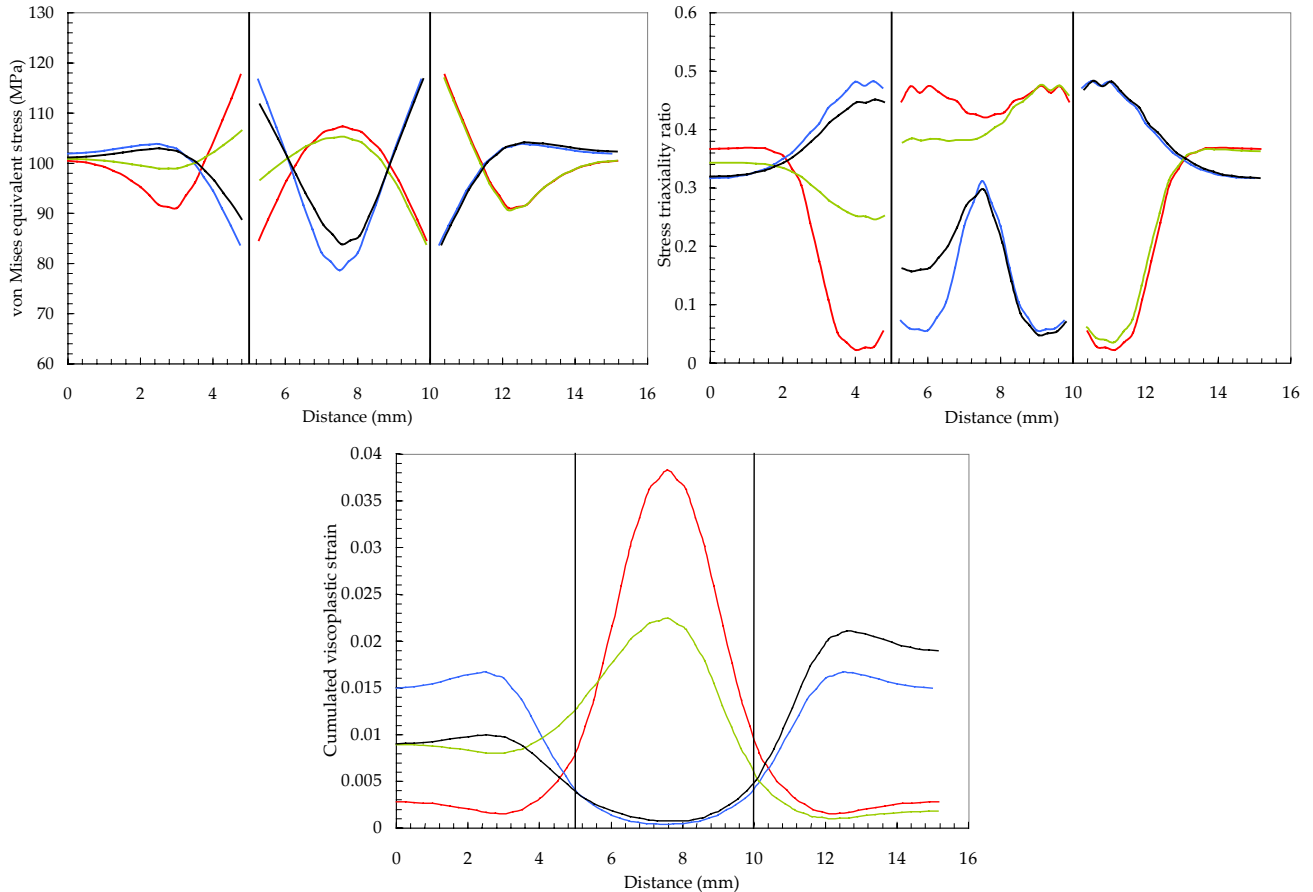


Figure D.I.2. Evolution of the mechanical parameters along the specimen axis red, blue, green and black lines respectively correspond to the situations (a), (b), (c) and (d) in the high stress creep regime

From the comparison of the four studied cases, the following conclusions can be drawn in the high stress creep regime (see **figure D.I.2**):

1. When a soft material is constrained by two hard materials:
 - The von Mises equivalent stress is maximum in the hard materials near the interface with $\sigma_{eq} = 1.2\sigma_{nom}$, but also reaches a local maximum at the centre of the soft material zone with $\sigma_{eq} = 1.1\sigma_{nom}$.
 - The stress triaxiality ratio and the cumulated creep strain are maximum at the centre of the soft material.
2. When a hard material is between two soft materials:
 - The von Mises equivalent stress is maximum in the hard materials near the interface with $\sigma_{eq} = 1.2\sigma_{nom}$ and a minimum is reached at the centre of the hard material zone with $\sigma_{eq} = 0.8\sigma_{nom}$.
 - The stress triaxiality ratio and the cumulated creep strain are maximum in the soft materials near the interface with $\tau = 0.45$ (i.e. slightly higher than 0.33).

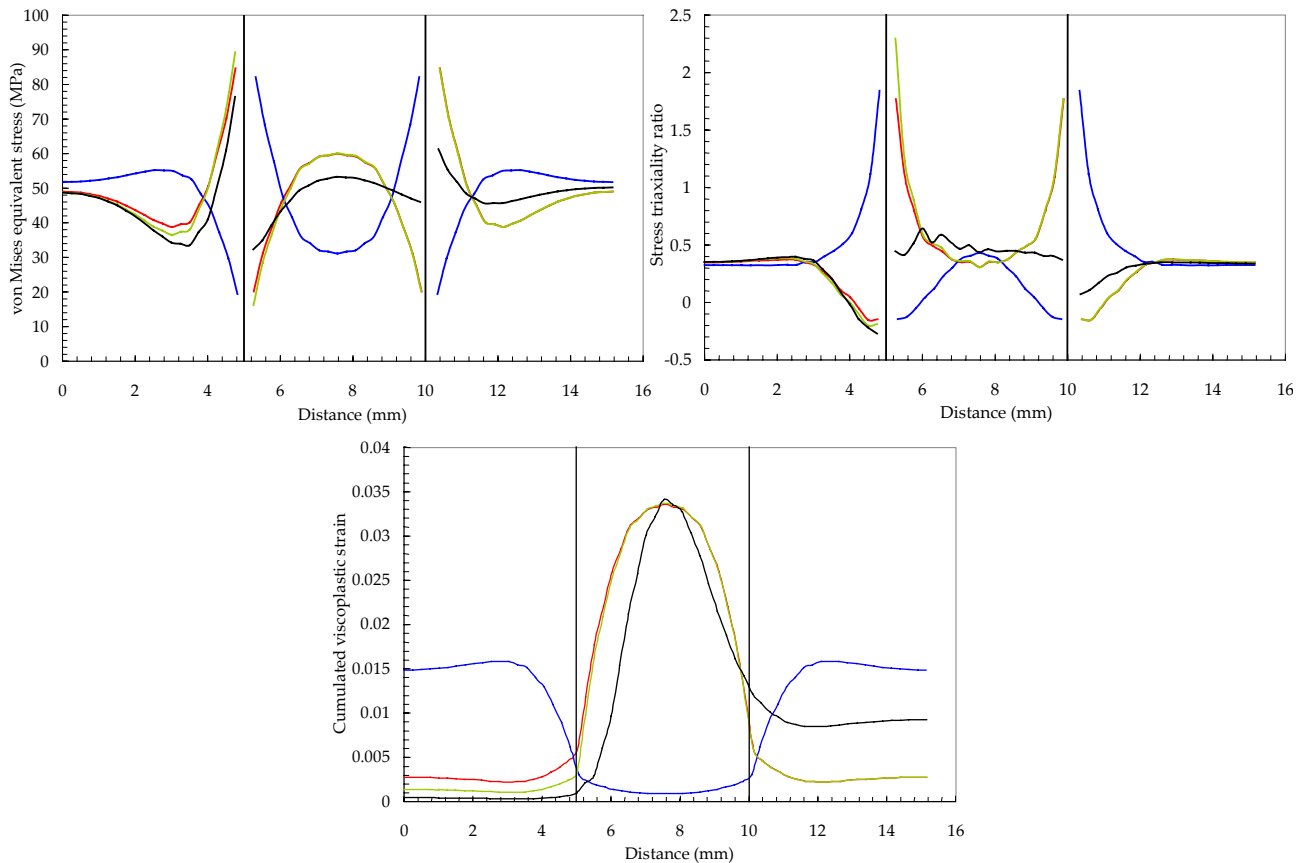


Figure D.I.3. Evolution of the mechanical parameters along the specimen axis red, blue, green and black lines respectively correspond to the situations (a), (b), (c) and (d) in the low stress creep regime

In the low stress creep regime the conclusions are quite similar at least for the von Mises equivalent stress and the cumulated creep strain distributions. The main changes concerned the distribution of the stress triaxiality ratio as:

1. The locally reached values of the stress triaxiality ratio can be very large with $\tau = 1.8$ which shows that τ may play a key role in damage development at low stress.
2. Distribution of the stress triaxiality ratio are quite abrupt with strong peaks on both sides of interfaces between the materials whereas it reaches the classical value of $1/3$ elsewhere.

4.2. Study of geometrical parameters on constraining effects

In this part, only the situation (a) of **figure D.I.1**, i.e. hard/soft/hard, is studied as this is the situation commonly encountered in Cr-Mo steels weldments. The influence of the following parameters was studied:

1. The specimen diameter.
2. The length of the “soft” material zone (this effect is obviously very similar to that of the specimen diameter).
3. The effect of a multiaxial loading (i.e. the effect of the stress triaxiality ratio).

To study the effect of the specimen diameter, FE calculations were performed with a specimen diameter twice larger than that used in the previous calculations i.e. $r = 5$ mm. The evolution of the von Mises stress, the stress triaxiality ratio and the cumulated viscoplastic strain were plotted, for a total specimen elongation of 1%, both in the low stress and in the high stress creep regime respectively in **figure D.I.4** and **D.I.5**. It was evidenced, both in the low stress and the high stress creep regimes, that when the specimen diameter increases:

1. The cumulated viscoplastic strain which is maximum in the soft material decreases (the constraint effect increases in the soft material).
2. The maximum of the stress triaxiality ratio which is located in the soft material is increased by a factor of 1.5 when increasing the specimen diameter by a factor of two.
3. The maximum of the von Mises equivalent stress which is located in the hard material slightly increases and the value of σ_{eq} more largely decreases in the soft material.

To study the effect of the length of the “soft2” material, the total length was kept constant but FE calculations were performed for three values of the “soft2” region i.e. 5 mm, 3 mm and 1 mm. The evolution of the von Mises equivalent stress, the stress triaxiality ratio and the cumulated viscoplastic strain were plotted, for a total specimen deformation of 1%, both in the low stress and in the high stress creep regime respectively in **figure D.I.6.** and **D.I.7.** It was evidenced that when the length of the soft material diminishes:

1. The stress triaxiality ratio largely increases in the soft material due to constraint effects.
2. The cumulated viscoplastic strain which is maximum in the HAZ is reduced by a factor of 3 when reducing the length of the HAZ from 5 mm to 1 mm.
3. When the HAZ length is too much lowered i.e. 1 mm the von Mises equivalent stress abruptly decreases in the HAZ.

In fact, reducing the length of the soft material zone and increasing the specimen diameter leads to the same changes in distributions of mechanical fields.

To study the effect of a multiaxial loading, FE calculations were performed both for a stress triaxiality ratio equal to 1/3 and 2.5. Note that for this simulation, the stress triaxiality ratio is imposed and consequently remains constant. The evolution of the von Mises equivalent stress, the stress triaxiality ratio and the cumulated viscoplastic strain were plotted, for a total specimen elongation of 1%, both in the low stress and in the high stress creep regime respectively in **figure D.I.8** and **D.I.9.** It was evidenced that when the stress triaxiality ratio is increased:

1. No maxima of cumulated viscoplastic strain is detected: i.e. the creep deformations of the soft and hard materials are homogeneous.
2. The evolution of the stress triaxiality ratio and the cumulated viscoplastic strains between the two materials is very abrupt for high stress triaxiality ratio (i.e. the effect is quite similar to that observed when decreasing the HAZ length). Moreover, the mismatch of τ between the two materials is larger.

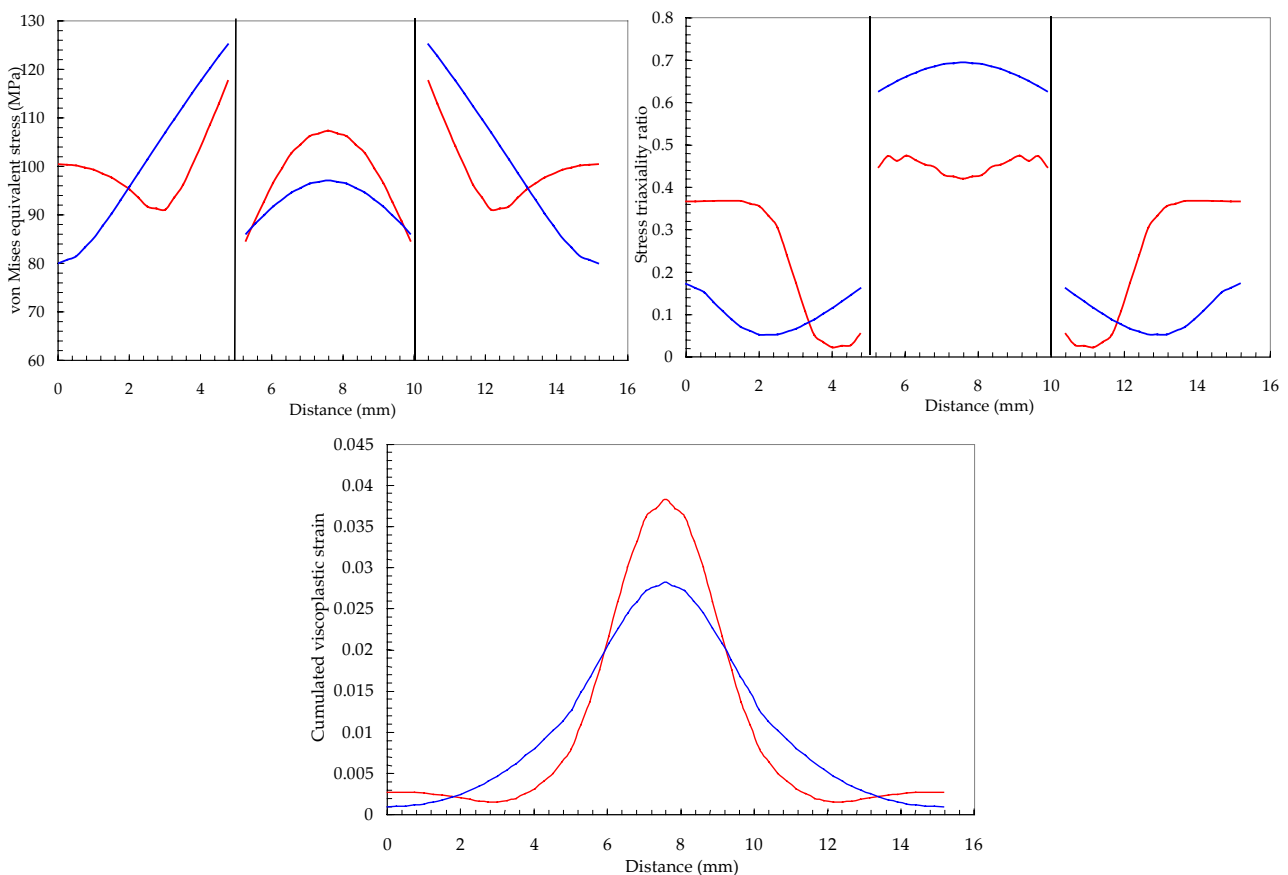


Figure D.I.4. Evolution of the mechanical parameters in the high stress creep regime along the specimen axis red and blue lines respectively correspond to specimens radius of 2.5 and 5 mm

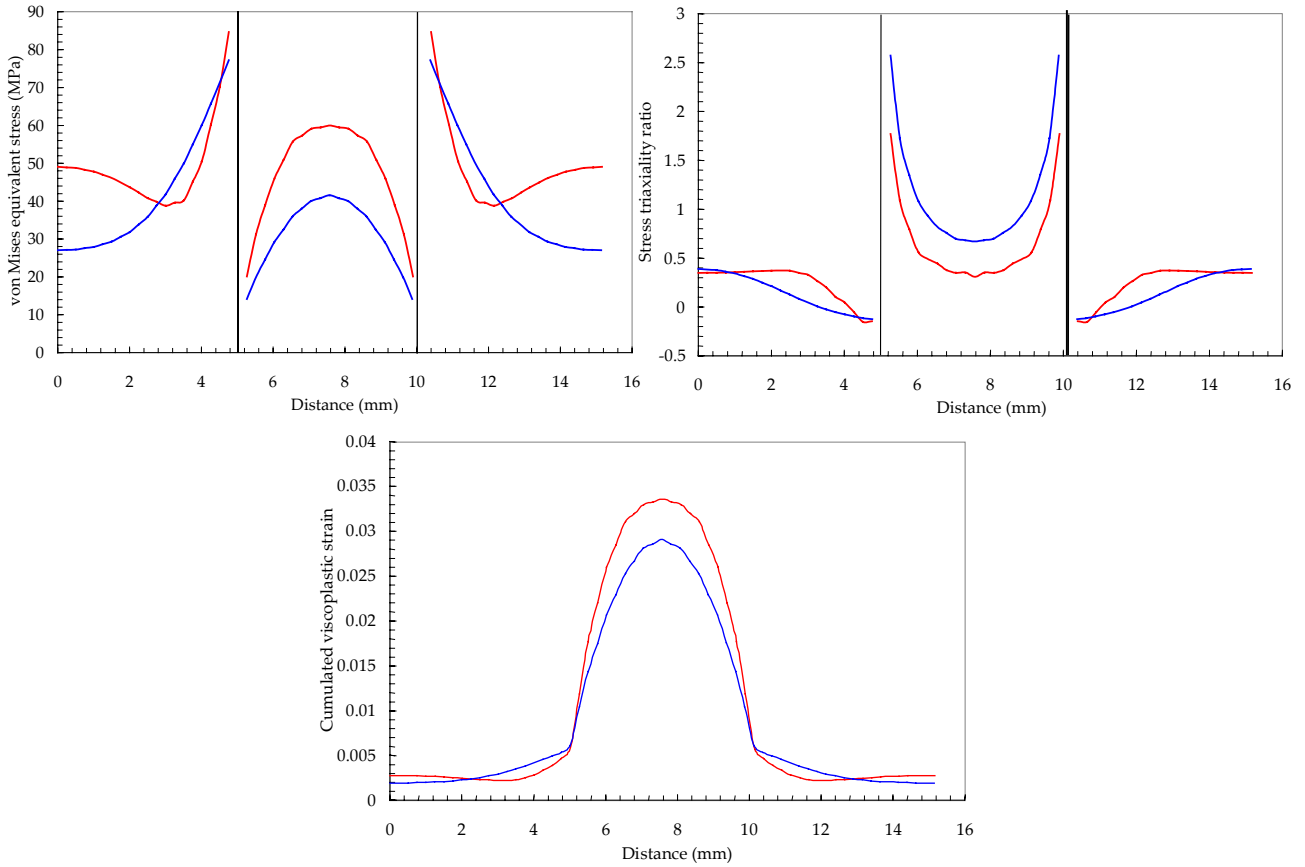


Figure D.I.5. Evolution of the mechanical parameters in the low stress creep regime along the specimen axis red and blue lines respectively correspond to specimens radius of 2.5 and 5 mm

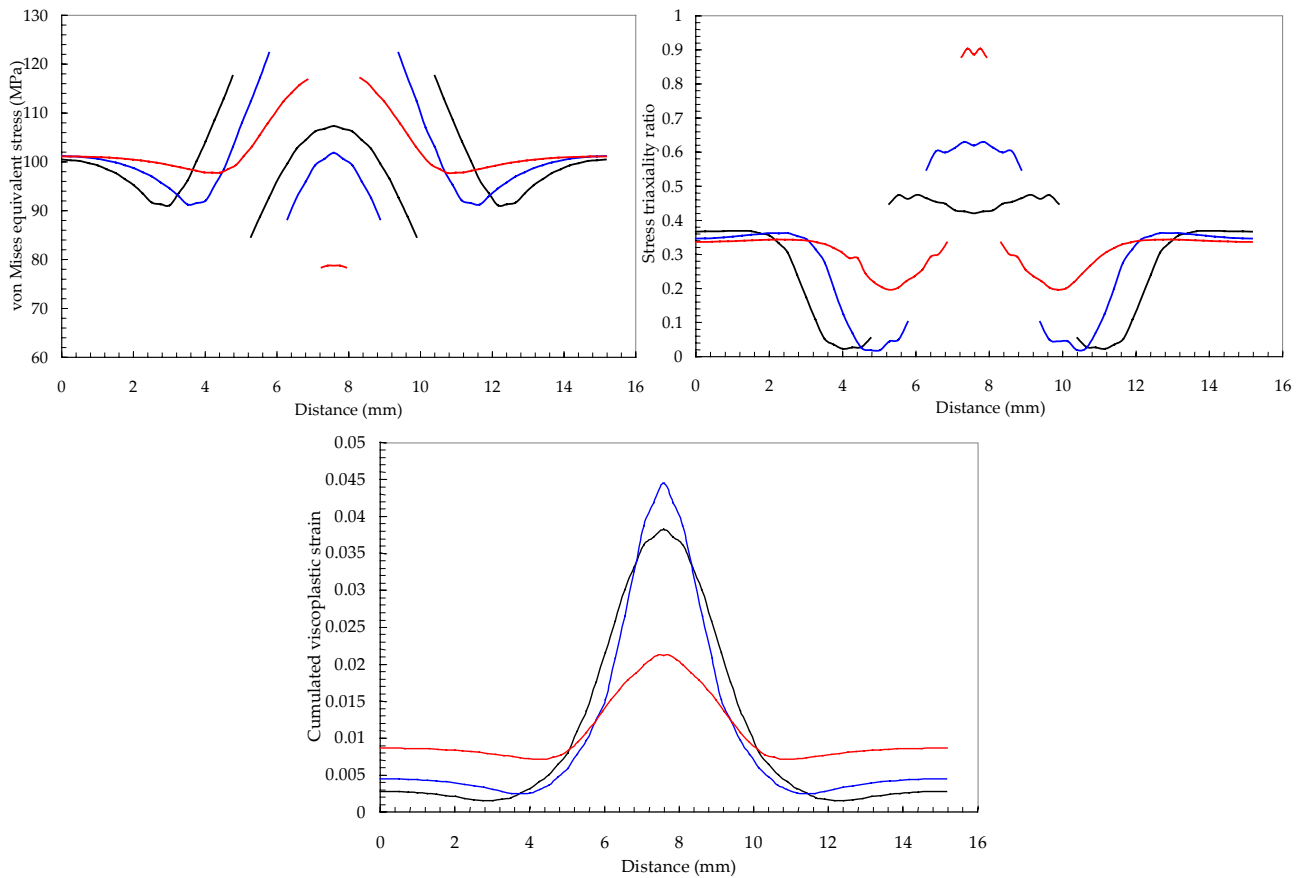


Figure D.I.6. Evolution of the mechanical parameters in the high stress creep regime along the specimen axis red, blue and black lines respectively correspond to $w = 1, 3$ and 5 mm

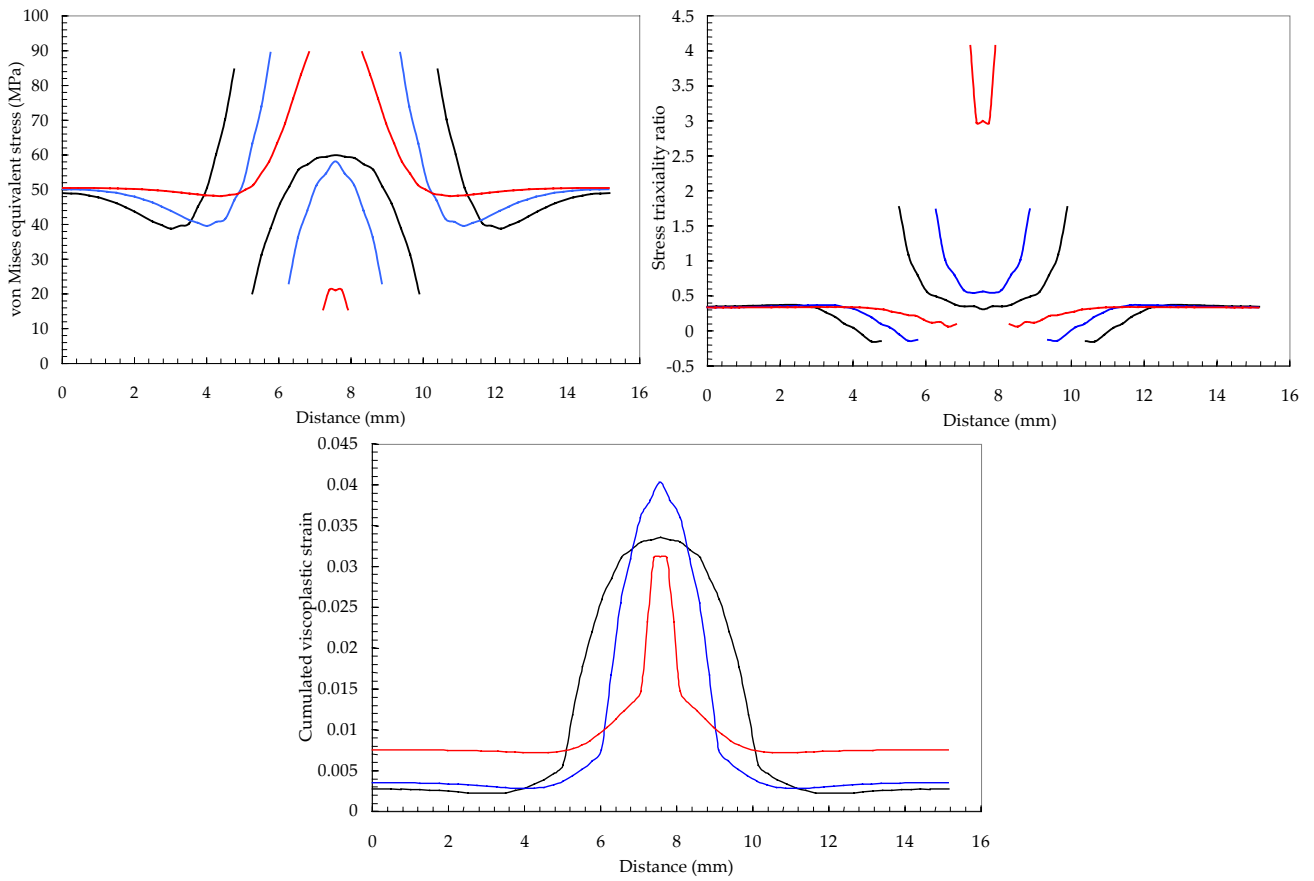


Figure D.I.7. Evolution of the mechanical parameters in the low stress creep regime along the specimen axis red, blue and black lines respectively correspond to $w = 1, 3$ and 5 mm

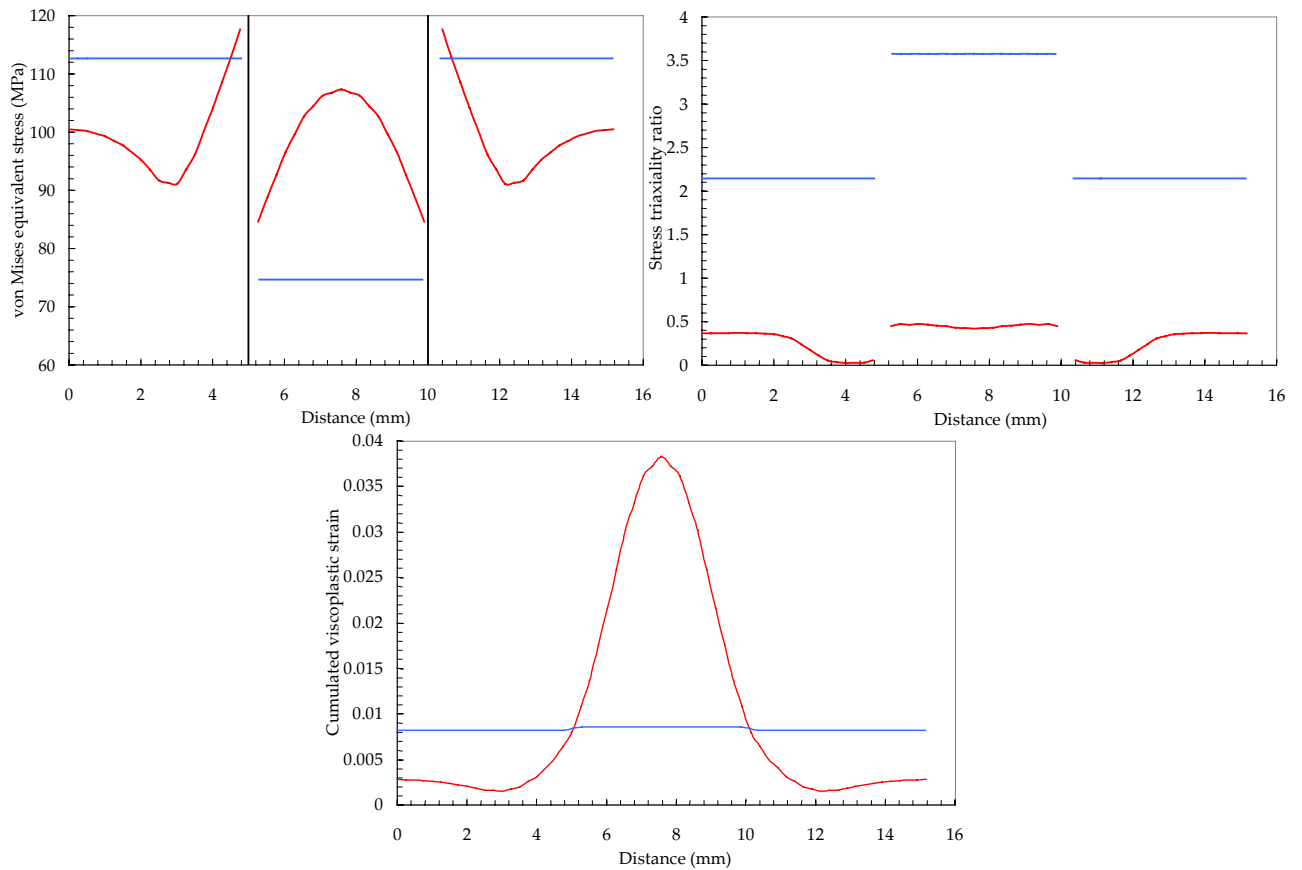


Figure D.I.8. Evolution of the mechanical parameters in the high stress creep regime along the specimen axis red and blue lines correspond to stress triaxiality ratio respectively equal to $1/3$ and 2.5

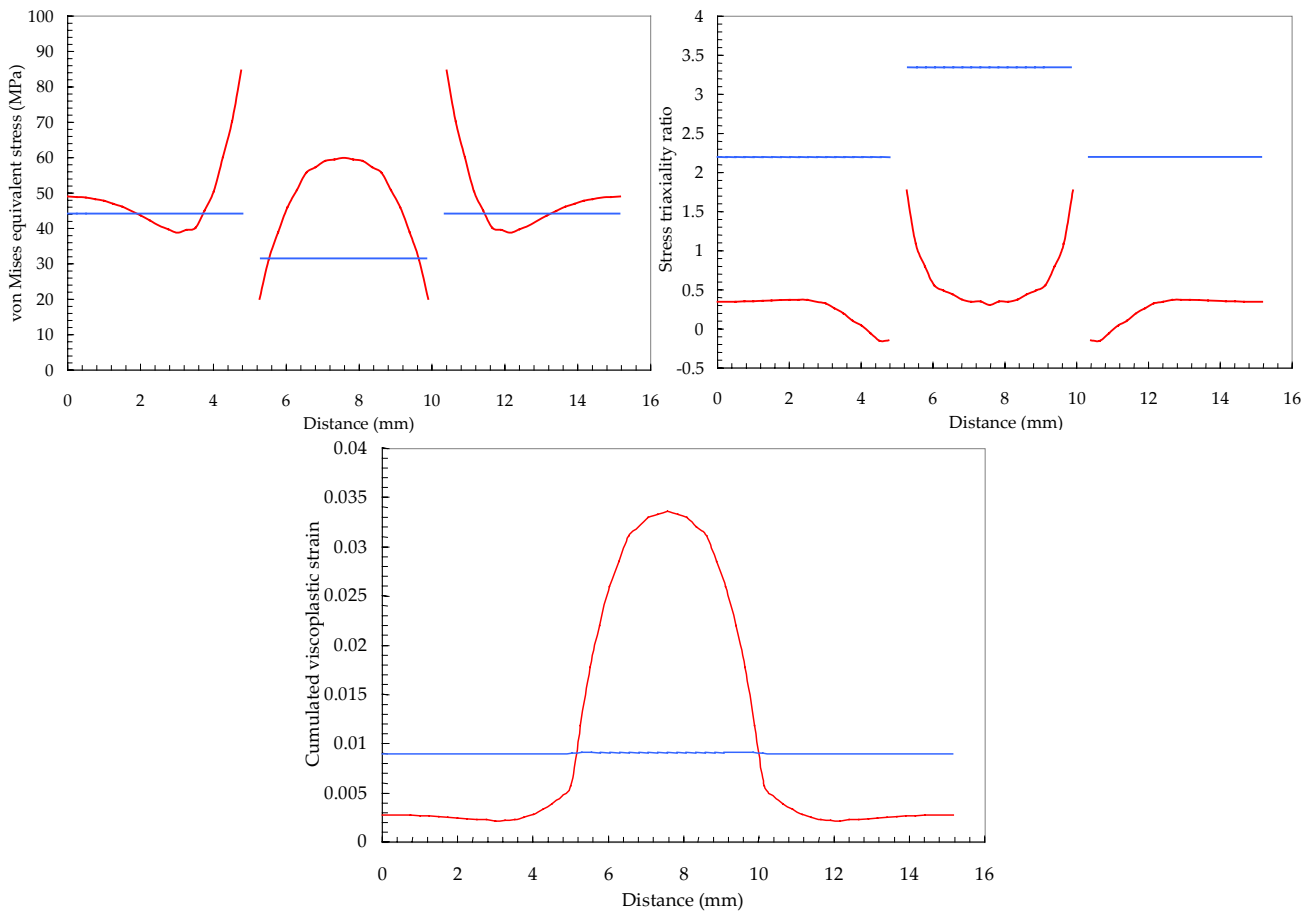


Figure D.I.9. Evolution of the mechanical parameters in the low stress creep regime along the specimen axis red and blue lines correspond to stress triaxiality ratio respectively equal to 1/3 and 2.5

5. Conclusions – Guidelines principles for studying creep properties of welded components

As evidenced by Anderson et al (1998), lifetime assessments on welds in high temperature components can not be based on material data only concerning the base metal. Indeed, the mismatch between the creep flow properties of the base metal, the weld metal and the HAZ leads to stress and strain redistributions and multiaxial loading conditions that strongly modify the predictions of creep lifetime.

The literature does not clearly investigate the effects of material mismatching and geometrical parameters on creep stress and strain redistributions so that a simple analysis of the problem was proposed in the present section. The following conclusions can be drawn:

1. The stress triaxiality ratio locally reaches a maximum in the softest material. The increase in the value of the stress triaxiality ratio can very large for material deforming in the diffusion low stress creep regime.
2. The von Mises equivalent stress locally reaches a maximum in the hardest material near the interface with the softest material.
3. The creep strain is mainly accumulated in the soft region but is constrained by the surrounding hard material.
4. Decreasing the HAZ length or increasing the specimen diameter have similar effects on stress and strain redistributions.

In addition to these phenomena, the weld angle, whose effect was not explored in the present study as it requires very time consuming 3D finite element calculations, also probably modify the loading state and by deduction the weldment creep lifetime.

The simple cases must be considered as reference cases and the following methodology is proposed to study the creep flow and damage behaviour of the weldments:

1. Creep experiments must be carried out on cross-weld specimens. These specimens must be examined with focusing attention on where damage develops and fracture occurs in terms of material (HAZ, base metal or weld metal) but

also location in the specimen geometry (at the inside or at the outside of the specimen for example). The shape of the specimen at the fracture stage will also be a useful information about constraining effects.

2. The geometry of the creep tested cross-welds specimens must be known especially the weld angle and the specimen diameter as they can influence stress and strain distributions.
3. The creep flow properties of each part of the weldment must be determined. A three material representation is, a priori, relevant. Note also that it was shown in **chapter C.II** that the HAZ creep flow properties can be evaluated from creep tests on cross-welds specimens even if a full study like that presented in **chapter C.III** and **chapter C.IV** would be preferable.
4. FE calculations using steady state creep flow properties of the constituents of the weldment must then be performed to evaluate the stress and strain redistributions in the cross-welds specimens (In fact the results must be obviously consistent with one of the four situations explored in **section 3 of the present chapter**). Moreover, as shown in **chapter C.II**, the length of the HAZ can be fitted by comparison with experimental results.
5. The comparison between the stress and strain redistributions with the rupture location can then be used to formulate an accurate predictive rupture criterion using for example the concept of the peak rupture stress.

Such a method will be explored in **chapter D.III**. A slightly different method which consists in determining coupled creep flow and damage behaviour of each constituents of the material is presented in **chapter D.II**. The main disadvantage is that it requires a full study of the HAZ creep flow and damage behaviour in comparison with the method proposed above. Then, the only parameter that must be fitted, is the length of the HAZ which is done following the method proposed in **chapter C.II**. Finally, multi-material FE calculations are performed and the results are compared with experiments on cross-welds specimens for validation. Studying the effects due to geometry is also possible and relevant as creep flow and damage properties of each constituents of the weldment have been previously and separately determined.

References

- Anderson P., Samuelson L.A., Segle P. (1998). The significance of weldment material mismatching on stress redistribution and creep cracking of high temperature components. *Materials at high temperature*. **15(3/4)**. 243-248.
- ASME Code case N-47 (1987). Class 1 components in elevated temperature service. *ASME, New York*.
- Browne R.J., Lonsdale D. and Flewitt P.E.J. (1982). Multiaxial stress rupture testing and compendium of data for creep resisting steels. *Journal of engineering materials technology*. **104**. 291-296.
- Budden P.J. (2003). Validation of the high temperature structural integrity procedure R5 by component testing. *International journal of pressure vessels and piping*. **80**. 517-526.
- Budden P.J. (1998). Analysis of the type IV creep failures of three welded ferritic pressure vessels. (1998). *International journal of pressure vessels and piping*. **75**. 509-519.
- Chellapandi P., Chetal S.C. (2000). Influence of mismatch of weld and base material creep properties on elevated temperature design of pressure vessels and piping. *Nuclear engineering and design*. **195**. 189-196.
- Coleman M.C., Parker, J.D., Walter D.J. (1985). The behavior of ferritic weldment in thick section of 1.25Cr0.5Mo-0.25V pipe at elevated temperature. *International Journal of Pressure Vessels and Piping*. **18**. 277-310.
- Coussement C., De Backer T., Dewitte M., Verelst L. (1994). Internal pressure creep testing on welded components of modified 9% Cr and 12%Cr steel. Second european conference on joining technology – EUROJOIN2. 461-479.
- Craine R.E, Newman M.G. (1996). *Journal of strain analysis*. **31**. 117-124.
- Holdsworth S.R. (2001). Creep damage zone development in advanced 9%Cr weldments. *International journal of pressure vessels and piping*. **78**. 773-778.
- Hyde T.H., Sun W. (2002). Effect of bending load on the creep failure behaviour of a pressurised thick walled CrMoV pipe weldment. *International journal of pressure vessels and piping*. **79**. 331-339.
- Hyde T.H., Sun W., Becker A.A. (2001). Creep crack growth in welds: a damage mechanics approach to predicting initiation and growth of circumferential cracks. *International journal of pressure vessels and piping*. **78**. 765-771.
- Hyde T.H., Sun W., Becker A.A. (2000). Failure prediction for multi-material creep test specimens using a steady state creep rupture stress. *International journal of mechanical sciences*. **42**. 401-423.
- Hyde T.H., Sun W., Becker A.A., Williams J.A. (2001). Effect of weld angle and axial load on the creep failure behaviour of an internally pressurised thick walled CrMoV pipe weld. *International journal of pressure vessels and piping*. **78**. 365-372.
- Hyde T.H., Tang A. (1998). Creep analysis and life assessment using cross weld specimens. *International materials reviews*. **43(6)**. 221-239.
- Hyde T.H., Xia L., Becker A.A. (1996). Prediction of creep failure in aeroengine materials under multiaxial stress states. *International journal of mechanics science*. **38(4)**. 385-403.
- Law M., Payten W. (1997). Weld performance under creep using finite element modelling. *International journal of pressure vessels and piping*. **72**. 45-49.

- Li X.Y., Hao Q., Shi Y.W., Lei Y.P., Marquis G. (2003). Influence of mechanical mismatching on the failure of welded joints by void nucleation and coalescence. *International journal of pressure vessels and piping*. **80**. 647-654.
- Newman M.G., Craine R.E. (1991). Creep failure in thin plates. *Mechanics of creep brittle materials edited by Cocks A.C.F. and Ponter A.R.S. - Elsevier applied - London*.
- Patel R.D. (2001). R5 creep life assessment of a welded component. *Abaqus UK users group conference*.
- Parker J.D. (1995). Creep behaviour of low alloy steel weldments. *International Journal of Pressure Vessels and Piping*. **63**. 55-62.
- Parker J.D., Stratford G.C. (1996). Strain localization in creep testing of samples with heterogeneous microstructures. *International Journal of Pressure Vessels and Piping*. **68**. 135-143.
- Perrin I.J., Hayhurst D.R., Ainsworth R.A. (2000). Approximate creep rupture lifetime for butt welded ferritic steel pressurised pipes. *European journal of mechanics A/Solids*. **19**. 223-258.
- Perrin I.J., Hayhurst D.R. (1999). Continuum damage mechanics analyses of type IV creep failure in ferritic steel crossweld specimens. *International journal of pressure vessels and piping*. **76**. 599-617.
- Perrin I.J., Hayhurst D.R. (1996). A method for the transformation of creep constitutive equations. *International journal of pressure vessels and piping*. **68**. 299-309.
- Prager M. (1992). Issues in the life assessment of chrome moly welds. *Serviceability of petroleum process and power equipment - ASME New-York*. **PVP239/MPC33**. 253-263.
- Samuelson L.A., Segle P., Anderson P. (1998). Creep stress concentrations in mis-matched weldments-starting points for early creep damage and creep cracking. *Materials at high temperature*. **15(3/4)**. 415-420.
- Segle P. (2002). Numerical simulation of weldment creep response. *PhD thesis - Royal institute of technology - Stockholm - Sweden*.
- Segle P., Tu S.T., Storesund J., Samuelson L.A. (1996). Some issues in life assessment of longitudinal seam welds based on creep tests with cross weld specimens. *International journal of pressure vessels and piping*. **66**. 199-222.
- Storesund J., Tu S.T. (1995). Geometrical effect on creep in cross weld specimens. *International Journal of Pressure Vessels and Piping*. **62**. 179-193.
- Tu S.T., Segle P., Gong J.M. (2003). Creep damage and fracture of weldments at high temperature. *International journal of pressure vessels and piping*.
- Tu S.T., Segle P., Gong J.M. (1996). Strength design and life assessment of welded structures subjected to high temperature creep. *International journal of pressure vessels and piping*. **66**. 171-186.
- Tvergaard V., Needleman A. (1984b). Analysis of the cup cone fracture in a round tensile bar. *Acta Metallurgica*. **32(1)**. 157-169.
- Vazda D. (1997). On concentration effects in circumferential welds due to dissimilar creep properties. *International journal of pressure vessels and piping*. **73**. 119-126.
- Wang Z.P., Hayhurst D.R. (1995). Characterisation of creep behaviour for multimaterials structures such as ferritic steel pipe weldments. *UMIST Report DMM.95.1*.
- Wang Z.P., Hayhurst D.R. (1993). Materials design data for design of ferritic pressure vessels weldments. *International journal of pressure vessels and piping*. **55**. 461-479.

**Modelling high temperature creep flow and damage behaviour
of 9Cr1Mo-NbV steel weldments**

V. Gaffard, J. Besson, A.F. Gourgues-Lorenzon

*Ecole Nationale Supérieure des Mines de Paris (E.N.S.M.P) - Centre des Matériaux
UMR CNRS 7633 BP 87, 91003 Evry Cedex France (corresponding author: jacques.besson@ensmp.fr)*

Abstract

The welding technology is one of the most commonly used method to join structural components in power-plants. This operation may lead to strong modifications of the mechanical properties of the base metal which is obviously the case for 9Cr1Mo-NbV steels. The present study aims at predicting the creep flow and damage behaviour of welded components made of 9Cr1Mo-NbV steels. To do so a three materials representation (i.e. weld metal, heat affected zone and base metal) was chosen. The present work is based on the results presented in Gaffard et al (2005a, 2005b, 2005c and 2005d) where creep flow and damage properties of respectively the base metal and the heat affected zone were experimentally studied then represented by a new model integrating multiple deformation and damage mechanisms. In the present study, an attempt is made to model, using a three materials representation, creep flow and damage behaviour of weldment for various kind of specimen geometry. It allows to study the influence of creep properties mismatch on the loading state and the deformation behaviour of the weldment.

Keywords: 9Cr-1MoNbV - Weldment – FE calculations

Introduction

The integrity of welded structures has focused the attention of both engineers and researchers so that simple design principles were introduced in design codes fifty years ago. It has been previously evidenced in Dewitte and Coussement (1991), Kojima et al (1995), Jakobova et al (1998), Laha et al (2000) Spigarelli and Quadrini (2002) and Gaffard et al (2005b) that welding has a large effect on the creep strength of 9Cr1Mo-NbV steels. The rupture occurs in the type IV region which is a relatively weak but ductile area supported by the base metal on one side and the weld metal on the other side. As both the base and weld metals are stronger than the HAZ, there is a constraint effect on the deformation of the type IV region so that this region is submitted to complex multiaxial loading conditions.

Due to these constraint effects, it was evidenced that the use of simple design criteria as these proposed in the ASME (1987) and R5 procedure did not allow to give good predictions of weldments creep lifetime. Therefore, attention was focused on performing finite element modelling of creep flow and damage behaviour of weldments with taking into account heterogeneities in materials properties (see Perrin and Hayhurst (2000)). Despite the complexity of the HAZ microstructure, the weldment is classically simplified using a three materials representation i.e. the weld metal (WM), the weakest heat affected zone (HAZ) and the base metal (BM) (see Hyde et al (2001), Perrin and Hayhurst (1999) and Eggeler et al (1994)). Note also that some authors like Storesund and Tu (1995) considered four main areas as they divide the HAZ into two main parts. The determination of the creep flow properties of each part of the weldment requires a lot of time consuming experiments. Moreover, to study the creep properties of the weakest HAZ, it is necessary to reproduce its microstructure on bulk specimens after determining the thermal cycle to which this part of the HAZ is submitted during the welding procedure.

Thus, Perrin and Hayhurst (1996) proposed methods to transform the creep constitutive equations of the base metal to account for creep flow and damage behaviour of the HAZ and the weld metal. If practical, these methods postulate that the physical mechanisms responsible for damage are the same in the HAZ, the base metal and the weld metal which is not necessary true. Some other authors, like Hyde and Tang (1998), Tu et al (1996) and Segle et al (1996) determined the creep flow and damage properties of the HAZ from multi-material FE calculations to account for experimentally measured weldments creep lifetime. But this method also neglects the determination of the physical mechanisms responsible for creep flow and damage.

Therefore, it is assumed in the present study that there is a strong need to perform a more systematic analysis, like that proposed by Eggeler et al (1994), which proceeds following three steps:

1. The characterisation of the creep flow and damage mechanisms in the weldment from creep tests on cross-weld specimens. The analysis of the tested specimens especially allows the determination of creep strain gradients and the rupture location in the weldment.

2. The characterisation of the creep flow and damage behaviour of various regions of the weldment chosen from the analysis of the creep response of the weldment (three regions i.e. the HAZ, the weld metal and the base metal in the present study).
3. The finite element modelling integrating the heterogeneities in materials creep properties. This method will be used to predict the weldment creep lifetime.

A strong effort was also made to understand the origins of the microstructural changes in the HAZ during welding before choosing a weld thermal cycle to reproduce the HAZ microstructure on bulk specimens (see Gaffard et al (2005c)). By comparison with the work of Eggeler et al (1994), the present study is supported by a finer analysis of the HAZ creep properties based on a larger experimental database. Creep tests on various type of U-notched axisymmetric specimens were especially included in the experimental database to investigate the effects of the stress triaxiality ratio on damage kinetics and creep tests were carried out up to 6,000 hours.

In addition, the modelling of the creep response is based in the present study on the use of a model integrating multiple deformation and damage mechanisms (see Gaffard et al (2005a)) which allows a description of the creep response from high to low stress with taking into account the changes in both deformation and damage mechanisms. Note that the constitutive equations representing each material were not refitted to account for the experimentally observed creep lifetime of cross-weld specimens.

Finally, it was possible to study the effects of the geometry on the creep flow behaviour and damage kinetics. The results of the present work are probably of better significance than these of Segle et al (1996) and Perrin and Hayhurst (1999) because the physical mechanisms responsible for damage development in the HAZ, i.e. the driving forces, were previously identified.

1. Materials and testing procedures

1.1. Materials

The weldment of this study consists in the circumferential welding of two pipes of 295 mm in outer diameter and 55 mm in thickness. The base metal and the weld metal are 9Cr1Mo-NbV steels whose chemical compositions are given in **table D.II.1**. Only slight variations between the chemical compositions of the two materials can be evidenced. The welding procedure was submerged metal arc welding which was divided into seventeenth runs with a heat input energy of 1296 Jmm⁻¹. To release the residual stresses and tempered the fresh martensite, a post weld heat treatment (PWHT) of two hours at 750°C was also performed.

	C	Si	Mn	P	S	Al	Cr	Ni	Mo	V	Nb	N	Cu
Base Metal	0.09	0.31	0.41	0.014	0.005	0.016	8.56	0.26	0.92	0.21	0.065	0.042	/
Weld Metal	0.091	0.369	0.409	0.028	0.013	0.07	8.44	0.27	0.92	0.24	/	0.038	0.04

Table D.II.1. Chemical compositions of the base metal

The main characteristics of the resulting microstructure in the tempered state are as follows:

1. The base metal exhibits a lath martensite (α) microstructure whose laths having the same crystallographic orientation are arranged in packets into the austenite grain (γ). Second phase particles, mainly $M_{23}C_6$ carbides (100 nm in average diameter) but also carbonitrides of type MX (20 nm in average diameter) were observed at grain boundaries.
2. The weld metal exhibits a microstructure very similar to that of the base metal except that the shape of the austenite grain is more elongated than equiaxed. Moreover, the presence of MnS particles (more than 500 nm in average diameter) was detected in the weld metal.
3. The welding operation affects the base metal properties in the so-called heat affected zone. This region is made of several microstructures whose properties depend on the peak temperature, T_{peak} , reached during the welding operation and especially the position of T_{peak} in comparison with the phase transformation points:
 - $T_{peak} \gg A_{c3}$ corresponds to the coarse grained heat affected zone (CGHAZ): the $\alpha \rightarrow \gamma$ phase transformation proceeds upon heating and the austenite grain growth is promoted by the high normalising temperature.
 - $T_{peak} \approx A_{c3}$ corresponds to the fine grained heat affected zone (FGHAZ): the $\alpha \rightarrow \gamma$ phase transformation proceeds upon heating but the austenite grain growth is on the contrary limited by the low normalising temperature.

- $A_{c1} < T_{peak} < A_{c3}$ corresponds to the intercritical heat affected zone (ICHAZ) as the $\alpha \rightarrow \gamma$ phase transformation only partially proceeds upon heating. A minimum of hardness is especially evidenced in this region.

The weakest microstructure with respect with the creep strength is the ICHAZ microstructure. This microstructure is characterised by:

1. Fine equiaxed gains (few microns in size) which have replaced the initial lath martensite morphology of the base metal.
2. A low dislocation density.
3. A larger size of $M_{23}C_6$ carbides whose average diameter reaches 200 nm (i.e. twice larger than in the base metal).

The microstructure of the ICHAZ was reproduced on bulk specimens using a Gleeble 1500 thermal-mechanical simulator following the thermal cycle described in **table D.II.2**. More details about the choice of the thermal cycle are given in Gaffard et al (2005c) where detailed microstructural analysis are reported. It is especially shown in Gaffard et al (2005c) that several thermal cycles corresponding to intercritical treatments can be performed but one of them is obviously of better significance. As also described in Gaffard et al (2005d), several type of metallurgical investigations (scanning electron microscope (SEM), transmission electron microscope (TEM), electron backscattered diffraction (EBSD) analysis and carbon extraction replica) allowed to ensure the correspondence between the simulated microstructure and the corresponding one in the real weldment.

Peak temperature	Heating rate	Cooling rate	PWHT
986°C	155°Cs ⁻¹	$\Delta t_{800 \rightarrow 500} = 16$ s	2 hours (760°C)

Table D.II.2. Thermal cycle corresponding to the weak HAZ

1.2. Testing procedures

Specimens were manufactured from the weldment along the longitudinal axis of the pipe. All the tests were performed at 625°C. All tensile creep tests were carried out under constant applied load in controlled atmosphere (20°C – 50% humidity). Load was applied using dead weights for smooth creep (SC) specimens or electrical mechanical testing machine for notched creep (NC) specimens. Temperature was monitored using three thermocouples spot welded onto the specimen surface. The temperature gradient between bottom and top did not exceed 2°C. The elongation of the specimen, measured by a linear variable differential transducer, was continuously recorded with a sensitivity of 1 μ m.

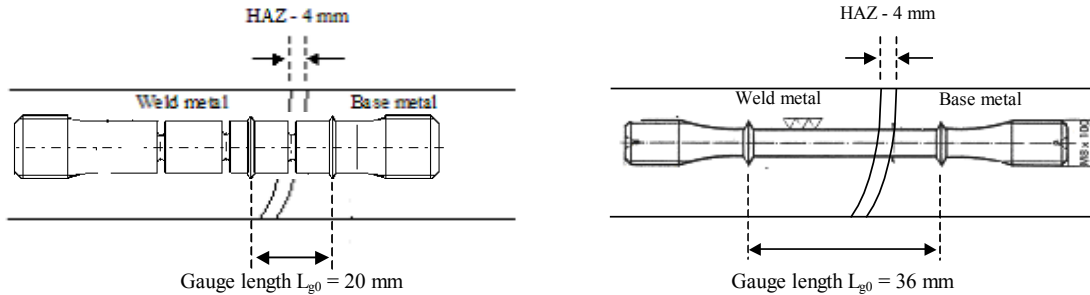


Figure D.II.1. Location of specimens in the weldment (NC1.2 and SC specimens)

First creep tests were performed on smooth round tensile bars (SC) having a gauge length of 36 mm and a minimum diameter of 5 mm. These tests allow to determine which part of the weldment has the worst creep strength.

Then creep tests were carried out on round U-notched bars (NC1.2 and NC4.0). It allows to determine the effect of the stress triaxiality ratio, which is defined as the ratio, $\tau = \frac{1}{3} \frac{\sigma_m}{\sigma_{eq}}$ where σ_m is the local hydrostatic stress and σ_{eq} is the local

von Mises equivalent stress, on the creep fracture properties. These specimens have a maximum diameter of 13 mm, a minimum diameter of 6 mm with notch radii of respectively 1.2 mm and 4.0 mm. Moreover, they were given respectively three and two widely separated notches. One of the notch was located in the HAZ and the two other ones in the base metal so that the damage development could be investigate in the two materials. Note that due to both the weld and the specimens geometry, the fusion line could not be set perpendicular to the loading axis but the weld angle did not exceed 30°.

Finally tensile creep tests were carried out on plate specimens (PC) under vacuum (10⁻³ Pa) in order to determine the gradient of creep strain throughout the weldment. The elongation of the specimen was not directly measured but the

displacement of the hydraulic jack was monitored to interrupt the creep tests at the onset of the creep fracture. Strain gradients could be evaluated by measuring the evolution of the specimen thickness in three regions of the weldment.

2. Creep flow and damage behaviour of the weldment

2.1. Results of creep tests

For tests on SC specimens, stress holding values were from 100 MPa to 50 MPa and corresponding times to failure were between 300 and 11,000 hours. For tests on NC4.0 specimens, stress holding values were from 120 MPa to 60 MPa and corresponding time to failure were between 150 hours and 3750 hours and for tests on NC1.2 specimens, stress holding values were from 135 MPa to 85 MPa and corresponding time to failure were between 200 hours and 3,000 hours. The corresponding creep curves are respectively given in figures D.II.2, D.II.3 and D.II.4. It can be noticed that the experimental scatter is quite large including the creep tests on NC1.2 specimens. This experimental scatter can be attributed to the heterogeneities in the weldment microstructure depending on the location of creep specimens in the weldment.

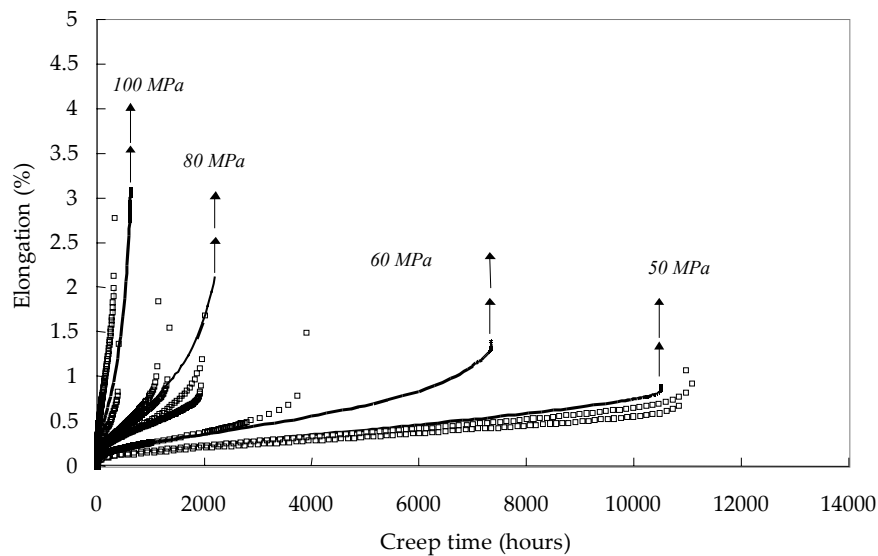


Figure D.II.2. Comparisons of experimental (symbols), 2D calculated (black lines) creep curves for creep tests on SC specimens

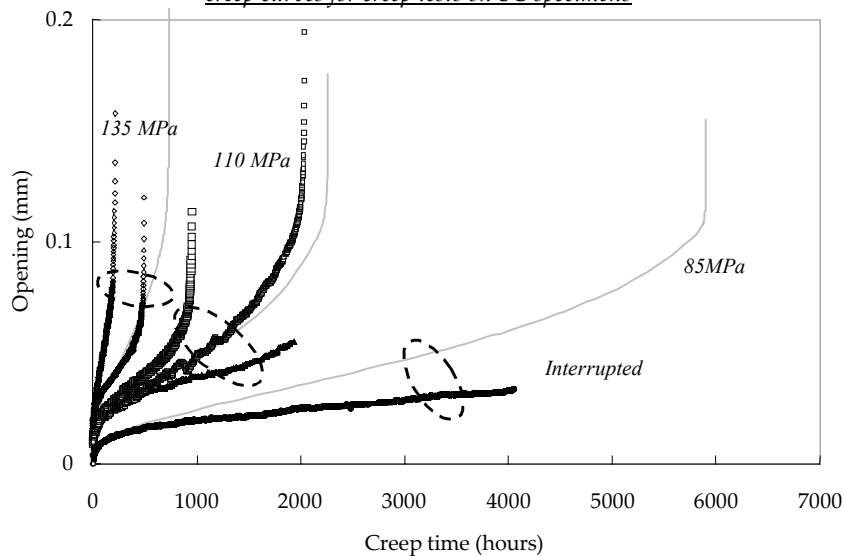


Figure D.II.3. Comparisons of experimental (symbols), 2D calculated (black lines) creep curves for creep tests on NC1.2 specimens

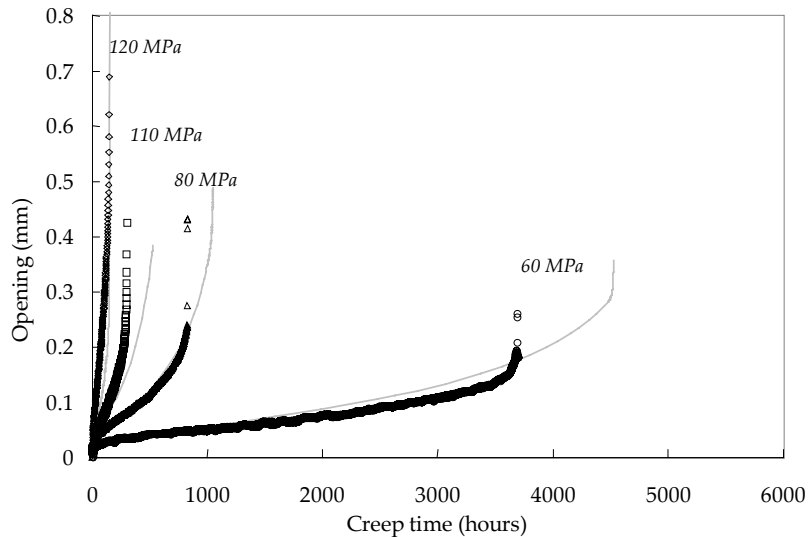


Figure D.II.4. Comparisons of experimental (symbols), 2D calculated (lines) creep curves for creep tests on NC4.0 specimens

2.2. Creep fracture properties of the weldment

In all cases, the creep failure of cross-weld NC1.2, NC4.0 and SC specimens was of type IV i.e. in the HAZ parallel to the fusion line. SEM investigations in SC cross-weld specimens cross-sections revealed that creep damage cavitation only occurred in the HAZ and in the base metal (see also Li et al (2003)). In addition, no damage was detected in NC specimens in the notches located in the base metal.

SEM investigations also show that the weld metal contains a population of perfectly round voids obviously corresponding to the decohesion of the matrix/MnS particles interface. This aspect will be taken into account in modelling. The evolution of the creep time to failure versus the applied engineering stress is plotted in **figure D.II.5** for SC and NC specimens. It shows that the notch has no strengthening effect from SC specimens to 4.0 mm notched specimens. A strengthening effect is however observed when decreasing the notch radius from 4.0 mm to 1.2 mm. It means that when the HAZ creep deformation is quite highly constrained, the weldment creep lifetime is increased at least in the high stress creep regime.

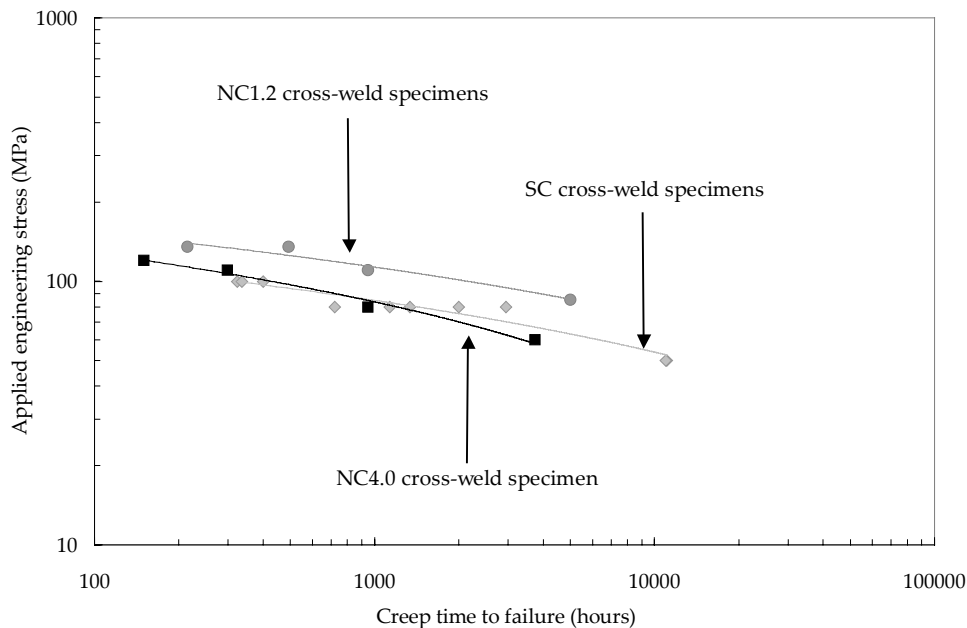
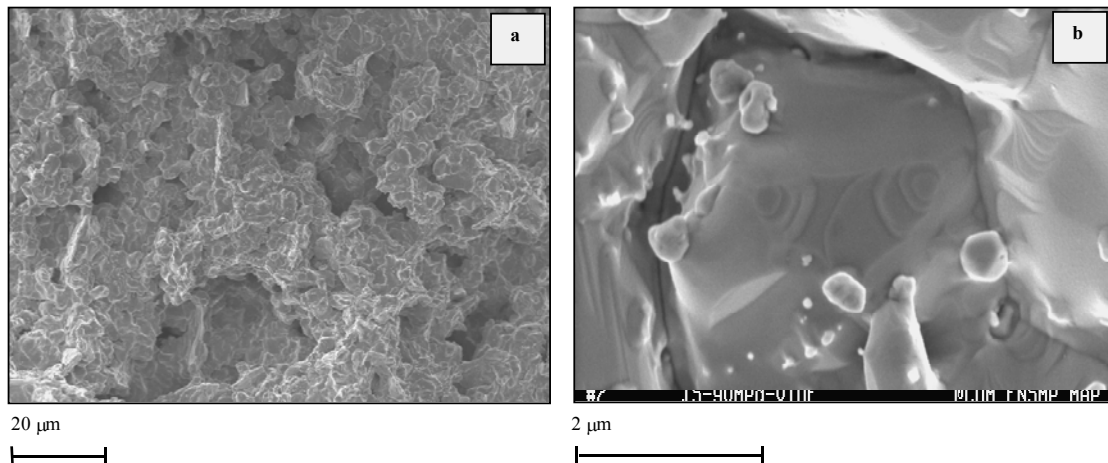


Figure D.II.5. Applied engineering stress versus creep time to failure Experimental results on SC, NC4.0 and NC1.2 specimens

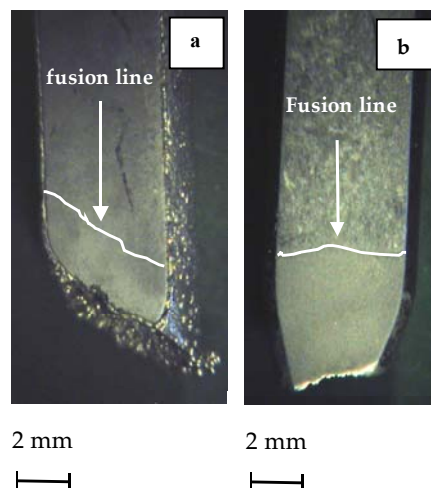
Fracture surfaces were also examined, especially these of the specimens tested under vacuum for which non extensive oxidation of the specimen surface has occurred. It is shown in **figure D.II.6a** and **D.II.6b** that intergranular fracture is

the dominating fracture mechanism. The comparison with the same observations on the base metal presented in Gaffard et al (2005a) shows that the contribution of intergranular fracture to the specimen fracture is really larger in the weldment than in the base metal.



*Figure D.II.6. Fracture surface of a creep specimen tested under vacuum (90 MPa – 1,000 hours)
SEM observation – (a) General view – (b) Closer view*

For better understanding of the creep fracture properties, attention was focused on the specimen necking and on the shape of the fracture surface. As shown in figures D.II.7a and D.II.7b, the necking of the creep tested specimen is largely lower for long term creep tests. It was also observed for all creep fractured specimens i.e. SC and NC specimens that the fracture surface does not exhibit a round shape. It shows that an anisotropy of mechanical properties probably exists in the weldment due to the multi-pass arc welding. Note about this point, that Brozda and Zeman (1996) evidenced an anisotropy of tensile properties in P91 steel weldments at high temperature (i.e. a difference of 10 MPa – 20 MPa in 0.2% proof stress and tensile strength between longitudinal and transverse direction).



*Figure D.III.7. Creep Fracture behaviour of the creep tested cross-weld specimens – Observation of longitudinal cross-section
(a) SC specimen - 50 MPa (b) SC specimen – 100 MPa*

2.3. Creep damage mechanisms in the weldment

SEM investigations of weldment specimens cross-sections evidence that damage is mainly intergranular cracking. This point can be observed in figure D.II.8a where a numbers of intergranular cracking are evidenced. More spherical cavities can also be found but they obviously result from intergranular cracking of small equiaxed grain boundaries as they exhibits polygonal edges (The metallographic preparation is probably responsible for the formation of this type of cavities). When preparing the specimens with a soft polishing which unfortunately strongly diminishes the backscattered electron (BSE) channelling contrast, the occurrence of intergranular cracking can be more clearly evidenced (see figure D.II.8b). Moreover, it is shown in figure D.II.8a that the cracks mainly developed at the boundaries of grain of approximately 30 µm in average size. Note also that the micrograph of figure D.II.8a was taken in

the cross-sections of a NC4.0 specimens at the onset of creep fracture (The creep test was interrupted in the late stage of tertiary creep), showing that only a small amount of grain boundaries, probably the prior packet boundaries, are concerned with intergranular cracking.

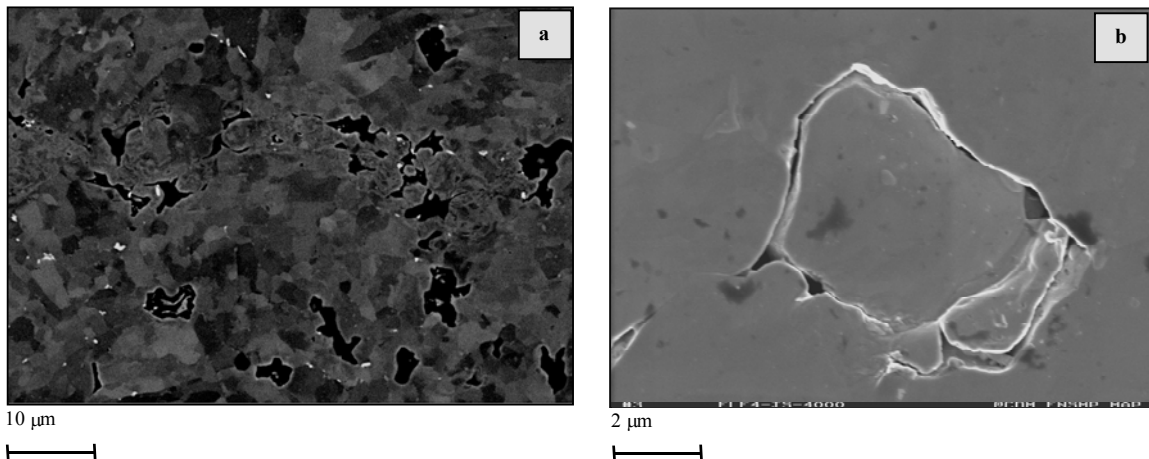


Figure D.II.8. Cavity growth in the HAZ of cross-weld specimens (SEM observation after mechanical polishing)

SEM investigations, using the BSE channelling contrast, of longitudinal cross-sections after colloidal silica also confirmed that rupture occurs in the fine equiaxed grain microstructure of the ICHAZ for all the creep tested specimens.

2.4. Determination of creep strain gradients in cross-weld specimens

Due to creep flow properties mismatch strain gradients developed in cross-weld specimens. It is important to determine these gradients of creep strains in the weldment as it has already shown by Smith et al (2003) and Tu et al (2004). To do so, in the present study, two creep tests on PC specimens were carried out under vacuum (10^{-4} Pa) for applied engineering stress of 90 MPa and 60 MPa. The creep time to failure were respectively of 350 hours and 1,100 hours. Post-mortem observations allowed to measure the evolution of the specimen width from the weld to the base metal. These variations of thickness which are plotted in **figure D.II.9**. It was first evidenced that the heat affected zone is the most deformed area whereas the base metal and the weld metal are little deformed. More precisely, it also allowed to evaluate the width of the deformed heat affected zone to near 5 mm. Taking into account that deformation reaches 5% with a gauge length of 19 mm, it follows that the initial width of the deformed area is obviously of 4 mm. This distance will be used in the FE calculations as the width of the simulated ICHAZ material.

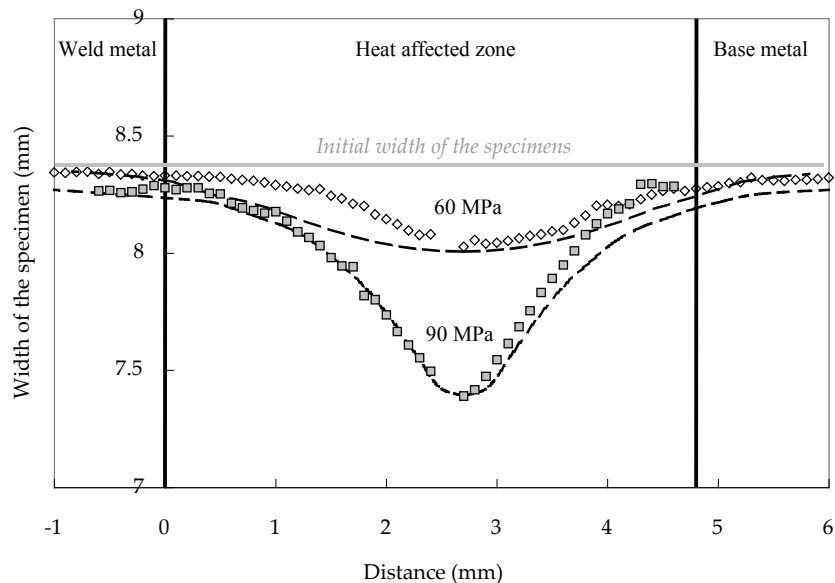


Figure D.II.9. Creep tests on PC specimens (WJP91 weldment): Width of the specimens, symbols = experiments and interrupted lines = calculated (FE simulations)

2.5. Conclusions

The creep flow and damage behaviour of 9Cr1Mo-NbV steels can be described as follow:

- Rupture is of type IV i.e. in the HAZ, and more precisely in the ICHAZ, parallel to the fusion line in all testing conditions at 625°C.
- Damage is mainly intergranular.
- The creep strain is concentrated within a region of four millimetres in length which nearly corresponds to the initial length of the HAZ.
- Creep damage was detected mainly in the HAZ but also in the base metal near the HAZ.
- Round voids corresponding to the decohesion of the MnS particles were observed in the weld metal. However due to the low creep strain rate in this area the size of these cavities only slightly increases during creep.

Therefore, the weldment will be represented as the assembly of three materials i.e. the weld metal, the weakest HAZ and the base metal. From experimental investigations, it is assumed that it is necessary to model both creep flow and damage behaviour of the base metal and the weakest HAZ whereas only the creep flow properties of the weld metal must be represented as no creep damage developed in this area.

3. Modelling creep flow and damage behaviour

In this part, the formulation of the model introduced by Gaffard et al (2005a) to represent high temperature creep flow and damage behaviour from high to low stress is first reminded. It consists in a model integrating and coupling multiple creep flow and damage mechanisms in the framework of the mechanics of porous media.

The model was fitted in Gaffard et al (2005a) and (2005d) to represent respectively the high temperature creep flow and damage behaviour of the base metal and the weakest HAZ (i.e. the ICHAZ) at 625°C. The corresponding model parameters are reminded whereas the creep flow properties of the weld metal, derived from experiments described in Gaffard et al (2005b), are also given.

3.1. Model formulation for the undamaged material

The model was designed to describe the three main mechanisms involved in creep namely quasi-plastic ('qp') loading deformation, matrix viscoplasticity ('vp') and grain boundary diffusion ('d'). An additive decomposition was chosen and the resulting strain rate tensor, is given by:

$$\dot{\underline{\epsilon}} = \dot{\underline{\epsilon}}_e + \dot{\underline{\epsilon}}_{qp} + \dot{\underline{\epsilon}}_{vp} + \dot{\underline{\epsilon}}_d \quad (\text{eq. D.II.1})$$

The strain rate tensor, $\dot{\underline{\epsilon}}_m$, is given by the normality rule:

$$\dot{\underline{\epsilon}}_m = \dot{p}_m \frac{\partial \phi_m}{\partial \underline{\sigma}} \quad (\text{eq. D.II.2})$$

For each mechanism ($m = qp, vp, d$), the equivalent strain rate is given by a Norton power-law:

$$\dot{p}_m = \left\langle \frac{\phi_m}{K_m} \right\rangle^{n_m} \quad (\text{eq. D.II.3})$$

where $\phi_m = \sigma_m^* - R_m$ describes the equipotential surface. σ_m^* is an effective scalar stress which is equal to the von Mises stress, σ_{eq} , for the undamaged material. R_m is the flow stress which is expressed as a function of an effective viscoplastic strain, \bar{p}_m , which accounts for cross hardening between the various deformation regimes:

$$\bar{p}_m = \sum_{m'} H_{mm'}^p \dot{p}_{m'} \quad (\text{eq. D.II.4})$$

The interaction matrix, $H_{mm'}^p$, which determined cross-hardening between deformation mechanisms is given by:

$$H_{mm'}^p = \begin{bmatrix} H_{11} & H_{12} & H_{13} \\ H_{21} & H_{22} & H_{23} \\ H_{31} & H_{32} & H_{33} \end{bmatrix} = \begin{bmatrix} 1 & 1 & 0 \\ 1 & 1 & 0 \\ 0 & 0 & 1 \end{bmatrix} \quad (1 \text{ for } m = qp, 2 \text{ for } m = vp \text{ and } 3 \text{ for } m = d) \quad (\text{eq. D.II.5})$$

The choice of the cross-hardening coefficients is explained in Gaffard et al (2005a) (**chapter B.III**).

3.2. Coupling damage and creep flow

Coupling between creep flow and damage properties is based on the mechanics of porous media (Besson and al (2001)). Three effective stresses σ_m^* , depending on damage, are defined in the quasi-plastic, viscoplastic and diffusional creep regimes. In the quasi plastic creep regime, the effective stress is defined following the description of the Gurson - Tvergaard - Needleman (GTN) model (1984) :

$$\frac{\sigma_{eq}^2}{\sigma_m^{*2}} + 2q_1 f^* \cosh\left(\frac{q_2}{2} \frac{\sigma_{kk}}{\sigma_m^*}\right) - 1 - q_1^2 f^{*2} \stackrel{\text{def.}\sigma_m^*}{=} 0 \quad (\text{eq. D.II.6})$$

where q_1 and q_2 are model parameters, and f^* is a function of the total porosity f_t which is defined to account for cavity coalescence in the later stage of the material creep life.

In the viscoplastic creep regime, the generalization of the Gurson model to high temperature deformation proposed by Leblond – Perrin – Suquet (LPS) (1994) is used:

$$\frac{\sigma_{eq}^2}{\sigma_m^{*2}} + f^* q_1 \left[h_m \left(q_2 \frac{1}{2} \frac{\sigma_{kk}}{\sigma_m^*} \right) + \left(\frac{1-m}{1+m} \right) \frac{1}{h_m \left(q_2 \frac{1}{2} \frac{\sigma_{kk}}{\sigma_m^*} \right)} \right] - 1 - q_1^2 \left(\frac{1-m}{1+m} \right) f^{*2} \stackrel{\text{def.}\sigma_m^*}{=} 0 \quad (\text{eq. D.II.7})$$

where q_1 and q_2 are model parameters, m is the strain hardening coefficient equal to the inverse of the apparent Norton power-law exponent ($m = 1/n$). The function $h_m(x)$ is given by:

$$h_m(x) = \left[1 + mx^{(1+m)} \right]^{1/m} \quad (\text{eq. D.II.8})$$

In the low stress creep regime, **equation D.III.5.** is simplified for $m \rightarrow 1$ leading to a description of the effective stress of the type of the elliptic model (Green (1972)):

$$\frac{1}{1-fq_1} \sigma_{eq}^2 + \frac{fq_1 q_2^2}{4(1-fq_1)} \sigma_{kk}^2 - \sigma_m^{*2} \stackrel{\text{def.}\sigma_m^*}{=} 0 \quad (\text{eq. D.II.9})$$

For the three creep mechanisms 'm', the strain rate tensor is modified to be:

$$\dot{\underline{\epsilon}}_m = (1-f_t) \dot{\underline{p}}_m \frac{\partial \phi_m}{\partial \underline{\sigma}} \quad (\text{eq. D.II.10})$$

where $\phi_m = \sigma_m^* - R_m \cdot \sigma_m^*$ is an effective scalar stress determined by **equation D.II.4, D.II.5** and **D.II.7.** for respectively the quasi-plastic regime, the viscoplastic and the diffusion creep regimes.

The yield stress function, R_m is given in the quasi-plastic regime by:

$$R_{qp}(\bar{p}_{qp}) = R_{oqp} + Q_{qp1}(1 - \exp(-b_{qp1} \bar{p}_{qp})) - Q_{qp2}(1 - \exp(-b_{qp2} \bar{p}_{qp})) \quad (\text{eq. D.II.11})$$

where $R_{oqp} + Q_{qp1}(1 - \exp(-b_{qp1} \bar{p}_{qp}))$ accounts for material hardening and $-Q_{qp2}(1 - \exp(-b_{qp2} \bar{p}_{qp}))$ accounts for material softening associated with the recovery of the microstructure observed for tensile specimens.

In the viscoplastic creep regime, the yield stress function was written as:

$$R_{vp}(\bar{p}_{vp}) = R_{ovp} + Q_{vp1}(1 - \exp(-b_{vp1} \bar{p}_{vp})) - \left\{ Q_{vp2}(1 - \exp(-b_{vp2}(\bar{p}_{vp} - p_c))) \right\} \quad (\bar{p}_{vp} > p_c) \quad (\text{eq. D.II.12})$$

where $R_{ovp} + Q_{vp1}(1 - \exp(-b_{vp1} \bar{p}_{vp}))$ represents material hardening in the first steps of creep deformation and $-Q_{vp2}(1 - \exp(-b_{vp2}(\bar{p}_{vp} - p_c)))$ is the softening function added to account for ageing and softening phenomena.

It was finally assumed that diffusion does not involve material hardening so that,

$$R_d(\bar{p}_d) = 0 \quad (\text{eq. D.II.13})$$

Then, as the macroscopic plastic work (left handside) is equal to the microscopic plastic work (right handside):

$$(1-f_t) \dot{\underline{p}}_m \sigma_m^* = \dot{\underline{\epsilon}}_m : \underline{\sigma} \quad (\text{eq. D.II.14})$$

The evolution of porosity is expressed using mass conservation and taking into account the nucleation of new voids:

$$\dot{f}_m = (1-f_t) \sum_m \text{trace}(\dot{\underline{\epsilon}}_m) + \dot{f}_n = (1-f)^2 \sum_m \dot{\underline{p}}_m \text{trace} \left(\frac{\partial \phi_m}{\partial \underline{\sigma}} \right) + \dot{f}_n \quad (\text{eq. D.II.15})$$

where nucleation is given by the summation of contributions of each mechanism to nucleation:

$$\dot{f}_n = \sum_m \dot{f}_{nm} \quad (\text{eq. D.II.16})$$

As the stress triaxiality ratio may play a key role in the nucleation kinetics (see McLean (1981) and Myers et al (1987)), for each mechanism, the kinetics of nucleation was described by:

$$\dot{f}_{nm} = \left(A_m + B_m \tau^{\alpha_m} \right) \dot{p}_m \quad (\text{eq. D.II.17})$$

where τ is the stress triaxiality ratio, A_m , B_m and α_m are adjustable parameters.

Coalescence starts when a critical porosity ratio is reached. The coarsening law in the high stress ('vp') creep regime was written as:

$$\dot{f}^* = f_t + \delta_c (f_{nm} + f_{gm} - f_{cm}) \quad \text{if } (f_{gm} + f_{nm}) > f_{cm} \quad (\text{eq. D.II.18})$$

$$\dot{f}^* = f_t \quad \text{if } (f_{gm} + f_{nm}) < f_{cm} \quad (\text{eq. D.II.19})$$

In the low stress creep regime ('d'), no coalescence law was used, as for $n = 1$ the stability of the material prevents from void coalescence until the later stage of the specimen creep failure. In fact, due to damage accumulation even in the low stress creep regime it is the viscoplastic creep behaviour that control creep fracture.

3.3. Model parameters

The model integrating multiple creep flow and damage behaviour was fitted for the base metal and the simulated HAZ in respectively Gaffard et al (2005a) and Gaffard et al (2005d). For the sake of simplicity and based on the investigations in cross-sections of cross-weld creep tested specimens, only the creep flow behaviour of the weld metal was considered. However, to take into account the presence of voids in the weld metal, an initial fraction of porosity $f_0 = 0.01$ was introduced in the weld metal.

		Weld Metal	Base Metal	Simulated HAZ
Young's modulus	E	145 GPa	145 GPa	145 GPa
Poisson's ratio	ν	0.3	0.3	0.3
Quasi plastic hardening at 625°C	R_{0qp}	/	173 MPa	145 MPa
	Q_{qp1}	/	128 MPa	30 MPa
	b_{qp1}	/	400	50
	Q_{qp2}	/	80 MPa	25 MPa
	b_{qp2}	/	7.3	10
Viscoplastic hardening at 625°C	R_{0vp}	0 MPa	0 MPa	0 MPa
	Q_{vp1}	40 MPa	40 MPa	40 MPa
	b_{vp1}	2120	569	200
	Q_{vp2}	/	40 MPa	20 MPa
	b_{vp2}	/	75	10
	p_c	/	0.03	0.01
Quasi plastic strain rate effect at 625°C	K_{qp}	/	112 MPah ^{-1/n_{qp}}	240 MPa h ^{-1/n_{qp}}
	n_{qp}	/	5.0	8.6
Viscoplastic strain rate at 625°C	K_{vp}	1233 MPah ^{-1/n_{vp}}	542 MPah ^{-1/n_{vp}}	395 MPa h ^{-1/n_{vp}}
	n_{vp}	3.8	5.38	4.95
Diffusion strain rate at 625°C	K_d	0.33 .10 ⁹ MP h ^{-1/n_d}	0.33 .10 ⁹ MPa h ^{-1/n_d}	0.020 .10 ⁹ MPa h ^{-1/n_d}
	n_d	1.0	1.0	1.0
LPS model	q_1	1.5		
	q_2	1.0		
	f_c	0.1		
	δ_c	6.0		
<i>Strain hardening coefficients</i>	m_{qp}	0.0	0.0	0.0
	m_{vp}	0.125	0.125	0.105
	m_d	1.0	1.0	1.0

Nucleation by the viscoplastic mechanism	A_{vp1}	0.0	0.01	0.05
	A_{vp2}	0.0	0.15	0.4
	α_v	0.0	2.0	2.0
Nucleation by the diffusional mechanism	A_{d1}	0.0	14.0	5
	A_{d2}	0.0	16.0	0.5
	α_d	0.0	2.0	2.0

Table D.II.3. Models parameters

4. Study of mismatch in creep flow and damage properties

Before performing the three material FE calculations, it is quite interesting to study the mismatch in tensile and creep properties of the three materials.

4.1. Mismatch in tensile properties

To start, the mismatch in tensile properties was determined from the experimental results given in Gaffard et al (2005a) and Gaffard et al (2005d) (**chapters B.III and C.IV**). Note that the tensile properties of the simulated HAZ were determined by finite element simulations after constitutive equations representing the tensile behaviour from inverse analysis. It is shown in **figure D.II.10** that for strain rates larger than 10^{-3} s^{-1} , the tensile properties of the base metal are increased by more than 50 MPa in comparison with those of the simulated HAZ. However, this difference tends to disappear as for strain rates lower than 10^{-4} s^{-1} the tensile properties of the two materials are quite similar.

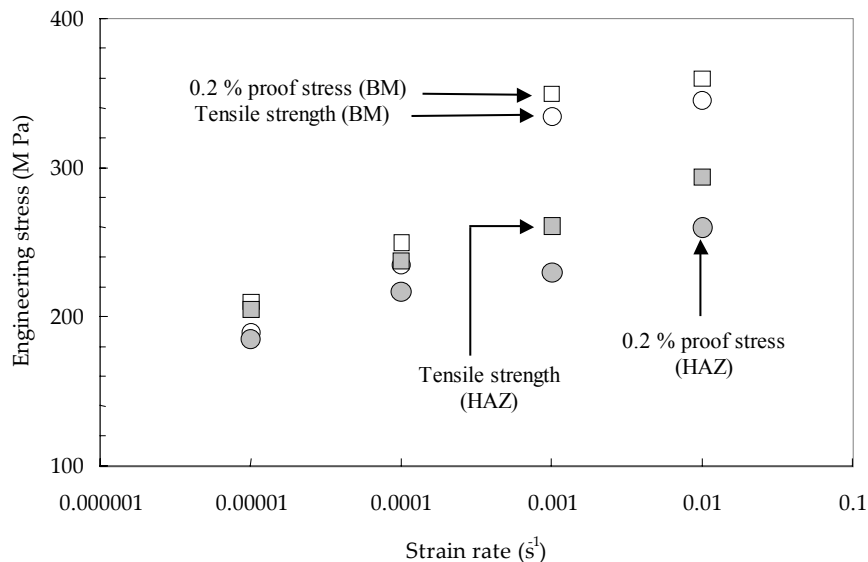
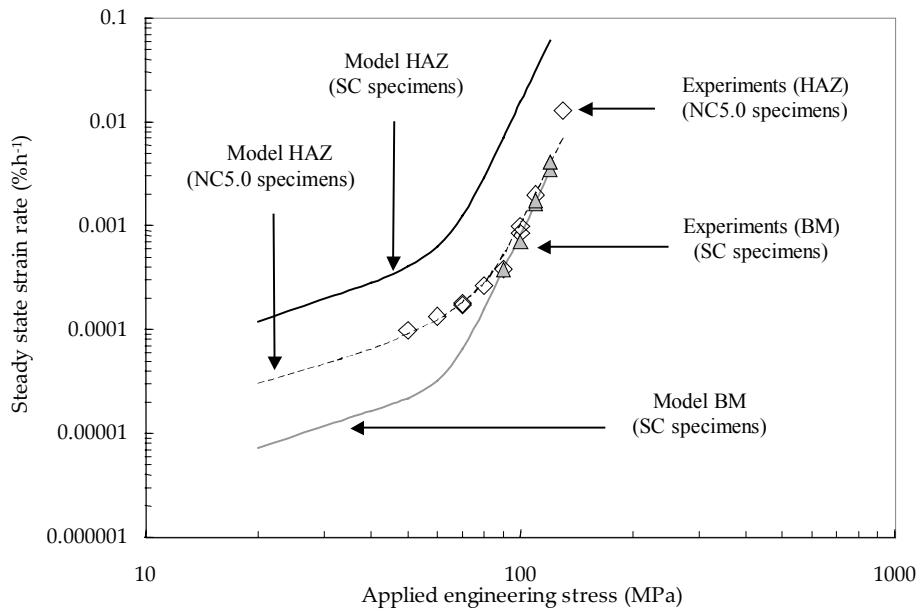


Figure D.II.10. Tensile properties (i.e. 0.2% proof stress and tensile strength) for the base metal and the simulated HAZ

4.2. Mismatch in creep flow properties

The creep flow properties of the simulated HAZ were determined in Gaffard et al (2005a) and Gaffard et al (2005d) (**chapters B.III and C.IV**) and are plotted in **figure D.II.11**. The Norton power-law exponents are quite similar both in the high stress and the low stress creep regimes. The transition stress between the two creep flow regimes is also the same for the base metal and the simulated HAZ i.e. 70 MPa. Nevertheless, the steady state creep strain rates are increased by approximately a factor of ten in the simulated HAZ. Note that for the sake of clarity the steady state creep flow properties of the weld metal are not reported in **figure D.II.11** as steady state creep strain rates of the weld metal are very closed to these of the base metal.

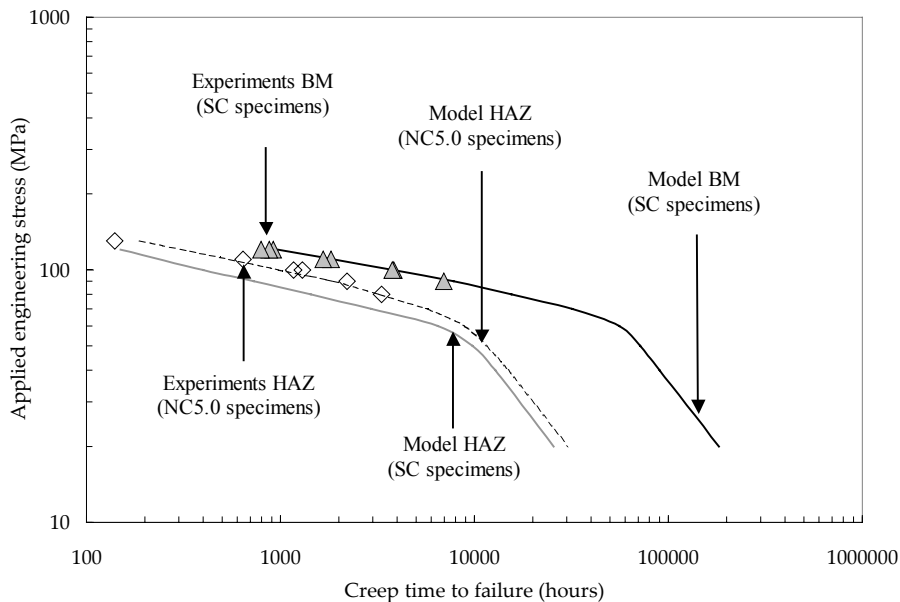


*Figure D.II.11. Steady state strain rate versus stress at 625°C for the base metal and the simulated ICHAZ
Experimental results (symbols) and Model (lines)*

Therefore, it can be concluded that the 9Cr1Mo-NbV steel weldments are hard/soft/hard weldments as the creep strain of the HAZ is obviously constrained by the lower creep strains of the base metal on one side and the weld metal on the other side.

4.3. Mismatch in creep fracture properties

The creep failure models determined in Gaffard et al (2005a) and Gaffard et al (2005d) (**chapter B.III** and **chapter C.IV**) allow to compare the creep fracture properties of the base metal and the ICHAZ. The plot in **figure D.II.12** shows that the transition between the two creep damage mechanisms occurs for creep lifetimes larger than 50,000 hours in the base metal and for creep lifetimes only larger than 9,000 hours in the simulated HAZ. In the high stress creep regime, the creep strength of the simulated HAZ is 30% lower than that of the base metal.



*Figure D.II.12. Steady state strain rate versus stress at 625°C for the base metal and the simulated ICHAZ
experimental results (symbols) and Model (lines)*

5. Modelling creep flow and mechanical behaviour of weldment

The aim of the present study is to integrate the creep flow and damage behaviour of the base metal, the weakest HAZ and the weld metal, separately determined, into multi-materials FE calculations of the weldment. The model parameters

are not fitted with the results of creep tests on cross-weld specimens. The ability of the method to well predict creep flow and damage behaviour of cross-weld specimens is investigated in the following.

5.1. Numerical procedures

The model was implemented in the finite element software Zebulon (Besson and Foerch (1997)). A fully implicit integration scheme was used to integrate the material constitutive equations, which allows the calculation of the consistent tangent matrix (Simo and Taylor (1985)). The method is derived from the one detailed in Besson et al (2001a), modified to deal with an arbitrary number of deformation mechanisms. Finite strains were treated using co-rotational reference frames (Besson et al (2001b)). The material was considered to be broken when f^* was greater than $\frac{1}{q_i} - \epsilon$,

where $\frac{1}{q_i}$ is the theoretical value for f^* at fracture and ϵ is taken equal to 0.01. As soon as the material was considered as

broken, its behaviour was replaced by an elastic behaviour with a very low stiffness (Young's modulus: $E_b = 1$ MPa). A similar technique was used in Liu et al (1994) showing convergence of the results for sufficiently low values of the Young's modulus E_b . Gauss points where these conditions are met are referred to as "broken Gauss points". In regions where damage develops, eight-node axisymmetric elements with reduced integration (ie. 4 Gauss points) were used. Elements containing two broken Gauss points were automatically removed by checking this condition after each time increment.

Both two and three dimensional axisymmetrical meshes were chosen. Specimens were divided into three parts corresponding to the base metal, the weld metal and the HAZ. The mesh size and mesh design play an important role in calculations involving crack initiation and propagation (Rousselier (1987); Tvergaard and Needleman (1984); Xia and al. (1995)). Due to the softening of the material, the mesh size influences the fracture energy and it is often argued that this quantity should be adjusted on experiments involving stable crack growth in order to fit the crack energy (Gullerud et al. (2000); Rousselier (1987)). The mesh size is then interpreted as some microstructural characteristic length (e.g. a multiple of the interparticle spacing or grain size). For 2D calculations, the elements, in the region where damage was expected to develop (i.e. in the HAZ), were quadratic squares (with reduced integration) whose edge size is equal to 100 μm . Note that this element size was used to fit the multiple creep flow and damage mechanisms model of the three materials. As 3D calculations were too much time consuming, the mesh size was increased but a particular attention has been focused on the refinement of the mesh within the HAZ to ensure that the surface boundary condition and the locally high stress gradients could be adequately represented.

5.2. Modelling creep tests on SC cross-weld specimens – Study of geometrical effects

5.2.1. Geometry

2D axisymmetric FE calculations were performed with setting the HAZ perpendicular to the fusion line. The most important geometrical parameter i.e. the width of the HAZ area, l_{HAZ} , was experimentally determined as $l_{\text{HAZ}} = 4\text{mm}$ in **section 3.4**. It has also already been shown, by means of simple analysis of creep strain in cross-weld specimens, in Gaffard et al (2005b) that this value of l_{HAZ} allows to well represent the cross-weld specimens creep deformation, at least when using a three materials representation but without integrating the effect of damage.

The constitutive equations of **section 3.1** and **section 3.2** were used to represent creep flow and damage behaviour of the base metal, the weld metal and the HAZ (see **table D.II.3** for model parameters). The significance of l_{HAZ} was ensured by comparing the 3D calculated PC specimens reduction in thickness with the same experimental measurements (see **figure D.II.9**).

5.2.2. Results - Description of mechanical fields in SC cross-weld specimens

For a better comprehension of the creep flow and damage behaviour of cross-weld specimens, it is very interesting to determine the effect of the mismatches in material creep properties on stress and strain redistributions. The general behaviour of the mechanical fields are given in **figure D.II.13**. It was evidenced that both the von Mises equivalent and principal stresses are maximum in the HAZ at the centre of the specimen and in both the weld and base metal near the HAZ at the outer face of the specimen. The stress triaxiality ratio is maximum in the HAZ at the interfaces between the HAZ and the weld and base metals. About this point, it was also evidenced that higher stress triaxiality ratios, which are concentrated at the materials interfaces, are reached at low stresses ($\tau_{\text{max}} > 1.0$) than at high stresses ($\tau_{\text{max}} < 0.5$).

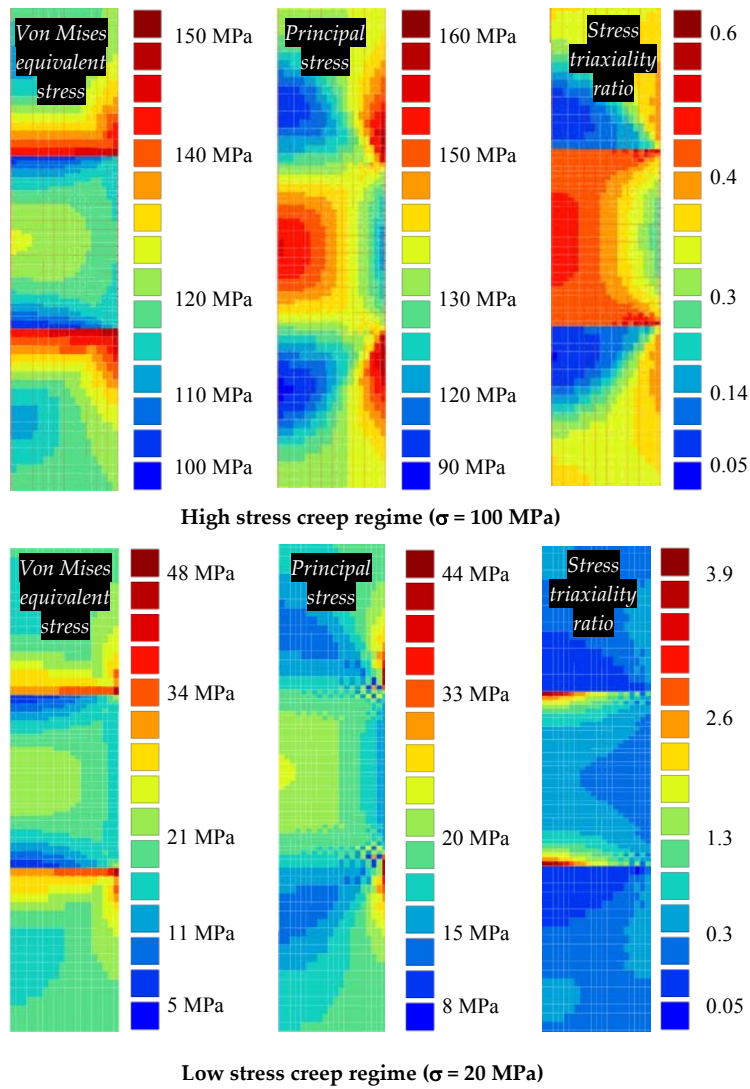


Figure D.II.13. Stress and strain distributions in SC cross-weld specimens in the steady state creep regime

The comparison between experiments and FE calculations exhibit a quite good agreement from high to low stress (see figure D.II.2). About this point, it is very important to notice that the creep models of the base metal, the weld metal and the simulated HAZ were not refitted to account for creep results on cross-weld specimens. The model and the three material representation also succeeds in predicting the specimen necking at the creep failure stage from high to low stress as can be shown in figure D.II.14 where the transition between high and low stress related creep fracture mechanisms is also evidenced.

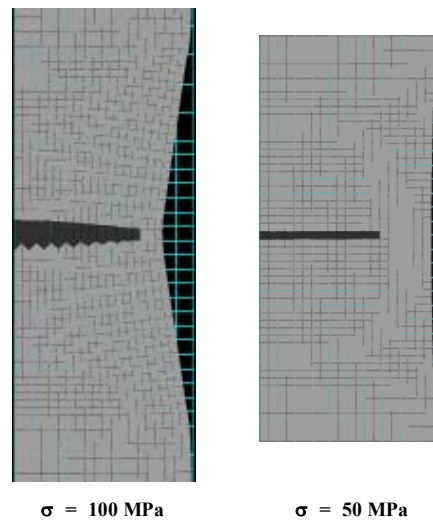


Figure D.II.14. Calculated specimen necking and cracking for creep tests on cross-weld SC specimens

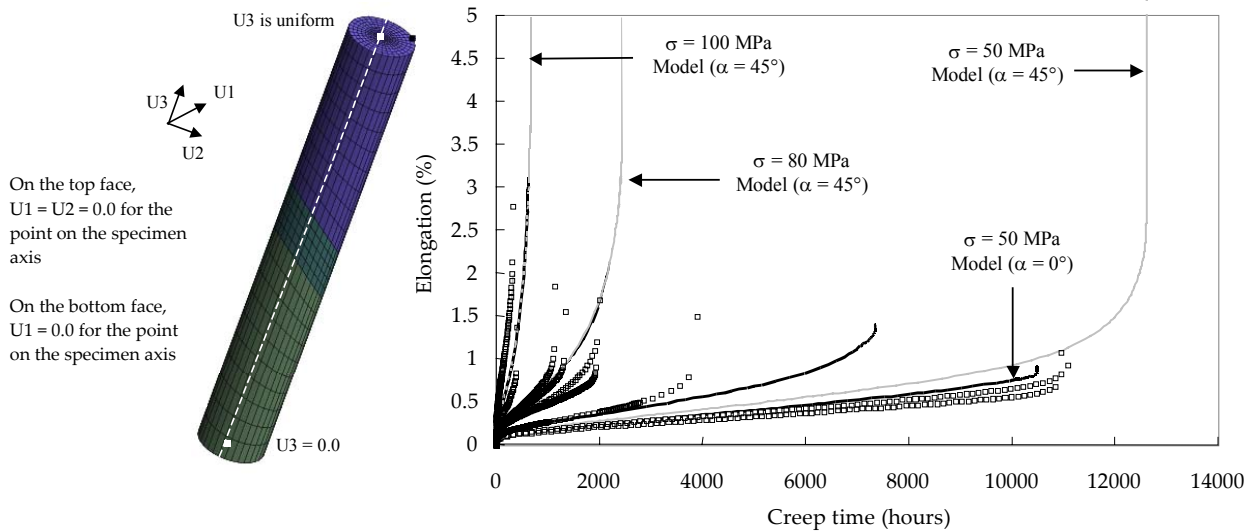
5.2.3. Effects of the geometrical parameters

The SC specimen geometry was used to study the effects of the geometrical parameters on the creep response. First the effect of the width of the HAZ area was explored. To do so, 2D axisymmetric calculations were performed with dividing the HAZ width by two: i.e. $l_{HAZ} = 2$ mm. A strong effect on creep lifetime was observed as can be shown in **table D.II.4.** at high stress as for $l_{HAZ} = 2$ mm, the creep lifetime is higher of approximately 40% than the creep lifetime for $l_{HAZ} = 4$ mm. The effect is however not so marked in the low stress creep regime as the difference in creep lifetime predictions is lower than 10% for an applied engineering stress of 50 MPa. These results also show that the value of the l_{HAZ} must be experimentally determined from creep tests at high stress level.

	100 MPa	80 MPa	60 MPa	50 MPa
t_r (4 mm) / t_r (2 mm)	0.68	0.72	0.86	0.92

*Table D.II.4. Effect of the HAZ width on creep lifetime of SC specimens
Results of 2D axisymmetric calculations*

Then, 3D calculations were performed for various values of the weld angle between the fusion line and the loading axis namely 0° , 22.5° and 45° (The FE mesh is shown in **figure D.II.15**). FE calculations showed that the stress triaxiality ratio is increased when the angle between the loading axis and the HAZ is increased. The effect of weld angle is opposed to that of the HAZ width as both the creep lifetime and the creep curves (i.e. the overall deformation of the specimens) are not affected in the high stress creep regime (for $\sigma = 100$ MPa and 80 MPa) but the creep lifetime is increased for higher value of the weld angle in the low stress creep regime (for $\sigma = 50$ MPa, the creep lifetime is increased by 10%) as can be shown in **figure D.II.15**. Note that Hyde et al (2001) have shown that the creep lifetime is increased by 10% when the weld angle is larger than 15° . 3D FE calculations revealed the shear of the specimens at the HAZ/base metal and HAZ/weld metal interfaces at low stresses, also experimentally observed, can explained the tendency for high values of the weld angle.



*Figure D.II.15. Effect of weld angle on cross-weld specimens creep response:
Black lines = 2D calculations i.e. $\alpha = 0^\circ$ - Grey lines = 3D calculations with $\alpha = 45^\circ$*

Finally, the effect of the specimen diameter has also already been largely studied by Storesund and Tu (1995) and Law and Payten (1997). They concluded that the cross-weld specimen creep lifetime can be largely increased when the diameter of the specimen is increased. To address this point, 2D axisymmetric calculations were performed for SC cross-weld specimens with varying the value of the specimen diameter (i.e. 2 mm, 3 mm, 10 mm, 20 mm and 30 mm). It allows to plot a graph that can be very useful for design purposes. Indeed, it shows how the results of creep tests on cross-weld SC specimens can be used to predict the creep failure properties of components thicker than the SC specimens. It was also shown that for a specimen diameter of 5.0 mm and $l_{HAZ} = 2$ mm the creep lifetime is the same from high to low stress than for a specimen diameter of 10.0 mm and $l_{HAZ} = 4$ mm which confirmed that constraint effects do not depend on the specimen diameter, ϕ , or the HAZ length, l_{HAZ} but on the ratio l_{HAZ} / ϕ . In **figure D.II.16**, the evolution of the ratio $(t_r / t_{r,ref})$ is plotted versus $(l_{HAZ} / \phi) / (l_{HAZ,ref} / \phi_{ref})$ were $\phi_{ref} = 5.0$ mm and $l_{HAZ,ref} = 4.0$ mm.

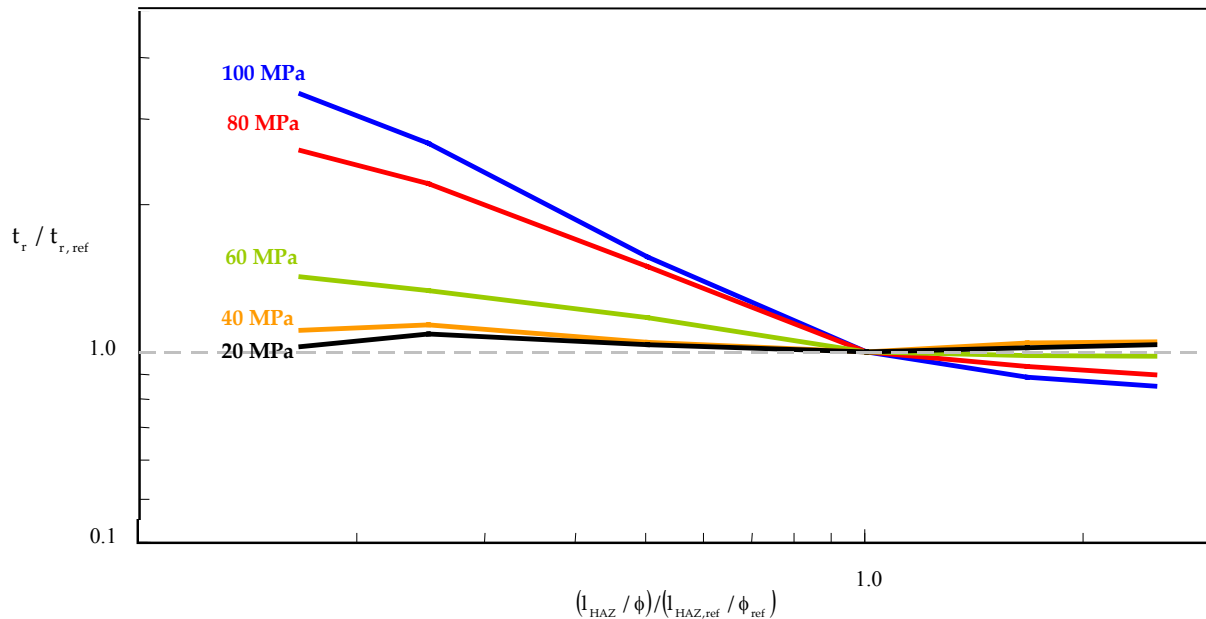


Figure D.II.16. Effect of the ratio (I_{HAZ} / ϕ) on weldment creep lifetime

Results plotted in **figure D.II.16** evidenced that the effect of the ratio (I_{HAZ} / ϕ) is especially quite strong in the high stress creep regime as the creep lifetime increases when the ratio (I_{HAZ} / ϕ) decreases (when the ratio (I_{HAZ} / ϕ) is reduced by a factor of 2, the creep lifetime is increased by a factor of 3), whereas the effect is not so marked at low stress. The insensitivity of the creep response to specimen geometry in the low stress crepe regime can probably be related to the absence of any stress redistributions in the diffusion creep regime.

5.3. Modelling creep tests on NC cross-weld specimens notched in the HAZ

For the sake of simplicity and as the study on cross-weld specimens have shown that the weld angle has little effect on the cross-weld specimens, 2D axisymmetric calculations were performed. As the base metal and the weld metal have the same creep flow properties, a two materials representation was also chosen (see **figure D.II.17**).

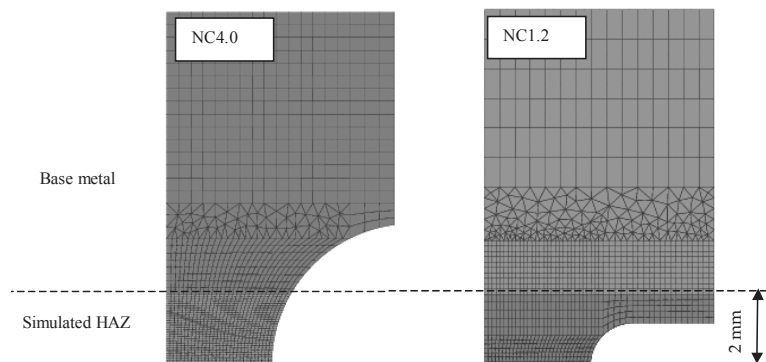


Figure D.II.17. Meshes for FE calculations on NC1.2 and NC4.0 cross-weld specimens

The agreement between experimental and calculated creep curves is quite good as can be shown in **figures D.II.3** and **D.II.4**.

5.4. Predictions of weldments creep lifetime

As the accuracy of the model to represent creep flow and damage behaviour of 9Cr1Mo-NbV weldments was ensured, a predictive curve of the creep lifetime of cross-weld specimens was established and compare to experimental results in **figure D.II.18**. The model for the simulated ICHAZ was also plotted on the same representation (see **figure D.II.18**). A

good agreement was found between experiments and predicted values even if the model is quite optimistic in comparison with the minimum values of the measured cross-weld SC specimens creep lifetimes. In addition, the results of the present study are quite pessimistic for the possible use 9Cr1Mo-NbV steels weldments service temperature as high as 625°C (50 MPa – 10,000 hours in comparison with the design criterion of 100 MPa – 100,000 hours).

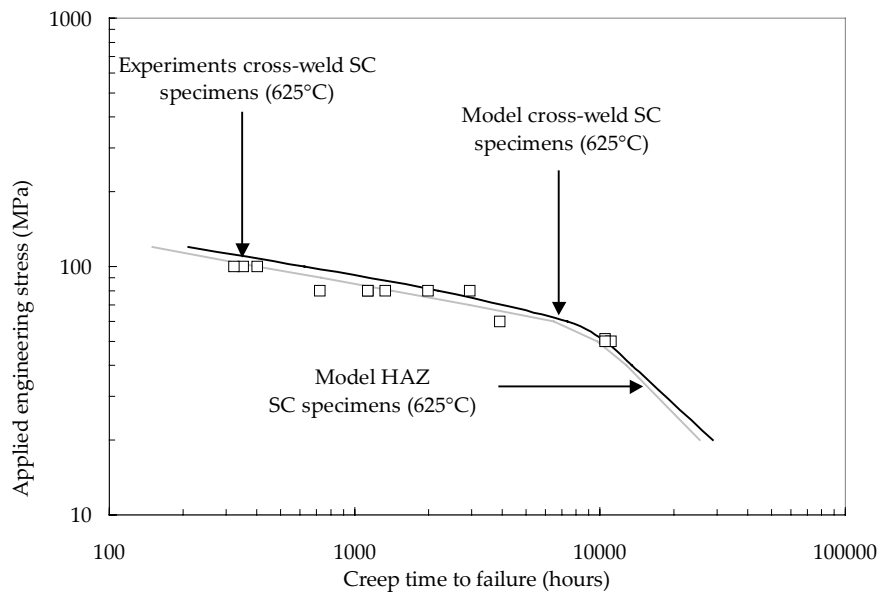


Figure D.II.18. Predictions of cross-weld specimens creep lifetime

Conclusions

In the present study, FE calculations with taking into account materials heterogeneities, were used to predict the creep response of 9Cr1Mo-NbV steels weldments. The originality of the work was to independently experimentally determine and model the creep flow and damage behaviour of the three materials chosen to represent the weldment.

When integrating the constitutive laws corresponding to the three materials into multi-material FE modelling, a satisfactory agreement was found between the predicted and experimentally measured weldment creep lifetimes.

Assuming that the physical mechanisms were finely taken into account, geometrical effects (weld angle, width of the HAZ, specimen diameter) could be studied with the conclusions that for 9Cr1Mo-NbV steel weldments:

1. The width of the HAZ strongly determines the weldment creep properties in the high stress creep regime due to constraint effects but the influence of constraint effects on the weldment creep lifetime tends to disappear in the low stress creep regime.
2. Comparison between 2D axisymmetric and 3D calculations with weld angles up to 45° shows that the weld angle has a little influence on the weldment creep response except at low stress probably due to the shear of the specimen at the interfaces between materials.

Finally, it is evidenced from experimental observations and especially from the large experimental scatter band observed for creep tests on cross-weld specimens, that other metallurgical phenomena have to be explored in a future work as:

1. The influence of anisotropy in creep properties which probably exists due to the multipass arc welding procedure and was experimentally evidenced by the ovalization of the fracture surfaces.
2. The presence of welding defects in the weld metal or near the fusion line which can largely affects the weldment creep strength.
3. The influence of the residual stresses whose study has focused little attention until now despite they may be locally high especially in thick welded components.

Acknowledgements

Financial and technical support from Electricité de France (EdF), Framatome and Le Commissariat à l'Énergie Atomique (CEA) is acknowledged.

References

- ASME Code case N-47 (1987). Class 1 components in elevated temperature service. *ASME, New York*.
- Besson J., Foerch R. (1997). Large scale object-oriented finite element code design. *Computer Methods in Applied Mechanics and Engineering*. **142**. 165-187.
- Besson J., Cailletaud G., Chaboche J.L., Forest S. (2001a). Mécanique non linéaire des matériaux. *Hermes – Paris* (in French).
- Besson J., Steglich D., Brocks W. (2001b). Modeling of crack growth in round bars and plane strain specimens. *International Journal of Solids and Structures*, **38 (46-47)**, 8259-8284.
- Brozda J., Zeman M. (1996). Weldability of 9Cr-1Mo-Nb, V P91 steel intended for service in the power industry. *Welding International*. **10(5)**. 370-380
- DeWitte M., Coussement C. (1991). Creep properties of 12%Cr and improved 9%Cr weldments. *Materials at high temperature*. **9(4)**. 178-184.
- Eggeler G., Rameke A., Coleman M., Chew B., Peter G., Burblies A., Hald J., Jefferey C., Rantal J., De Witte M., Mohrmann R. (1994). Analysis of creep in a welded 'P91' pressure vessel. *International journal of pressure vessels and piping*. **60**. 237-257.
- Gaffard V., Besson J., Gourgues-Lorenzon A.F. (2005a). Creep failure model of a tempered martensitic stainless steel integrating multiple deformation and damage mechanisms. *Submitted to International journal of fracture*.
- Gaffard V., Gourgues-Lorenzon A.F., Besson J. (2005b). High temperature creep flow and damage properties of 9Cr1Mo-NbV steels: base metal and weldment. *Submitted to Nuclear engineering and design*.
- Gaffard V., Gourgues-Lorenzon A.F., Besson J. (2005c). High temperature creep flow and damage properties of the weakest area of 9Cr1Mo-NbV steel weldments. *Submitted to ISIJ International*.
- Gaffard V., Besson J., Gourgues-Lorenzon A.F. (2005d). Modelling creep flow and damage behaviour of the weak area of the weakest area of 9Cr1Mo-NbV steel weldments. *Submitted to Engineering fracture mechanics*.
- Green R. (1972). A plasticity theory for porous solids. *International journal of mechanical science*. **14**. 215-224.
- Gullerud A.S., Gao X., Dodds Jr.R. and Haj-Ali R. (2000). Simulation of ductile crack growth using computational cells: numerical aspects. *Engineering Fracture Mechanics*. **66**. 65-92
- Hyde T.H., Sun W. (2002). Effect of bending load on the creep failure behaviour of a pressurised thick walled CrMoV pipe weldment. *International journal of pressure vessels and piping*. **79**. 331-339.
- Hyde T.H., Sun W., Becker A.A. (2001). Creep crack growth in welds: a damage mechanics approach to predicting initiation and growth of circumferential cracks. *International journal of pressure vessels and piping*. **78**. 765-771.
- Hyde T.H., Sun W., Becker A.A. (2000). Failure prediction for multi-material creep test specimens using a steady state creep rupture stress. *International journal of mechanical sciences*. **42**. 401-423.
- Hyde T.H., Sun W., Becker A.A., Williams J.A. (2001). Effect of weld angle and axial load on the creep failure behaviour of an internally pressurised thick walled CrMoV pipe weld. *International journal of pressure vessels and piping*. **78**. 365-372.
- Hyde T.H., Tang A. (1998). Creep analysis and life assessment using cross weld specimens. *International materials reviews*. **43(6)**. 221-239.
- Hyde T.H., Xia L., Becker A.A. (1996). Prediction of creep failure in aeroengine materials under multiaxial stress states. *International journal of mechanics science*. **38(4)**. 385-403.
- Jacobova A., Vodarek V., Hennhofer K., Foldyna V. (1998). Microstructure and creep properties of P91 steel and weldments. *Materials for advanced power engineering - 6th Liege Conference*. 373-382.
- Kojima T., Hagashi K., Kajita T. (1995). HAZ softening and creep rupture strength of high Cr ferritic steel weldments. *ISIJ International*. **35(10)**. 1284-1290.
- Koplik J., Needleman A. (1988). Void growth and coalescence in porous plastic solids. *International Journal of Solids and Structures*. **24(8)**. 835-853.
- Laha K., Chandravathi K.S., Bhanu Santara Ras K., Mannan S.L. (2000). Microstructural evolution, creep deformation and rupture behaviour of 9Cr1Mo steel base metal, weld metal and weld joint. *Transactions of the Indian Institute of metals*. **55(3)**. 217-221.
- Law M., Payten W. (1997). Weld performance under creep using finite element modelling. *International journal of pressure vessels and piping*. **72**. 45-49.
- Leblond J.B., Perrin G., Suquet P. (1994). Exact results and approximate models for porous viscoplastic solids. *International journal of plasticity*. **10(3)**. 213-235.
- Li X.Y., Hao Q., Shi Y.W., Lei Y.P., Marquis G. (2003). Influence of mechanical mismatching on the failure of welded joints by void nucleation and coalescence. *International journal of pressure vessels and piping*. **80**. 647-654.

- McLean D. (1981). Damage accumulation in creep. *Annales de chimie*. **6**.124-139.
- Myers M.R., Pilkington R. , Needham N.G. (1987). Cavity nucleation and growth in a 1%Cr-0.5%Mo steel. *Materials Science and Engineering*. **95(2)**. 81-91.
- Parker J.D., Stratford G.C. (1996). Strain localization in creep testing of samples with heterogeneous microstructures. *International Journal of Pressure Vessels and Piping*. **68**. 135-143.
- Perrin I.J., Hayhurst D.R., Ainsworth R.A. (2000). Approximate creep rupture lifetime for butt welded ferritic steel pressurised pipes. *European journal of mechanics A/Solids*. **19**. 223-258.
- Perrin I.J., Hayhurst D.R. (1999). Continuum damage mechanics analyses of type IV creep failure in ferritic steel crossweld specimens. *International journal of pressure vessels and piping*. **76**. 599-617.
- Perrin I.J., Hayhurst D.R. (1996). A method for the transformation of creep constitutive equations. *International journal of pressure vessels and piping*. **68**. 299-309.
- Rousselier G. (1987). Ductile fracture models and their potential in local approach of fracture. *Nuclear Engineering and Design*. **105**. 97-111.
- Segle P., Tu S.T., Storesund J., Samuelson L.A. (1996). Some issues in life assessment of longitudinal seam welds based on creep tests with cross weld specimens. *International journal of pressure vessels and piping*. **66**. 199-222.
- Simo J.C, Taylor R.L. (1985). Consistent tangent operators for rate-independent elastoplasticity. *Computer Methods in Applied Mechanics Engineering*. **48(1)**. 101-118.
- Spigarelli S., Quadrini E. (2002). Analysis of the creep behaviour of a modified P91 (9Cr1Mo-NbV) welds. *Materials and design*. **23**. 547-552.
- Storesund J., Tu S.T. (1995). Geometrical effect on creep in cross weld specimens. *International Journal of Pressure Vessels and Piping*. **62**. 179-193.
- Tu S.T., Segle P., Gong J.M. (2004). Creep damage and fracture of weldments at high temperature. *International journal of pressure vessels and piping*. **81**. 199-209.
- Tu S.T., Segle P., Gong J.M. (1996). Strength design and life assessment of welded structures subjected to high temperature creep. *International journal of pressure vessels and piping*. **66**. 171-186.
- Tvergaard V., Needleman A. (1984). Analysis of the cup cone fracture in a round tensile bar. *Acta Metallurgica*. **32(1)**. 157-169.
- Wang Z.P., Hayhurst D.R. (1995). Characterisation of creep behaviour for multimaterials structures such as ferritic steel pipe weldments. *UMIST Report DMM.95.1*.
- Wang Z.P., Hayhurst D.R. (1993). Materials design data for design of ferritic pressure vessels weldments. *International journal of pressure vessels and piping*. **55**. 461-479.
- Xia L., Shih C.F., Hutchinson J. W. (1995). A computational approach to ductile crack growth under large scale yielding conditions. *Journal of the Mechanics and Physics of Solids*. **43(3)**. 389-413.

Chapter D.III. Predictions of creep lifetime of cross-weld specimens by means of elasto-viscoplastic calculations and the use of a rupture criterion in post-calculation

The aim of the present chapter is to propose a method to predict weldments creep lifetime based on elasto-viscoplastic finite elements calculations. A rupture criterion derived from both the peak rupture stress method and the Monkman-Grant relationship is then used in post-treatment.

1. Presentation of FE calculations

In the present chapter, multi material FE calculations are performed using the models determined for the base metal and the simulated heat affected zone without taking into account any contribution of damage. Following the procedure described in the previous chapter, FE calculations were performed on simple assemblies of two materials as it was shown that base and weld metals exhibit quite similar creep flow properties (see description of **figure D.III.1**).

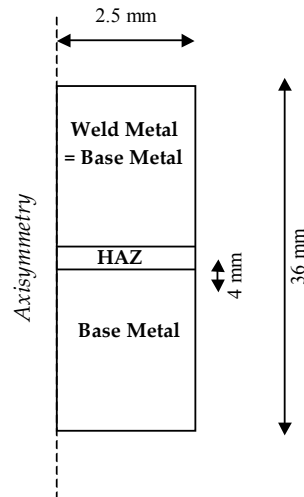


Figure D.III.1. Geometry of specimen for FE 2D axisymmetric calculations

FE calculations were performed using the constitutive laws describing the creep flow properties of the base metal and simulated HAZ without taking into account any damage contribution (i.e. only the primary and steady state creep regimes are represented). Moreover, only the two creep mechanisms were considered i.e. the quasi-plastic creep regime was neglected so that the strain rate tensor was written as:

$$\dot{\underline{\epsilon}} = \dot{\underline{\epsilon}}_e + \dot{\underline{\epsilon}}_{vp} + \dot{\underline{\epsilon}}_d \quad (\text{eq. D.III.1})$$

The elastic strain tensor $\dot{\underline{\epsilon}}_e$ is related to the stress tensor by the Hooke's law: $\underline{\sigma} = \underline{\underline{C}} : \underline{\epsilon}_e$ where $\underline{\underline{C}}$ is the fourth order stiffness tensor. The Young's modulus was taken to 145 GPa and the Poisson ratio to 0.3. The non-elastic (viscoplastic and diffusion) strain rates tensor are given by the normality rule:

$$\dot{\underline{\epsilon}}_{vp} = \frac{3}{2} \dot{p}_{vp} \frac{\underline{s}}{\sigma_{eq}} \quad \text{and} \quad \dot{\underline{\epsilon}}_d = \frac{3}{2} \dot{p}_d \frac{\underline{s}}{\sigma_{eq}} \quad (\text{eq. D.III.2})$$

where \underline{s} is the stress deviator, σ_{eq} is the von Mises equivalent stress and the viscoplastic multipliers are assumed to be given by Norton power-laws so that:

$$\dot{p}_{vp} = \left\langle \frac{\sigma_{eq} - R_{vp}}{K_{vp}} \right\rangle^{n_{vp}} \quad \text{and} \quad \dot{p}_d = \left\langle \frac{\sigma_{eq}}{K_d} \right\rangle^{n_d} \quad (\text{eq. D.III.3})$$

where the yield stress function is given by:

$$R_{vp}(\bar{p}_{vp}) = R_{ovp} + Q_{vp1}(1 - \exp(-b_{vp1} \bar{p}_{vp})) - \left\{ Q_{vp2}(1 - \exp(-b_{vp2}(\bar{p}_{vp} - p_c))) \right\} \quad (\bar{p}_{vp} > p_c) \quad (\text{eq. D.III.4})$$

The model parameters for the multiple damage mechanism model without any damage contributions are given for both the base metal and the simulated HAZ in **table D.III.1**.

		Base Metal	Simulated HAZ
Young's modulus	E	145 GPa	145 GPa
Poisson's ratio	ν	0.3	0.3
Viscoplastic hardening at 625°C	R_{0vp}	0 MPa	0 MPa
	Q_{vp1}	40 MPa	40 MPa
	b_{vp1}	569	200
	Q_{vp2}	40 MPa	20 MPa
	b_{vp2}	75	10
	p_c	0.03	0.01
Viscoplastic strain rate at 625°C	K_{vp}	542 MPah ^{-1/n_{vp}}	395 MPah ^{1/n_{vp}}
	n_{vp}	5.38	4.95
Diffusion strain rate at 625°C	K_d	0.33 · 10 ⁹ MPah ^{-1/n_d}	0.020 · 10 ⁹ MPah ^{1/n_d}
	n_d	1.0	1.0

Table D.III.1. Creep flow properties of the base metal and the simulated HAZ at 625°C

2. Results of FE calculations

The FE calculations were used to determine the distribution of the von Mises equivalent stress, σ_{eq} , the principal stress, σ and the stress triaxiality ratio, τ in the steady state creep flow regime.

Sketches of the distributions of these quantities are represented in **figure D.III.2** (Please note that information given by **figure D.III.2** is only qualitative as the color key are not given and are not the same from one image to another). Note that the distributions of σ_{eq} and σ are nearly the same both at high stress and low stress. There is however a difference in the distribution of the stress triaxiality ratio between high and low stress.

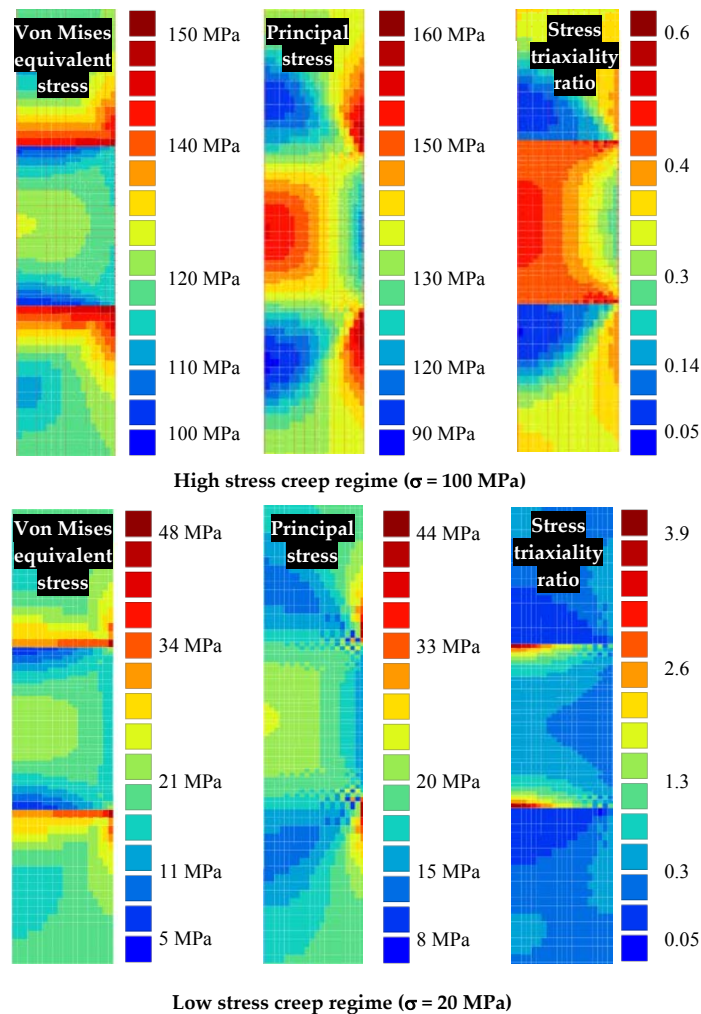


Figure D.III.2. Distributions of σ_{eq} , σ and τ in cross-weld specimens in the steady state creep regime

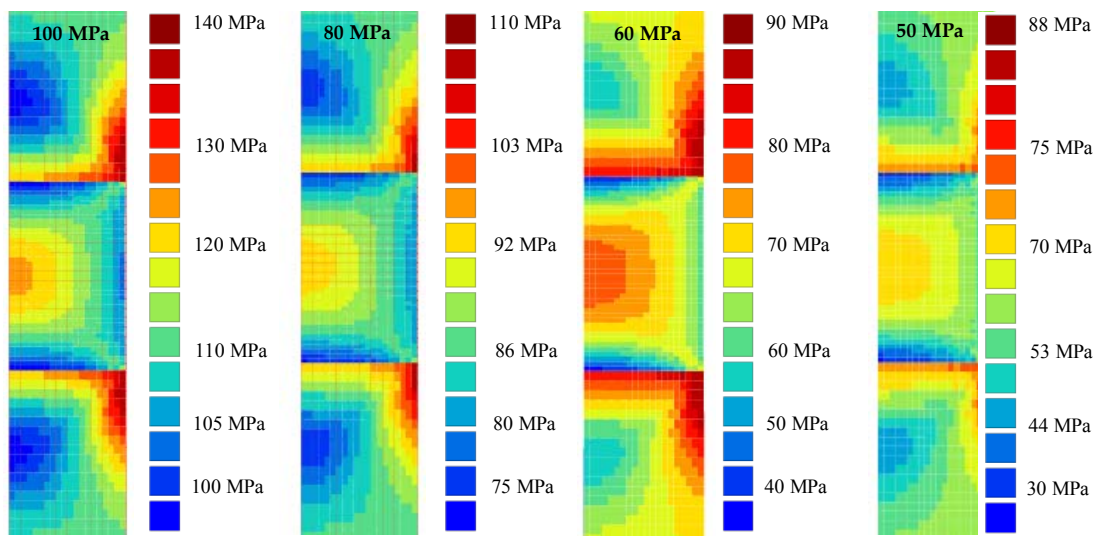
3. Definition of a criterion to predict creep lifetime of weldments

The stress redistributions evidenced in the previous section must be compared with experimental results which showed that the specimen failure occurs in the HAZ and starting from the centre of the specimen. One should then easily assumed that both the principal stress and the von Mises equivalent stress obviously promote the creep failure of cross-welds specimens. Therefore, the use of the “peak rupture stress” introduced by Storesund and Tu (1995) may be interesting. The expression of the peak rupture stress is reminded in **equation D.III.5**:

$$\sigma_{rs} = \alpha \sigma_1 + (1 - \alpha) \sigma_{eq} \quad (\text{eq. D.III.5})$$

Using the values of σ_{eq} and σ_1 determined by elasto-viscoplastic calculations, the peak rupture stress σ_{rs} could be calculated by a post-processor routine at every Gauss point at a time increment in the steady state creep regime. Note that the method, proposed in the present chapter, is based on the steady state creep properties so that it is not necessary to run the post-processor for each time increment.

The α parameter was set to the value classically found in the literature, i.e. 0.43, and the corresponding calculated σ_{rs} , in the steady state creep regime are plotted in **figure D.III.3**.



*Figure D.III.3. Distribution of the peak rupture stress in cross-weld SC specimens in the steady state creep regime
(Results of post calculations)*

Then, a method to predict the creep lifetime of SC specimens based on the use of the computed peak rupture stresses is proposed. The steady state creep strain rate can be described respectively in the high stress (before the onset of material softening) and in the low stress creep regime as:

$$\dot{\epsilon}_{vp,ss} = \left\langle \frac{\sigma_{eq} - Q_{vp1}}{K_{vp}} \right\rangle^{n_{vp}} \quad (\text{eq. D.III.6})$$

$$\dot{\epsilon}_{d,ss} = \left\langle \frac{\sigma_{eq}}{K_d} \right\rangle \quad (\text{eq. D.III.7})$$

For the sake of simplicity, Monkman-Grant relationships were used to represent the creep fracture properties of the base metal and the simulated HAZ. The corresponding values of C_{MG} , m , A and n are reported in **table D.III.2**. In the high stress creep regime the coefficients of the MG relationship were fitted to experimental data (see **chapter B.III** and **chapter C.IV**). In the low stress creep regime the Monkman-Grant relationships were fitted to the results given by the models determined in the present study as no experimental data is available at low stress for both the base metal and the simulated HAZ.

		Base metal	Simulated HAZ
Damage properties	High stress	$C_{MG}^{vp,BM} = 0.058 h^{0.06}$ $m_{vp,BM} = 0.94$	$C_{MG}^{vp,HAZ} = 0.28 h^{0.2}$ $m_{vp,HAZ} = 0.8$
	Low Stress*	$C_{MG}^{d,BM} = 0.07435 h^{0.12}$ $m_{d,BM} = 0.88$	$C_{MG}^{d,HAZ} = 0.28 h^{0.2}$ $m_{d,HAZ} = 0.8$

Table D.III.2. Values of MG parameters for both the base metal and the simulated HAZ at 625°C (*determined from the results of modelling in chapter B.III for the base metal and in chapter C.IV for the HAZ)

Then, using the Norton power-laws and the MG fits, the predicted creep lifetime corresponding to the calculated peak rupture stresses could be determined both in the base metal and the simulated HAZ:

$$t_R^{vp,BM} = \frac{C_{MG}^{vp,BM}}{\left[\frac{\left(\frac{\sigma_{rs,BM} - Q_{vp1,BM}}{K_{vp,BM}} \right)^{n_{vp,BM}}}{K_{vp,BM}} \right]^{m_{vp,BM}}} \quad t_R^{d,BM} = \frac{C_{MG}^{d,BM}}{\left[\frac{\sigma_{rs,BM}}{K_{d,BM}} \right]^{m_{d,BM}}} \quad (\text{eq. D.III.8})$$

$$t_R^{vp,HAZ} = \frac{C_{MG}^{vp,HAZ}}{\left[\frac{\left(\frac{\sigma_{rs,HAZ} - Q_{vp1,HAZ}}{K_{vp,HAZ}} \right)^{n_{vp,HAZ}}}{K_{vp,HAZ}} \right]^{m_{vp,HAZ}}} \quad t_R^{d,HAZ} = \frac{C_{MG}^{d,HAZ}}{\left[\frac{\sigma_{rs,HAZ}}{K_{d,HAZ}} \right]^{m_{d,HAZ}}} \quad (\text{eq. D.III.9})$$

The relationships of equations D.III.8 and D.III.9 were integrated to a post-calculation treatment at every Gauss point at a time increment in the steady state creep regime (the same time increment than that used for the calculations of the peak rupture stress), so that maps of evaluated creep lifetimes could be plotted in figure D.III.4. Note that only the maximum and the minimum values of predicted creep lifetime in each part of the weldment are given. In all cases, rupture is likely to occur in the HAZ and starting from the centre of the HAZ.

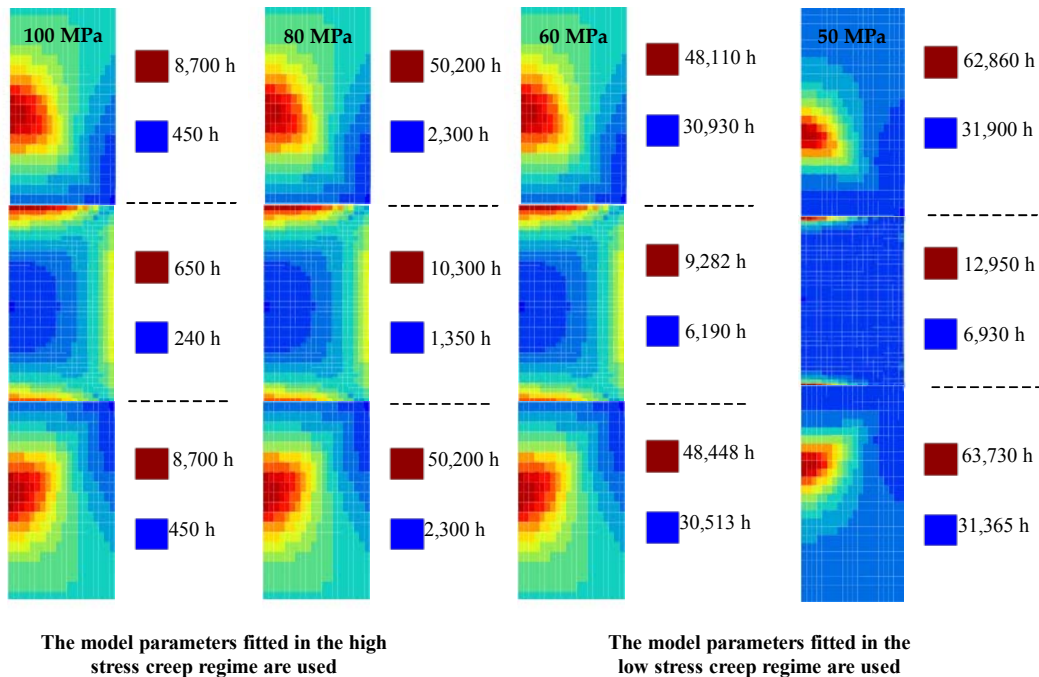
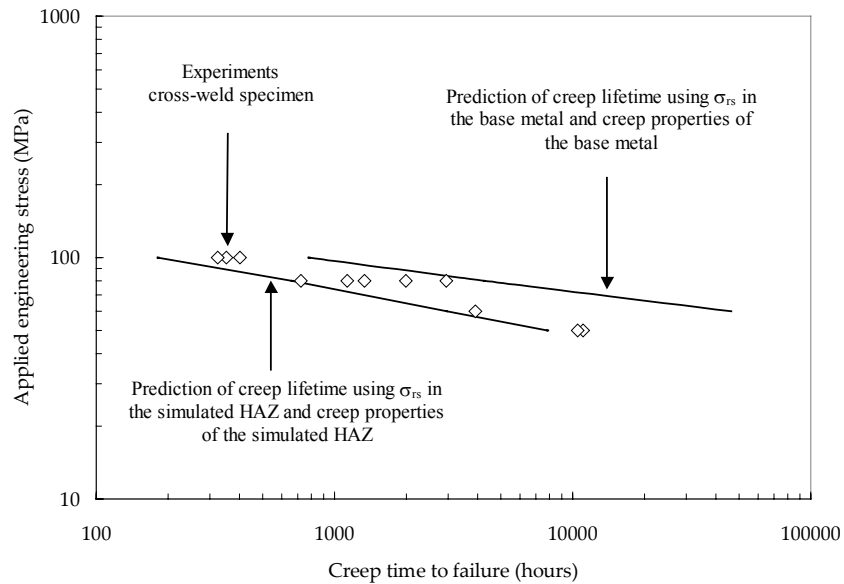


Figure D.III.4. Evaluation of creep lifetime in cross-weld SC specimens using the peak rupture stress method and the relationship of equation D.III.8 and D.III.9

The resulting predictions were plotted in figure D.III.5 and compared to the results of creep tests on cross-weld specimens. When the creep lifetime is calculated with σ_{rs} in the base metal and the creep damage properties of the base metal, the specimen failure is likely to occur in the base metal near the HAZ and to start from the outside of the specimen. When the creep lifetime is calculated with σ_{rs} in the HAZ and the creep damage properties of the HAZ, the specimen failure is likely to occur in the HAZ and to start from the centre of the specimen.



*Figure D.III.5. Predictions of cross-weld specimens creep lifetime using peak rupture stresses
Comparison with experimental data*

The result of this simple study are very interesting as the curves of lifetime predictions well delimit the scatter-band of experimental results of creep tests on cross-weld specimens. If extrapolating the curves, one should also notice that the two predictive curves would probably intersect for $\sigma = 120$ MPa and evidences a shift of the creep fracture location from the HAZ to the base metal at high temperature.

4. Use of the procedure to predict creep lifetime of notched specimens

As it has already been explained in **chapter D.II**, several creep tests were also performed on cross-weld notched in the HAZ specimens at 625°C.

Two of them corresponding to applied engineering stresses of respectively 135 MPa and 110 MPa were chosen and the corresponding FE calculations were performed following the same procedure than for SC cross-welds specimens. The distributions of σ_{eq} , σ_1 and τ are plotted in **figure D.III.6**.

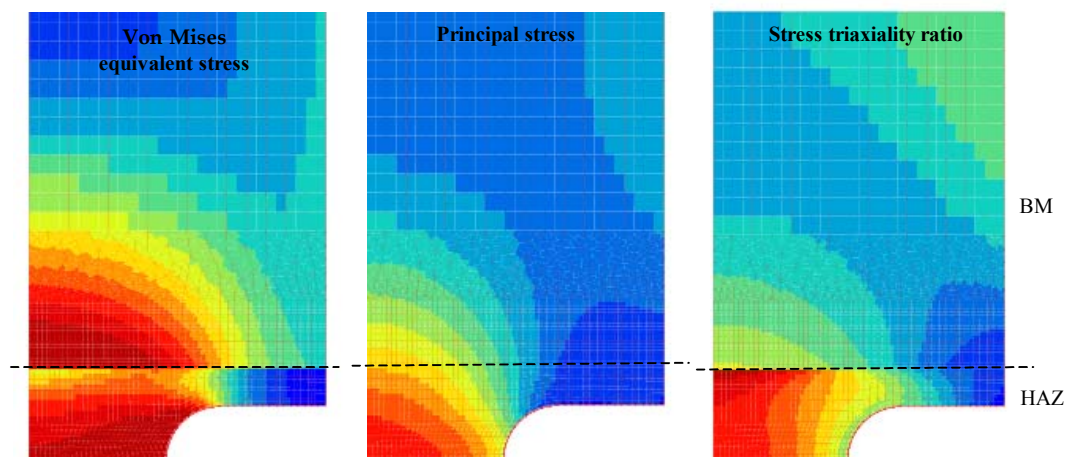


Figure D.III.6. Distributions of σ_{eq} , σ_1 and τ in cross-weld specimens (red areas represent the maxima)

A post-processor routine was then carried out on elasto-viscoplastic calculations to determine the peak rupture stresses at every Gauss point at every time increment. The distributions of peak rupture stresses in the steady state creep regime are represented in **figure D.III.7** for two tests on NC1.2 specimens. It is shown that the peak rupture stress is maximum in the HAZ at the centre of the specimen and that its value is slightly lower than that of the applied engineering stress.

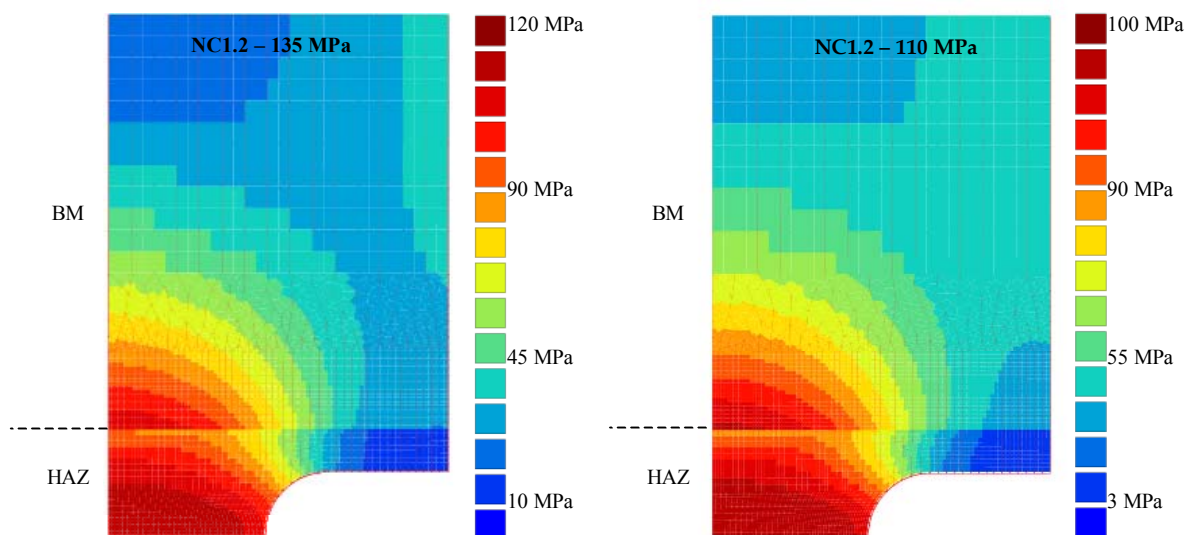
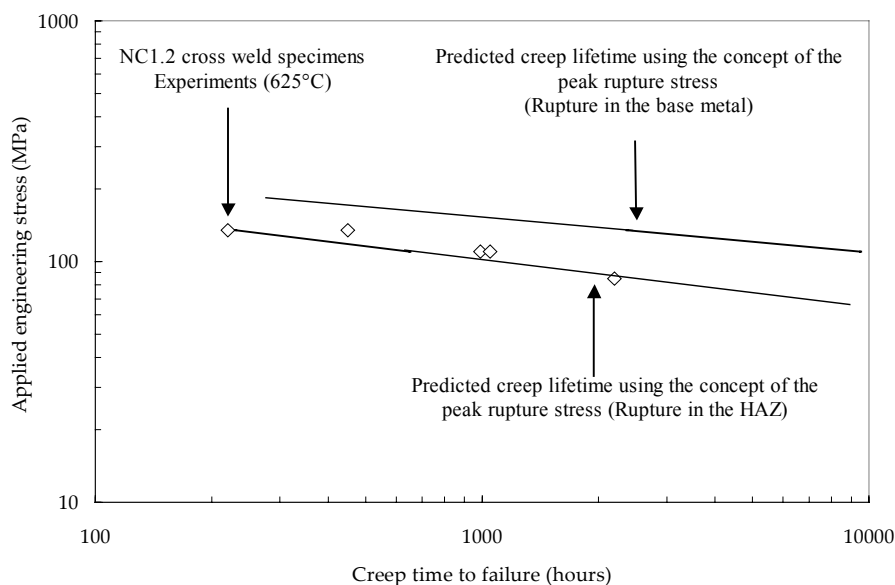


Figure D.III.7. Distribution of peak rupture stress in NC1.2 cross-weld specimens

As already done in the previous section, creep flow and damage properties of the base metal and the simulated heat affected zone and the calculated peak rupture stresses, were used to predict the creep lifetime of cross-welds notched specimens (see **figure D.III.8**). Note that in the two studied cases, it is predicted that creep fracture will start from the centre of the specimen.



*Figure D.III.8. Predictions of cross-weld notched specimens creep lifetime using peak rupture stresses
Comparison with experimental data*

The experimental results quite well lie between the two predictive curves but the agreement is not as good as for the cross-welds SC specimens. Moreover, due to the notch effect, the von Mises equivalent stress and the principal stress distributions are separated contrary to in the SC specimens. Therefore, the expression of the peak rupture stress is probably no more valid. In fact, these last results show that such quite interesting but too much simple criteria like the peak rupture stress are not likely to be used in case of complex multi-axial loading.

5. Conclusions

The peak rupture stress is a relevant method to evaluate the constraints effects in cross-weld SC specimens provided it is carefully used. In the present study, it is proposed to combine the evaluation of the peak rupture stress to Monkman-Grant predictive relationships. To do so, such relationships must previously be determined for both the base metal and the HAZ. The main difficulty is that the MG fits can be only determined using experimental data in the high stress creep regime. The model integrating multiple deformation and damage mechanisms had to be used to determine the MG fits in the low stress creep regime.

In fact, the significance of the peak rupture stress method is assumed provided creep flow properties of the base metal and the HAZ are known and provided the creep fracture properties are known in both the high stress and the low stress creep regime. When all this elements are taken into account, it was shown in the present chapter that the creep lifetime predictions are in quite good agreement with experimental results. Therefore, the method is recommended by the author to perform a first level analysis of the weldment creep failure properties without needing to implement the multiple deformation and damage mechanism in your own finite element software.

A more simplified method which consists in describing creep flow properties by means of a simple Norton power-law without a threshold stress (see **equation D.III.10**) can also be proposed. The resulting creep lifetime criteria are given by **equation D.III.11** and **equation D.III.12**. The corresponding model parameters are given in **table D.III.3**.

$$\dot{\epsilon}_{ss} = B\sigma^n \quad (\text{eq. D.III.10})$$

$$t_f^{BM} = \frac{C_{MG}^{BM}}{\left[\left(B_{BM} \sigma_{rs,BM} \right)^{n_{BM}} \right]^{m_{BM}}} \quad (\text{eq. D.III.11})$$

$$t_f^{HAZ} = \frac{C_{MG}^{HAZ}}{\left[\left(B_{HAZ} \sigma_{rs,HAZ} \right)^{n_{HAZ}} \right]^{m_{HAZ}}} \quad (\text{eq. D.III.12})$$

		Base metal	Simulated HAZ
Damage properties	High stress	$C_{MG}^{vp,BM} = 0.058 \text{ h}^{0.06}$ $m_{vp,BM} = 0.94$	$C_{MG}^{vp,HAZ} = 0.28 \text{ h}^{0.2}$ $m_{vp,HAZ} = 0.8$
	Low Stress	$C_{MG}^{d,BM} = 0.07435 \text{ h}^{0.12}$ $m_{d,BM} = 0.88$	$C_{MG}^{d,HAZ} = 0.28 \text{ h}^{0.2}$ $m_{d,HAZ} = 0.8$
Flow properties	High stress	$B_{vp,BM} = 3.03 \cdot 10^{-22} \text{ MPa}^{-8.6} \text{ h}^{-1}$ $n_{vp,BM} = 8.1$	$B_{vp,HAZ} = 2.13 \cdot 10^{-24} \text{ MPa}^{-9.6} \text{ h}^{-1}$ $n_{vp,HAZ} = 9.6$
	Low Stress	$B_{d,BM} = 4.55 \cdot 10^{-9} \text{ MPa}^{-1} \text{ h}^{-1}$ $n_{d,BM} = 1.0$	$B_{d,HAZ} = 5.0 \cdot 10^{-8} \text{ MPa}^{-1} \text{ h}^{-1}$ $n_{d,HAZ} = 1.0$

Table D.III.3. Values of MG parameters for both the base metal and the simulated HAZ

Reference

Storesund J., Tu S.T. (1995). Geometrical effect on creep in cross weld specimens. *International Journal of Pressure Vessels and Piping*. 62. 179-193.

Chapter D.IV. Creep flow and damage behaviour of the T91 steel at 450°C and 550°C

1. Experimental study

1.1. Experimental procedure

Mechanical tests of type tensile and creep tests were carried out at 450°C and 550°C. Creep tests were performed only on cross-weld smooth round tensile bars (SC) having a gauge length of 36 mm and a gauge diameter of 5 mm. These specimens were machined from the WJT91 weldment (see **figure D.IV.1**) in areas corresponding to both the sequence 2 and the sequence 3 of the welding procedure.

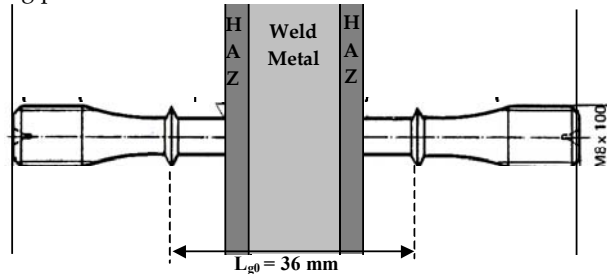


Figure D.IV.1. Specimen location in the WJT91 weldment

These tests were carried out at 450 and 550°C under constant applied load in controlled laboratory atmosphere (20°C ± 2°C and 50% relative humidity). The load was applied using dead weights. The temperature was monitored using three thermocouples spot welded onto the specimen surface. The temperature gradient between top and bottom ends of the specimen did not exceed 2°C. The elongation measured using linear variable differential transducers was continuously recorded with a sensitivity of 1 µm as:

$$\varepsilon = \frac{\Delta L_g}{L_{g0}} \quad (\text{eq.D.IV.1})$$

where L_{g0} is the initial gauge length and ΔL_g is the actual elongation of the initial gauge length. One should notice in **figure D.IV.1** that two HAZ areas are tested in the gauge length.

1.2. Results

The initial values of the applied engineering stresses at 550°C (load divided by the initial area of the minimum section) range from 140 MPa to 185 MPa and corresponding times to failure range from 300 hours to 8,500 hours (**figure D.IV.2**). At 450°C, the initial values of the applied engineering stresses range from 340 MPa to 400 MPa and corresponding times to failure range from 10 hours to 3,500 hours. The results of these experiments are reported in **appendix A table A.D.3** and **A.D.4**.

2. Creep flow and damage behaviour of WJT91 weldments at 450°C and 550°C

2.1. Creep flow properties

The steady state strain rate were represented using a Norton power-law:

$$\dot{\varepsilon}_{ss} = B\sigma^n \quad (\text{eq.D.IV.2})$$

where the model parameters, B and n , were fitted from experimental data. The values of B and n for the base metal, the weldment and the HAZ are given in **table D.IV.1**.

Temperature	Material	B (h ⁻¹ MPa ⁻ⁿ)	n
450°C	Base metal (BM) - Experiments	8.12 10 ⁻¹⁰⁶	39.02
	Weldment - Experiments	1.34 10 ⁻¹⁰⁰	37.30
	HAZ – Calculated with l _{HAZ} = 3.5 mm	2.69 .10 ⁻⁹⁹	37.04
550°C	Base metal (BM) - Experiments	1.13 10 ⁻³¹	11.51
	Weldment - Experiments	3.06 10 ⁻⁵⁴	21.75
	HAZ – Calculated with l _{HAZ} = 3.5 mm	9.12 10 ⁻⁵⁶	22.82

Table D.IV.1. Norton power-law parameters for base metal, weldment specimens and HAZ at 450°C and 550°C

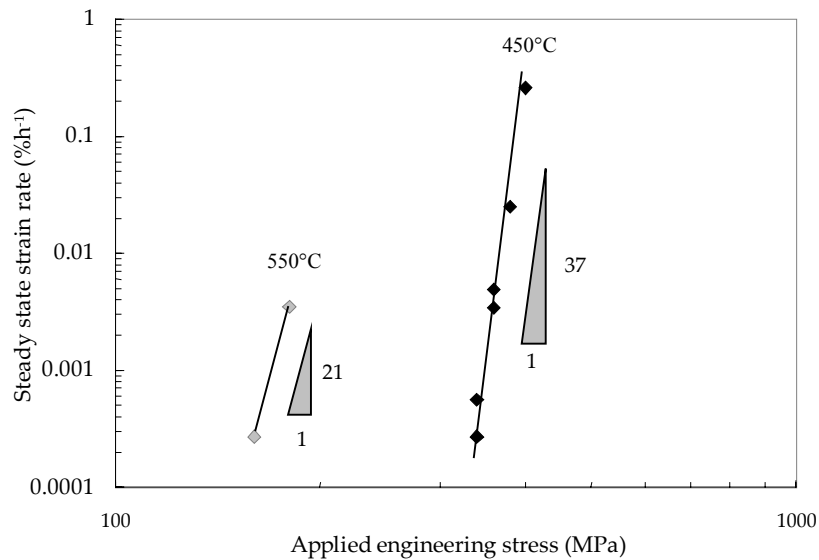


Figure D.IV.2. Steady state strain rate versus applied engineering stress of weldments at 450°C and 550°C: Experimental results

2.2. Creep fracture properties

Empirical Monkman-Grant and Larson-Miller relationships could be used to predict creep lifetime of the weldments at both 450°C and 550°C. Due to the creep strain heterogeneities in the weldment, the Larson-Miller relationship is more relevant than the Monkman-Grant fit which requires the evaluation of the steady state creep strain rates (see **chapter C.II.** for more detail). The Larson-Miller relationship is written as:

$$P_{LM} = [20 + \log(t_R)] \frac{T(K)}{1000} = f(\sigma) \quad (\text{eq. D.IV.2})$$

where the Larson-Miller parameter was fitted as:

$$P_{LM}(T = 450^\circ\text{C}) = -0.06\sigma + 40.3 \quad (\text{eq. D.IV.3})$$

$$P_{LM}(T = 550^\circ\text{C}) = -0.04\sigma + 26.1 \quad (\text{eq. D.IV.4})$$

The comparison between experimental data and the LM predictions can be shown in **figure D.IV.3.** Note that the Larson-Miller relationships are strictly valid in the domain experimentally investigated, predictions for longer creep lifetime are highly questionable as no change in both creep flow and damage mechanisms is taken into account.

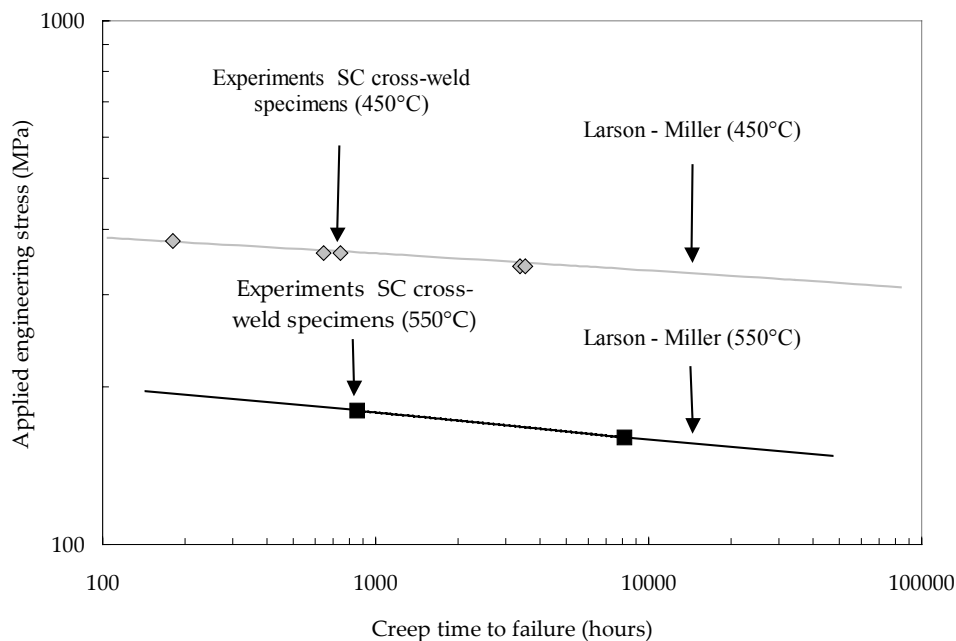
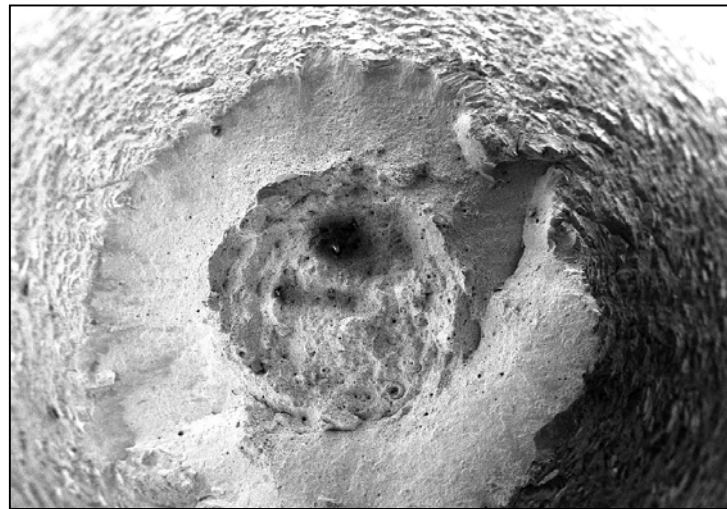


Figure D.IV.3. Applied engineering stress versus creep time to failure for weldments at 450°C and 550°C: Experimental results

2.3. Creep damage characteristics in weldments at 450°C and 550°C

The fracture surfaces exhibit the same characteristics than these of the T91 base metal at 450°C and 550°C. The “cup-cone” fracture is evidenced in the fractography of **figure D.IV.4** which shows that the specimen fracture starts from the centre of the specimen.

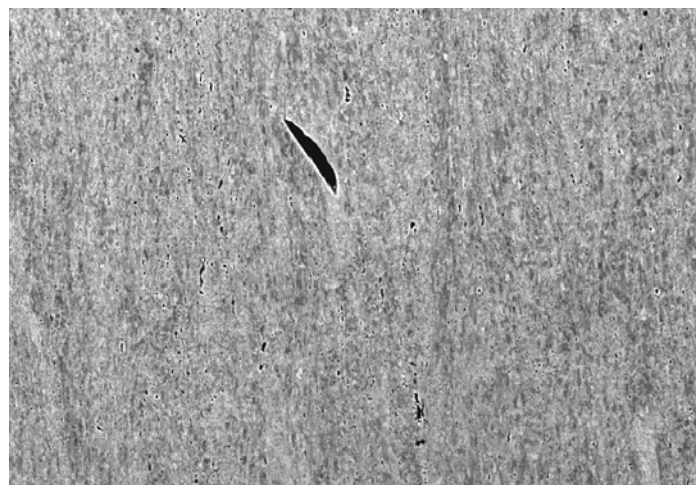


200 μm



Figure D.IV.4. Example of a fracture surface of the WJT91 weldment (Creep test at 450°C, 340 MPa)

Longitudinal cross-sections of cross-weld specimens were polished using colloidal silica and were examined with backscattered electron (BSE) channelling contrast in the SEM. It was evidenced that rupture occurs in the base metal but near the HAZ and parallel to the fusion line. Damage was observed in both the HAZ and the base metal. It could be evidenced in **figure D.IV.5** that the characteristics of damage are quite similar to these observed in the base metal (see **figure B.VI.9** in **chapter B.VI**). Cavities mainly nucleate at the interface between the matrix and second phase particles. Damage is mainly constituted of small round cavities and larger intergranular cavities are sometimes observed as it can be shown in **figure D.IV.5**. The material is however little damage and the dominating mechanism which lead to the softening and the failure of specimens is obviously the recovery of the initial lath martensite microstructure. The final microstructure observed in specimens longitudinal cross-sections is composed of fine equiaxed grains as it can be evidenced in **figure D.IV.5**.



10 μm



Figure D.IV.5. Micrograph representative of damage behaviour in cross-welds specimen: observations on longitudinal cross-sections of crept specimens

3. Modelling coupled creep flow and damage behaviour of the WJT91 weldment at 450°C and 550°C

3.1. Evaluation of l_{HAZ}

It was shown in **chapter C.II** that a very simple analysis of the creep deformation of cross-weld specimens by means of a simple one dimensional model and bi-material FE calculations gives useful information especially to determine l_{HAZ} . Taking into account the geometry of the specimen, the model is written:

$$l_{tot} \dot{\epsilon}_{ss} = 2l_{HAZ} \dot{\epsilon}_{HAZ} + l_{BM} \dot{\epsilon}_{BM} \quad (\text{eq.D.IV.5})$$

where $l_{tot} = 36\text{mm}$.

The width of the HAZ can be evaluated to $l_{HAZ} = 3.5\text{ mm}$ using the hardness profile in **figure D.IV.6** so that $l_{BM} = 29\text{ mm}$. Therefore, the steady state creep properties of the HAZ were determined from **equation D.IV.1** with taking $l_{HAZ} = 3.5\text{ mm}$. The corresponding values of B and n of the HAZ are given in **table D.IV.1**.

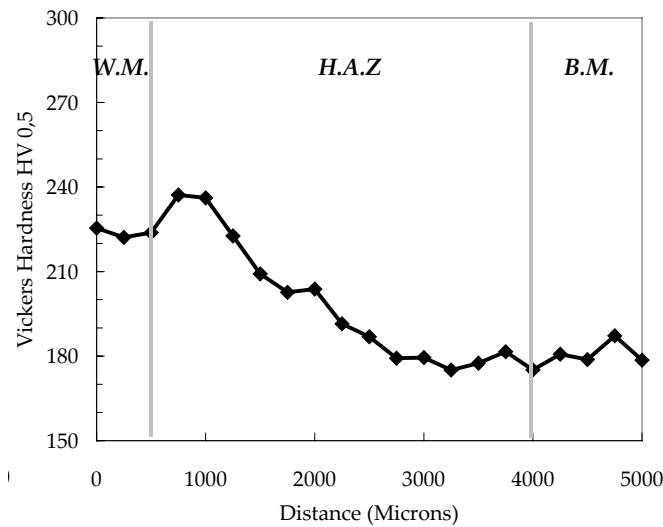


Figure D.IV.6. Hardness profile in the WJT91 weldment

Then, 2D axisymmetric FE calculations using a bi-material representation were performed with the FE software Zebulon (Besson and Foerch (1997)). Taking into account symmetry relationships, a half of SC specimens was meshed with the HAZ representing 3.5 mm of the total gauge length equal to 18 mm. The HAZ area was finely meshed with quadratic squares (with reduced integration) of $100\ \mu\text{m}$ in size. Norton power-law coefficients of **table D.IV.1** were integrated to constitutive laws describing the creep flow properties of the base metal and the HAZ. The strain rate tensor was written as:

$$\dot{\epsilon} = \dot{\epsilon}_e + \dot{\epsilon}_{vp} \quad (\text{eq. D.IV.6})$$

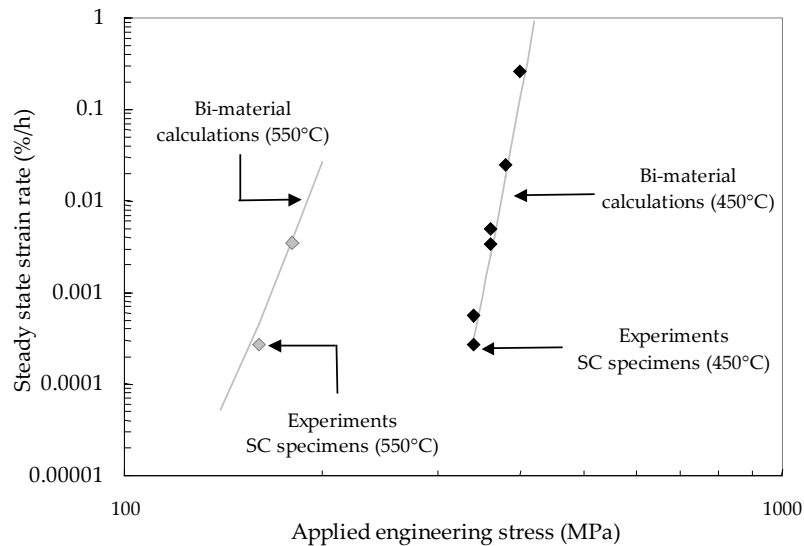
The elastic strain tensor $\dot{\epsilon}_e$ is related to the stress tensor by Hooke's law: $\dot{\sigma} = \underline{\underline{C}} : \dot{\epsilon}_e$ where $\underline{\underline{C}}$ is the fourth order stiffness tensor. The Young's modulus was taken to 145 GPa and the Poisson ratio to 0.3. The non-elastic (viscoplastic) strain rate tensor is given by the normality rule:

$$\dot{\epsilon}_{vp} = \frac{3}{2} \dot{p} \frac{\underline{s}}{\sigma_{eq}} \quad (\text{eq. D.IV.7})$$

where \underline{s} is the stress deviator, σ_{eq} is the von Mises equivalent stress and the viscoplastic multiplier, \dot{p} , is assumed to be given by a Norton power-law:

$$\dot{p} = B \sigma_{eq}^n \quad (\text{eq.D.IV.8})$$

The creep flow properties of the weldments were calculated from the bi-material FE simulations and compared to experimental data in **figure D.IV.7**. A quite good agreement was found between experimentally measured steady state creep strain rates and the results of FE calculations. Therefore, it was concluded that the value of $l_{HAZ} = 3.5\text{ mm}$ allows to rightly represent constraints effects in the WJT91 weldment.



*Figure D.IV.7. Steady state creep strain rate versus applied engineering stress
Comparison between bi-material calculations (line) and experimental results at both 450°C and 550°C (symbols)*

FE calculations were performed until the specimen fracture. Only the creep flow properties are represent and no damage development is taken into account. It means that the creep time to failure given by the model corresponds to the time when the reduction of loading section becomes high. The results are plotted in **figure D.IV.8** and compared with experimental results. Contrary to the case of the WJP91 weldment (see **chapter C.II**), the predicted creep lifetime are not overestimated but are in very good agreement with experimental results both at 450°C and 550°C whereas no contribution of damage is taken into account.

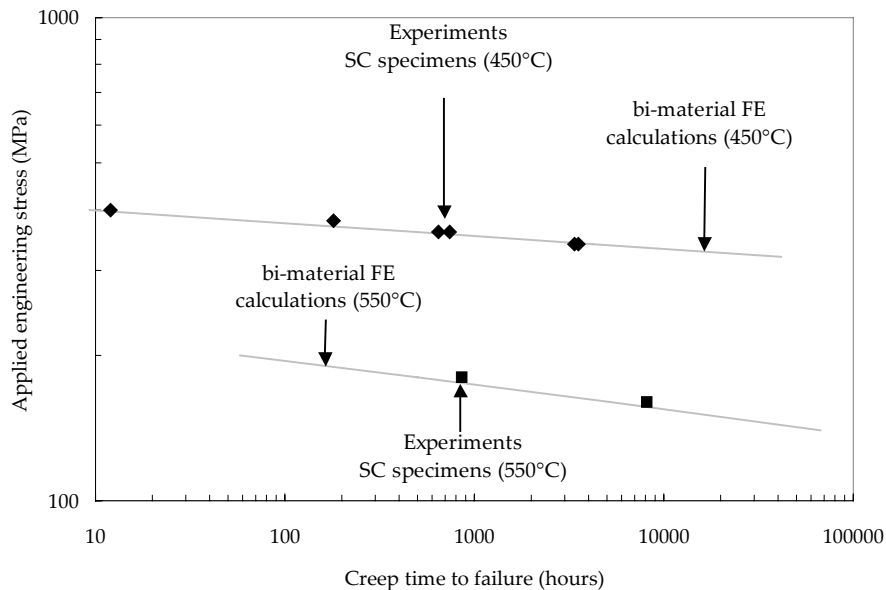


Figure D.IV.8. Applied engineering stress versus creep time to failure - Comparison between bi-material calculations without taking into account damage (line) and experimental results at both 450°C and 550°C (symbols)

The analysis of creep flow and damage behaviour of the WJT91 weldment by the use of a simple uniaxial model of creep allowed to set l_{HAZ} to 3.5 mm. It was also evidenced that damage development probably does not play a key role in specimens fracture at both 450°C and 550°C at least in the stress domain experimentally investigated and for the SC specimen geometry.

3.2. Formulation of the model

The lack of experimental data concerning the tensile properties of the simulated HAZ at 550°C leads to use a simplified version of the model to two inelastic contributions with neglecting the quasi plastic creep regime. Therefore, the resulting strain rate tensor, was given by:

$$\dot{\underline{\epsilon}} = \dot{\underline{\epsilon}}_e + \dot{\underline{\epsilon}}_{vp} + \dot{\underline{\epsilon}}_d \quad (\text{eq. D.IV.9})$$

where $\dot{\underline{\epsilon}}_e$ is the elastic strain rate tensor, $\dot{\underline{\epsilon}}_{vp}$ accounts for power-law creep and $\dot{\underline{\epsilon}}_d$ accounts for low stress grain boundary diffusion creep. The corresponding subscripts vp and d will be used to designate these two mechanisms in the following. As the details about the model were reminded several times in the present manuscript, it will not be done here (Please report to **chapter D.II** for example).

The model for the base metal at 550°C was previously determined in **chapter B.VI**. As it was evidenced that the weld and base metal exhibit quasi-similar creep flow properties in 9Cr1Mo-NbV steel weldments, for the sake of simplicity, a two material representation was chosen here (Note that this approximation is commonly used for Cr-Mo weldments, see Perrin and Hayhurst (1999)).

The model of the ICHAZ at 550°C was evaluated from that determined at 625°C with keeping constant the damage parameters assuming that no change in damage mechanism occur. Model parameters for both the base metal and the ICHAZ are reported in **table D.IV.2**.

		Base Metal	ICHAZ
1. Young's modulus	E	163 GPa	163 GPa
2. Poisson's ratio	ν	0.3	0.3
3. Viscoplastic hardening at 550°C	R_{0vp}	0 MPa	0 MPa
	Q_{vp1}	100 MPa	120 MPa
	b_{vp1}	224	120
	Q_{vp2}	35 MPa	20 MPa
	b_{vp2}	25	10
	p_c	0.05	0.02
4. Viscoplastic strain rate at 625°C	K_{vp}	$460 \text{ MPa h}^{-1/n_{qp}}$	$352 \text{ MPa h}^{1/n_{vp}}$
	n_{vp}	7.14	7.14
5. Diffusion strain rate at 550°C	K_d	$2.53 \cdot 10^9 \text{ MPa h}^{-1/n_d}$	$0.153 \cdot 10^9 \text{ MPa h}^{1/n_d}$
	n_d	1.0	1.0
6. LPS model	q_1		1.5
	q_2		1.0
	f_c		0.1
	δ_c		6.0
<i>Strain hardening coefficients</i>	m_{vp}	0.087	0.045
	m_d	1.0	1.0
<i>Nucleation by the viscoplastic mechanism</i>	A_{vp1}	0.01	0.05
	A_{vp2}	0.15	0.4
	α_v	2.0	2.0
<i>Nucleation by the diffusional mechanism</i>	A_{d1}	14.0	5
	A_{d2}	16.0	0.5
	α_d	2.0	2.0

Table D.IV.2. Model parameters

3.3. Prediction of creep lifetime

The model was used to predict creep lifetime of cross-weld specimens at 550°C in the stress range between 60 MPa and 200 MPa. The corresponding predictions are given in **figure D.IV.9**. There is no deny that more experimental results are necessary to confirm these predictions. The transition in creep damage mechanisms especially appears quite soon.

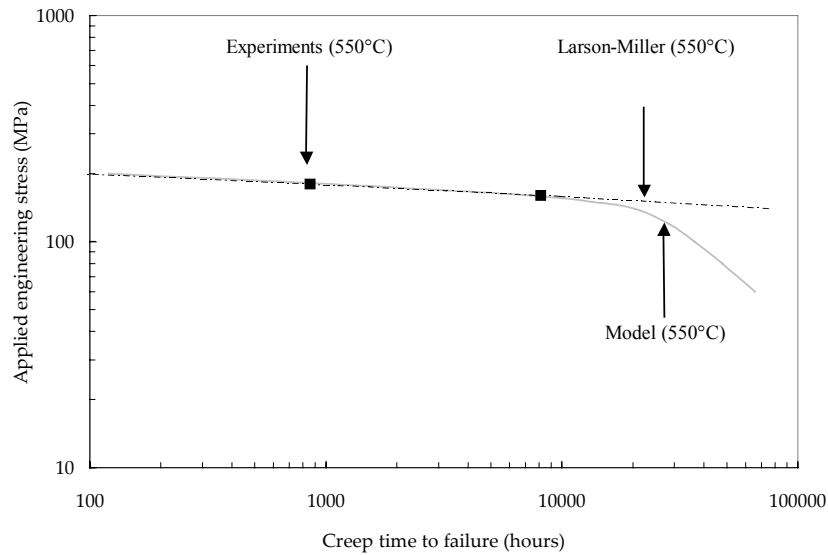


Figure D.IV.9 Stress versus creep time to failure for cross-weld SC specimens at 550°C (model and experiments)

Taking into account that one can be interested in performing a study similar than that performed in **chapter D.III**, the creep damage properties (i.e. the Monkman-Grant parameters) were evaluated for the base metal and the weakest heat affected zone from the results of the multiple deformation and damage mechanisms model (see **table D.IV.3**).

		Base metal	Simulated HAZ
Damage properties	High stress	$C_{MG}^{vp,BM} = 0.074$ $m_{vp,BM} = 1.0$	$C_{MG}^{vp,HAZ} = 0.0127 h^{-0.18}$ $m_{vp,HAZ} = 1.18$
	Low stress	$C_{MG}^{d,BM} = 0.098 h^{0.12}$ $m_{d,BM} = 0.88$	$C_{MG}^{d,HAZ} = 0.437 h^{0.21}$ $m_{d,HAZ} = 0.79$

Table D.IV.3. MG fit for the base metal and the weakest HAZ at 550°C (Evaluated from the results of FE simulations)

4. Simulation of the microstructure of the weakest HAZ

In the present study, it was not possible to perform creep tests on the simulated HAZ of the WJT91 weldment because of a lack of time. However, metallurgical investigations similar to these presented in **chapter C.III** were performed. A model of Rosenthal (1941) modified by Rykalin (1957) was fitted to represent weld thermal cycle corresponding to various microstructural states in the HAZ.

To start, the effect of the heating rates on the position of the phase transformation points namely A_{c1} and A_{c3} was investigated. It can be evidenced in **figure D.IV.10** that the effect of the heating rate on phase transformations temperatures in the T91 steel is more limited than in the P91 steel.

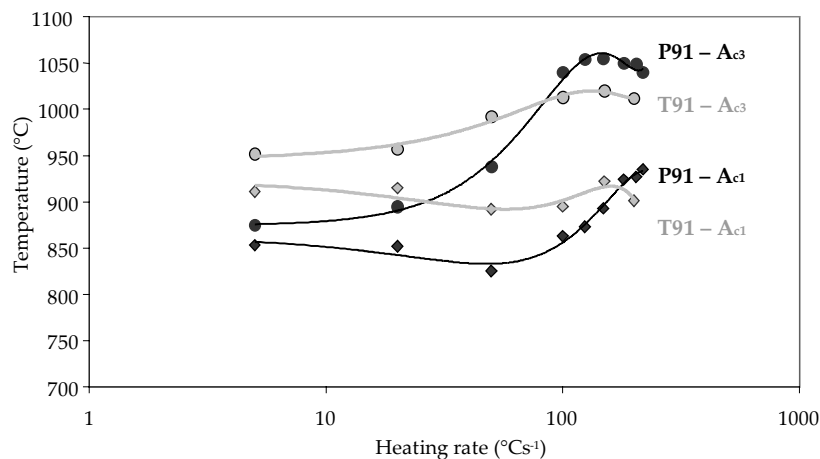


Figure D.IV.10. Effect of the heating rate on A_{c1} and A_{c3} temperature (dilatometry)

All parameters needed to calculate welding thermal cycles are reported in **table D.IV.4**. The cooling parameter is slightly higher than that of welding thermal cycles of the WJP91 weldment (i.e. 16 s) due to the higher thickness of the component and the higher heat input energy.

Thermal conductivity	$\Gamma = 28 \text{ Wm}^{-1}\text{K}^{-1}$ (at 225°C)
Heat input energy	$H = 1700 \text{ Jmm}^{-1}$
Arc displacement rate	$v_a = 1.75 \cdot 10^{-3} \text{ ms}^{-1}$.
Preheat temperature	$T_0 = 225^\circ\text{C}$
Thickness of the component	$e = 150 \text{ mm}$
Cooling parameter	$\Delta t_{800 \rightarrow 500} = 21 \text{ s}$
Heat source position	5.0 mm from the fusion line

Table D.IV.4. Model parameters

Several treatments were calculated and then applied to round bars of 5 mm in diameter, using the Gleeble 1500 thermal-mechanical simulator (see **appendix B.F** for a description of the experimental facility) for various distances from the fusion line. The characteristics of the corresponding heat cycles are given in **table D.IV.5**. Phase transformations were continuously monitored using in-situ dilatometric measurements of the specimen diameter. It allowed to address the position of the peak temperature of the welding thermal cycle with respect to the phase transformation points (Note that heat treatments were performed under vacuum to prevent from extensive oxidation of the specimen).

Distance from the fusion line	Peak temp.	Heating rate	Specificity
2.00 mm	1270°C	155°Cs ⁻¹	$A_{c3} < T_{\text{peak}}$
2.50 mm	1156°C	143°Cs ⁻¹	$A_{c3} < T_{\text{peak}}$
3.00 mm	1060°C	124°Cs ⁻¹	$A_{c3} < T_{\text{peak}}$
3.50 mm	1020°C	115°Cs ⁻¹	$A_{c3} \approx T_{\text{peak}}$
4.00 mm	965°C	104°Cs ⁻¹	$A_{c1} < T_{\text{peak}} < A_{c3}$
4.25 mm	911°C	98°Cs ⁻¹	$A_{c1} < T_{\text{peak}} < A_{c3}$
4.50 mm	862°C	90°Cs ⁻¹	$T_{\text{peak}} < A_{c1}$

Table D.IV.5. Model parameters

For each weld thermal cycle two specimens were treated and only one of two was submitted to the post weld heat treatment (i.e more than 15 hours at 750°C), so that the properties of the simulated microstructures could be compared to those of the microstructures of the weldment before and after the PWHT. It is shown in **figure D.IV.11** that hardness values of the simulated and tempered microstructures are very close to the hardness profile in the tempered weldment. It is a first validation of the method used to reproduce weld thermal cycles.

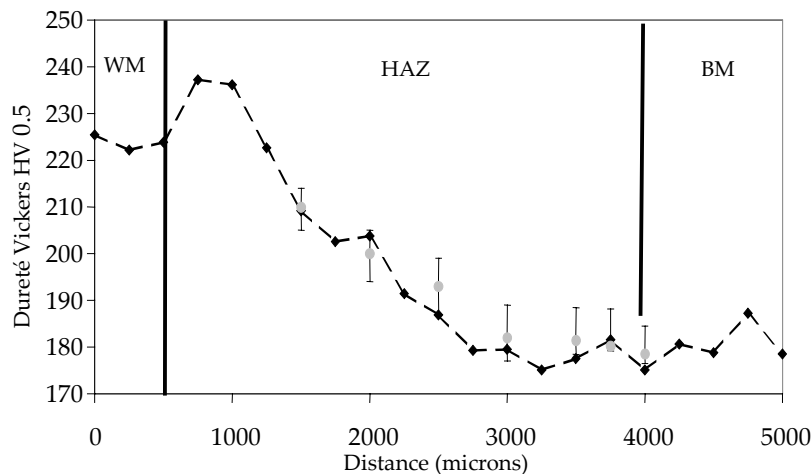


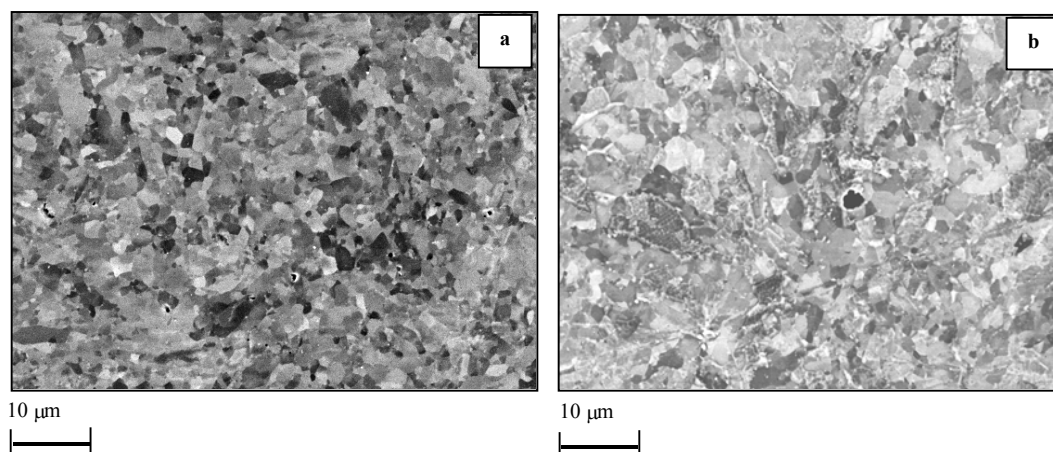
Figure D.IV.11. Hardness comparison after PWHT: grey symbol = simulated HAZ and black symbols = welded joint

Even if the present study is not as detailed as that performed on the WJP91 weldment in **Part C** of the present study, a weld thermal cycle obviously corresponding to the weakest HAZ can be proposed. The characteristics of this weld thermal cycle are given in **table D.IV.6**.

Peak temperature	Heating rate	Cooling rate	PWHT
962°C	104°Cs ⁻¹	$\Delta t_{800 \rightarrow 500} = 21 \text{ s}$	15 hours 18 minutes (750°C)

Table D.IV.6. Thermal cycle corresponding to the soft HAZ

The simulated microstructure corresponding to the weld thermal cycle of **table D.IV.6** is shown in **figure D.IV.12b** and exhibits a quite good agreement with the corresponding microstructure in the WJT91 weldment (see **figure D.IV.12a**).



*Figure D.IV.12. Comparison between actual (a) and simulated (b) microstructure ($T_{peak} = 965^\circ\text{C}$)
Colloidal silica polishing - SEM (BSE) observations*

5. Conclusions

Creep test experiments were performed at 450°C and 550°C on cross-weld specimens machined from the WJT91 weldment. For the two temperatures, in the stress domain experimentally investigated, rupture was located in the base metal parallel to the fusion line. SEM investigations in longitudinal cross-sections of the specimens showed that damage little develop and that softening mechanism are obviously mainly responsible of specimens fracture.

Following the same procedure than that used in **chapter C.I**, a uniaxial model was used to evaluate the length of the HAZ area. Then, creep flow and damage behaviour of the simulated HAZ at 625°C were extrapolated at 550°C. The corresponding constitutive equations and these of base metal (see **chapter B.VI**) were integrated into multi-materials FE calculations. It allowed to predict cross-weld specimens creep lifetimes even if more experimental data would be necessary to confirm the validity of the model.

Finally, the method to reproduce bulk specimens having the same microstructure than that of the weakest HAZ is described. It would allow to determine experimentally the creep flow and damage behaviour of the weakest HAZ of the WJT91 weldment with performing experiments and using the creep model of the present study as described in **chapter C.III** and **chapter C.IV**.

References

- Besson J., Foerch R. (1997). Large scale object-oriented finite element code design. *Computer Methods in Applied Mechanics and Engineering*. **142**. 165-187.
- Perrin I.J., Hayhurst D.R. (1999). Continuum damage mechanics analyses of type IV creep failure in ferritic steel crossweld specimens. *International journal of pressure vessels and piping*. **76**. 599-617.

Chapter D.V. Use of the model to predict creep lifetime of welded components for industrial applications

The models developed in the framework of the local approach to fracture can be used for designing structural components. It was reminded in **chapter B.III** that the mesh size plays an important role on the crack growth kinetics. In a presence of a defect, it is obviously necessary to refine the mesh around the defect with the same element size than that use for the model identification on laboratory specimens. Such works have been performed as reported in Berdin et al (2004).

It is however possible, in the absence of any defect, to use meshes with larger element size to model the evolution of volume damage in structural components. This is the scope of the present chapter.

1. Investigations of the creep rupture behaviour of the WJP91 welded pipe under internal pressure

1.1. Description of the FE calculations

The model determined in the previous chapters were used to evaluate the creep lifetime of the WJP91 welded pipe under internal pressure. The dimension of the geometry are these of the WJP91 welded pipe namely an outer diameter of 295 mm and a thickness of 55 mm. The loading and limit conditions are shown in **figure D.V.1**. One can see that two situations were considered whether the pipe was constrained (**figure D.V.1a**) or not (**figure D.V.1b**).

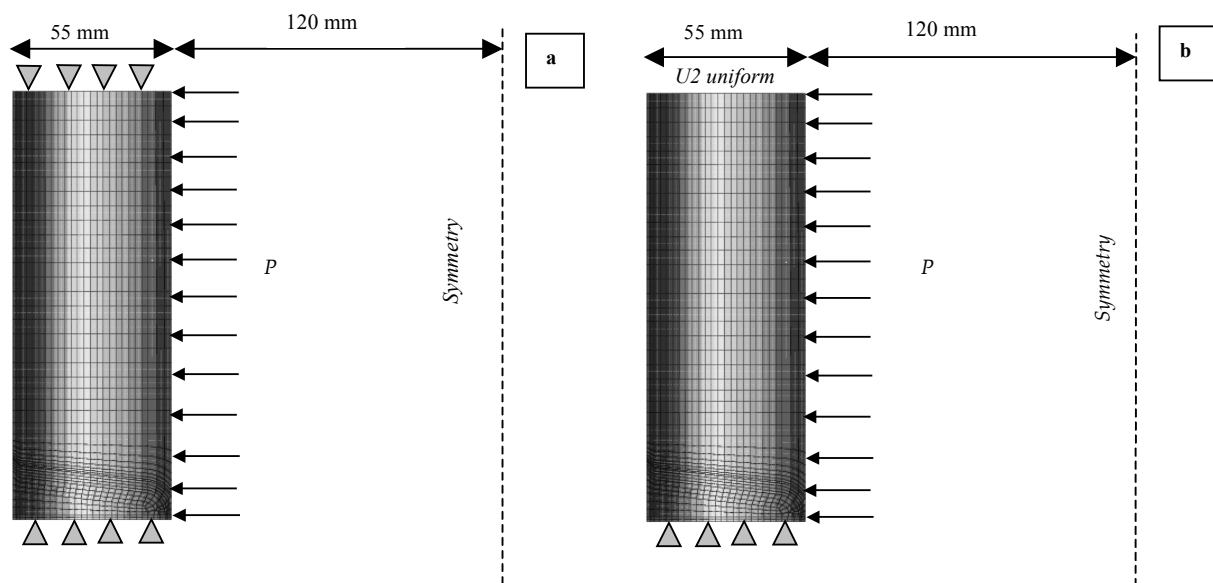


Figure D.V.1. Loading and limit conditions for FE calculations on the WJP91 welded pipe

2D axisymmetric representations were chosen with using square elements with reduced integration for the mesh. The internal pressure P was set to $P = 30$ MPa. The model formulation and the model parameters used for this study are these given in **table D.II.3**.

1.2. Results

First, the constraint effect on the stress and strain distributions was explored. It can be shown in **figure D.V.2** that the stress triaxiality ratio is larger in the constrained pipe than in the unconstrained pipe. It is evidenced by the results reported in **table D.V.1** that when the pipe is constrained, the creep strain in the HAZ is more constrained.

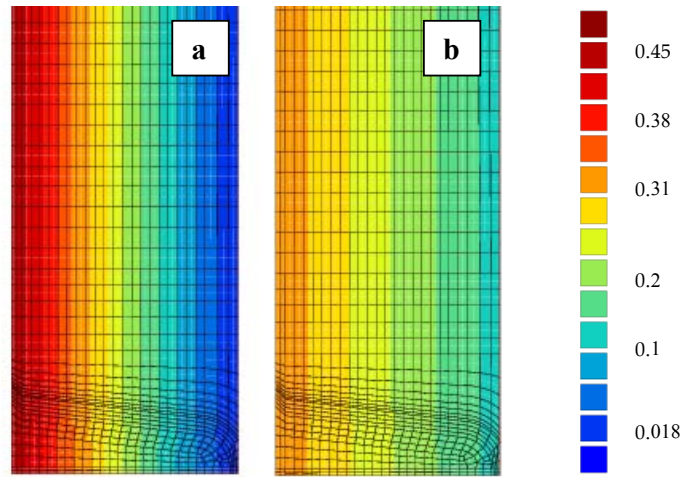


Figure D.V.2 Stress triaxiality ratio at the end of the loading stage (a) the pipe is constrained (b) the pipe is not constrained

Constraint	Temperature	$p_v = 0.05$	$p_v = 0.075$	$p_v = 0.1$
The pipe is not constrained	625°C	5,750 hours	12,050 hours	18,200 hours
The pipe is constrained	625°C	8,850 hours	14,600 hours	20,950 hours

Table D.V.1. Time to locally reach $p_v = 0.05, 0.075, 0.1$ and failure for pipe in the two configurations

These differences in stress and strain distributions should affect the damage kinetics. To address this point, the time for which the local total porosity reaches 0.1, 0.15 and the creep time to failure were determined for the two situations. It is shown that damage kinetics is faster in the constrained pipe than in the free one. Nevertheless, the creep times to failure are nearly equal.

Constraints	Temperature	$f_t = 0.1$	$f_t = 0.15$	Failure
The pipe is not constrained	625°C	15,300 hours	21,500 hours	26,500 hours
The pipe is constrained	625°C	12,000 hours	17,700 hours	26,150 hours

Table D.V.2. Time to locally reach $f_t = 0.1, 0.15, 0.2$ and failure for pipe in the two configurations

1.3. Comparison of the predictions of the present study with predictions given by the peak rupture stress method

A method based on elasto-viscoplastic calculations and the use of a post-calculation of a rupture criterion, at every gauss point and at a time increment in the steady state creep regime, was introduced in **chapter D.III**. This method first requires the calculation of the peak rupture stress:

$$\sigma_{rs} = \alpha \sigma_1 + (1 - \alpha) \sigma_{eq} \quad (\text{eq. D.V.1})$$

where σ_1 is the local principal stress and σ_{eq} is the local von Mises equivalent stress. The calculated peak rupture stresses in the steady state creep regime lead to the distributions given in **figure D.V.3** for the two pipes.

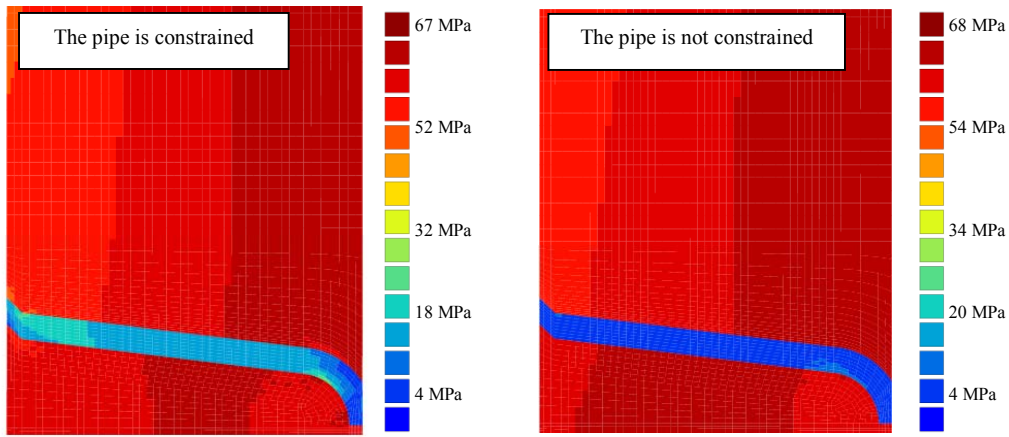


Figure D.V.3. Distributions of the peak rupture stress in the steady state creep regime

As the stress level is low in the pipes under an internal pressure of 30 MPa, the predicted creep lifetimes are calculated respectively in the base metal and the HAZ from:

$$t_R^{d,BM} = \frac{C_{MG}^{d,BM}}{\left[\left(\frac{\sigma_{rs,BM}}{K_{d,BM}} \right)^{m_{d,BM}} \right]} \quad (\text{eq. D.V.2})$$

$$t_R^{d,HAZ} = \frac{C_{MG}^{d,HAZ}}{\left[\left(\frac{\sigma_{rs,HAZ}}{K_{d,HAZ}} \right)^{m_{d,HAZ}} \right]} \quad (\text{eq. D.V.3})$$

where the values of the Monkman-Grant parameters are given in **table D.V.3**.

	Base metal	Simulated HAZ
Low stress*	$C_{MG}^{d,BM} = 0.07435 \text{ h}^{0.12}$ $m_{d,BM} = 0.88$	$C_{MG}^{d,HAZ} = 0.28 \text{ h}^{0.2}$ $m_{d,HAZ} = 0.8$

Table D.V.3. Monkman-Grant parameters for the base metal and the simulated HAZ in the low stress creep regime at 625°C
(*evaluated thanks to the results of the multiple deformation and damage mechanisms model)

A post-calculation at every Gauss point and for the same time increment than that at which the peak rupture stress was evaluated was performed to determine the predicted creep lifetime from **equation D.V.2**. The results of these post calculations are given in **figure D.V.4** where the three zones of the weldment have been separated as for a better visualisation the colour key are not the same for each zone. The values reported in **figure D.V.4** for the three regions of the welded pipes correspond to the minimum and maximum creep lifetimes predicted by **equation D.V.2** in the base metal and **equation D.V.3** in the HAZ.

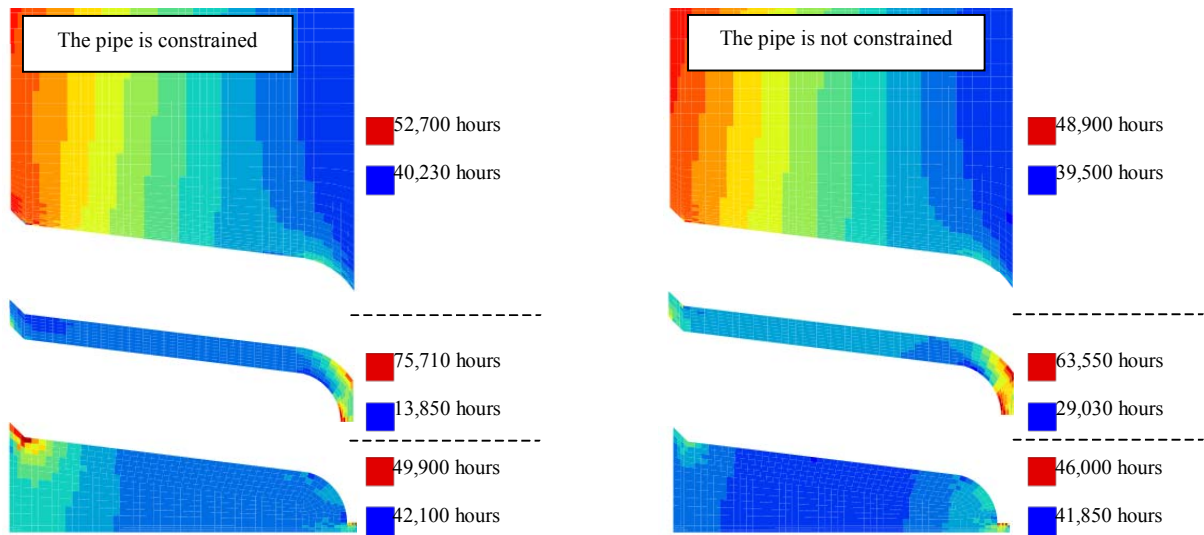


Figure D.V.4. Evaluation of the creep lifetimes of the welded pipe using the calculated peak rupture stresses and the MG fit for the base metal and the simulated HAZ

It is shown in **figure D.V.4** that in the two cases, rupture is likely to occur in the HAZ. When the pipe is not constrained, the prediction is quite in good agreement with that given by the multi-material calculation coupling creep flow and damage. However, the agreement is not so good when the pipe is constrained as the predicted creep lifetime is twice lower than that given by the multi-material calculation coupling creep flow and damage. It obviously shows that a unique expression of the peak rupture stress cannot be used when geometry and limit conditions induce complex loading conditions and constraint effects.

2. Investigations of the creep rupture behaviour of a vessel under internal pressure at 550°C (Creep properties of the WJT91 weldment)

2.1. Geometry and loading conditions

A vessel of 400 mm of inner diameter and 20 mm in thickness was modelled. A 2D axisymmetric representation was chosen and the mesh was refined in the heat affected zone where damage is expected to mainly develop. The loading state corresponds to an internal pressure which was set to 15 MPa and 10 MPa.

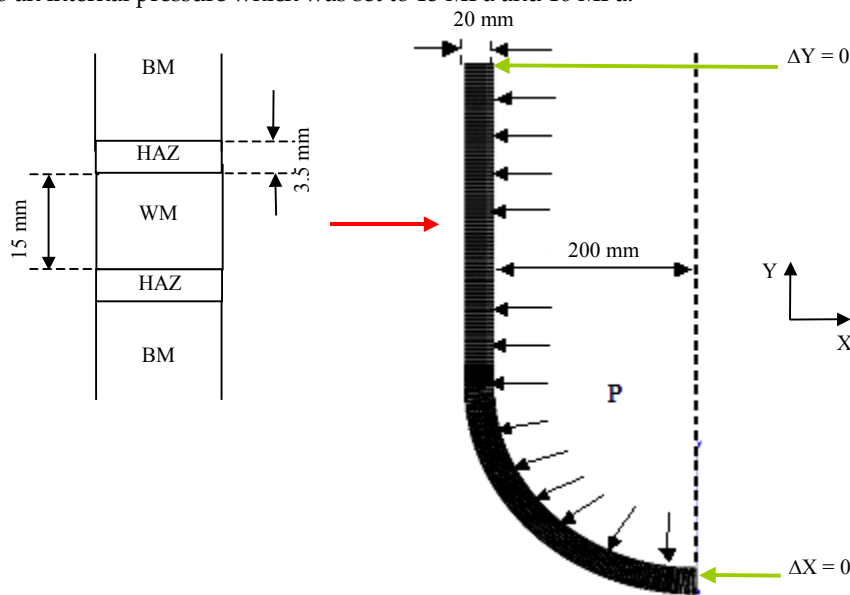


Figure D.V.5. Geometry of the vessel

2.2. Model parameters

The model parameters are those determined in **chapter D.IV** to represent creep flow and damage properties of the WJT91 weldment at 550°C. The model parameters are reminded in **table D.V.4**.

		Base metal	ICHAZ	
1. Young's modulus	E	163 GPa	163 GPa	
2. Poisson's ratio	ν	0.3	0.3	
3. Viscoplastic hardening at 550°C	R_{0vp}	0 MPa	0 MPa	
	Q_{vp1}	100 MPa	120 MPa	
	b_{vp1}	224	120	
	Q_{vp2}	35 MPa	20 MPa	
	b_{vp2}	25	10	
	p_c	0.05	0.02	
4. Viscoplastic strain rate at 625°C	K_{vp}	$460 \text{ MPah}^{-1/n_{qp}}$	$352 \text{ MPah}^{1/n_{vp}}$	
	n_{vp}	7.14	7.14	
5. Diffusion strain rate at 550°C	K_d	$2.53 \cdot 10^9 \text{ MPah}^{-1/n_d}$	$0.153 \cdot 10^9 \text{ MPah}^{1/n_d}$	
	n_d	1.0	1.0	
6. LPS model	q_1	1.5	1.5	
	q_2	1.0	1.0	
	f_c	0.1	0.1	
	δ_c	6.0	6.0	
	<i>Strain hardening coefficients</i>	m_{vp}	0.087	0.045
		m_d	1.0	1.0
	<i>Nucleation by the viscoplastic mechanism</i>	A_{vp1}	0.01	0.05
		A_{vp2}	0.15	0.4
		α_v	2.0	2.0
	<i>Nucleation by the diffusional mechanism</i>	A_{d1}	14.0	5
		A_{d2}	16.0	0.5
		α_d	2.0	2.0

Table D.V.4. Model parameters fitted at 550°C from experimental data on the WJT91 weldment

2.3. Results of FE calculations

The distributions of the von Mises equivalent stress and the stress triaxiality ratio were first investigated. Both of them are plotted at the end of the loading stage (see **figure D.V.6**).

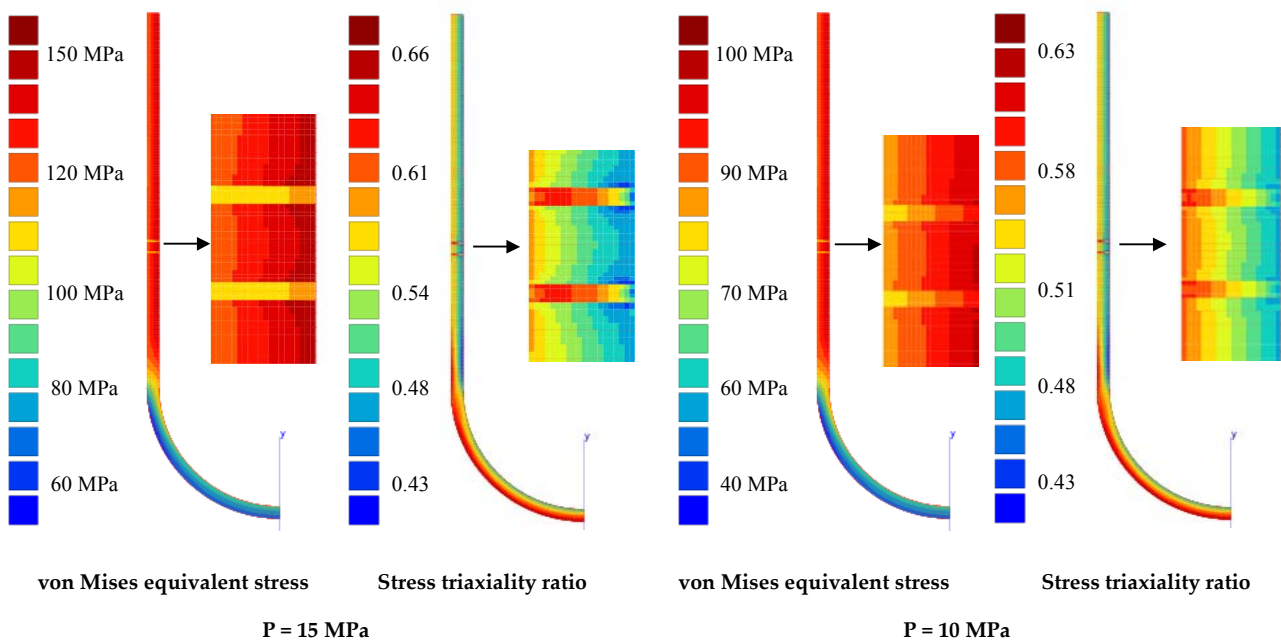


Figure D.V.6. Distributions of the von Mises equivalent stress and the stress triaxiality ratio at the end of the loading stage

Damage develops in the HAZ but also in the base metal as for a local maximum porosity ratio of 10% in the HAZ, the porosity ratio reaches 2% in the base metal. The evolution of the total porosity ratio during the creep lifetime is reported in **table D.V.5**.

Internal pressure	Temperature	$f_t = 0.05$	$f_t = 0.1$	$f_t = 0.15$	Failure
15 MPa	550°C	15,100 hours	30,605 hours	44,000 hours	47,530 hours
10 MPa	550°C	29,605 hours	54,400 hours	76,605 hours	92,575 hours

Table D.V.5. Model predictions of creep lifetime at 550°C

A post-calculation treatment at a time increment in the steady state creep regime allows to determine the peak rupture stress at every Gauss point. The distributions of the peak rupture stress in the steady state creep regime are shown in **figure D.V.7**.

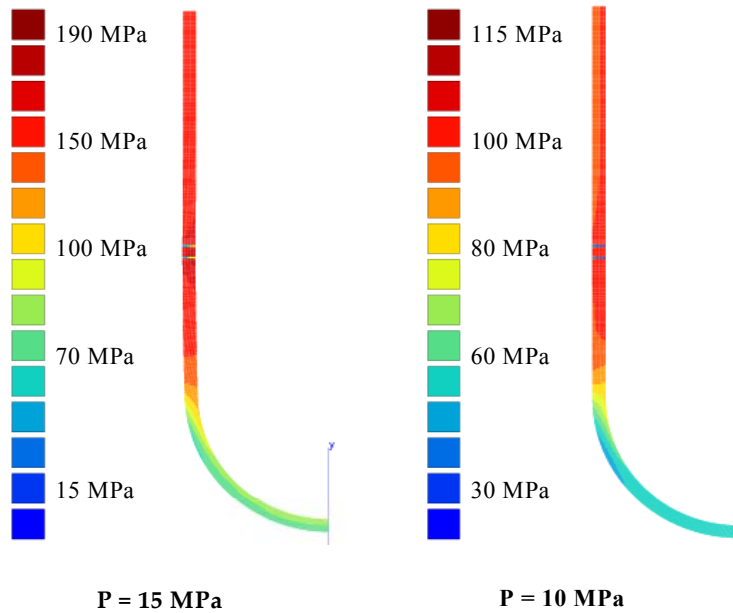


Figure D.V.7. Distribution of the peak rupture stress in the steady state creep regime

Then, using **equation D.V.2** and **equation D.V.3**, creep lifetime were respectively evaluated for the base metal and the heat affected zone using the Monkman-Grant relationships in the low stress creep regime. The model parameters of the MG fit in the low stress regime are reminded in **table D.V.6**. The creep lifetimes determined by post-calculation treatment are shown in **figure D.V.8**.

	Base metal	Simulated HAZ
Low stress*	$C_{MG}^{d,BM} = 0.098 h^{0.12}$ $m_{d,BM} = 0.88$	$C_{MG}^{d,HAZ} = 0.437 h^{0.21}$ $m_{d,HAZ} = 0.79$

*Table D.V.6. Monkman-Grant parameters for the base metal and the simulated HAZ in the low stress creep regime at 550°C
(*evaluated thanks to the results of the multiple deformation and damage mechanisms model)*

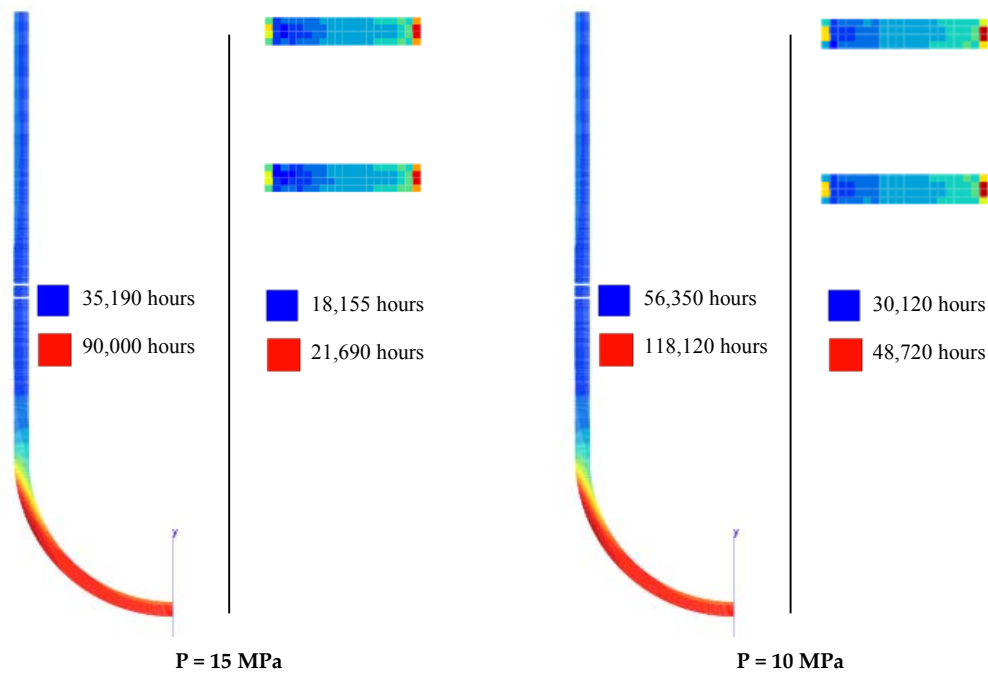


Figure D.V.8. Creep lifetimes predicted by the creep rupture stress method

It is shown that the creep lifetime predicted by using the post-calculation fracture criterion are largely pessimistic i.e. the predicted creep lifetime is twice lower than that predicted by the multi-material calculations integrating constitutive equations of the multiple deformation and damage mechanisms model coupling creep flow and damage development.

3. Prediction of the creep lifetime of a welded pipe for industrial use

3.1. Aim of the study

The aim of the present study is to show how the model and the multi-material approach can be used to evaluate the integrity of a component used in a thermal power-plant. The effect of the pipe geometry is especially investigated as well as the effect of the presence of a welded area.

3.2. Calculations procedure

3.2.1. Geometry and loading conditions

2D FE simulations were performed on two pipe geometry:

1. A perfectly round tube whose thickness is constant.
2. A pipe having the same radius than the tube but exhibits a roof geometry in the welded region.

The corresponding meshes are presented in **figure D.V.9**. The dimensions of the pipe cannot be given for confidentiality reasons. Note that the FE calculations were performed with the hypothesis of generalised plane strain i.e. the total creep strain is supposed to be homogeneous in the plane perpendicular to that of the 2D mesh.

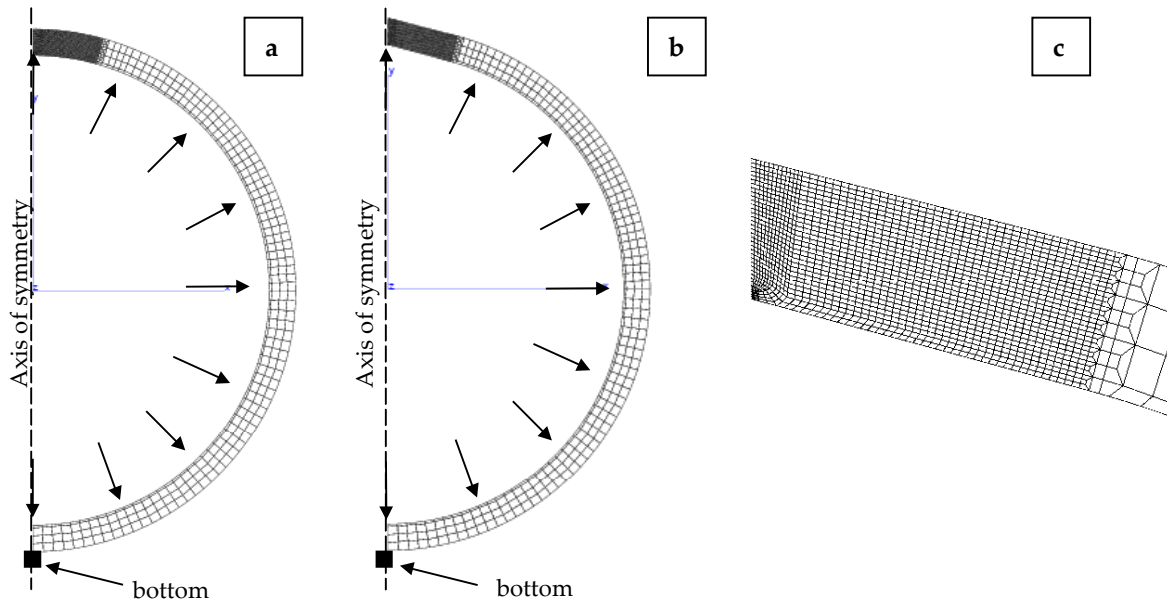


Figure D.V.9. Geometry: General view of the tube (a) and the pipe (b) and closer view of the pipe in the welded area (c)

The situation studied in this part is that of a tube under constant internal pressure that is not constrained at its extremities. As shown in **figure D.V.9**, the two pipes were submitted to a constant internal pressure. The limits conditions consist in avoiding the displacement following Y for the node called « bottom » and the displacement following X for the axis of symmetry. For the weldment, the HAZ was finely meshed within an area of 4 mm in length.

3.2.2. Calculations

The finite element simulations were performed for the two structures composed both of only the base metal and of the weldment (i.e. the base metal, the weld metal and the HAZ). In addition, these calculations were carried for two temperatures: 580°C and 625°C. The conditions of the FE simulations are reported in **table D.V.7**.

Material	base metal	base metal	base metal	base metal	Weldment	weldment	weldment	weldment
Geometry	tube	tube	pipe	pipe	Tube	tube	pipe	pipe
Temperature	580°C	625°C	580°C	625 °C	580°C	625°C	580°C	625 °C

Table D.V.7. Conditions of the FE calculations

For all the calculations the internal pressure was set to 4.1 MPa. The model coefficients extrapolated at 580°C and used for the present calculations are given in **table D.V.8**. Note that a simplified version of the model which has already been used in **chapter D.IV** was used, i.e. two deformation mechanisms are considered.

		Weld metal	Base metal	ICHAZ
1.Young's modulus	E	160 GPa	160 GPa	160 GPa
2.Poisson's ratio	ν	0.3	0.3	0.3
3.Viscoplastic hardening at 625°C	R_{0vp}	0 MPa	0 MPa	0 MPa
	Q_{vp1}	75 MPa	75 MPa	75 MPa
	b_{vp1}	1500	369	200
	Q_{vp2}	/	40 MPa	20
	b_{vp2}	/	75	10
	p_c	/	0.04	0.02
4.Viscoplastic flow rule at 625°C	K_{vp}	$1110 \text{ MPah}^{-1/n_{vp}}$	$493 \text{ MPah}^{-1/n_{vp}}$	$357 \text{ MPah}^{-1/n_{vp}}$
	n_{vp}	5.0	6.25	6.25
5.Diffusion flow rule at 625°C	K_d	$2.6 \cdot 10^9 \text{ MPah}^{-1/n_d}$	$2.6 \cdot 10^9 \text{ MPah}^{-1/n_d}$	$6.5 \cdot 10^7 \text{ MPah}^{-1/n_d}$
	n_d	1.0	1.0	1.0

6. LPS model	q ₁	1.5		
	q ₂	1.0		
	f _c	0.1		
	δ _c	6.0		
<i>Strain hardening coefficient</i>	m _{vp}	0.125	0.125	0.105
	m _d	1.0	1.0	1.0
	f ₀	/	0.01	/
<i>Nucleation by the viscoplastic mechanism</i>	A _{vp}	/	0.01	0.05
	B _{vp}	/	0.15	0.4
	α _{vp}	/	2.0	2.0
<i>Nucleation by the diffusional mechanism</i>	A _d	/	14	5
	B _d	/	16	0.5
	α _d	/	2.0	2.0

Table D.V.8. Model parameters extrapolated at 580°C

3.3. Results

3.3.1. Predictions of pipes creep lifetimes at 625 and 580°C

The evolution of damage in the components as well as the creep times to failure were determined from FE calculations and are reported in **table D.V.9**. Note that for all calculations on welded pipes, both creep damage development and creep failure occur in the heat affected zone.

Geometry	Material	Temperature	f_t = 0.1	f_t = 0.15	f_t = 0.2	Failure
Tube	base metal	625°C	56,800 hours	76,300 hours	77,450 hours	77,450 hours
Tube	weldment	625°C	10,700 hours	14,800 hours	16,700 hours	16,700 hours
Pipe	Base metal	625°C	13,000 hours	15,900 hours	<i>Not reached</i>	16,840 hours
Pipe	weldment	625°C	6,300 hours	9,500 hours	<i>Not reached</i>	11,500 hours
Tube	Base metal	580°C	440,000 hours	<i>Not reached</i>	<i>Not reached</i>	445,000 hours
Tube	weldment	580°C	29,300 hours	42,250 hours	52,250 hours	54,100 hours
Pipe	Base metal	580°C	132,900 hours		<i>Not reached</i>	142,200 hours
Pipe	weldment	580°C	15,100 hours	21,150 hours	28,100 hours	32,000 hours

Table D.V.9. Model predictions of creep lifetime at 580°C and 625°C

Strong differences in the creep time to failure between the two geometry were found and can be easily evidenced in **figure D.V.10**. For the same geometry and testing conditions, the welded component exhibits a creep lifetime between 4 and 5 times lower than that of the same component made of only base metal. An effect of the geometry was also evidenced as the roof effect induces a reduction of the creep lifetime by 40% for the same material in the same testing conditions. The effect of the geometry is investigated in the next section.

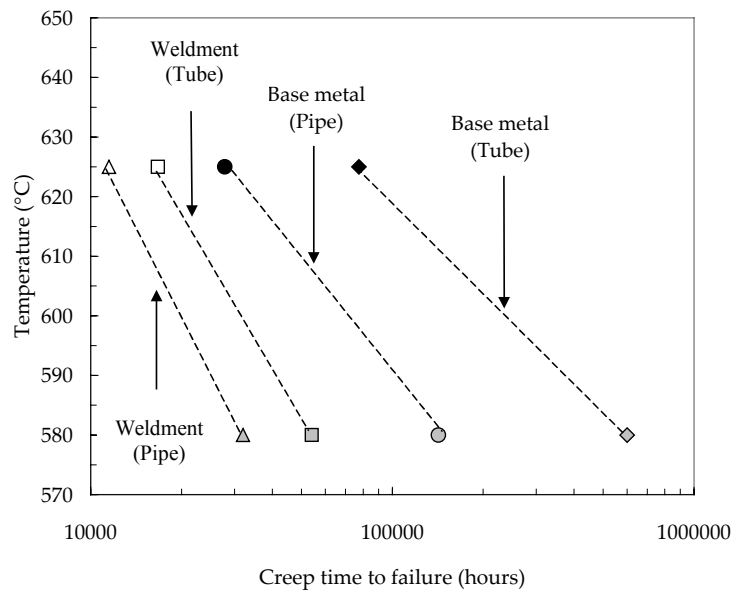


Figure D.V.10. Creep lifetime of the tube and the pipe made in base metal and weldment at 580°C and 625°C

3.3.2. Investigations of geometrical effects

FE calculations revealed that for the same temperature and loading conditions, the tube exhibits a creep lifetime very larger than that of the pipe with the roof effect both for components with and without weld. Therefore, further investigations were necessary to determine the origins of this loss of creep strength. The distributions of the von Mises equivalent stress at the end of the loading stage are plotted in **figure D.V.11** for the two geometries (i.e. (a) = tube and (b) = pipe with roof effect). Note that for the sake of simplicity, the results of **figure D.V.11** concern components made of only base metal.

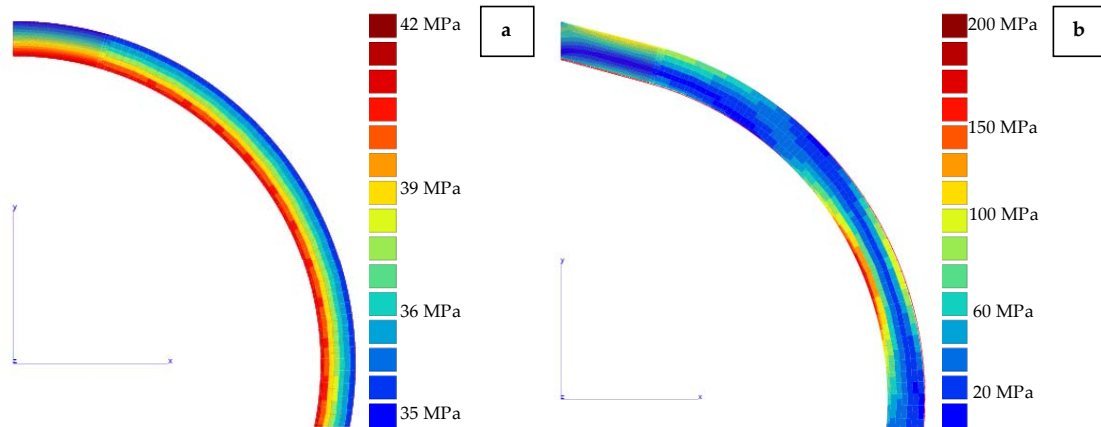


Figure D.V.11. von Mises equivalent stress at the end of the loading stage for components made of base metal (a) Tube (b) Pipe

For the tube, the maximum local von Mises equivalent stress is equal to 40 MPa whereas it locally reaches more than 150 MPa in the pipe with the roof effect. Therefore, it is evidenced that the roof effect leads to a complex loading state and very large increase in locally reached stress values.

3.4. Comparison of the predictions of the present study with predictions given by the peak rupture stress method

The locally coupled approach was used to predict creep lifetime of the welded component at 625°C under an internal pressure of 4.1 MPa. To start with, as already largely described for the previous cases and in **chapter D.III**, the peak rupture stress (see **equation D.V.1**) was calculated at every gauss point at a time increment in the steady state creep regime. The resulting distribution of the peak rupture stress in the steady state creep regime is given in **figure D.V.13**.

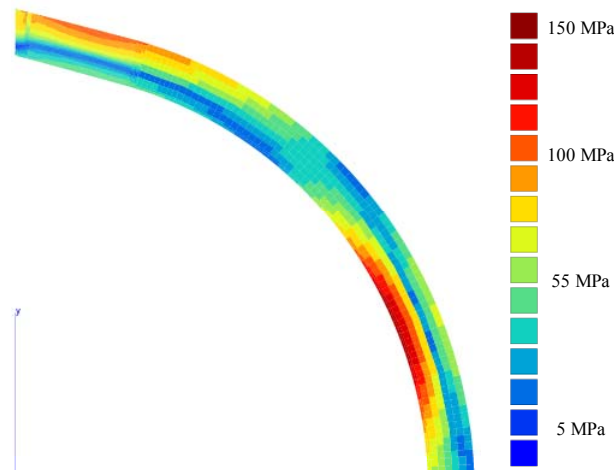


Figure D.V.13. Distribution of the peak rupture stress for the welded pipe (4.1 MPa – 625°C)

Equation D.V.2 and **equation D.V.3** were then used to calculate the creep lifetime respectively in the base metal and in the HAZ. The corresponding predicted creep lifetimes are plotted in **figure D.V.14**. The predicted creep lifetime exhibits a poor agreement with the results of multi-material coupled creep flow and damage calculation (the predicted lifetime is twice lower). Moreover, a steady state creep regime is never really reached as stress redistributes due to the creep flow properties mismatch.

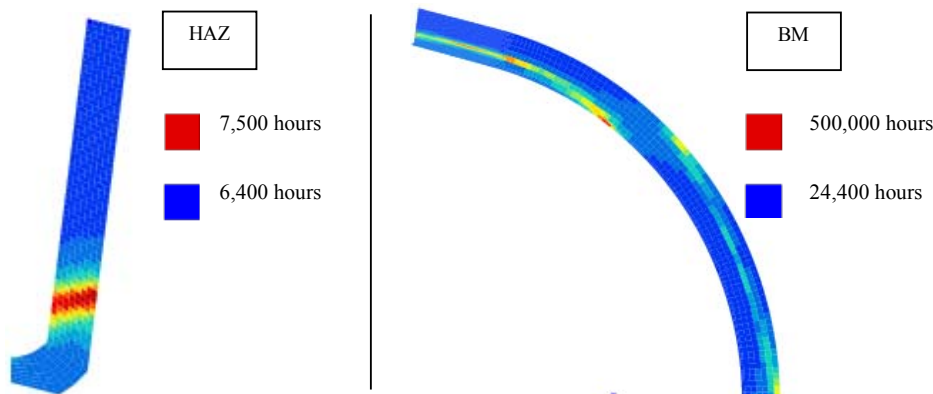


Figure D.V.14. Prediction of creep lifetime in the weldment – 625°C – 4.1 MPa (HAZ = close view and BM)

3.5. Comparison of the result of the present study with curves established from observed in service worst cases of type IV cracking in 9Cr1Mo welded components

The representations in **figure D.V.15** (extracted from Parrot and Shibli (2004)) gives the onset of type IV cracking versus the hoop stress. The use of these abacus requires:

1. A finite element elasto-viscoplastic calculation of the pipe made of only base metal.
2. The determination of the maximum hoop stress taking into account that the hoop stress can evolve due to geometry effect.

The hoop stress for a perfect pipe under internal pressure is given by:

$$\sigma_{\text{hoop}} = \frac{PR}{e} \quad (\text{eq. D.V.4})$$

where, P is the internal pressure in MPa, R is the radius of the pipe in mm and e is the thickness of the pipe in mm. The analytically calculated value is typically that found in the FE calculations at the end of the loading stage (i.e. 36 MPa at 4.1 MPa). Then, especially due to the roof effect, the value of the hoop stress largely increases after nearly 1,000 hours of creep.

The value of the hoop stress, evaluated from FE calculations, was reported in **figure D.V.15** (red lines). It shows that the results of the multi-material FE simulation of the present study are in quite good agreement with the curves established from observed in service worst case of type IV cracking.

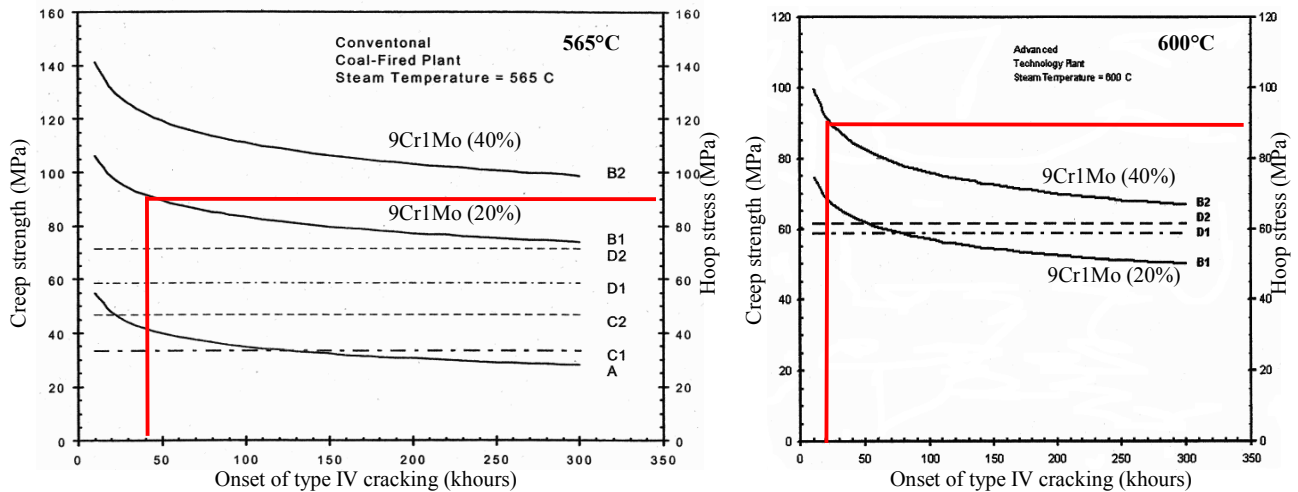


Figure D.V.15. Comparison of worst case type IV cracking of grade 22 and 91 steels (from Parrot and Shibli (2004))

3. Conclusions

Examples of application of the model as a support for designing welded components showed that:

1. The integration of the multiple creep flow and damage mechanism model into multi-material FE calculations allow to predict with a quite good agreement, the creep lifetime of welded components of various kind of geometry.
2. The geometry plays a key role as it was evidenced that only a roof shape in the welded area may lead, locally, to a large increase of the equivalent stress and so on to a large decrease in the creep lifetime.

The method introduced in **chapter D.III** and derived from the Monkman-Grant formalism and the peak rupture stress method gives quite interesting results for the predictions of the creep lifetime of welded components at least for not too much complex geometries. Indeed, the method does not give good results when geometry as well as mismatch in creep properties lead to a complex multiaxial loading state and continuous stress redistributions.

References

- Berdin C., Besson J., Bugat S., Desmorat R., Feyel F., Forest S., Lorentz E., Maire E., Pardoën T., Pineau A., Tanguy B. (2004). Local approach to fracture. Edited by J. Besson in *les presses de l'école des mines de Paris*. Examples of application. 176-191.
- Coussement C., De Backer T., Dewitte M., Verelst L. (1994). Internal pressure creep testing on welded components of modified 9%Cr and 12%Cr steel. *Second european conference on joining technology - EUROJOIN2*. 461-479.
- Parrot A., Shibli A. (2004). Performance du P91 et des autres aciers martensitiques à 9% Cr : Expérience industrielle et en laboratoire. *EdF report n°HT-26/02/006/A*. In French (Private communication).
- Shibli I.A. (2002). Performance of P91 thick section welds under steady state and cyclic loading conditions: power plant and research experience. *OMMI*. **1(3)**.

Main Results of Part D

Creep fracture behaviour of 9Cr1Mo-NbV weldments

At 625°C, creep fracture of 9Cr1Mo-NbV weldments occurs in the type IV region and more precisely in the intercritical heat affected zone (ICHAZ) parallel to the fusion line. At 450°C and 550°C, rupture occurs in the base metal but near the HAZ.

SEM investigations in longitudinal cross sections of cross-weld specimens revealed that damage mainly developed in the HAZ and in the base metal near the HAZ in the temperature range between 450°C and 625°C. Strong creep strain gradients were also observed in cross-weld specimens as creep strain mainly occurs in the HAZ (even at 450 and 550°C) whereas both the base metal and the weld metal were little deformed. Therefore 9Cr1Mo-NbV weldments are obviously hard/soft/hard weldments.

Creep flow and fracture properties mismatch in 9Cr1Mo-NbV weldments

Creep flow properties were respectively identified in **chapter B.III** for the base metal and in **chapter C.IV** for the HAZ. It allows to investigate both the creep flow and the creep fracture properties mismatches. It was found that for the same applied engineering stress, the steady state creep strain rate is more than ten times higher in the weakest HAZ than in the base metal. In terms of creep fracture properties, it was concluded that the weakest HAZ exhibits a creep strength 30% lower than that of the base metal.

Multi material finite element simulations

A multi-material approach was used to model creep flow and damage behaviour of the weldment. For the sake of simplicity a three material representation was chosen:

1. The weld metal because damage little develops in this zone, only the creep flow behaviour of the weld metal was described.
2. The HAZ which was reduced to its weakest part. The creep behaviour of the weakest HAZ was represented using the multiple deformation and damage mechanisms model, coupling creep flow and damage, fitted in **chapter C.IV**.
3. The base metal whose creep behaviour was represented using the multiple deformation and damage mechanisms model, coupling creep flow and damage, fitted in **chapter B.III**.

The key point of multi-material finite element modelling was to determine the length of the HAZ, l_{HAZ} which strongly determine the constraint effects in the weldment. l_{HAZ} was determined from experimental measurements of creep strain gradients in cross-weld creep specimens and nearly reaches the value of the initial length of the HAZ evidenced by hardness measurements at room temperature.

Modelling creep flow and damage properties of 9Cr1Mo-NbV steel weldments

One of the key point of the present study is that constitutive equations were fitted to independently represent the creep flow and damage behaviour of the weld metal, the HAZ and the base metal. When integrating these constitutive equations into multi-material FE calculations, a good agreement was found between calculated and experimentally measured cross-weld specimens creep lifetimes for various kind of geometry.

Use of the results of the present study for design purposes

The multi-material approach was finally used to model the creep flow and damage behaviour of welded components having various geometry. The case of a welded pipe was especially investigated. The predicted creep lifetime of the welded pipe under internal pressure exhibited a quite good agreement with abacuses established from observed in-service failures.

A simplified method is also proposed. It is based on elasto-viscoplastic finite element calculations and the use of a post-calculation treatment at every gauss point and a time increment in the steady state creep regime. It integrates the evaluation of the peak rupture stress which accounts for the effects of the multiaxial loading state on damage development and the use of the classical Monkman-Grant predictive relationship. The method gives not so bad results except for too much complex geometries and/or loading states.

Conclusions and further work

Conclusions

The present work was concerned with the experimental study of creep flow and damage behaviour of 9Cr1Mo-NbV steels at high temperature i.e. in the temperature range between 550°C and 650°C.

In the first part of this work, the metallurgical and general mechanical properties as well as the changes in metallurgical and mechanical properties due to ageing of both the base metal and the weldment were investigated. The following conclusions can be drawn:

1. The base metal exhibits a high dislocation density lath martensite morphology and laths of close crystallographic orientation are gathered into packets within the prior austenite grain (100 μm - 150 μm in mean size). The steel is strengthened by the precipitation of M_{23}C_6 carbides and a fine dispersion of MX particles which both proceed during the high temperature tempering (typically 2 hours at 765°C). In addition, molybdenum exerts a solid solution strengthening effect.
2. The high temperature tensile properties of the base metal are quite good with a tensile strength of 350 MPa for a strain rate of 10^{-3} s^{-1} at 625°C. One particularity of the base metal is its very low uniform elongation before the onset of material softening. A strong sensitivity of the tensile properties to the strain rate was also observed for temperatures larger than 450°C. The present study also confirmed that the base metal is probably sensitive to dynamic strain ageing for temperatures lower than 450°C.
3. During thermal ageing, many metallurgical changes occur. First, M_{23}C_6 carbides start to coarsen after only 1,000 hours of ageing in the temperature range between 450°C to 625°C. Then, Laves phase precipitation of type $(\text{Fe,Cr})_2\text{Mo}$ or Fe_2Mo occurs after 1,000 hours of ageing in the temperature range between 550°C and 625°C. In addition, the initial lath martensite microstructure recovers i.e. dislocation density decreases, subgrains formed and grow within the prior lath martensite. These metallurgical changes affect the material tensile strength as it is reduced by 20 MPa – 30 MPa after 10,000 hours of ageing in the temperature range between 550°C and 625°C.
4. The base metal exhibits a good weldability, and even if some defects can be detected both in the weld metal and at the fusion line, they do not affect the creep properties of the weldments.
5. The main metallurgical changes occurs in the intercritical heat affected zone (i.e. in areas where the temperature, T_{peak} , locally reached during the welding thermal cycle is set within the intercritical domain: $A_{c1} < T_{\text{peak}} < A_{c3}$). This area, exhibits a totally recovered microstructure made of low dislocation density fine equiaxed grains (5 μm – 10 μm in size). The M_{23}C_6 carbides are also twice larger in size i.e. 200 nm than in the base metal. The tensile properties (i.e. 0.2% proof stress and tensile strength) of the weldment are reduced by 50 MPa - 60 MPa in comparison with those of the base metal.

Creep flow and damage behaviour of the base metal were experimentally studied especially at 625°C using a large experimental database including creep tests on various kind of U-notched axisymmetric specimens. The following conclusions can be given:

1. The experiments of the present study and the literature data of Kloc and Sklenika (1997) evidenced that 9Cr1Mo-NbV steels exhibit two main creep flow mechanisms: a power-law creep regime, where deformation is accommodated by dislocation climb or cross-slip, at high stress ($n = 8.0$) and a diffusion creep regime, where deformation is accommodated by grain boundary diffusion, at low stress ($n = 1.0$). The transition stress between the two regimes was evaluated to 70 MPa.
2. Cavity nucleation mainly occurs at the interface between second phase particles (M_{23}C_6 carbides and Laves phase) and at triple points. It was also evidenced that the stress triaxiality ratio plays a key role in damage nucleation.
3. The fracture mode of the steel could then be called “intergranular then ductile”, as fracture starts from intergranular cavitation at grain and subgrain boundaries and then develops by growth and coalescence of cavities in a ductile manner.
4. Scanning electron microscope (SEM) investigations also showed that the recovery of the initial lath microstructure largely promotes the material softening for low creep elongation ($\approx 1\%$) and the acceleration of the creep strain rate in the tertiary creep regime.
5. Creep tests on materials aged for 10,000 hours at 625°C showed that prior thermal ageing significantly reduces the material creep strength.

Based on experimental investigations, a model was designed in the framework of the mechanics of porous media. This model aimed at representing various deformation mechanisms, corresponding to various stress levels, and aimed at coupling the creep flow and damage behaviour.

1. Three main deformation mechanisms were considered: a quasi-plastic regime (to represent deformation during loading and fracture by necking without any cavitation at high strain rates), a viscoplastic creep regime (high stress i.e. > 70 MPa), and diffusion creep regime (low stress i.e. < 70 MPa). These three deformation mechanisms were coupled in terms of hardening by introducing an effective creep strain.
2. For each mechanism, cavity nucleation, growth and coalescence were represented by both the Gurson-Tvergaard-Needleman model and the extension proposed by Leblond, Perrin and Suquet to high temperature deformation.
3. The model was fitted to represent creep flow and fracture properties of the base metal at 625°C for various kinds of axisymmetric specimen geometry.
4. The model was validated as it succeeds in predicting creep damage location in notched specimens, and in representing creep crack growth in compact tension specimens. The extension of the model in the temperature range between 600°C and 650°C was also used to represent experimental data given in the literature.
5. A simplified formulation of the model that can be used in post processor was proposed. This version of the model was implemented by Y. Lejeail at the CEA Cadarache.
6. The model was also successfully used to represent creep flow and damage behaviour at 550°C without modifying the model parameters accounting for damage. The model validity is however not ensured out of the temperature range between 550°C and 650°C. Indeed, for temperatures lower than 450°C, dynamic strain ageing may affect the creep flow and damage mechanisms and for temperature higher than 650°C, as the austenite start transformation temperature can be reached near carbides where the matrix is depleted in chromium and carbon. In the temperature range between 450°C and 550°C, the model validity can not be totally ensured due to the absence of any experimental results.

Creep flow and damage behaviour of the weldment were then investigated. To do so, creep tests were performed at 625°C up to 11,000 hours. It was shown that:

1. Type IV cracking occurs in the weldment i.e. creep failure occurs in the heat affected zone, more precisely in the intercritical heat affected zone (ICHAZ), parallel to the fusion line.
2. The weldment exhibits a creep strength 30% lower than that of the base metal.
3. Scanning electron microscope (SEM) investigations revealed that damage mainly develops in the HAZ and in the base metal near the HAZ. Moreover, intergranular cracking was found to be the dominating damage mechanism.
4. Measurements of strain gradients in the weldment allow to determine the length of the area where creep deformation is concentrated.

To understand, the creep flow and damage behaviour of weldments, it was necessary to determine the creep flow and damage behaviour of the weakest HAZ i.e. the ICHAZ. To do so, it was first necessary to investigate the metallurgical changes in the ICHAZ both during the weld thermal cycle and the post weld heat treatment of 2 hours at 760°C. A model specifically designed by Rosenthal and Rykalin to represent the weld thermal cycles experienced during manual arc welding was fitted. It allows to reproduce various microstructures of the HAZ. Metallurgical investigations were then performed to ensure the validity of the model:

1. Hardness measurements evidenced a good agreement between simulated and real HAZ microstructures.
2. Analysis of the precipitation on carbon extraction replica evidenced a difference of only 10 nm between the measured average particles size in simulated and real microstructures.
3. Transmission electron microscopy (TEM) and electron backscattering diffraction (EBSD) analysis ensured a good agreement between the simulated and real ICHAZ.

Thanks to these simulations, the metallurgical changes that occur in the ICHAZ and especially the extensive recovery of the initial lath structure during the post weld heat treatment could be investigated. It was concluded that:

1. During heat treatment in the intercritical domain, due to kinetics factors, the dissolution of $M_{23}C_6$ precipitates is very limited.
2. As their solubility limit is very high, MX precipitates are non dissolved in a large part of the heat affected zone.
3. The martensite that forms during cooling exhibits a strong lack in carbon so that this martensite is very sensitive to softening during the PWHT.

The weld thermal cycle corresponding to the weakest HAZ was represented by $T_{peak} = 986^\circ\text{C}$ and $\Delta t_{800 \rightarrow 500} = 16 \text{ s}$. Then, the weakest HAZ microstructure was reproduced on bulk specimens using a Gleeble 1500 thermal-mechanical simulator. Various kind of axisymmetric U-notched specimens were machined to investigate the effects of the stress triaxiality ratio on creep flow and damage behaviour. Creep flow and damage behaviour of the weakest HAZ were determined as:

1. The weakest HAZ microstructure exhibits two main creep flow mechanisms: a power-law creep regime at high stress ($n = 9.6$) and a grain boundary diffusion creep regime at low stress ($n = 1$). The transition stress between the two regimes was evaluated to 70 MPa as for the base metal. It was also evidenced that the steady state creep flow rates of the HAZ are more than ten times higher for the weakest HAZ than for the base metal.
2. SEM investigations also revealed that the damage mechanisms in the weakest HAZ were very similar to these observed in cross-weld specimens (It was a supplementary validation for the choice of the weld thermal cycle).

A three material representation i.e. the base metal, the weld metal and the weakest HAZ, was chosen to model creep flow and damage behaviour of weldments. Therefore, finite element (FE) calculations were performed with using the models fitted for the three materials. The results of FE calculations exhibits a quite good agreement with experiments on cross-weld specimens. It was finally shown that the model can be used to predict the creep lifetime of industrial components.

Further work

Development of chromium martensitic stainless steels and weldment

Many research programs are concerned with improving the creep strength of chromium martensitic stainless steels. There is no deny that the most interesting developments come from Japan due to their very good knowledge in the metallurgy of chromium stainless steels. They especially understand the great importance of the strengthening effect of MX precipitates which is all the more interesting as MX precipitates are very stables even for long term creep exposures (see Taneike et al (2003)). The representation given by Masuyama (2001) in **figure Co.1** can be used as a guideline for the development of new chromium heat resistant steels.

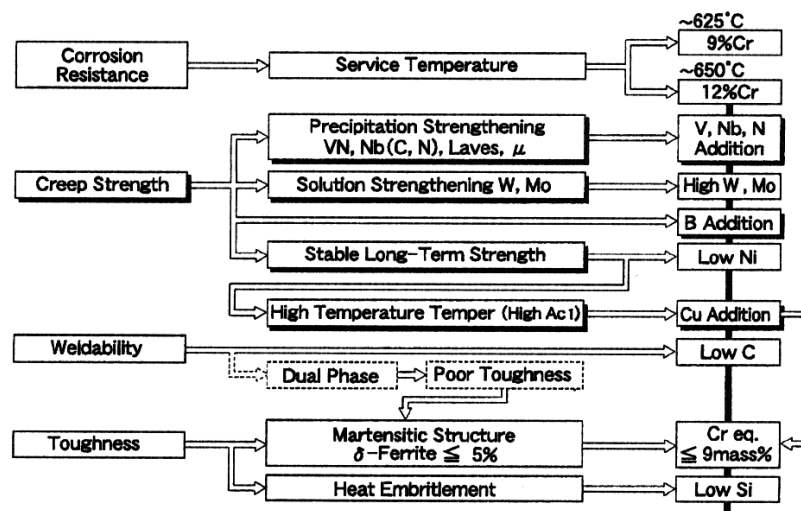


Figure Co.1. Optimisation of the chemical composition of chromium martensitic steels (Extracted from Masuyama (2001))

The present study shows that 9Cr1Mo-NbV steels should not be used at temperatures larger than 585°C to respect the criterion 100 MPa – 100,000 hours. For use at temperatures near 450°C as it is envisaged for the vessel of nuclear power plants, it is necessary to build the corresponding experimental database. As ageing phenomena strongly affects the material creep strength, it is recommended, if possible, to perform creep tests on previously long term ($\approx 10,000$ hours) aged materials.

Improving the creep strength of weldments is a great challenge. Indeed, it was shown that even if the creep strength of the base metal is improved the gap in creep strength between the base metal and the weldment is still high. The solutions to limit the loss of creep strength due to welding are obviously the optimisation of the post weld heat treatment. A normalising treatment of the welded components would be the best way to improve the weldment creep strength but this operation is hardly realisable on industrial components. The half tempering procedure which consists in a tempering of the base metal in the temperature range between 600°C and 650°C and a post weld heat treatment at 750°C is also probably quite interesting. The main point is, in fact, to limit the effects of the welding procedure on the precipitation state especially that of MX precipitates.

Modelling creep flow and damage behaviour

The model of the present study can probably be used to represent high temperature creep flow and damage behaviour of other materials like the austenitic stainless steels which also exhibits a transition in creep flow mechanisms at low stress.

Moreover, the model formulation can be improved on several points:

1. The description of cavity coalescence as the concept of effective porosity of the Gurson-Tvergaard-Needleman model is not satisfactory. The integration of the model proposed by Thomason (1985) and its last developments (Zhang et al (2000), Pardo T. and Hutchinson J. (2000)) is one of the future development of the model.
2. It would be interesting to integrate the extension of the Gurson model proposed by Gologanu et al (1993 and 1994) as it would give a better representation of cavity growth for low stress triaxiality ratio (in this case, cavities are generally elongated following the loading axis) and as creep cavities are rather elongated than spheroidal in high temperature creep conditions especially at low stress.
3. It would be of great interest to include a description of the precipitation state in terms of average diameter and volume fraction of particles. Indeed, the material softening is largely promoted by the evolution of the precipitation state and such a formulation would be more physical than the integration in of softening effects in the hardening function as proposed in the present study.
4. To describe high temperature creep flow and damage behaviour at temperatures lower than 500°C, it would be necessary to include constitutive equations as these proposed by Yaguchi and Takahashi (2001) for materials deforming in the dynamic strain ageing domain, into the model of the present study (i.e. with coupling with damage evolution). Note that the work currently performed at the Ecole Nationale Supérieure des Mines de Paris by Graff et al (2004) can also be used.

Finally, performing unit and void cells calculations would also be very interesting to study the effects of each parameters (q_1 , q_2 but also the coefficients of the interactions matrix) on the description of cavity growth. It requires, however, a very huge number of calculations because of the coupling between creep flow and damage mechanisms.

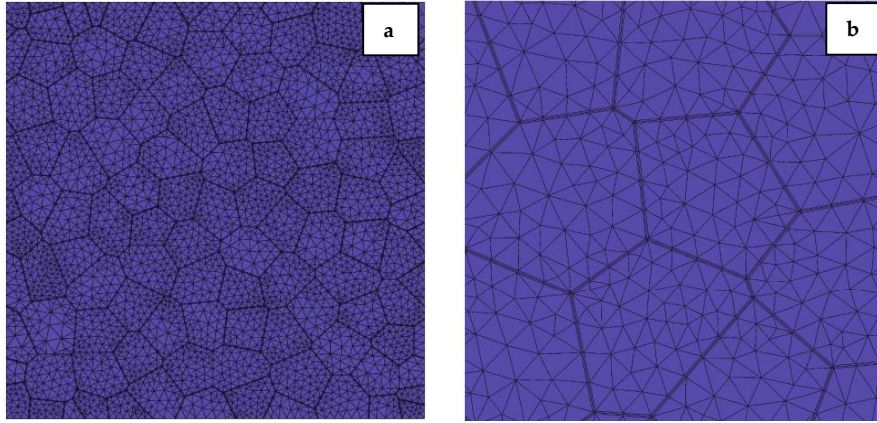
Taking into account the effect of welding residual stresses in calculations

The present study was not concerned with the evaluation of welding residual stresses in 9Cr1Mo-NbV weldments. Nevertheless, in components as thick as those studied in the present work, it is possible that all the residual stresses are not relaxed during the post weld heat treatment. Although it was not done in the present work, the effects of residual stresses on creep flow behaviour can easily be taken into account as the model allows to represent several creep flow mechanisms from high to low stress.

Integration of the model in polycrystalline aggregates FE calculations

Several studies have been performed at the Centre des Matériaux of the Ecole Nationale Supérieure des Mines de Paris concerning the development of polycrystalline aggregates FE calculations ((Diard (2001) and Musienko (2004)). The possibility to use the model of the present study in polycrystalline aggregates FE calculations was investigated. Such a use of the model may be quite interesting as polycrystalline aggregates FE calculations especially allow to study constraint effects due to both, the misorientation between grain boundaries and the loading axis, and the creep flow properties mismatch between grains and grain boundaries.

The work presented below uses a 3D representation of the real microstructure with both grains and grain boundaries as can be shown in **figure Co.2**. In the mesh presented in **figure Co.2**, the volume fraction of grain boundaries is equal to 4%. Note also that the mesh is three dimensional with a single grain in the thickness.



*Figure Co.2. 2D view of the 3D FE mesh of a polycrystalline aggregate (designed by Musienko (2004))
(a) General view and (b) closer view*

The model designed in the present study was used to perform polycrystalline aggregates FE calculations. Grains were given the creep flow and damage behaviour in the viscoplastic creep regime:

$$\dot{\epsilon}_g = \dot{\epsilon}_e + \dot{\epsilon}_{vp} \quad (\text{eq. Co.1})$$

whereas grain boundaries were given the coupled creep flow and damage behaviour between the viscoplastic creep regime and the diffusion creep regime:

$$\dot{\epsilon}_g = \dot{\epsilon}_e + \dot{\epsilon}_{vp} + \dot{\epsilon}_d \quad (\text{eq. Co.2})$$

The model parameters fitted for the base metal at 625°C were used in the following (see **chapter B.III**). The values of K_d , A_d and B_d need to be adapted as diffusion only occurs at grain boundaries. To do so, taking into account that the volume fraction of grain boundaries is only equal to 4%, K_d was set to $0.0132 \cdot 10^9 \text{ MPah}^{-1}$ and then A_d and B_d were respectively set to 0.56 and 0.64. The loading conditions are described in **figure Co.3**.

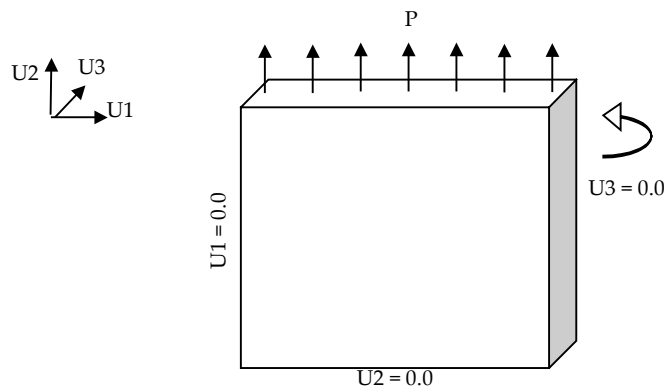


Figure Co.3. Loading conditions for polycrystalline aggregates FE calculations

FE calculations were performed for applied engineering stresses, $\sigma = 120 \text{ MPa}$, 80 MPa and 40 MPa . The steady state creep strain rates versus the applied engineering stress were plotted in **figure Co.4** where they are also compared to the results given by the multiple deformation and damage mechanism model. It is evidenced that the results are in good agreement with FE calculations on the homogenous material. Nevertheless, it is shown that polycrystalline aggregates calculations leads a lower steady state creep strain rate in the low stress creep regime which is probably due to geometry effects.

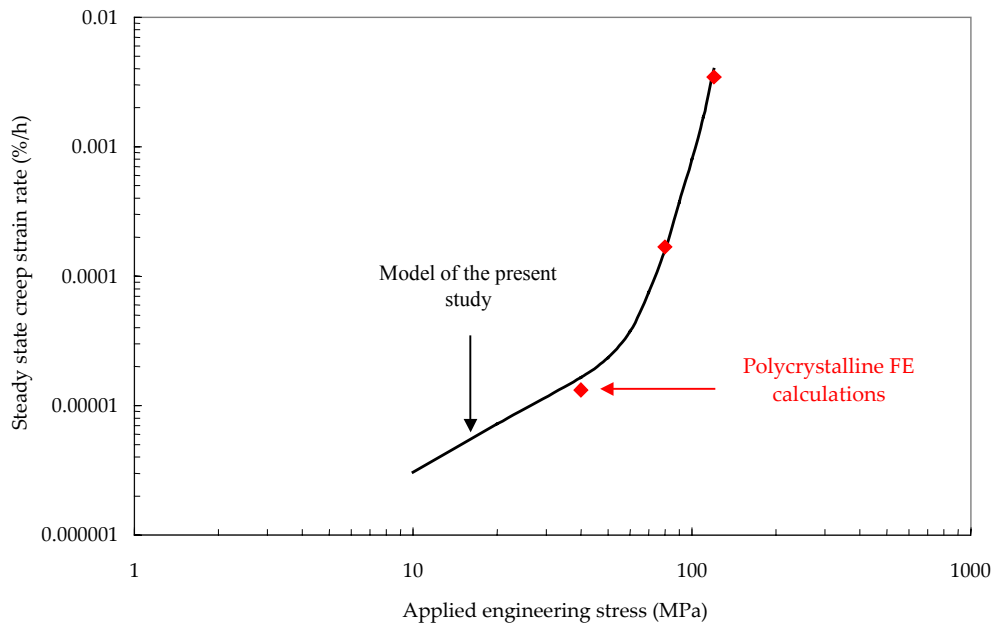


Figure Co.4. Steady state creep strain rate versus applied engineering stress for the base metal at 625°C: Comparison calculations on the homogeneous material (line) and polycrystalline aggregates FE calculations (red symbols)

It was also very interesting to compare, in **figure Co.5** and **figure Co.6**, the creep damage behaviour between the high stress (i.e. $\sigma = 120$ MPa) and the low stress creep regime (i.e. $\sigma = 40$ MPa). It is shown that at both high and low stress, damage mainly develops at grain boundaries. In the high stress creep regime (**figure Co.5**), damage development little depends on the orientation of the grain boundaries whereas it strongly depends on it at low stress. It is shown in **figure Co.6** that damage mainly develops in grain boundaries perpendicular to the loading direction in the low stress creep regime.

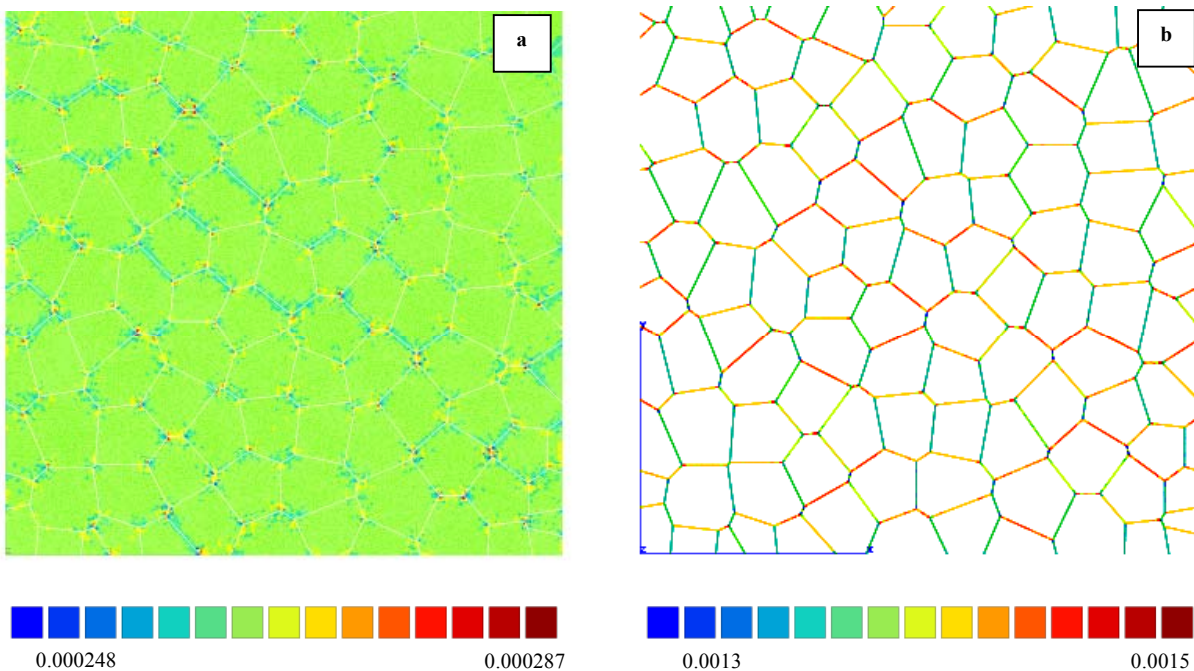


Figure Co.5. Creep damage development for a cumulated viscoplastic strain $p_v = 0.01$ (a) in grains (b) in grain boundaries at high stress ($\sigma = 120$ MPa)

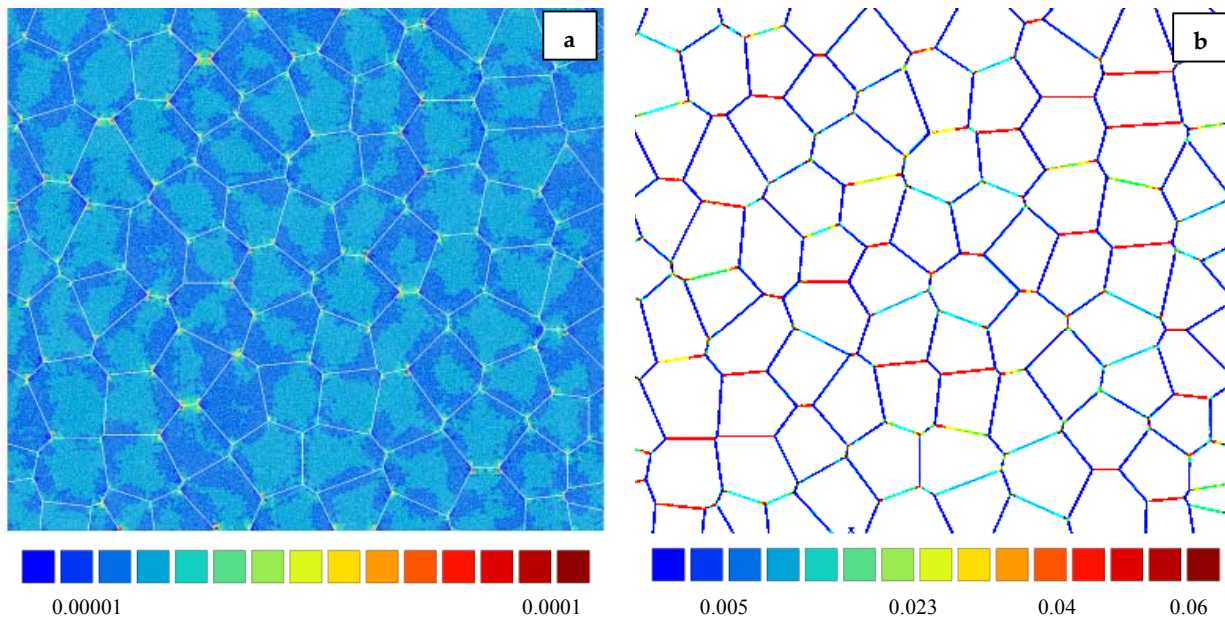


Figure Co.6. Creep damage development (a) in grains (b) in grain boundaries at low stress ($\sigma = 40$ MPa)

The first results presented above evidenced that the model can be quite easily integrated into polycrystalline aggregates FE calculations. Despite the quite long calculation time, FE polycrystalline aggregates calculations may be very interesting as they allow to take into account constraint effects due to geometry (grain size, orientation of grain boundaries with respect to the loading axis ...).

References

- Diard O. (2001). Un exemple de couplage, comportement – endommagement – environnement, dans les polycristaux. Application à l'interaction pastille-gaine. *PhD thesis of the Ecole Nationale Supérieure des Mines de Paris (In French)*.
- Gologanu M., Leblond J., Devaux J. (1993). Approximate models for ductile metals containing non spherical voids- case of axisymmetric prolate ellipsoidal cavities. *Journal of mechanics and physics of solids*. **41(11)**. 1723-1754.
- Gologanu M., Leblond J., Devaux J. (1994). Approximate models for ductile metals containing non spherical voids- case of axisymmetric oblate ellipsoidal cavities. *Journal of engineering material technology*. **116**. 290-297.
- Graff S., Forest S., Strudel J.L., Prioul C., Pilvin P., Béchade J.L. (2004). Strain localization phenomena associated with static and dynamic strain ageing in notched specimens: experiments and finite element simulations. *Materials science and engineering*. To be published.
- Kloc L., Sklenicka V. (1997). Transition from power law to viscous creep behavior of P91 type heat treated steel. *Materials Science Engineering*. **A234-236**. 962-965.
- Masuyama F. (2001). History of power plants and progress in heat resistant steels. *ISIJ International*. **41(6)**. 612-625.
- Musienko A. (2004). Fissuration intergranulaire et transgranulaire dans les agrégats polycristallins – Application à la corrosion sous contrainte et aux gaines de combustible nucléaire. *PhD thesis of the Ecole Nationale Supérieure des Mines de Paris (In English)*.
- Taneike M., Abe F., Sawada K. (2003) Creep strengthening of steel at high temperatures using nano sized carbonitride dispersions. *Letters to nature*. **424**. 294-296.
- Yaguchi M., Takahashi Y. (2000). A viscoplastic constitutive model incorporating dynamic strain ageing effect during cyclic deformation conditions. *International journal of plasticity*. **16**. 241-262.
- Zhang Z.L., Thaulow C., Odegaard J. (2000). A complete Gurson model approach for ductile fracture. *Engineering fracture mechanics*. **67**. 155-168.
- Pardoën T., Hutchinson J. (2000). An extended model for void growth and coalescence. *Journal of mechanics and physics of solids*. **48(12)**. 2467-2512.

Appendices

Table of contents

Appendix A. Synthesis of experimental results.

Appendix B. Specimens geometry and location - Experimental Techniques.

Appendix C. Experiments on tubular creep specimens.

Appendix A

Synthesis of experimental results

In the present appendix, a synthesis of all the experimental results of the tests which were carried out during the PhD is given. It mainly concerns mechanical tests (tensile and creep) at 450°C, 550°C and 625°C, performed on the P91 steel, the T91 steel, the WJP91 weldment, the WJT91 steel and the simulated heat affected zone. For the sake of clarity all the results are reported in tables.

A. Tests on the P91 base metal at 625°C

A.1. Tensile tests on smooth tensile (ST) specimens at 450°C, 550°C and 625°C

Test - geometry	Traverse displacement rate	Strain rate	$R_p^{0.2}$ (MPa)	R_m (MPa)	R_{rupt} (MPa)	$\Delta l/l_0$ (R_m) %	$\Delta l/l_0$ rupt. %	Z (%)
ST - L	57.0 mm min ⁻¹	5.0 .10 ⁻² s ⁻¹	360	380	104	1.5	17.3	78.9 %
ST - L	11.4 mm min ⁻¹	1.0 .10 ⁻² s ⁻¹	345	360	68	0.9	15.4	79.6 %
ST - L	11.4 mm min ⁻¹	1.0 .10 ⁻² s ⁻¹	345	360	68	0.9	15.4	79.4 %
ST - T	11.4 mm min ⁻¹	1.0 .10 ⁻² s ⁻¹	346	363	62	1.2	15.5	79.5 %
ST - T	11.4 mm min ⁻¹	1.0 .10 ⁻² s ⁻¹	345	360	64	0.9	15.4	79.9 %
ST - L	5.7 mm min ⁻¹	5.0 .10 ⁻³ s ⁻¹	341	353	59	1.2	15.5	79.9 %
ST - L	5.7 mm min ⁻¹	5.0 .10 ⁻³ s ⁻¹	342	356	62	1.0	15.2	79.8 %
ST - T	5.7 mm min ⁻¹	5.0 .10 ⁻³ s ⁻¹	344	358	63	1.0	15.8	79.3 %
ST - T	5.7 mm min ⁻¹	5.0 .10 ⁻³ s ⁻¹	339	352	61	0.9	15.6	79.6 %
ST - L	1.14 mm min ⁻¹	1.0 .10 ⁻³ s ⁻¹	326	348	58	0.9	15.6	79.4 %
ST - L	1.14 mm min ⁻¹	1.0 .10 ⁻³ s ⁻¹	328	350	55	0.8	15.3	79.4 %
ST - T	1.14 mm min ⁻¹	1.0 .10 ⁻³ s ⁻¹	332	355	52	1.1	15.9	78.9 %
ST - T	1.14 mm min ⁻¹	1.0 .10 ⁻³ s ⁻¹	335	350	61	0.8	15.3	79.2 %
ST - L	0.114 mm min ⁻¹	1.0 .10 ⁻⁴ s ⁻¹	241	255	21	0.9	16.8	79.1 %
ST - L	0.114 mm min ⁻¹	1.0 .10 ⁻⁴ s ⁻¹	238	252	20	0.8	16.4	79.6 %
ST - L	0.114 mm min ⁻¹	1.0 .10 ⁻⁴ s ⁻¹	235	250	19	0.7	16.8	79.8 %
ST - L	0.0114 mm min ⁻¹	1.0 .10 ⁻⁵ s ⁻¹	185	208	12	0.9	15.8	78.6 %
ST - L	0.0114 mm min ⁻¹	1.0 .10 ⁻⁵ s ⁻¹	190	210	16	1.1	16.1	78.7 %

Table A.A.1. Tensile tests on the P91 steel at 625°C

Test - geometry	Traverse displacement rate	Strain rate	$R_p^{0.2}$ (MPa)	R_m (MPa)	R_{rupt} (MPa)	$\Delta l/l_0$ (R_m) %	$\Delta l/l_0$ rupt. %	Z (%)
ST - L	11.4 mm min ⁻¹	1.0 .10 ⁻² s ⁻¹	408	452	191	5.2	14.8	70.2 %
ST - L	5.7 mm min ⁻¹	5.0 .10 ⁻³ s ⁻¹	395	443	186	4.4	15.2	69.8 %
ST - L	1.14 mm min ⁻¹	1.0 .10 ⁻³ s ⁻¹	390	435	182	2.6	15.8	69.3 %

Table A.A.2. Tensile tests on the P91 steel at 550°C

Test - geometry	Traverse displacement rate	Strain rate	$R_p^{0.2}$ (MPa)	R_m (MPa)	R_{rupt} (MPa)	$\Delta l/l_0$ (R_m) %	$\Delta l/l_0$ rupt. %	Z (%)
ST - L	11.14 mm min ⁻¹	1.0 .10 ⁻² s ⁻¹	484	572	361	5.2	15.2	56.7 %
ST - L	5.7 mm min ⁻¹	5.0 .10 ⁻³ s ⁻¹	462	565	354	5.1	15.8	55.1 %
ST - L	1.14 mm min ⁻¹	1.0 .10 ⁻³ s ⁻¹	450	550	342	4.9	15.6	54.2 %

Table A.A.3. Tensile tests on the P91 steel at 450°C

A.2. Creep tests on smooth creep (SC) specimens at 625°C

Test - geometry	Applied engineering stress	Steady state strain rate	Time to failure	End of steady state	(R ₀ -R _t)/R ₀
1545 - SC	120 MPa	3.9 .10 ⁻³ % h ⁻¹	907 h	280 h	57.6 %
1546 - SC	120 MPa	3.5 .10 ⁻³ % h ⁻¹	916 h	281 h	58.4 %
1547 - SC	120 MPa	4.1 .10 ⁻³ % h ⁻¹	878 h	275 h	58.0 %
1548 - SC	120 MPa	4.1 .10 ⁻³ % h ⁻¹	792 h	260 h	59.5 %
1549 - SC	110 MPa	1.6 .10 ⁻³ % h ⁻¹	1,826 h	530 h	50.7 %
1575 - SC	110 MPa	1.7 .10 ⁻³ % h ⁻¹	1,666 h	490 h	49.9 %
1573 - SC	100 MPa	8.0 .10 ⁻⁴ % h ⁻¹	3,831 h	1,020 h	18.4 %
1574 - SC	100 MPa	7.1 .10 ⁻⁴ % h ⁻¹	3,765 h	1,060 h	16.2 %
1702 - SC	90 MPa	3.8 .10 ⁻⁴ % h ⁻¹	6,972 h	1,500 h	10.5 %

Table A.A.4. Creep tests on P91 steel SC specimens at 625°C

Test - geometry	Applied engineering stress	Steady state strain rate	
		Increasing load	Decreasing load
SC	60 MPa	3.8 .10 ⁻⁵ % h ⁻¹	3.6 .10 ⁻⁵ % h ⁻¹
	80 MPa	7.9 .10 ⁻⁵ % h ⁻¹	7.6 .10 ⁻⁵ % h ⁻¹
	100 MPa	4.9 .10 ⁻⁴ % h ⁻¹	4.5 .10 ⁻⁴ % h ⁻¹
	120 MPa	3.7 .10 ⁻³ % h ⁻¹	

Table A.A.5. Load varying test with steps on a P91 steel SC specimen at 625°C

A.3. Creep tests on notched creep (NC1.2, NC4.0 and NC0.25) specimens at 625°C

Test - geometry	Applied engineering stress	Steady state strain rate	Time to failure	(R ₀ -R _t)/R ₀
112 – NC1.2	218 MPa	2.8 .10 ⁻³ % h ⁻¹	234 h	38.5 %
115 – NC1.2	218 MPa	2.1 .10 ⁻³ % h ⁻¹	265 h	36.2 %
114 – NC1.2	218 MPa	3.1 .10 ⁻³ % h ⁻¹	202 h	40.4 %
1115 – NC1.2	175 MPa	4.9 .10 ⁻⁴ % h ⁻¹	1,050 h	24.1 %
1117 – NC1.2	175 MPa	3.5 .10 ⁻⁴ % h ⁻¹	1,150 h	23.2 %
117 – NC1.2	175 MPa	2.2 .10 ⁻⁴ % h ⁻¹	1,835 h	14.9 %
1113 – NC1.2	150 MPa	1.2 .10 ⁻⁴ % h ⁻¹	2,916 h	1.7 %
1119 – NC1.2	150 MPa	1.1 .10 ⁻⁴ % h ⁻¹	2,908 h	1.1 %

Table A.A.6. Creep tests on P91 steel NC1.2 notched specimens at 625°C

Test - geometry	Applied engineering stress	Steady state strain rate	Time to failure	(R ₀ -R _t)/R ₀
111 – NC4.0	175 MPa	3.3 .10 ⁻³ % h ⁻¹	163 h	34.2 %
113 – NC4.0	175 MPa	1.2 .10 ⁻² % h ⁻¹	108 h	36.7 %
116 – NC4.0	175 MPa	4.4 .10 ⁻³ % h ⁻¹	161 h	35.4 %
1110 – NC4.0	145 MPa	5.4 .10 ⁻⁴ % h ⁻¹	873 h	29.6 %
1116 - NC4.0	145 MPa	4.7 .10 ⁻⁴ % h ⁻¹	1,200 h	26.7 %
1112 – NC4.0	100 MPa	9.0 .10 ⁻⁶ % h ⁻¹	7,657 h	19.8 %

Table A.A.7. Creep tests on P91 steel NC4.0 notched specimen at 625°C

Test - geometry	Applied engineering stress	Steady state strain rate	Time to failure
NC0.25	250 MPa	$6.2 \cdot 10^{-1} \% h^{-1}$	17 h
NC0.25	200 MPa	$2.7 \cdot 10^{-3} \% h^{-1}$	625 h
NC0.25	180 MPa	$1.0 \cdot 10^{-3} \% h^{-1}$	1,296 h
NC0.25	160 MPa	$5.6 \cdot 10^{-4} \% h^{-1}$	1,344 h

Table A.A.8. Creep tests on P91 steel notched creep specimens (NC0.25) at 625°C

A.4. Creep tests on plate notched (PNC) specimens under vacuum at 625°C

Test - geometry	Applied engineering stress	Steady state strain rate	Time to failure
PNC - 1	200 MPa	$8.2 \cdot 10^{-1} \% h^{-1}$	8.2 h
PNC - 2	170 MPa	$2.3 \cdot 10^{-2} \% h^{-1}$	185 h
PNC - 3	140 MPa	$4.8 \cdot 10^{-3} \% h^{-1}$	719 h
PNC - 4	120 MPa	$2.0 \cdot 10^{-3} \% h^{-1}$	1,854 h

Table A.A.9. Creep tests on P91 steel PNC specimens at 625°C

A.5. Creep tests on tubular (TC) tests specimens at 625°C

Test - Geometry	Shear stress	Creep time
TC - 1	65 MPa	130 h
TC - 2	38 MPa	3,055 h

Table A.A.10. Creep tests on P91 steel tubular creep specimens at 625°C

A.6. Creep tests on compact tension (CT) tests specimens at 625°C

Test - geometry	Applied engineering stress	Time to failure
CT - 1	30 MPa	1,256 h (interrupted)
CT - 2	25 MPa	2,850 h (interrupted)

Table A.A.11. Creep tests on P91 steel CT specimens at 625°C

* = The test was interrupted and restart because of the furnace failed.

A.7. Tensile and creep tests on aged smooth (ST and SC) specimens at 625°C

Test - geometry	Ageing conditions	Traverse displacement rate	Strain rate	$R_p^{0.2}$ MPa	R_m MPa	R_{rupt} MPa	$\Delta l/l_0$ (R_m) %	$\Delta l/l_0$ rupt. %	Z (%)
ST - L	550°C - 10,000 h	11.4 mm min ⁻¹	$1.0 \cdot 10^{-2} s^{-1}$	310	330	63	1.3	16.9	67.7 %
ST - L	550°C - 10,000 h	1.14 mm min ⁻¹	$1.0 \cdot 10^{-3} s^{-1}$	280	290	38	1.1	18.4	76.9 %
ST - L	550°C - 10,000 h	0.114 mm min ⁻¹	$1.0 \cdot 10^{-4} s^{-1}$	235	245	25	1.0	20.0	77.2 %
ST - L	550°C - 10,000 h	0.0114 mm min ⁻¹	$1.0 \cdot 10^{-5} s^{-1}$	190	200	41	1.5	16.8	75.2 %
ST - L	625°C - 10,000 h	11.4 mm min ⁻¹	$1.0 \cdot 10^{-2} s^{-1}$	310	330	95	1.5	17.8	73.9 %
ST - L	625°C - 10,000 h	1.14 mm min ⁻¹	$1.0 \cdot 10^{-3} s^{-1}$	270	280	36	0.9	16.5	78.5 %
ST - L	625°C - 10,000 h	0.114 mm min ⁻¹	$1.0 \cdot 10^{-4} s^{-1}$	225	235	32	0.8	16.1	79.6 %
ST - L	625°C - 10,000 h	0.0114 mm min ⁻¹	$1.0 \cdot 10^{-5} s^{-1}$	185	195	45	1.5	15.2	79.7 %

Table A.A.12. Tensile tests on aged P91 steel at 625°C

Test - geometry	Ageing conditions	Applied engineering stress	Steady state strain rate	Time to failure	End of steady state	(R ₀ -R _t)/R ₀
2002 - SC	10,000 h – 625°C	120 MPa	4.9 .10 ⁻³ % h ⁻¹	646 h	256 h	65.9 %
2012 – SC	10,000 h – 625°C	110 MPa	3.3 .10 ⁻³ % h ⁻¹	1,091 h	680 h	62.4 %

Table A.A.13. Creep tests on aged P91 steel SC specimens at 625°C

B. Tests on the T91 base metal at 450°C and 550°C

B.1. Tensile tests on smooth tensile (ST) specimens at 450°C and 550°C

Test – geometry	Traverse displacement rate	Strain rate	$R_p^{0.2}$ (MPa)	R_m (MPa)	R_{rupt} (MPa)	$\Delta l/l_0$ (R_m) %	$\Delta l/l_0$ rupt. %	Z (%)
ST	11.4 mm min ⁻¹	1.0 .10 ⁻² s ⁻¹	358	453	265	4.8	16.0	49.8 %
ST	11.4 mm min ⁻¹	1.0 .10 ⁻² s ⁻¹	415	470	245	5.4	15.4	50.0 %
ST	5.7 mm min ⁻¹	5.0 .10 ⁻³ s ⁻¹	357	455	258	5.0	16.1	50.1 %
ST	5.7 mm min ⁻¹	5.0 .10 ⁻³ s ⁻¹	355	468	255	5.6	16.2	50.8 %
ST	1.14 mm min ⁻¹	1.0 .10 ⁻³ s ⁻¹	352	468	271	5.2	15.6	54.4 %
ST	1.14 mm min ⁻¹	1.0 .10 ⁻³ s ⁻¹	348	457	228	4.3	15.8	52.3 %
ST	1.14 mm min ⁻¹	1.0 .10 ⁻³ s ⁻¹	410	460	281	3.7	13.6	53.5 %
ST	0.114 mm min ⁻¹	1.0 .10 ⁻⁴ s ⁻¹	390	460	238	3.7	13.2	57.9 %
ST	0.057 mm min ⁻¹	5.0 .10 ⁻⁵ s ⁻¹	392	465	247	3.4	12.7	59.9 %
ST	0.0114 mm min ⁻¹	1.0 .10 ⁻⁵ s ⁻¹	382	451	251	3.2	12.5	63.6 %
ST	0.0114 mm min ⁻¹	1.0 .10 ⁻⁵ s ⁻¹	385	455	258	3.2	11.6	62.2 %

Table A.B.1. Tensile tests on the T91 steel at 450°C

Test – geometry	Traverse displacement rate	Strain rate	$R_p^{0.2}$ (MPa)	R_m (MPa)	R_{rupt} (MPa)	$\Delta l/l_0$ (R_m) %	$\Delta l/l_0$ rupt. %	Z (%)
ST	11.4 mm min ⁻¹	1.0 .10 ⁻² s ⁻¹	348	397	155	4.1	17.8	60.8 %
ST	11.4 mm min ⁻¹	1.0 .10 ⁻² s ⁻¹	350	400	152	3.7	17.2	61.0 %
ST	5.7 mm min ⁻¹	5.0 .10 ⁻³ s ⁻¹	325	404	145	3.8	17.1	63.1 %
ST	5.7 mm min ⁻¹	5.0 .10 ⁻³ s ⁻¹	332	395	141	3.3	16.8	62.6 %
ST	1.14 mm min ⁻¹	1.0 .10 ⁻³ s ⁻¹	330	409	153	2.9	19.5	66.3 %
ST	1.14 mm min ⁻¹	1.0 .10 ⁻³ s ⁻¹	345	375	102	2.6	18.1	65.5 %
ST	1.14 mm min ⁻¹	1.0 .10 ⁻³ s ⁻¹	340	380	105	2.4	17.5	66.0 %
ST	0.114 mm min ⁻¹	1.0 .10 ⁻⁴ s ⁻¹	330	345	56	1.2	15.5	71.0 %
ST	0.057 mm min ⁻¹	5.0 .10 ⁻⁵ s ⁻¹	325	346	53	1.8	18.5	70.8 %
ST	0.0114 mm min ⁻¹	1.0 .10 ⁻⁵ s ⁻¹	295	312	53	1.2	14.8	72.5 %
ST	0.0114 mm min ⁻¹	1.0 .10 ⁻⁵ s ⁻¹	300	320	55	1.1	15.5	72.7 %

Table A.B.2. Tensile tests on the T91 steel at 550°C

B.2. Creep tests on smooth creep (SC) specimens at 450°C and 550°C

Test – geometry	Applied engineering stress	Steady state strain rate	Time to failure	End of steady state	(R ₀ -R _t)/R ₀
1941 - SC (T91 - 2)	250 MPa	1.1 ·10 ¹ % h ⁻¹	1.2 h	0.33 h	62.8 %
1943 - SC (T91 - 4)	215 MPa	9.0 ·10 ⁻³ % h ⁻¹	606 h	196 h	67.6 %
1946 – SC (T91 - 6)	215 MPa	7.6 ·10 ⁻³ % h ⁻¹	567 h	226 h	67.8 %
1940 - SC (T91 - 1)	200 MPa	2.9 ·10 ⁻³ % h ⁻¹	1,776 h	620 h	63.2 %
1950 - SC (T91 - 9)	200 MPa	2.3 ·10 ⁻³ % h ⁻¹	1,480 h	421 h	67.1 %
1947 - SC (T91 - 7)	185 MPa	1.9 ·10 ⁻³ % h ⁻¹	4,689 h	3,000 h	67.2 %
1948 – SC (T91 - 8)	185 MPa	2.7 ·10 ⁻³ % h ⁻¹	2,035 h	835 h	64.0 %

Table A.B.3. Creep tests on T91 steel SC specimens at 550°C

Test – geometry	Applied engineering stress	Steady state strain rate	Time to failure	End of steady state	(R ₀ -R _t)/R ₀
1942 - SC (T91 - 3)	435 MPa	3.6 ·10 ⁻¹ % h ⁻¹	16 h	5 h	51.0 %
1951 - SC (T91 - 10)	420 MPa	1.0 ·10 ⁻¹ % h ⁻¹	57 h	32 h	53.8 %
1957 - SC (T91 - 11)	410 MPa	7.7 ·10 ⁻² % h ⁻¹	156 h	45 h	53.7 %
1960 - SC (T91 - 15)	400 MPa	1.8 ·10 ⁻¹ % h ⁻¹	32 h	12 h	53.4 %
1977 - SC (T91 - 13)	390 MPa	3.4 ·10 ⁻² % h ⁻¹	116 h	56 h	55.5 %
2006 - SC (T91 - 17)	390 MPa	3.5 ·10 ⁻² % h ⁻¹	78 h	51 h	56.6 %
1944 - SC (T91 - 5)	380 MPa	9.3 ·10 ⁻⁴ % h ⁻¹	3,306 h	1,200 h	49.9 %
1976 - SC (T91 - 12)	380 MPa	8.5 ·10 ⁻⁴ % h ⁻¹	2,801 h	1,580 h	54.6 %

Table A.B.4. Creep tests on T91 steel SC specimens at 450°C

C. Tests on the WJP91 weldment at 625°C

C.1. Tensile tests on smooth tensile specimens (ST) at 625°C

Test – geometry	Traverse displacement rate	Strain rate	$R_p^{0.2}$ (MPa)	R_m (MPa)	R_{rupt} (MPa)	$\Delta l/l_0$ (R_m) %	$\Delta l/l_0$ rupt. %	Z (%)
ST	1.14 mm min ⁻¹	1.0 10 ⁻³ s ⁻¹	242	317	62	1.7	18.2	76.2 %
ST	1.14 mm min ⁻¹	1.0 10 ⁻³ s ⁻¹	236	295	50	1.1	20.0	79.9 %
ST	1.14 mm min ⁻¹	1.0 10 ⁻³ s ⁻¹	236	292	55	1.1	18.0	76.5 %
ST	1.14 mm min ⁻¹	1.0 10 ⁻³ s ⁻¹	236	297	58	1.3	17.7	72.3 %
ST	11.4 mm min ⁻¹	1.0 10 ⁻² s ⁻¹	300	320	78	1.9	16.5	68.7 %
ST	1.14 mm min ⁻¹	1.0 10 ⁻³ s ⁻¹	265	280	52	0.9	22.1	80.0 %
ST	0.114 mm min ⁻¹	1.0 10 ⁻⁴ s ⁻¹	230	240	50	1.2	19.3	77.3 %
ST	0.0114 mm min ⁻¹	1.0 10 ⁻⁵ s ⁻¹	190	205	36	1.0	14.7	76.3 %

Table A.C.1. Tensile tests on the WJP91 cross-weld ST specimens at 625°C

C.2. Creep tests on smooth creep (SC) specimens at 625°C

Test – geometry	Applied engineering stress	Steady state strain rate	Time to failure	Distance between rupture location and fusion line	(R ₀ -R _t)/R ₀
1632 – SC	100 MPa	4.2 .10 ⁻³ % h ⁻¹	323 h	HAZ 3.0 mm	52.2 %
1934 – SC	100 MPa	3.8 .10 ⁻³ % h ⁻¹	336 h	HAZ 3.0 mm	52.1 %
1935 – SC	100 MPa	1.4 .10 ⁻³ % h ⁻¹	401 h	HAZ 2.7 mm	51.4 %
1936 – SC	80 MPa	1.3 .10 ⁻³ % h ⁻¹	721 h	HAZ 2.8 mm	32.2 %
1932 – SC	80 MPa	4.2 .10 ⁻⁴ % h ⁻¹	1,336 h	HAZ 3.4 mm	28.2 %
1937 – SC	80 MPa	3.0 .10 ⁻⁴ % h ⁻¹	2,952 h	HAZ 3.2 mm	20.3 %
1939 – SC	80 MPa	5.7 .10 ⁻⁴ % h ⁻¹	1,131 h	HAZ 2.6 mm	16.8 %
1700 – SC	80 MPa	3.3 .10 ⁻⁴ % h ⁻¹	1,996 h	HAZ 2.8 mm	29.2 %
1647 – SC	60 MPa	1.1 .10 ⁻⁴ % h ⁻¹	3,906 h	HAZ 3.1 mm	19.3 %
1700 – SC	51.1 MPa	2.9 .10 ⁻⁵ % h ⁻¹	10,492 h	HAZ 2.9 mm	12.2 %
1931 – SC	50 MPa	6.9 .10 ⁻⁵ % h ⁻¹	11,085 h	HAZ 3.1 mm	11.8 %
1938 – SC	50 MPa	6.5 .10 ⁻⁵ % h ⁻¹	10,955 h	HAZ 3.2 mm	9.6 %

Table A.C.2. Creep tests on WJP91 cross-weld SC specimens at 625°C

C.3. Creep tests on notched creep (NC1.2, NC4.0 and PNC) specimens at 625°C

Test – geometry	Applied engineering stress	Steady state strain rate	Time to failure	(R ₀ -R _t)/R ₀
PNC	90 MPa	5.7 .10 ⁻³ % h ⁻¹	970 h	/
JS6B – NC4.0	120 MPa	1.5 .10 ⁻³ % h ⁻¹	150 h	38.2 %
JS6A – NC4.0	110 MPa	5.8 .10 ⁻⁴ % h ⁻¹	298 h	36.7 %
JS5B – NC4.0	100 MPa	3.5 .10 ⁻⁴ % h ⁻¹	948 h	32.4 %
JS5A – NC4.0	80 MPa	5.3 .10 ⁻⁵ % h ⁻¹	Interrupted 3,750 h	19.6 %
JS4B – NC1.2	135 MPa	1.3 .10 ⁻³ % h ⁻¹	215 h	26.7 %
JS4A – NC1.2	135 MPa	3.1 .10 ⁻⁴ % h ⁻¹	494 h	23.8 %
JS2B – NC1.2	110 MPa	2.1 .10 ⁻⁴ % h ⁻¹	948 h	19.6 %
JS2A – NC1.2	110 MPa	4.6 .10 ⁻⁵ % h ⁻¹	Interrupted *	/
JS1A – NC1.2	110 MPa	4.4 .10 ⁻⁵ % h ⁻¹	2,032 h	14.3 %
JS1B – NC1.2	85 MPa	1.8 .10 ⁻⁵ % h ⁻¹	Interrupted *	/

Table A.C.3. Creep tests on WJP91 cross-weld NC specimens notched in the heat affected zone (NC1.2 and NC4.0) at 625°C

C.4. Creep tests on plate creep specimens (PC) under vacuum at 625°C

Test – Geometry	Applied engineering stress	Steady state strain rate	Time to failure
PC – 1	90 MPa	$5.7 \cdot 10^{-3} \% h^{-1} *$	330 h
PC – 2	60 MPa	$7.7 \cdot 10^{-4} \% h^{-1} *$	1,055 h

Table A.C.4. Creep tests on WJP91 cross-weld PC specimens at 625°C (measured by traverse displacement)*

C.5. Creep tests on tubular creep (TC) specimens at 625°C

Test – Geometry	Shear stress	Creep time
TC	65 MPa	Interrupted 43 h
TC	38 MPa	Interrupted 294 h
TC	26 MPa	Interrupted 4,660 h

Table A.C.5. Creep tests on WJP91 weldment tubular creep specimens at 625°C

D. Tests on the WJT91 weldment at 450°C and 550°C

D.1. Tensile tests on smooth tensile (ST) specimens at 450°C and 550°C.

Test – geometry	Traverse displacement rate	Strain rate	$R_p^{0.2}$ (MPa)	R_m (MPa)	R_{rupt} (MPa)	$\Delta l/l_0$ (R_m) %	$\Delta l/l_0$ rupt. %	Z (%)
ST	11.4 mm min ⁻¹	1.0 10 ⁻² s ⁻¹	325	427	257	4.0	14.4	54.2 %
ST	5.7 mm min ⁻¹	5.0 10 ⁻³ s ⁻¹	324	428	269	3.6	17.0	54.8 %
ST	1.14 mm min ⁻¹	1.0 10 ⁻³ s ⁻¹	349	453	234	2.0	19.2	56.5 %

Table A.D.1. Tensile tests on WJT91 cross-weld ST specimens at 450°C

Test – geometry	Traverse displacement rate	Strain rate	$R_p^{0.2}$ (MPa)	R_m (MPa)	R_{rupt} (MPa)	$\Delta l/l_0$ (R_m) %	$\Delta l/l_0$ rupt. %	Z (%)
ST	11.4 mm min ⁻¹	1.0 10 ⁻² s ⁻¹	298	385	160	3.8	12.1	63.2 %
ST	1.14 mm min ⁻¹	1.0 10 ⁻³ s ⁻¹	300	351	124	4.4	22.5	68.2 %

Table A.D.2. Tensile tests on WJT91 cross-weld ST specimens at 550°C

D.2. Creep tests on smooth creep (SC) specimens at 450°C and 550°C

Test – geometry	Applied engineering stress	Steady state strain rate	Time to failure	Distance between rupture location and fusion line	(R_0-R_t)/ R_0
1958 - SC (WJT91 - 9)	400 MPa	2.6 .10 ⁻¹ % h ⁻¹	12 h	BM - 5.2 mm	51.2 %
1961 - SC (WJT91 - 7)	380 MPa	2.5 .10 ⁻² % h ⁻¹	181 h	BM – 5.0 mm	56.3 %
1975 - SC (WJT91 - 6)	360 MPa	4.9 .10 ⁻³ % h ⁻¹	742 h	BM - 4.8 mm	57.2 %
2001 - SC (WJT91 - 5)	360 MPa	3.4 .10 ⁻³ % h ⁻¹	646 h	BM – 4.9 mm	55.6 %
1996 - SC (WJT91 - 12)	340 MPa	5.6 10 ⁻⁴ % h ⁻¹	3,376 h	BM - 4.3 mm	55.9 %
1986 - SC (WJT91 - 8)	340 MPa	2.7 .10 ⁻⁴ % h ⁻¹	3,530 h	BM - 4.1 mm	55.6 %

Table A.D.3. Creep tests on WJT91 cross-weld SC specimens at 450°C

Test – geometry	Applied engineering stress	Steady state strain rate	Time to failure	Distance between rupture location and fusion line	(R_0-R_t)/ R_0
1962 - SC (WJT91 - 1)	180 MPa	3.5 .10 ⁻³ % h ⁻¹	856 h	BM - 4.5 mm	66.6 %
1988 - SC (WJT91 - 2)	160 MPa	2.7 .10 ⁻⁴ % h ⁻¹	8,150 h	/	/

Table A.D.4. Creep tests on WJT91 cross-weld SC specimens at 550°C (= not finished)*

E. Creep tests on the WJP91 weld metal at 625°C

Test - geometry	Applied engineering stress	Steady state strain rate	
		Increasing load	Decreasing load
WMP91 – PCMLL (625°C)	40 MPa	/	/
	60 MPa	$1.9 \cdot 10^{-4} \% \text{ h}^{-1}$	/
	80 MPa	$3.4 \cdot 10^{-4} \% \text{ h}^{-1}$	/
	100 MPa	$1.4 \cdot 10^{-3} \% \text{ h}^{-1}$	/
	120 MPa	specimen fracture	

Test – geometry	Applied engineering stress	Steady state strain rate	
		Increasing load	Decreasing load
WMP91 – PCMLL (625°C)	40 MPa	/	/
	60 MPa	$2.1 \cdot 10^{-4} \% \text{ h}^{-1}$	$1.8 \cdot 10^{-4} \% \text{ h}^{-1}$
	80 MPa	$3.6 \cdot 10^{-4} \% \text{ h}^{-1}$	$3.3 \cdot 10^{-4} \% \text{ h}^{-1}$
	100 MPa	$1.5 \cdot 10^{-3} \% \text{ h}^{-1}$	$1.3 \cdot 10^{-3} \% \text{ h}^{-1}$
	120 MPa	$3.5 \cdot 10^{-3} \% \text{ h}^{-1}$	

Table A.E.1. Load varying creep tests on WMP91 weld metal PCMLL specimens at 625°C

F. Tests on simulated intercritical heat affected zone (ICHAZ) at 625°C

F.1. Tensile tests on Gleeble treated notched tensile specimens (GTNT) at 625°C

Test - geometry	Traverse displacement rate	Strain rate	$R_p^{0.2}$ (MPa)	R_m (MPa)	R_{rupt} (MPa)	$\Delta l/l_0$ (R_m) %	$\Delta l/l_0$ rupt. %	Z (%)
GTNT	0.057 mm min ⁻¹	1.10 ⁻⁴ s ⁻¹	237	267	22	0.5	23.4	69.6 %
GTNT	0.57 mm min ⁻¹	1.10 ⁻³ s ⁻¹	316	336	25	0.7	23.7	70.8 %
GTNT	1.14 mm min ⁻¹	2.10 ⁻³ s ⁻¹	325	362	37	0.8	23.2	70.7 %
GTNT	5.7 mm min ⁻¹	1.10 ⁻² s ⁻¹	330	373	64	1.2	20.9	76.7 %

Table A.F.1. Tensile tests on simulated ICHAZ ST specimens at 625°C

F.2. Creep tests on Gleeble treated notched creep specimens (GTNC5.0, GTNC4.0, GTNC1.2, GTNC0.25) at 625°C

Test - geometry	Applied engineering stress	Steady state strain rate	End of steady state	Time to failure	(R ₀ -R _t)/R ₀
ZS-1 – GTNC5.0	130 MPa	1.3 .10 ⁻² % h ⁻¹	80 h	140 h	69.3 %
ZS-2 – GTNC5.0	110 MPa	2.0 .10 ⁻³ % h ⁻¹	380 h	642 h	54.8 %
ZS-3 – GTNC5.0	100 MPa	9.8 .10 ⁻⁴ % h ⁻¹	490 h	1,169 h	51.7 %
ZS-4 – GTNC5.0	100 MPa	6.5 .10 ⁻⁴ % h ⁻¹	560 h	Interrupted 952 h	/
ZS-5 – GTNC5.0	90 MPa	3.8 .10 ⁻⁴ % h ⁻¹	650 h	2,209 h	44.9 %
ZS-6 – GTNC5.0	80 MPa	2.7 .10 ⁻⁴ % h ⁻¹	1,100 h	3,313 h	36.4 %
ZS-7 – GTNC5.0	70 MPa	1.7 .10 ⁻⁴ % h ⁻¹	Not finished	Not finished	Not finished
ZS-9 - GTNC1.2	120 MPa	6.1 .10 ⁻⁴ % h ⁻¹	640 h	1,118 h	23.6 %
ZS-10 - GTNC1.2	80 MPa	9.0 .10 ⁻⁵ % h ⁻¹	4,250 h	6,485 h	11.2 %
ZS-11 - GTNC4.0	100 MPa	7.7 .10 ⁻⁴ % h ⁻¹	600 h	1,163 h	41.8 %

Table A.F.2. Creep tests on simulated ICHAZ GTNC5.0, GTNC4.0 and GTNC1.2 specimens at 625°C

Geometry	Applied engineering stress	Steady state strain rate	Time to failure
ZSAXI-1 GTNC0.25-1	140 MPa	4.4 .10 ⁻³ % h ⁻¹	415 h
ZSAXI-2 GTNC0.25-1	130 MPa	2.1 .10 ⁻³ % h ⁻¹	764 h
ZSAXI-3 GTNC0.25-1	110 MPa	3.3 .10 ⁻³ % h ⁻¹	2256 h
ZSAXI-4 GTNC0.25-2	130 MPa	2.0 .10 ⁻³ % h ⁻¹	550.5 h
ZSAXI-5 GTNC0.25-2	120 MPa	2.6.10 ⁻⁴ % h ⁻¹	2035 h
ZSAXI-6 GTNC0.25-2	110 MPa	2.1 .10 ⁻⁴ % h ⁻¹	2631 h

Table A.F.3. Creep tests on simulated ICHAZ GTNC0.25 at 625°C

Test - geometry	Applied engineering stress	Steady state strain rate	
		Increasing load	Decreasing load
ZS-8 – GTNC5.0	40 MPa	/	
	50 MPa	9.85 .10 ⁻⁵ % h ⁻¹	2.0 .10 ⁻⁵ % h ⁻¹
	60 MPa	1.35 .10 ⁻⁴ % h ⁻¹	2.9 .10 ⁻⁵ % h ⁻¹
	70 MPa	1.85 .10 ⁻⁴ % h ⁻¹	

Table A.F.4. Load varying creep test on simulated ICHAZ GTNC5.0 specimen at 625°C

G. Thermal ageing tests

Material	Ageing temperature	Ageing times		
P91 base metal	550°C	1,000 h	5,000 h	10,000 h
P91 base metal	625°C	1,000 h	5,000 h	10,000 h
T91 base metal	450°C	1,000 h	5,000 h	10,000 h
T91 base metal	550°C	1,000 h	5,000 h	10,000 h
WJP91 weldment	550°C	1,000 h	5,000 h	10,000 h
WJP91 weldment	625°C	1,000 h	5,000 h	10,000 h
Simulated ICHAZ	550°C	1,000 h	5,000 h	10,000 h
Simulated ICHAZ	625°C	1,000 h	5,000 h	10,000 h

Table A.G.1. Ageing conditions for the P91 steel, the T91 steel, the WJP91 weldment and the simulated ICHAZ

Appendix B
Specimens geometry and location - Experimental Techniques

Appendix B.A. Specimens Geometry

The following specimens were used for the present study:

1. Figure B.A.1. Smooth tensile specimen (ST).
2. Figure B.A.2. Smooth creep specimen (SC).
3. Figure B.A.3. Plate notched creep specimen (PNC).
4. Figure B.A.4. Plate creep specimen for multiple load level tests (PC-MLL).
5. Figure B.A.5. Notched creep specimen with a notch radius $R = 1.2$ mm (NC1.2).
6. Figure B.A.6. Notched creep specimen with a notch radius $R = 4.0$ mm (NC4.0).
7. Figure B.A.7. Notched creep specimen with a notch radius $R = 0.25$ mm (NC0.25).
8. Figure B.A.8. Compact tension (CT) creep specimen without pre-crack.
9. Figure B.A.9. Tubular creep specimen (TC) with circumferential crack.
10. Figure B.A.10. Gleeble treated notched tensile specimen (GTNT).
11. Figure B.A.11. Gleeble treated notched creep specimen with a notch radius $R = 1.2$ mm (GTNC1.2).
12. Figure B.A.12. Gleeble treated notched creep specimen with a notch radius $R = 4.0$ mm (GTNC4.0).
13. Figure B.A.13. Gleeble treated notched creep specimen with a notch radius $R = 5.0$ mm (GTNC5.0).
14. Figure B.A.14. Gleeble treated notched creep specimen with a notch radius $R = 0.25$ mm (GTNC0.25-1).
15. Figure B.A.15. Gleeble treated notched creep specimen with a notch radius $R = 0.25$ mm (GTNC0.25-2).
16. Figure B.A.16. Plate creep specimens (PC).

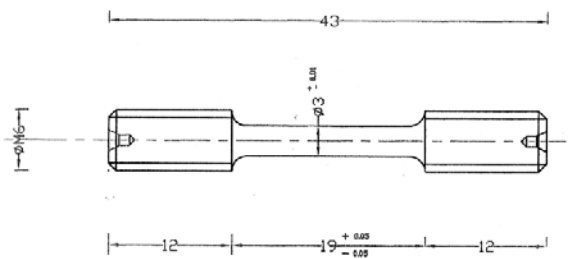


Figure B.A.1. Smooth tensile specimen (ST)

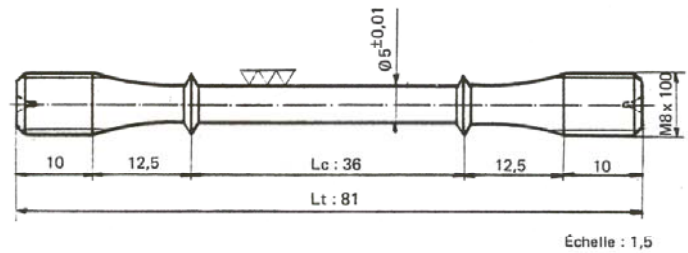


Figure B.A.2. Smooth creep specimen (SC)

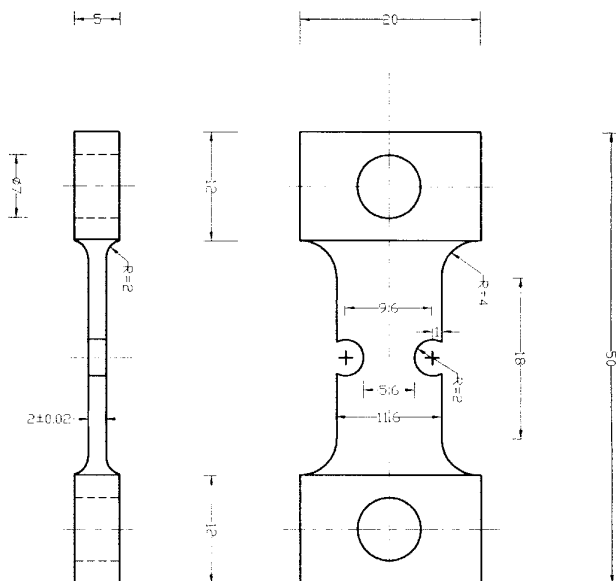


Figure B.A.3. Plate notched creep specimen (PNC)

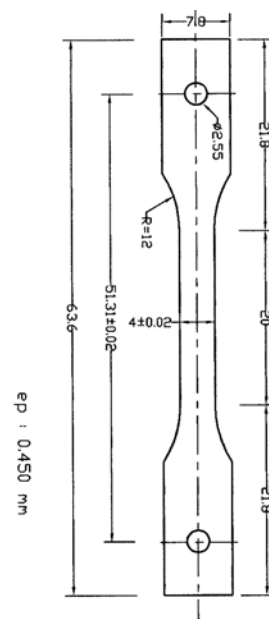


Figure B.A.4. Plate creep specimen (PC-MLL)

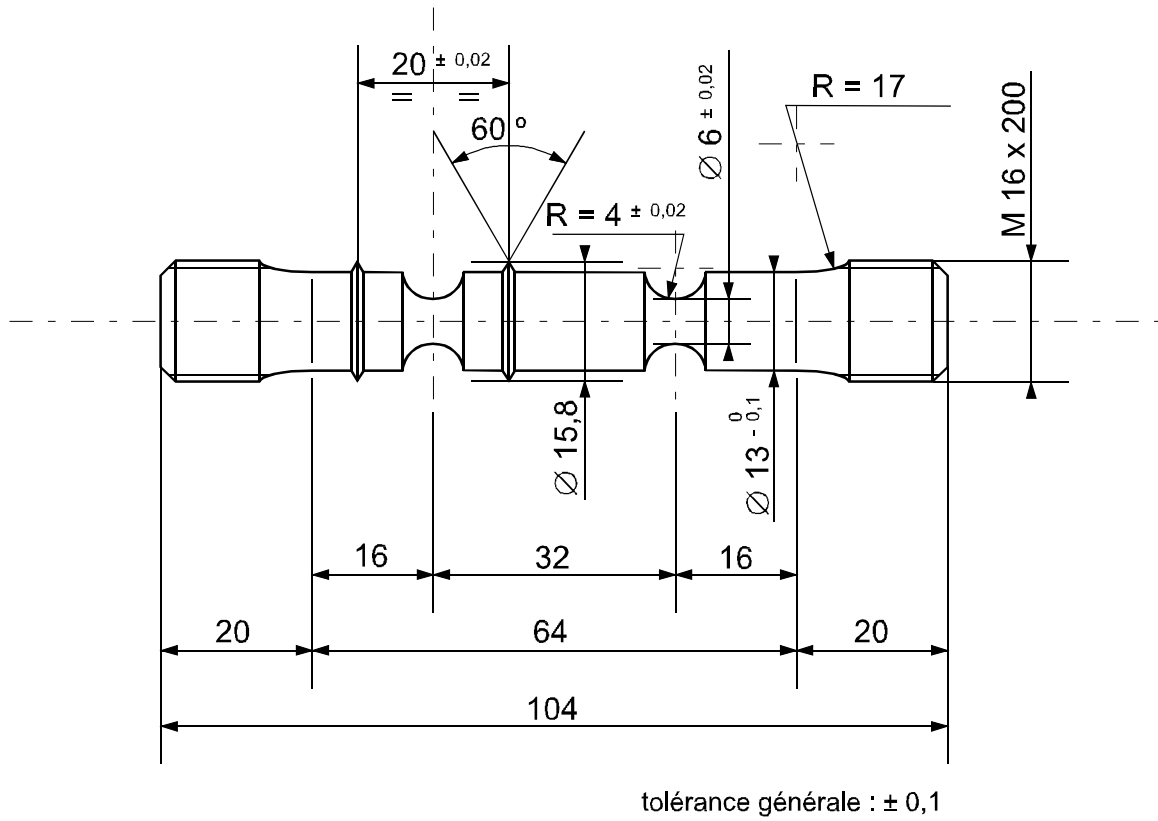


Figure B.A.5. Notched creep specimen R = 1.2 mm (NC1.2)

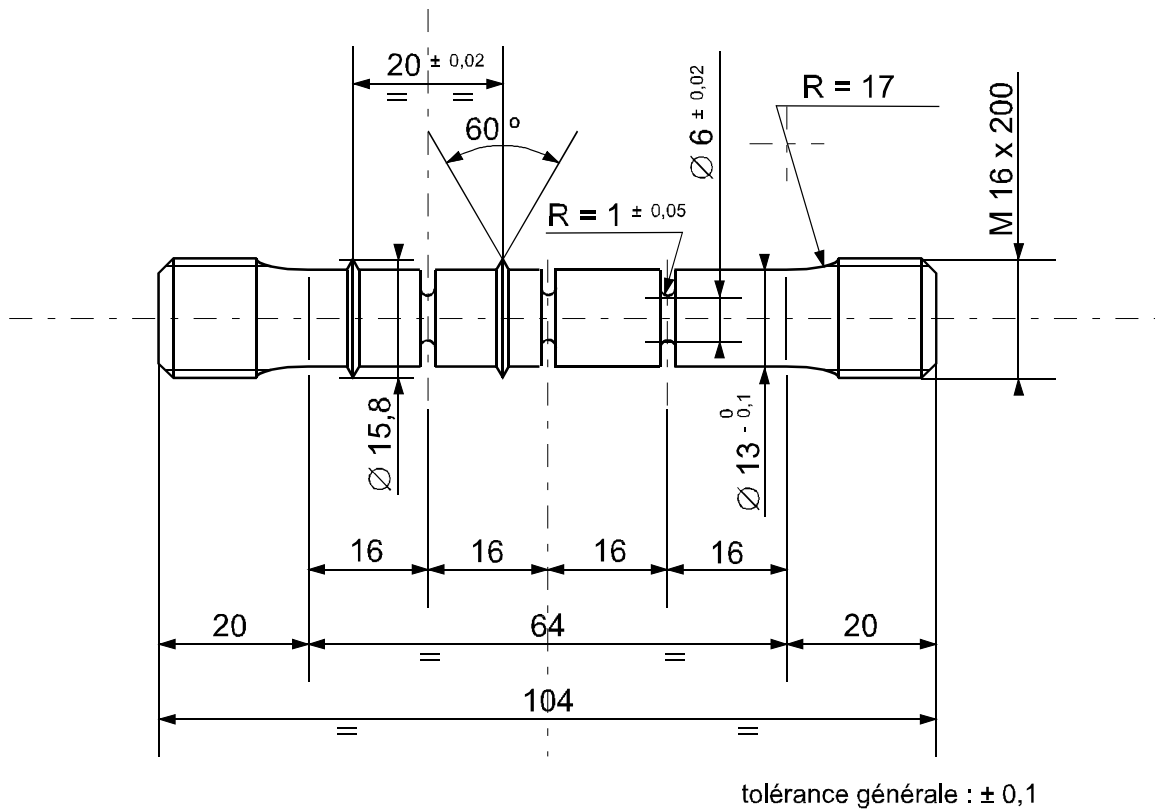


Figure B.A.6. Notched creep specimen R = 4.0 mm (NC4.0)

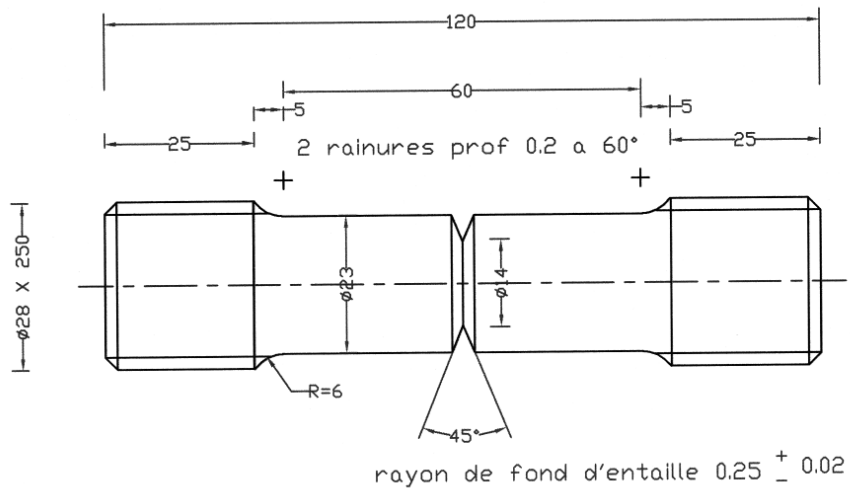


Figure B.A.7. Notched creep specimen $R = 0.25$ mm (NC0.25)

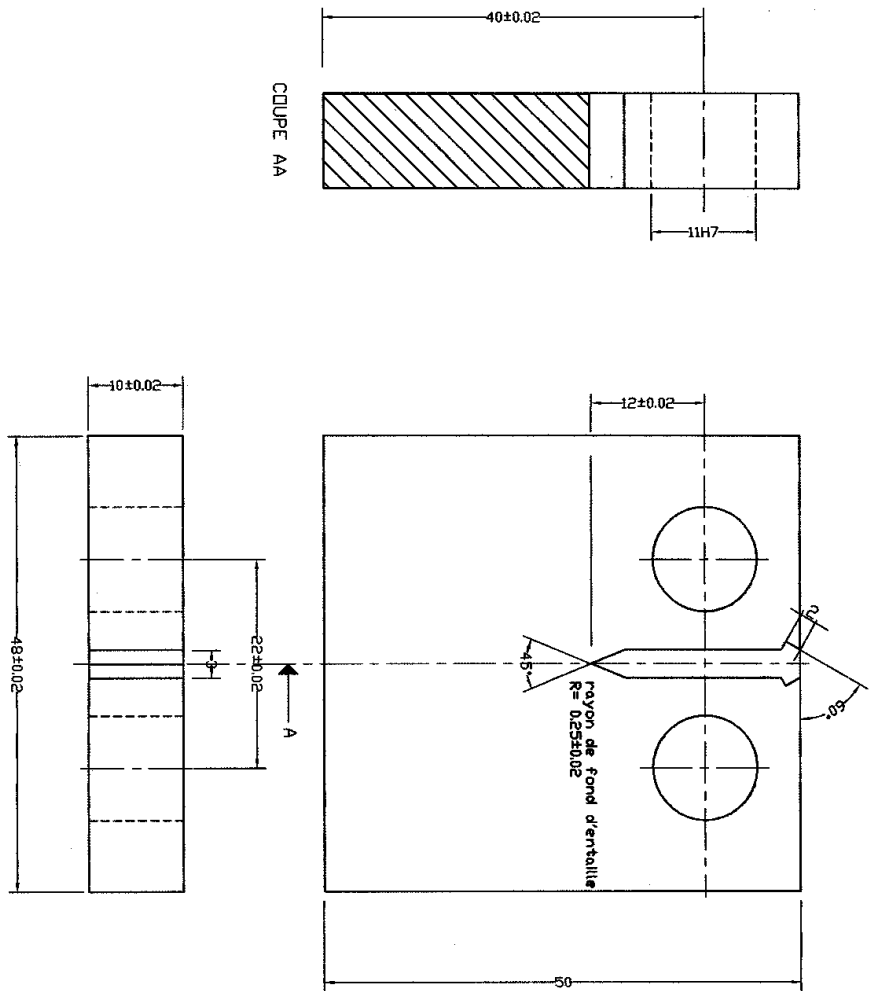


Figure B.A.8. Compact tension (CT) creep specimen without pre-crack

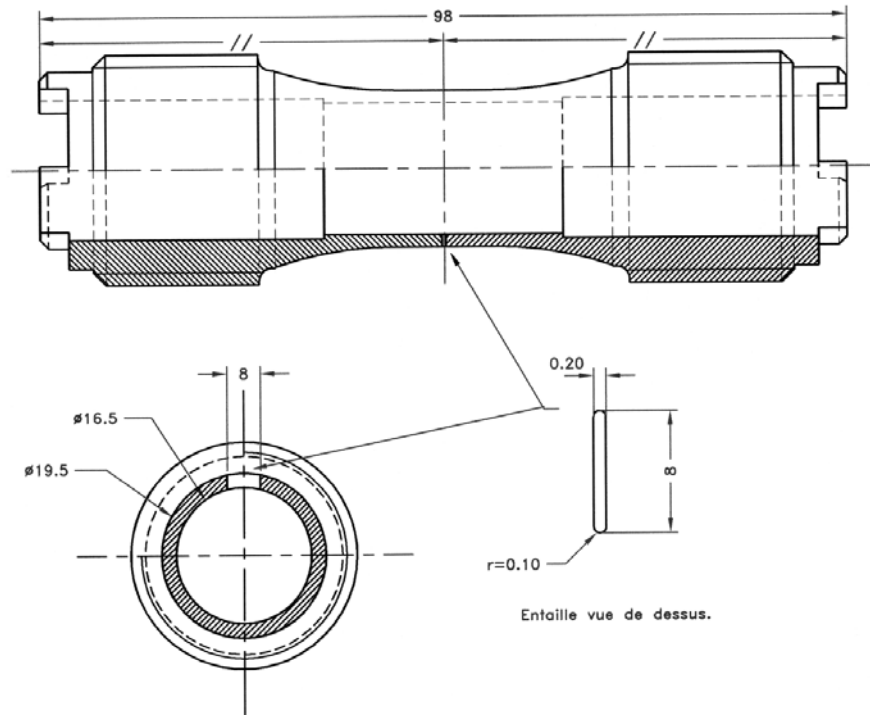


Figure B.A.9. Tubular creep specimen (TC) with circumferential crack

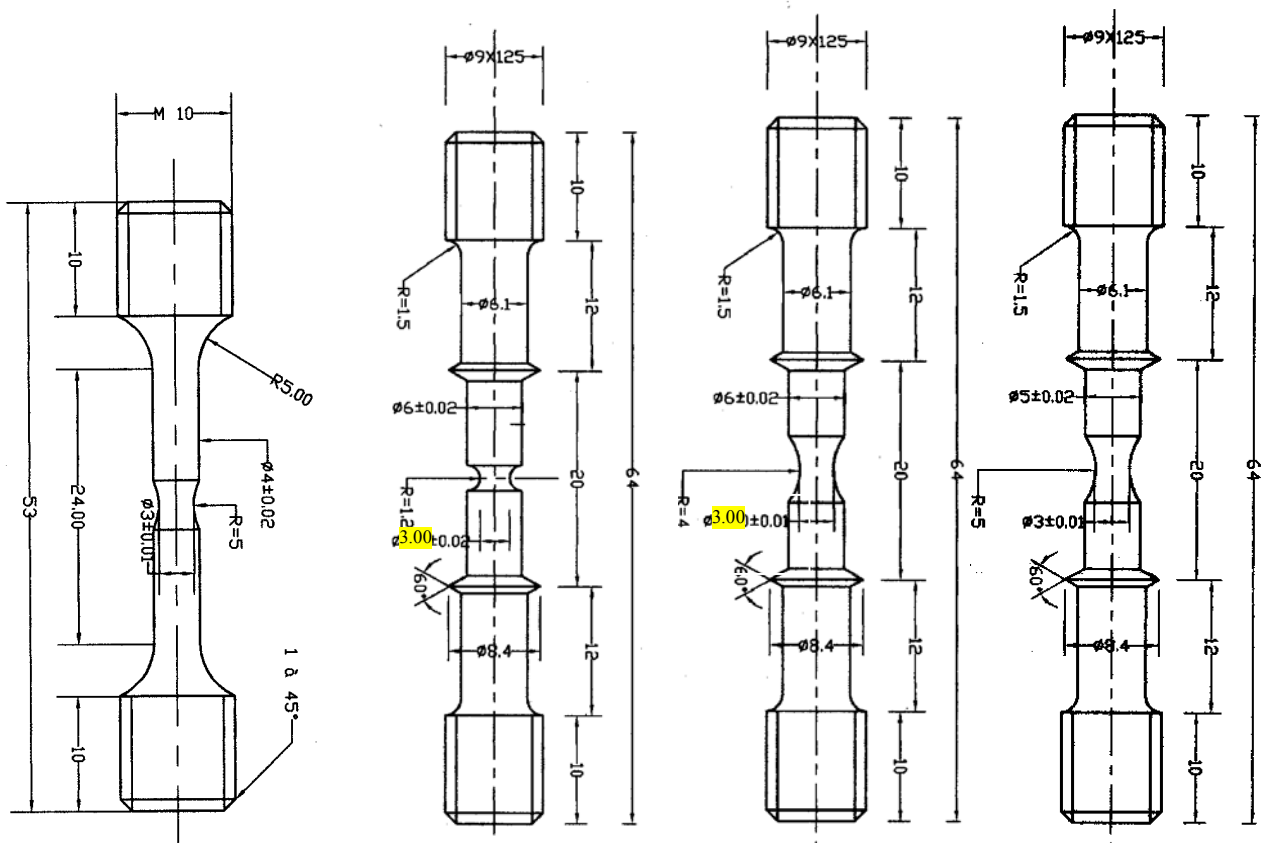


Figure B.A.10. Gleeble treated notched tensile specimen (GTNT)

Figure B.A.11. Gleeble treated notched creep specimen $R = 1.2 \text{ mm}$ (GTNC1.2)

Figure B.A.12. Gleeble treated notched creep specimen $R = 4.0 \text{ mm}$ (GTNC4.0)

Figure B.A.13. Gleeble treated notched creep specimen $R = 5.0 \text{ mm}$ (GTNC5.0)

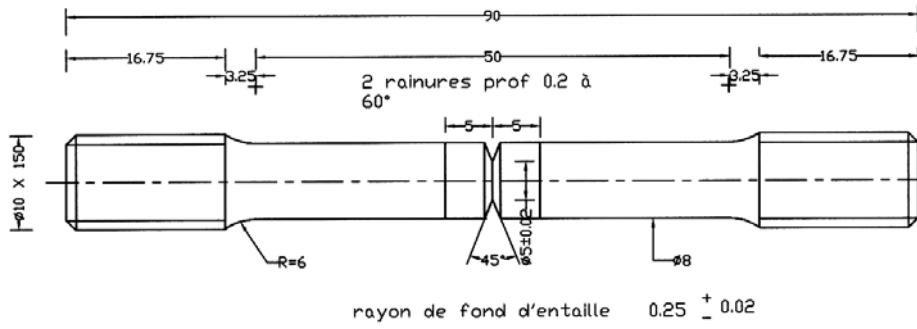


Figure B.A.14. Gleeble treated notched creep specimen $R = 0.25$ mm (GTNC0.25-1)

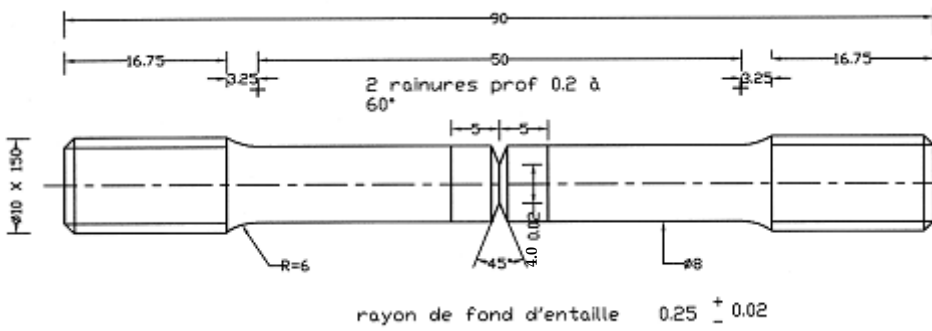


Figure B.A.15. Gleeble treated notched creep specimen $R = 0.25$ mm (GTNC0.25-2)

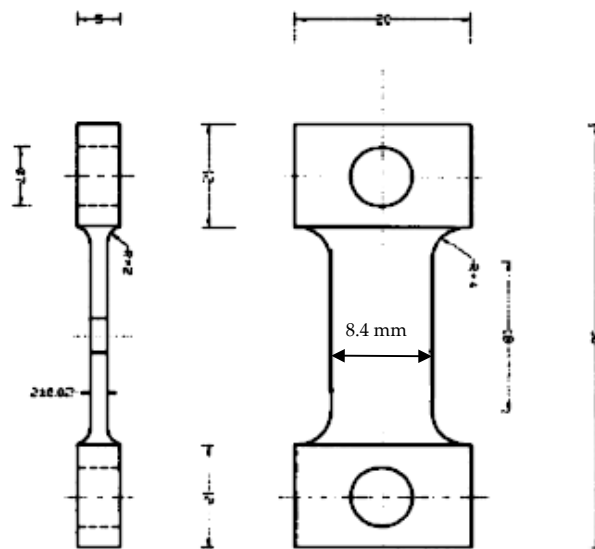


Figure B.A.16. Plate creep specimens (PC)

Appendix B.B. Location of the outlines of specimens for mechanical testing

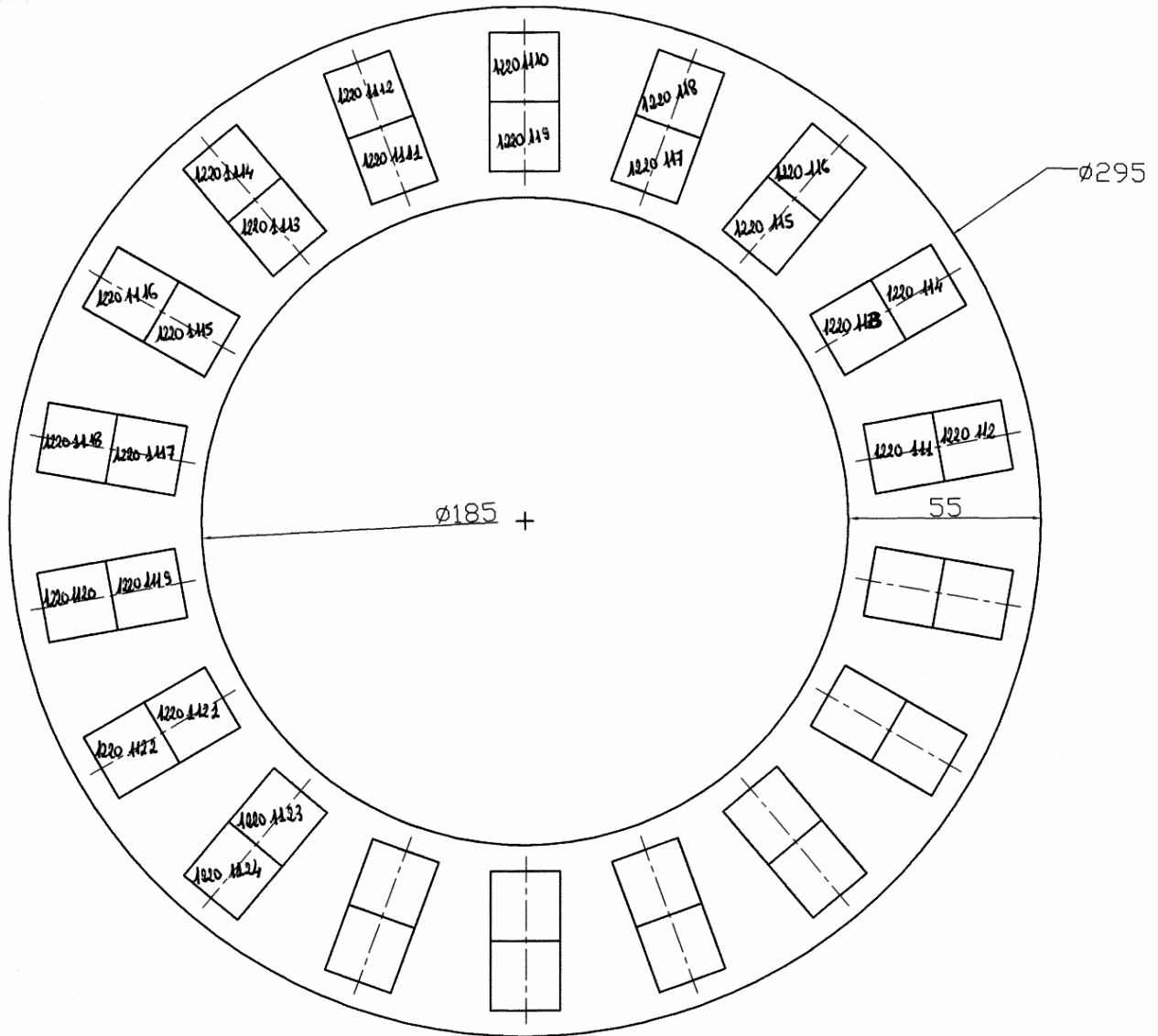


Figure B.B.1. Location of creep test specimens in the P91 steel (1)

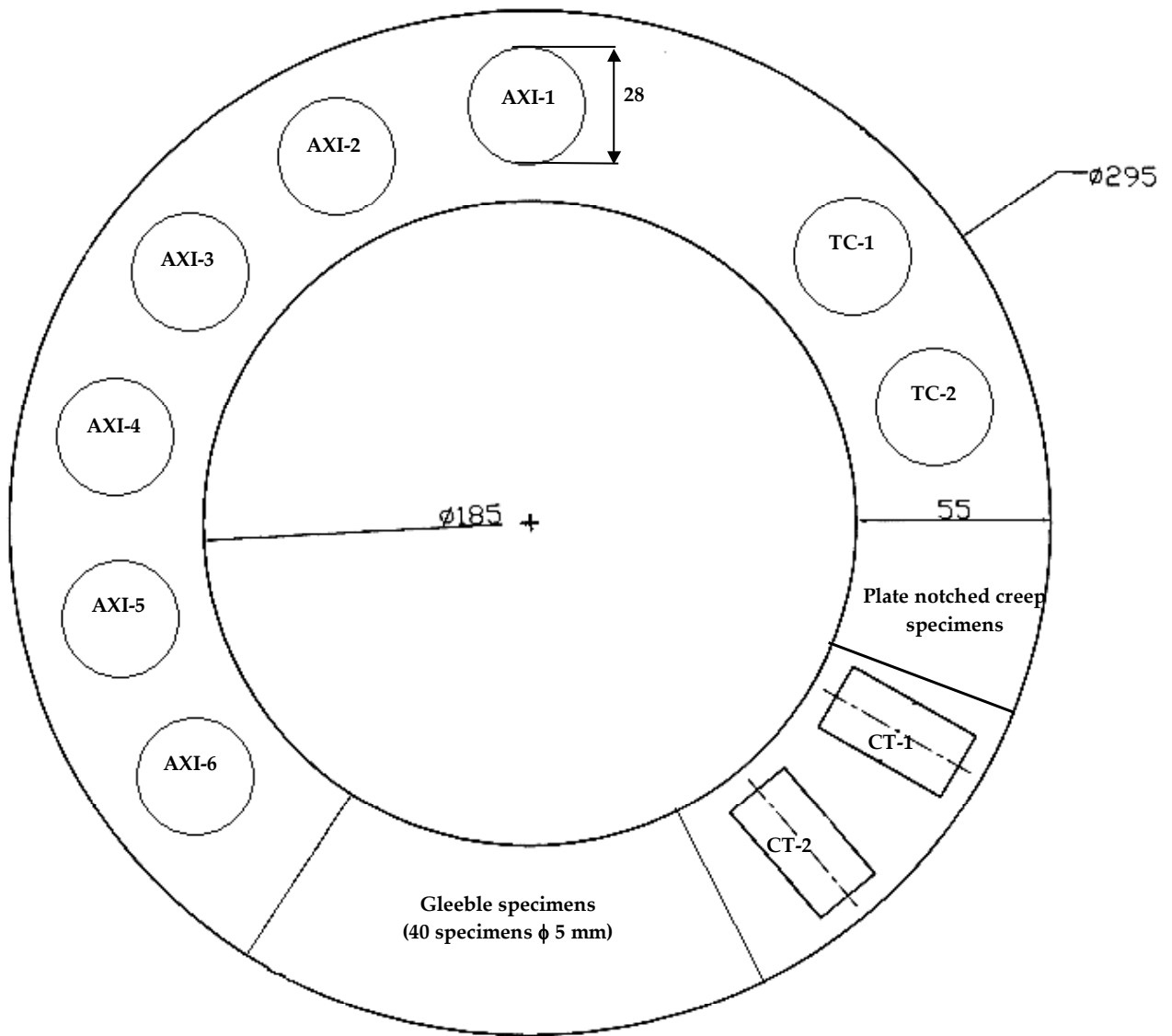


Figure B.B.2. Location of creep test specimens in the P91 steel (2)

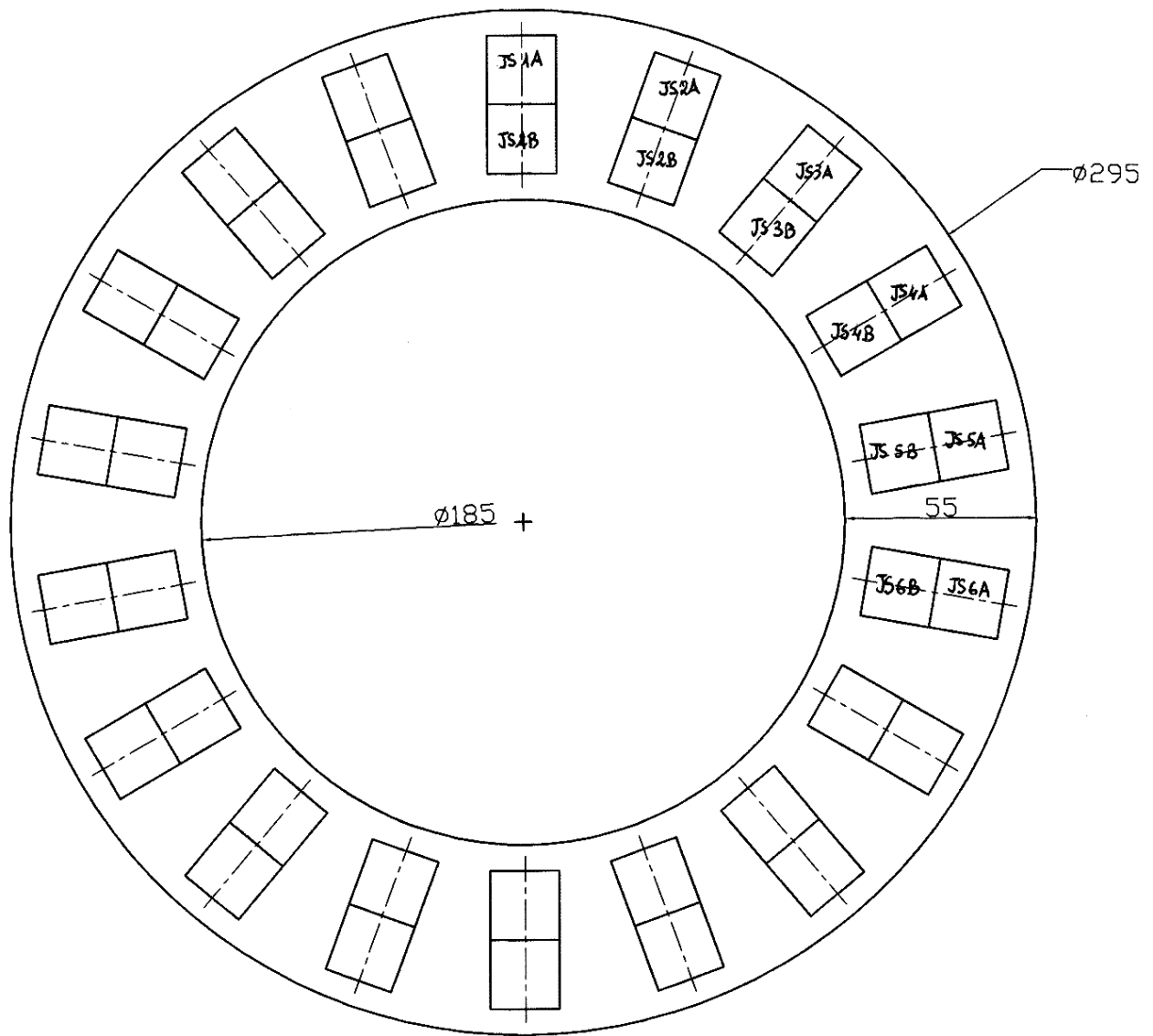


Figure B.B.3. Location of creep test specimens in the WJP91 weldment

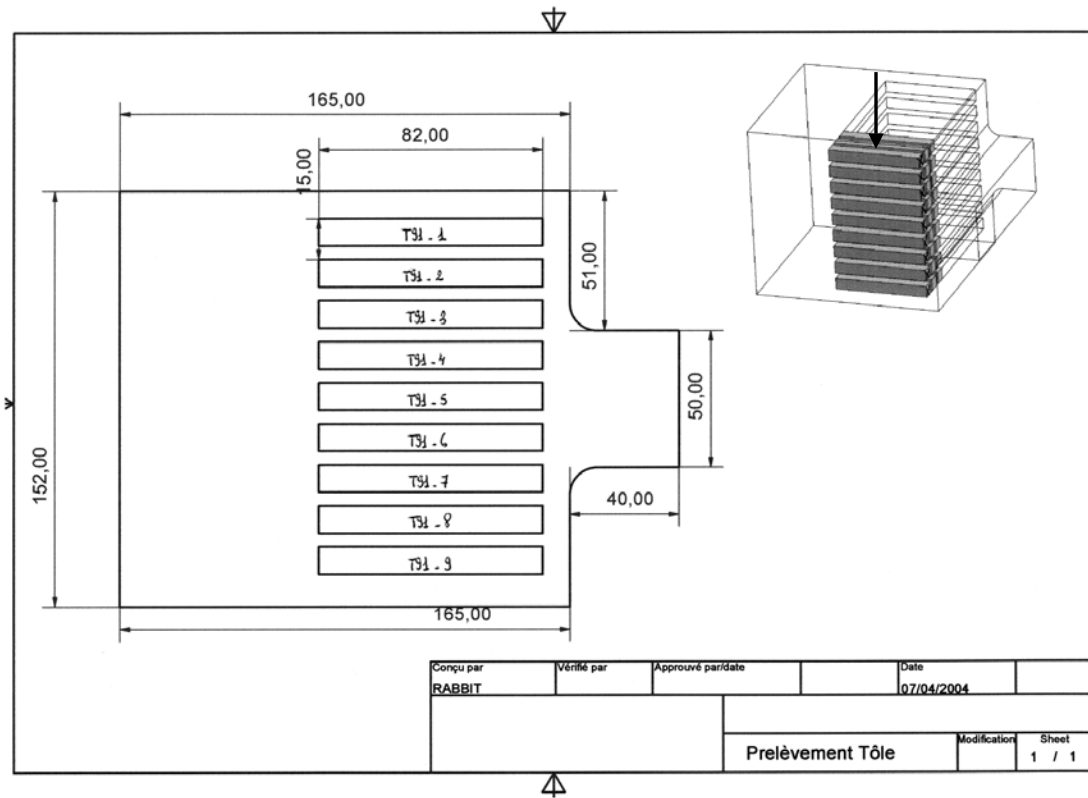


Figure B.B.4. Location of creep test specimens in the sheet made of T91 steel (1)

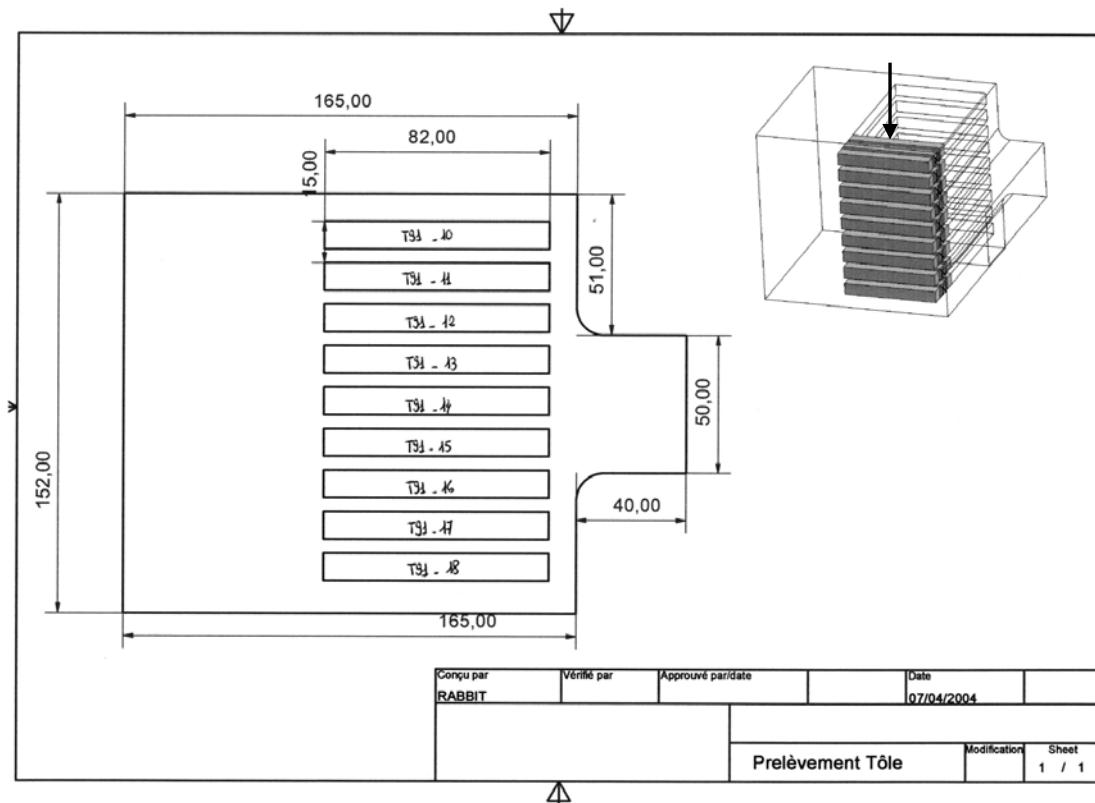


Figure B.B.5. Location of creep test specimens in the sheet made of T91 steel (2)

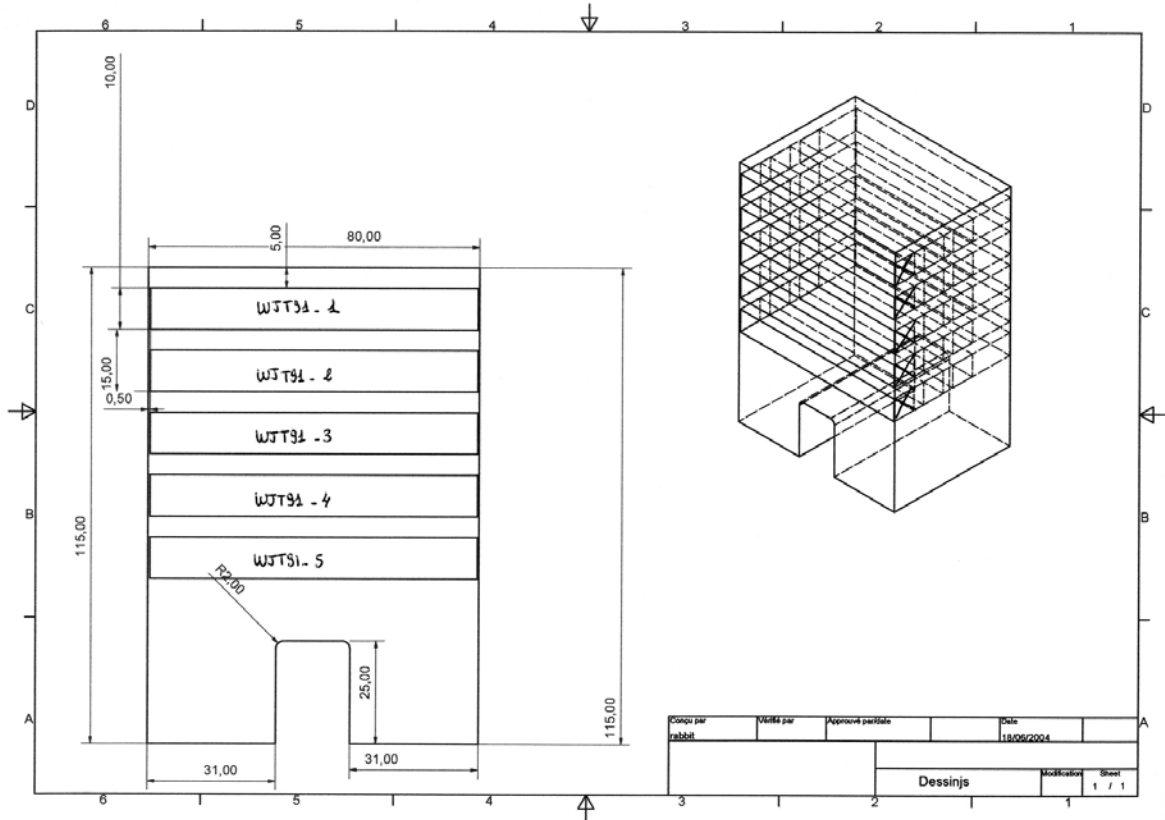


Figure B.B.6. Location of creep test specimens in WJT91 weldment (1)

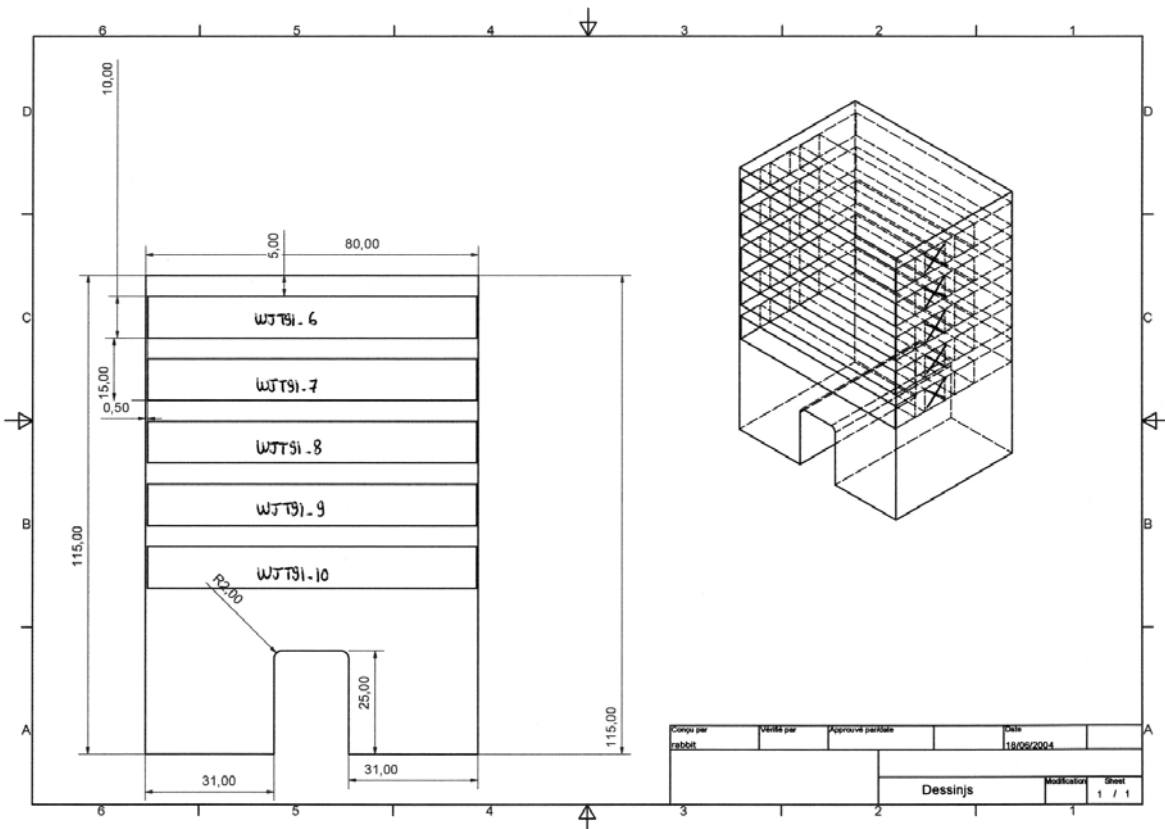


Figure B.B.7. Location of creep test specimens in the WJT91 weldment (2)

Appendix B.C. Creep tests facilities

1. Creep test facilities for creep tests on the base metal

1.1. Description of test facilities

Test Facility	Load application	Load Cell	Extensometer	Heating	Heat control
Machine for tests on notched creep specimens (NC1.2 and NC4.0)	Electrical jack	1,000 N	Linear variable differential transducer (+/- 2.5 mm)	Three zones resistance furnace	Three thermocouples spot welded onto the specimen surface
Machine for tests on notched creep (NC0.25) specimens	Electrical jack	10,000 N	Displacement transducer	Three radiation lamps (1.2 kW)	Two thermocouples spot welded onto the specimen surface
Machine for test on smooth creep (SC) specimens (EDF-Renardières)	Dead weights	/	Capacitive transducer (0-20 mm)	Three zones resistance furnace	Three thermocouples spot welded onto the specimen surface

Table B.C.1. Description of tests facilities for creep tests on the base metal

2. Creep test facilities for creep tests on the simulated HAZ

Considering the specimen geometry, the load cells have been changed for testing the Gleeble treated creep specimens.

Test Facility	Load application	Load Cell	Extensometer	Heating	Heat controll	Other facilities
Machine for tests on notched creep specimens (GTNC1.2, GTNC4.0 and GTNC5.0).	Electrical jack	250 N	Linear variable differential transducer	Three zones resistance furnace	Three thermocouples spot welded on specimen surface	
Machine for tests on notched creep (GTNC0.25) specimens.	Electrical jack	5,000 N	Displacement transducer	Three radiation lamps (total power of 3.6 kW)	Two thermocouples spot welded onto the specimen surface	Electrical potential drop facility

Table B.C.2. Description of tests facilities for creep tests on the simulated HAZ

3. Creep test facilities for creep test on axisymmetric V notched specimen

Creep test on smooth V-notched specimens facility does not strongly differ from classical creep test facilities. They are performed on specimens geometry of type NC0.25 and GTNC0.25 (**figure B.A.7**, **figure B.A.14** and **figure B.A.15**). Their specificity is that the crack initiation and growth is followed using the four points direct current potential drop method. The potential measurements are made in the centre of the specimen on each side of the notch between two points located on the outer edges of the notched area (see **figure B.C.I**).

Creep crack propagation was related to potential drop measurements throughout the calibration curve established by Hourlier (1982):

$$\frac{\phi_0}{\phi} = -0.5832 + 1.7497 \left(\frac{V}{V_0} \right)^{0.5} - 0.1644 \left(\frac{V}{V_0} \right) \quad (\text{eq. B.C.1})$$

where, V_0 and $V(t)$ are respectively the initial and for time t , measured values of the potential drops.

The crack advance is given by:

$$a = \frac{\phi_0 - \phi}{2} \quad (\text{eq. B.C.2})$$

An example of the resulting evolution of the crack propagation is given in **figure B.C.2**. It allows to determine the time to crack initiation and the crack propagation rate. Post-mortem observations of the fracture surface (see **figure B.C.3**) also allowed to determine the size of the stable crack propagation area, as, due to the slow propagation rate combined to the high temperature exposure, the specimen is largely oxidised in this area in comparison with the less oxidised fracture surface corresponding to the late stage of the creep lifetime.

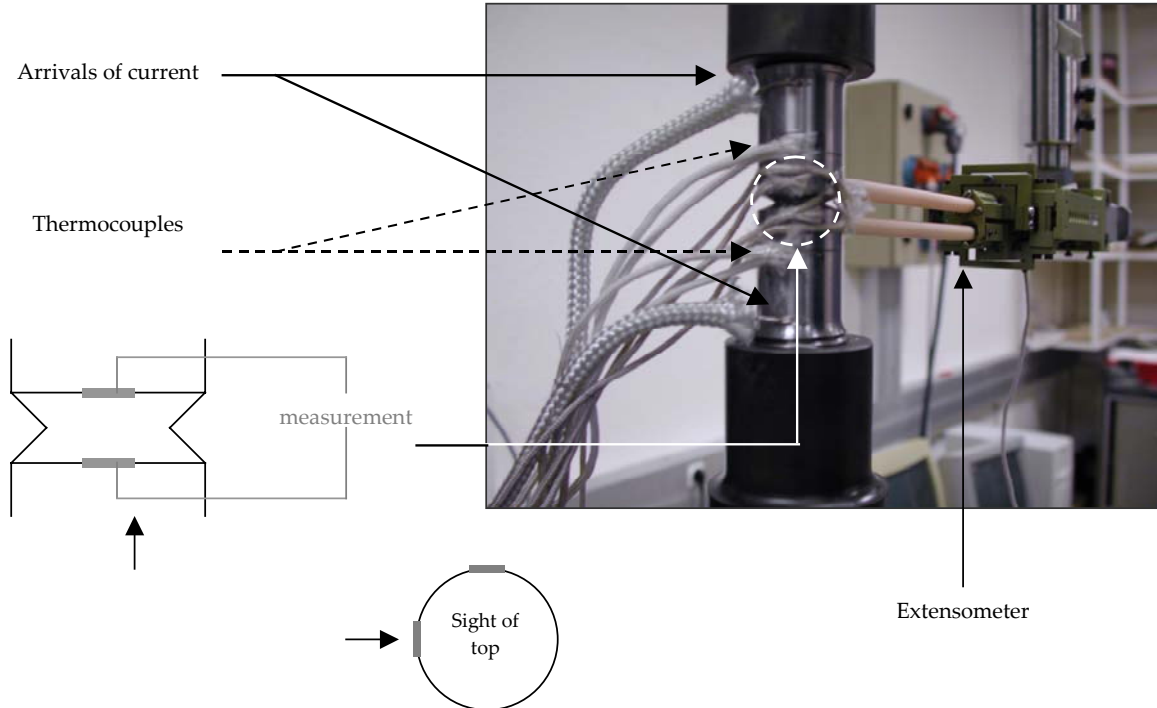


Figure B.C.1. Description of the creep test on V-notched specimens

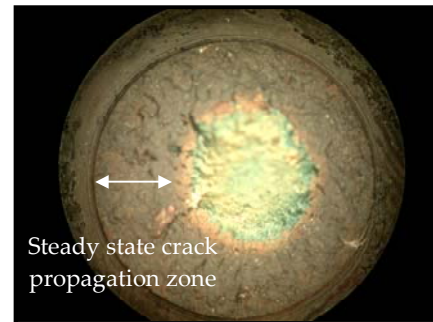
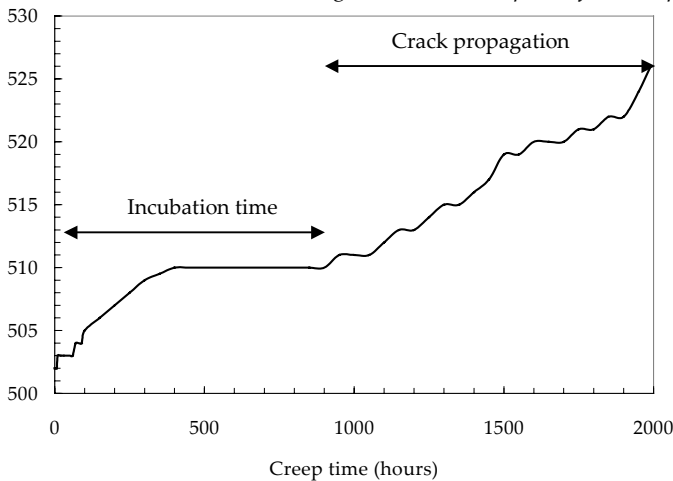


Figure B.C.2. Example of crack evolution followed by the potential drop method *Figure B.C.3. Observation of the fracture surface*

4. Creep test facilities for creep tests under vacuum

Creep tests under vacuum were carried out on specimens whose geometry is given in **figure B.A.3**. Experimental facility consists in a vacuum chamber (10^{-3} Pa). Specimens are heated using a radiation lamps furnace which surrounds the specimen and provides the heating (the heating power of the furnace is 3.6 kW). The temperature is regulated by a thermocouple spot welded onto the specimen surface. Load is applied using an electrical mechanical facility.

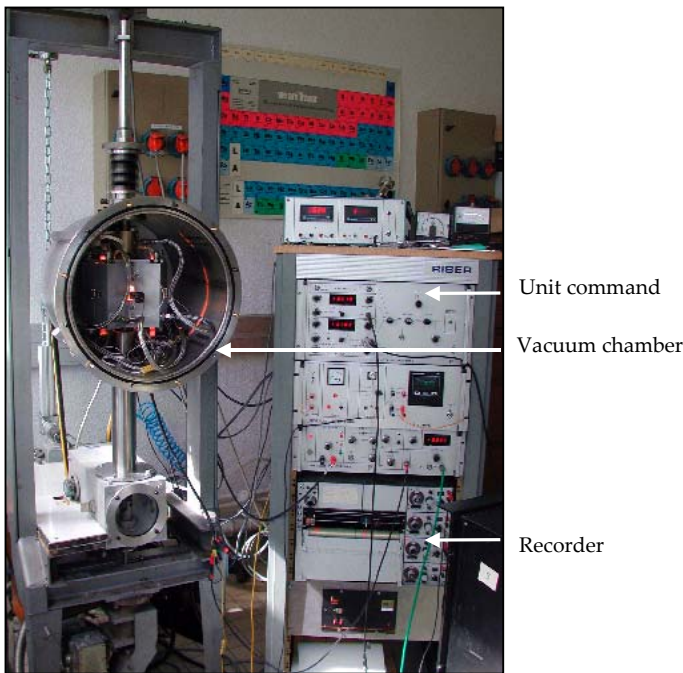


Figure B.C.4. Testing machine for creep tests under vacuum

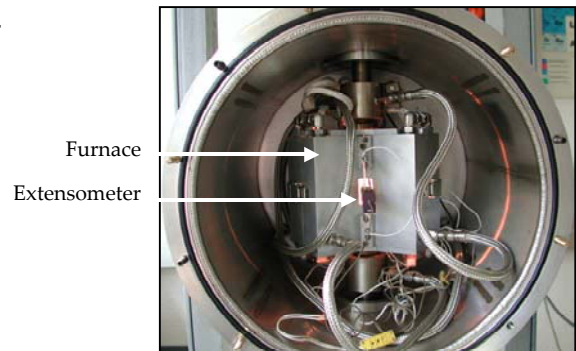


Figure B.C.5. Closer view of the chamber

The elongation of the specimen is measured by a MTS clip-on extensometer specifically designed for measuring crack opening displacement in high-temperature environment.

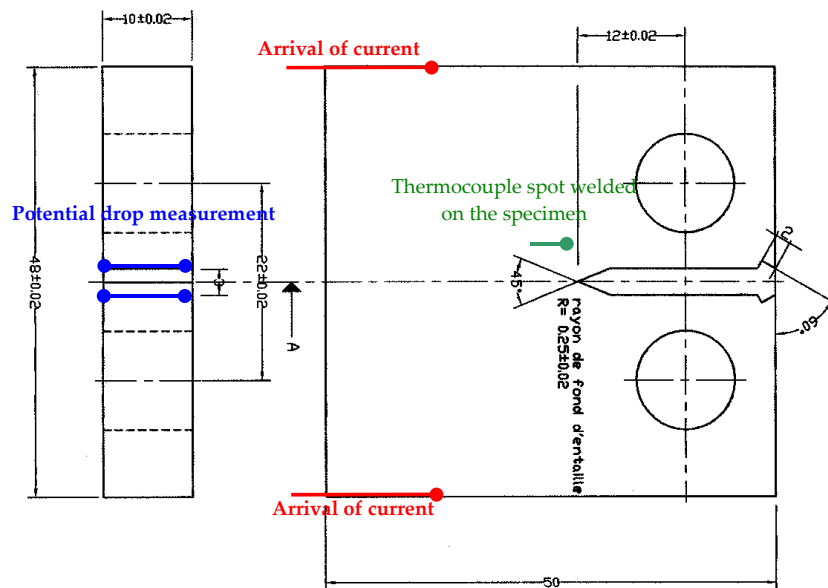


Figure B.C.7. Position of arrivals of current, points of potential measurements and thermocouple

The same test facility was used to perform creep tests on CT specimens. Those tests were however not performed under vacuum as this PhD is not concern with studying environmental effects on creep crack initiation and growth.

References

Hourlier F. (1982). Propagation de fissures de fatigue sous sollicitations polymodales. *PhD Thesis – Ecole Nationale Supérieure des Mines de Paris, Paris, France.*

Appendix B.D. Tensile test facility

High temperature (450°C, 550°C and 625°C) tensile tests on ST and GTNT tensile specimens were carried out using a Zwick testing machine. For all tests a loading cell of 1,000 daN was used to follow the evolution of the load applied on the specimen section. All the tests were carried at constant strain rate controlled by the jacks of the mechanical testing machine. A two radiation lamps furnace surrounds the specimen and provides the heating. The heating power of the furnace was 2.4 kW. Temperature was regulated by a thermocouple spot welded onto the specimen surface. The gradient between bottom and top did not exceed 5°.



Figure B.D.1. General view of the Zwick testing machine used to perform tensile tests at high temperature

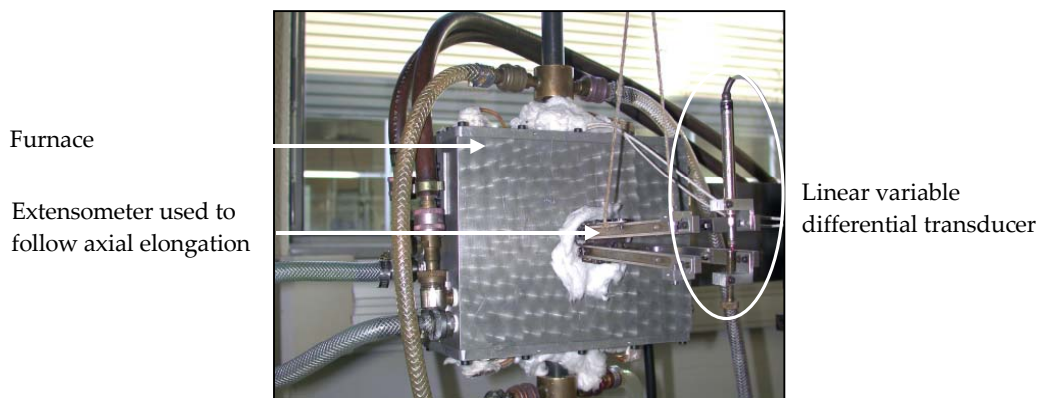


Figure B.D.2. Closer view: The furnace and the extensometer

Load, the displacement of the jack and the elongation of the specimen measured by the linear variable differential transducer were monitored and continuously recorded during the tensile tests.

Appendix B.E. Torsion test facility

Torsion tests at high temperature were carried out on tubular (TC) specimens containing a defect (Geometry of the specimens is given **figure B.F.1**).

Several characteristics of the torsion test facility can be given:

1. Specimen heating is assured by a radiation lamps furnace of 4.8 kW in total power which is regulated by a thermocouple spot welded onto the specimen surface near the crack.
2. Load is applied using dead weights through a pulley.
3. Angular displacement is measured with a displacement transducer.
4. A strain gauge was fixed on the grip to measure the applied torque.
5. The electrical drop technique was used to detect crack initiation and follow crack propagation. The potential measurements were made in the centre of the tube, on each side of the notch between two point distant from 1 mm.

Angular displacement, temperature, loading and potential drop were continuously recorded during tests.

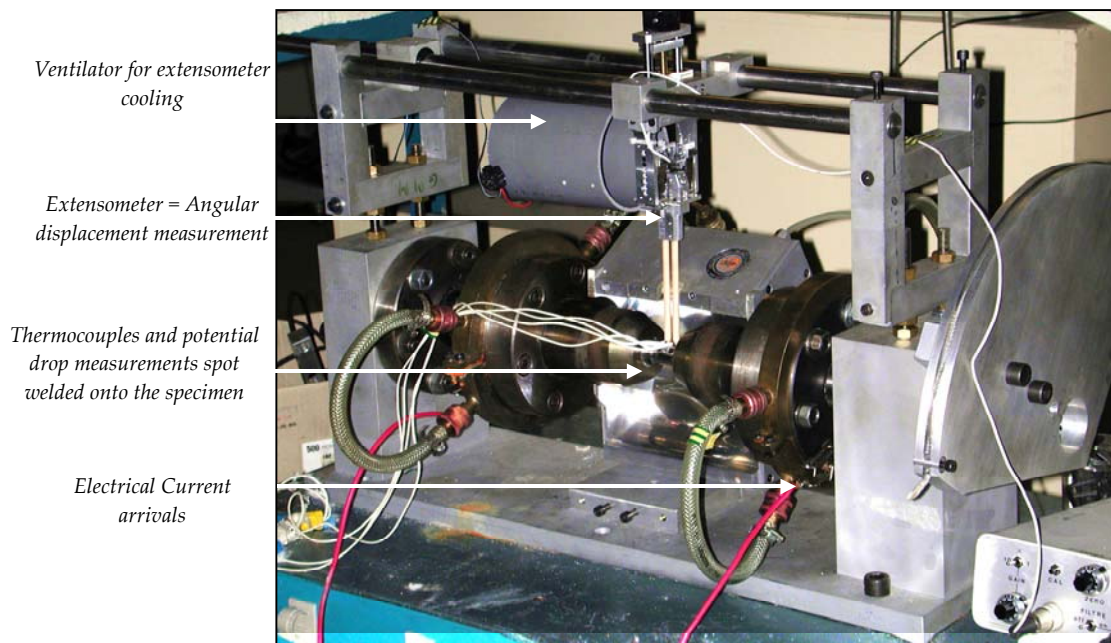


Figure B.E.1. Torsion test facility

Unfortunately, no calibration curve is available for this specimen geometry. Consequently, potential drop measurements could not be used to calculate the evolution of the crack propagation in mmh^{-1} . However:

1. Time to crack initiation may be considered to be the time when the potential drop starts to change significantly.
2. Steady state crack propagation rate may be determined from two type of measurements: the measurement of the final crack length and the evaluation of the duration of the steady state crack propagation from potential drop measurements.

Appendix B.F. Gleeble 1500 facility

Gleeble 1500 test facility is currently use to reproduce welding thermal cycles as heating rate can be very fast. The principle is very simple. A Gleeble 1500 thermal-mechanical machine which is capable of heating specimens by direct resistance heating. This employs a low voltage 50Hz AC current which is passed directly through the specimen by the Joule effect, so that the resistance of the specimen itself generates the heat. By the way, Gleeble 1500 simulator is able to heat specimens at very high strain rates corresponding to those encountered in welding. Temperature is controlled by a thermocouple spot welded onto the specimen surface. A closed loop feedback signal enables precise control of the heat input based on the temperature measured at any instant.

Moreover the Gleeble 1500 simulator used for this study has been adapted to measure dilatation of specimens during heat cycles. A linear differential variable transducer, presented in figure B.F.3, has been added to measure specimen diametral dilatation. To ensure validity of measurements, main parts of oxidation phenomena are avoided as tests are done under vacuum of 10^{-2} Torr. The great interest of such a system is the ability to follow phase transformations in out of equilibrium conditions.

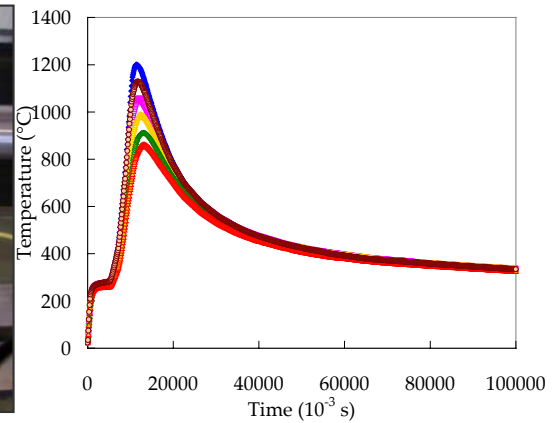
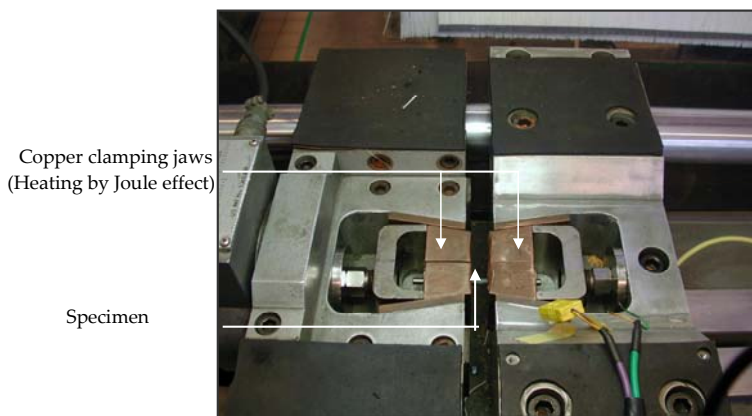


Figure B.F.1. The Gleeble 1500 simulator

Figure B.F.2. Examples of simulated weld thermal cycles

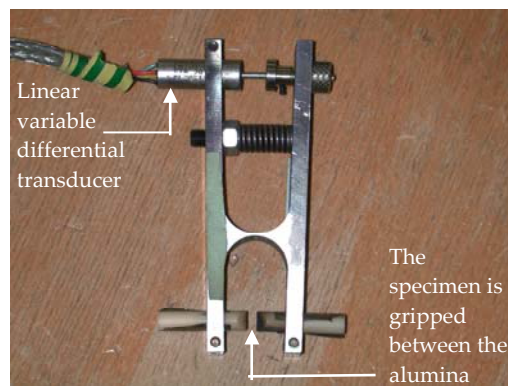


Figure B.F.3. Close view of the displacement transducer

Appendix B.G. Quantification of damage

Specimens preparation

1. Creep specimens were cut according to the longitudinal direction in the maximum section.
2. They were polished from mechanical grinding to OPS polishing.
3. Attention was specially focused on specimens cleaning to release impurities from cavities.

Observations

Observations were made using a LEO 1450VP scanning electron microscope with programming the displacement of the turntable. A particular care was taken to ensure a good image quality and a good accordance in terms of histogram of grey scales between the images.

Damage quantification using image analysis

Image analysis was performed using the image processing toolbox of Matlab®. The first step of the treatment consists in a threshold of the initial image which is converted into binary image. Note that for the automation of the process, a great attention must be taken to keep a quasi similar grey scales histogram from one image to another. During the second step of the image analysis process, three operations are performed:

1. The cavities are filled by successive erosion and dilatation operations.
2. The cavities which touch the edges of the image are eliminated.
3. The cavities which do not exceed a minimum size (100 pixels²) are also eliminated.

The image of **figure B.G.1c** is finally used to determine the characteristics of the cavities i.e. the surface of the cavity, major axis of the circumscribed ellipse, the orientation of the cavity with respect to the loading axis.

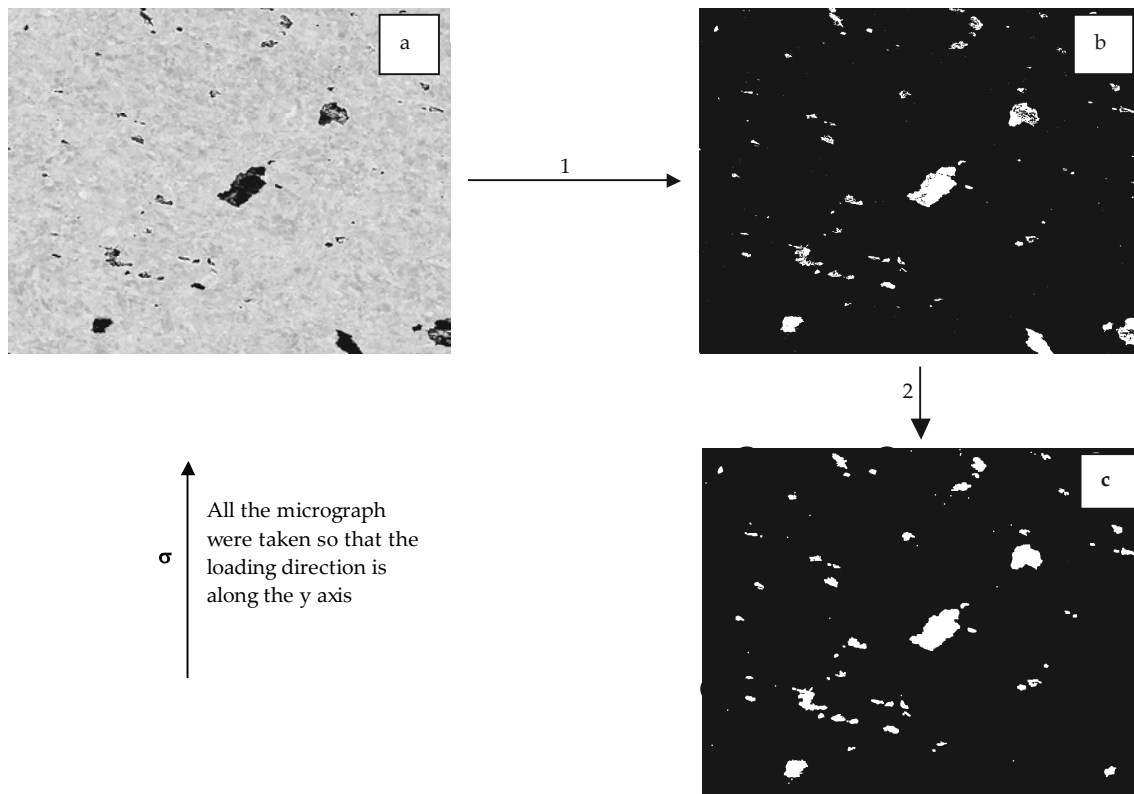


Figure B.G.1. Treatment of images for analysis of the cavity population

Histograms of cavity orientation with respect to the loading axis could for example be plotted for NC1.2 specimens in **figure B.G.2** where it is shown that there is no preferential cavity orientation.

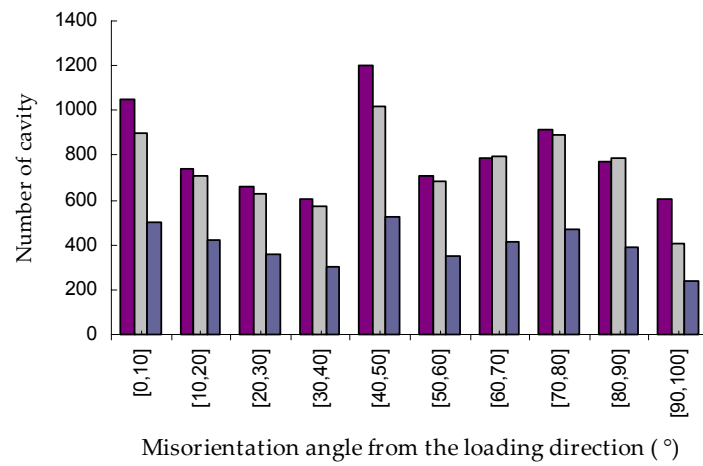


Figure B.G.2. Example of histogram of cavity orientation with respect to the loading axis (NC1.2 specimens)

As underlined in **chapter B.II**, the relevant cavity parameter to compare experiments to the results of the model was the surface of the circle which surrounds the cavity. The image analysis allowed to determine the length of the major axis of the circumscribed ellipse, b . This length was used to determine the effective cavity surface as:

$$S = \pi \left(\frac{b}{2} \right)^2 \quad (\text{eq. B.G.1})$$

Appendix B.H. Procedure of carbon extraction replicas for stainless chromium martensitic steels and transmission electron microscopy facility

Extraction on carbon extraction replicas was performed so as to determine the size and the chemical composition of precipitates in stress and stress free ageing conditions.

The procedure is divided into four steps:

1. Specimen polishing: mechanical and with diamond paste up to 1 μm .
2. Villela etching (100 ml methanol, 5 ml hydrochloric acid and 1g picric acid).
3. Carbon deposition under vacuum.
4. Extraction in Villela and cleaning in methanol before deposition on 3 mm diameter copper grids.

Then, carbon extraction replicas were observed with a field emission gun scanning electron microscope of type Gemini. Example of SEM observation of carbon extraction replica is given in **figure B.I.1**.

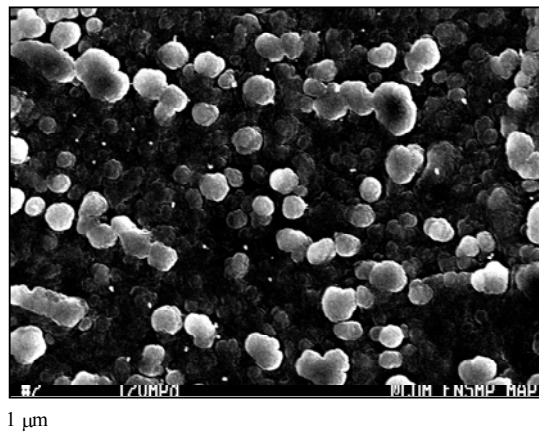


Figure B.H.1. Observation of particles on carbon extraction replicas

Image analysis could then be done using the Scion® public domain image analysis software so as to determine particle sizes. To do so, the particles were first traced from the SEM image and then scanned. Image analysis was performed on the resulting image (see **figure B.H.2b**).

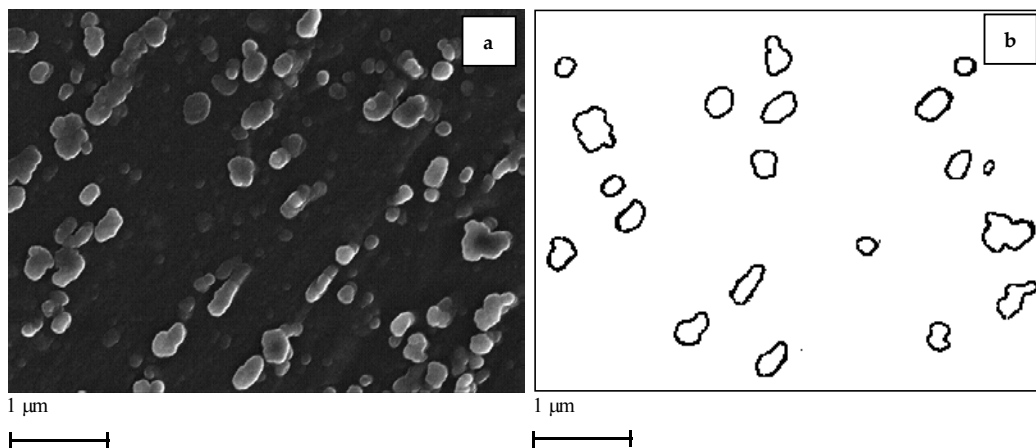


Figure B.H.2. Image analysis procedure to determine the size of second phase particles

Image analysis of **figure B.H.2b** allowed to determine the surface of each cavity so that the diameter of the equivalent sphere in surface could be determined as $d_{\text{eq}} = 2\sqrt{\frac{S}{\pi}}$. Histograms of particles diameter could then be plotted as shown in **figure B.H.3**.

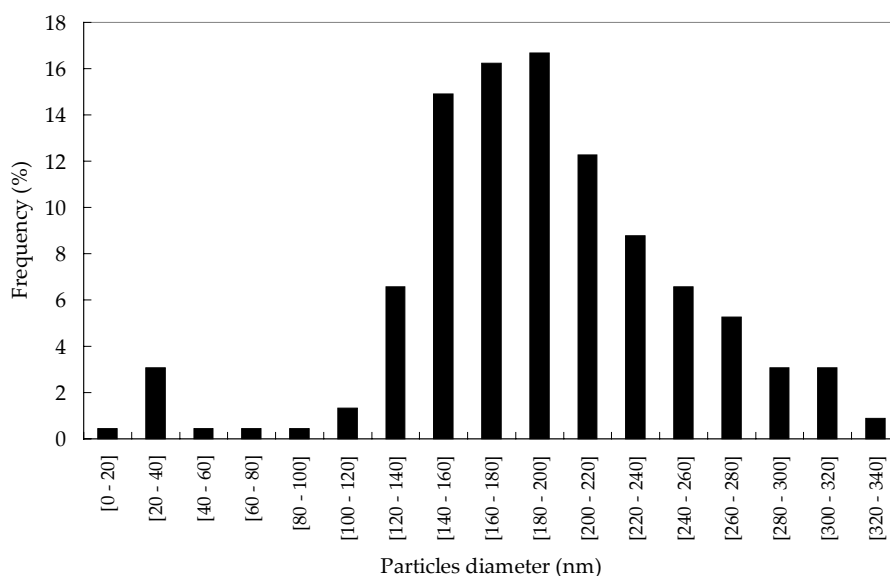


Figure B.H.3. Example of an histogram of particle size

X-Ray energy dispersive spectroscopy analysis was also performed in the FEG-SEM Gemini DSM 982. The measured chemical compositions are only half-quantitative using this system but give valuable information for identification of particle type and changes in their chemical composition during ageing.

TEM investigations: sample preparation and transmission electron microscope

Cylinder of 3 mm were machined using an electrical discharge machining (EDM). Then, the first step of the preparation consists in preparing blades by mechanical polishing until they are 100 μm in maximum thickness. The thinning of the foils was then done using a reagent containing:

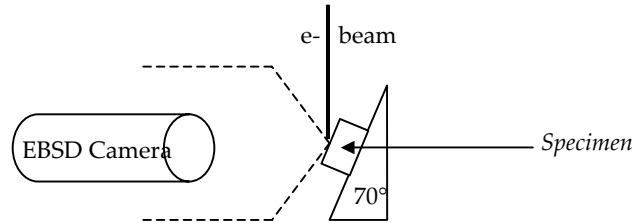
1. 45 % butoxyethanol
2. 45% acetic acid
3. 10% perchloric acid

Thinning conditions were: 40 V and 0°C. The transmission electron microscope of the present study (CEA Grenoble) was of type JEOL2000FX with an acceleration voltage of 200kV. It was also equipped with a scanning facility and an EDS detector for X-ray analysis.

Appendix B.I. Electron backscattering diffraction

Principle

The electron beam of a scanning electron microscope (SEM) is used to strike a crystalline material mounted at an incline around 70°. In such a case, the electron beam is diffracted at the specimen surface depending on the local crystal orientation. Electron backscatter patterns are imaged by a phosphor screen that is set near the specimen.



Use

Figure B.I.1. Position of the specimen in the FEG-SEM for EBSD analysis

An example of a backscatter pattern is shown **figure B.I.2**. The bands in the pattern are the Kikuchi lines and are directly related to the crystal lattice structure. First step of the process is to identify properly each band of the pattern. To do so, crystal structure of the material must be previously determined: in the case of the present study, body centred cubic. Indeed, due to the low carbon content 0.1 wt%, in the martensite matrix, the martensite tetragonality:

$$\frac{c}{a} = 1.000 + 0.045[C]_{ss} = 1.0045$$

where c and a are the lattice parameters, so that the diffraction patterns could be indexed with the reference patterns of a body centred cubic crystal.

The TSLOIM® software is able to index pattern by comparison with reference tables at each step of the specimen scanning process. Each pattern is described in a three dimensional space by three Euler angles: $\varphi_1, \phi, \varphi_2$ (**see figure B.I.3**).

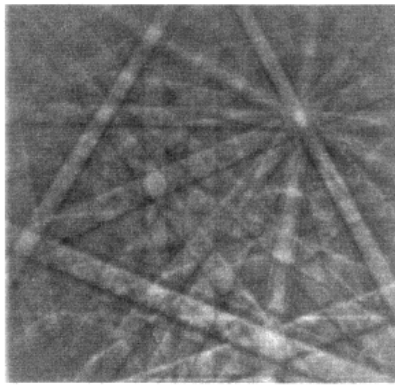


Figure B.I.2. Kikuchi pattern

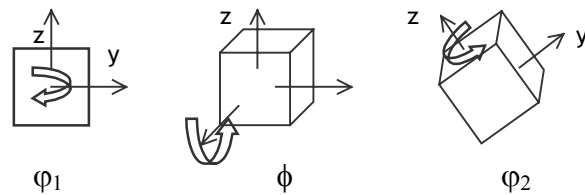


Figure B.I.3. Euler angles

Several opportunities are given for using EBSD data: phase identification, visualisation of microstructure, texture determination etc ...

(Further information concerning EBSD abilities are given at <http://www.edax.com/technology/EBSD/index.html>).

In the present study, the EBSD was used for two aims:

1. To characterise the microstructure and more especially to determine the nature of grain boundaries (high or low misorientation) which is particularly interesting in microstructures such complex as that of 9Cr1Mo-NbV steels.
2. To determine the position of nucleation sites with respect to the microstructure.

Appendix C
Experiments on tubular creep specimens

During the PhD several torsion creep tests on tubular creep specimens, made of both base metal and weldment, were carried out. The results of these tests are given in the present appendix as many difficulties to model their creep flow and damage behaviour were encountered. The measured steady state creep strain rates were especially very larger than these predicted by the model. Two main reasons can be given to explain the bad accordance between experiments and modelling:

1. An experimental problem (temperature control ...).
2. The anisotropy of the material creep properties even if no anisotropy of tensile properties was evidenced (see **chapter A.I**).

A. Creep torsion tests on base metal tubular creep specimens

1. Experiments and results

Torsion creep tests on tubular (TC) specimens were performed at 625°C with adding a crossing defect of 8 mm in length and 0.2 mm in width. For these tests, load was applied using dead weights through a pulley at one side of the thin tubular specimen whereas the other side was locked. The angular displacement was continuously recorded using an angular displacement transducer. Temperature was monitored using one thermocouple spot welded onto the specimen surface near the defect. The temperature gradient between right and left did not exceed 3°C. The tests were carried out in controlled laboratory atmosphere i.e. 20°C ± 2°C and 50% relative humidity). The experimental facility is described in **appendix B.E**.

For tests on TC specimens made of base metal, the values of the couples were C = 50 Nm and C = 35 Nm and the corresponding shear stresses, τ , could be determined as:

$$\tau = \frac{2C}{\pi(R_{ext}^2 - R_{int}^2)(R_{ext} + R_{int})} = 1.31C \quad (\text{eq. C.A.1})$$

where R_{ext} and R_{int} are respectively the inner and outer radii in m, C is the couple in Nm and τ is calculated in MPa. It follows that the two values of shear stresses are respectively $\tau = 65.5$ MPa and 46 MPa and the experimentally measured corresponding times to failure were 130 hours and 3,055 hours. In addition, both the creep time to crack initiation and the steady state crack propagation, could be identified using the electrical potential drop technique. The creep curves i.e. angular displacement versus creep time, are plotted in **figure C.A.1**.

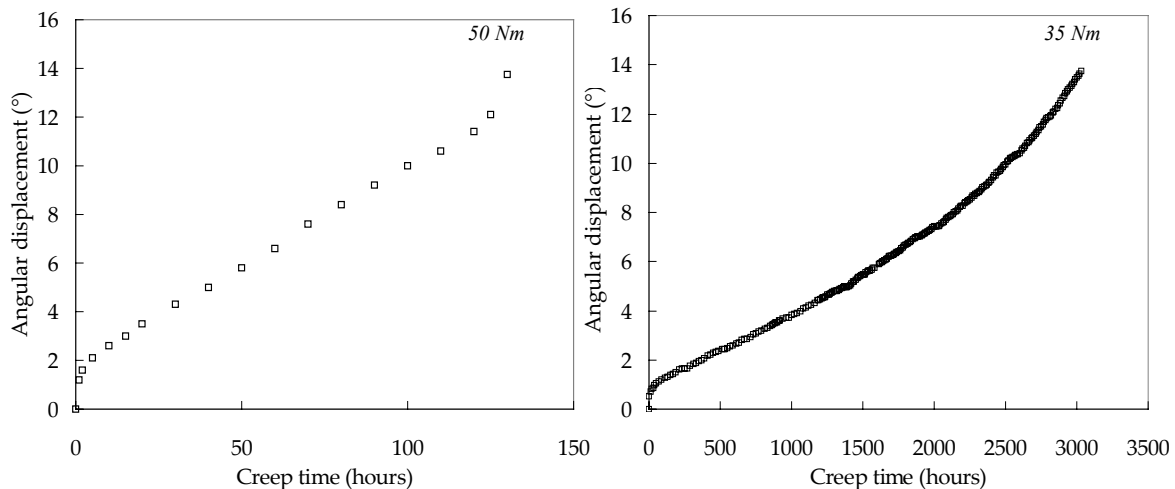


Figure C.A.1. Experimental results of torsion tests on base metal TC specimen at 625°C

2. Interpretation of torsion tests experimental results

Torsion tests on TC specimens are said to be in mode II because principal stress is maximum at the tip of the defect with a misorientation of 45° from its axis and the equivalent viscoplastic strain is maximum straight ahead the defect following its axis. Therefore, creep tests on tubular creep specimens are very useful to determine the driving force for cavity nucleation. SEM investigations were performed on TC specimens after creep exposure. Deviation from the initial crack axis was investigated for short and long term creep tests. For short term creep torsion test, the direction of the

crack propagation is deviated from the initial crack axis from near 30°. It was also evidenced that the strain level is very high at the end of the torsion test. Photographs of the two specimens at the end of the test are given in **figure C.A.2**.

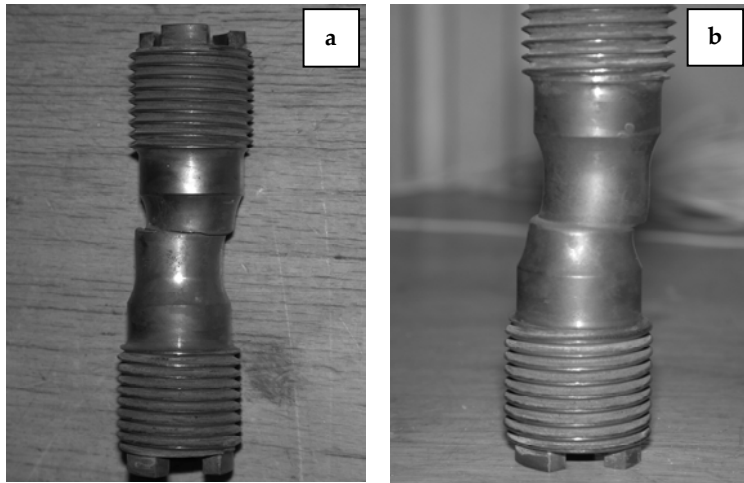


Figure C.A.2. Shape of the TC specimens at the end of the test (a) $\tau = 65$ MPa (b) $\tau = 46$ MPa

For long term creep torsion test, as shown in **figure CA.3**, the crack initiated at the right side of the crack tip but, then its propagation followed the initial crack axis.

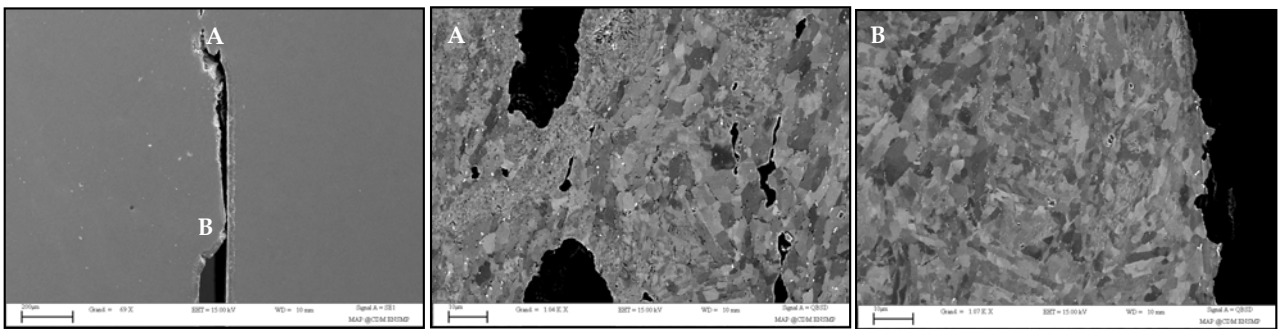


Figure C.A.3. SEM Investigations of crack propagation in TC specimen ($\tau = 46$ MPa) – SEM(BSE) observations after colloidal silica polishing.

3. FE calculations for torsion tests on TC specimens

The mesh, loading and limits conditions are given in **figure C.A.4** with a closer view of the mesh near the defect (see **figure C.A.4b**). For the sake of simplicity, as Poquillon (1997) and Chabaud Reytier (1999), FE calculations were performed on a 3D meshed sheet form which corresponded to the unrolled tube. It was necessary to add conditions of alignment as shown in **figure C.A.4a**. The load was applied as a shear stresses τ given by **equation C.A.1**. 3D FE calculations were performed on a sheet without any defect and compared with a 3D FE calculations on a tube. These calculations ensured that the simplified representation of a sheet well represents the torsion creep response of the tube.

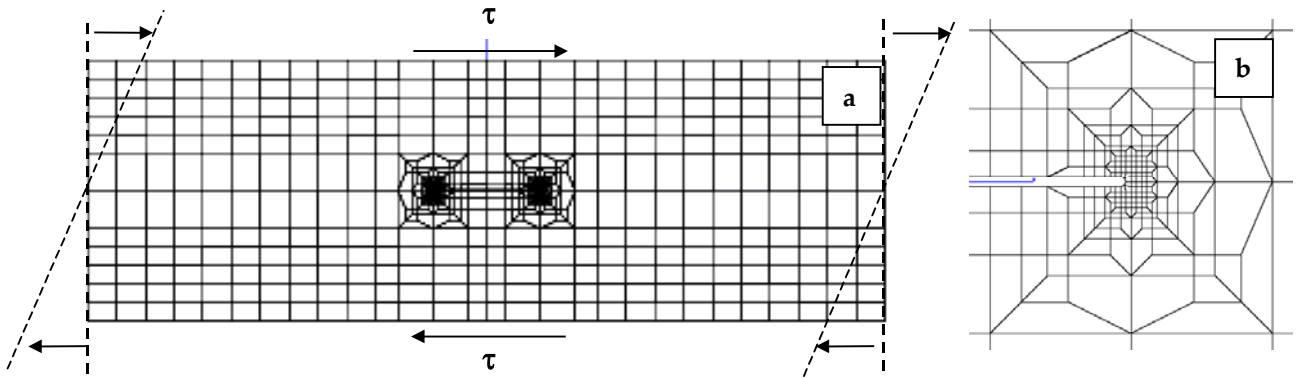


Figure C.A.4. Mesh, load and limit conditions

To start, the mechanical fields were determined from the FE calculations. The stress and the strain fields near the defect are plotted in **figure C.A.5**. It shows that the loading conditions at the crack tip are of mode II: the strain is maximum in the direction of the axis of the defect (see **figure C.A.5**) whereas the maximum stress is maximum at 45° from the axis of the defect (see **figure C.A.5**).

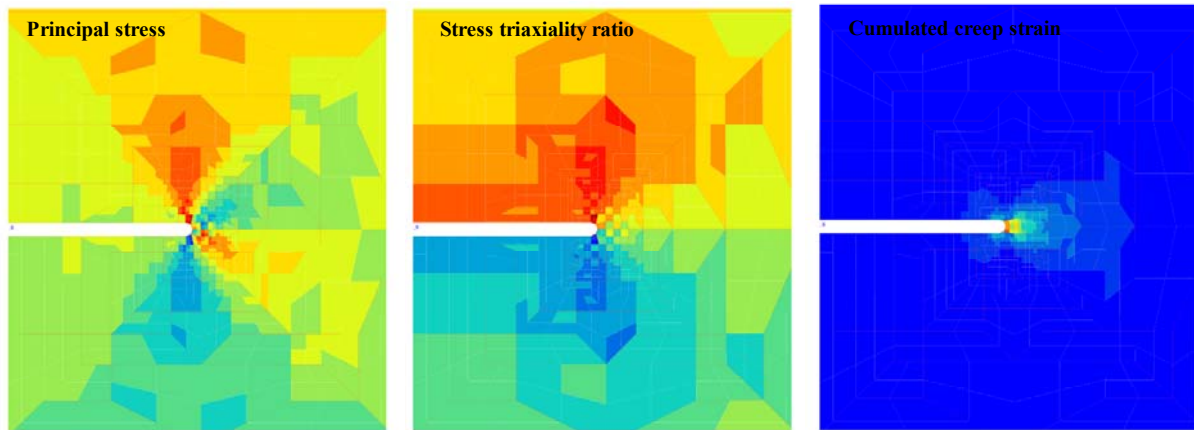


Figure C.A.5. Mechanical fields near the crack for TC specimens

Note that a useful formulation of the von Mises equivalent stress was proposed by Huddleston (1981) as:

$$\sigma_{eq} = \sqrt{3} \frac{\sigma_{sh}}{\exp(b)} \quad (\text{eq.C.A.2})$$

where σ_{sh} is the shear stress and b was evaluated to 0.16 by Huddleston (1981). It was verified that the von Mises equivalent stresses calculated with **equation C.A.2** are in very good agreement with these given by FE calculations.

B. Creep torsion tests on weldment tubular creep specimens

1. Experiments and results

The experimental facility and procedure is the same than that described for torsion creep test on the base metal. It is just necessary to precise that the defect was set in the heat affected zone near the base metal (i.e. in the intercritical heat affected zone). For tests on TC specimens, the values of couples were from 50 Nm, 35 Nm and 20 Nm and the corresponding shear stresses, τ , were respectively $\tau = 65.5$ MPa, 46 MPa and 26 MPa. The experimental curves are shown in **figure C.B.1**. Note that the torsion creep test corresponding to $C = 20$ Nm was interrupted.

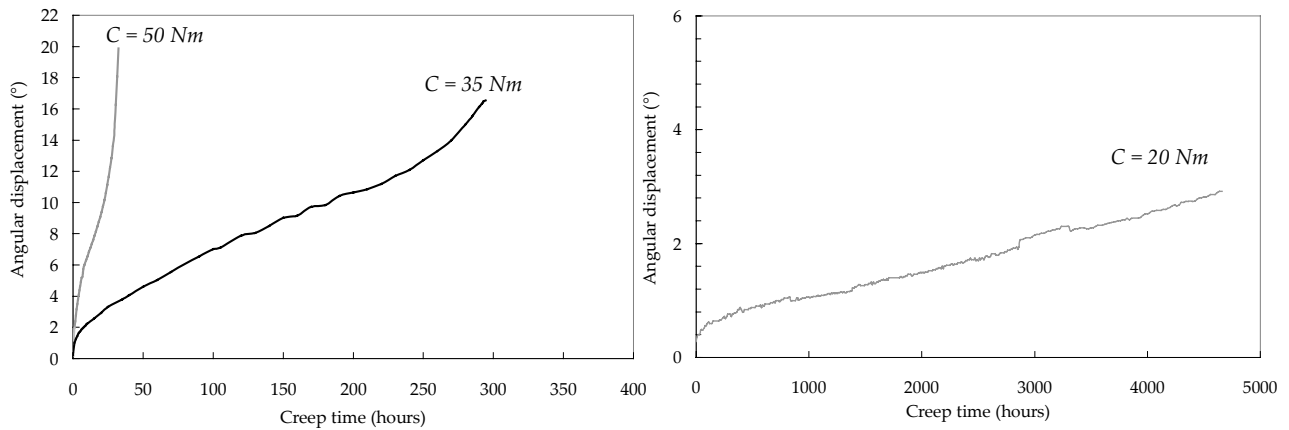


Figure C.B.1. Experimental results of torsion tests on weldment TC specimen at 625°C

2. Interpretation of torsion tests experimental results

For the three creep tests, it was observed that the crack propagation proceeds in the direction of the axis of the defect. There is however a competition between the influence of the cumulated creep strain and the principal stress. A crack initiated at the tip of the defect and which propagates in a direction misoriented by 30° from the axis of the defect, was also evidenced in **figure C.B.2b**.

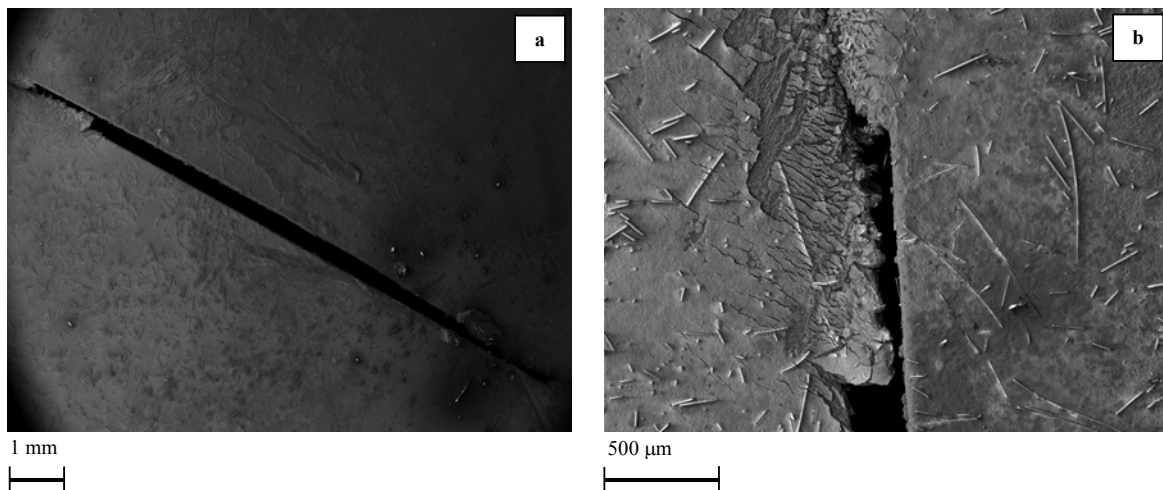


Figure C.B.2. Crack propagation behaviour at 625°C (C = 35 Nm)

The electrical potential drop technique also allows to follow the evolution of the crack. As no detailed calibration curve is available, only a qualitative comparison can be proposed from results given in **figure C.B.3**. It is shown that the crack initiation occurs very soon in the creep lifetime. This observed tendency is largely different from that observed for NC0.25 specimens for which the time to the crack initiation was the longest stage.

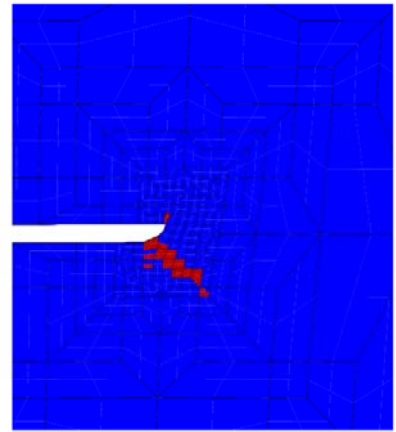
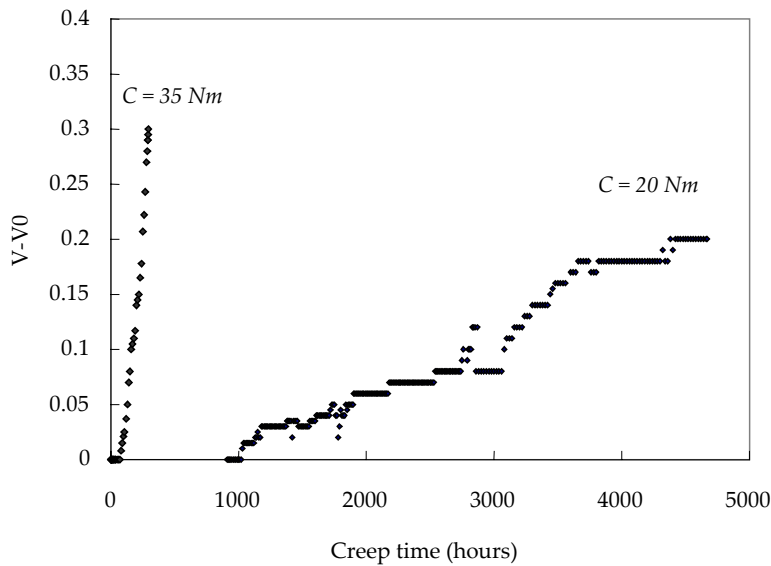


Figure C.B.3. Crack propagation followed by the electrical potential drop technique Figure C.B.4. Finite element modelling simulation of crack initiation

It is shown in **figure C.B.4** that the model predicts the initiation and growth of the creep crack at 45° from the axis of the defect.

3. Summary of creep tests on tubular creep specimens

The results of torsion creep tests on tubular creep specimens for both the base metal and the weldment are plotted in **figure C.B.4**. They are plotted as the shear stress versus the creep time to failure. The creep fracture property mismatch between the base metal and the weldment is the same than that evidenced by creep tests on axisymmetric smooth creep specimens.

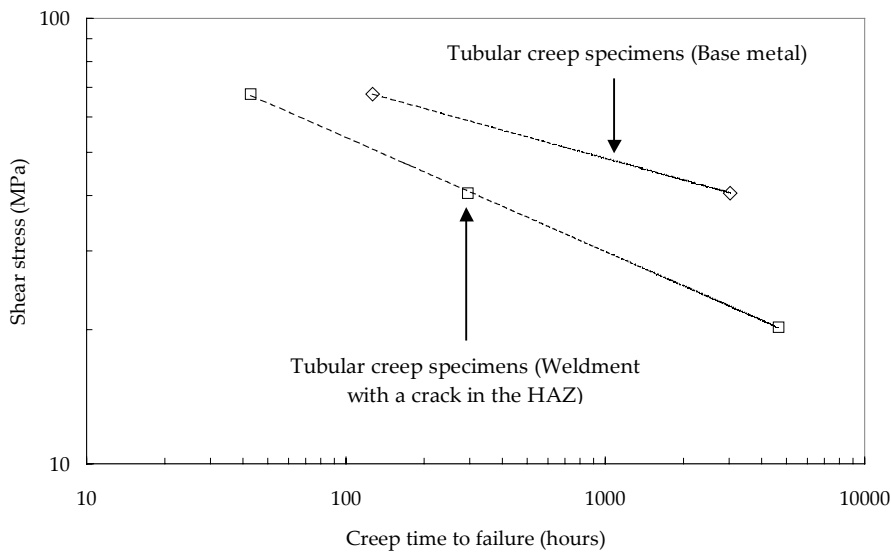


Figure C.B.5. Creep fracture properties mismatch (Torsion creep)

C. Conclusions

The model failed at predicting both the experimentally measured creep strain rates and the experimentally observed direction of crack propagation. In fact, the bad prediction of the direction of the crack propagation probably results from the too low calculated steady state creep strain rate. Another point which requires further investigations is that, contrary to NC0.25 specimens, the creep crack initiation stage is quite short.

References

- Chabaud-Reytier M. (1999). Etude de la fissuration différée par relaxation d'un acier inoxydable austénitique stabilisé au titane. *PhD Thesis – Ecole Nationale Supérieure des Mines de Paris, Paris, France (in French)*.
- Huddleston R.L. (1981). An improved multiaxial creep rupture strength criterion. *ASME International journal of pressure vessels and piping*. **107**. 421-429. *PhD Thesis – Ecole Nationale Supérieure des Mines de Paris, Paris, France (in French)*.
- Poquillon D. (1997). Approche locale/ fissuration à haute température dans un acier inoxydable sous chargements thermomécaniques. Simulations numériques et validations expérimentales.
- Poquillon D., Cabrillat M.T., Pineau A. (1999). Mode II creep crack initiation in 316LN stainless steel: experiments and modelling. *Materials at high temperatures*. **16(2)**. 99-107.

Abstract

Chromium martensitic stainless steels are under development since the 70's with the prospect of using them as structural components in thermal and nuclear power plants. The modified 9Cr1Mo-NbV steel is already used, especially in England and Japan, as a material for structural components in thermal power plants where welding is a commonly used joining technique. New generations of chromium martensitic stainless steels with improved mechanical properties for high pressure and temperature use are currently under development. However, observations of several in-service premature failures of welded components in 9Cr1Mo-NbV steel, outline a strong need for understanding the high temperature creep flow and damage behaviour of 9Cr1Mo-NbV steels and weldments.

The present study aimed at experimentally determining and then modelling the high temperature creep flow and damage behaviour of both 9Cr1Mo-NbV steels and weldments (typically in the temperature range from 450°C to 650°C).

The base metal was first studied as the reference material. It was especially evidenced that tempered chromium martensitic steels exhibit a change in both creep flow and damage behaviour for long term creep exposure. As a consequence, the classically performed extrapolation of 1,000 hours creep data to 100,000 hours creep lifetime predictions might be very hazardous. Based on experimental observations, a new model, integrating and coupling multiple creep flow and damage mechanisms, was developed in the framework of the mechanics of porous media. It was then successfully used to represent creep flow and damage behaviour of the base metal from high to low stress levels even for complex multiaxial loading conditions.

Although the high temperature creep properties of the base metal are quite good, the occurrence of premature failure in weldments in high temperature creep conditions largely focused the attention of the scientific community. The lower creep strength of the weld component was also experimentally confirmed in the present study. The evaluation of creep flow and damage behaviour of the weldment requires two types of investigations, namely, the determination of the effect of welding on creep strength of the material especially in the heat affected zone (HAZ), and the investigation of the effect of the mismatch in creep properties between the weld metal, the base metal and the HAZ.

To do so, the microstructure of the weakest HAZ was first reproduced on bulk specimens. These specimens were used to experimentally investigate the creep flow and damage behaviour of the weakest HAZ microstructure. The results of experiments allowed to fit a creep model for the simulated HAZ derived from the one designed for the base metal.

The integration of constitutive equations of base metal, weld metal and simulated HAZ in finite element calculations of the heterogeneous weldment allows to study the effect of mismatch on creep properties and finally to predict creep lifetime of 9Cr1Mo-NbV welded components.

Résumé

Les aciers inoxydables martensitiques au chrome sont développés depuis les années 70 avec pour objectif aujourd'hui de les utiliser comme matériau de structure dans les centrales thermiques (Circuits de refroidissement, turbine) et nucléaires (Cuve du réacteur...). L'acier de l'étude i.e. l'acier 9Cr1Mo-NbV est déjà utilisé dans des centrales thermiques principalement en Angleterre et au Japon. Compte tenu de l'importance des composants, l'assemblage par soudage est une technique largement utilisée. Un intérêt tout particulier est porté dans cette étude à l'évaluation de la durée de vie des composants soudés en acier 9Cr1Mo-NbV après la constatation de plusieurs ruptures en service prématurées au niveau des soudures.

L'étude réalisée avait donc pour objectif d'identifier expérimentalement et de modéliser le comportement, l'endommagement et la rupture en fluage haute température (typiquement dans le domaine de température 450°C - 650°C) de composants soudés en acier 9Cr1Mo-NbV.

Pour cette étude, le métal de base a d'abord été étudié comme matériau de référence. Il est notamment démontré que les résultats expérimentaux à 1000 heures ne peuvent pas être utilisés, comme il est usuel de le faire, pour prédire la durée de vie en fluage à 100000 heures. La raison de cette impossibilité est l'existence d'un changement de mécanisme de comportement et d'endommagement aux temps longs. Pour représenter ce changement de mécanisme, un modèle de fluage couplant comportement et endommagement et intégrant plusieurs mécanismes de déformation a été développé suivant les développements de la mécanique des milieux poreux initiés par Gurson. Le modèle a été identifié sur la base de résultats expérimentaux sur diverses géométries d'éprouvettes permettant notamment de prendre en compte les effets de la triaxialité sur le développement de l'endommagement. L'étude a par ailleurs mis en évidence une bonne capacité du modèle à prédire les lieux de rupture ainsi que l'amorçage et la propagation stable de fissure.

L'attention a ensuite été portée à la tenue en fluage des composants soudés qui présentent une résistance au fluage très inférieure à celle du métal de base due à la faiblesse de la zone affectée thermiquement (ZAT). Pour ce faire, deux niveaux d'investigation ont du être explorés. D'une part, le soudage induit des modifications métallurgiques et donc des modifications locales des propriétés mécaniques du métal de base : c'est un effet matériau. D'autre part, les différences de propriétés mécaniques rendent complexes l'état de chargement de l'assemblage soudé : c'est un effet de structure.

L'effet matériau a été étudié en identifiant la ZAT faible des composants soudés, en la reproduisant sur échantillons massifs, puis en testant des éprouvettes de fluage usinées dans ces mêmes échantillons massifs. Il a été ainsi possible d'utiliser le modèle multi-mécanismes développé pour l'étude sur métal de base afin de modéliser le comportement et l'endommagement de fluage haute température de la ZAT faible dans toute la gamme de contrainte.

Finalement, des calculs éléments finis multi-matériaux ont été réalisés en considérant le composant soudé comme l'assemblage de trois microstructures : le métal d'apport, le métal de base et la ZAT faible dont les équations constitutives respectives ont été intégrées aux calculs. Il a ainsi été possible d'identifier les effets de type structure mais surtout de prédire la durée de vie des composants soudés en acier 9Cr1Mo-NbV y compris pour des composants industriels.